KfK 5271
Dezember 1993

IEA Implementing Agreement for a Programme of Research and Development on Fusion Materials

Workshop on Beryllium for Fusion Applications

Karlsruhe, Germany, 4-5 October 1993

M. Dalle Donne
Institut für Neutronenphysik und Reaktortechnik
Projekt Kernfusion
Association KfK-EURATOM

Kernforschungszentrum Karlsruhe

KERNFORSCHUNGSZENTRUM KARLSRUHE

Institut für Neutronenphysik und Reaktortechnik
Projekt Kernfusion
Association KfK-EURATOM

KfK 5271

IEA Implementing Agreement for a Programme of Research and Development on Fusion Materials

Workshop on Beryllium for Fusion Applications

Karlsruhe, Germany, 4 - 5 October 1993

Editor: M. Dalle Donne

Kernforschungszentrum Karlsruhe GmbH, Karlsruhe

Kernforschungszentrum Karlsruhe GmbH
Postfach 3640, 76021 Karlsruhe

ISSN 0303-4003

TABLE OF CONTENTS

IEA - Implementing Agreement for a Programme of Research and Development on Fusion Materials

WORKSHOP ON BERYLLIUM FOR FUSION APPLICATIONS - Karlsruhe 4 - 5 October 1993

Executive Summary

As shown by recent developments beryllium has become one of the most important materials in the development of fusion reactors. It is practically the only neutron multiplier available for blankets with ceramic breeder materials and can be used with liquid metal breeders as well. It is one of the most likely materials to be used on the surface of the first walls and of the divertor.

The neutron irradiation behavior of beryllium in a fusion reactor is not well know. Beryllium was extensively irradiated about 25 -40 years ago and has been used since then in material testing reactors as reflector. In the meantime, however, beryllium has been improved quite considerably. Today it is possible to obtain commercially beryllium which is much more isotropic and contains smaller amounts of oxide. There are already indications that these new kinds of beryllium behave better under irradiation.

Due to the importance of beryllium for the fusion reactors a considerable amount of work on this material has been initiated in the recent years in Europe, Japan, the United States and Russia. So far this work is not well coordinated. A more effective exchange of information and of comparison and discussion of results is clearly required. It has therefore been decided to held a two days Workshop in Karlsruhe on this matter.

The Workshop was attended by 52 people from various countries (Belgium, Canada, China, France, Germany, Italy, Japan, Sweden, U.S.A.) and international organizations (EC, ITER, JET, NET). Twenty papers were presented. A considerable amount of time during the meeting was taken up by discussions.

The main themes of the workshop are summarized below.

1. Beryllium manufacturing

It was recognized that the understanding of the manufacturing capabilities, functional integrity of various forms (pebbles, low density blocks) and impurity control is important and needs more work. Manufacturing Sciences Corporation

(MSC) makes melted ingot beryllium with very low oxygen content. Pebbles produced by the rotating electrode process have a smoother surface, a more regular spherical form and less oxygen content than those obtained by product screening from the Be-MgF_2 process, but they are more expensive.

2. Beryllium irradiation behavior

The main neutron-irradiation issues of beryllium are swelling, embrittlement and tritium retention. At the workshop Billone showed swelling data evaluated in terms of helium content. Gelles et al. showed the importance of material condition and oxygen content. Scaffidi-Argentina et al., showed good agreement between measured swelling data and calculations with the code ANFIBE. The major questions remaining are the lack of data from high temperature in-pile irradiations to high neutron fluences and the ability of high porosity to relieve helium gas and thus reduce swelling.

Irradiation induced embrittlement is influenced by the isotropicity and BeO content of the material. New grades of beryllium behave better. A systematic irradiation program has been started in the Mol BR2 reactor.

Evidence points to interaction of tritium with BeO at the grain boundaries and at trapping in helium bubbles. It is not clear if other impurities are trapping the tritium as well. Porous beryllium shows a faster tritium release. Data is required on tritium retention during in-pile high temperature irradiation.

Various beryllium specimens have been irradiated in FFTF and EBRII for doses up to 30 dpa in the temperature range 370 - 550 °C, however no money is available at present for post-irradiation examinations. Japanese irradiations are under way and new data will come soon.

3. Compatibility issues

Compatibility between beryllium and austenitic steel limits the contact temperature to 600 °C. Kawamura et al., showed a considerable improvement by the use of ceramic coating (Cr_2O_3 + SiO_2) which could also reduce the tritium permeation.

4. Safety and waste disposal

Safety concerns are mainly connected to the tritium retention and permeation in beryllium, especially in the case of beryllium as plasma facing material. Beryllium

could react with steam by temperatures ≥ 600 °C. Especially in case of porous beryllium uncontrolled self sustaining reactions could develop. INEL has started experimental investigations on these topics.

MSC recycles radiative beryllium from weapons. A real time beryllium air concentration monitor has been developed in Los Alamos. Beryllium dust, probably related to oxygen, has been observed in JET. There is a need to clarify the waste disposal requirements, especially as regards the hazardous materials classification.

5. Specific issues related to the use of beryllium as a plasma facing component

Los Alamos National Laboratory has obtained relatively high density beryllium (95 %) by plasma spraying on copper surfaces. The oxygen and gas content in plasma sprayed beryllium is low, however its thermal conductivity is only ⅓ of that of fully dense beryllium.

Deuterium ions have been implanted on plasma sprayed beryllium at the Idaho National Engineering Laboratory. The experiments indicate that, due to the porosity of the material, the reemission of deuterium molecules is relatively fast, which means a relatively low tritium permeation to the first wall coolant system and a low deuterium inventory. However porous beryllium is more brittle than fully dense one.

Beryllium bonding by HIP-ing of beryllium disks, 3 to 9 mm thick, to copper and vanadium has been achieved at MSC. Improvements are still required to increase the shear strength of the joint. Bonding of beryllium with CuCrZr by brazing has been achieved by JET.

Tests, performed at the JET Neutral Beam Test Bed, with 2 mm thick castellated beryllium tiles brazed on CuCrZr hypervapotrons, have shown that this arrangement can survive up to 10^3 cycles with a heat flux of 12 MW/m^2 with only minor damage. It is clear that for ITER applications supplementary data is needed such as fatigue-crack propagation and ductility including neutron irradiation effects.

A study of the NET-Team indicates that, for heat fluxes significantly above 1 MW/m^2, beryllium should be used merely as amour bonded to a suitable structural material as heatsink.

M. Dalle Donne

Workshop on Beryllium for Fusion Applications

Karlsruhe, Germany

October 4–5, 1993

ABSTRACT

Optimization of Beryllium for Fusion Blanket Applications

by

M. C. Billone
Fusion Power Program
Argonne National Laboratory
Argonne, IL 60439 USA

The primary function of beryllium in a fusion reactor blanket is neutron multiplication to enhance tritium breeding. However, because heat, tritium and helium will be generated in and/or transported through beryllium and because the beryllium is in contact with other blanket materials, the thermal, mechanical, tritium/helium and compatibility properties of beryllium are important in blanket design. In particular, tritium retention during normal operation and release during overheating events are safety concerns. Accommodating beryllium thermal expansion and helium–induced swelling are important issues in ensuring adequate lifetime of the structural components adjacent to the beryllium. Likewise, chemical/metallurgical interactions between beryllium and structural components need to be considered in lifetime analysis. Under accident conditions the chemical interaction between beryllium and coolant and breeding materials may also become important.

The performance of beryllium in fusion blanket applications depends on fabrication variables (e.g., grain size, porosity, and impurity content) and operational parameters (heat generation rate and temperature profile, tritium generation rate profile, helium generation rate profile, displacement damage rate profile, external stresses, etc.). First the properties database is reviewed to determine our state of knowledge of beryllium performance as a function of these variables. Several design calculations are then performed to indicate ranges of fabrication and operation variables that lead to optimum beryllium performance. Finally, areas for database expansion and improvement are highlighted based on the properties survey and the design sensitivity studies.

INTRODUCTION

- **Applications**

  - ITER/CDA

    Blanket multiplier and thermal barrier:
    68–85% dense sintered blocks (US)
    Pebble bed (JPN)

    Blanket multiplier:
    Dense hollow cylinder (EC)

  - EC/DEMO

    Blanket multiplier:
    Dense plates

  - ITER/EDA

    Plasma facing component (PFC)

- **Performance Parameters**

  - Thermal
  - Tritium
  - Helium
  - Mechanical
  - Compatibility

- **Optimization**

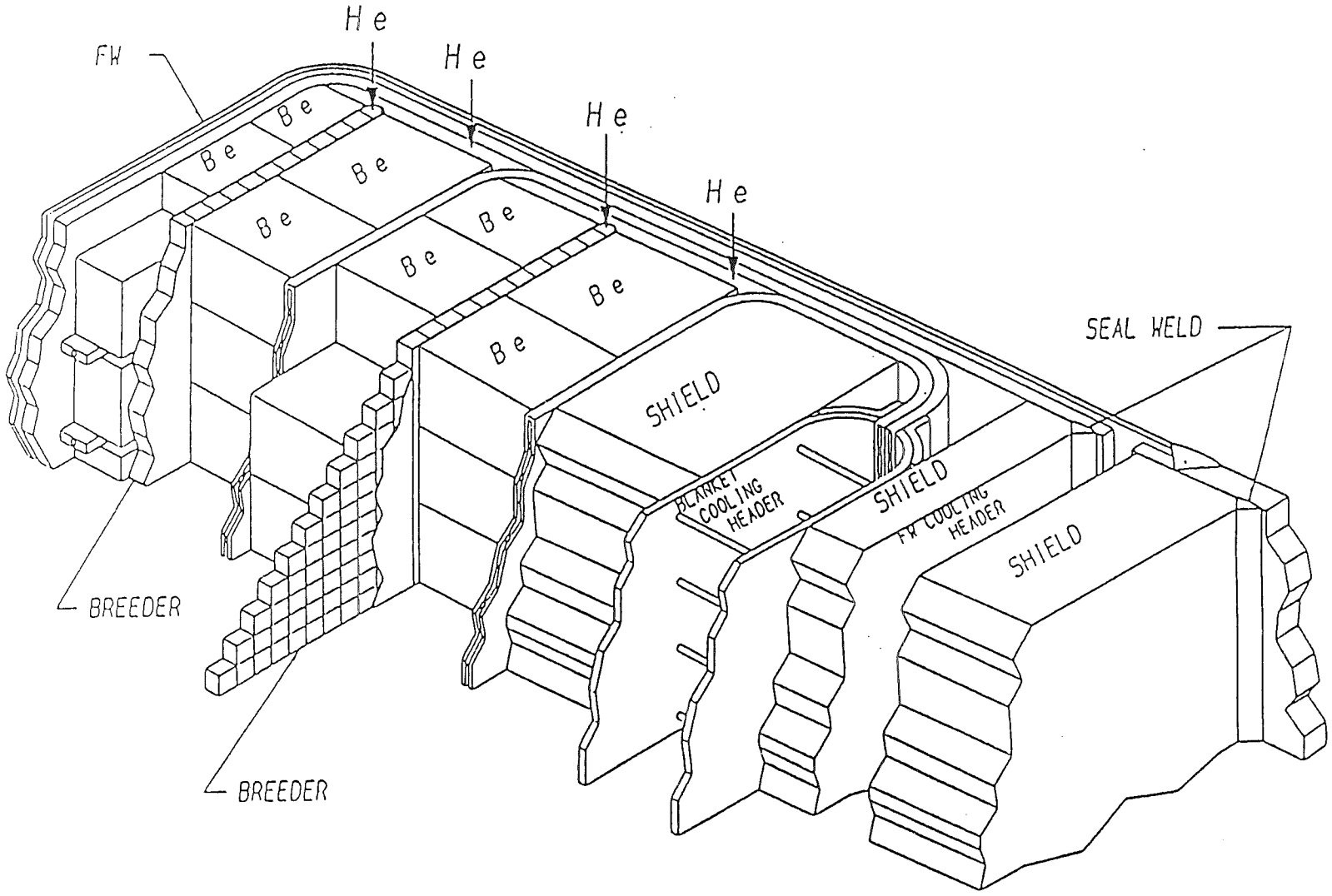

Figure 1. Layered ceramic blanket design.

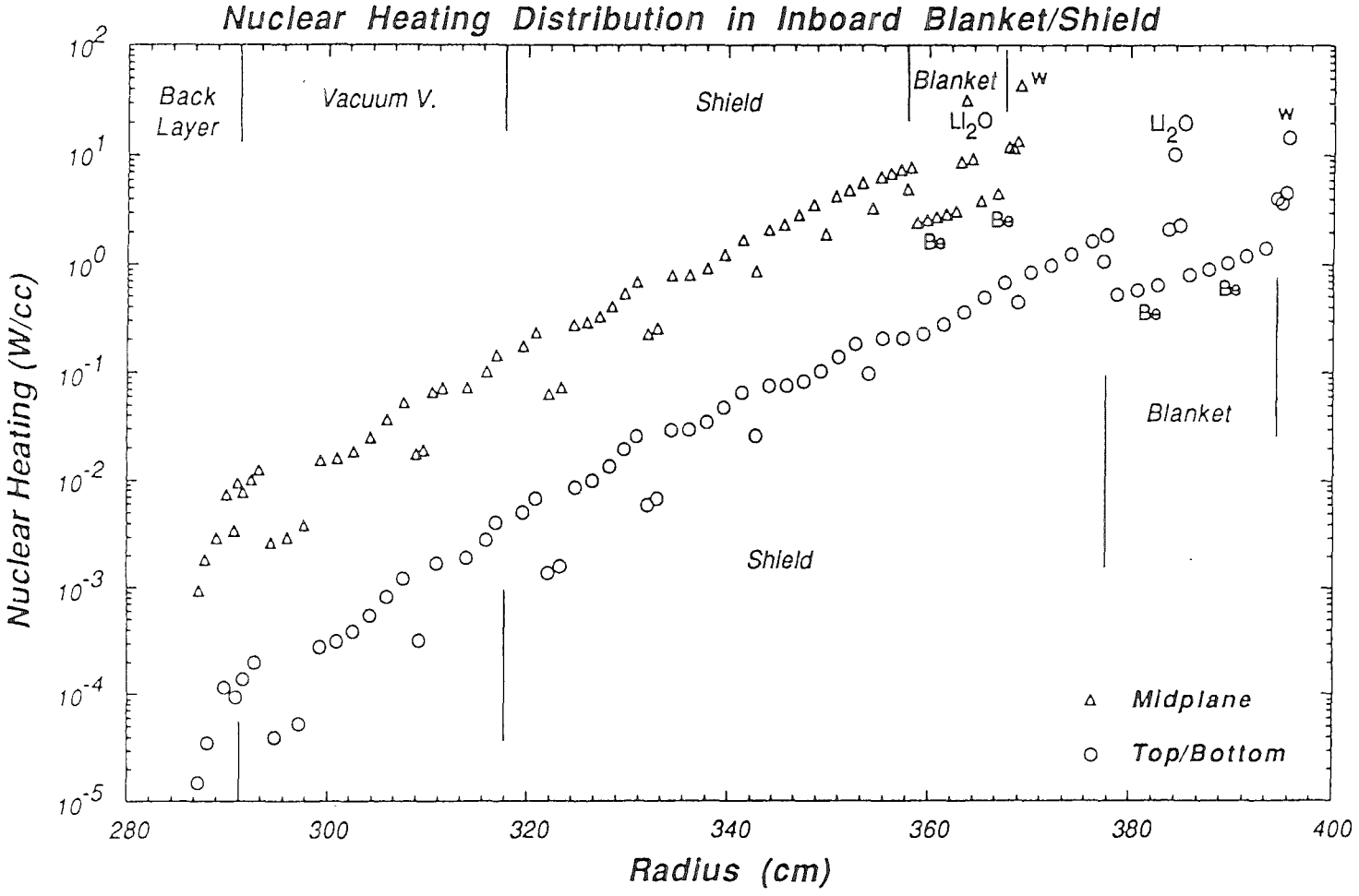
Nuclear Heating Distribution in Inboard Blanket/Shield
Nuclear Heating (W/cc)
Radius (cm)
Back Layer
Vacuum V.
Shield
Blanket
W
Li_2O
Be
Shield
Blanket
Midplane
Top/Bottom

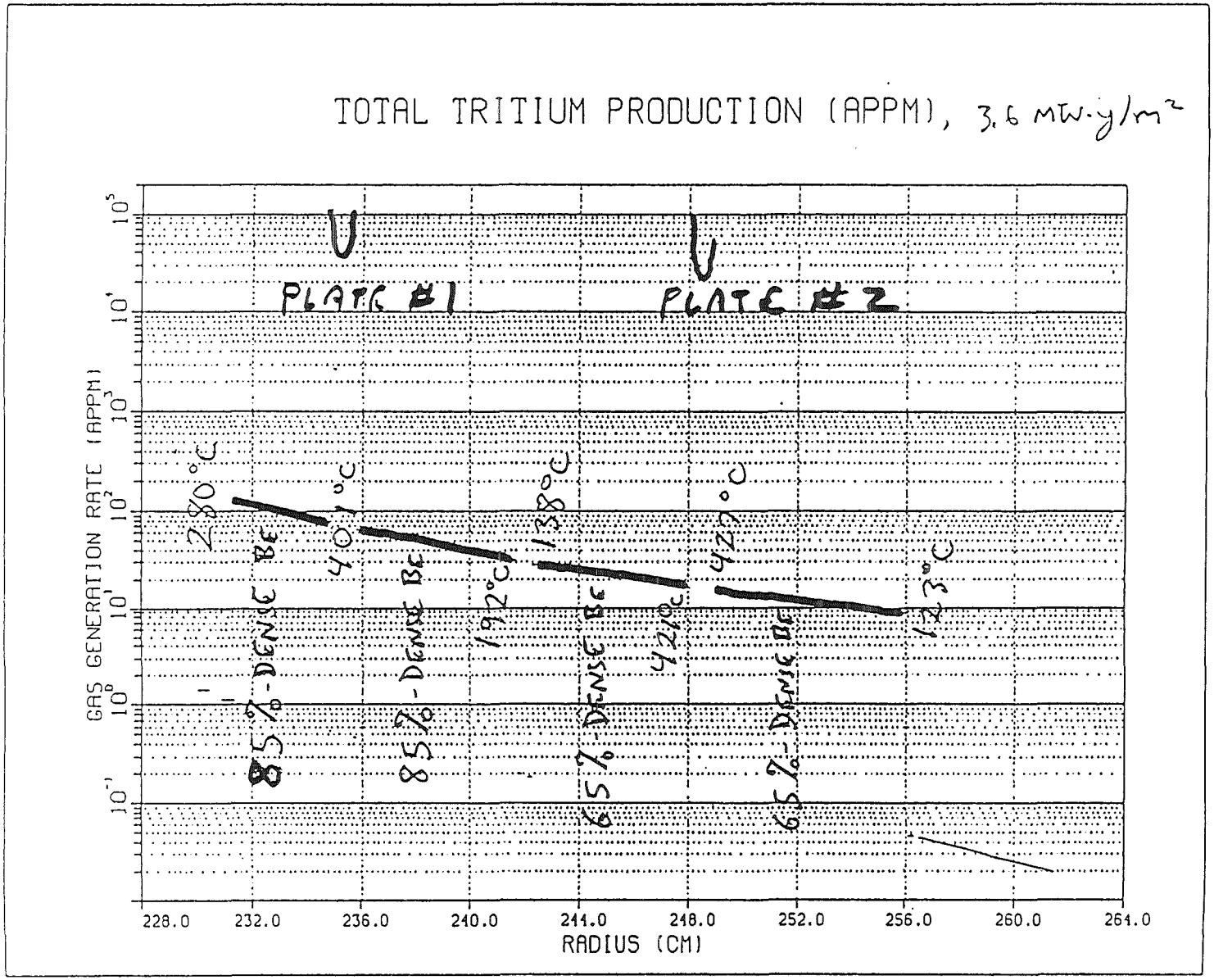
TOTAL TRITIUM PRODUCTION (APPM), 3.6 MW·y/m²
PLATE #1
PLATE #2
280 °C
410 °C
192°C
138°C
427°C
421°C
123°C
85% - DENSE BE
85% - DENSE BE
65% - DENSE BE
65% - DENSE BE
GAS GENERATION RATE (APPM)
RADIUS (CM)
228.0
232.0
236.0
240.0
244.0
248.0
252.0
256.0
260.0
264.0

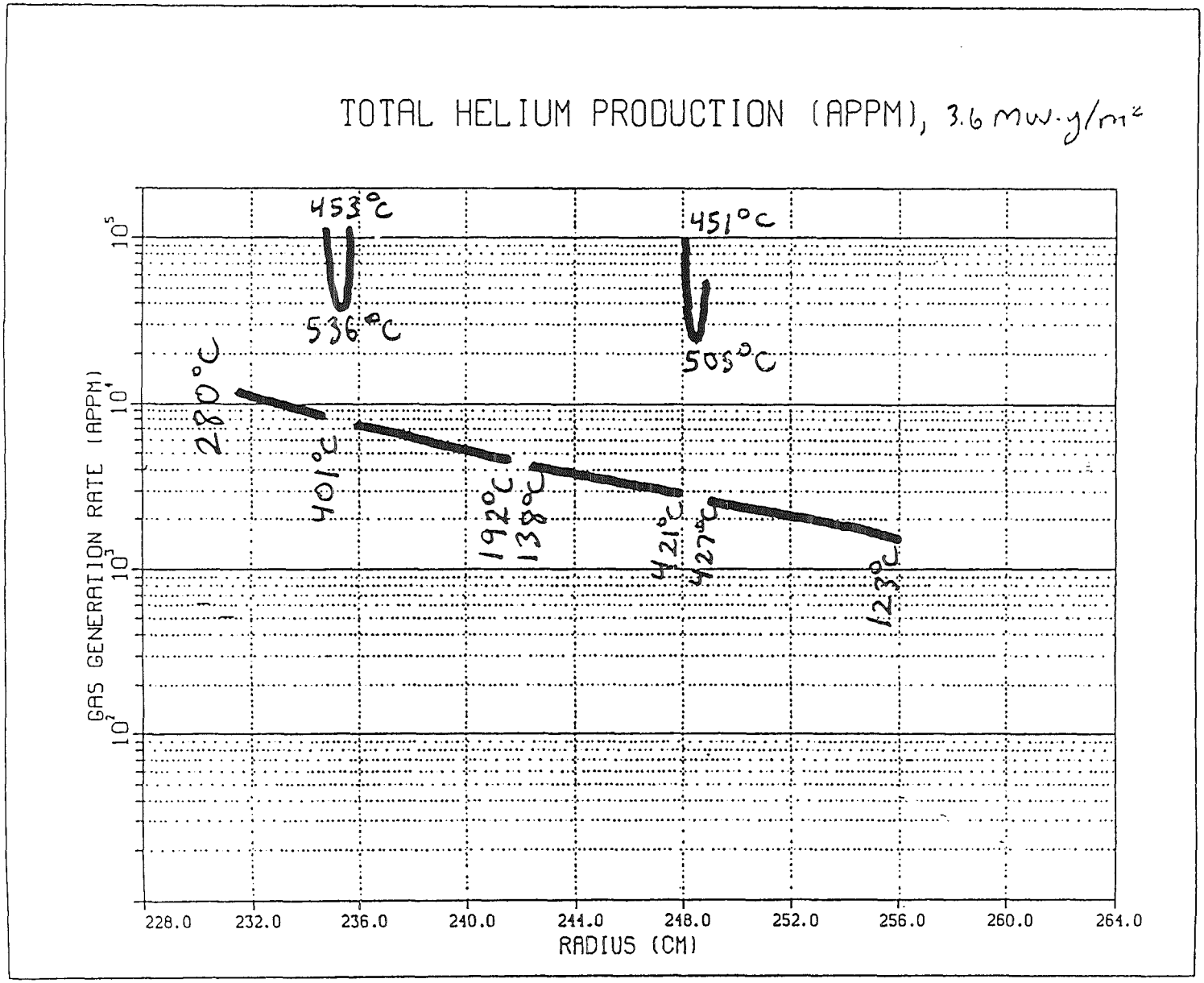
TOTAL HELIUM PRODUCTION (APPM), 3.6 MW·y/m²
453°C
536°C
451°C
505°C
280°C
401°C
192°C
138°C
421°C
427°C
123°C
GAS GENERATION RATE (APPM)
10⁵
10⁴
10³
10²
228.0
232.0
236.0
240.0
244.0
248.0
252.0
256.0
260.0
264.0
RADIUS (CM)

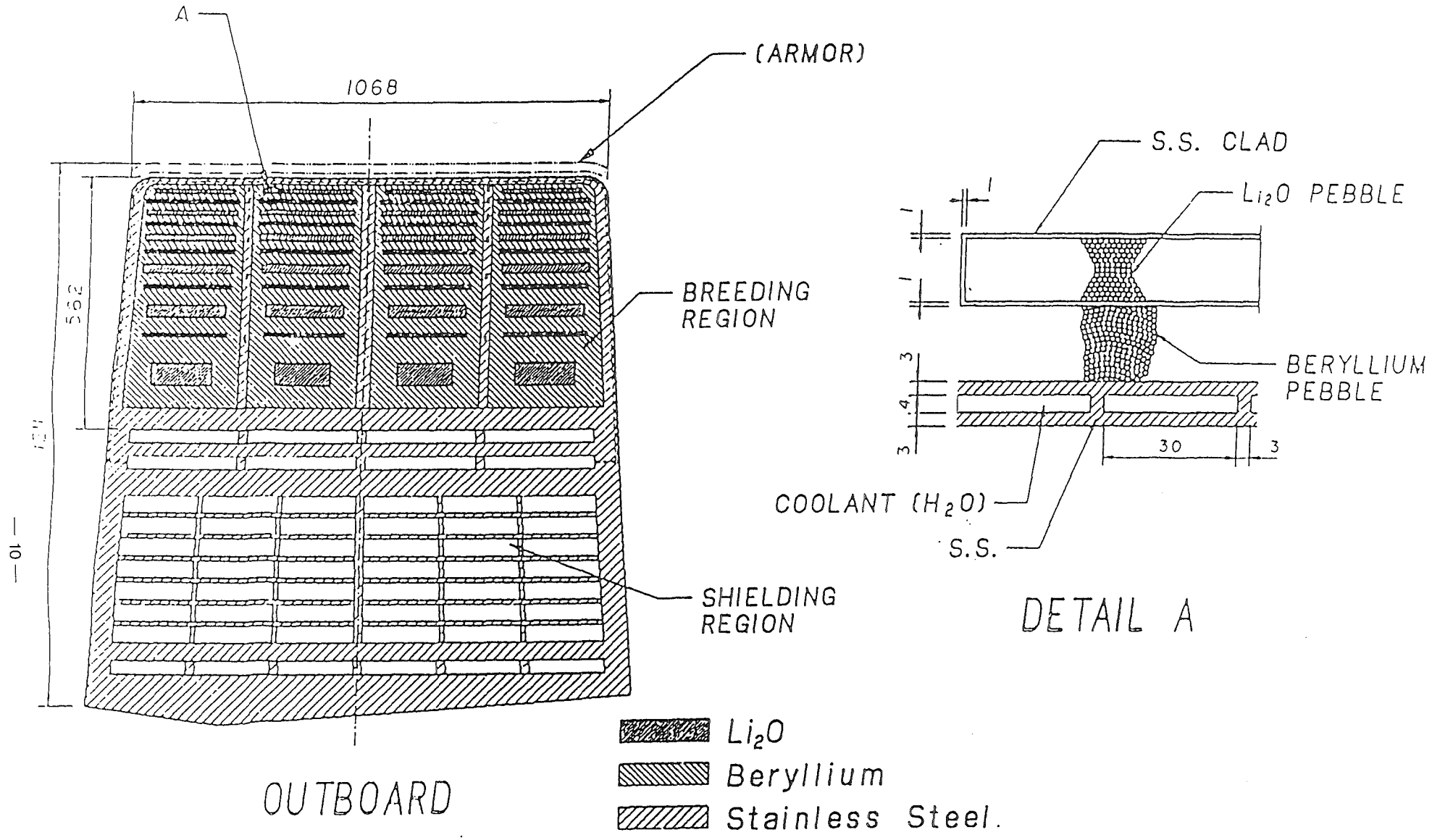

Figure 2. Ceramic blanket "layered" concept --pebble bed design--.

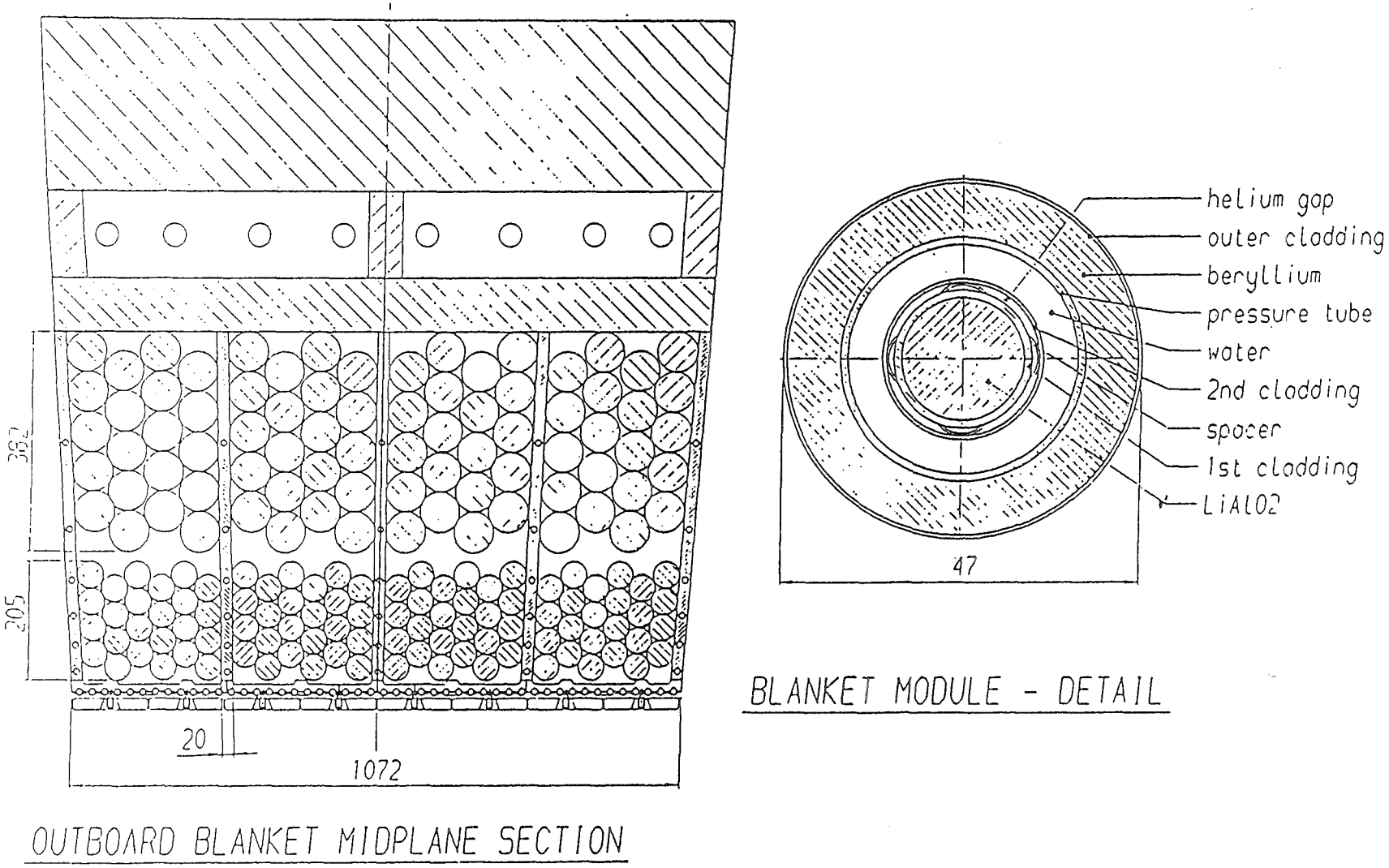

Figure 3. BIT blanket design.

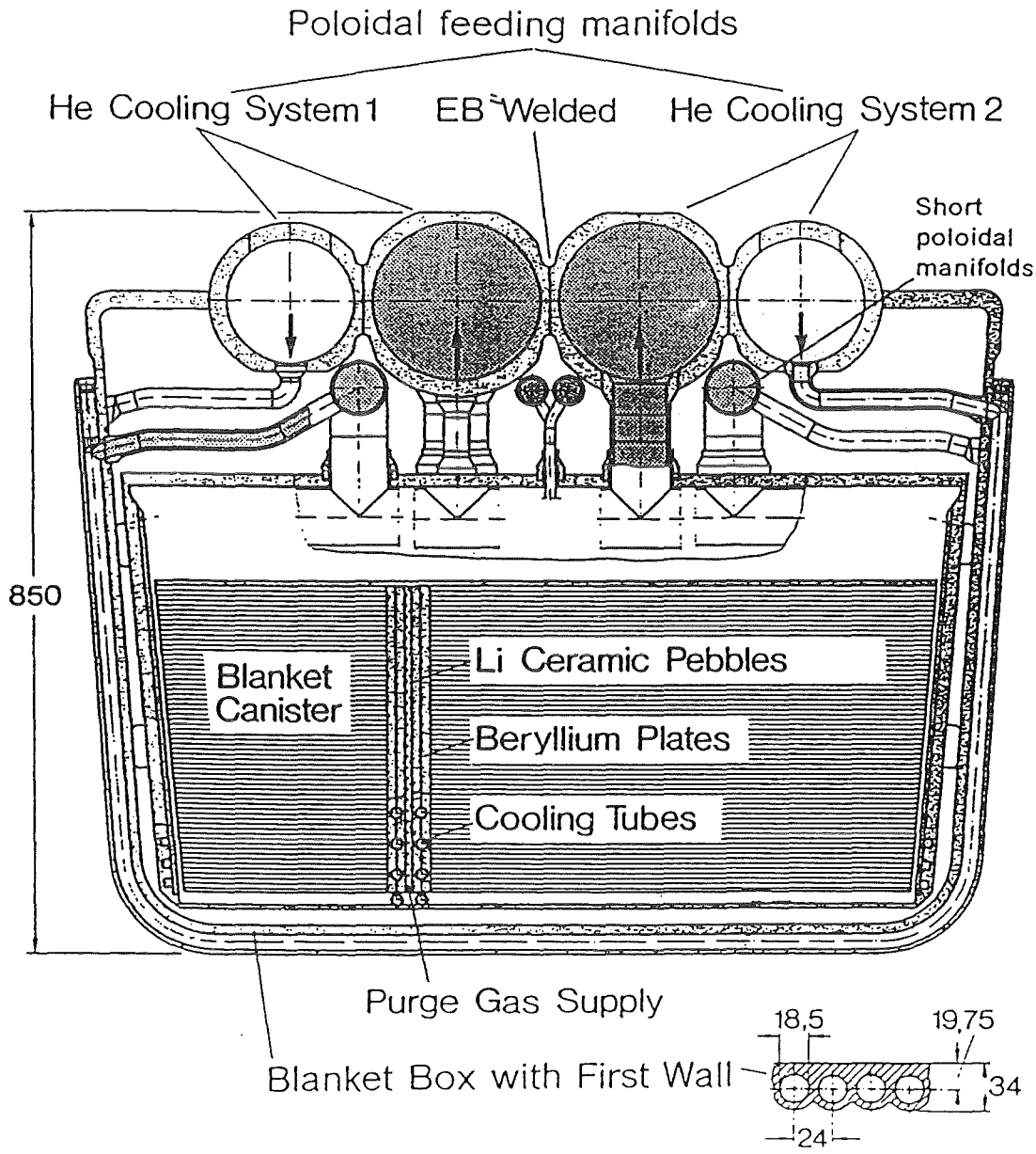

Figure 4. Radial-toroidal cross section at the equatorial plane of the outboard blanket box and (below) radial-poloidal section of the first wall (dimensions in mm).

ITER Blanket Module (Typical 48 Places)

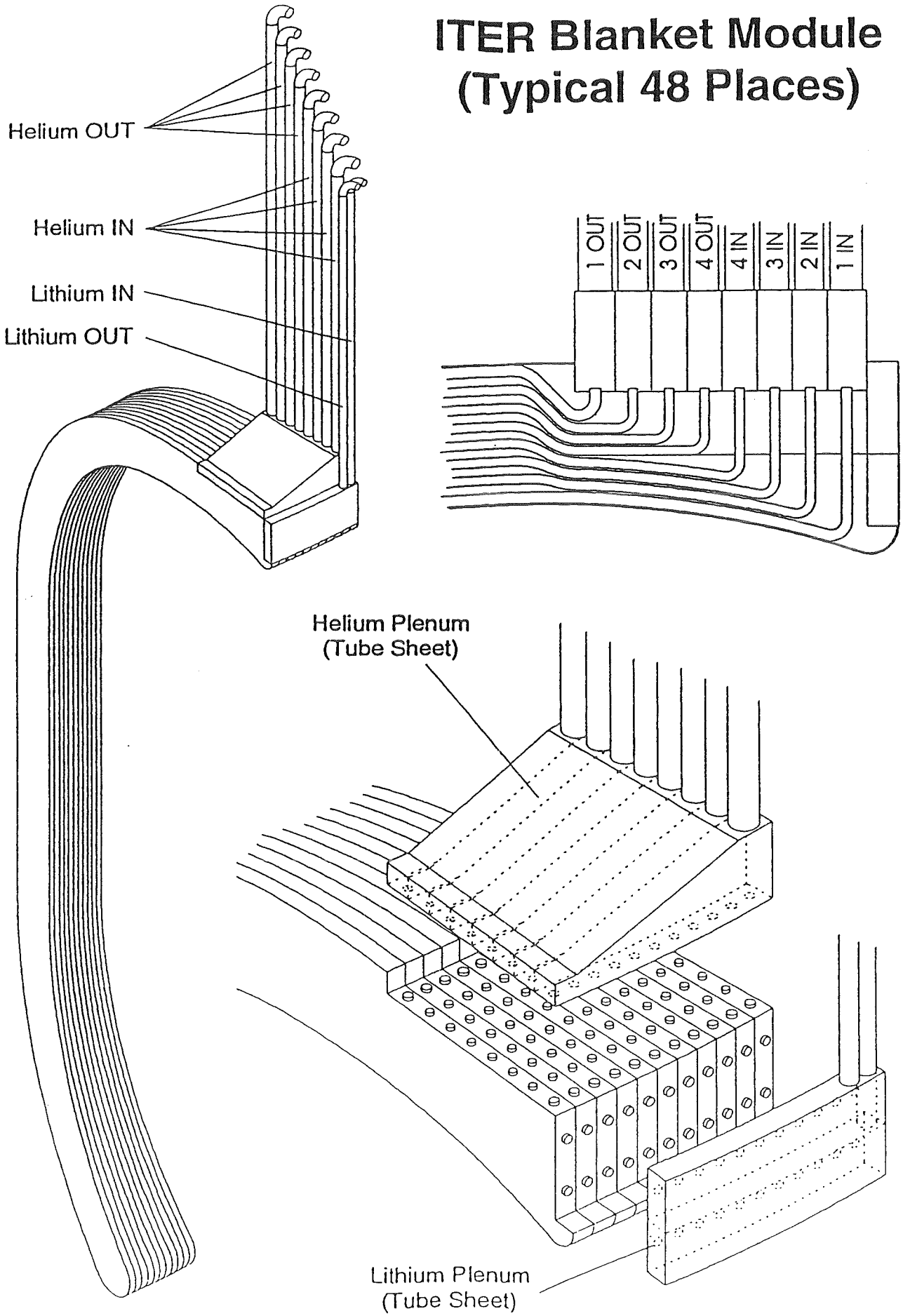

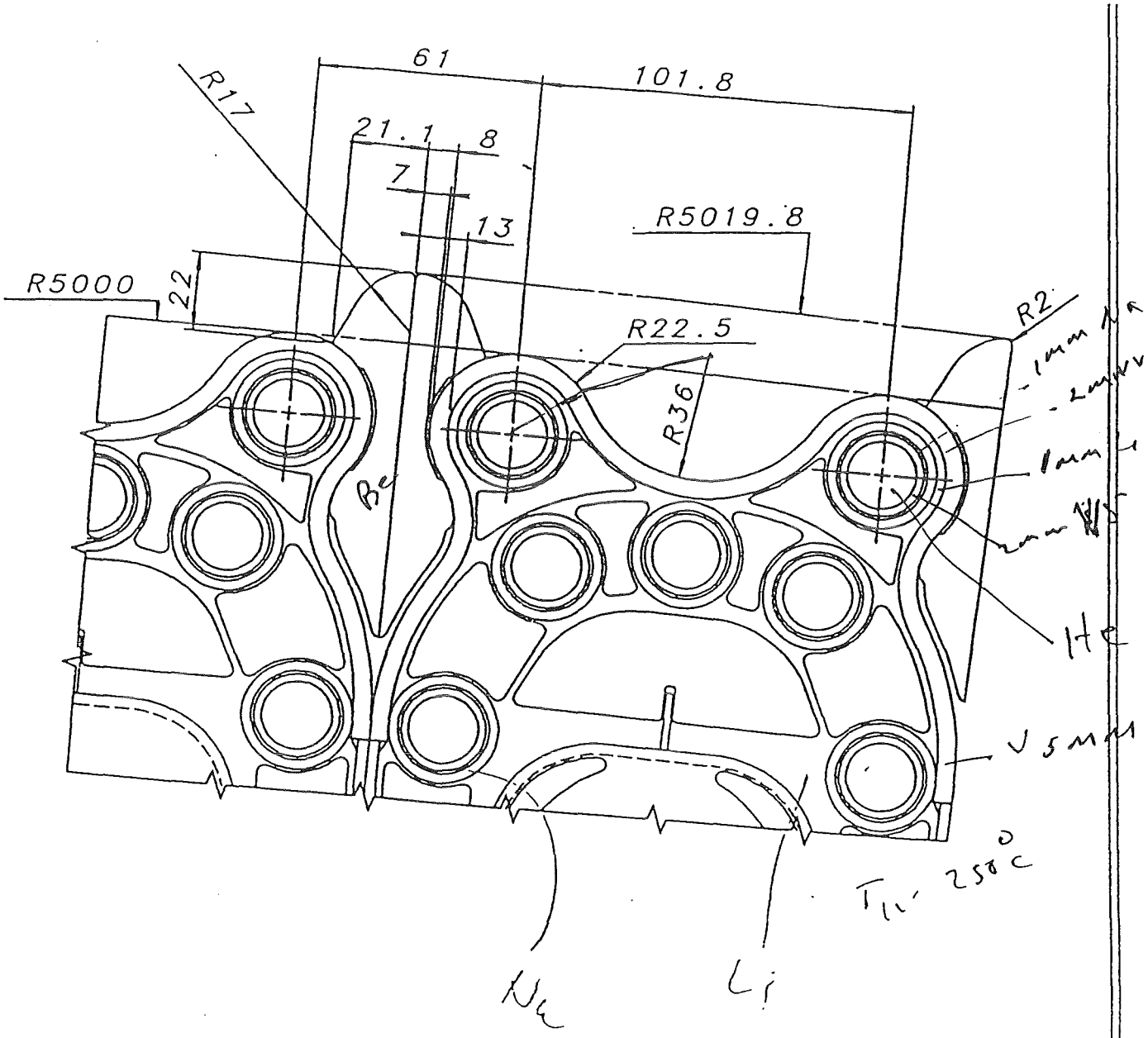

THIS IS PROVISIONAL WORKING INFORMATION ONLY. MUST NOT BE TRANSMITTED TO ANY THIRD PARTY.

INBOARD BLANKET SECTION ON EQUATORIAL PLANE

ITER

MAY 16 1993

WORKING PROPOSAL

LEVEL : SKETCH

SAN DIEGO CO-CENTER

PERFORMANCE PARAMETERS

- **Thermal Performance**

  - 100% dense Be: thermal conductivity well characterized; no degradation with neutron damage
  - Porous Be: some "holes" in the data base
  - Pebble-bed Be: new data

- **Tritium Performance**

  - 100% dense Be

    Diffusivity: difficult to measure; probably higher than for ceramics

    Solubility: difficult to measure; probably lower than for ceramics

    Trapping: chemical?
    neutron-damage-induced?
    He induced?
    Higher than for ceramics

  - Porous Be (80% TD)

    Good tritium release

- **Helium Performance**

  - 100% dense Be

    Good swelling data base; high He retention

  - Porous Be

    No swelling data base, high He retention

- **Mechanical Performance**

  - 100% dense Be

    Ductility very sensitive to impurities
    Neutron damage and He;
    No irradiation creep data

  - Porous Be

    Poor ductility; limited data base

- **Compatibility**

  Good data base

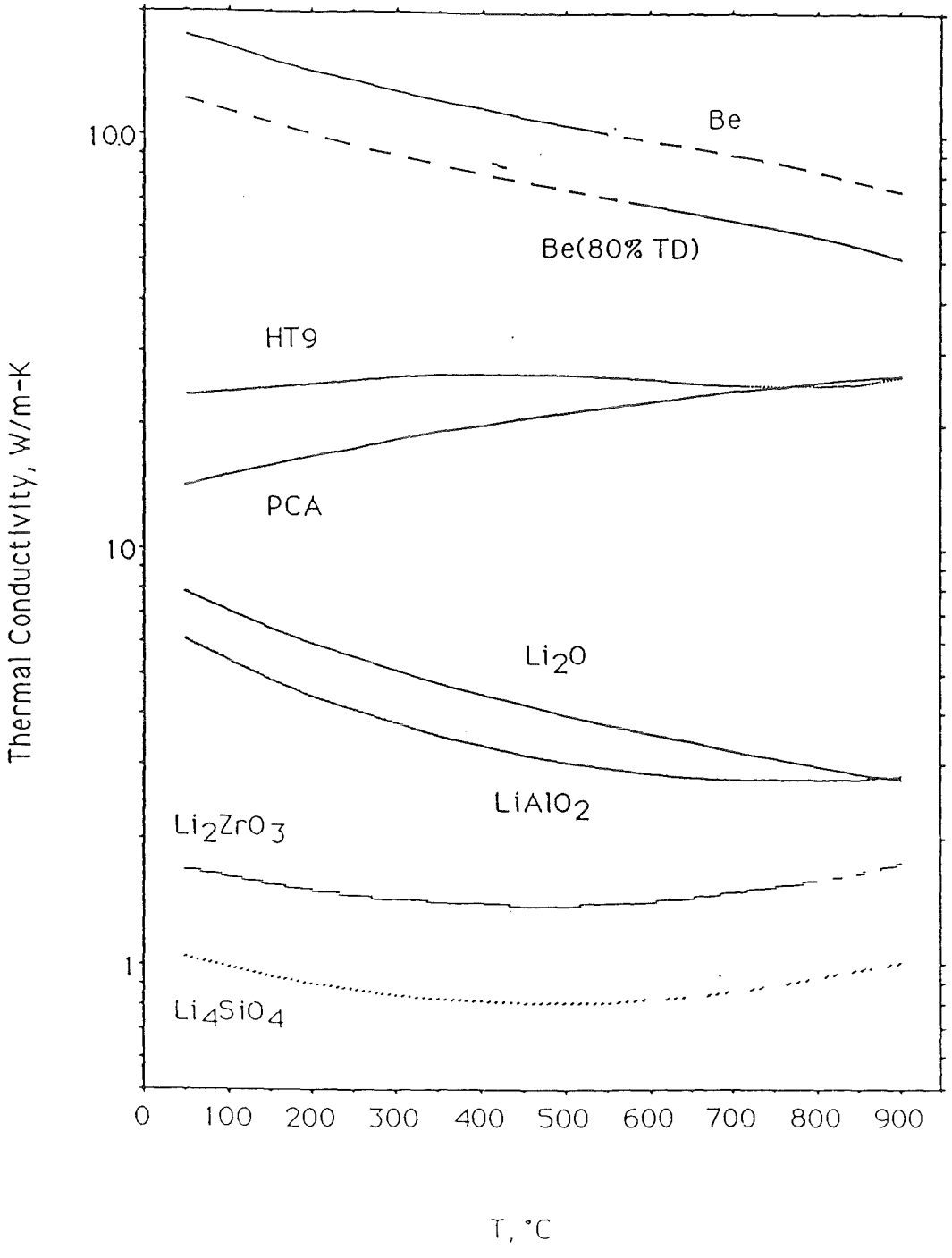

Thermal conductivity of 80%-dense solid breeder materials.

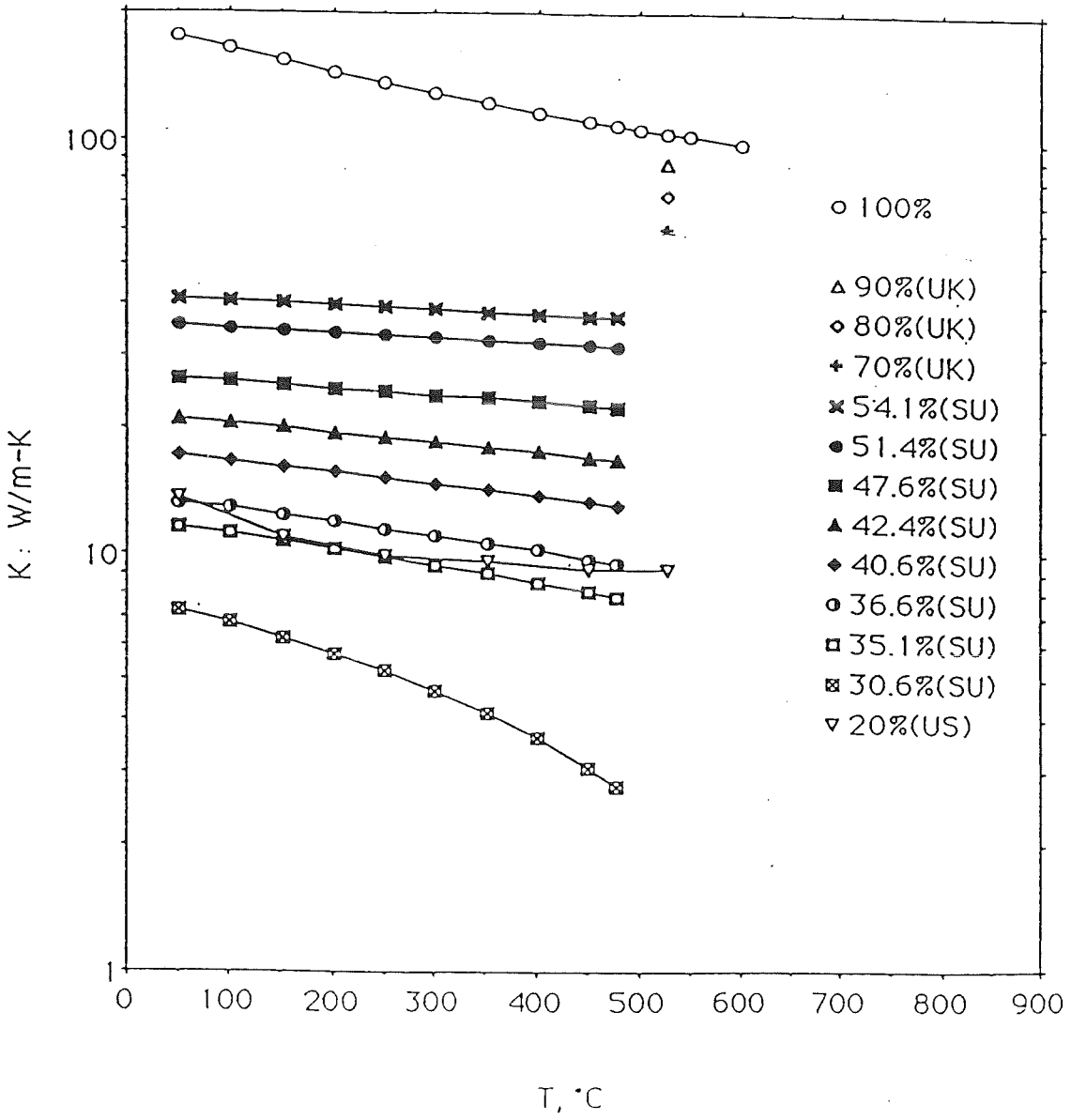

Figure 38. Beryllium thermal conductivity data vs. temperature and density (in % TD).

Low temperature swelling data for 100% dense, hot-pressed beryllium.

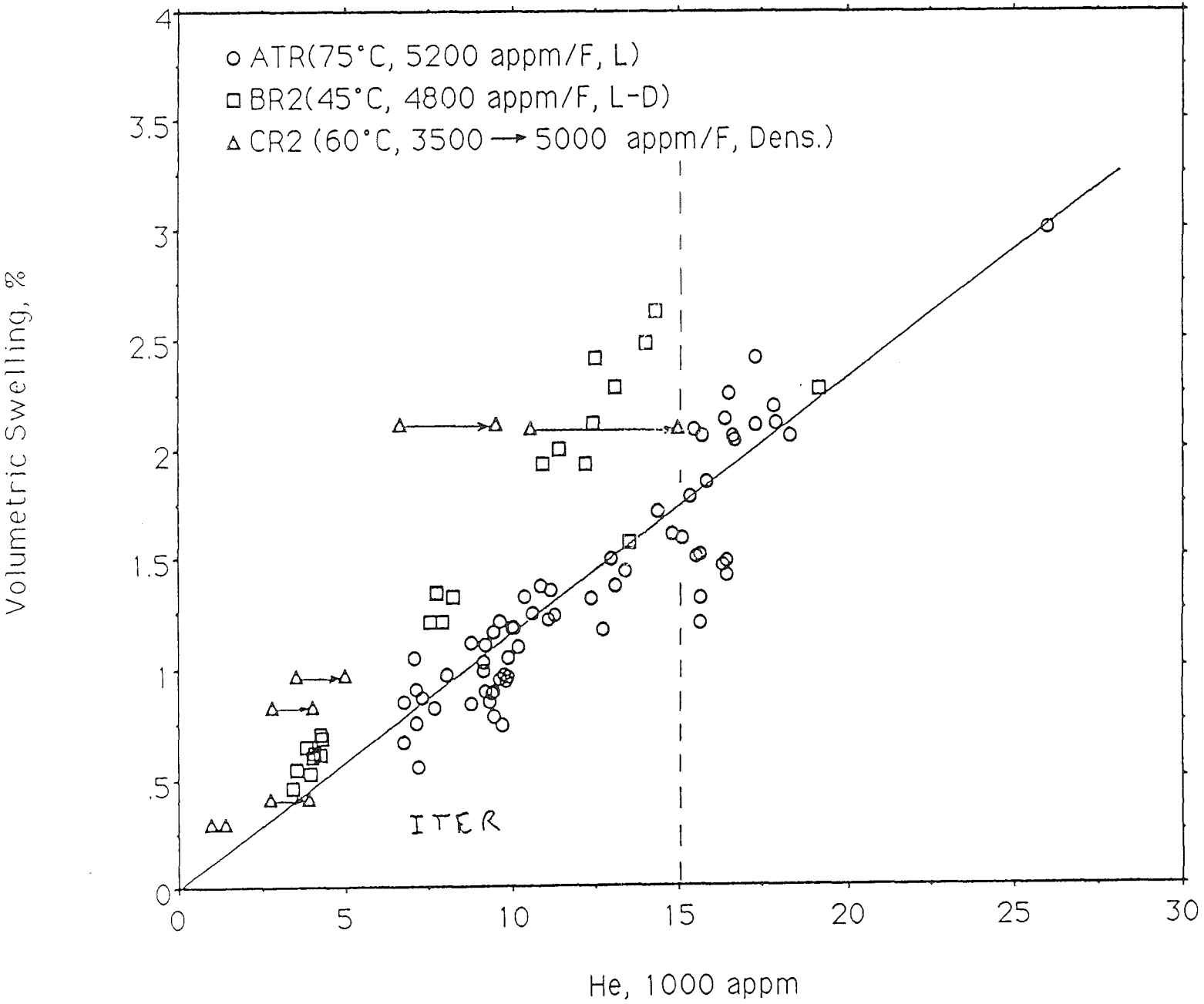

High temperature swelling data for 100 % dense, hot-pressed beryllium.

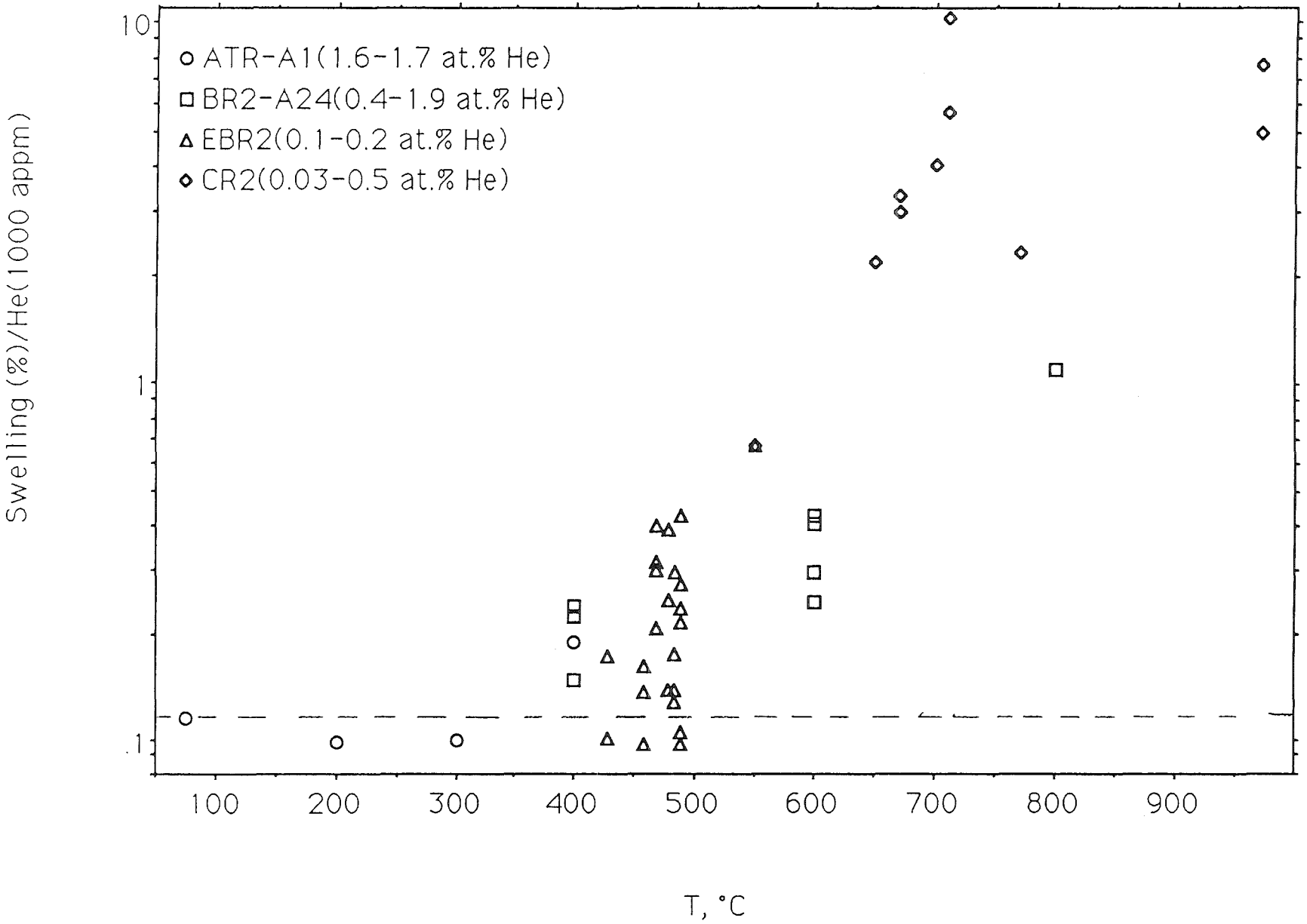

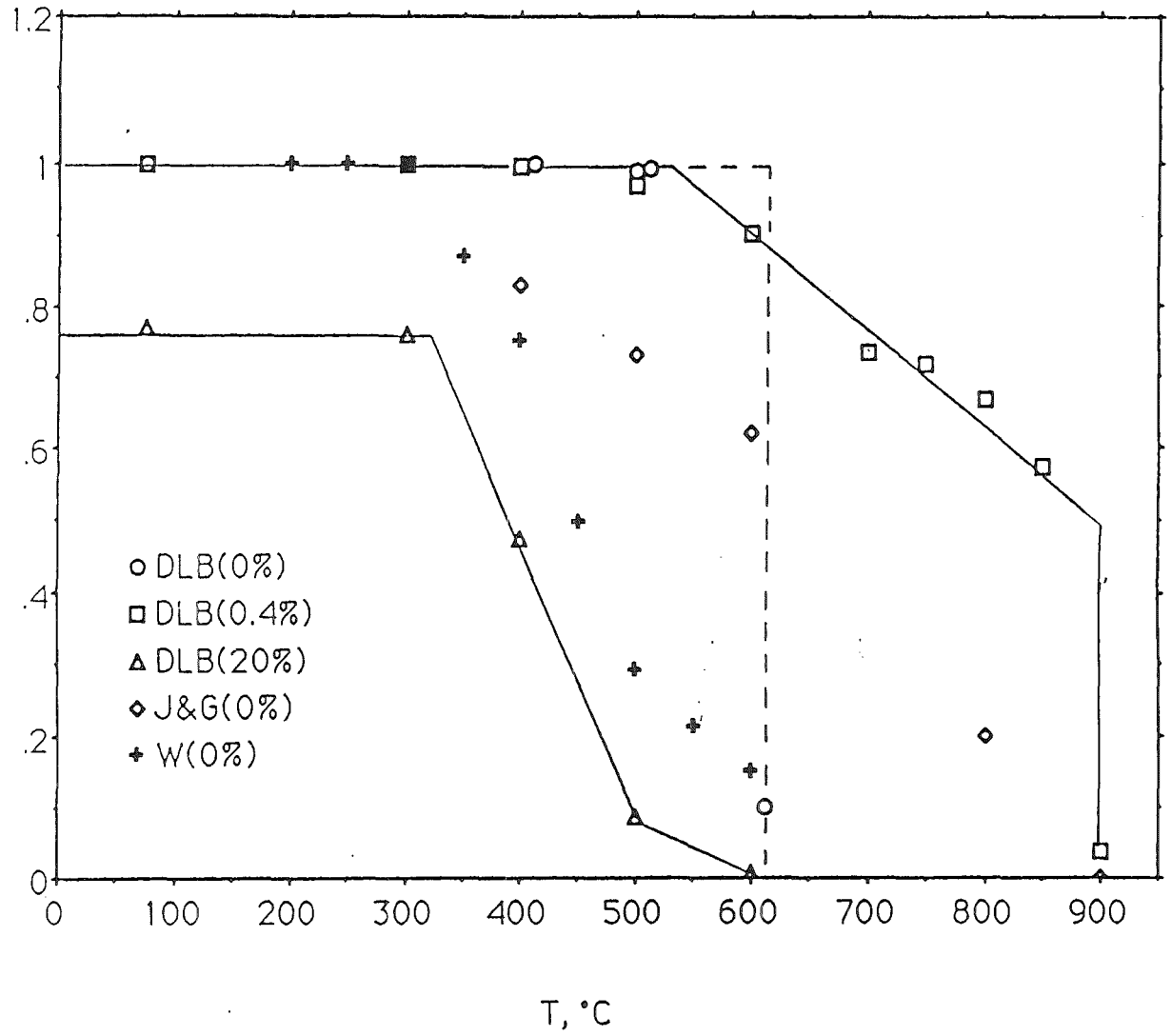

Figure 46. Laboratory annealing data for fractional tritium retention in dense and porous Be.

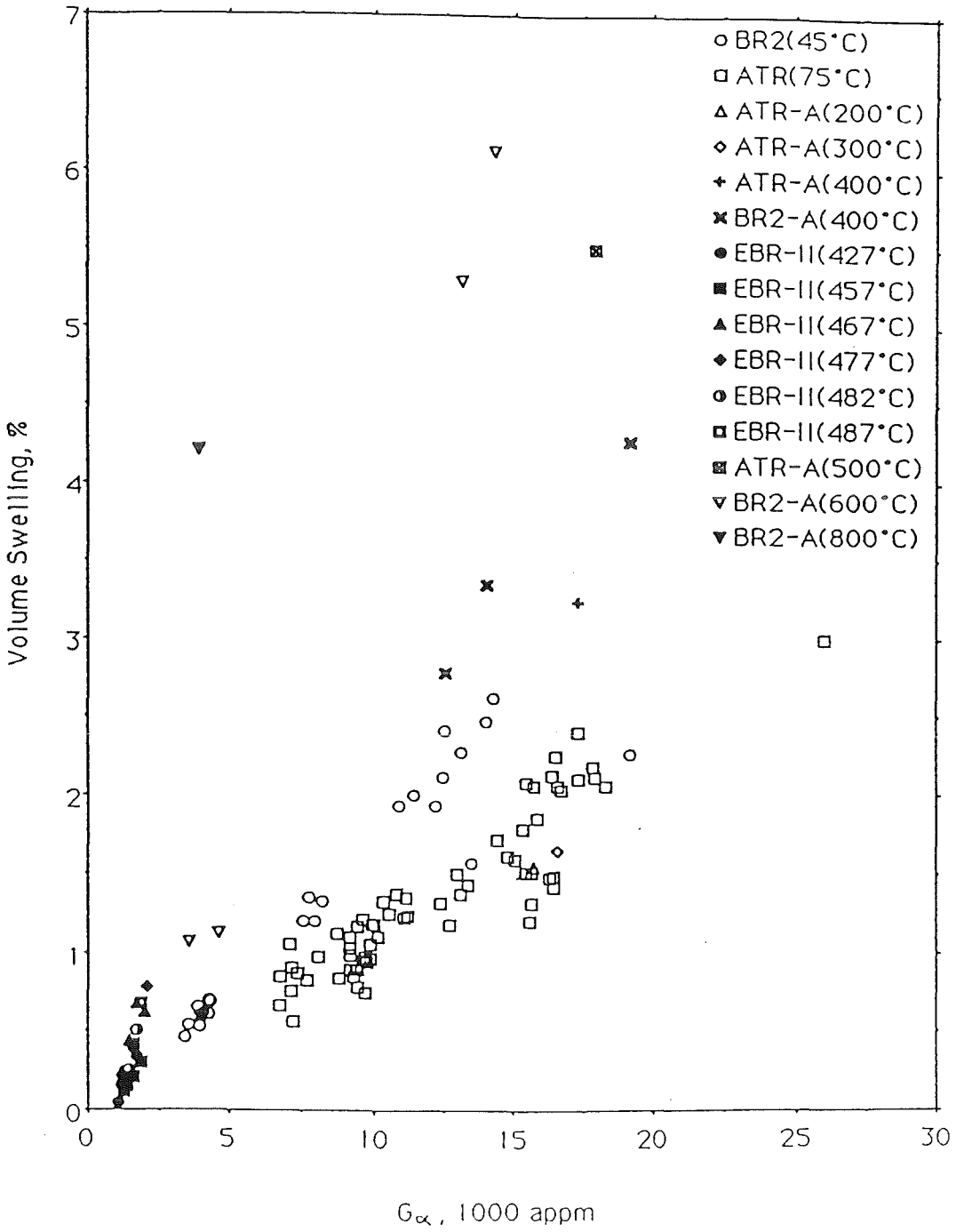

Figure 47. Swelling data for 100% dense hot-pressed beryllium.

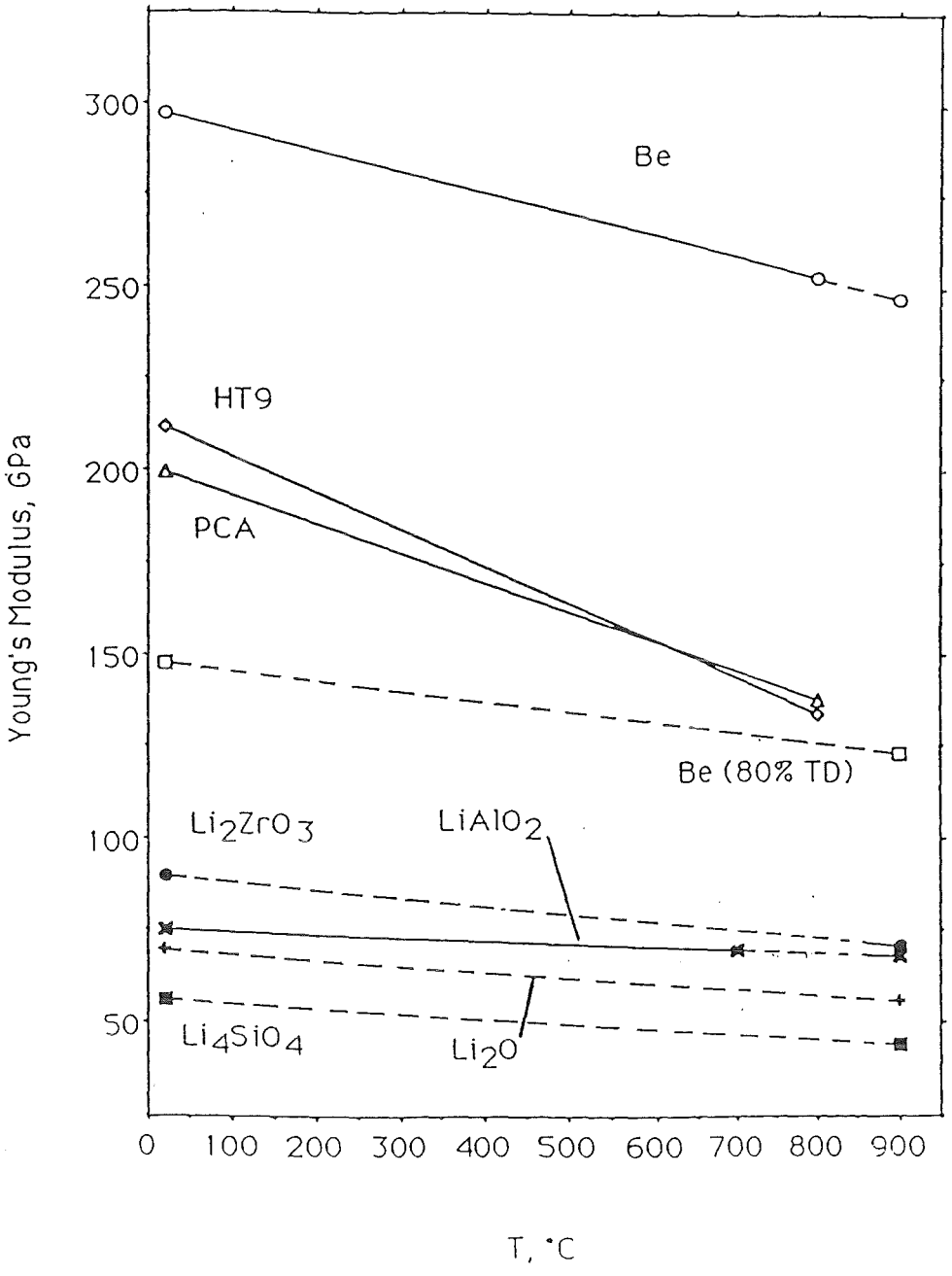

Figure 54. Young's modulus of 80%-dense solid breeder materials

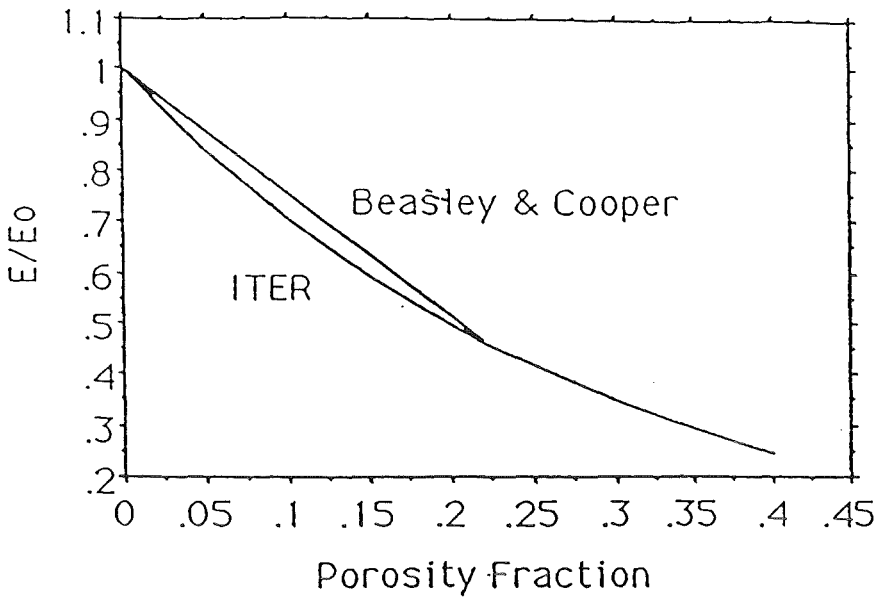

FIgure 41a. Porosity dependence of Young's modulus for Be at room temperature.

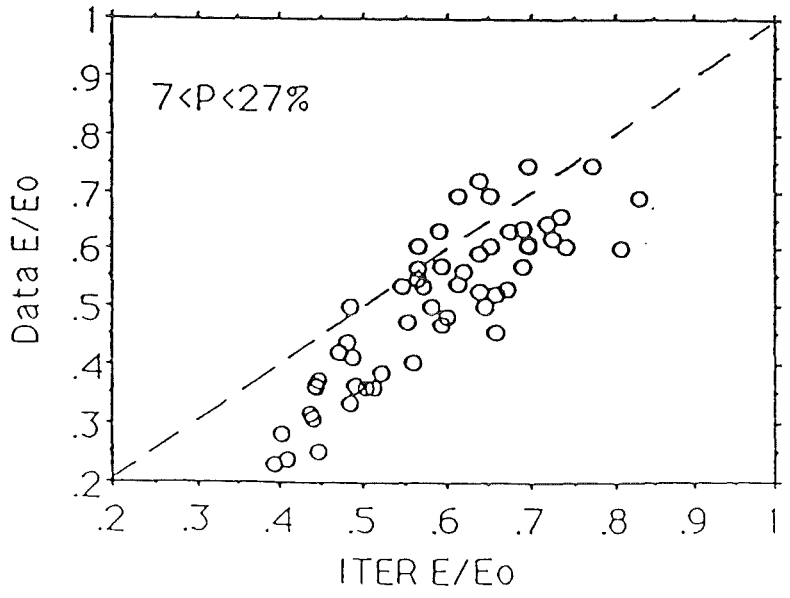

Figure 41b. Comparison of ITER correlation to data for E/Eo for 0.07<P<0.27.

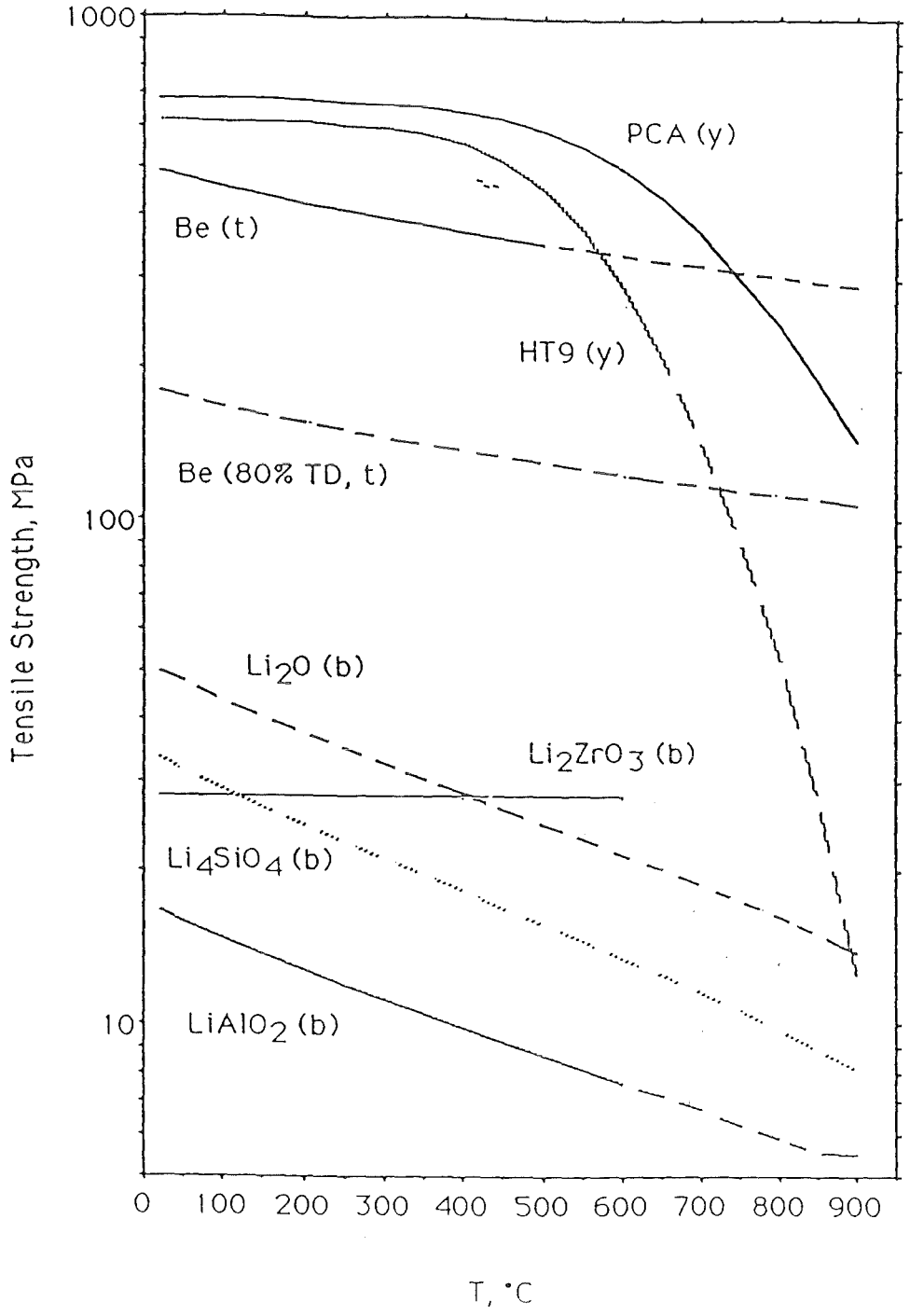

Figure 55. Bending (b) strength of 80%-dense, 10-micron grain size breeder materials.

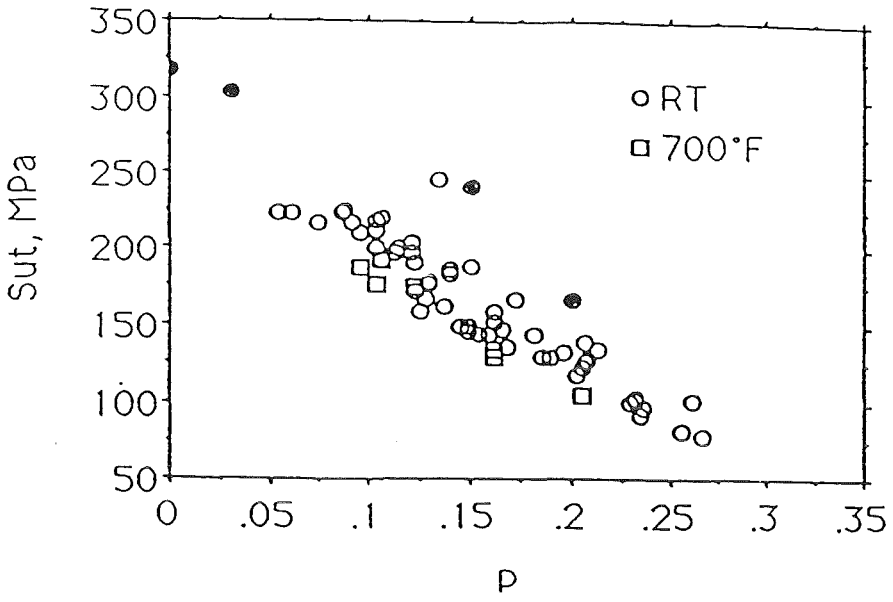

Figure 42a. Ultimate tensile strength data for CIP/S Be vs. porosity (P).

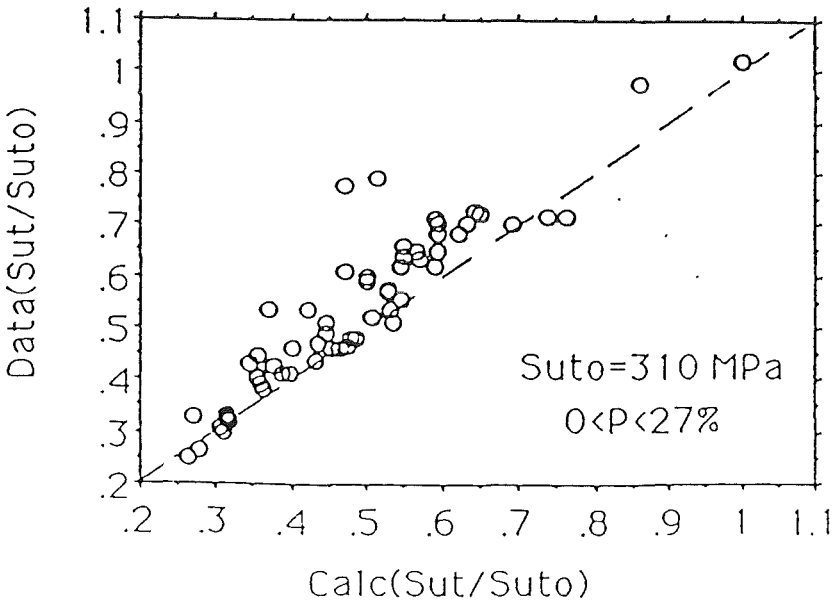

Figure 42b. Comparison of ITER correlation to data for RT tensile strength.

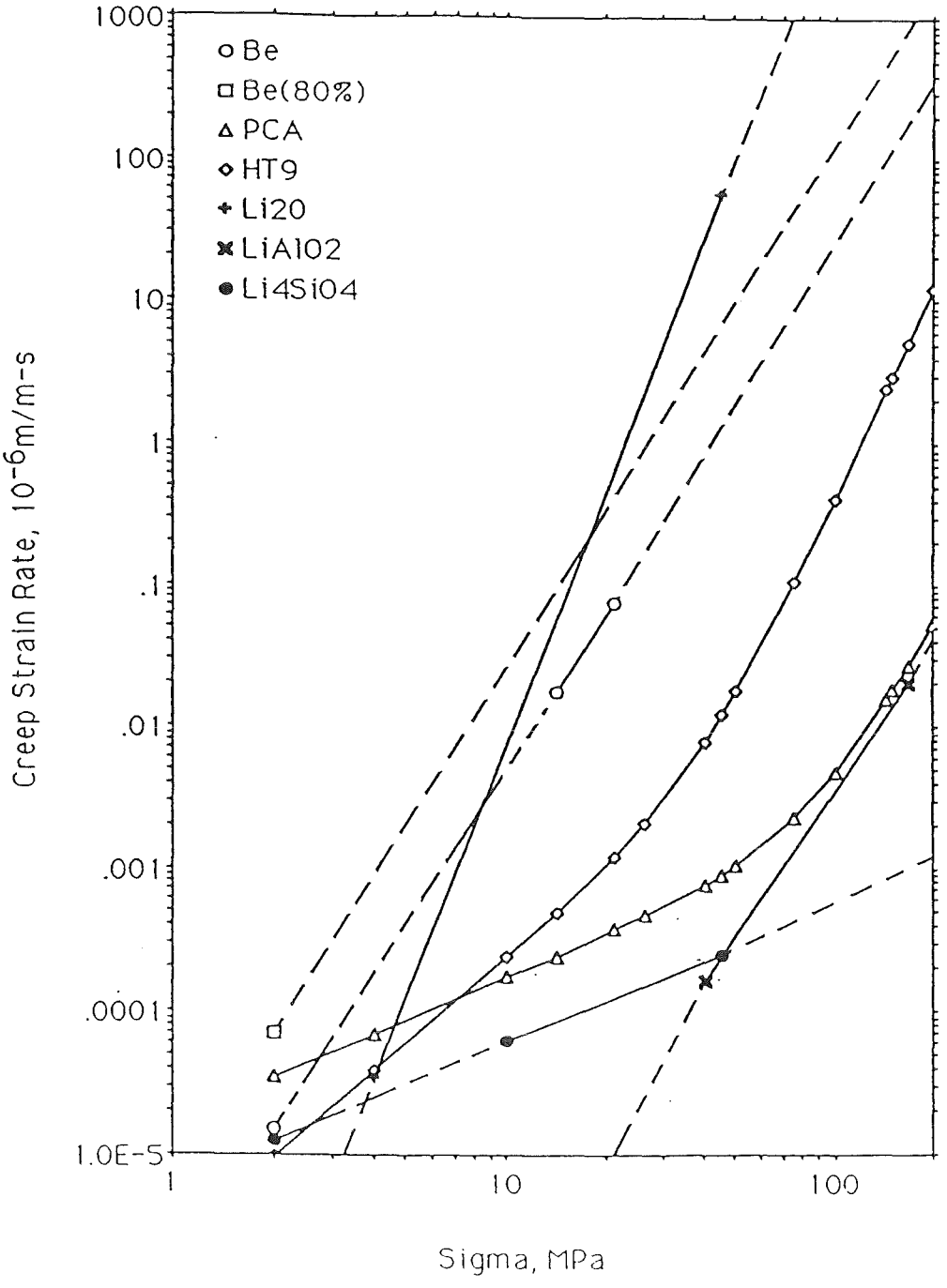

Figure 56a. Thermal creep strain rate of 80%-dense breeder materials (700°C).

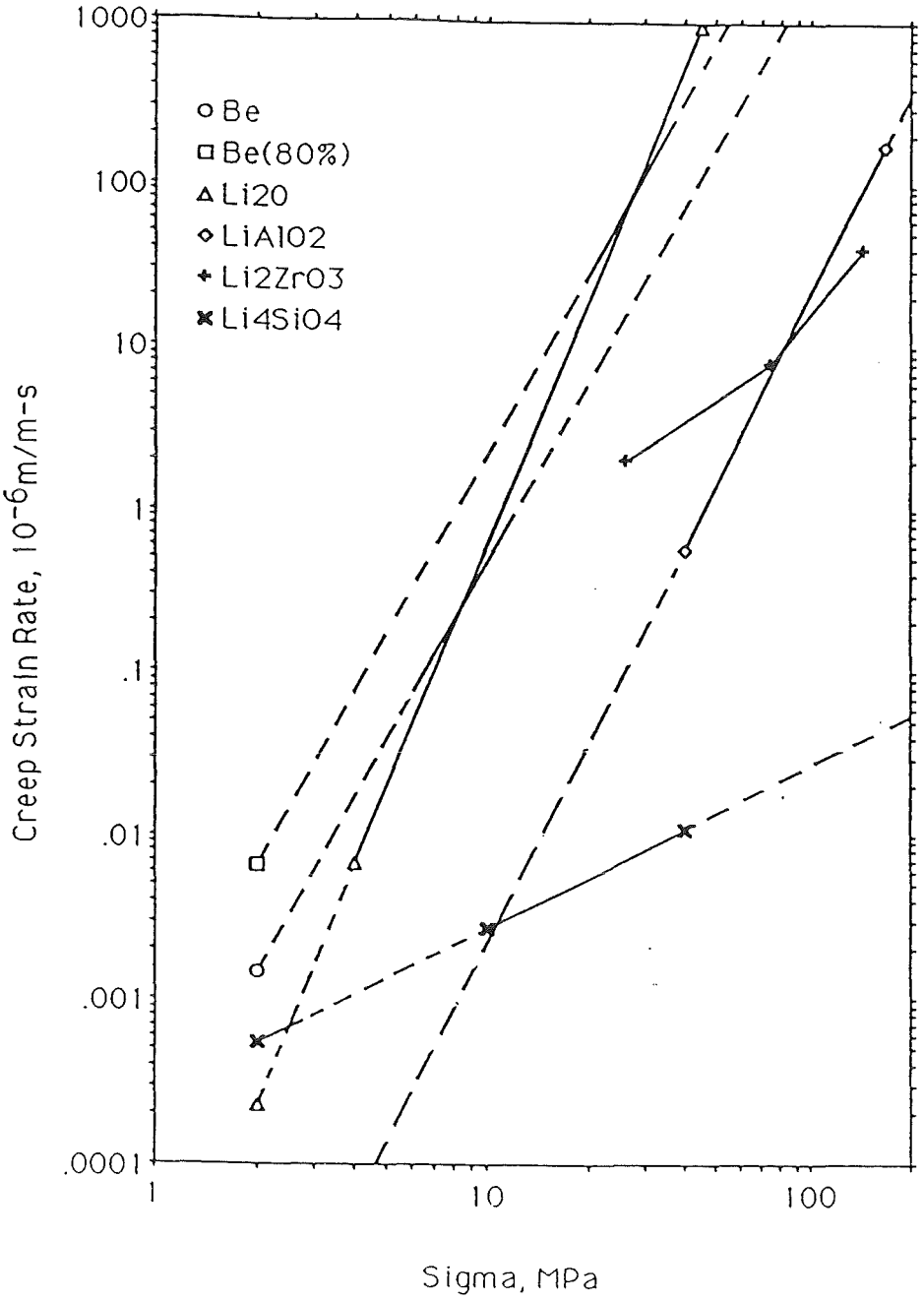

Figure 56b. Thermal creep strain rate of 80%-dense breeder materials (900°C).

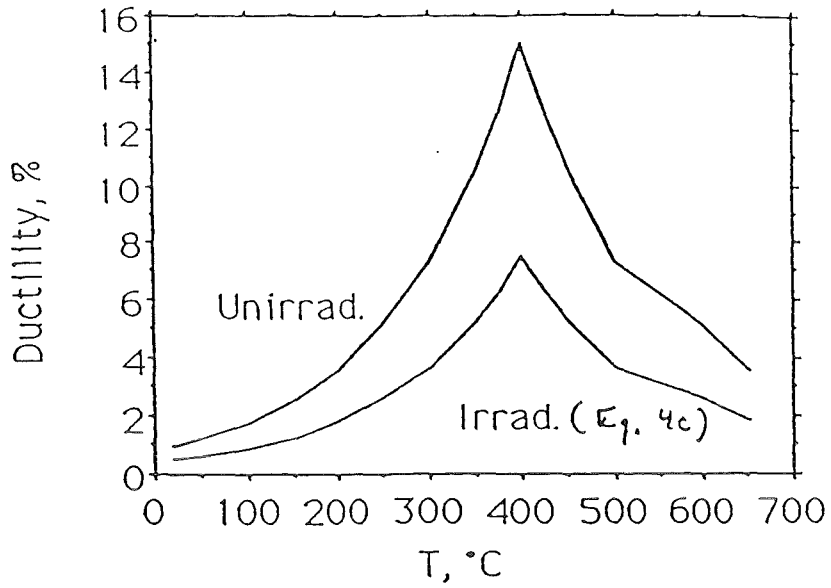

Figure 44a. ITER correlation for Be ductility with porosity > 10%.

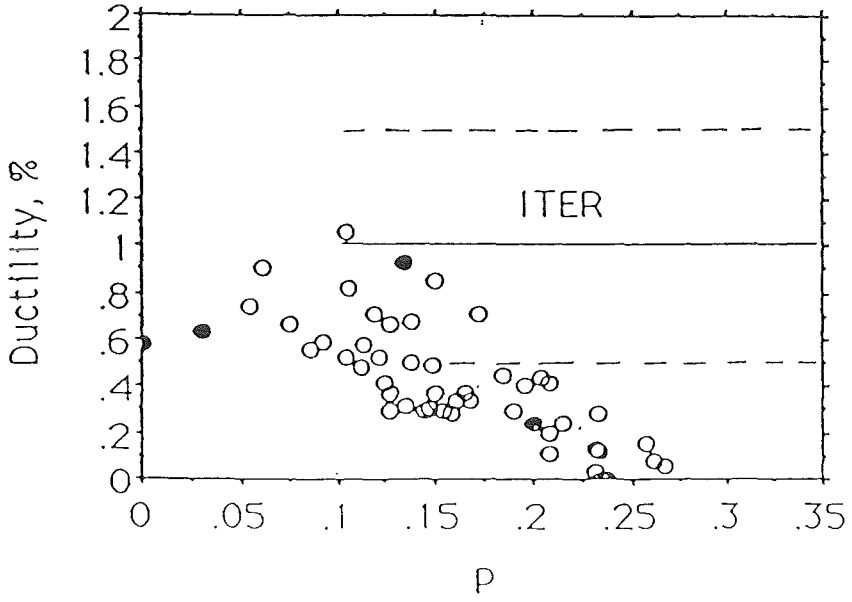

Figure 44b. Room temperature ductility for CIP/S Be.

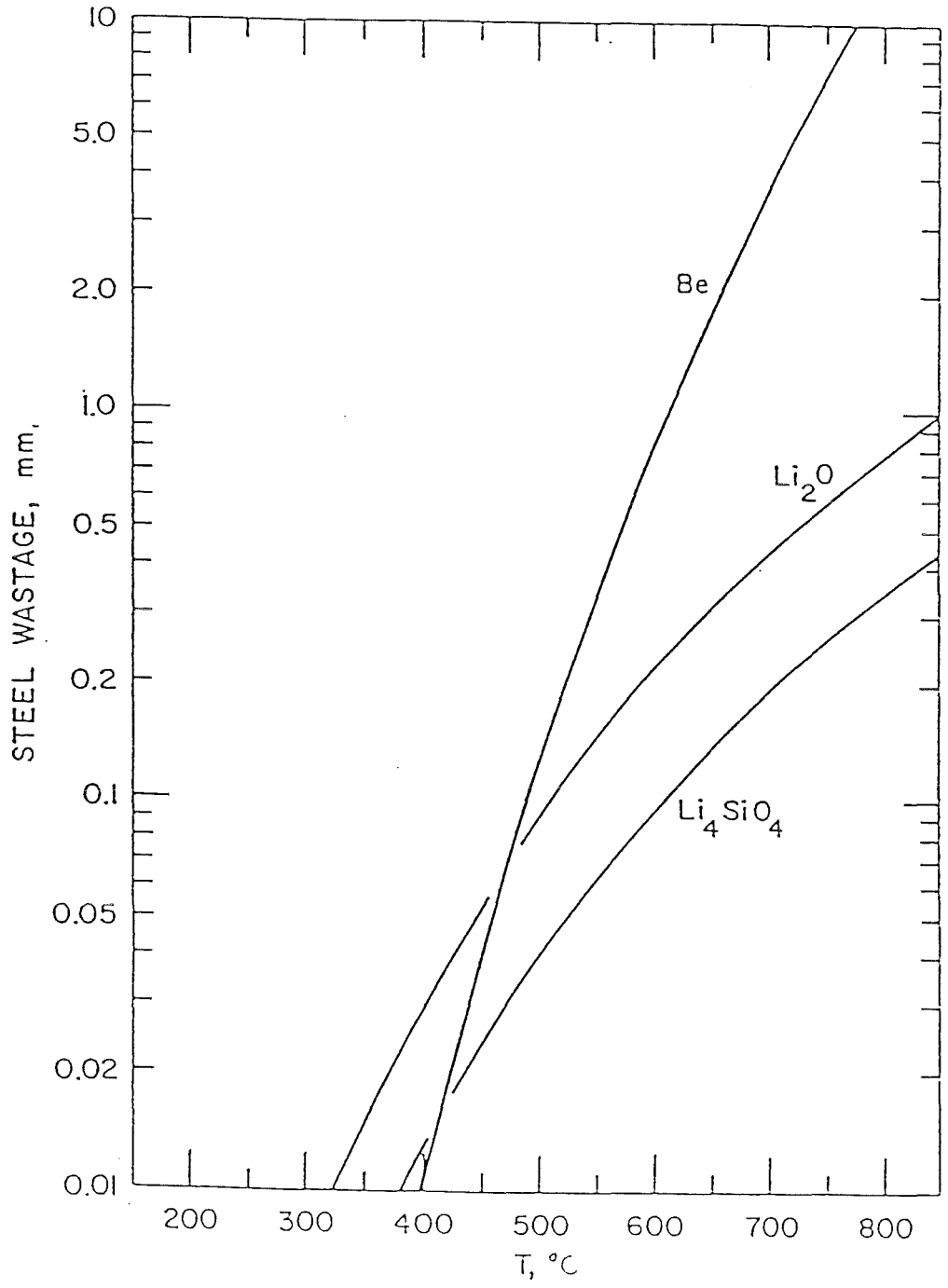

Figure 60. Extrapolation of wastage correlations to an ITER lifetime of 3 MW-y/m^2 (3.792 full power years).

Fig. 1. Temperature drop across interfaces with 1 micron roughness, 0.5 MW/m2, and 300°C sink temperature.

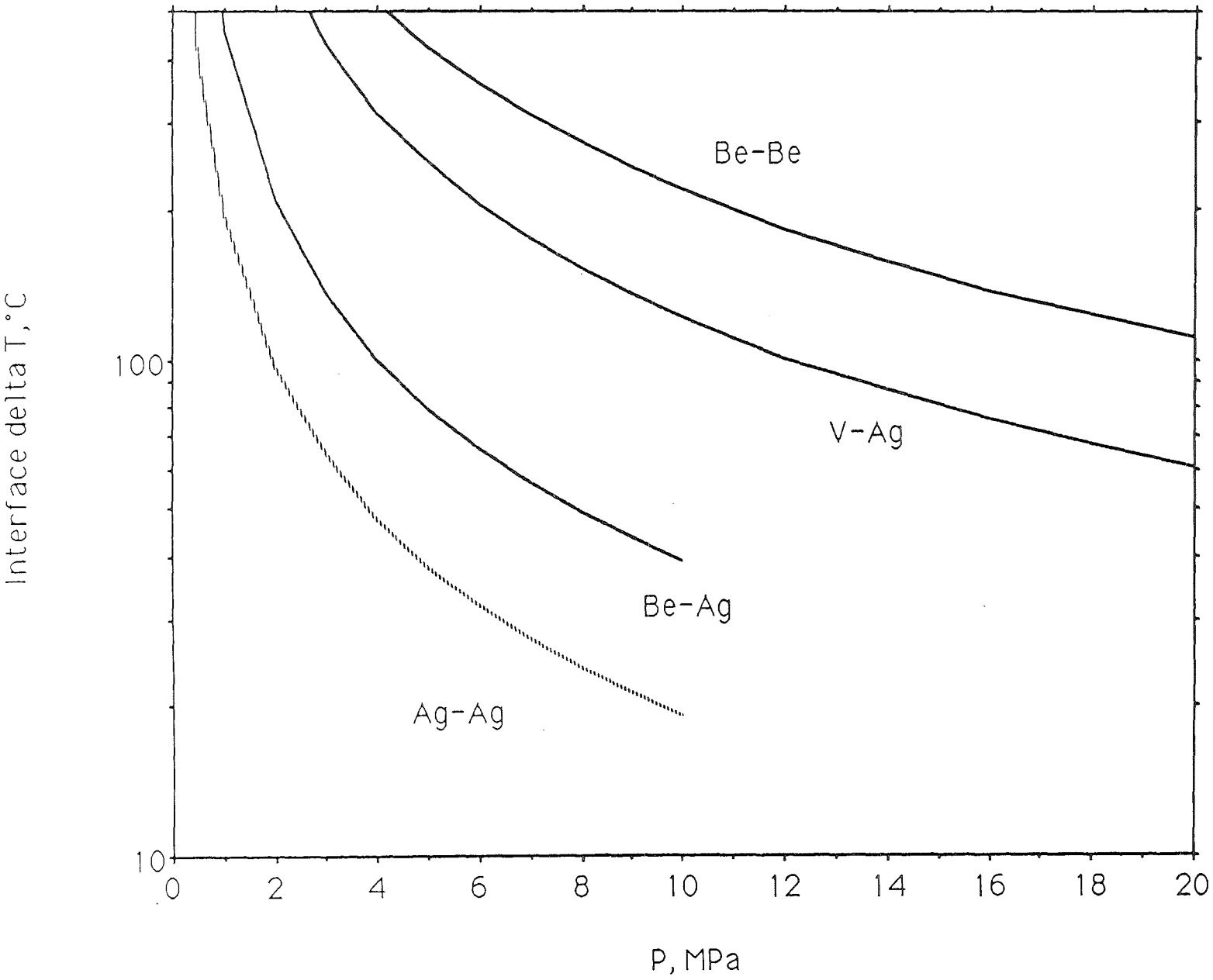

SAMPLE DESIGN CALCULATIONS

- **Thermal Performance**

  Be/metal contact in vacuum

- **Tritium and Helium**

  Tritium release and swelling vs. temperature for porous Be

- **Swelling and Creep of Constrained Be**

  Increase in stress with time vs. strength

Sensitivity of tritium release fraction and swelling in Be to temperature.

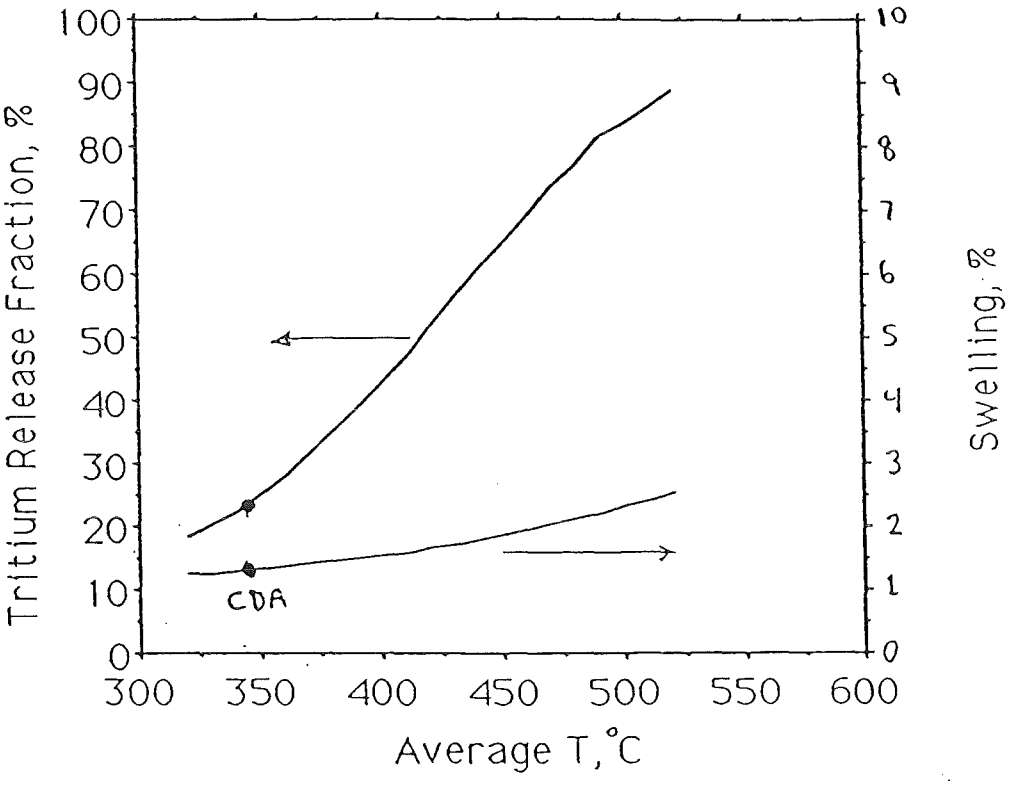

Swelling-induced stress in constrained Be near the first wall.

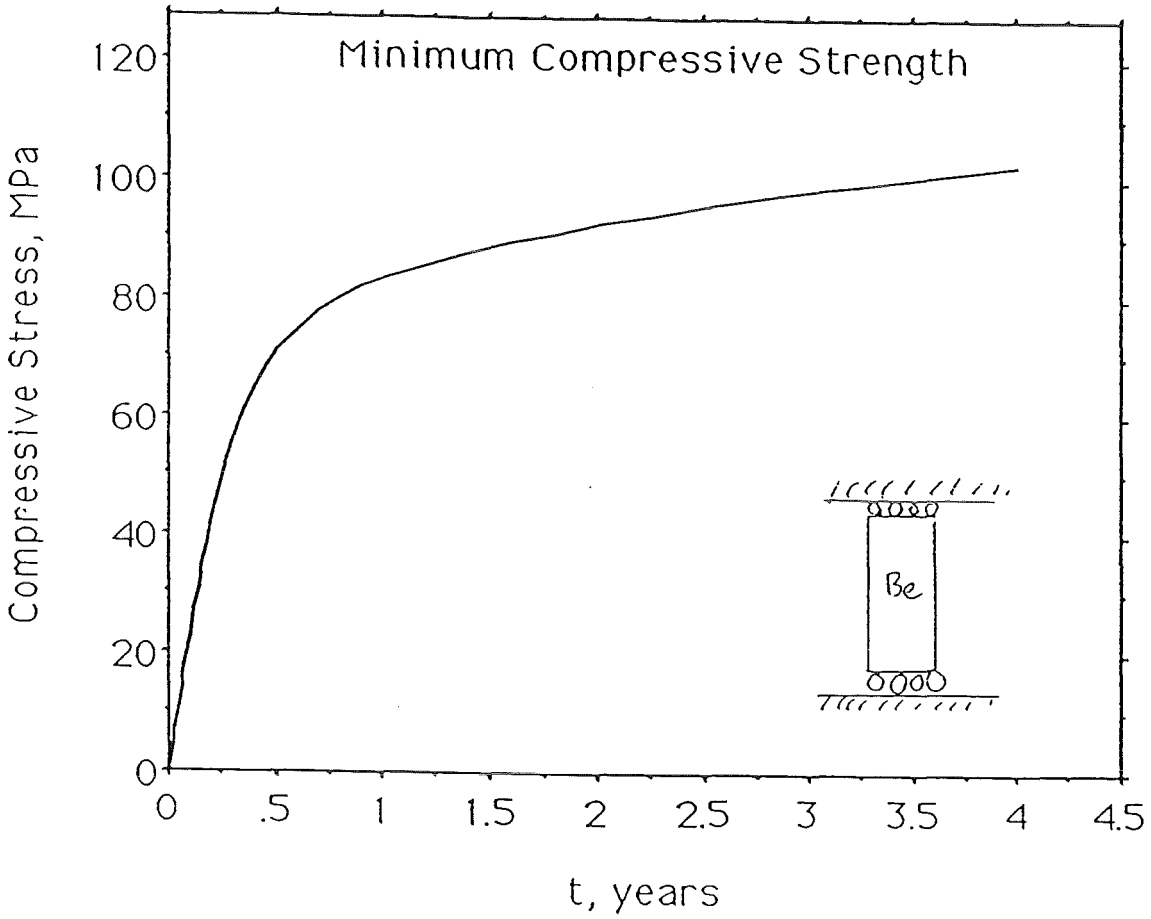

OPTIMIZATION

- **Increasing Temperature**

  Good for tritium release

  Poor for thermal performance; swelling, and compatibility

- **Increasing Porosity**

  Good for tritium release

  May be good for swelling

  Good for Be/structural–material mechanical interaction

  Poor for thermal performance and ductility

- **Decreasing BeO Content**

  Good for ductility

  Good for tritium release???

  Good for swelling???

- **Decreasing Grain Size and Texture**

  Good for ductility

  Good for tritium release???

  Good for swelling???

PNL-SA-22668FP

Radiation Effects in Beryllium Used for Plasma Protection

D. S. Gelles

M. Dalle Donne[a]

G. A. Sernyaev[b]

H. Kawamura[c]

September 21, 1993

To be included in Fusion Reactor Materials Semiannual Progress Report for the Period ending September 30, 1993, DOE/ER-0313/15 and to be submitted as an invited paper for the Sixth International Conference on Fusion Reactor Materials to be held September 27 to October 1, 1993, in Stresa, Italy

Work supported by
the U.S. Department of Energy
under Contract DE-AC06-76RLO 1830

Pacific Northwest Laboratory
Richland, Washington 99352

(a) Kernforschungszentrum Karlsruhe, Germany
(b) SF NIKIET, Russia Federation
(c) JAERI, Tokai-mura, Japan

RADIATION EFFECTS IN BERYLLIUM USED FOR PLASMA PROTECTION

D. S. Gelles
Pacific Northwest Laboratory*
Richland, WA 99352, USA

M. Dalle Donne
Kernforschungszentrum
Karlsruhe
Postfach 36 40
D-7500 Karlsruhe 1, Germany

G. A. Sernyaev
SF NIKIET
Zarechnyi
Russia Federation

H. Kawamura
Blanket Irradiation and Analysis
Laboratory, JMTR,
Oarai Research Establishment, JAERI
Oarai-machi, Nigashi Ibaraki-gun
Japan, 311-13

Abstract

This paper reviews the literature on beryllium, emphasizing the effects of irradiation on essential properties. Swelling and embrittlement experiments as a function of irradiation temperature and dose, and and as a function of neutron spectrum are described, and the results are quantified, where possible. Effects of impurity content are also reported, from which optimum composition specifications can be defined. Microstructural information has also been obtained to elucidate the processes controlling the property changes.

The available information indicates that beryllium divertors can be expected to embrittle quickly and may need frequent replacement.

Introduction

Beryllium is presently a leading candidate material for fusion reactor first wall coating and divertor applications. This is largely a result of improved performance in the Joint European Torus (JET) after evaporated beryllium, and then beryllium tiles as a plasma facing material were installed in the limiter area. [1] In comparison with graphite that had been used previously, beryllium reduced the plasma radiation, increased the density limit, reduced the incidence of disruptions, and enhanced the deuteron pumping. Based in part on its good thermal and physical properties, but also a result of operating experience in JET, beryllium has recently been identified as the material of choice for the International Thermonuclear Experimental Reactor (ITER) both as a plasma facing material and as a divertor material. In that application, it would provide the interface material between plasma and confinement structure in the first fusion reactor to generate significant quantities of 14 MeV neutrons.

Beryllium is also the candidate material of choice as the neutron multiplier in a solid breeder blanket design. In that capacity, it would provide additional neutrons for tritium production in a blanket containing lithium ceramics. However, design optimization studies have shown that the blanket must contain at least 70% beryllium to maximize tritium production. If beryllium is used as a plasma facing material, a divertor material, and blanket neutron multiplier in a fusion reactor design, it is apparent that

*Operated for the U.S. Department of Energy by Battelle Memorial Institute under Contract DE-AC06-76RLO 1830.

the fusion reactor will incorporate beryllium as a major fraction of the materials making up the reactor design. Operating such a fusion reactor may therefore be very dependent on the response of beryllium to 14 MeV neutron damage.

However, beryllium is degraded by radiation damage, both as a result of displacement damage and of transmutation. Displacement damage leads to point defect clustering, irradiation hardening, and embrittlement. Transmutation produces helium (and lithium), resulting in high levels of gas-driven swelling and embrittlement at high temperatures. It is not yet clear what limitations this damage will place on fusion reactor applications. Results of experiments seem to be contradictory. The purpose of this review is to present data concerning effects of irradiation on essential properties. Swelling and embrittlement experiments as a function of irradiation temperature and dose and as a function of the neutron spectrum are described, and the results are quantified where possible. Effects of impurity content are also reported, and the optimum composition specifications can be defined. Microstructural information has also been obtained to explain the processes controlling the property changes. Previously published reviews on this subject may be noted. [2-5]

Neutronic considerations

A major contributor to radiation damage in beryllium, in addition to displacement damage, is the production of helium and tritium from (n,2n) and (n,α) reactions. Each beryllium atom can transmute to two helium atoms upon absorption of a high energy neutron. Absorption of a lower energy neutron produces two helium atoms and one tritium atom. The controlling reactions are as follows:

$$^{9}Be + n \rightarrow {}^{8}Be + 2n \qquad \text{(effective threshold energy 2.7 MeV)}$$
$$^{8}Be \rightarrow 2\,^{4}He \qquad (1)$$

$$^{9}Be + n \rightarrow {}^{6}He + {}^{4}He \qquad \text{(effective threshold energy 1.4 MeV)}$$
$$^{6}He \rightarrow {}^{6}Li$$
$$^{6}Li + n \rightarrow {}^{4}He + {}^{3}H \qquad \text{(Primarily thermal neutrons)} \qquad (2)$$

As a consequence, under high energy neutron bombardment, helium is generated in much greater quantities in beryllium than in any other metal. It has been estimated that for a 14 MeV neutron wall loading of 1 MW/m^2, 4.73 dpa/yr will be produced at a helium generation rate of 617 appm-He/dpa or 2920 appm-He/yr. [3]

Point Defect Accumulation and Swelling

Radiation damage in beryllium can best be characterized by distinguishing between point defect accumulation, point defect coalescence, and gas driven swelling.

Gol'tsev and coworkers [6] have noted that at low temperatures where mobility of point defects is high enough to efficiently recombine and accumule at point defect sinks, but gas atoms are practically immobile, swelling in beryllium can be determined by the expression:

$$\Delta V/V_o \simeq 8.2x10^{-25}\phi t \qquad (3)$$

where ϕt is fast fluence in n/cm^2, E > 0.85 MeV. This is based on irradiations at 60°C, but can be used over the range of temperatures where helium remains in supersaturated solid solution.

From this expression, it can be noted that at a fluence of 10^{22} n/cm^2, a swelling level of 0.8% is predicted. Sernyaev [7] has published swelling data for various grades of pure beryllium irradiated at between 450 and 500°C to doses between $5.7x10^{21}$ and $1.02x10^{22}$ n/cm^2, E > 0.85 MeV. Swelling levels of between 0.4 and 0.8% were recorded, the higher values corresponding to higher fluence levels. Sannen and De Raedt [8] have published swelling data for vacuum hot pressed beryllium irradiated at 40 to 50°C to fluences of 0.8, 2.8, and $3.9x10^{22}$ n/cm^2, E > 1 MeV. Swelling values of 0.65, 1.57, and 2.27% were obtained, and a somewhat lower correlation factor of 0.58 ± 0.3 was recommended for expression (3). Koonen [9] has published swelling data for vacuum hot-pressed beryllium irradiated at 40 to 50°C to fluences as high as $8x10^{22}$ n/cm^2, E > 1 MeV with a maximum of 2.2% diametral swelling (corresponding to 6.6% volumetric swelling if swelling were isotropic.) Finally, Burmistrov and coworkers [10] published measurements on the beryllium core moderator block of an MIR reactor irradiated to a fluence of $3.2x10^{22}$ n/cm^2 at 40°C, noting that the swelling did not exceed 0.3%, but that this was in agreement with expression (3). Therefore, the correlation factor of $8.2x10^{-25}$ may not be valid for all materials.

For example, based on the review by Dalle Donne and co-workers, [11] it can be shown that product form can control swelling response at low irradiation temperatures. Figure 1 provides a plot of volumetric swelling at temperatures below 100°C as a function of helium content, which is proportional to fluence. Significant differences are found between the swelling measurements of Sernyaev [12] and those obtained in western experiments. [13-15] The Sernyaev data points all fall above the trend line defining western measurements. The difference is attributed to modern beryllium production and processing. The Sernyaev results are based on beryllium irradiated in the 1960s, whereas the western data in Figure 1 are more recent and show response on modern beryllium production technology. The earlier Russian beryllium is very anisotropic, with large grains and relatively high amounts of impurities (BeO and others) whereas modern beryllium made by powder processing techniques is fine grained and more isotropic. This therefore emphasizes an effect of microstructure on low temperature swelling response.

An effect of higher fluence is demonstrable from the Koonen measurements [9] where beryllium was irradiated at 40 to 50°C in the BR2 Research Reactor. Non-linear response can be identified for fluences above $6.4x10^{22}$ n/cm^2, E > 1 MeV so that swelling increases either in a bilinear or quadratic fashion from that dose. Based on this response, safety issues have been satisfied to allow irradiation of beryllium as BR2 in-core structural components to this fluence of $6.4x10^{22}$ n/cm^2, E > 1 MeV. This

decision attests to the use of modern hot-pressed beryllium for use in high fluence irradiation applications.

Beeston and Miller [16] provide a somewhat different expression that includes a temperature dependence that applies to the temperature range 400 to 600°C:

$$\Delta V/V_o = 1.83x10^{-58}(\phi t)^2 T^4 \quad (4)$$

where ϕt is fast fluence in n/cm^2, E > 1 MeV, and T is the temperature in K. This dependence was derived from density change measurements made from a beryllium cylinder that was irradiated in a flux gradient in a fast breeder reactor for 4 years and cut into pieces, providing 26 samples with fluences between 0.7 and 1.3x10^{22} n/cm^2, E > 1 MeV, at irradiation temperatures between 427 and 482°C. From this expression, it can be noted that at 500°C and a fluence of 10^{22} n/cm^2, a swelling level of 0.65% is predicted, in reasonable agreement with the data from Sernyaev [7]. However, for an irradiation temperature of 50°C and a fluence of 10^{22} n/cm^2, expression (4) predicts 0.02%, and therefore, this equation cannot predict the results of Sannen and De Raedt [8] or Koonen. [9]

At temperatures where helium and tritium mobility becomes large enough to allow consolidation into large bubbles, the swelling accumulation during neutron irradiation is larger by over an order of magnitude, and the swelling dependence is different. The dependence can be described by the expression from Sernyaev [7]

$$\Delta V/V_o \approx M \cdot T \cdot \exp[-Q/(4kT)](\phi t)^{3/2} \quad (5)$$

where M is a structure-sensitive factor and T, Q, k, and ϕt have their usual meaning. Sernyaev has analyzed available data and found that Q is 2.1 ± 0.1 eV/at and M varies from 0.31 to 1.65x10^{-34} K^{-1} (n/cm^2)$^{-3/2}$. The dependence of M on materials parameters was found to correlate best with a processing procedure such that hot pressing produced significantly higher values for M than did extrusion. However, given a specific processing procedure, M was found to increase with decreasing oxygen content and with increasing grain size. Therefore, to minimize high temperature swelling, extruded materials with oxygen levels on the order of 3% and grain diameters between 10 and 20 μm would be recommended.

Examples of swelling in beryllium irradiated at high temperatures are given in Figure 2. Figure 2 (a) shows the data of Sernyaev [7] from which the structure-sensitive factor analysis described above is based and Figure 2 (b) gives results from Burmistrov. [10] Swelling as high as 18% can be noted in hot-pressed 56 μm grain size beryllium irradiated to 8.9x10^{21} n/cm^2, E > 0.85 MeV. In both plots, it is apparent that swelling in beryllium is sensitive to manufacturing and processing variables.

To understand the consequences on swelling of helium present in beryllium, a number of experiments have been performed where specimens irradiated at low temperatures were subsequently heated to higher temperatures, and the resultant increases in swelling were measured. [16-22] Often, these experiments used 1 hour annealing increments, but many followed the same condition at temperature for many hours. The swelling produced depended somewhat on the neutron fluence, because higher doses produced higher

helium levels. Doses were poorly quantified, but ranged from $5x10^{20}$ to 10^{22} n/cm^2. The general response of annealing experiments can be summarized as follows. Effects of annealing on swelling were only observed for temperatures of 600°C and above, but at 600 and 700°C, all annealing experiments produced swelling levels of 1% or less. [17,21] One hour anneals at 800°C produced swelling levels as high as 14% [17], but generally the values were negligible [18-20,22] or between 3 and 5.5%. [21] One hour anneals at 900°C raise the swelling somewhat, giving values ranging from 0.5 to 17%, and 1000°C anneals raised the maximum values to about 32%, [17] but still higher annealing temperatures of 1100 and 1200°C produced swelling only on the order of 40%. [17,20] The data have been analyzed to show Arhenius behavior (with an activation energy of 40 kcal/mole, about the value for self-diffusion in beryllium) for 1 hour anneals over the temperature range 600 to 900°C, but a saturation in behavior at higher temperatures occurred, corresponding to about 30% (after heating to about 1000°C for 1 hour.) [17]

When longer annealing times were used, [19,20,22] swelling sometimes increased to much higher levels, approaching saturation behavior as noted above. For example, at 800°C where 1 hour anneals produced negligible swelling, anneals for 20 hours [20] and 1000 hours [22] produced swelling on the order of 10%, and at 900°C, anneals for 700 hours produced 10% swelling [22] and for 10 hours produced 25% swelling. [20] The swelling as a function of annealing time has been shown to give linear behavior on log-log plots, and an activation energy of 22 kcal/mole was calculated for the controlling process. [22] However, two examples of rapid swelling after apparent saturation are reported [20], probably similar in process to the tritium burst-release identified in more recent experiments. [8,23]

More recently, Sernyaev [23] has studied the initiation and growth of helium gas bubbles in single crystal beryllium irradiated at 60°C to fluences of 2.6 and $5.1x10^{21}$ n/cm^2, $E > 0.8$ MeV, and then annealed at temperatures of 100 to 1100°C with 1 hour hold times. Techniques employed included small angle x-ray scattering (SAS), differential microcalorimetry (DMC), and transmission electron microscopy (TEM), and it was possible to demonstrate that bubble nucleation occurred at temperatures from 350 to 600°C and that bubbles grew above 600°C. The SAS measurement also allowed estimates of mean bubble diameter as a function of annealing time, with the interesting result that the specimen irradiated to lower fluence developed larger bubbles at temperatures above 775°C with bubbles approaching 12.5 nm in diameter.

Mechanical properties - hardening and embrittlement

Beryllium metal has the hexagonal close packed (HCP) crystal structure with a c/a ratio of 1.5677 at temperatures below 1254°C. As with other HCP and body centered cubic crystal structures, beryllium displays a thermally activated deformation response at low temperatures, leading to increasing yield strength with decreasing temperature, and a tendency for twinning and brittle fracture at low temperatures. Slip has been observed on basal, prism, and pyramidal planes in beryllium, but due to the thermal activation process that controls at low temperatures, slip can become difficult, and embrittlement results if the temperature is low enough. However, beryllium differs from other metals in that the elastic moduli are very high, the interatomic distance is very short, the Poisson's ratio is very low, and

the Debye temperature is very high. [24] All are indications of strong interatomic forces, and therefore beryllium is more sensitive than most metals to embrittlement at low temperatures.

However, manufacturers have successfully produced beryllium with reasonable room temperature mechanical properties. In general, two approaches are responsible: higher purity and refined grain size. This has generally necessitated the use of powder metallurgy fabrication techniques. However, there are few producers of beryllium in the world.

Irradiation adversely affects the mechanical properties of beryllium due to two processes. Point defects produced by radiation damage can cluster to form obstacles to dislocation motion, and helium can migrate to point defect sinks to form bubbles which again produce obstacles to dislocation and grain boundary motion. These bubbles can provide nucleation sites for cracking. Restrictions to dislocation motion are manifested as hardening, strength increases, ductility decreases, fracture toughness decreases, and embrittlement. A large number of studies on beryllium have included experiments to study these phenomena. [17-20,22,25-42] These include results on strength and ductility changes due to irradiation, [18-20,22,25-38] bend test response, [17,38] hardness, [17,18,20,25,27,36,39] fracture toughness, [40-42] and stress rupture. [36,39] However, most of those studies were performed about 30 years ago when an international effort was made to develop beryllium as a fuel cladding material for fission reactors. As a consequence, the dosimetry is crude, and it is very difficult to quantitatively compare results of the different studies. The database on irradiation effects to mechanical properties has been reviewed previously. [36,43]

Studies on strength and ductility changes due to irradiation have shown that, as with swelling studies, irradiation temperature affects response. At low irradiation temperatures, strength increase due to irradiation is most evident, whereas at high irradiation temperatures on the order of 650°C, irradiation embrittlement can occur without significant strength increase. To minimize the possibility of zero ductility response, a number of yield strength measurement techniques have been applied including uniaxial tensile strength, compressive strength, shear strength, splitting tensile strength, flexural strength and three point bend tests.

However, the general trend of the response following low-temperature irradiation is for strength to begin to increase at fluences on the order of 10^{19} n/cm^2 (E > 1 MeV), to saturate as ductility approaches zero, and then to decrease with further fluence. An example is shown in Figure 3 (a) providing comparison of available data for increase in tensile yield strength as a function of fluence. The original plot, provided by Hickman, [43] predicted linear behavior based on the "x" symbols, but more recent data do not support a linear description. Figure 3 (b), originally provided by Beeston and coworkers, [32] shows compressive fracture or yield strength as a function of fluence for specimens irradiated at 120°C and emphasizes the tendency for reduced strength beyond fluences where saturation occurs. Note that saturation in compressive tests can be expected to occur at a higher fluence because compression allows testing to higher levels of strength before failure.

Hardness measurements further demonstrate linear response in strength with fluence at low temperatures. Figure 4 (a) shows diamond pyramid hardness

for beryllium irradiated in the temperature range 35 to 100°C, originally compiled by Hickman, [43] but now including further data, [29] plotted logarithmically as a function of fluence. Hardness values begin to increase at fluences on the order of 2×10^{19} n/cm^2, similar to the yield strength response. The plot is linear with only a hint of saturation.

However, response following irradiation at higher temperatures gives reduced hardening. Figure 4 (b) has been prepared to show this effect. The trend line from Figure 4 (a) is reproduced, and available data points showing hardness increase are plotted and labelled with the irradiation temperature. The tendency is for 280 to 400°C data points to lie close to the trend line, but as irradiation temperature is increased, hardness increase is reduced. Irradiation at 700°C [39] produces softening, and those data points have not been included.

Strength changes following irradiation at 280°C and above follow these trends, but the dependence of strength increase as a function of fluence may be different. Walters [34] has noted that yield strength as a function of dose is linear when plotted as $(\phi t)^{\frac{1}{4}}$ for specimens irradiated at 350°C. Similar slopes are produced by the data from other experiments following irradiation from 280 to 500°C. This response is shown in Figure 5.

At still higher temperatures, such as 650°C and above, the strength behavior is more complicated. About half the experiments indicate a strength increase, [25,26,30] and the rest show a decrease. [18,27,33,39] An explanation is provided in Figure 6, which shows an example of compressive yield strength at room temperature in beryllium specimens irradiated at 650°C. [38] The strength is found to increase to a maximum at fluences on the order of 6×10^{20} n/cm^2, E > 0.85 MeV, and then to decrease to levels significantly lower than the unirradiated strength. This response would explain why, in Figure 4 (b), the hardness values for several lower fluence, high temperature irradiation conditions appear near or on the trend line.

Concurrent with irradiation induced strengthening, reduction in ductility and embrittlement occurs. This was generally because ultimate tensile strength reduced with fluence, and therefore, the allowable plastic deformation was reduced. A number of examples are found in the literature where irradiation resulted in negligible ductility or complete embrittlement during bend testing [16] and tensile testing. [20,21,29,37,38] This included irradiations at temperatures of 100°C or below to fluences as low as 4×10^{21} n/cm^2, [17,20,29], irradiations at 280 to 400°C to fluences of 10^{21} n/cm^2, [20,37,38] and irradiation at 650°C to 10^{21} n/cm^2. [38] However, it is likely that in all cases, the sources of beryllium used older production techniques. No results on hot pressed powder products are reported showing completely brittle response.

Three reports have addressed the issue of fracture toughness degradation due to irradiation. [40-42] However, the first two consider irradiation at liquid nitrogen temperature and are therefore not fusion relevant. Moderate reductions in fracture toughness were found in those cases following low fluence irradiation (8×10^{18} [40] and 7×10^{17} n/cm^2 [41]). They mainly serve to demonstrate the thermal activation nature of beryllium; testing at lower temperature gives lower fracture toughness values. A report by Beeston is more relevant. [42] The material studied was nuclear-grade hot-pressed beryllium, including a porous product intended to expand understanding of

porous material response, and irradiation was to fluences of 3.5 to 5.0×10^{21} n/cm^2, E > 1 MeV at 66°C. The fracture toughness of solid beryllium was found to be reduced from 12.0 MPa $m^{\frac{1}{2}}$ by 60% due to irradiation, and the fracture toughness of porous beryllium with a sightly higher unirradiated value of 13.1 MPa $m^{\frac{1}{2}}$ was reduced 68%.

Microstructural investigations

A number of studies have included efforts to examine microstructural features to better understand irradiation phenomena in beryllium. These have included fractographic examinations to reveal bubbles on grain boundaries, transmission electron microscopy to reveal bubble distributions, and transmission electron microscopy to reveal dislocation loops and black spot damage. Early workers relied on either replica techniques, scanning microscopy, or even optical microscopy to show fracture initiation sites. [17,20,25,26,28,30,33,39,44] Helium bubble investigations considered smaller bubble sizes by using transmission electron microscopy, [10,16,20,23,37,45-48] and often employed annealing experiments to better understand bubble development. [17,19,20,22,23,32,34,44-48] Several studies have noted dislocation loop development as well. [19,23,32,34,37,49-51]

These microstructural investigations confirmed the different regimes of response as a function of temperature noted previously. At irradiation temperatures of 400°C and below, damage consisted of black spot or loop damage. [19,23,32,34,37,45,47,49,50] Burgers vector analysis of the loop structure in irradiated beryllium, when attempted, gave differing results. Following neutron irradiation at 350°C to 2×10^{20} fast n/cm^2, dislocation loops 20 to 70 nm in diameter were generally found on $\{11\bar{2}0\}$ planes, but additional small numbers were also observed on $\{10\bar{1}0\}$, $\{\bar{1}101\}$, and $\{11\bar{2}2\}$ planes, and the Burgers vector responsible in these latter cases was expected to be $\frac{1}{3}\langle\bar{1}123\rangle$. [49] Following neutron irradiation to 4×10^{21} n/cm^2, E > 1 MeV, at 400°C, a low density of $\frac{a}{3}\langle 11\bar{2}0\rangle$ dislocation tangles and a high density of c<0002> loops, approximately 20 nm in diameter, were found. [37] Finally, following 1 MeV electron irradiation at 100°C to a dose of 4 dpa, loops appeared to be close to end-on orientation near $\{11\bar{2}0\}$ planes, and therefore, a Burgers vector of $\frac{a}{3}\langle 11\bar{2}0\rangle$ was indicated. This probably means that the common Burgers vector for loops in irradiated beryllium is $\frac{a}{3}\langle 11\bar{2}0\rangle$, but loops with a $\vec{c}$ component do form at a slower rate.

At higher temperatures, the microstructural product of irradiation is mainly bubbles. Helium bubbles are observed at grain boundaries following irradiation in the temperature range 325 to 400°C, [16,37] and are reported on dislocations within grains following irradiation at 450 to 550. [20,37,46,47] However, following irradiation at temperatures of 600°C and above, all investigators report bubbles, generally on grain boundaries. [10,19,25,26,28,30,33,39,44,46,47] Many of the fractographic studies revealed that large bubbles located on grain boundaries were facetted. This was also noted for smaller cavities, [37,46,47] but in general, bubbles were considered to be spherical.

Many studies included microstructural examinations following high temperature annealing treatments. [17,19,20,22,23,32,34,44-48] The results reported can be summarized with three observations: bubbles formed

on dislocations as a result of anneals in the temperature range 300 to 900°C, [20,39,45,46,48] dislocation loops were annihilated following annealing in the temperature range 500 to 600°C, [19,34,47,48] and only bubbles were present following anneals at 600°C and above. [17,20,22,32,34,48] Also of note is an observation of Shiozawa and co-workers [46,47] that bubbles attached to dislocation networks did not change size and distribution below 900°C. Bubble growth under annealing conditions was presumed to occur only under dislocation and grain boundary sweeping conditions. However, this observation may only apply to annealing experiments; under neutron irradiation, helium atom migration was feasible.

Composition optimization

Three examples of composition optimization have been provided above. Beryllium fabrication is optimized by purification and refined grain size. Analysis of swelling response at high temperatures by Sernyaev [7] showed that swelling is increased (when the M parameter is increased) with decreasing oxygen content and with increasing grain size. Extruded materials with oxygen levels on the order of 3% and grain diameters between 10 and 20 μm would be recommended to minimize swelling at high temperatures. Finally, comparison of swelling response at low temperatures [11] showed that modern fine-grained isotropic materials provide greater swelling resistance than older, coarse grained, anisotropic material with high levels of impurity. All three optimizations indicated that modern fine-grained beryllium will be more serviceable for plasma protection than the materials on which early experiments were based.

Health issues

Use of beryllium is associated with a hazard to health. It has been reputed to be one of the most toxic elements known. However, the toxicity of beryllium metal and its oxide is usually manifested as a lung disease, resulting from inhaling the powder. [52,53] Now known by the name berylliosis, the disease is understood to arise from inhaling powder particles of sufficient fineness (<5 μm) to reach certain lung membranes where they can cause allergic reaction. Large amounts of particles can overwhelm the lungs and lead to respiratory failure. This response may occur relatively soon after excessive exposure, or after a latent period of several years, and the severity of response is variable from one person to another. In fact, other health risks from beryllium, such as cancer, are now discounted. [53]

Therefore, the use of beryllium, per se, in a fusion device does not constitute a hazard to health. Only inhaling significant quantities of fine powders of beryllium leads to berylliosis. It can be argued that the presence of tritium in a fusion device constitutes a much greater health risk.

Discussion

The preceding description of neutron damage to beryllium indicates that beryllium components must be designed with care. Response is different as a function of irradiation temperature, and damage at low temperatures can

lead to gross property changes following heating to higher temperatures. The basic mechanisms controlling behavior are displacement damage and gas production by transmutation. Response can best be divided into four regimes of temperature: (1) low temperature (<RT) response where point defects are created, but mobility is so low that coalescence is rare, (2) somewhat higher temperatures (RT to 300°C), where point defects are mobile, but gas atoms are practically immobile, (3) still higher temperatures (300 to 600°C), where gas atoms become mobile, and (4) very high temperatures where gas pressure driven swelling becomes dominant (>600°C). The lowest temperature regime has been ignored in this report.

Microstructural evolution in these temperature regimes is as follows. At temperatures where point defects are mobile, but gas atoms are not, point defects coalesce into dislocation loops, and the loops grow and evolve into a complex dislocation network with basal and non-basal Burgers vectors represented. Gas atoms become trapped in the microstructure. Therefore, at these temperatures, beryllium displays swelling, at a modest rate, and hardening, which leads to embrittlement. Growth (change in shape under irradiation) can also be anticipated. At temperatures where gas atoms become mobile, gas bubbles form, most visibly on grain boundaries, but are also probably present on dislocations. The accumulation of helium at bubbles is probably by a mechanism similar to solute segregation, dragging impurity atoms to point defect sinks by interaction with moving point defects. Therefore, swelling and mechanical property degradation occur at somewhat different rates than for lower temperature response. Finally, at high enough temperatures where gas bubbles can come into thermal equilibrium, bubbles grow in response to internal pressurization, leading to enhanced swelling and the creation of very large bubbles on grain boundaries. These large bubbles provide crack nucleation sites resulting in embrittlement without significant increases in strength.

Mechanical property degradation can be severe. Examples are provided showing complete ductility loss in beryllium following irradiation to doses on the order of 10^{21} n/cm^2. However, it is apparent that large variations in response are possible, depending on fabrication procedures andthe resultant product form. Results on more modern materials prepared by powder processing and hot pressing give acceptable ductility and fracture toughness, or reduced swelling, and even porous beryllium made in this way gives acceptable ductility and toughness. [31,42] Therefore, it appears that the disappointing results obtained during beryllium fuel cladding development efforts are overly pessimistic.

Given significant property degradation, it should be possible to design blanket and first wall areas so that beryllium components are not required to provide structural support. For example, beryllium can be encapsulated in the blanket and can be replaced by plasma spraying procedures on the first wall. The divertor design should produce greater problems.

However, it must be emphasized that available database information is extremely limited with regard to prototypic material. Also, all irradiation tests have been performed using fission reactors where the major transmutation response is defined by equation (2). As a consequence, effects of lithium and tritium production are overemphasized, and the effects of helium production are somewhat reduced in comparison with the fusion condition where large numbers of neutrons have energies above 2.7 MeV, and therefore equation (1) applies. A more complete database is

required, using prototypic materials irradiated at high temperatures appropriate for divertor applications. Also, high energy neutron irradiation is needed.

Conclusions

This review of neutron irradiation effects to beryllium demonstrates that swelling and embrittlement are significant. They can be expected to be of concern for divertor applications, and may contribute to flaking of first wall coatings. However, more modern fabrication techniques provide materials with greater radiation resistance, and there is cause for hope that they will provide sufficient properties to allow components to operate to fluences on the order of 6×10^{22} n/cm^2, E > 1 MeV or higher.

A much more complete testing program, including high energy neutron irradiation, is required to qualify these newer materials for fusion applications and to determine lifetime limits.

References

[1] P. R. Thomas and the JET Team, presented at the 9th International Conference on Plasma Surface Interactions and Controlled Fusion Devices, held in Bournemouth, UK, 21-25 May 1990, reproduced in JET-P (90) 41,1,

[2] M. F. Smith and A. W. Mullendore, J. Nucl. Mater., 122 & 123 (1984) 855.

[3] W. G. Wolfer and T. J. McCarville, Fusion Tech., 8 (1985) 1157.

[4] J. B. Mitchell, J. Fusion Energy, 5 (1986) 327.

[5] K. L. Wilson, R. A. Causey, W. L. Hsu, B. E. Mills, M. F. Smith, and J. B. Whitley, J. Vac. Sci. Technol., A, 8 (1990) 1750.

[6] V. P. Gol'tsev, G. A. Sernyaev, and Z. I. Chechetkina, Radiatsionnoe Materialovedenie Berilliya, Minsk: Nauka i Tekhnika (1977) 38.

[7] G. A. Sernyaev, "Swelling of Beryllium in a Mode of High-Temperature Neutron Irradiation," Voprosy Atomnoi Nauki i Tekniki, No 2 (56), (1991) 16, PNL-TR-488.

[8] L. Sannen and Ch. De Raedt, "The Effects of Neutron Irradiation on Beryllium," presented at 17th Symposium on Fusion Technology, Rome Sept. 14-18, 1992.

[9] E. Koonen, in Proceedings of the International Symposium on Research Reactor Safety, Operations and Modification, AECL-9926, Vol. 3 (1990) 737.

[10] V. N. Burmistrov, Yu. D. Goncharenko, V. A. Kazakov, O. Yu. Shvedov, V. A. Gorokhov, and I. B. Kupriyanov, "Certain Aspects of the Radiation Stability of Beryllium with Application to Synthesis

Reactor Conditions from Results of Tests in a Fission Reactor," presented at the Second International Conference on Effects of Irradiation on Materials for Fusion Reactors, held September 21-24, 1992 in St. Petersburg, Russia, PNL-TR-487.

[11] M. Dalle Donne, F. Scaffidi-Argentina, C. Ferrero and C. Ronchi, "Modelling of Swelling and Tritium Release in Irradiated Beryllium," proceeding of ICFRM-6.

[12] G. A. Sernyaev, "Some Physical Properties of Beryllium as a Material for Neutron Multiplier," in Modular Variant of ITER Ceramic Blanket (ITER, Garching, Germany, July 1990).

[13] J. M. Beeston, "Properties of Irradiated Beryllium: Statistical Evaluation, EG&G Idaho Report TREE-1063 (1976).

[14] E. Koonen, "Study of Irradiation Effects and Swelling of Irradiated Beryllium," CEN/SCK Report, Reactor Safety Analysis BR2 Department (1989). (See also [9])

[15] J. M. Beeston, G. R. Longhurst, L. G. Miller, and R. A. Causey, "Gas Retention in Irradiated Beryllium," EGG-FSP-9125 (1990).

[16] J. M. Beeston, L. G. Miller, E. L. Wood, Jr., and R. W. Moir, J. Nucl. Mater., 122 & 123 (1984) 802.

[17] J. B. Rich, G. B. Redding, and R. S. Barnes, J. Nucl. Mater., 1 (1959) 96.

[18] B. S. Hickman, in The Metallurgy of Beryllium, Inst. of Metals Monograph No. 28 (Institute of Metals, London, 1961) 410.

[19] J. B. Rich and G. P. Walters, in The Metallurgy of Beryllium, Inst. of Metals Monograph No. 28 (Institute of Metals, London, 1961) 362.

[20] J. B. Rich, G. P. Walters, and R. S. Barnes, J. Nucl. Mater., 4 (1961) 287.

[21] C. E. Ells and E. C. W. Perryman, J. Nucl. Mater., 1 (1959) 73.

[22] S. Morozumi, S. Goto, and M. Kinno, J. Nucl. Mater., 68 (1977) 82.

[23] G. A. Sernyaev, "The Formation of Helium Bubbles and Energy Phenomena in Beryllium," Voprosy Atomnoi Nauki i Tekniki, No 2 (56), (1991) 82, PNL-TR-490.

[24] D. McLean in Conference Internationale sur la Metallurgie du Beryllium (Presses Universitaires de France, Grenoble, 1965) 3.

[25] B. S. Hickman, G. Bannister, J. H. Chute, J. G. McCracken, R. Smith, and J. C. Bell, "Irradiation of Beryllium at Elevated Temperatures," TRG Report 540, UKAEA, 1963.

[26] B. S. Hickman and G. Bannister, "Irradiation of Beryllium at Elevated Temperatures," Part II, AAEC/E-115, 1963, also issued as TRG Report 532.

[27] B. S. Hickman and G. T. Stevens, "The Effect of Neutron Irradiation on the Mechanical Properties of Irradiation of Beryllium at Elevated Temperatures," Part II, AAEC/E-115, 1963, also issued as TRG Report 532.

[28] G.T. Stevens and B. S. Hickman, "Effect of Irradiation on the Mechanical Properties of Beryllium Metal," AAEC/E-133, 1965.

[29] M. H. Bartz, in Proceedings of the 2nd United Nations International Conference on the Peaceful Uses of Atomic Energy, Vol. 5 (United Nations, Geneva, 1958) 466.

[30] J. M. Beeston, in Effects of Radiation on Structural Materials, ASTM STP 426, (ASTM, Philadelphia PA, 1967) 135.

[31] J. M. Beeston, G. R. Longhurst, R. S. Wallace, and A. P. Abeln, J. Nucl. Mater., 195 (1992) 102.

[32] J. M. Beeston, M. R. Martin, C. R. Brinkman, G. E. Korth, and W. C. Francis, in Symposium on Materials Performance in Operating Nuclear Systems, M. S. Wechsler and W. H. Smith, Eds., CONF-730801 (1973) 59.

[33] E. D. Hyam and G. Sumner, in Radiation Damage in Solids, I (IAEA, Vienna, 1962) 323.

[34] G. P. Walters, J. Less Common Metals, 11 (1966) 77. (Earlier version in Conference on the Physical Metallurgy of Beryllium, Gatlinburg, 1963, CONF-170, 138.)

[35] E. H. Smith, J. L. Liebenthal, B. V. Winkel, J. M. Beeston, and W. C. Francis, in Symposium on Materials Performance in Operating Nuclear Systems, M. S. Wechsler and W. H. Smith, Eds., CONF-730801 (1973) 41.

[36] J. M. Beeston, Nucl. Engineering and Design, 14 (1970) 445.

[37] D. S. Gelles and H. L. Heinisch, J. Nucl. Mater., 191-194 (1992) 194.

[38] V. Barabash, "Brief Review of Be Study for Plasma Facing Component in RF for ITER Reactor," presented at the US/RF Exchange Meeting, September 17-19, 1992, in St. Petersburg, Russia.

[39] J. R. Weir, in The Metallurgy of Beryllium, Inst. of Metals Monograph No. 28 (Institute of Metals, London, 1961) 395.

[40] D. L. Harrod, T. F. Hengstenberg and M. J. Manjoine, J. Materials, 4 (1969) 618.

[41] R. L. Kesterson, Trans. Amer. Nucl. Soc., 14 (1971) 607.

[42] J. M. Beeston, in Effects of Radiation on Structural Materials, ASTM STP 683, (ASTM, Philadelphia PA, 1979) 309.

[43] B. S. Hickman, in Studies in Radiation Effects, Series A, Vol. 1, G. J. Dienes, Ed. (Gordon & Breach Science Publishers, Inc., N.Y., 1966) 72.

[44] R. Sumerling and E. D. Hyam, in The Metallurgy of Beryllium, Inst. of Metals Monograph No. 28 (Institute of Metals, London, 1961) 381.

[45] R. S. Barnes in The Metallurgy of Beryllium, Inst. of Metals Monograph No. 28 (Institute of Metals, London, 1961) 372.

[46] Y. Mishima, S. Ishino, and S. Shiozawa, in Beryllium 1977, (The Royal Society, London, 1977) 25/1.

[47] S. Shiozawa, thesis, "The Electron Microscopic Studies on the Irradiated and Deformed Hexagonal-Close-Packed Metals, University of Tokyo, 1977.

[48] R. Nagasaki, S. Ohashi, S. Kawasaki, Y. Karita and N. Tsuno, J. Nucl. Sci. Tech., 8 (1981) 546.

[49] G. P. Walters, C. M. Van Der Walt, and M. J. Makin, J. Nucl. Mater., 11 (1964) 335. (Earlier version in Conference on the Physical Metallurgy of Beryllium, Gatlinburg, 1963, CONF-170, 126.)

[50] G. J. C. Carpenter and R. G. Fleck, in Beryllium 1977, (The Royal Society, London, 1977) 26/1.

[51] R. G. Fleck, in Effects of Radiation on Materials, ASTM STP 782, (ASTM, Philadelphia PA, 1982) 735.

[52] W. Jones Williams, in Beryllium 1977, (The Royal Society, London, 1977) 47/1.

[53] O. P. Preuss, Fusion Tech., 8 (1985) 1137.

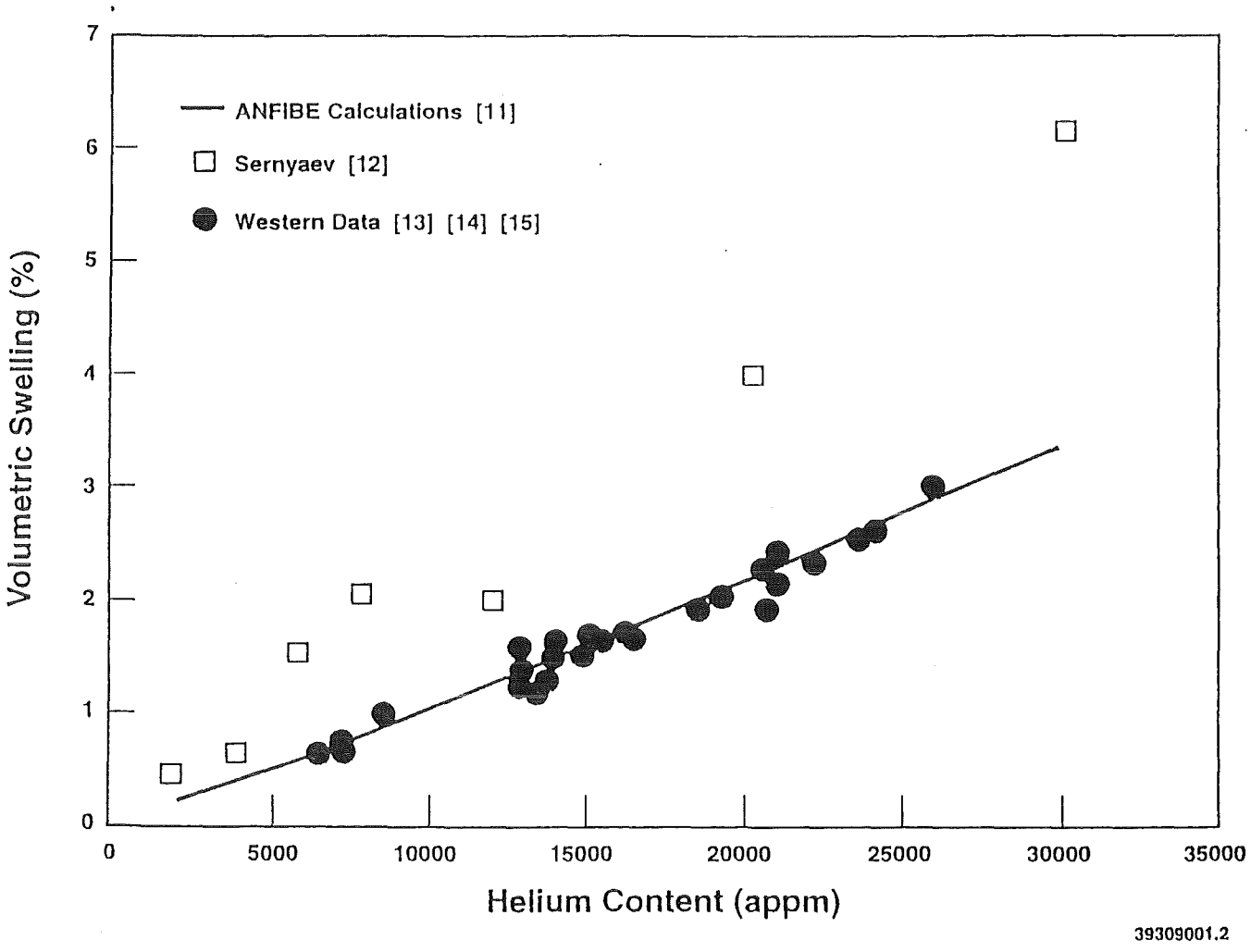

Figure 1. Swelling in beryllium irradiated at temperatures below 100°C as a function of helium content.

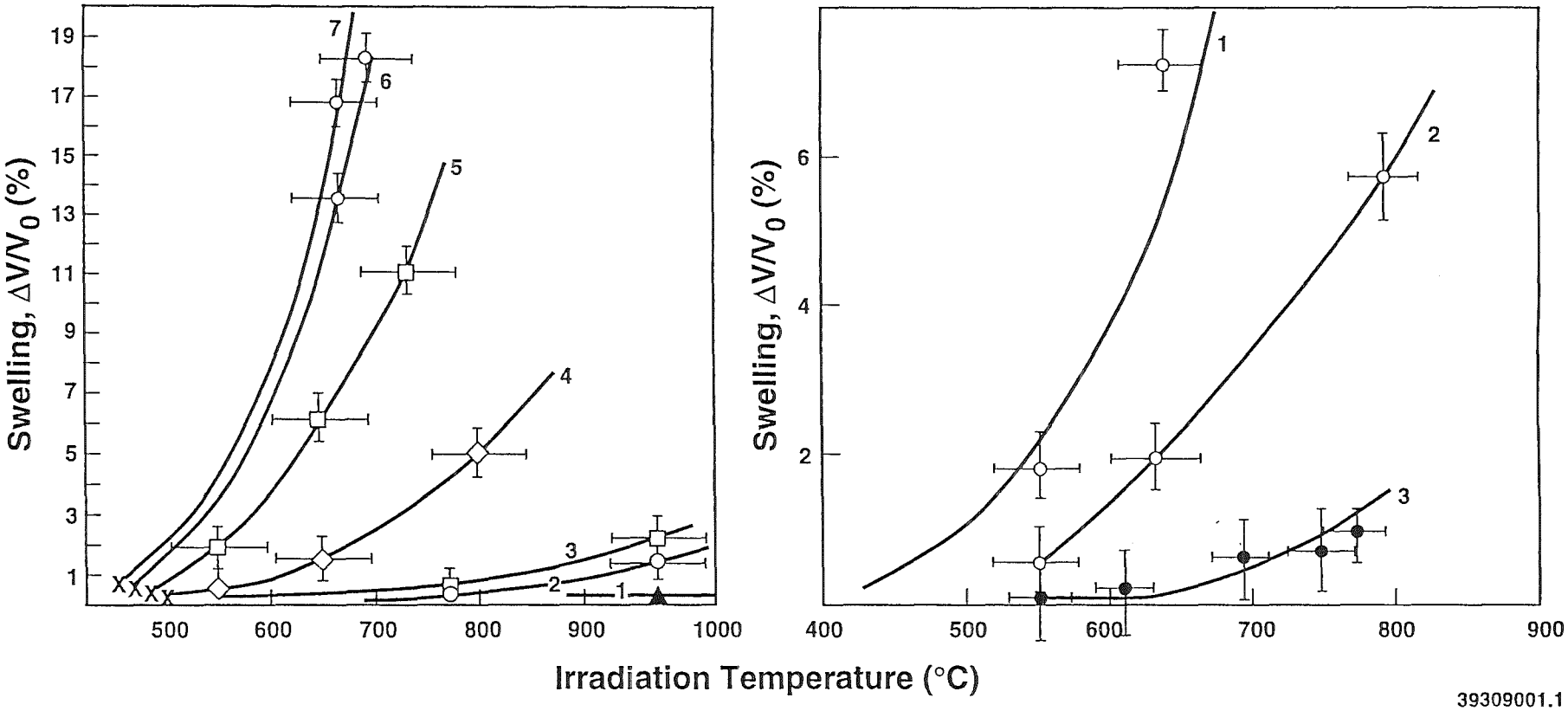

Figure 2. Swelling in Beryllium as a function of irradiation temperature (a) from [7] and (b) from [10]. Notation in (a) is as follows: (1) is single crystal; (2, 6, 7) are hot pressed, grain size (g.s.) 56 μm; (3,5) are hot pressed, g.s. 600 μm; (4) is thermally extruded, g.s. 400 μm. Also, (1-3) are at 6×10^{20}, (4,5) are at 5.7×10^{21}, (6) is at 8.9×10^{21} and (7) is at 1.02×10^{22} n/cm^2, E > 0.85 MeV.; notation in (b) is as follows: (1) g.s. 30 μm, (2) g.s. 20 μm, and (3) g.s. 8 to 13 μm and fluences for (1,2) 5.7×10^{21}, and for (3) 3.5×10^{21} n/cm^2 (E > 0.1 MeV).

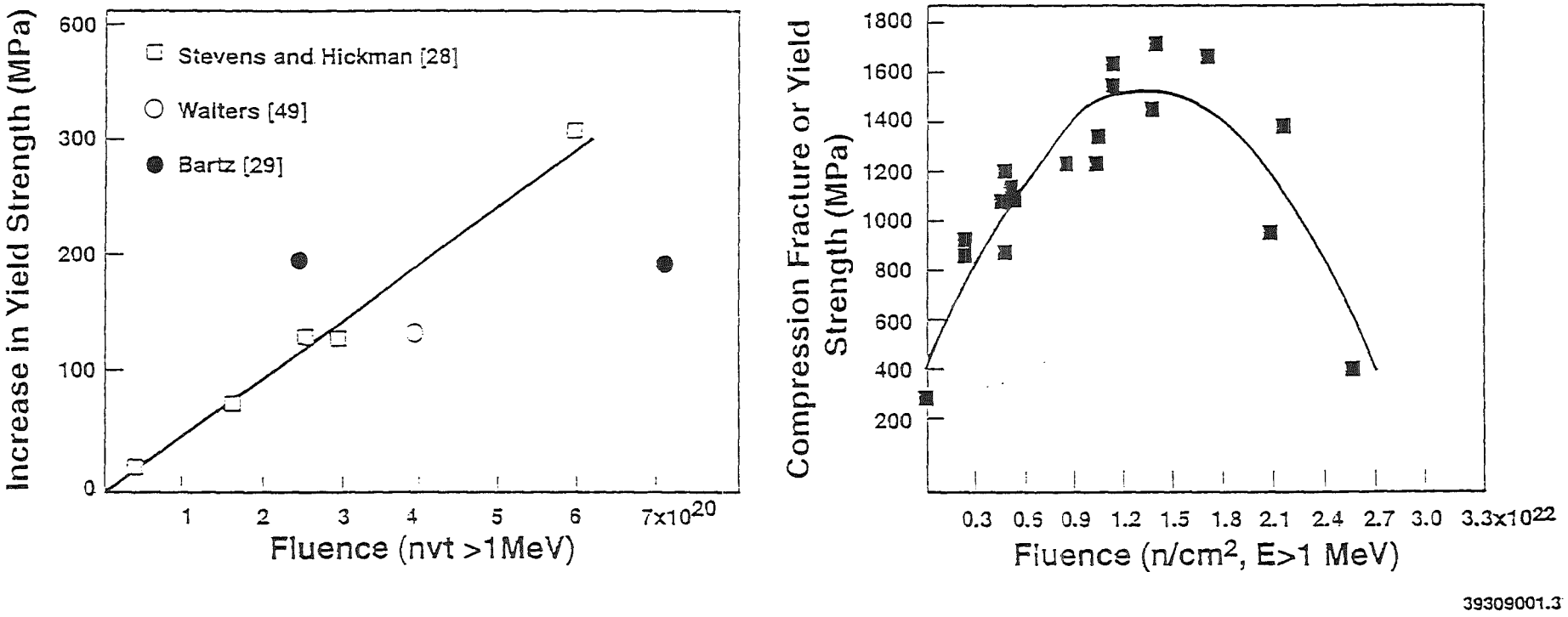

Figure 3. Tensile strength increase (a) or compressive fracture or yield strength (b) as a function of Fluence (E > 1 MeV) for beryllium specimens irradiated at 75 to 125°C.

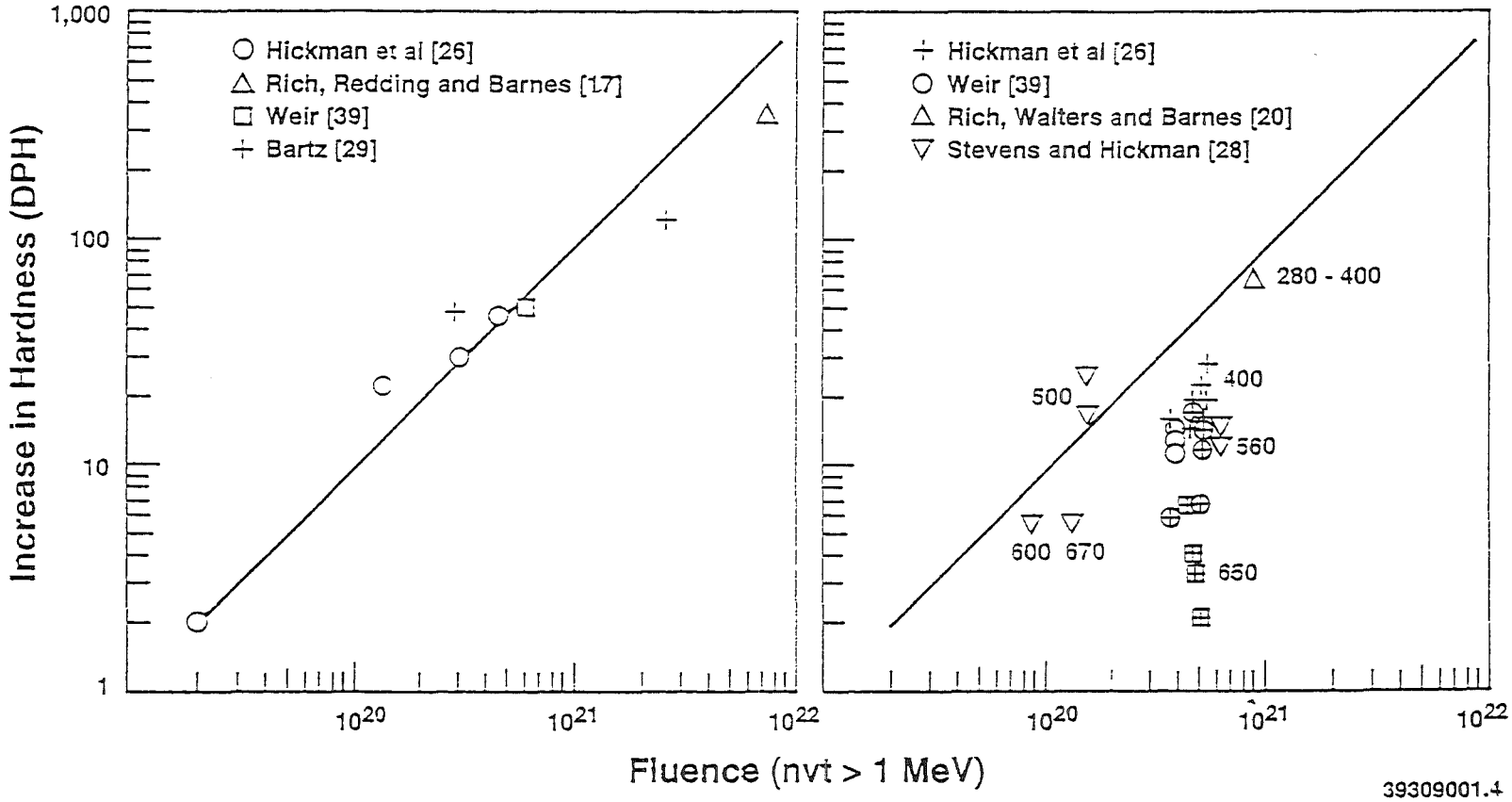

Figure 4. Increase in hardness as a function of fluence for beryllium specimens (a) irradiated at 35 to 100°C and (b) irradiated at 280 to 650°C.

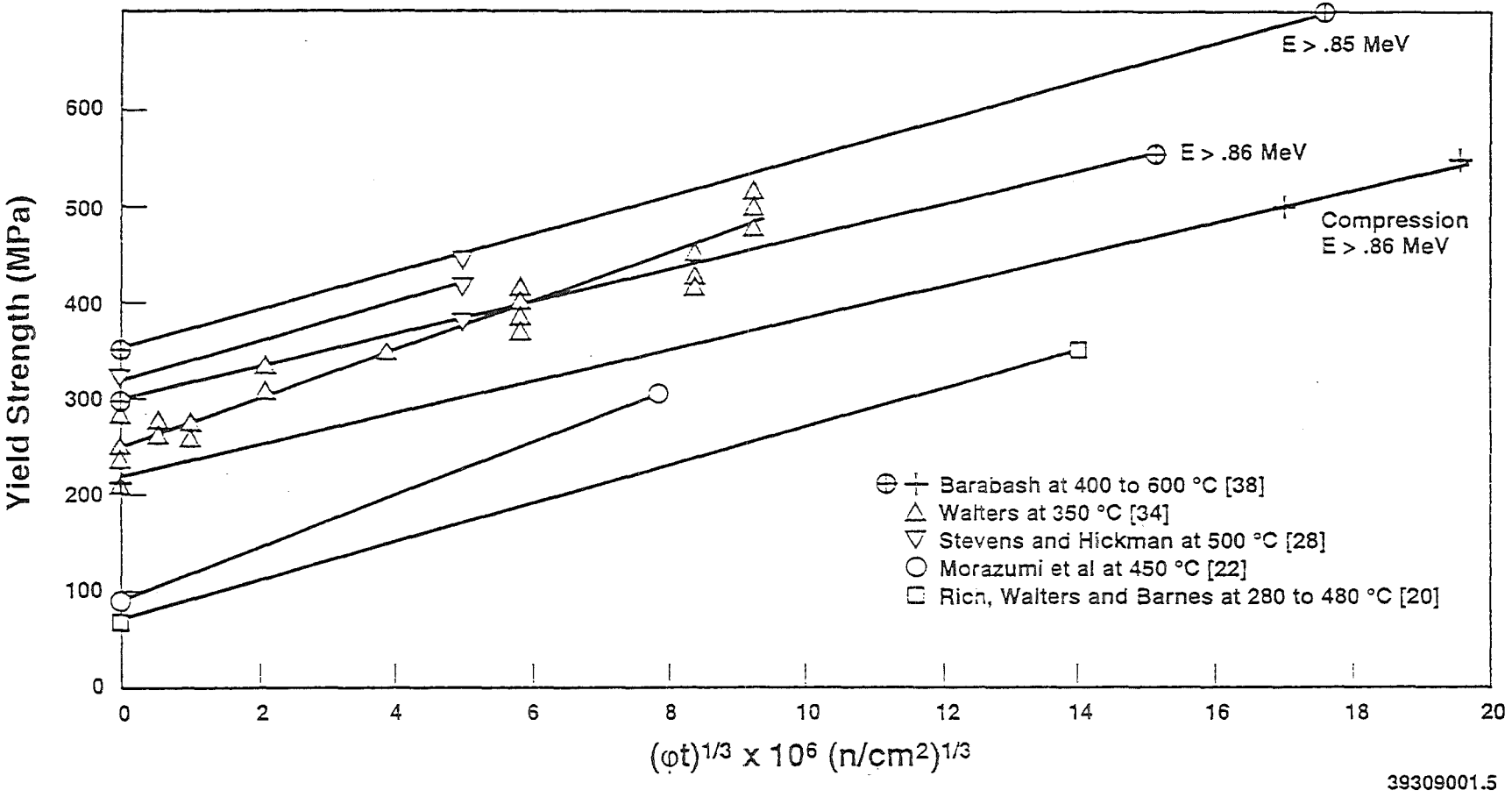

Figure 5. Increase in yield strength as a function of fluence to the 1/3 power for intermediate irradiation temperatures as per Walters. [34] All measurements are in tension and for fluences of E > 1 MeV except where noted.

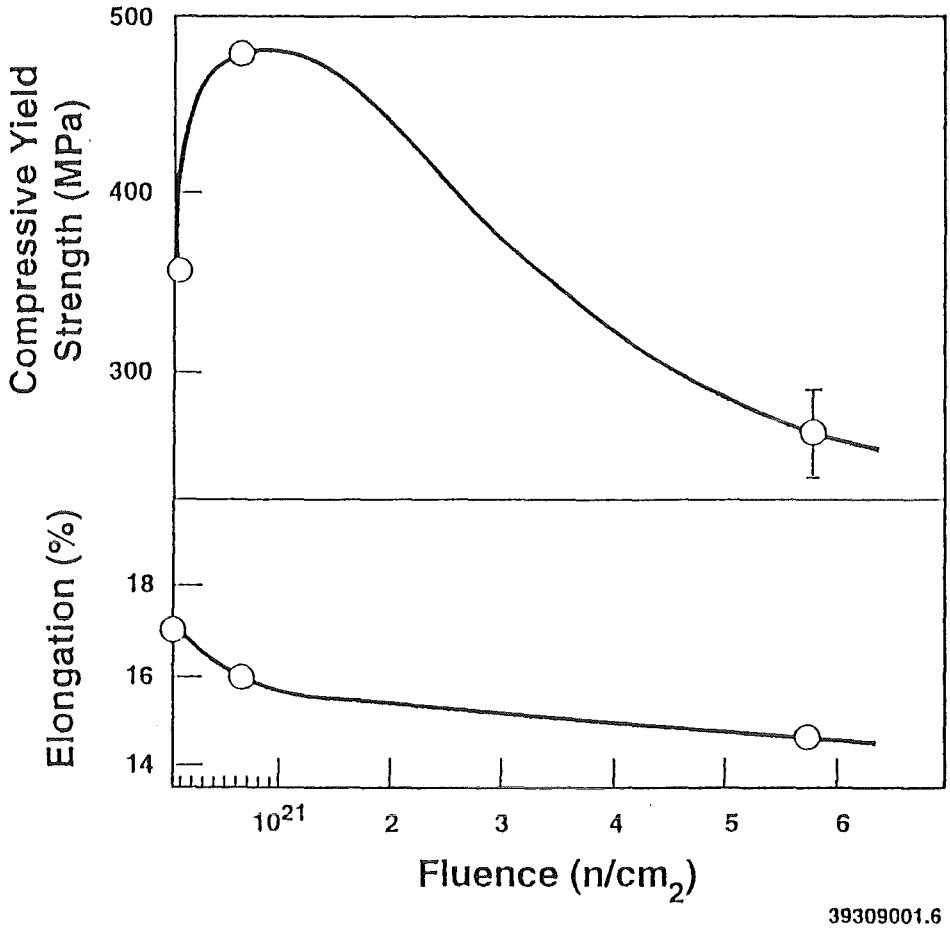

Figure 6. Compressive strength and Elongation as a function of fluence (E > 0.85 MeV) for beryllium specimens irradiated at 650°C. [38]

STATUS OF Be IRRADIATION EXPERIMENTS IN USA

Be SPECIMENS HAVE BEEN INCLUDED IN STRUCTURAL MATERIALS IRRADIATION EXPERIMENTS IN FFTF & EBR-II

- FFTF IRRADIATIONS IN MOTA
  USING Li FILLED TZM CAPSULES

- EBR-II IRRADIATIONS IN A WEEPER CANISTER
  USING He FILLED SS CAPSULES

DOSES ARE IN THE RANGE 10 TO 30 DPA

FFTF/MOTA 2A MATRIX

SPECIMENS AT 425°C

V460	.375 OD x 2.5	2 0.30" Be cylinders & 3 TEMs/Li (.19)
V461	.375 OD x 2.5	2 0.30" Be cylinders & 3 TEMs/Li (.19)
V462	.375 OD x 2.5	2 0.30" Be cylinders & 3 TEMs/Li (.18)
V463	.375 OD x 2.5	2 0.30" Be cylinders & 3 TEMs/Li (.18)
V464	.375 OD x 2.5	2 0.30" Be cylinders & 3 TEMs/Li (.19)

FFTF/MOTA 2B MATRIX

V308	370°C	.375 OD x 2.5	4 0.30" Be cylinders/Li (.22)
V309	370°C	.375 OD x 2.5	4 0.30" Be cylinders/Li (.21)
V310	370°C	.375 OD x 2.5	2 0.30" Be cylinders & 12 TEMs/Li (.21)
V311	370°C	.375 OD x 2.5	2 0.30" Be cylinders & 7 TEMs/Li (.21)
V312	370°C	.375 OD x 2.5	0.30" Be cylinder & 7 TEMs/Li (.23)
V487	425°C	.375 OD x 2.5	4 0.30" Be cylinders/Li (.21)
V488	425°C	.375 OD x 2.5	4 0.30" Be cylinders/Li (.24)
V489	425°C	.375 OD x 2.5	2 0.30" Be cylinders & 12 TEMs/Li (.21)
V490	425°C	.375 OD x 2.5	2 0.30" Be cylinders & 7 TEMs/Li (.21)
V491	425°C	.375 OD x 2.5	0.30" Be cylinder & 3 TEMs/Li (.24)
V566	550°C	.375 OD x 2.5	4 0.30" Be cylinders/Li (.23)
V567	550°C	.375 OD x 2.5	3 0.30" Be cylinders & 2 Discs/Li (.22)
V568	550°C	.375 OD x 2.5	2 0.30" Be cylinders & 11 TEMs/Li (.23)
V569	550°C	.375 OD x 2.5	3 0.30" Be cylinders & 6 TEMs/Li (.20)
V570	550°C	.375 OD x 2.5	0.30" Be cylinder & 3 TEMs/Li (.23)
V571	550°C	.375 OD x 2.5	0.30" Be cylinder/Li (.24)

EBR-II/COBRA 1A MATRIX

D03	.75 OD x 9.25	18 0.30" Be cylinders, many 1 mm and 5 mm balls & Mo spacer/He
C03	.75 OD x 9.42	18 0.30" Be cylinders, many 1 mm, 3 mm and 5 mm balls & Mo spacer/He

FUTURE IRRADIATION PLANS

SPECIMENS IRRADIATED IN MOTA 1B AT 425°C ARE TO BE REIRRADIATED IN EBR-II TO ABOUT DOUBLE THE PRESENT DOSE

HOWEVER, NO MONEY HAS BEEN MADE AVAILABLE TO OPEN ANY OF THE IRRADIATED CAPSULES

- SAM BERK IS WORKING ON THE PROBLEM

- LACK OF COMMITTMENT FROM ITER FOR BLANKET DEVELOPMENT IS A MAJOR DIFFICULTY

Defect Formation in Single Crystalline Beryllium

F. Mücklich, U. Scholz and G. Petzow
Max-Planck-Institut für Metallforschung, Stuttgart, PML,
Heisenbergstr.5, D-70569 Stuttgart

ABSTRACT

The paper presents some studies on the mechanisms of dislocation formation in single crystalline Beryllium.
Due to the low solubilities of only ppm for most of the impurity atoms in the Beryllium lattice, precipitation formation limits the single crystal growth very strictly. Therefore measurements with high sensitivity such as Rutherford Backscattering have been applied to find reliable estimations for absolute solubilities of the most critical impurities and for their local distribution with respect to defect arrangements such as subgrain boundaries.
The strong mechanical anisotropy of the hexagonal Beryllium lattice is a key factor controlling the dislocation formation procedures during crystal growth and also during crystal annealing as well as during deformation procedures.

INTRODUCTION

Dealing with single crystalline material is done in many cases to study a well defined model case. This is of course also valid for single crystalline beryllium. Moreover, beryllium exhibits an extraordinary combination of properties which emphasise its unique potential as a monochromator material for neutrons as well as for X-rays, in particular for synchrotron radiation [88Fre]. Therefore, defect structure design for a controlled scattering behaviour are an additional part of motivation for the investigations in single crystalline beryllium.
Fig.1 illustrates some of the relevant properties of beryllium in comparison to the conventional materials in use so far. The coherent cross section for neutrons is the highest of the elements which can practically applied. In the same time the incoherent losses are smaller than for the other elements. For the monochromatization of synchrotron radiation especially the better thermal properties together with the very low absorption (Fig.2) play the dominating role for the expected superior monochromator behaviour. In both cases (neutrons as well as X-rays) the small lattice distances improve the resolution functions and therefore the quality of monochromized beams. The low absorption of X-rays enables quite new experimental arrangements (e.g. Fig.3), where beryllium crystals are applied in transmission (so called Laue case) and extract only the desired wavelength out of the polychromatic beam. The rest of the spectra penetrates the crystal with only low absorption losses (and corresponding thermal effects) and can be used for additional monochromatization of other wavelengths by similar crystals with slightly different angular positions [93Als].
The different proposed variants of application call for a real defect structure design. Whereas the neutron monochromator applications need a high concentration of dislocations which corresponds to misorientations of lattice planes up to 0.5 degree,

the X-ray applications should have very low defect concentrations but also homogeneous distributed dislocation ensembles corresponding to lattice misorientations which do not exceed 30 seconds of arc. In both cases homogeneous distributions without subgrain boundary arrangements are preferred.
To get insights into this subject, basic experiments concerning defect formation in single crystalline beryllium are necessary.

REMARKS TO THE STRUCTURAL PECULIARITIES

The discussion of lattice defect formation in beryllium should be concentrated on dislocations, because they are the most effective defects also for the scattering behaviour. In hexagonal crystal structures the c/a ratio plays an important role for the dislocation formation and propagation in the real lattice. Fig. 4 indicates, that Be has the smallest of all c/a-ratios. That means a higher density of atoms in the prismatic planes than in the basal planes. Nevertheless the basal plane is still the primary slip plane because only in the basal plane the electron overlap is strong and represents a metallic behaviour whereas in the c-direction significant covalent parts of bond have been realised [79Ald]. This corresponds to a strong anisotropy of the mechanical behaviour. Fig. 5 shows the well known diagram of Critical Resolved Shear Stresses for the different lattice planes versus temperature. For example at room temperature the ratio between the shear stresses for the different slip systems is 1:40:2000 MPa. Of course this has significant effects also for the defect formation in the single crystalline state and for the chances of single crystal growth itself.

CONSEQUENCES FOR CRYSTAL GROWTH

A number of different attempts for a single crystal growth had been undertaken in the past. Most of conventional growth techniques such as Czochralski (Univ. Grenoble, Physico-Technical Inst. Kharkov) and Bridgman techniques (Franklin Inst.) or direct crystallisation from the vapour phase (Kharkov) failed in growing macroscopic crystals. Successful crystal growth have been established using the procedure of crucibleless zone melting. This growth technique uses a special version of sample heating by a mirror furnace (Fig. 6)[79Jön]. In comparison to other growth techniques, the energy is focused on a small lateral region, producing a strong temperature gradient in the crystal axis.
Close to the melting point of pure Be (1287°C) a phase transition from the bcc to the hcp crystal structure takes place (1254°C) [79Pet]. This phase transition is connected with a significant volume effect of 4.9% and a high transition enthalpy of 837 kJ/kg [72Hul]. Therefore a quick transition to the hcp structure without a complete formation of the high temperature bcc-phase might improve the chances of higher lattice perfection in the hcp lattice. This is done in the mirror furnace due to its strong temperature gradient at the solidification front.
The first results of crystal growth exhibit still significant subgrain formations which can be detected by Gamma-ray diffraktometry (each rocking curve represents the orientation distribution of the reflecting lattice plane in the penetrated volume through the crystal). The micrograph of such a subgrain boundary (Fig. 8) exhibits

the fan out of dislocations in its neighbourhood (note the different dislocation arrangements on basal (vertical) and prismatic planes (horizontal) due to the strong lattice anisotropy).

IMPURITY INFLUENCES

Annealing experiments at sufficient temperatures to reorganise the dislocation arrangements of the subgrain boundary showed different results. In Fig. 9 subgrain boundaries of type I have significantly been affected by a reduction of the width of the rocking curve which corresponds to a reduction of the misorientation or even dissolution of the subgrain boundary. In contradiction to that the subgrain boundaries of type II only show an increased perfection of each individual subgrain but no reduction of the misorientation between them. The difference of subgrain boundaries of type I and II has been characterized by careful local measurements of the chemical composition with high sensitivity. Therefore, Rutherford Backscattering (RBS) was helpful to measure a significantly increased concentration of critical elements in the region of subgrain boundaries of type II. Figure 10 is the result of RBS scans across a subgrain boundary type II which indicates impurity concentrations of more than 200 ppm also in the depth at the boundary. In samples of TEM prepared from this regions different types of precipitations have been found, which are clearly the pinning centres of dislocations (Fig. 11). If the annealing is insufficient for the dissolution of these precipitations, also the subgrain boundary withstands the annealing [93Müc].
Of course this calls for a sufficiently low impurity content in the raw material for single crystal growth. Nevertheless, even an impurity content below the limits of solubility can be hazardous, because RBS scans along cross sections of a single crystal clearly show the local enrichments of impurity concentrations which are the projections of striations of a slightly convex solidification front. The spiral path of the impurity enrichments corresponds to oscillations of the impurity concentrations, which are incorporated at the solidification front due to mechanisms of constitutional supercooling. In order to compensate these local enrichments the concentration of impurities should be further reduced. As a nondestructive and practical characterization of the impurity content of the purified raw material the measurement of residual resistance ratio has been established. Resistance ratios exceeding 8-12 indicate a sufficient purification state of the polycrystalline rod. This has been adjusted by a number of measurements along single crystals with high lattice perfections.

MANIPULATION OF DEFECT STRUCTURES

If the problem of subgrain boundary formation is solved mainly by avoiding overcritical concentrations of impurity concentrations, further reduction of the dislocation content can be achieved by manipulations of the growth conditions. The scheme in Fig. 14 illustrates the sources of dislocation creation and their interactions which result in stable configurations for crystal growth processes. Additional to the general situation also constitutional stresses due to the already mentioned phase transition must be taken into account.

As an example for variations of growth conditions Fig. 15 shows different crystals (diameter 15mm, length around 100mm) with different crystallographic orientations of the crystal with respect to the nonradial temperature field. The free grown surface exhibits different shapes of the former solidification front, represented by the striations. As a consequence of these experiments a strong symmetry of low indexed lattice planes towards the higher temperature gradients perpendicular to the mirror axis must be adjusted. The higher thermal conductivity in these directions ensures the minimum sagging of the solidification front and controls a minimum concentration of incorporated defects.

The temperature gradient during phase transition has already been mentioned as a key factor for the stress creation and therefore the dislocation incorporation. An improved (increased) temperature gradient at the solidification front combined with a reduced gradient during cooling has been modelled theoretically (Fig. 16) by the defocusing of the light sources (Fig. 17), which have been proofed also experimentally.

The result of these manipulations was an increase in lattice perfection corresponding to a decrease of the angular width of the Gamma-Rocking curve from around 4-6 min of arc down to 40-60 seconds of arc. Simultaneously the peak intensity increased by more than 100 % (Fig.18).

Nevertheless the defect structure is very anisotropic which is indicated by the White Beam X-ray Topography images in Fig. 20. Whereas the upper reflections exhibit a rather homogeneous lattice perfection, the lower ones clearly indicate a "plate-like" defect structure. That means different defect concentrations are simulated in different reflections. The scheme in Fig. 19 explains the situation. If crystals are grown in a prismatic direction (which is the most suitable case), the thermal stresses during cooling are able to create dislocations in particular on the basal plane (horizontal lines), due to the very low critical resolved shear stresses in this slip system (comp. Fig.5). The highest Schmid factor for this slip system is valid around the 45° case (double arrows). As a consequence the dislocations are concentrated mainly in each quarter as indicated. An analogous situation is valid for the prismatic slip system (right part of the scheme).

Beside the anisotropic distribution of the dislocations also the effect of each dislocation on Bragg scattering is not isotropic corresponding to the projection of the chosen scattering vector onto the strain field of this dislocation. If the scattering vector is perpendicular to the Burgers vector of the dislocation, its strain effect is rather small (edge dislocations) or even zero (screw dislocations). Therefore by rotating the crystal lattice around the scattering vector, type and concentrations of the dislocations can be measured independently (Fig. 21). On the prismatic planes stress induced edge dislocations can be detected ($b=1/3\langle 110\rangle$) with concentrations of 10^5 per cm^2. Concentrations of basal dislocations with the same Burgers vector are between 10^3 and 10^4 per cm^2. They can significantly be reduced by annealing. In contradiction to these types the grown in networks often parallel to the growth axis and with c-type Burgers vectors are much more stable.

SUMMARY

Single crystalline beryllium material can be achieved by careful crucible free growth procedures. For the occurrence of stable subgrain boundaries in particular overcritical impurity concentrations should be responsible. Due to constitutional supercooling the overall impurity level must be lowered even below the equilibrium solubility limit. Concentrations of dislocations can be significantly reduced by optimized crystal growth experiments. The defect concentrations remain at different levels in the different lattice planes as a consequence of the strong mechanical anisotropy of the crystal lattice.
Further manipulations of the defect structure should include attempts for the reduction of the mechanical anisotropy of the crystal lattice itself. This seems to be possible by doping with elements such as copper [92Müc].
In general a defect structure design should be carried out within the tetrahedron of crystal growth, annealing, deformation and doping. In this way single crystalline beryllium has a good chance to become a new functional material.

Acknowledgement

The authors very much appreciate the X-ray topography work of F.Zontone and J.Baruchel from ESRF in Grenoble.

References

[72Hul] R. Hultgren, R.L. Orr, K.K. Kelley, Supplement Values of Thermodynamic Properties of Metals and Alloys (University of California, Berkeley, 1972)

[79Ald] F. Aldinger, in: Beryllium Science and Technology, Eds. D. Webster and G.J.London, Plenum Press, New York, London, 1979, pp.7-107,

[79Jön] S. Jönsson, A. Freund and F. Aldinger, Metall 12(1979)1257

[79Pet] F. Aldinger and G. Petzow, dto., pp. 235-295

[79Sto] A.J. Stonehouse, dto., pp. 181-204

[88Fre] A.K. Freund, Nucl.Instr.&Methods A266(1988)461-466,

[92Müc] F. Mücklich, workshop on "Development of new Materials for Monochromators", MPI Stuttgart, 2.11.1992

[93Als] J. Als-Nielsen, A.K. Freund, Rev.Sci, Instr. to be publ.

[93Müc] F.Mücklich and G. Petzow, in: Mineral Processing and Extractive Metallurgy Review, Gordon & Breach Science Publishers, Beryllium Issue, 1993

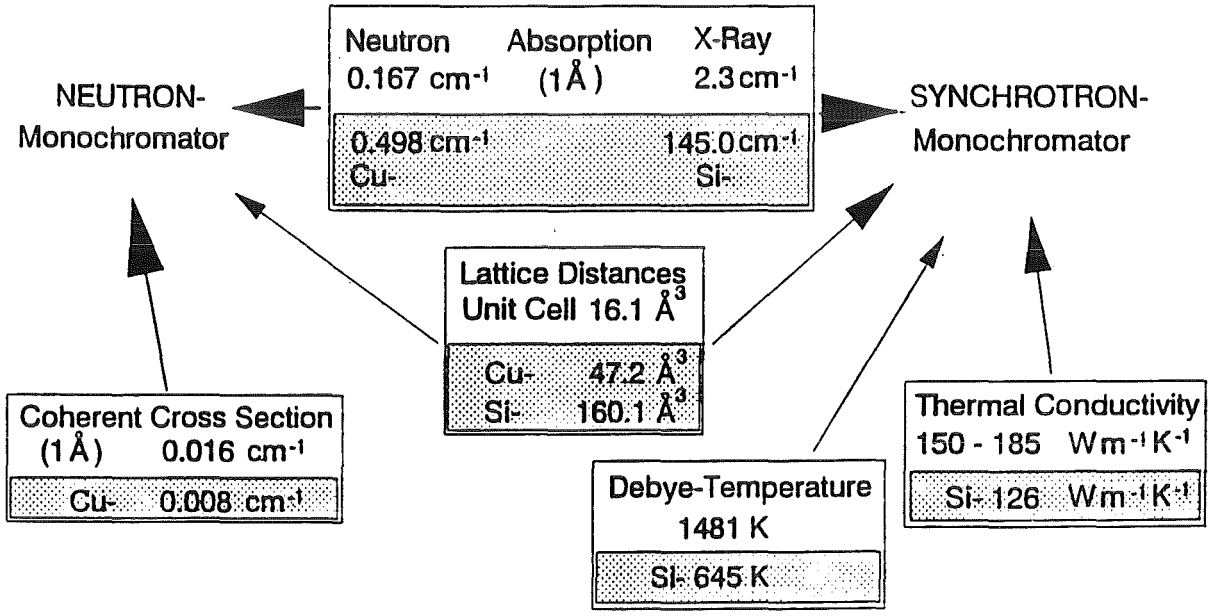

Fig. 1: Physical properties related to the scattering behaviour of beryllium.

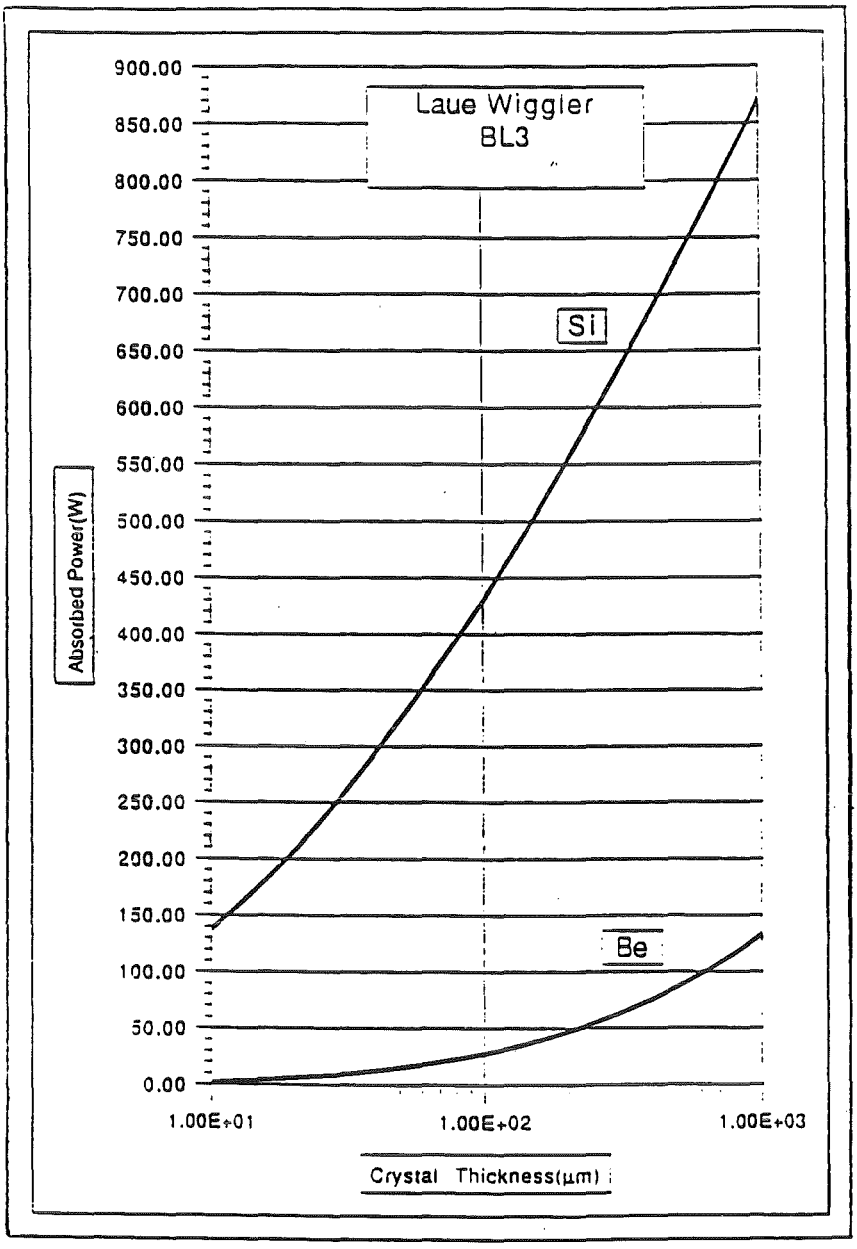

small *source size*: ≈ 200 μm
very small *beam divergence*: ≈ 20 - 200 μrad
very high *heat load*:
total power up to 5 kW
power density up to 200 Wmm^{-2}.

Fig. 2: The power absorbed by Si and Be as a function of crystal thickness in the wiggler beamline BL3 at the ESRF. (A.K.Freund, et al., Rev. Sci. Instr., 1993)

beam dimensions			5mm x 50μm ————
reflectivity			50 %
flux	(10^8 s^{-1})	<<	1.5 * 10^{12} s^{-1}
heat load (18 W/mm^2)			$\leq$ + 11 Kelvin
thermal deformation			< mosaic spread

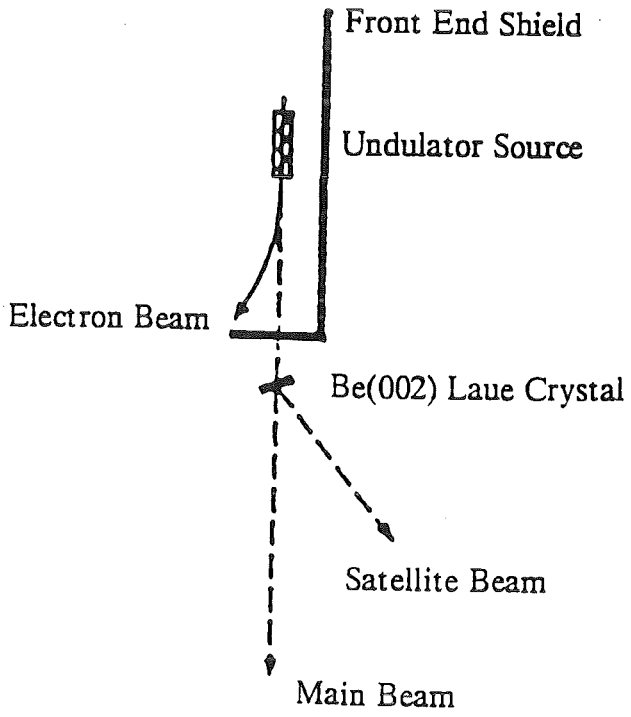

Fig. 3: Beryllium monochromator on a synchrotron undulator source for liquid surface studies. (J.Als-Nielsen, A.K.Freund 1991)

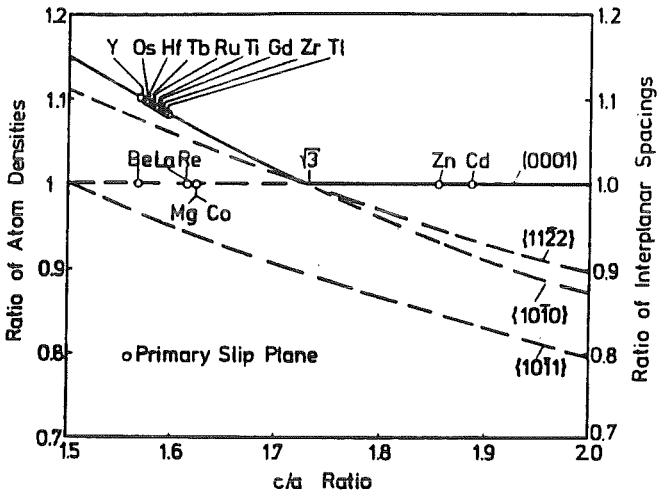

(F. Aldinger 1979)

Fig. 4: Ratio of atom densities of lattice planes versus the c/a ratio.

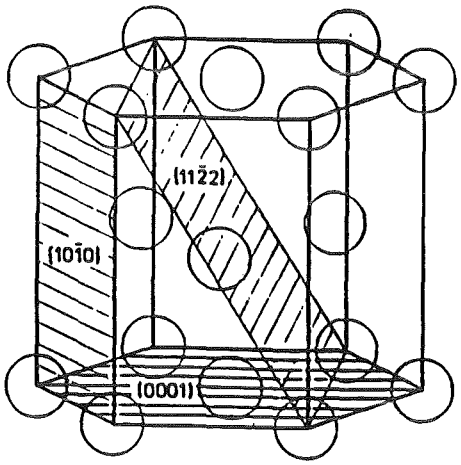

a)

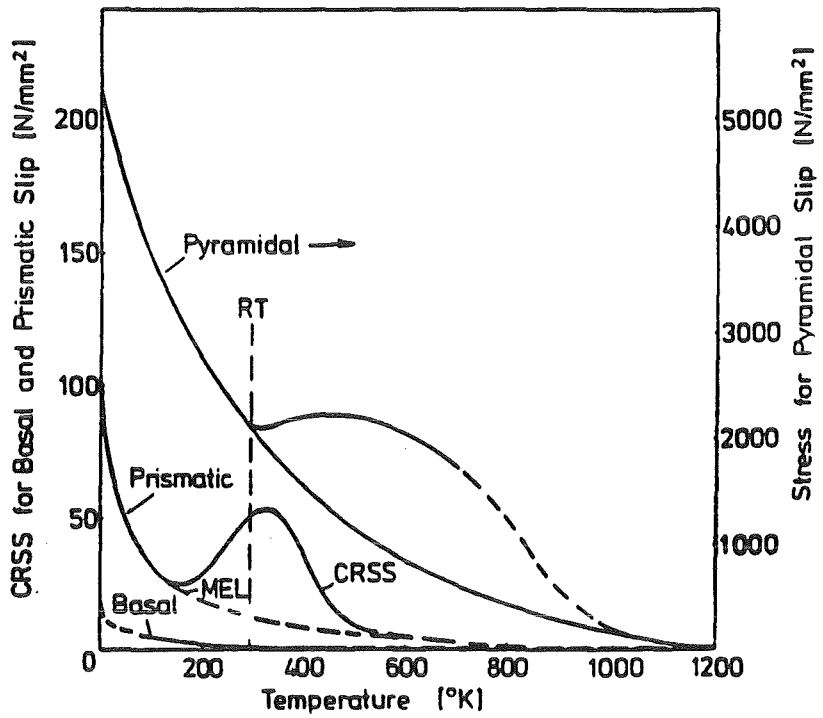

b) Flow stress for basal, prismatic and pyramidal slip versus temperature (F. Aldinger 1979)

Fig. 5: a) Hexagonal close-packed structure.
b) Critical resolved shear stresses (CRSS) versus temperature for different slip systems. At room temperature the ratio for basal : prismatical : pyramidal slip is known to be approximately 1 : 40 : 2000 MPa.

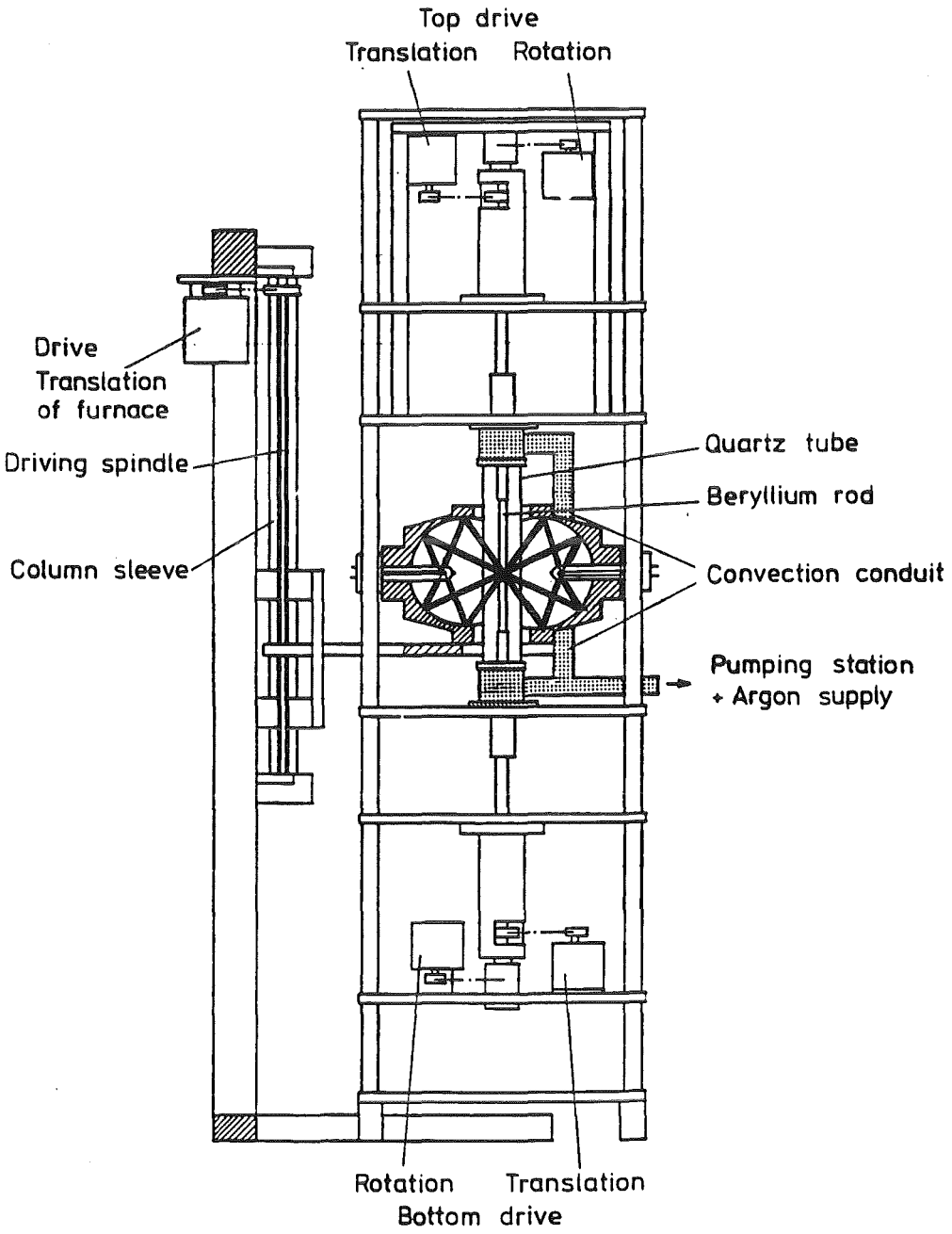

Fig. 6: Scheme of a crucibleless mirror furnace.

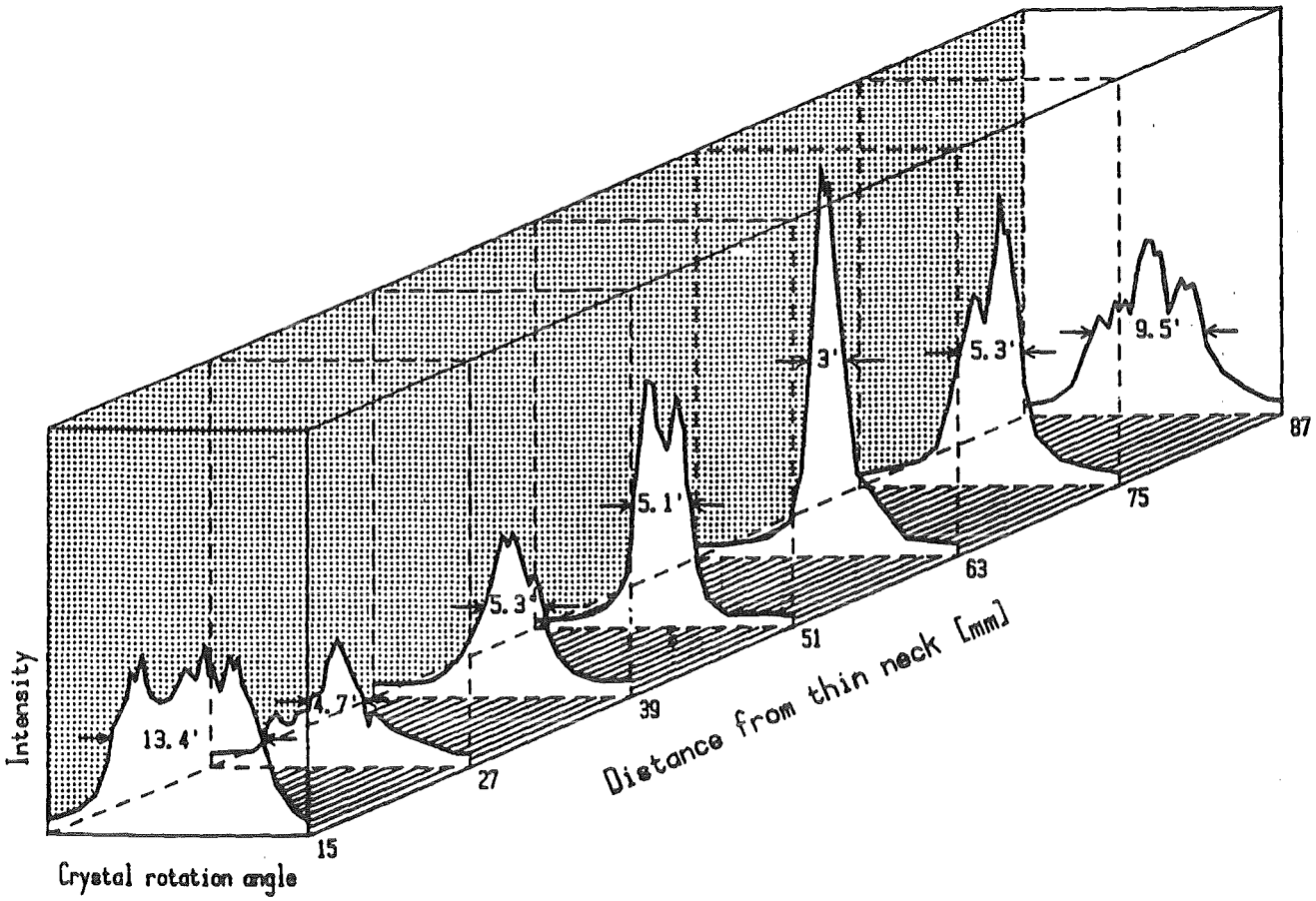

Fig. 7: Diffraction properties of a beryllium single crystal. (γ-rocking curves)

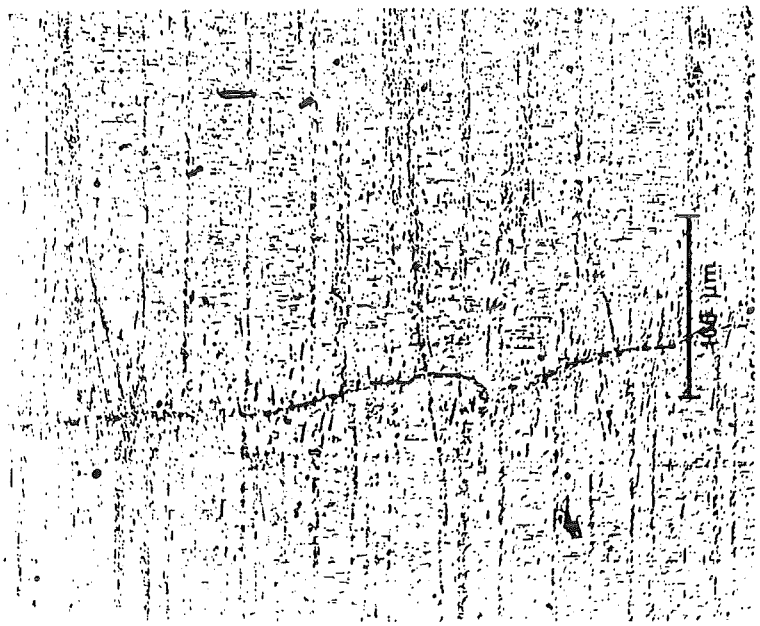

Fig. 8: Subgrain boundary in a beryllium single crystal. (section plane is the $(11\bar{2}0)$ plane)

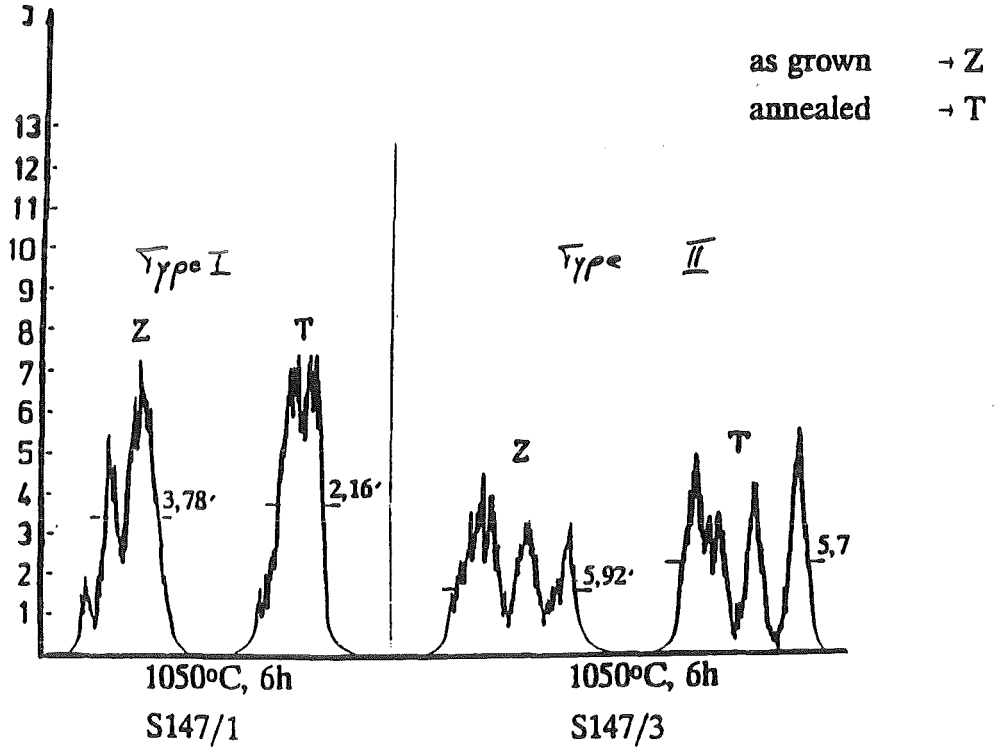

Fig. 9: Influence of crystal lattice defects on rocking curves by modifications in crystal growth and annealing processes.

Type I: Healing effect of subgrain boundaries during a 1323 K annealing of 8 h compared with the as grown state.

Type II In regions of higher impurity content of the same crystal, subgrain boundaries seem to be stabilised by precipitation arrangements.

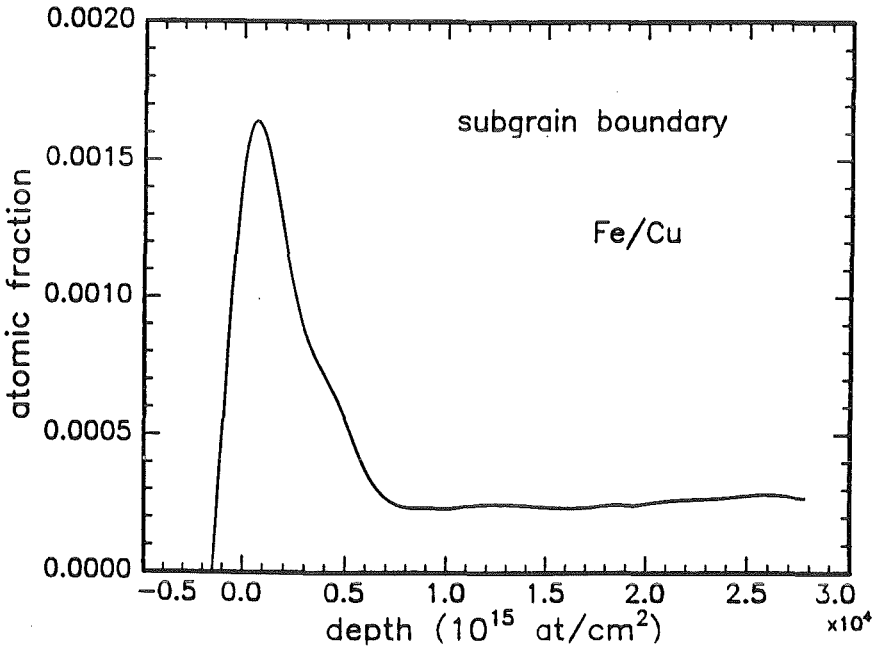

Fig. 10: Result of Rutherford Back Scattering (RBS) spectrum generated directly at the subgrain boundary with significant concentrations of iron and/or copper.

precipitations: Cr, Ti, Al, Si, (less Cu)

different coefficients of thermal expansion ⇒ release of strain by dislocations

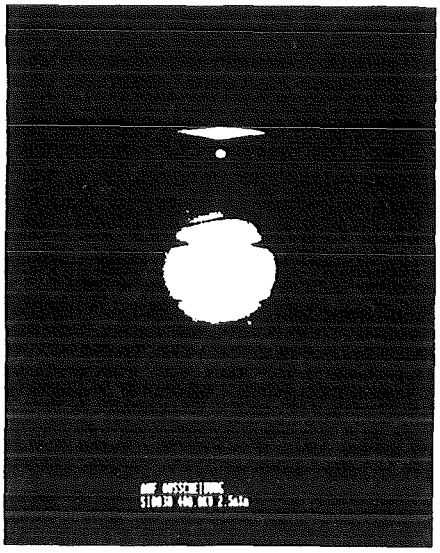

diffuse scattering pattern (subgrain boundary.⇒ migrating Kikuchi line while sample tilting)

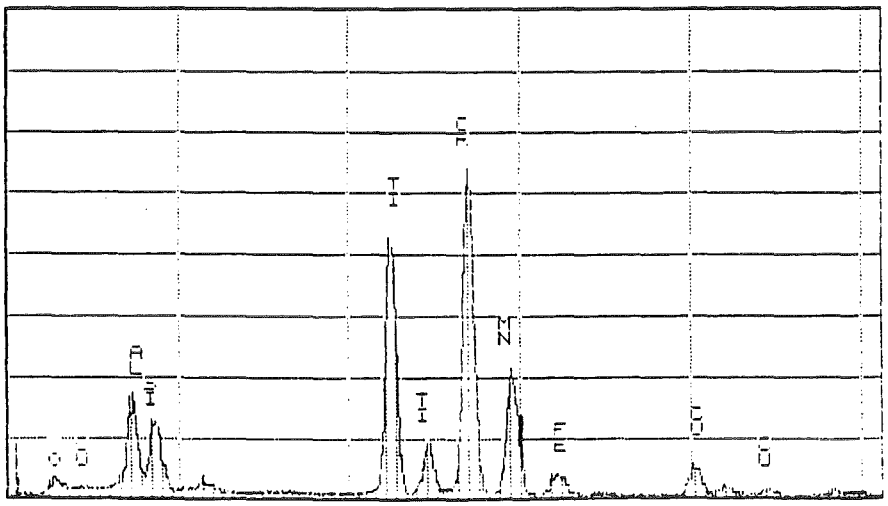

Fig. 11: Typical precipitation at the subgrain boundary with dominating contents of chromium and titanium but also aluminium and silicon. TEM-image indicated a weak misorientation between the upper left and lower right region by a shift of the corresponding Kikuchi lines. Small dark points are residual enrichments of copper caused by spark erosion.

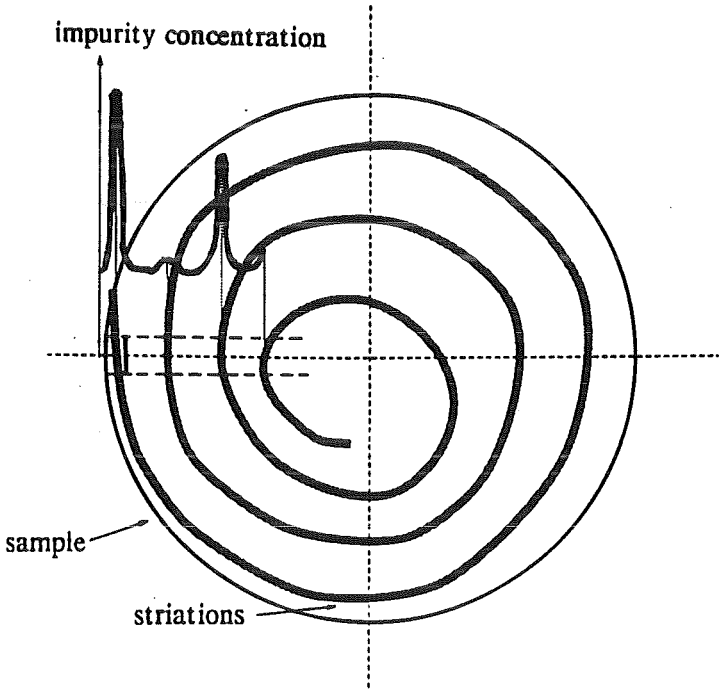

Fig. 12: Linescan of RBS measurement along the radius of a section perpendicular to the growth direction of a beryllium single crystal. Enhanced concentrations of iron and carbon coincide with each striation line.

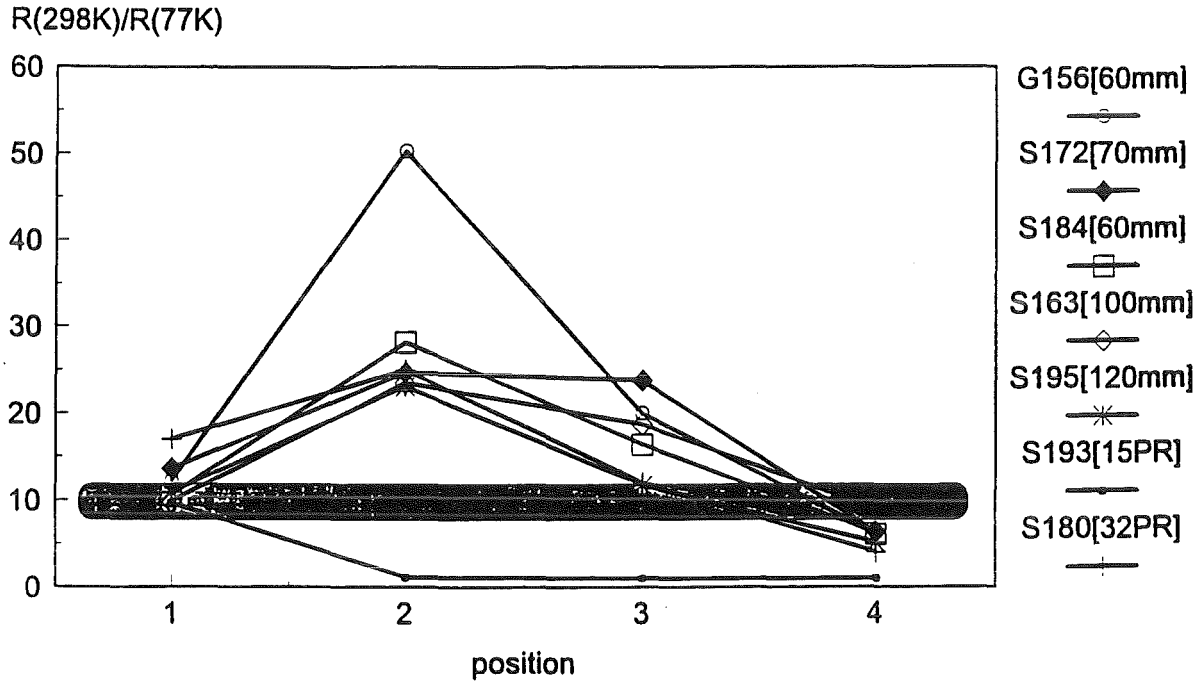

Fig. 13: Residual Resistance Ratio (RRR) along beryllium crystals, purified by zone refining.

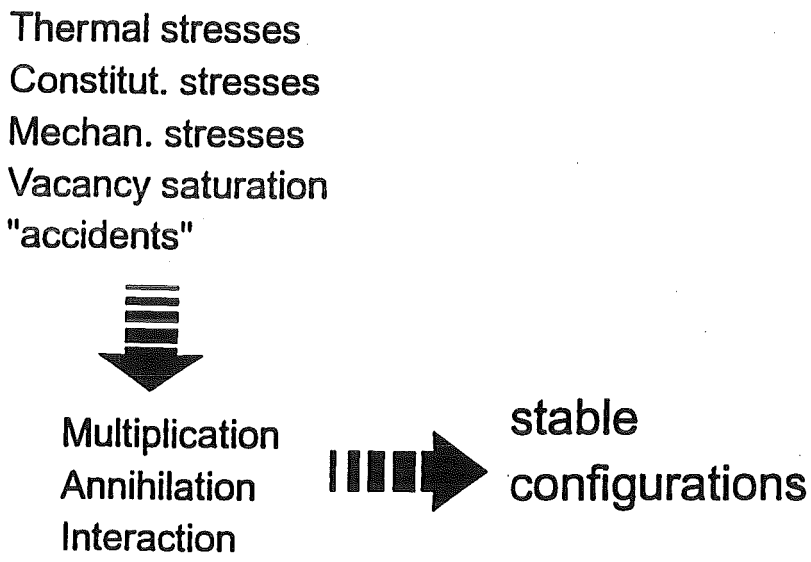

Fig. 14: Generation of dislocations and dislocation arrangements.

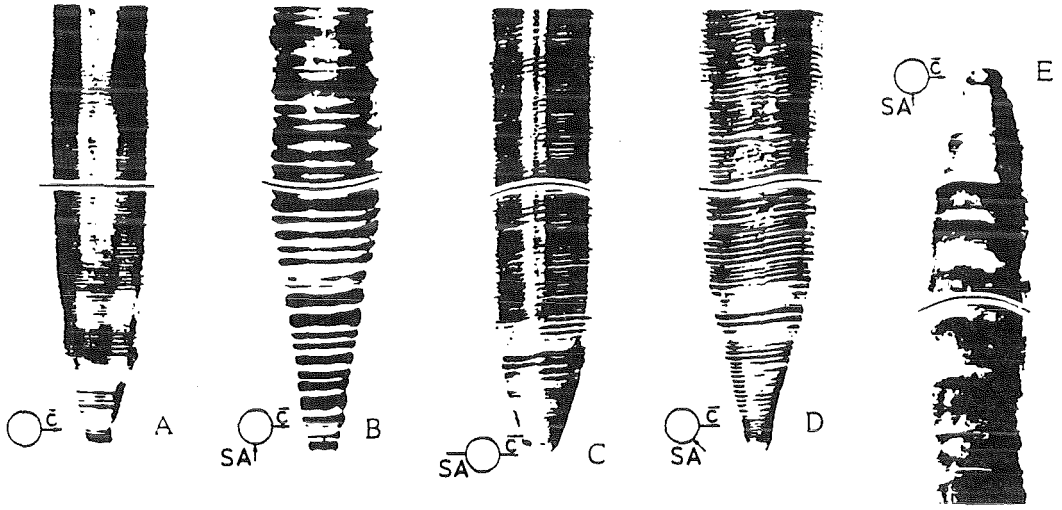

Fig. 15: Typical shape of beryllium single crystals, grown under different angular positions of c-axis to the symmetry axis of the heating system. Note the different shape of the surfaces due to striation development.

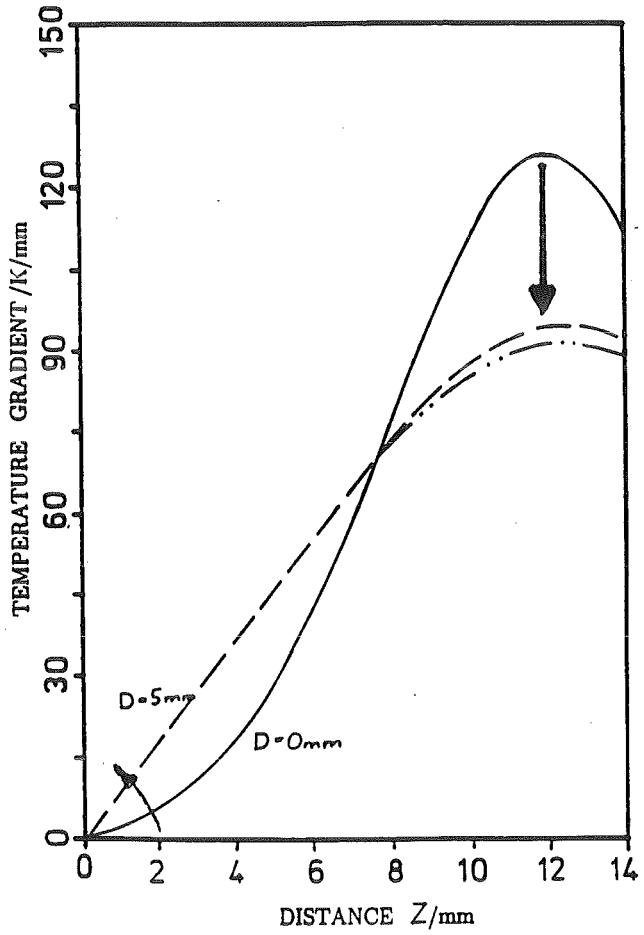

Fig. 16: The temperature gradient versus vertical distance from the solidification front. The defocusing experiment clearly shows a reduction of maximum gradient but the phase transition (at 1523 K) is shifted to shorter distances from the solidification front.

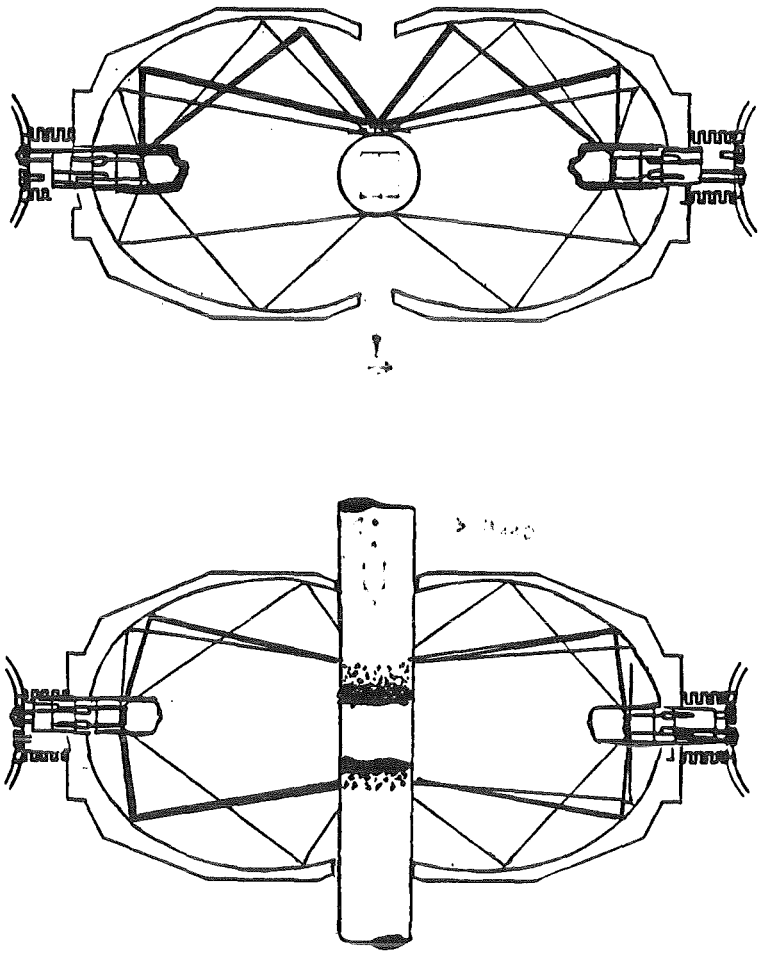

Fig. 17: Scheme of the beam geometry in the double-ellipsoid furnace. The axial temperature gradient in the beryllium rod can reduced by defocusing.

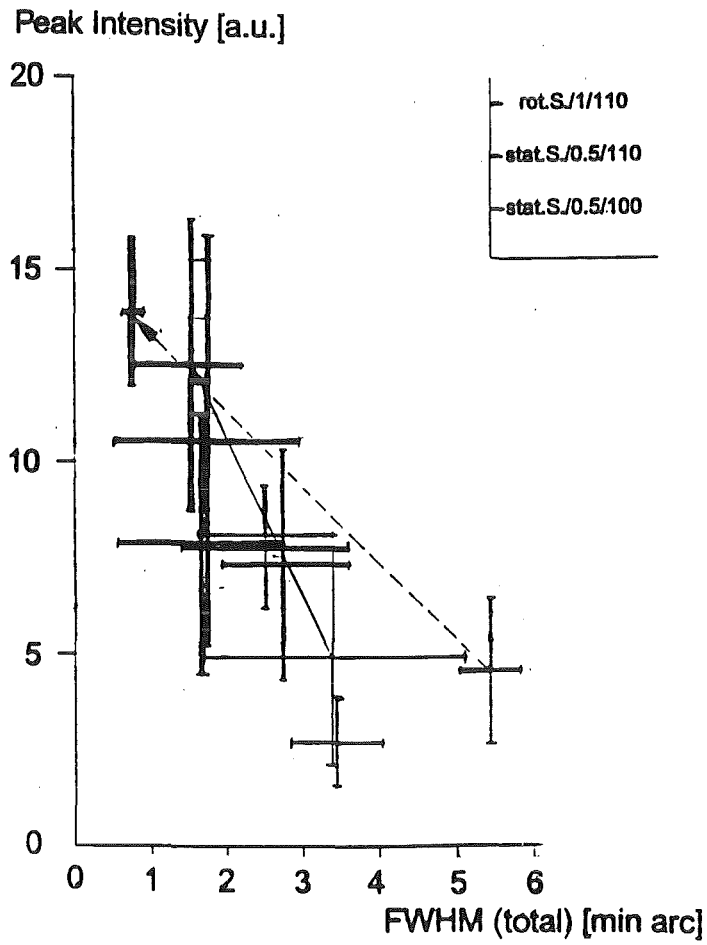

Fig. 18: Peak intensity versus angular width of the γ-rocking curve. Initial widths around 4-6 min of arc can be significantly reduced by optimized growth conditions up to 40-60 sec of arc. Simultaneously the peak intensities exceed the doubled level.

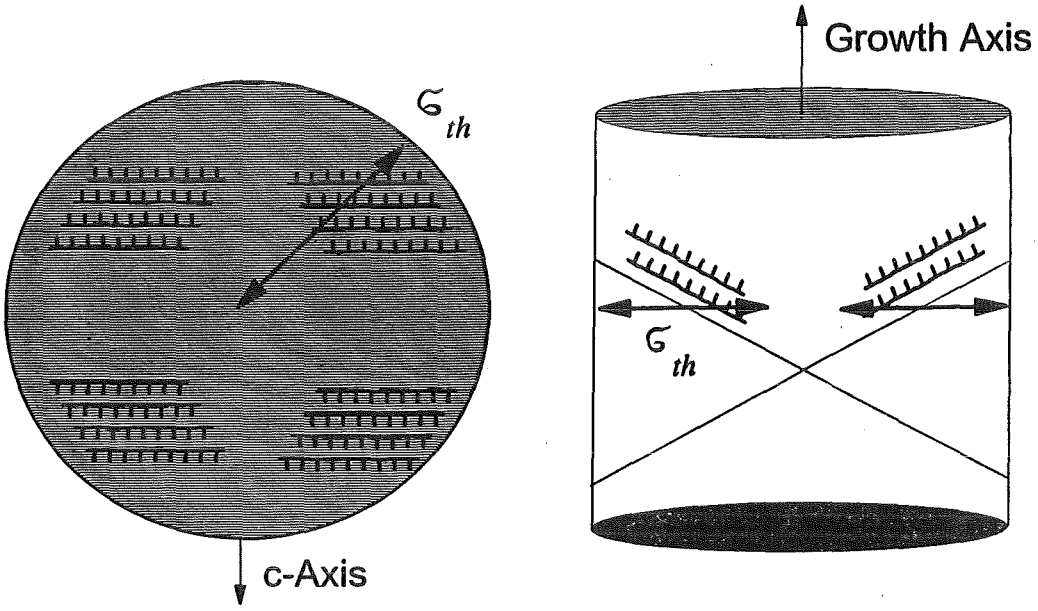

Fig. 19: Dislocation formation during crystal cooling.

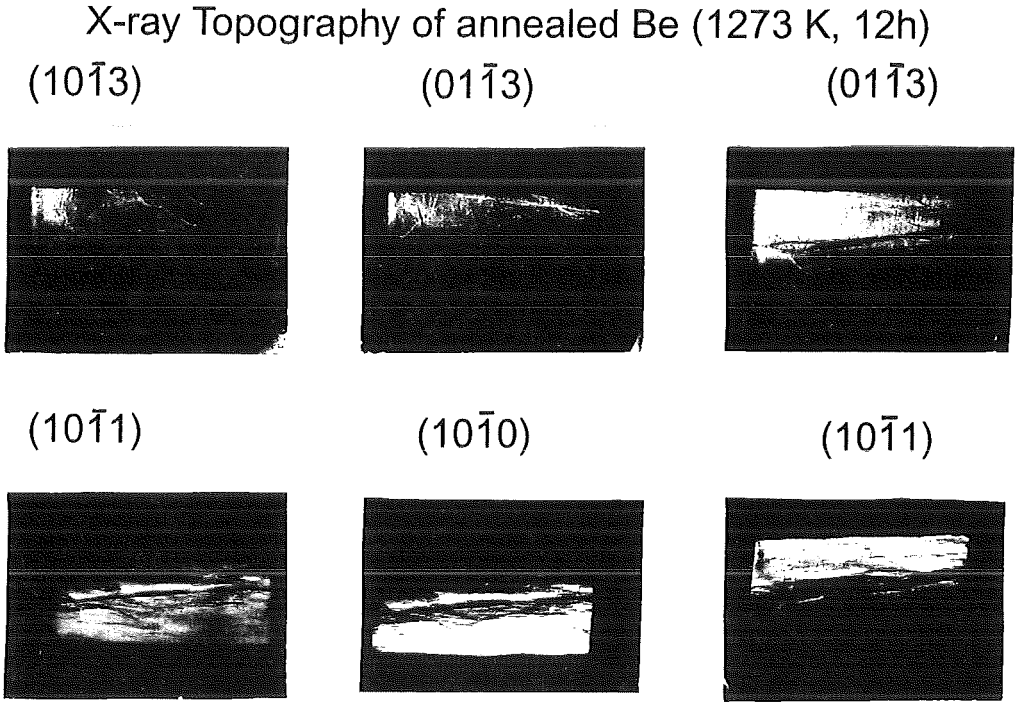
X-ray Topography of annealed Be (1273 K, 12h)
(10$\bar{1}$3)
(01$\bar{1}$3)
(01$\bar{1}$3)
(10$\bar{1}$1)
(10$\bar{1}$0)
(10$\bar{1}$1)

Fig. 20:

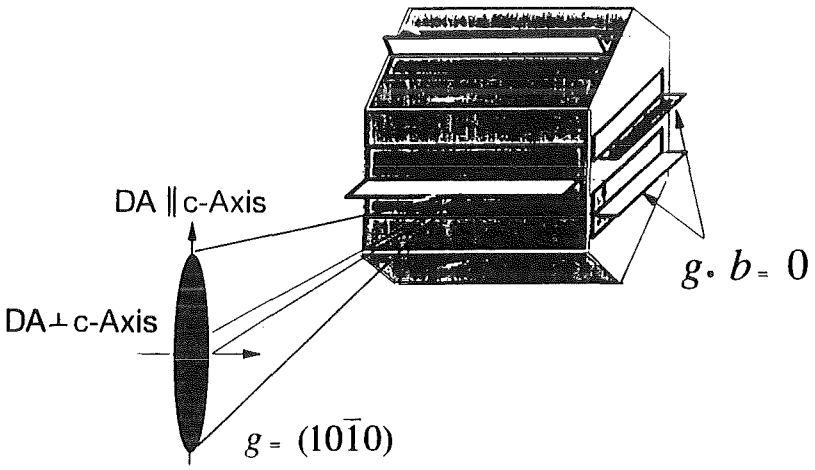

Fig. 21: Strain effect of dislocation types.

FT/Mol/93-07 Mol, September 17th 1993.

Helium Content and Swelling of Low Temperature Irradiated / Post-Irradiation Annealed Beryllium

---

L. SANNEN, F. MOONS, Y. YAO*
S.C.K./C.E.N., Boeretang 200, B-2400 Mol, Belgium

*Nuclear Power Institute of China
P.O. Box 291-106, Chengdu, 610005, P.R. China

Paper presented at the IEA "Workshop on Beryllium for fusion applications" at Karlsruhe, 4-5 october 1993.

STUDIECENTRUM VOOR KERNENERGIE / CENTRE D'ETUDE DE L'ENERGIE NUCLEAIRE
S.C.K. / C.E.N.
Reactor Material Research - RMO
Laboratory of High and Medium level Activity - LHMA
Boeretang, 200 Tel. : -32-(0)14/333000
B-2400 MOL (Belgium) Fax : -32-(0)14/321216

ABSTRACT

Beryllium is one of the leading candidate materials for use in blanket and first wall of fusion reactors. As swelling and embrittlement of beryllium occurs under high neutron fluence, the available data based on fission neutron irradiation at high fast fluence and high temperature are important for predicting the behaviour of beryllium used under fusion conditions.

Beryllium specimens produced by vacuum hot pressing have been irradiated since 1980 in BR2, the material testing reactor of the nuclear research centre in Mol, Belgium, up to a fast fluence of 4 x 10^{22} n/cm^2 (E > 1 MeV) at 40-50°C. The helium production and induced swelling of beryllium have been determined as a function of neutron fluence. The enhancement of the swelling as due to post-irradiation annealing up to 800°C for 24 h has also been evaluated and correlated with the neutron fluence and annealing temperature.

The main experimental results are as follows :

- Both irradiation swelling and helium content show a linear dependence on fast neutron fluence (E > 1 MeV) : the swelling rate amounts to 0.581 % per 10^{22} n/cm^2 fluence, and the helium production rate is 4880 appm/10^{22} n/cm^2.
- The swelling after post-irradiation annealing can be correlated with the neutron fluence to the second power and with the annealing temperature to the fourth power.
- The helium content measurements on the post-irradiation annealed specimens show that no helium is released during the annealing time considered (24 h max.) except at high temperature (800°C).

1. INTRODUCTION.

Beryllium has been chosen by designers for fusion reactor blankets because of its unique neutron multiplication and thermalisation. Beryllium is also a leading candidate material for the surface of the first wall and other high flux components due to its very low-Z value, high resistance against thermal shocking and low hydrogen retention and sputtering yield.

The crucial drawback seems to be the embrittlement and swelling under high fluence irradiation as a result of large amounts of helium produced through the neutron multiplication reaction :

$$^{9}Be + n \longrightarrow {}^{8}Be + 2\,n \qquad \text{(threshold energy 2.7 MeV)}$$

$$^{8}Be \xrightarrow[10^{-16}\,sec]{} 2\ {}^{4}He$$

Due to the lack of real fusion reactor conditions and a 14 MeV high dose neutron source, the investigation of data from high fluence and elevated temperature fission neutron irradiation is important for predicting the behaviour of beryllium under the fusion conditions.

In the present work performed at SCK/CEN, helium content and swelling have been studied for beryllium irradiated up to a fast fluence of 4×10^{22} n/cm² at 40-50°C. Post-irradiation annealing treatment at different temperatures in the range 200 - 800°C for periods of 1 h and 24 h has been conducted. A correlation of induced swelling as a function of fast neutron fluence and annealing temperature has been derived. In addition, helium content and its release during the annealing process are being discussed.

2. EXPERIMENTAL PROCEDURES.

The beryllium available for the study is manufactured by vacuum hot-pressing. The average grain size amounts to 10-13 μm. With beryllium metal content of 98 % and BeO content of 2 %, initial bulk density of 1.852 g/cm³ corresponds to 99.5 % theoretical density [1].

The beryllium samples have been irradiated in BR2, the material test reactor at SCK/CEN at 40-50°C up to three different fast neutron fluences (E > 1 MeV) 0.789, 2.767 and 3.925 x 10^{22} n/cm².

The experimental measurement techniques used are described else [1-2]. Density measurement for swelling determination is performed by remote mechanical mercury pycnometry with a measurement accuracy of ± 0.1 % (1 σ). Helium content is obtained by means of hot vacuum extraction. The sample is degassed at 1250 °C for 5-30 minutes and the quantity of helium released is analysed by a quadrupole mass spectrometer. The precision of the ^{4}He measurement is ± 3 % (1 σ). Post-irradiation annealing process is carried out in a quartz tube vacuum furnace in the temperature range of 200°C to 800°C for a period of 1 h and 24 h.

3. EXPERIMENTAL RESULTS.

3.1. Swelling.

The unirradiated bulk beryllium density D_0 = 1.852 g/cm³ is taken as the reference for swelling measurement. The $\frac{\Delta D}{D_0}$ x 100 (i.e. Vol % swelling) results of irradiated, annealed and non-annealed specimens are given in Table 1.

The post-irradiation swelling shows a linear dependence on the neutron fluence (Fig. 1) :

$$\frac{\Delta D}{D_0} \times 100 = (0.581 \pm 0.031) \times \Phi \times 10^{-22} \quad \text{vol.\%} \qquad (1)$$

where Φ is the fast (E > 1 MeV) neutron fluence in n/cm². For the irradiation conditions in BR2, swelling of beryllium, exposed to fast neutron fluence from 0.789 to 3.925 x 10^{22} n/cm², amounts from 0.65 to 2.27 vol %.

The density measurements after annealing show more swelling, much more that the initial one caused by the irradiation. Two equations of swelling for the two different annealing periods (1 h - equation (2) and 24h -

equation (3)) are deduced from the data in Table 1 :

$$\frac{\Delta D}{D_0} x100 = (0.58 \pm 0.03).\Phi.10^{-22} + (0.286 \pm 0.002).10^{-55}.\Phi^2.T^4 \qquad (2)$$

$$\frac{\Delta D}{D_0} x100 = (0.58 \pm 0.03).\Phi.10^{-22} + (0.372 \pm 0.005).10^{-55}.\Phi^2.T^4 \qquad (3)$$

where Φ is fast neutron fluence in n/cm² and T is the annealing temperature in °C.
The equations (2) and (3) give excellent agreement with the measurement data as can be seen in fig. 2 and 3. The observed correlation includes two parts : a first linear part representing the neutron fluence induced swelling without annealing and a second part reflecting the enhancement of swelling induced during the post-irradiation annealing process. This last annealing induced swelling increases as a function of fluence to the second power and annealing temperature to the fourth power. Meanwhile, the coefficient of the multiple power term for equation (3), being 30 % higher than the corresponding coefficient in equation (2), indicates that the swelling degree at a certain annealing temperature increases with annealing time.

3.2. Helium content

The helium content results are also depicted in Table 1. A linear relationship of helium concentration in function of neutron fluence, as derived from the non-annealed specimens (fig. 4), is as following :

$$C_{He} = (4880 \pm 90) \times \Phi \times 10^{-22} \quad \text{appm} \qquad (4)$$

where Φ is the fast (E > 1 MeV) neutron fluence in n/cm². The helium production rate of beryllium is 4880 appm He per 10^{22} n/cm².

The helium content measurements on post-irradiation annealed specimens (Table 1) indicate that at or beow 400°C, no helium is released from the irradiated beryllium specimens annealed up to 24 h. However, it is noticeable that 70 % initial helium content is released from the specimen irradiated up to 0.782 x 10^{22} n/cm², after annealing at 800°C for 24 h even though its helium content remains unchanged when annealed at the same temperature for only 1 h.

4. DISCUSSION OF THE RESULTS.

Many investigations have been made on helium induced swelling of beryllium in thermal and fast neutron spectra at different temperature ranges [3]. As the "solid helium" theory for beryllium at low irradiation temperature (≤ approx. 250°C) mentions [4], helium atoms produced in (n, 2n) reaction are probably trapped by immobile vacancies in the beryllium lattice and held in enforced solid solution while self-diffusion is insignificant. Therefore, according to this theory, at low irradiation temperature the formation and growth of helium bubbles is an athermal process and swelling rate is linear proportional to the helium concentration C_{He}.

More systematic investigations, although mostly covering restricted fluence ranges, give consistent swelling/fluence ratios of 0.52 - 0.55 vol% per 10^{22} n/cm² and helium concentration/fluence ratios of 2000 - 6000 appm per 10^{22} n/cm² [5-6]. The swelling rate and helium production rate in the present work are in these ranges.

At elevated temperature when helium and vacancies are more mobile, self-diffusion allows bubbles to grow by absorption of thermal vacancies so that the beryllium swelling becomes more important and also dependent upon temperature. Such "helium bubble promoted swelling" has been recognised as the predominant mechanism for the dimensional changes of irradiated Be [6]. From experimental results and theoretical calculation, it is proved that both neutron fluence and temperature play an important role in the swelling behaviour of beryllium in elevated irradiation temperature condition.

J.M. Beeston presented a swelling correlation from the data of beryllium irradiated in EBR at 427 to 487°C up to a fluence of 1.2 x 10^{22} n/cm² (E > 1 MeV) [7] :

$$\frac{\Delta V}{V} = 1.83 \times 10^{-58} . \Phi^2 . T^4 \qquad (5)$$

Good agreement was found by J.M. Beeston between measured swelling data, as obtained from high temperature irradiated (427-487°C), low helium content (1850 appm at 1.2 x 10^{22} n/cm²) beryllium, and theoretical calculated swelling according to equation (5).

As a comparison with the correlation in the present work, the form of equations (2) and (3) is similar to J.M. Beeston's correlation (equation (5)). Thus the same swelling mechanism seems to govern the temperature dependent swelling despite the quite different experimental conditions (high temperature irradiation against low temperature irradiation with post-irradiation annealing).
The fact that the coefficient of the $\Phi^2 T^4$ term in the equation (2) and (3) is significantly higher than that in equation (5) (two orders of magnitude), can be attributed to the following. The helium production rate observed in the present work is approximately three times higher than the one observed by J.M. Beeston (4880 appm/10^{22} n/cm² in the BR2 reactor against 1540 appm/10^{22} n/cm² in the EBR-II reactor). This can be due both to a different neutron spectrum and the release of helium during the high temperature irradiation in the EBR-II reactor. Since helium is the controlling factor regarding the swelling this will result in an enhanced swelling and thus a larger coefficient in the correlation.

From fig. 2 and 3, it is obvious that the onset temperature of the annealing swelling shifts to a lower value with the increase in neutron fluence. If 1.800 g/cm³ (2.8 % density decrease) is taken as a density limitation for the swelling threshold temperature [8], the swelling thresholds are approximately 705°C, 450°C and 260°C respectively for 0.789, 2.767 and 3.925 x 10^{22} n/cm² (E > 1 MeV) exposure in case of the 24 h annealed beryllium. Collating the temperature swelling threshold results of R. Tromp [8] in fig. 5, the present data show a proper match to and extrapolation from the previous low neutron fluence irradiation data.

For the first wall fluence of 7.4 MW.y/m², corresponding to approximately 2.6 x 10^{22} n/cm² (E > 1 MeV) and 18000 appm He in beryllium by the ITER design [9], an irreversible decrease of density of 2.8 % could be predicted to occur at 460°C according to the present test results.

Reviewing the self-diffusion equation of beryllium in reference [10] :

$$D_{He} = 0.52 \exp(-1.63 \text{ eV} / kT) \quad \text{cm}^2/\text{sec} \qquad (6)$$

self diffusion will rise very steeply in Be from about 250°C because of its low activity energy. Under the assumption that swelling of Be is due to the formation of gas bubbles at the grain boundaries caused by migration of the helium formed in the matrix towards the grain boundaries, and that this migration is governed by the self-diffusion of Be (as stipulated above, according to the "solid helium" theory), one can estimate the time for a diffusion path length, L, of 6 μm (conservative distance from the center of a grain towards the grain boundary) as :

$$t = L^2 / D_{He} \quad \text{sec} \qquad (7)$$

By applying foregoing equation at 400°C resp. 800°C it comes out that it would take 13 days resp. 30 seconds for helium to migrate to the boundaries. This may explain why the beryllium irradiated at the low neutron fluence of 0.789 x 10^{22} n/cm² after annealing for 24 h at 800°C releases 70 % of its initial helium content while no helium is released neither by the same specimen annealed only for 1 h nor by any sample when annealed at or below 400°C for both 1 h and 24 h. This might explain as well the low helium production rate as observed by J.M. Beeston since during the four years of irradiation at 427-487°C, a considerable amount of the helium produced might have escaped.

All foregoing observations clearly demonstrate that the quantitative evaluation of the swelling behaviour of Be irradiated at higher temperature is complicated by the continuous long term annealing effect which results from two factors :

- an enhanced swelling arising from helium bubble formation promoted at elevated temperatures ;
- and a reduced swelling due to a release of He produced.

5. CONCLUSIONS.

Beryllium irradiated in the BR2 reactor at low temperature (40-50°C) up to a fluence of 4.0 x 10^{22} n/cm² does show swelling of 2.27 vol % and helium content of 21,000 appm. A post-irradiation swelling rate of 0.58 vol % per 10^{22} n/cm² fast neutron fluence and a He production rate of 4880 appm per 10^{22} n/cm² fast neutron fluence have been found.

Post-irradiation annealing treatment (up to 800°C and 24 h) enhances strongly the swelling. This swelling enhancement is correlated with the second power of the neutron fluence and the fourth power of the annealing temperature.

Helium measurements on the post-irradiation annealed specimens did show that no helium was released except when annealing at higher temperature (800 °C) for longer period (24 h).

All these observations

- of linear correlation of both swelling and helium content with fast neutron fluence at lower temperatures (< 250 °C) ;
- of strongly enhanced swelling after post-irradiation annealing at higher temperatures (> 250 °C) ;
- and of helium release after post-irradiation annealing at higher temperatures and longer period ;

can be explained on the base of the "solid helium" and self-diffusion theory.

As related to the fusion reactor engineering aspect, the data presented in this work concern

- Be irradiation up to a high fast neutron fluence of 4 x 10^{22} n/cm²,
- at low temperature,
- followed by post-irradiation annealing up to 800 °C and 24h,
- with no helium release below 450 °C.

As such

- large amounts of helium are produced,
- which all of them are available to promote the annealing produced swelling.

Consequently the data are well suited to estimate the swelling behaviour of high temperature irradiated beryllium from a conservative point of vue, i.e. the upbound of swelling that can be expected.

7. REFERENCES.

1. L. Sannen.
Characterisation of Irradiated Beryllium.
FT/Mol/92-01, Mol, July 1992.

2. L. Sannen, Ch. De Raedt.
The Effects of Neutron Irradiation on Beryllium.
Paper presented at the 17th Symposium on Fusion Technology, Roma, Italy, Sept. 1992.
Proceedings, Fusion Technology Vol.2, 1993, 1474-1478.

3. L.G. Miller and J.M. Beeston.
Fusion Technology Vol.8, July 1985, 1152-1156.

4. T.J. McCarville, D.H. Derwald and W. Wolfer.
Technical Issues for Beryllium use in Fusion Blanket Applications.
UCIC-20319, DE85 005856.

5. W.G. Wolfer and T.J. McCarville.
Fusion Technology Vol.8, July 1985, 1157-1164.

6. J.M. Beeston, M.R. Martin, C.R. Brinkman, C.E. Korth and W.C. Francis.
Symposium on Materials Performance in Operating Nuclear Systems, CONF-730801, Ames Laboratory, Ames, Iowa, Aug. 1973.
Nuclear Metallurgy Vol.19, 59-87.

7. J.M. Beeston, L.G. Miller, E.L. Wood Jr. and R.W. Moir.
J. Nucl. Mater. Vol.122-123, 1984, 802-809.

8. R. Tromp.
Quaterly Progress Report : Irradiation Effects on Reactor Structural Materials.
BNWL-128, Aug. 1965, 12.9-12.15.

9. R.W. Moir.
Beryllium Usage in Fusion Blankets and Beryllium Data Needs.
CONF-880417-8, April 1988.

10. N.L. Peterson.
J. Nucl. Mater. Vol.69-70, 1970, 3.

Table 1 : Swelling and He content of irradiated both annealed and non-annealed Be

Annealing		Fast neutron fluence (x 10^{22} n/cm²), E > 1 Mev					
		0.789		2.767		3.925	
Temp. (°C)	Time (h)	^{4}He-content appm	swelling (%)	^{4}He-content appm	swelling (%)	^{4}He-content appm	swelling (%)
non annealing		3798	0.65	12830	1.57	20670	2.27
200	1				1.51		2.16
250							2.43
300						21211	2.59
350						21010	2.92
400			0.65	12994	2.11	21065	3.56
450					2.48		
500					2.75		4.91
650			1.03				
800		3880	2.54				
200	24				1.67		2.27
250							2.59
300						21096	2.92
350						21103	3.24
400			1.19	13333	2.43	20886	4.27
450					2.70		
500					3.29		5.45
650			1.35				
800		1163	4.21				

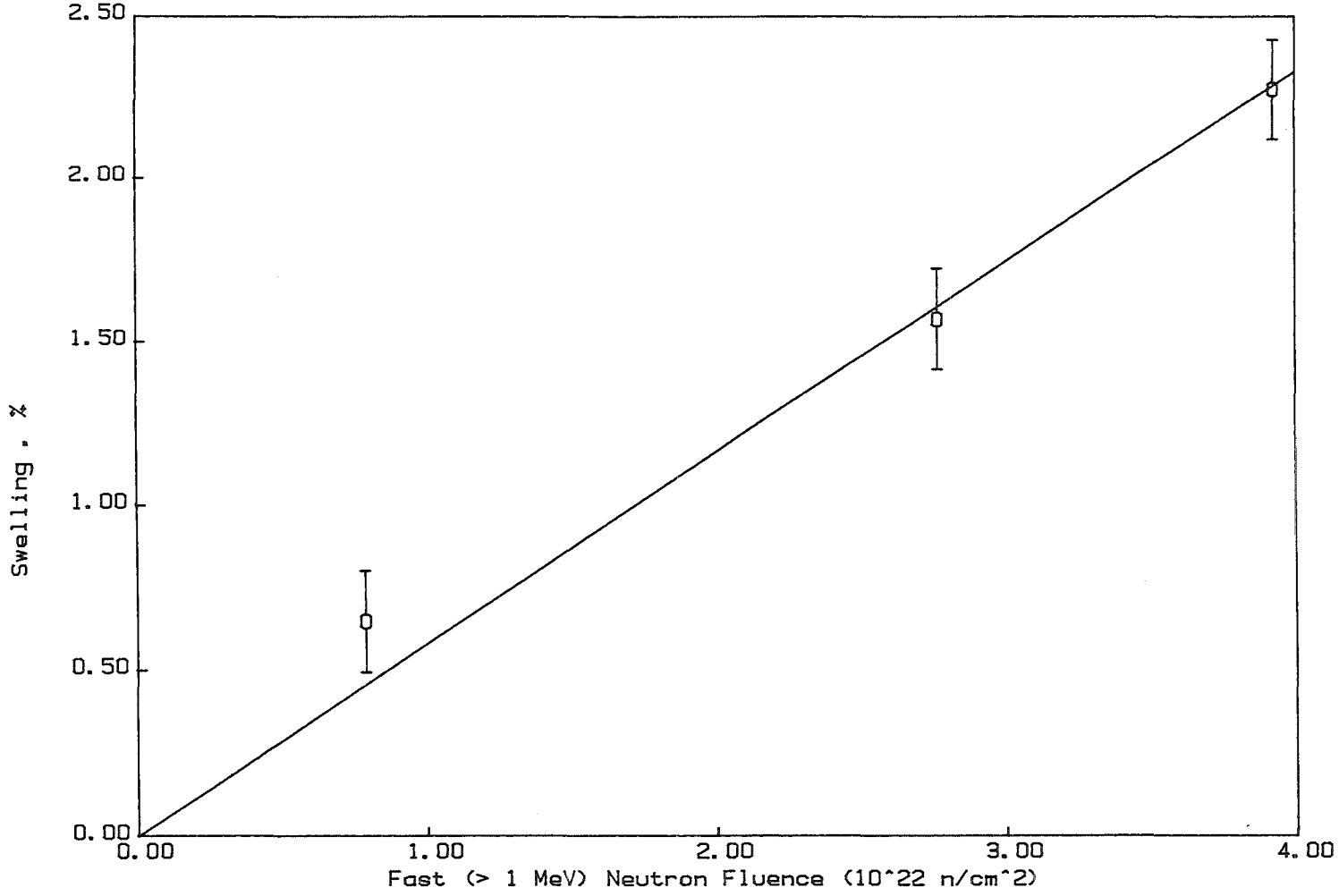

Fig. 1 : Swelling of low temperature irradiated Beryllium as a function of the fast neutron fluence (E > 1 MeV).

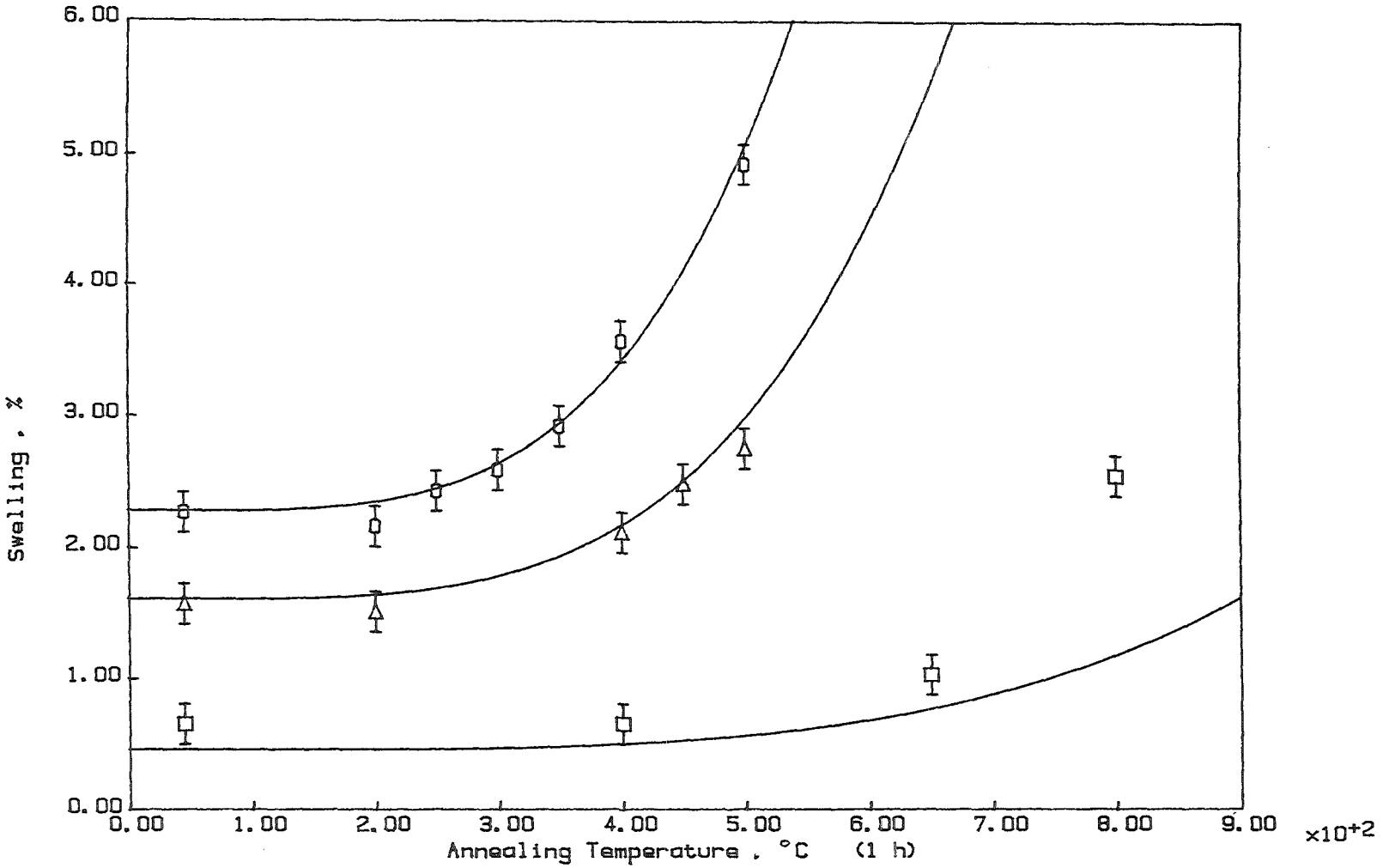

Fig. 2 : Swelling of Beryllium after post-irradiation annealing for 1 h, as a function of annealing temperature at three different fast neutron fluences (E > 1 MeV) : □ 0.789 x 10^{22} n/cm²
△ 2.767 x 10^{22} n/cm²
0 3.925 x 10^{22} n/cm².

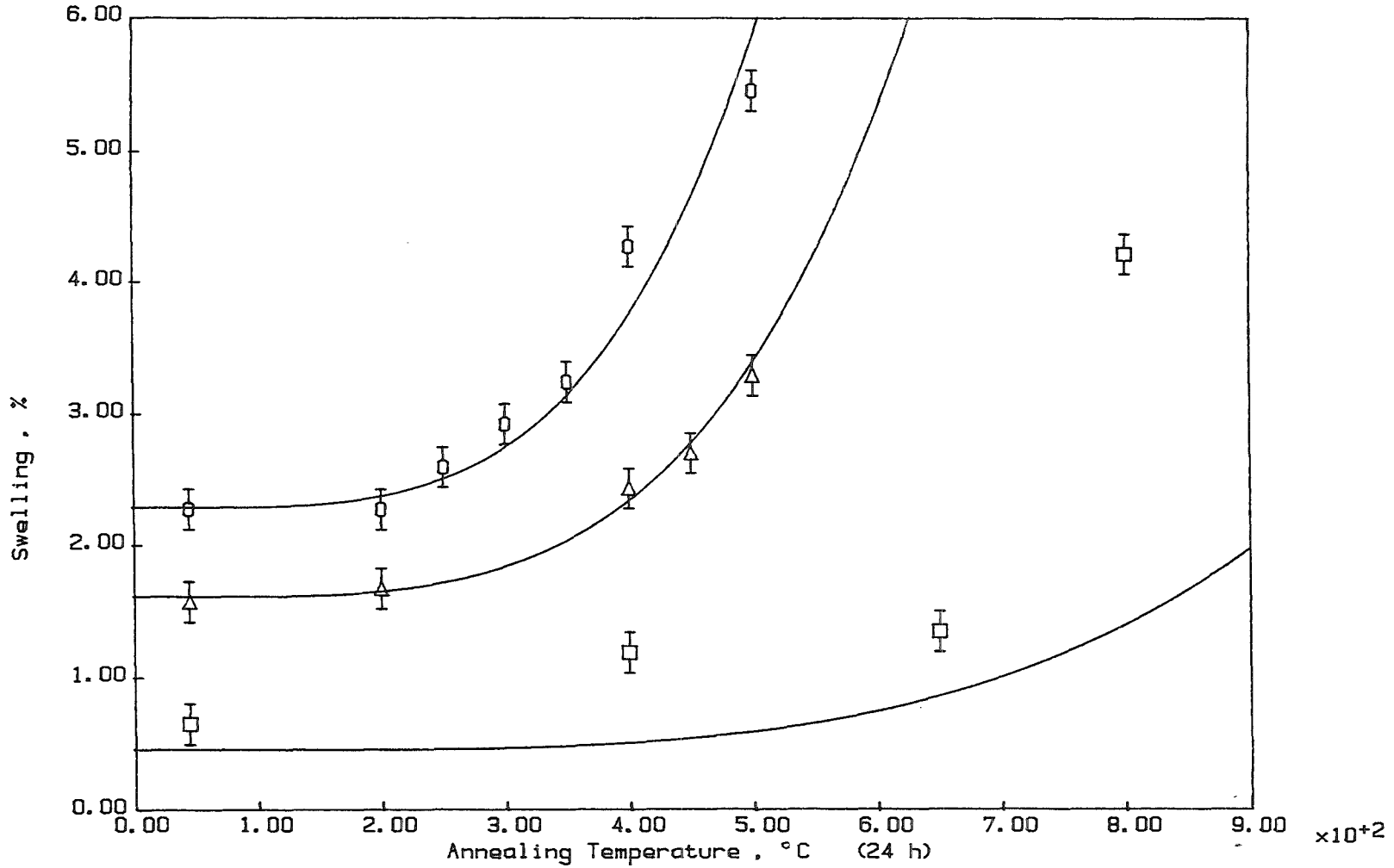

Fig. 3 : Swelling of Beryllium after post-irradiation annealing for 24 h, as a function of annealing temperature at three different fast neutron fluences (E > 1 MeV) : □ 0.789 x 10^{22} n/cm²
△ 2.767 x 10^{22} n/cm²
0 3.925 x 10^{22} n/cm².

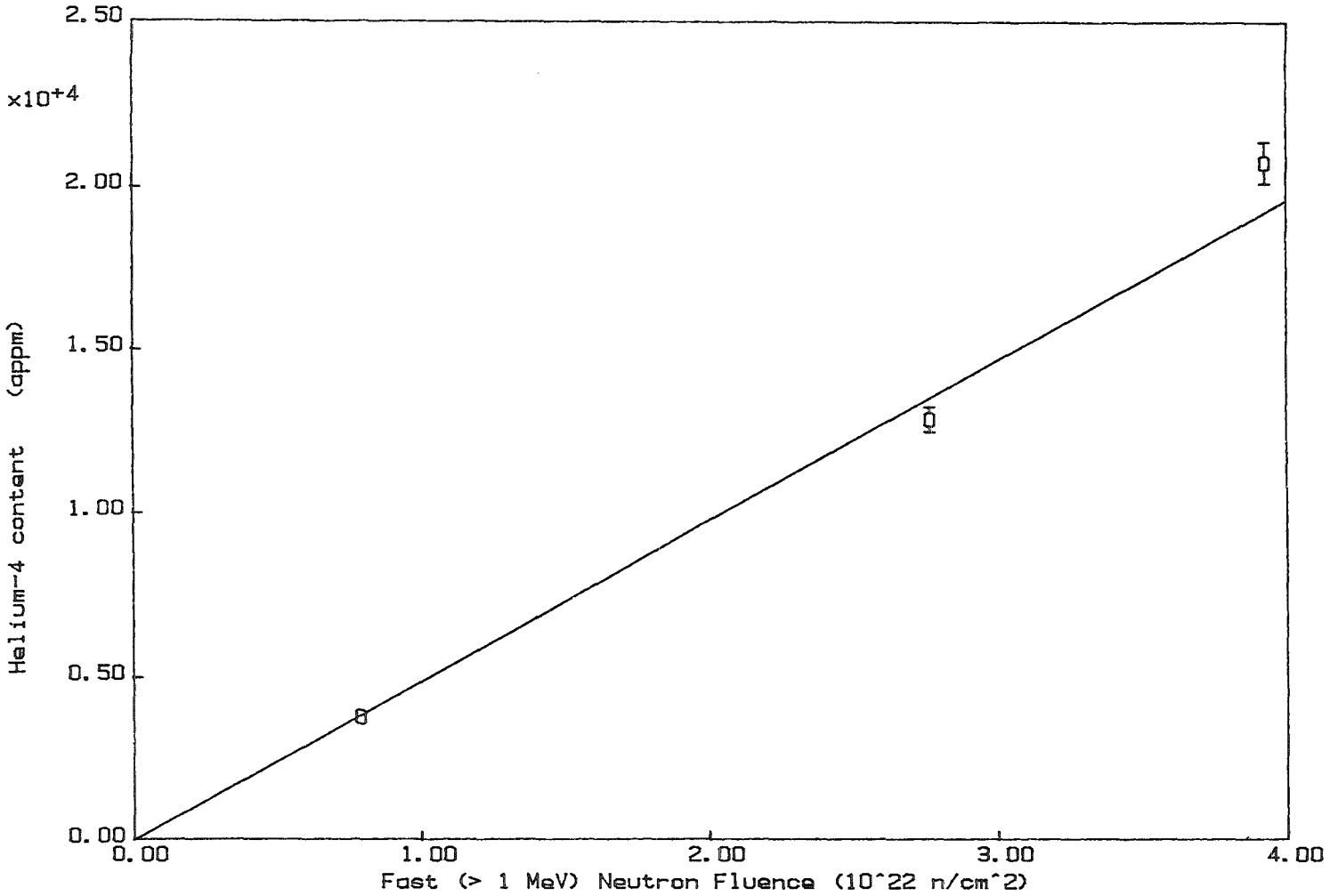

Fig. 4 : Helium content of low temperature irradiated Beryllium as a function of the fast neutron fluence (E > 1 MeV).

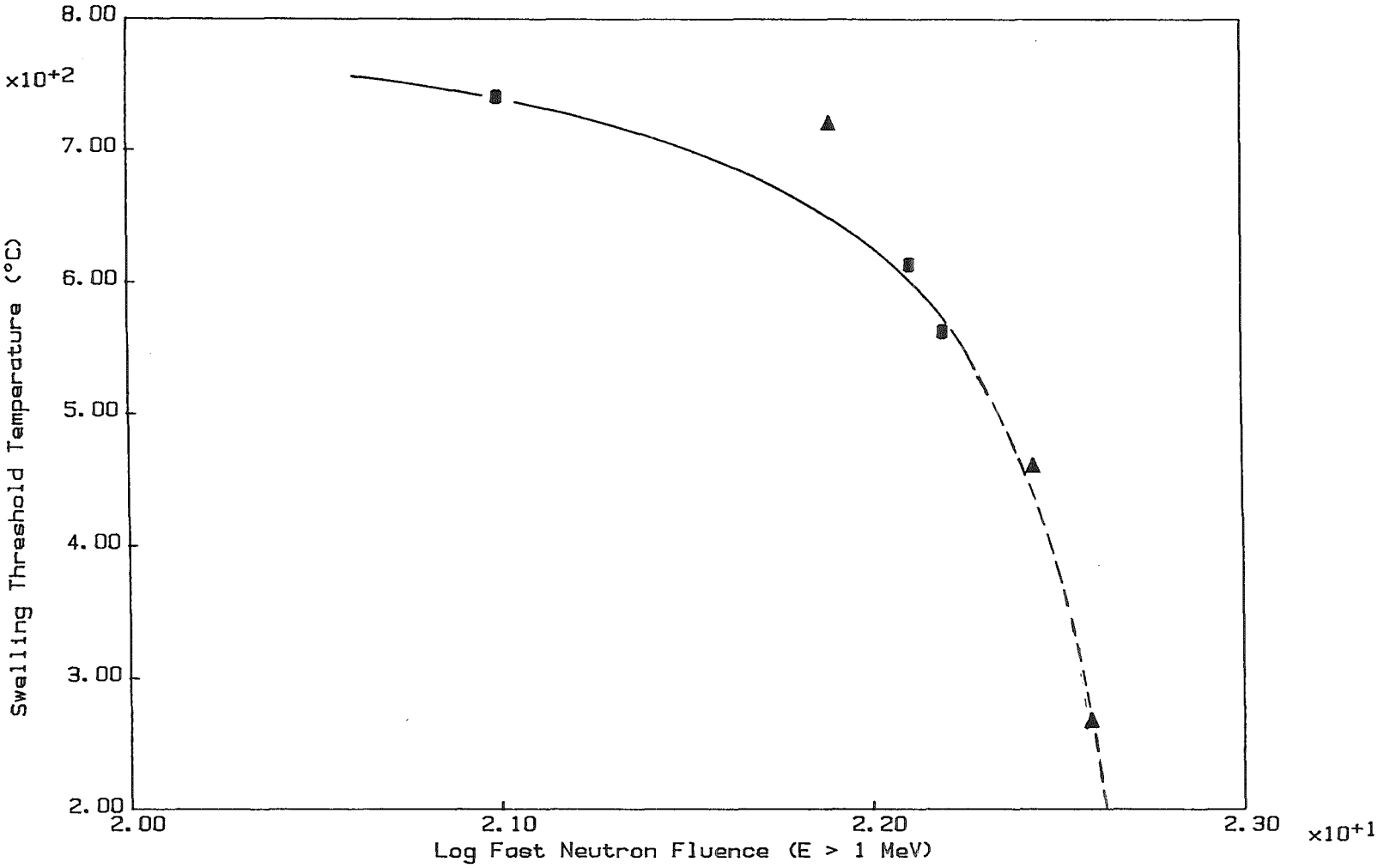

Fig. 5 : Swelling Threshold Temperature of Beryllium (arbitrary criterium of 2.8 vol % swelling) as a function of fast neutron exposure.

- ● irradiated at ambient temperature, ref. [8]
- ▲ irradiated at 40-50 °C in present work.

MODELLING HE-INDUCED SWELLING IN BERYLLIUM DURING FAST NEUTRON IRRADIATION

M. DALLE DONNE, F. SCAFFIDI-ARGENTINA

Kernforschungszentrum Karlsruhe, Institut für Neutronenphysik und Reaktortechnik
P.O. Box 3640, D-76021 Karlsruhe, Federal Republic of Germany

C. FERRERO

European Synchrotron Radiation Facility
B.P. 220, F-38043 Grenoble Cedex, France

C. RONCHI

Commission of the European Communities, Joint Research Centre, Karlsruhe Establishment,
European Institute for Transuranium Elements
P.O. Box 2340, D-76125 Karlsruhe, Federal Republic of Germany

ABSTRACT

The most important effects of neutron irradiation on beryllium are swelling, embrittlement and tritium retention. The helium produced by the $^{9}Be(n,2n)2\,^{4}He$ reaction is the cause of beryllium swelling which is the main limiting lifetime factor for the material. It was, therefore, decided to develop a computer code capable of describing the helium behaviour in beryllium; the approach used was to modify an existing code available for the modelling of the UO_2 performance in fission reactors. The resulting code ANFIBE (ANalysis of Fusion Irradiated BEryllium) allows the calculation of gas distribution, induced swelling and helium release from beryllium. Good agreement between experimental and calculated swelling has been found.

1. INTRODUCTION

The operating conditions in the blanket of the European DEMO Fusion Reactor [1] (fast neutron fluence $\simeq 2.5\,10^{22}\ n/cm^2$ ($E_n > 1\ MeV$), operation time $\simeq 20000\ h$, helium content$\simeq$ 17000 *appm*) dictate the necessity of evaluating beryllium behaviour under fast neutron irradiation conditions typical of the next generation of fusion reactors. To our knowledge, no com-

puter codes are as yet available which describe the possible processes occurring during beryllium irradiation. Despite the complexity of the problem, which is influenced by stochastic factors too, a mechanistic analysis is, in most cases, a viable and useful solution [2]. It was thus decided to develop a mechanistic code to predict the performance of beryllium in the blanket up to high neutron fluences.

A code, previously written at the Institute for Transuranium Elements in Karlsruhe for analysing the behaviour of fuel pellets in fission reactors [2], was modified to model all the relevant processes which are thought to affect gas behaviour and swelling in beryllium.

To evaluate the performance of the new computer code, calculations for a wide range of irradiation conditions were carried out. Additionally, a first analysis for the European BOT Solid Breeder Blanket [1] was also performed. The aim of this study is to describe the analytical approach used in the new code and to discuss the results obtained.

2. COMPUTER CODE MODEL

The gas kinetics and dynamics of the helium-induced swelling in beryllium have been described by a system of reaction-rate differential equations. All the relevant effects occurring in irradiated beryllium under stationary or transient temperature conditions have been considered from a microscopic (lattice and subgranular volume elements), structural (metallographic features of the material) and geometrical (specimen design parameters) point of view.

The beryllium specimen was ideally considered as an arrangement of spherical grains in which helium, mainly generated by the reaction [1]:

$$^{9}Be + n \rightarrow 2^{4}He + 2n \qquad (1)$$

(which has a theoretical neutron energy threshold of 1.70 MeV and an effective threshold at 2.7 MeV), migrates to the free surfaces and/or precipitates into intragranular bubbles. These can also migrate (at much lower rate than the free atoms) through the grains to the grain boundaries to form grain-face bubbles and grain-edge bubbles (intergranular bubbles) usually larger than the intragranular ones. Bubbles may grow by capture of gas and coalesce to create larger bubbles with a lower restraint capillarity pressure. The growth of intragranular and intergranular bubbles causes a plastic deformation of the medium resulting in material swelling. For relatively large volume increases, grain-face and grain-edge bubbles can become interlinked and merge into an open porosity network through which the gas can escape from the specimen.

---

1 A second (n,α) reaction is responsible for helium production, but for fast reactor fusion irradiations the (n,2n) reaction is dominant.

2.1 THE REACTION-RATE EQUATIONS

The developed mathematical model is expressed by a system of seven reaction-rate differential equations which describe the helium short-and long-range transport. Each term of the equations presented below represents a source or loss term of the respective concentrations, due to a distinct elementary mechanism. The definition of the symbols used is listed at the end of this paper.

Concentration of gas in dynamical solution:

$$\frac{\partial c}{\partial t} = \beta - \chi k_i^2 D(c - c^0) - k_g^2 Dc - \frac{\chi \pi r_i^2 N_i DcQ\Delta T}{RT^2} - \frac{\alpha DcQ\Delta T}{aRT^2} - \frac{6\pi r_i cN_i D_i}{\lambda} - \pi r_i^2 cN_i V_i + \eta b - \psi c \quad (2)$$

Concentration of gas in intragranular bubbles:

$$\frac{\partial b}{\partial t} = \chi k_i^2 D(c - c^0) + \frac{\chi \pi r_i^2 N_i DcQ\Delta T}{RT^2} + \frac{6\pi r_i cN_i D_i}{\lambda} - \eta b - \frac{3v_i b}{a} - k_{gb}^2 D_i b - \psi b \quad (3)$$

Intragranular-bubble density:

$$\frac{\partial N_i}{\partial t} = \chi 16\pi\lambda DN_n cA^2 - \eta^{\times} N_i - \alpha' r_i^2 v_i N_i^2 - 16\pi r_i D_i N_i^2 - \frac{\alpha 3v_i N_i}{a} - k_{gb}^2 D_i N_i \quad (4)$$

Concentration of gas in grain-face bubbles:

$$\frac{\partial g}{\partial t} = Fk_g^2 Dc + Fk_{gb}^2 D_i b + \frac{F3v_i b}{a} + \frac{F\alpha DcQ\Delta T}{aRT^2} + F\psi(c + b) \quad (5)$$

Grain-face-bubble density:

$$\frac{\partial N_f}{\partial t} = \frac{F3v_i N_i}{a} + Fk_{gb}^2 D_i N_i - \frac{\alpha v_f N_f}{a_f} - \alpha' r_f^2 v_f N_f^2 - 16\pi r_f D_f N_f^2 \quad (6)$$

Concentration of gas in grain-edge bubbles:

$$\frac{\partial w}{\partial t} = (1 - F)k_g^2 Dc + (1 - F)k_{gb}^2 D_i b + (1 - F)\frac{3v_i b}{a} + (1 - F)\frac{\alpha DcQ\Delta T}{aRT^2} + (1 - F)\psi(c + b) \quad (7)$$

Grain-edge-bubble density:

$$\frac{\partial N_e}{\partial t} = (1 - F)\frac{3v_i N_i}{a} + (1 - F)k_{gb}^2 D_i N_i + \frac{\alpha v_f N_f}{a_f} - \alpha' r_e^2 v_e N_e^2 - 16\pi r_e D_e N_e^2 \quad (8)$$

Equations 2 to 8 are integrated by using the three bubble radii r_i, r_f, r_e calculated from additional expansion equations resulting from the interplay of all forces (i.e. gas pressure, capillarity stresses, internal stresses, etc.) acting on the intragranular, grain-face and grain-edge bubbles, respectively. A major part of the present work consisted in reformulating the constitutive relations used in these equations and selecting the parameters specific to beryllium, the most important of which are listed in Tab. 1.

2.2 BUBBLE NUCLEATION AND RE-SOLUTION

Once helium is generated in beryllium by the $^{9}Be(n,2n)2\,^{4}He$ reaction, due to its effective insolubility in the metals, it quickly supersaturates the lattice and precipitates to form embryonic intragranular bubbles on nucleation centres (i.e. vacancies, dislocation loops and nodes, etc.). The precipitation rate into intragranular bubbles is a diffusion-dependent process in which, during its random migration, a He-atom encounters a pre-existing cluster, and is expressed by the product Dk_i^2c, where $k_i^2 = 4\pi N_i r_i$ is the sink strength of the intragranular bubbles. However, it has been shown [3] that the precipitation of gas in solids under very strong supersaturation conditions is not governed by a simple random capture process, but it is also controlled by the vacancy flux into the bubbles. In fact, the pressure exerted by the gas on the surrounding lattice is gradually released if vacancies are captured providing more free volume for the precipitated gas. Thus the vacancy capture process goes on until the gas phase attains a pressure p equal to the elastic capillarity restrain $\frac{2\gamma}{r}$ (where γ is the surface tension and r the size of the bubble). Because the vacancy flux is driven by the compressive stress gradient around the bubbles, it follows that the resulting precipitation rate is significantly delayed if a large overpressure in the bubble is created, and it can be expressed by the product of the random capture precipitation with a *delaying factor* $\chi \leq 1$. Therefore, this factor, which is proportional to the vacancy concentration and tends to one when the equilibrium is reached, favours the migration of free gas atoms to the grain boundaries, where a larger vacancy availability is present.

The bubbles may grow by capture of free atoms, by coalescence and, of course by thermal expansion of the medium. On the other hand, due to the intense neutron irradiation, the gas bubbles can be destroyed as the gas atoms are re-injected into the lattice by elastic collisions at a frequency described by the *re-solution parameter* η. At the same time, the large number of vacancies generated by neutrons enhances the diffusion processes, so that the rate of bubble nucleation and growth is expressed by the balance between gain due to precipitation and loss due to re-solution.

2.3 BUBBLE MOTION

Once the bubbles are formed, they can move randomly through the lattice (*brownian motion*) or migrate in the direction of the acting forces produced by the local thermal gradients (*biased motion*). The most important mechanisms for bubble motion occur via volume diffusion and surface diffusion. The first mechanism arises when vacancies diffuse through the lattice from one side of a bubble to the other, while the second arises when the vacancies move through more effective atomic jumps along the bubble surface, causing a displacement of the centre of gravity of the bubble. Both mechanisms of motion are expressed by a diffusion coefficient which is written in terms of the atomic *self-diffusion coefficient* and *surface diffusion coefficient*, respectively, and of the size of the bubble. Due to the uncertainty in the experimental measurements of the surface diffusion coefficient of beryllium, this

quantity has been provisionally taken equal to the self-diffusion coefficient. The global bubble-diffusion coefficient considered in the code takes into account all the possible mechanisms which affect bubble motion in beryllium[2] .

2.4 GRAIN GROWTH AND GAS SWEEPING

For high irradiation temperatures and fluences, beryllium grains grow at a rate which is strongly dependent on temperature. From the microscopic point of view grain growth is caused by lattice atoms which tend to reduce the average curvature of the grain boundaries, resulting in a growth of the larger grains and in a shrinkage of the smaller ones. This mechanism causes a reduction of the specific area of the grain boundaries. Due to the motion of the grain boundaries part of the dynamically soluted gas and of the bubbles are swept and irreversibly trapped at the grain boundary (where bubbles can subsequently easier coalesce). This phenomenon is expressed by a *grain boundary sweeping coefficient* $\psi = \frac{3}{a}\frac{da}{dt}$, a being the mean grain radius. It should be noted that grain growth is limited by the intergranular bubbles which preclude the enlargement of the grains when the covering ratio (fraction of the grain surface area covered by intergranular bubbles) approaches one. When these conditions are met, the grain growth process is allowed to proceed further only after the reduction of the covering ratio, tipycally caused by venting of intergranular gas and re-sintering.

2.5 BUBBLE GROWTH AND MATERIAL SWELLING

As it has been previously remarked, bubbles may grow by capture of free gas atoms and by coalescence. When two bubbles collide, they tend to coalesce generating a larger bubble with lower restraint capillarity pressure. The new bubble is initially instable and becomes finally stable when the equilibrium of all locally acting forces is reached, namely when:

$$p = \frac{2\gamma}{r} + p_{ext}$$

p being the gas pressure, γ the surface tension, r the bubble radius and p_{ext} the pressure given by the existing external forces, which is generally dependent on the overall swelling. Since in its final equilibrium state the coalescence of two bubbles is a surface-preserving and not a volume-preserving process, it follows that the new bubble has an equilibrium volume which is larger than the sum of the separated bubble volumes. The bubble growth is therefore a process driven by the mechanical stress gradient created around the bubble by the bubble inner overpressure. The growth rate equation was thus written as a diffusional creep rate equation around the various pressurized cavities (intragranular bubbles, face and edge-bubbles) and involving a spherical volume whose diameter is equal to the

---

[2] A third mechanism of motion arises when bubbles move by transport of evaporating matter. It is also accounted for in the code although it is acting at very high temperatures only.

pertinent bubble interdistances. The expansion process is calculated starting from the simplest cell arrangement (one intragranular bubble surrounded by 100%-dense material). Then a more complex cell is considered, containing an intergranular bubble in the center surrounded by a medium consisting of dense material and intragranular bubbles and so on. The overall strain-stress relations are simultaneously calculated accounting for the plastic deformations of the individual cells. The following cell subdivision has been considered:

- *Micro-cell* centered around an intragranular bubble. The expansion of this cell can be produced only by point defect motion (i.e. Schottky vacancies and/or gas atoms).
- *Local cell* centered around a grain-face bubble and constructed from a finite number of micro-cells. The expansion of this cell is due to micro-cell deformations and by the face-bubble expansion.
- *Macro-cell* centered around an edge-pore and made up of a set of local cells. The deformation of this cell can be produced by the inter- and intragranular bubbles expansion, and by the edge-pore expansion.
- *Geometrical cell* (cylindrical macroscopic sample), the only cell having an annular shape, which consists of an ensemble of macro-cells. This cell can expand by macrocell growth and by shear in the geometrical stress field of the sample.

On the basis of the previously calculated variables (i.e. bubble density, bubble size, etc.), and taking into account the imposed boundary conditions (i.e. external pressure, etc.), the code provides the integration of the stress-strain equations for the four above-described cells, evaluating the material swelling rate which is given by the resulting strain rate of the geometrical cell.

2.6 GAS RELEASE

For relatively large swelling, grain-face and grain-edge bubbles can become interlinked and merge into an open porosity network through which the gas can escape from the specimen. The modelling of the interlinkage of intergranular bubbles and pores is based on percolation theory [4].
According to this theory, intergranular bubbles and pores are considered as being distributed on a branching pattern describing the potential porosity channel network. The sites of this pattern are defined as *occupied* if they contain a pore or a bubble. Let P be defined as the fraction of occupied sites relatively to the total number N of sites of the pattern. The occupied sites tend to form clusters, the size of which depends on the fraction P. If two clusters are connected to each other, they form a chain which is defined as *unbounded* if connected to open porosity. It has been demonstrated [4] that, for each type of pattern there exists a critical value P_c of P below which an occupied site belongs certainly to a *bounded* chain, namely a chain which is not connected to open porosity. For each value of P greater than P_c there is a finite probability that a given occupied site belongs to an unbounded interlinked chain. This probability is known as *percolation probability* $p(P)$ and it is obviously zero for $P \leq P_c$. For calculation purposes the intergranular bubbles and pores have been supposed to be

distributed on a pattern in which each node is connected with three bonds. For this type of pattern, named *expanded cactus*, it can be demonstrated that the critical value of P is equal to 0.637. This means that the gas cannot escape from the material until at least 63.7% of the total sites of the pattern are occupied by intergranular bubbles and/or pores. Therefore, according to this model the percolation probability is evaluated from the previous calculated grain size and intergranular pore distribution. Finally, the open-pore fraction being known, gas release from porosity can be calculated.

3. RESULTS

At present a first version of the code based on the above-mentioned assumptions is available, and is being validated by comparison with a large number of experiments. Beryllium in-pile irradiations [5] [6] [7] [8] [9] have been considered for our calculations. A comparison of the calculated swelling with in-pile experimental data for a wide range of irradiation conditions (i.e. irradiation temperatures from 50 $°C$ to 700 $°C$, neutron fluences from $2.1\ 10^{21}\ n/cm^2$ ($E_n > 1\ MeV$) to $5.0\ 10^{22}\ n/cm^2$ ($E_n > 1\ MeV$), helium contents from 1155 *appm* to 26100 *appm*) is shown in Fig. 1 and Fig. 2.

These data cover the range of irradiation temperatures and neutron fluences applicable to the European BOT DEMO blanket. Experimental data for combined high temperatures and fluences are, as yet, unavailable. The agreement between calculated swelling and experimental data is excellent (mean error 0.9%, standard deviation 13.3 %), whereby the discrepancies are probably due to the uncertainty in the experimental conditions (i.e. fast flux, helium generation rate, volumetric heat generation, etc.) and in knowledge of the relevant beryllium properties (i.e. creep law, helium diffusion coefficient, etc.) which may be affected by the manufacturing processes and impurity content. In order to evaluate beryllium swelling and helium release during normal reactor operating conditions, a first calculation for the proposed European BOT DEMO blanket [1] was performed. Calculations for beryllium pebbles under a variety of irradiation temperatures and fluences appropriate to the European DEMO blanket have been carried out. The results of the swelling calculations are shown in Fig. 3.

It can be noticed that swelling, initially, increases with irradiation temperature; for higher fluences, however, this trend is inverted due to release of helium. At higher irradiation temperatures the initial trend of the swelling behaviour is found again, due to the rapid coalescence of the gas bubbles and to the reduction of the mechanical strength of the material, involving an easier deformation of the metal under the thrust of the bubble for overpressure.

4. CONCLUSIONS AND FUTURE WORK

The ANFIBE code satisfactorily describes the beryllium swelling in in-pile tests. However, to improve the reliability of the code predictions, further in-pile experiments at high temperatures and neutron fluences are clearly needed. Additional code development is also in progress in order to de-

scribe both the behaviour of beryllium at temperatures higher than 700 °C (as some of the correlations used in the code are valid only up to this temperature) and the behaviour of beryllium with fabricated open porosity.

NOMENCLATURE

a	beryllium mean grain radius (cm).
A	Avogadro number (atoms/mole).
a_f	grain face radius (cm).
b	gas atoms in the bubbles per unit volume of beryllium (moles/cm^3).
c	intragranular gas atoms in dynamical solution per unit volume of beryllium (moles/cm^3).
c^0	equilibrium solubility of the helium gas atoms per unit volume of beryllium (moles/cm^3).
D	atomic diffusion coefficient of the gas (cm^2/s).
D_e	edge bubble diffusion coefficient (cm^2/s).
D_f	face bubble diffusion coefficient (cm^2/s).
D_i	intragranular bubble diffusion coefficient (cm^2/s).
D_s	atomic surface diffusion coefficient (cm^2/s).
D_v	atomic vacancy diffusion coefficient (cm^2/s).
e	index to define the grain-edge variables.
f	index to define the grain-face variables.
F	ratio of the face-bubble to specific surface.
g	index to define the grain boundary.
g	gas atoms in the face bubbles per unit volume of beryllium (moles/cm^3).
gb	index to define the grain boundary for bubbles.
i	index to define the intragranular variables.
k_e^2	sink strength of the edge bubbles (1/cm^2).

k_f^2 sink strength of the face bubbles ($1/cm^2$).

k_g^2 sink strength of the grain boundary ($1/cm^2$).

k_{gb}^2 sink strength of the grain boundary for bubbles ($1/cm^2$).

k_i^2 sink strength of the intragranular bubbles ($1/cm^2$).

N_e concentration of edge bubbles ($1/cm^3$).

N_f concentration of face bubbles ($1/cm^3$).

N_i concentration of intragranular bubbles ($1/cm^3$).

N_n concentration of vacancy clusters produced by recoil atoms ($moles/cm^3$).

Q heat of transport for thermodiffusion (erg/mole).

R gas constant (erg/mole).

r_e edge bubble radius (cm).

r_f face bubble radius (cm).

r_i intragranular bubble radius (cm).

t irradiation time (s).

T absolute temperature (K).

v_e edge bubble biased-migration velocity (cm/s).

v_f face bubble biased-migration velocity (cm/s).

v_i intragranular bubble biased-migration velocity (cm/s).

w atoms in the edge bubbles per unit volume of beryllium ($moles/cm^3$).

Greek letters

α Parameter ($0 \leq \alpha \leq 1$), evaluated from the bubble size distribution, which represents a positive source term due to the nucleation rate.

α' equivalent to α, but for another term in the equation.

β gas production rate ($moles/cm^3 s$).

ΔT temperature gradient (K/cm).

η atomic re-solution rate (atoms/s).

$\eta^{\times}$ bubble destruction rate (bubbles/s).

λ beryllium lattice spacing (cm)

χ precipitation delaying factor due to bubble overpressure.

ψ grain-boundary sweeping rate due to the grain growth under irradiation. (1/s).

ACKNOWLEDGEMENTS

This work was performed in the framework of the KfK Nuclear Fusion Project and is supported by the European Communities within the European Fusion Technology Program.

REFERENCES

[1] M. Dalle Donne et al., in: Proc. of the 17th Symposium on Fusion Technology (Rome, 1992) p. 1236.

[2] C. Ronchi and J. Van de Laar, EUR Report, 11387 EN (1988).

[3] C. Ronchi, J. Nucl. Mater. 148 (1987) 316

[4] C. Domb and M.S. Green, "Phase Transitions and Critical Phenomena", Vol. II, (Academic Press, London, 1972) p. 197.

[5] J.M. Beeston, "Properties of Irradiated Beryllium: Statistical Evaluation", EG&G Idaho Report, TREE-1063 (1976).

[6] J.M. Beeston et al., J. Nucl. Mater. 122 & 123 (1984) 802.

[7] E. Koonen, "Study on Irradiation Effects and Swelling of Irradiated Beryllium", CEN/SCK Report, Reactor Safety Analysis, BR2 Department, (1989).

[8] J.M. Beeston et al., "Gas Retention in Irradiated Beryllium", EG&G Idaho Report, EGG-FSP-9125 (1990).

[9] V. Levy, "Rapport Final du Contrat SBB-BS1", CEA Report, Centre d'Etudes de Saclay, N.T. SRMA 92-1955 F.A 3591-532 (1992).

[10] M.C. Billone, Private Communication (1993).

[11] M.C. Billone et al., Fusion Technol. 19 (1991) 1707.

[12] Brush Wellman Inc., Private Communication (1992).

[13] "Ullmann's Encyclopedia of Industrial Chemistry", Vol. A4, (VCH, Weinheim, 1985) p. 12

[14] L. Murr, "Interfacial Phenomena in Metals and Alloys", (Addison-Wesley Publishing Company, Reading, 1975) p. 130.

[15] J.M. Dupoy et al., Mém. Scientif. Rev. Metallurg. 63 (1966) 481.

[16] C Ronchi, J. Nucl. Mater. 84 (1979) 55.

[17] A.G. Bespalov et al., Tr. Fiz.-Energ. Inst. (1974) 443.

[18] M.C. Billone: Private Communication (1992).

[19] W.G. Wolfer and T.J. McCarville, "An Assessment of Radiation Effects in Beryllium", Presented at the Sixth Topical Meeting on the Technology of Fusion Energy (San Francisco, 1985).

[20] N.P. Pinto, "Beryllium Science and Technology", (Plenum Press, New York, 1979) p. 342.

Tab.1 Material properties.

Properties	Correlations used in the code		Ref.
Solid surface tension [dyn/cm]	$\gamma = 3130.24$ $\gamma = 1960 - 1.5 \times (T - 1560.16)$ $\gamma = 1960$	$T < 780\ K$ $T < 1560\ K$ $T \geq 1560\ K$	[12] [13]
Grain boundary surface energy [erg/cm^2]	$\gamma_{gb} = 1076.08$ $\gamma_{gb} = 686 - 0.5 \times (T - 1560.16)$ $\gamma_{gb} = 686$	$T < 780\ K$ $T < 1560\ K$ $T \geq 1560\ K$	[14]
Self-diffusion coeff. [cm^2/s]	$D_{v\perp} = 0.52 \times \exp(-18916.15/T)$ $D_{v\parallel} = 0.62 \times \exp(-19844.55/T)$ $D_v = 3.14 \times 10^{-6} \times \exp(-9105.03/T)$	$T \geq 838\ K$ $T \geq 838\ K$ $T < 838\ K$	[15]
Surface-diffusion coeff. [cm^2/s]	$D_{v\perp} = 0.52 \times \exp(-18916.15/T)$ $D_{v\parallel} = 0.62 \times \exp(-19844.55/T)$ $D_v = 3.14 \times 10^{-6} \times \exp(-9105.03/T)$	$T \geq 838\ K$ $T \geq 838\ K$ $T < 838\ K$	
Bubble-diffusion coeff. [cm^2/s]	$D_b = (3\lambda^3/2\pi r^3 f)D_v + (3\lambda^4/2\pi r^4)D_s$		[16]
Helium-diffusion coeff. [cm^2/s]	$D_{He} = 3.1 \times 10^{-2} \times \exp(-25817.8/T)$ $D_{He} = 9.889 \times 10^{-13} \times \exp(-4718.87/T)$	$T \geq 873\ K$ $T < 873\ K$	[17]
Thermal creep rate [$1/s$]	$\dot{\varepsilon}_t = 0.02 \times \sigma^{3.6} \times \exp(-26000/T)$	$T \leq 973\ K$	[18]
Irradiation creep rate [$1/dpa$]	$\dot{\varepsilon}_i = 3.2 \times 10^{-12} \times \sigma$		[19]
Vapour pressure [atm]	$\log p = 6.186 + 1.454 \times 10^{-4} \times T - 16734/T$		[20]

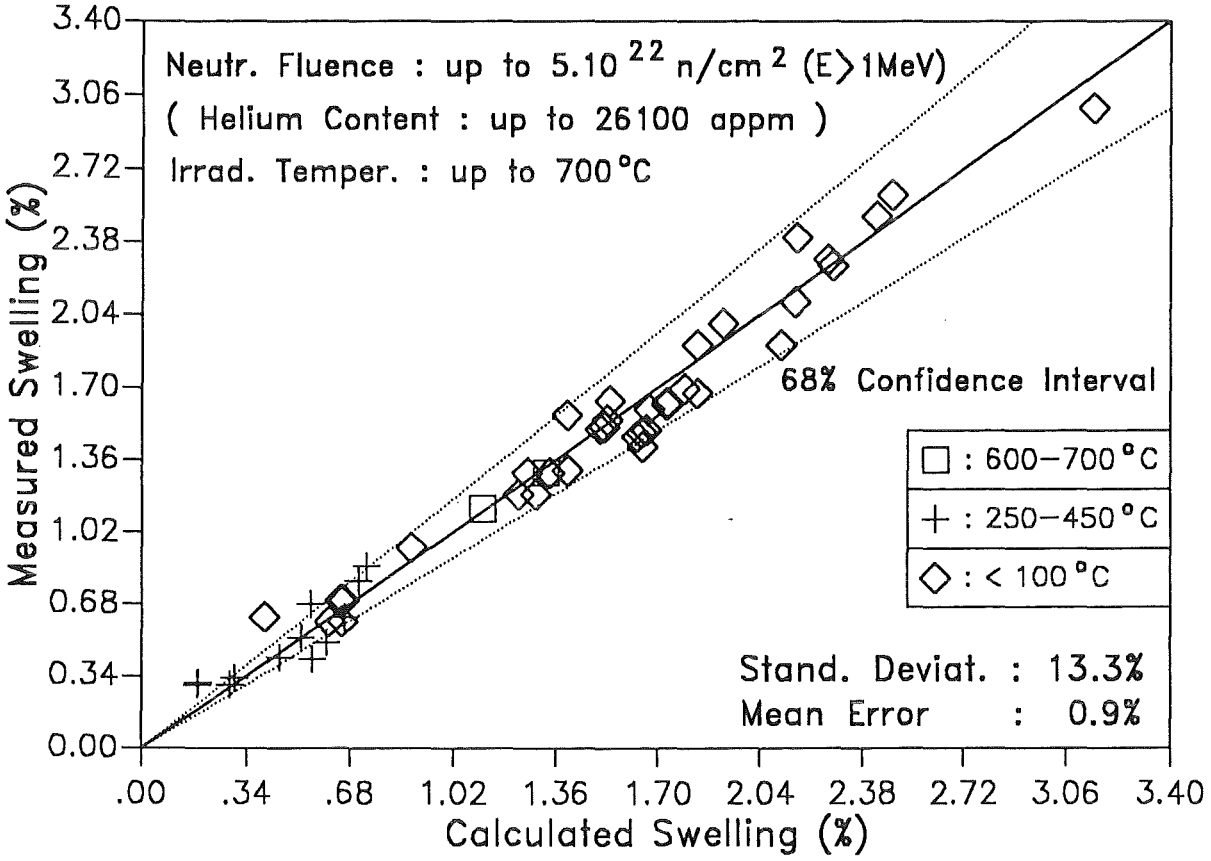

Fig.1 Comparison of calculated and experimental swelling data for in-pile irradiated beryllium [5] [6] [7] [8] [9], classified according to irradiation temperature.

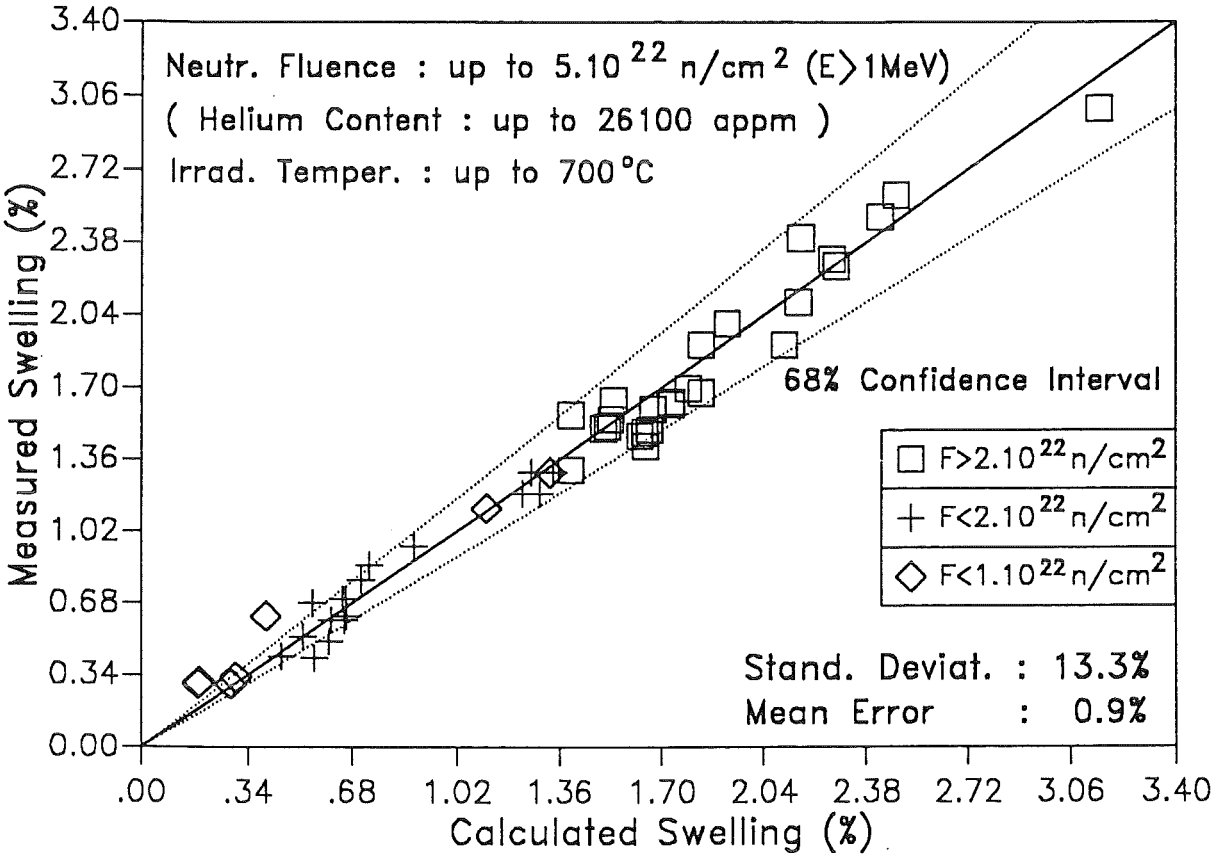

Fig.2 Comparison of calculated and experimental swelling data for in-pile irradiated beryllium [5] [6] [7] [8] [9], classified according to fast neutron fluence.

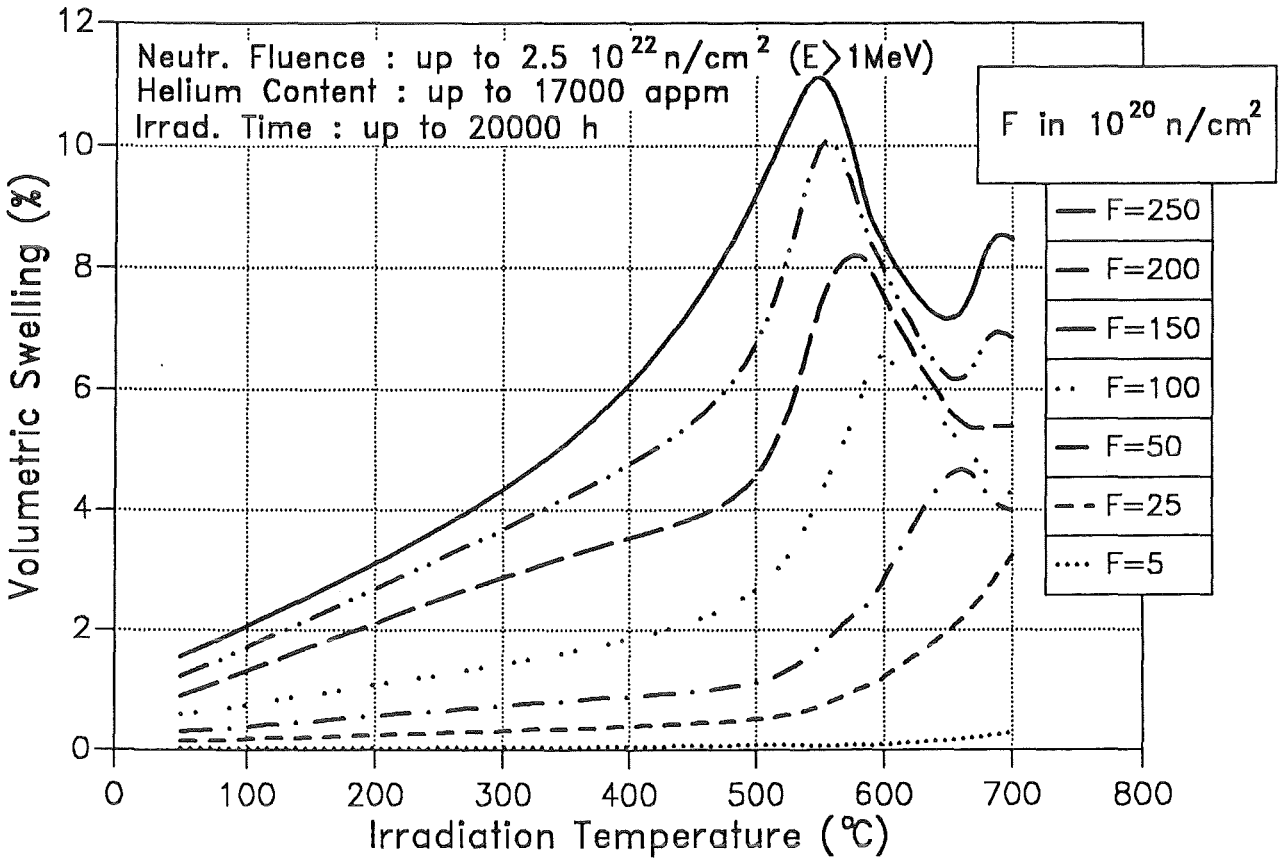

Fig.3 Volumetric swelling vs. irradiation temperature at different fast neutron fluences for the DEMO BOT [1] beryllium, as predicted by ANFIBE.

TRITIUM RELEASE STUDIES OF IRRADIATED BERYLLIUM

by
David L. Baldwin
Battelle, Pacific Northwest Laboratory
Richland, WA

Presented at the Workshop on Beryllium for Fusion Applications
October 4-5, 1993, Karlsruhe, Germany

INTRODUCTION

This presentation is a summary of Be studies, conducted at the Pacific Northwest Laboratory[a], relating stepped isothermal anneal tritium release measurements with thermal-ramp temperature programmed desorption measurements. Three ATR-irradiated Be specimens, covering the density range of 81% to 100% TD, have been tested by a stepped-thermal anneal technique. Data analysis of the tritium release curves using a diffusion/desorption model has yielded effective tritium diffusion coefficients, desorption-rate constants and the corresponding activation energies. The results from this model show diffusion to be the predominant rate-limiting mechanism under isothermal conditions with small and varying contribution by surface desorption. The 100% TD Be has also been tested by a thermal-ramp temperature-programmed desorption technique. Results from the stepped-thermal anneal and temperature-programmed desorption technique is summarized and compared.

EXPERIMENTAL FOR STEPPED ISOTHERMAL ANNEALS

Stepped isothermal anneal ^{3}H release testing of both low-density (81%) and high-density (99%) Be irradiated in the Advanced Test Reactor (ATR), over 1500 h periods, was recently performed. A description of the Be test materials can be found in [1]. These Be test materials were fabricated and irradiated to meet conditions relevant to the International Thermonuclear Experimental Reactor (ITER). 100% TD Be was previously tested and release curves reported earlier [2,3].

Using the experimental apparatus described previously [2], the 81% TD sample was heated at 573 to 873 K, in isothermal steps of 100 K, with about 400 h holds at each temperature. The 99% TD sample was heated in similar fashion from 573 to 973 K, then in 50 K steps to 1173 K. The hold times for the 973

(a) Pacific Northwest Laboratory is operated by Battelle Memorial Institute for the U.S. Department of Energy under Contract DE-AC06-76RLO 1830.

to 1173 K range were 24 h per step to determine the presence and temperature of a burst release. Purge gas (He-0.1%H_2) at 100 scm^3/min swept the wafer-shaped samples in a quartz system. Important modifications of the previously described apparatus include eliminating the Zn reducer bed, adding 10 scm^3/min moist air just before the CuO oxidizer column, and adding a pair of sequential HTO collection bubblers, replacing the molecular sieve columns. Tritium and helium assay and release results are shown in Table 1.

DIFFUSION / DESORPTION MODEL

A combined diffusion/desorption model solving for the release fraction, $f_r=R_t/R_\infty$, as function of time, was derived by Billone [1] from Carslaw and Jaeger [4].

The diffusion portion of the model assumes that the tritium released after long time, R_∞, at an isothermal annealing temperature, is uniformly distributed and available for transport in the bulk at the beginning of the anneal. The characteristic path length for diffusion is the half-width, ℓ, of the wafer-like samples. The diffusivity determined by matching predictions to data is considered an "effective" diffusivity, D_{eff}.

The surface-desorption portion of the model assumes first-order kinetics. The rate constant for this process is also considered to be an "effective" constant, k_{eff}. The diffusion/desorption equation is

$$f_r = 1 - 2\,h^2 \sum_{n=1}^{\infty} \frac{\exp(-\beta_n^2 t/\tau_1)}{\beta_n^2[\beta_n^2 + h(h+1)]}$$

where

f_r	=	Tritium Release Fraction, R_t/R_∞
h	=	$k_{eff}\ell/D_{eff}$
$\beta_n \tan\beta_n$	=	h
τ_1	=	ℓ^2/D_{eff}
D_{eff}	=	$D_o \exp(-Q_1/RT)$ in m^2/s
k_{eff}	=	$k_o \exp(-Q_2/RT)$ in m/s
t	=	time in s
ℓ	=	slab half-thickness in m
R	=	8.314×10^{-3} kJ/mol-K
T	=	temperature in K

The effective tritium diffusivities, D_{eff} (m^2/s), and desorption rate constants, k_{eff} (m/s), for these materials, and D_{eff} from new data analysis of previously reported 100% TD material, are shown in Table 2.

The diffusion/desorption model provides evidence for a changing mechanism over both temperature and density and indicates that diffusion is the primary mechanism with a small and changing contribution from surface desorption.

Table 1: Tritium and Helium Assay and Release Characteristics

Parameter		81% TD	99% TD	100% TD
^{3}H Assay (pre-anneal)		6600 MBq/g	8570 MBq/g	302000 MBq/g
		55.3 appm	71.8 appm	2530 appm
^{4}He Assay (pre-anneal)		1.82 cm^{3}STP/g	2.17 cm^{3}STP/g	65.0 cm^{3}STP/g
		733 appm	872 appm	26100 appm(3)
He Generation Rate (appm/10^{22} n/cm^2)		2820	3350	5300 ±300
^{3}H Fractional Release (%) at Temperature:	573 K (2)	3.2	0.10	0.01
	673 K	38	0.55	0.25
	773 K	89	3.3	0.6
	873 K	99 (4)	9.7	90 (4)
	973 K	(1)	26.4	(1)
	1073 K	(1)	33.2	(1)
	1173 K	(1)	96.5 (4)	(1)
^{3}H Retention (post-anneal)		1.4%	(1)	10%
He Retention (post-anneal)		91.7%	(1)	(1)
Sample Weight		0.353 g	0.112 g	0.473 g
Sample Thickness		5.25 mm	4.50 mm	3.2 mm
^{3}H Content in Sample		2330 MBq	960 MBq	143000 MBq

Notes:

(1) not measured.
(2) Actual release temperatures of 100% TD test: 573, 684, 784, 884 K.
(3) The value of 26100 appm He for the 100% TD Be is a revised value from earlier published data [1] and based on new measurements. This revised value is due to improvements in the analytical method for measuring retained He.
(4) Burst release of ^{3}H observed.

Table 2: Summary of Tritium Diffusivity and Desorption Rate Constant

Be Density	Time Regime	Diffusivity, D_{eff} (m^2/s)	Surface Desorption Rate Constant, k_{eff} (m/s)
81% TD	50< t <150 h	1.7×10^{-11} exp(-3.5 kJ/mol/RT)	8.8×10^{-5} exp(-18 kJ/mol/RT)
99% TD	25< t <400 h	1.6×10^{-10} exp(-9.5 ±3.0 kJ/mol/RT)	4.8×10^{-8} exp(-4.6 kJ/mol/RT)
100% TD	1< t <25 h	1.4×10^{-10} exp(-11.5 kJ/mol/RT)	

Applying the diffusion/desorption model to the 81% and 99% TD data sets, a changing h-parameter, as a function of temperature and density, was observed, implying changing mechanisms with temperature and density.

as $h \rightarrow \infty$, diffusion is rate-limiting
as $h \rightarrow 1$, diffusion and desorption are equally rate-limiting
as $h \rightarrow 0$, desorption is rate-limiting

For both densities, the h-parameter was found to range from 1 to >100 for all temperatures, implying the rate-limiting mechanism ranged from mixed diffusion and desorption (h=1) to primarily diffusion (h=>100). In the high-density (99% TD) Be case, with increasing temperature from 573 to 773 K, the h-parameter decreased from 10 to 1, implying primarily diffusion at the lower temperatures and mixed diffusion and desorption at the higher temperature. In the low-density (81% TD) Be case, the reverse was observed, with the h-parameter increasing from 10 to >100 with increasing temperature, still indicating primarily diffusion with only a small contribution from desorption.

TEMPERATURE PROGRAMMED DESORPTION

An alternative to the often used stepped isothermal anneal heating method is the method of temperature programmed desorption under the conditions of a constantly increasing thermal ramp. Several data analysis methods are available to extract information from the release curve. The method utilized here is the Heating Rate Variation Method. In this method, the release rate curve is measured, under thermal ramp conditions, at varying ramp rates. The ramp rates used should span at least one order of magnitude.

The heating rate variation method equation is

$$\ln(T_m^2/\beta) = E_a/RT_m + \ln(E_a/AR)$$

where
T_m = temperature of $Peak_{max}$
β = heating rate
E_a = activation energy
R = gas constant
A = pre-exponential

Then the plotting of $\ln(T_m^2/\beta)$ versus $1/T_m$ provides:

slope = E_a/R
intercept = $\ln(E_a/AR)$

Using this method, three specimens of the 100% TD ATR-irradiated Be was tested and the data analyzed. A single release peak was observed in each case. The data for 100% TD ATR Beryllium is shown in Table 3.

Table 3: Data for Heating Rate Variation Model

T_m ($Peak_{max}$, K)	β (Heating Rate, K/min)	$\ln(T_m^2/\beta)$
997	2.0	13.12
955	0.5	14.42
939	0.2	15.30

From plot of $\ln(T_m^2/\beta)$ versus $1/T_m$, the regression is:

$$y = -21.17 + 34140x$$

resulting in:

$$E_a = 280 \text{ kJ/mol}$$

$$A = 5.3 \times 10^{13}$$

Now, summarizing all activation energies from the stepped isothermal anneal tests and the thermal-ramp tests, the comparative results are shown in Table 4. As can be seen, Q_1 for diffusion and Q_2 for desorption, both under isothermal conditions, show relatively low activation energies, ranging from 4 to 18 kJ/mol. The activation energy, Q_3 for surface release under thermal-ramp conditions, is a very high 280 kJ/mol.

Table 4: Summary of Activation Energies

Activation Energy	Conditions	Temperature Range	Value (kJ/mol)
Q_1 (diffusion)	Isothermal conditions	573 to 873 K	4 - 12
Q_2 (desorption)	Isothermal condition	573 to 873 K	5 - 18
Q_3 (surface release)	Thermal-ramp conditions	$Peak_{max}$ = 939-997 K	280

There is no other known work in the literature for tritium release from beryllium under thermal-ramp conditions using the heating rate variation method for determining activation energy. In evaluating the meaning of this very high activation energy, it should be recalled [2] that the 100% TD Be has very high BeO and probable high surface BeO. Therefore, perhaps a useful comparison can be made to activation energies in the literature on tritium diffusion from pure BeO, single-crystal and sintered material. As shown in Table 5, Fowler and Chandra, et al., reported very high values of 203 to 220 kJ/mol, very similar to the 280 kJ/mol reported in Table 2. This comparison leads to the possible conclusion that tritium release under thermal-ramp conditions is very sensitive to surface BeO, while tritium release under isothermal conditions is less sensitive to surface BeO.

Table 5: Comparison to Literature Values for Diffusion in BeO

Sample Material Type	Q (kJ/mol)
single-crystal BeO	220
sintered BeO	203
BeO Powder	70

Ref: Fowler, Chandra, et al., J Amer Cer Soc., Vol 60, No. 3-4, March 1977

In summarizing the work on the temperature programmed desorption studies on irradiated Be, the following points can be concluded:

1. Single release peaks were observed for tritium release, implying a single release site, single release mechanism, and single activation energy,

2. The reported Q_3 is over order-of-magnitude larger than Q_1 or Q_2 in irradiated Be,

3. The measured very high Q_3 (280 kJ/mol) is similar to Q_1 for BeO (220 kJ/mol),

4. Concluding that the activation energy of surface release, Q_3, measured under thermal ramp conditions may be very sensitive to surface BeO, while the activation energy of diffusion or desorption under isothermal-anneal conditions may be less sensitive to surface BeO.

TRITIUM BURST RELEASE

A tritium burst release, first predicted [7] in 1985 to occur at about 923 K due to the migration of He bubbles to form interconnected grain-edge tunnels to the surface, has been observed in all these Be materials.

Accumulated evidence includes

1) wide burst-release peak-widths,
2) non-diffusional-shaped release peak,
3) nearly complete loss of remaining tritium inventory,
4) before and after SEM photographs showing extensive restructuring and void formation,
5) 0 to 7 hour time-lag of the release burst, dependent upon Be density, presumably caused by the time required for He bubble coalescence and restructuring to occur.

The observed burst release temperature (873 to 1173 K) and observed time lag appear to be sensitive to density, He content, and irradiation temperature. The burst release for the low He-content 81% TD and high He-content 100% TD Be occurred at 873 K. The burst release for the low He-content 99% TD Be occurred at 1173 K, releasing the entire remaining inventory of over 50% of the total.

References

1. Baldwin, D. L., M. C. Billone, to be published in Proceedings of ICFRM6, Stresa, Italy, September 27-October 1, 1993.

2. Baldwin, D. L., O. D. Slagle, and D. S. Gelles, J. Nucl. Matl. 179&181 (1991) 329-334.

3. Billone, M. C., C. C. Lin, and D. L. Baldwin, Proceedings of the Ninth Topical Meeting on Fusion Technology, Oakbrook, IL, October 1990.

4. Carslaw, H. S. and J. C. Jaeger, University Press, Oxford, 1959.

5. Verrall, R. A., Proceedings of the International Workshop on Ceramic Breeder Blanket Interactions", Clearwater, FL, November 22-23, 1991, 92-105.

6. Bertone, P. C., J. Nucl. Matl., 151 (1988) 281-292.

7. Baker, C. C., J. N. Brooks, D. A. Ehst, D. L. Smith, and D. K. Sze, FY 1985", ANL/FPP/85-2, 4-304.

8. Jones, P.M.S. and R. Gibson, J. Nucl. Matl., 21 (1967) 353.

9. Abramov, E., M. P. Riehm, D. A. Thompson, and W. W. Smeltzer, CFFTP-G-9013, May 1990.

10. Kawamura, H. and E. Ishituka, Proceedings of the International Workshop on Ceramic Breeder Blanket Interactions, Clearwater, FL, November 222-23, 1991, 164-168.

11. Pemsler, J. P. and E. J. Rapperport, Trans. Metall. Soc. AIME, 230 (1964) 90.

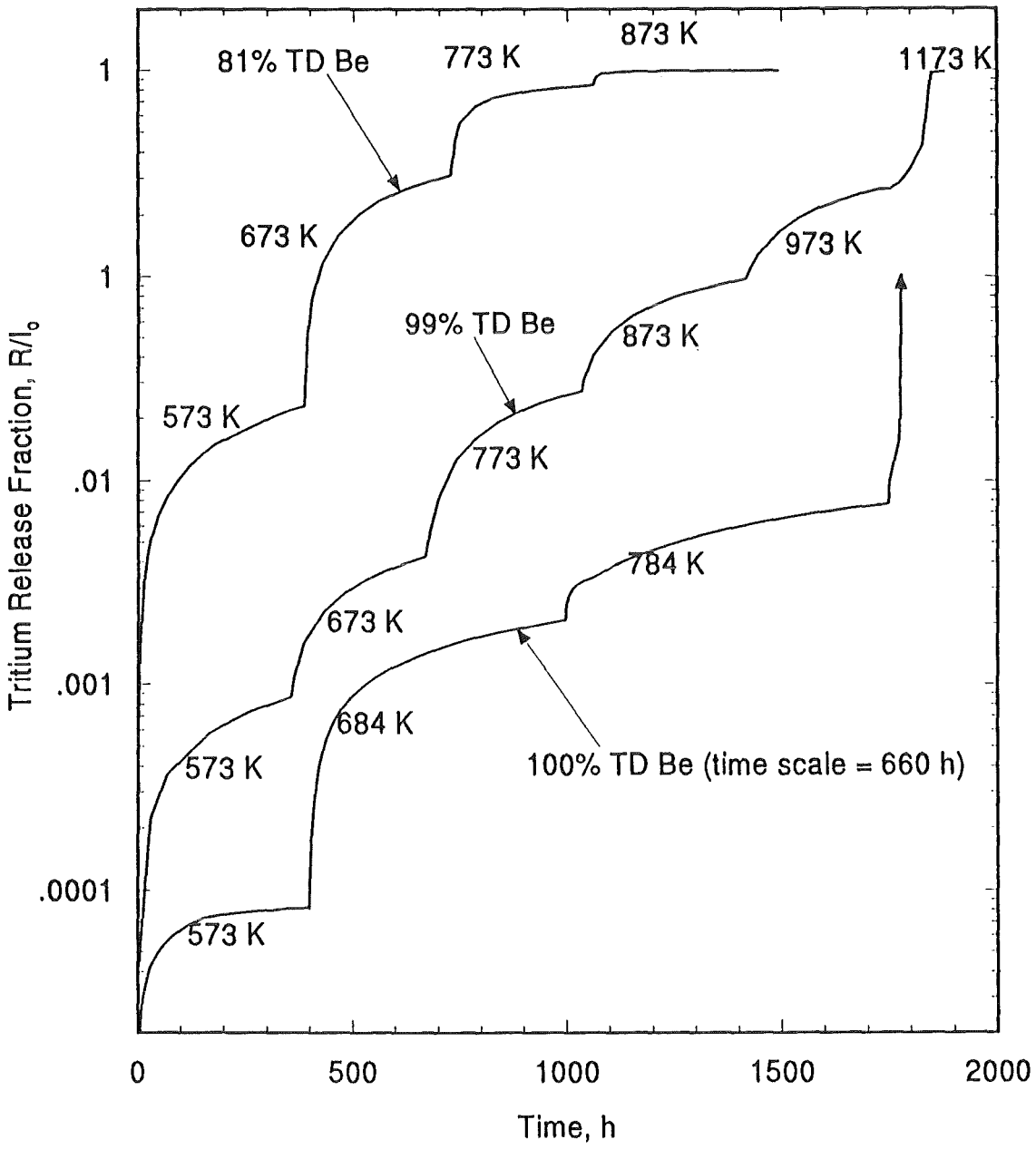

Tritium Release Curves for Beryllium

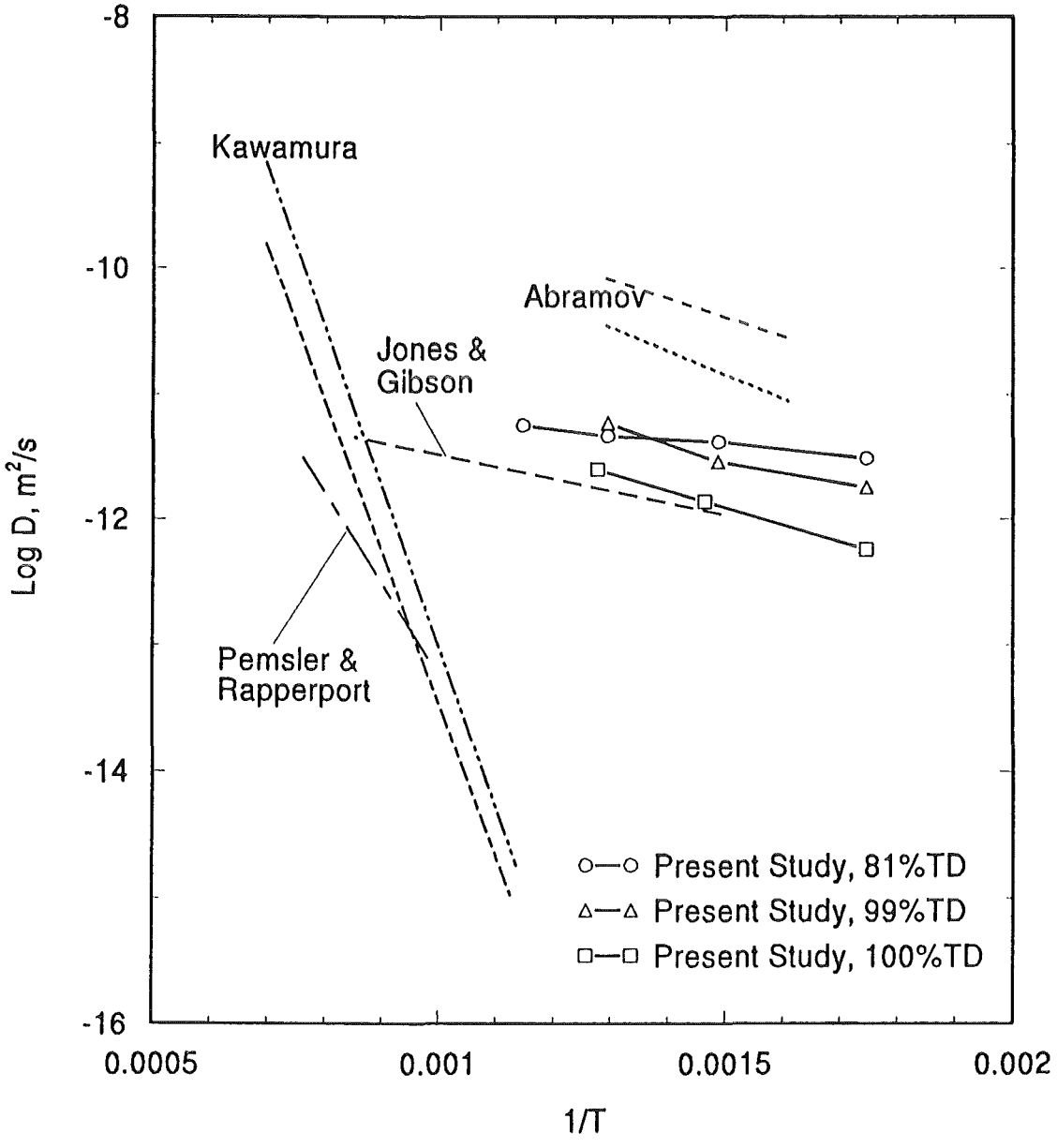

Tritium Diffusivity in Beryllium

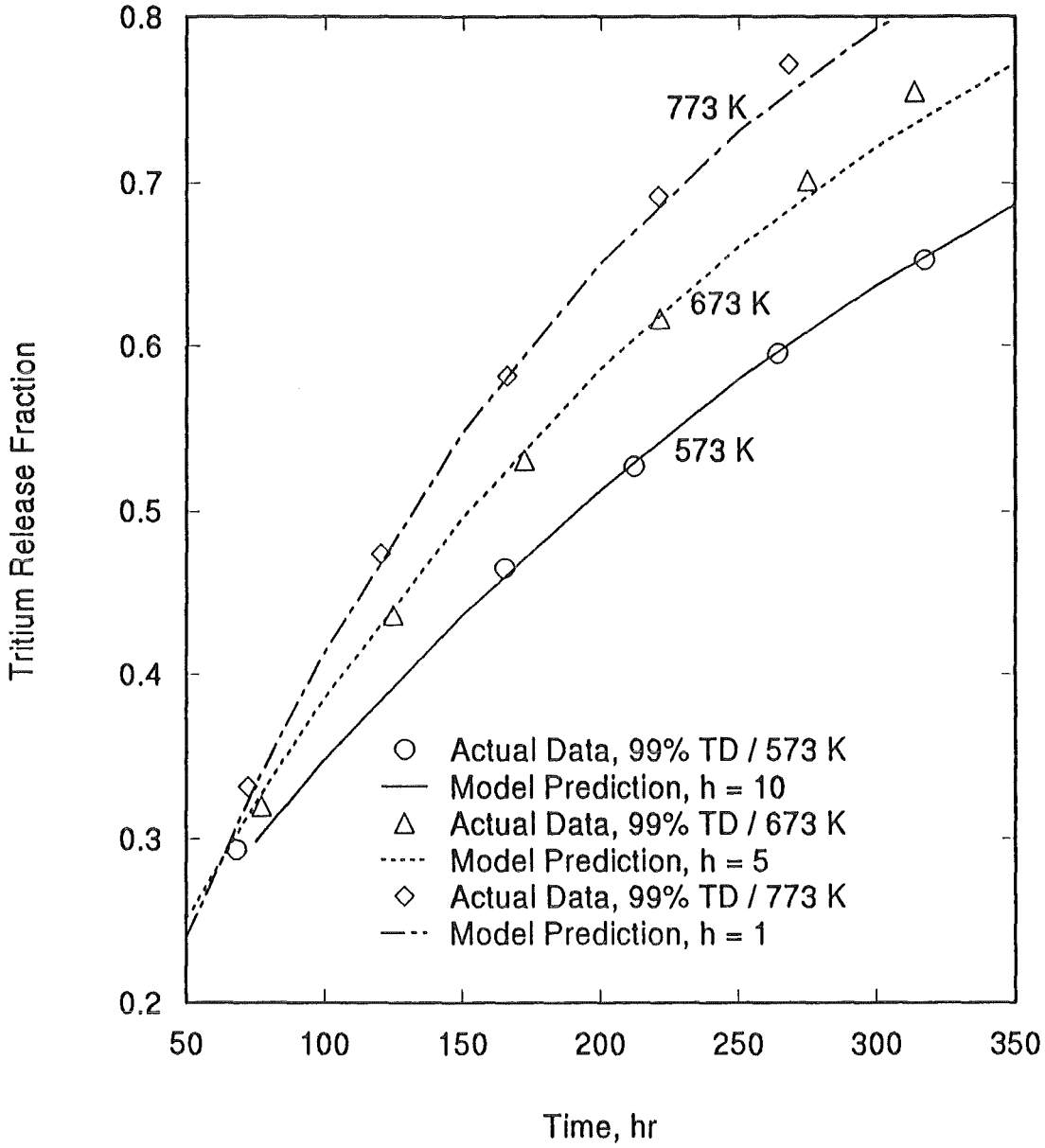

Model Prediction vs Actual Release Data for 99% TD Be

SUMMARY

* Stepped thermal-anneal release measurements at 573 K to 1173 K
  - 81% TD Be
  - 99% TD Be

* Diffusion/Desorption model allows determination of D_{eff} and k_{eff}

* D_{eff} (m^2/s), for these materials, and from new data analysis of previously reported 100% TD material, were found to be

  81% TD Be: 1.7×10^{-11} exp(-3.5 kJ/mol/RT)

  99% TD Be: 1.6×10^{-10} exp(-9.5 kJ/mol/RT)

  100% TD Be: 1.4×10^{-10} exp(-11.5 kJ/mol/RT)

* Diffusion is determined as the primary mechanism, with contribution from surface desorption

TEMPERATURE PROGRAMMED DESORPTION

HEATING RATE VARIATION METHOD

Heating Rate Variation Model Equation:

$$\ln(T_m^2/\beta) = E_a/RT_m + \ln(E_a/AR)$$

where T_m = temperature of $Peak_{max}$
β = heating rate
E_a = activation energy
R = gas constant
A = pre-exponential

Plotting of $\ln(T_m^2/\beta)$ versus $1/T_m$ provides:

slope = E_a/R
intercept = $\ln(E_a/AR)$

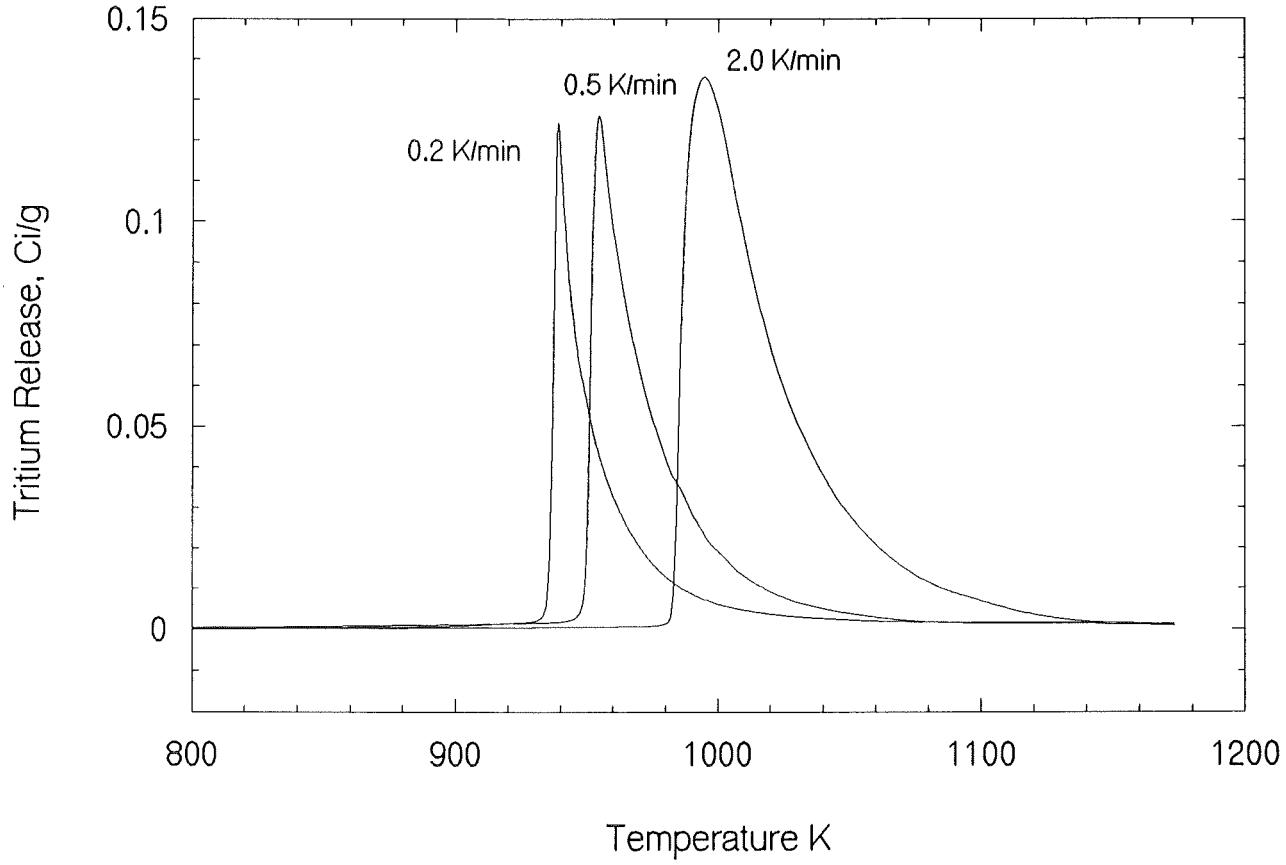

Thermal Ramp Release for 100% TD Be

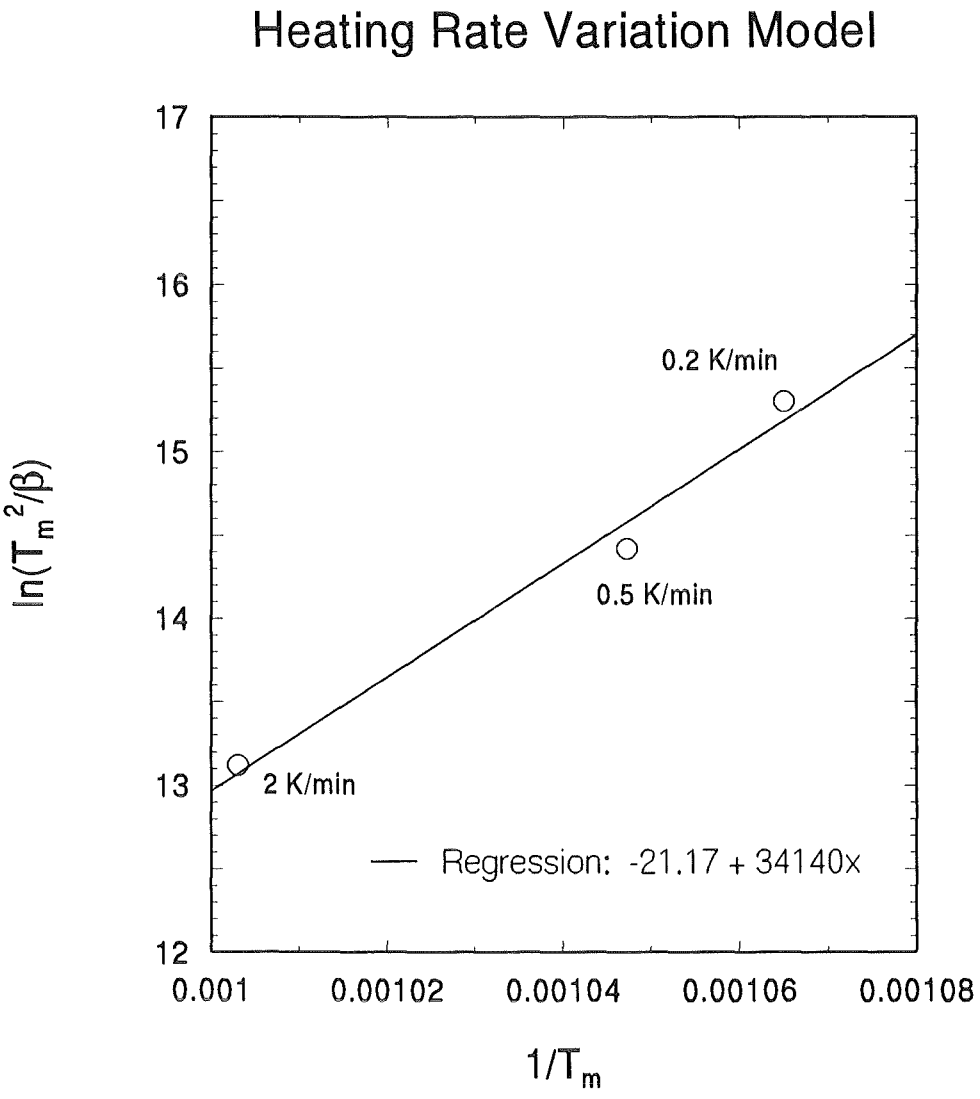
Heating Rate Variation Model
17
16
15
14
13
12
0.001
0.00102
0.00104
0.00106
0.00108
ln(T_m^2/β)
1/T_m
0.2 K/min
0.5 K/min
2 K/min
Regression: -21.17 + 34140x

TEMPERATURE PROGRAMMED DESORPTION

Data for 100% TD ATR Beryllium

Table: Data for Heating Rate Variation Model

T_m ($Peak_{max}$, K)	β (Heating Rate, K/min)	$\ln(T_m^2/\beta)$
997	2.0	13.116
955	0.5	14.417
939	0.2	15.299

From plot of $\ln(T_m^2/\beta)$ versus $1/T_m$, regression is:

$$y = -21.17 + 34140x$$

$$E_a = 280 \text{ kJ/mol}$$

$$A = 5.3 \times 10^{13}$$

SUMMARY OF ACTIVATION ENERGIES

Table: Summary of Activation Energies

Activation Energy	Conditions	Temperature Range	Value (kJ/mol)
Q_1 (diffusion)	Isothermal conditions	573 to 873 K	4 - 12
Q_2 (desorption)	Isothermal condition	573 to 873 K	5 - 18
Q_3 (surface release)	Thermal-ramp conditions	$Peak_{max}$ = 939-997 K	280

Table: Comparison to Literature Values for Diffusion in BeO

Sample Material Type	Q (kJ/mol)
single-crystal BeO	220
sintered BeO	203
BeO Powder	70

Ref: Fowler, Chandra, et al., J. Amer. Cer. Soc., Vol 60, No. 3-4, March 1977

Long-time Tritium Release from Irradiated Beryllium (SIBELIUS Irradiation)

L. Dörr[2], T. Eberle[2], J. Lebkücher[1], H. Werle[1]

Kernforschungszentrum Karlsruhe GmbH

Institut für Neutronenphysik und Reaktortechnik[1]

Hauptabteilung Versuchstechnik[2]
Postfach 36 40, D-76021 Karlsruhe, Germany

Projekt Kernfusion

Association KfK-Euratom

Abstract

Tritium is produced in beryllium, which is used as neutron-multiplier in ceramic fusion blankets, by fast neutrons. Although the production rate is about two to three orders of magnitude smaller than that of the breeder ceramic, initial tritium release tests with beryllium samples from the SIBELIUS irradiation indicated that, because of the very slow release at typical blanket temperatures (400 - 700 °C), the inventory might become large during the DEMO blanket lifetime ($\simeq$ 3 y). An extrapolation of the short-time (several days) tritium release tests to longer times is difficult because the inventory decrease with time is not exponential.

Therefore a long-time annealing test with beryllium samples from the SIBELIUS irradiation has been started February 1993. Samples are purged and annealed up to 12 months at 380, 450, 550 and 650 °C. Residual inventories after annealing are determined by purging and heating to 850 °C. Results for not-annealed and 3-, respectively 6-month annealed samples are presented.

1. Introduction

Solid breeder blankets require the use of beryllium in order to achieve adequate tritium breeding. Among the concerns related to the use of beryllium are

compatibility with other blanket materials (ceramic and steel), tritium retention and swelling.

The main objective of the SIBELIUS experiment [1, 2], a common EC-US program, was to investigate the oxidation kinetics of beryllium in contact with ceramics and the nature and extent of beryllium interaction with steel in a neutron environment. In addition, tritium release characteristics of the ceramic/beryllium/steel compacts were checked inpile and tritium and helium retention in beryllium was determined out-of-pile after irradiation.

An extensive post-irradiation examination (PIE) program is performed by US laboratories, CEA and KfK. CEA PIE and inpile results have been presented earlier [2, 3]. Initial SIBELIUS PIE work at KfK was concerned with chemical compatibility of beryllium with ceramics and steel and with tritium retention in ceramics and beryllium and has been described previously [4]. The most important result concerning tritium release of beryllium was, that the tritium generated by fast neutrons is released very slowly at typical blanket temperatures (400 - 700 °C). Therefore, although the tritium production rate of the ceramic is two to three orders of magnitude larger than that of beryllium, the inventory in beryllium may become comparable or even exceed that of the ceramic. Reliable estimations of tritium inventories for times comparable with the DEMO blanket lifetime ($\approx$ 3 y) are not possible with available data. Therefore a long-time annealing (up to 12 months) test with SIBELIUS beryllium samples has been started February 1993. Results on tritium release of beryllium from the initial PIE and from long-time annealing (0, 3 and 6 months, respectively) are presented.

2. SIBELIUS irradiation

The design of the irradiation device and experimental conditions are reported in [1, 2]. Eight capsules have been irradiated (Fig. 1). At KfK, samples from capsule 1, 2, and 5 were investigated. These capsules contained stacks of beryllium, steel and Li_4SiO_4 pebbles (capsule 1), Li_4SiO_4 pellets (capsule 2) and Li_2O pellets (capsule 5). The irradiation temperature of the beryllium pellets of capsule 1 was 270 °C, for that of capsule 2 and 5 550 °C.

The investigated beryllium pellets (8 mm ∅ x 2 mm) were made by Brush-Wellman (specification B-26, arc cast, BeO $<$ 300 ppm). The structure is characterized by grains as large as 2 mm and some intergranular cracks. A cold worked layer resulting from machining is observed on the surface [2]. The density

determined from the masses and dimensions varied between 1.79 and 1.82 g/cm^3 and was in the average 1.805 g/cm^3 (98 % TD) [5].

The ceramic specimens were degassed at 600 °C for four hours in vacuum to eliminate moisture, then all specimens were assembled in a dry glove box. Similar precautions were taken against moisture after irradiation: a moisture-tight argon enclosure was specially designed and installed in the hot cells for dismantling operations. Transport and handling of samples after irradiation was done under inert atmosphere.

The irradiation was performed in the core of the SILOE reactor at CEN Grenoble from April to October 1990 for 1690 h (4 reactor cycles). Neutron fluxes in the device midplane were: thermal 1.1 x 10^{14}, fast (> 1 MeV) 1.0 x 10^{14} 1/cm^{2}s. Calculated beryllium dpa is 0.7 [2, 3].

3. Tritium release of not-annealed samples

The experimental setup for the tritium release measurements has been described earlier [6]. The main characteristics are: the sample chamber is connected by a short, heated line (≈ 300 °C) to a Zn reductor (390 °C). The reductor transforms any tritium water to tritium gas. This avoids problems with tritium water adsorption and allows quantitative tritium measurements. The tritium activity is measured in parallel with an ionization chamber and a proportional counter. In all cases, the agreement of the time-dependant activity between the two detectors was excellent. Therefore only the ionization chamber data are given.

The samples were purged with 50 standard-cm^3/min He + 0.1 % H_2 (purity 99.9999 %). Two heating procedures were used: linear ramps with 5 °C/min up to about 850 °C, which is hold for 6 - 31 h or fast, stepwise temperature increase, holding each temperature level for about 2 h, up to 850 °C (2 - 6 h).

The tritium inventory is determined by integrating the measured release rate over the time. Because tritium release of beryllium is slow, even after heating several hours at 850 °C not all tritium is released. The residual inventory has been estimated assuming an exponential decrease of inventory with time (which is known to be a bad assumption), and has been added to the measured release to determine experimental inventories. The estimated residual inventories amounted to 5 - 25 % of the total experimental inventory.

In a neutron field, tritium is generated in beryllium by the following reactions: ^{9}Be(n, t)^{7}Li (threshold 11.6 MeV) and ^{9}Be(n, α)^{6}He → ^{6}Li(n, α)t. In addition, a fraction of the tritium (2.74 MeV tritons) produced in the surface layer of the

ceramic is injected into those beryllium pellets, which are in contact with ceramic. The amount of injected tritium has been estimated numerically based on calculated tritium production rates in the ceramic [5].

Measured, calculated neutron-generated [5] and estimated injected inventories are given in table 1. Pellet 1 of capsule 1 was irradiated at ≤ 270 °C and was not in contact with ceramic. Assuming, based on Baldwin's observations [7], that at 270 °C the release of neutron-generated tritium is negligible, the experimental inventory should agree with the calculated neutron-produced inventory. This is not the case and checks indicated that very probably the calibration factor of the tritium detection (ionization chamber) was too high.

The following conclusions drawn from the experimental inventories are independent of this uncertainty in the absolute values of inventories:

1. Capsule 1 (irradiation temperature 270 °C)

   The much higher inventory of pellet 6 (contact with ceramic) compared to that of pellet 1 indicates, that at 270 °C a remarkable fraction of the injected tritium is retained during irradiation

2. The inventories of the pellets of capsule 2 and 5 (irradiation temperature 550 °C) are comparable to that of pellet 1 of capsule 1. This indicates that at 550 °C essentially all injected tritium, but only a small fraction of the neutron-generated tritium is released during irradiation.

In accordance with the conclusions based on the experimental inventories, studies of tritium release kinetics (Fig. 2) demonstrate that the injected tritium is released at lower temperatures (> 400 °C, Fig. 2 top) than the neutron-generated (≥ 600 °C, Fig. 2 bottom). A crude estimation of the residence time of neutron-generated tritium based on kinetics yielded > 1 month for temperatures ≤ 600 °C.

Because of the very slow and very uncertain release of neutron-generated tritium a long-time annealing test (up to 12 months) was started February 1992.

4. Long-time annealing

SIBELIUS beryllium pellets from previous metallographic investigations have been cleaned and cut axially to quarter of pellets for this investigation. The samples were inserted at definite positions in a tube furnace to achieve the desired annealing temperatures of 380, 450, 550 and 650 °C and are purged with 5 l/h He. The inventory after annealing is determined by heating the samples 3 h at 850 °C

and purging with He + 0.1 vol % H_2. As discussed earlier, even after heating several hours at 850 °C the samples contain a remarkable residual inventory (Fig. 3), which is estimated to be several ten to hundred percent of the released tritium and this determines essentially the uncertainty (errors bars in Fig. 4).

In the table below, measured absolute values of released tritium and relative values based on the release of a not-annealed similar sample are given. Values for 12 months annealing are not yet available. The samples investigated up to now contained essentially only neutron-generated tritium.

Capsule no.	Irrad. temp. (°C)	Pellet no.	Contact	Released tritium after annealing (MBq/g) / (rel. units)			
				Anneal. temp. (°C)	Anneal. time (months)		
					0	3	6
1	270	3	steel	380	376/1.0	--	234/0.62
2	550	13	Li_4SiO_4/steel	550	845/1.0	608/0.72	214/0.25
5	550	11/13	Li_2O/steel	650	892/1.0	66/0.07	62/0.07

Whereas the absolute values of released tritium for the not-annealed samples of capsule 2 and 5 are in reasonable agreement with the previous measurements (table 1), that of capsule 1 is about a factor three lower. The reason for this discrepancy is not clear.

Relative inventories are plotted in Fig. 4 as a function of annealing time. From these data a first very crude estimation of the residence time of neutron-generated tritium in high-density beryllium yields 13, 5 and 2 months for 380, 550 and 650 °C, respectively, in accordance with the previous estimation.

5. Conclusions

In the blanket the mass of beryllium is comparable with that of the ceramic, therefore the ratio of tritium inventory in beryllium to that in the ceramic is given by $I(Be)/I(ceramic) \approx (p \times \tau)_{Be} / (p \times \tau)_{ceramic}$. The specific tritium production rate p of beryllium is two to three orders of magnitude lower than that of the ceramic. On the other side the tritium residence time τ is estimated to be three to four orders of magnitude larger (for lithium orthosilicate τ is 10 and 0.3 h for 380 and

550 °C, respectively). Therefore the neutron-generated tritium inventory in beryllium may become comparable or even exceed that in the ceramic during the lifetime (≈ 3 y) of the DEMO blanket.

The tritium inventory in beryllium is an important issue in safety considerations. Further studies concerning tritium release of beryllium for DEMO blanket relevant temperatures and times are required.

Acknowledgements

This work was performed in the framework of the KfK Nuclear Fusion Project and is supported by the European Communities within the European Fusion Technology Program.

References

[1] N. Roux, H. Briec, M. Bruet, T. Flament, C. Johnson, M . Masson A. Terlain, F. Tournebize, J. Nucl. Mater. 179 - 181 (1991) 827

[2] N. Roux, J.J. Abassin, M. Briec, D. Cruz, T. Flament, I. Schuster, "Compatibility Behavior of Beryllium with $LiAlO_2$ and Li_2ZrO_3 Ceramics, with 316L and 1.4914 Steels in SIBELIUS", 5th Int. Conf. on Fusion Reactor Materials (ICFRM-5), Clearwater, Fla, Nov. 17 - 22, 1991, paper PA 22

[3] M. Briec, "The SIBELIUS Experiment", CEN Grenoble, Note Technique DTP/SEC/90/90, Dec. 6, 1990

[4] W. Dienst, D. Schild, H. Werle, "Tritium Release of Li_4SiO_4, Li_2O and Beryllium and Chemical Compatibility of Beryllium with Li_4SiO_4, Li_2O and Steel (SIBELIUS Irradiation)", KfK 5109, Dec. 1992

[5] N. Roux, CEN Saclay, private communication

[6] W. Breitung, H. Elbel, J. Lebkücher, G. Schumacher, H. Werle, J. Nucl. Mater. 155 - 157 (1988) 507

[7] D.L. Baldwin, "Comparison of Results of Tritium and Helium Behavior in Irradiated Beryllium", Beryllium Technology Workshop, Clearwater, Fla, Nov. 20, 1991, (G.R. Longhurst, INEL, ed.)

Table 1 Tritium inventories from initial PIE (samples not annealed)

Capsule no.	Beryllium pellets				Titium inventory / pellet (MBq)		
	No.	Mass (g)	Irrad. temp. (°C)	Contact	Invent. exp.	Neutron-gen. calc.	Injected estim.
1	1	0.1890	≤ 270	steel	191	73	0
	6	0.1711	270	Li_4SiO_4	719	65	666
2	9	0.1877	550	Li_4SiO_4/steel	238	105	792
	15	0.1761	550	Li_4SiO_4/steel	244	98	792
5	9	0.1868	550	Li_2O/steel	229	152	503
	15	0.1720	550	Li_2O/steel	271	140	503

DISTRIBUTION OF SPECIMENS FOR P.I.E.

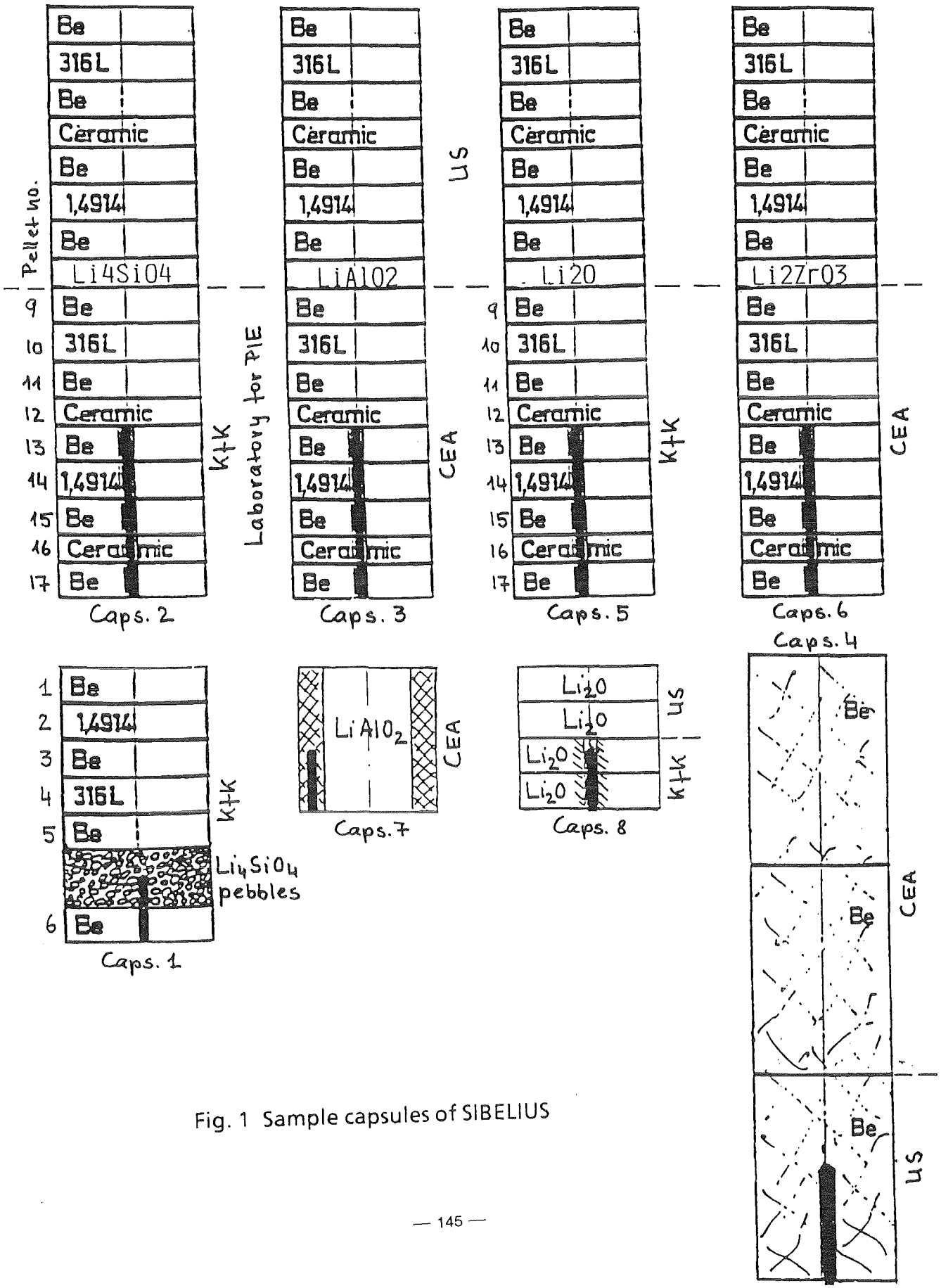

Fig. 1 Sample capsules of SIBELIUS

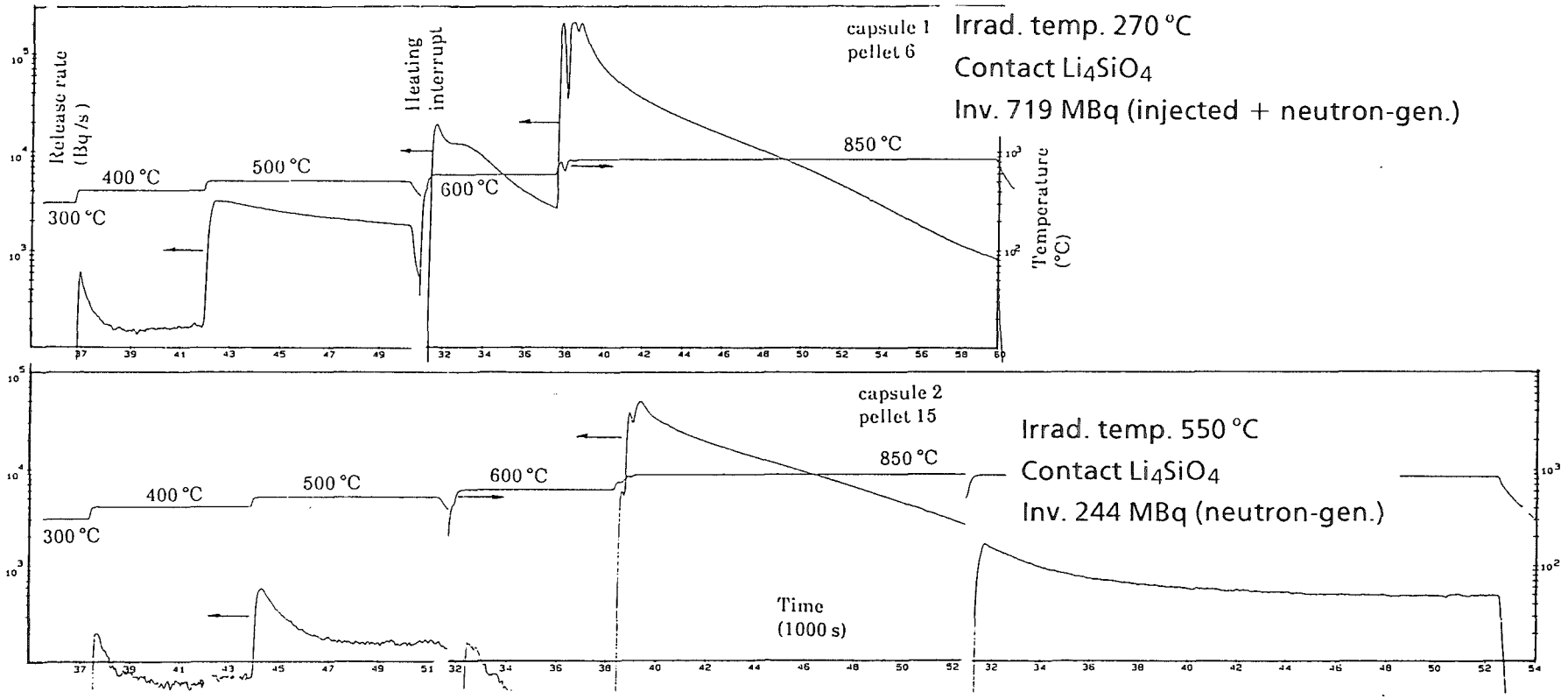

Fig. 2 Tritium release of beyllium, initial PIE (samples not annealed), temperature steps, purge gas He + 0.1 % H_2

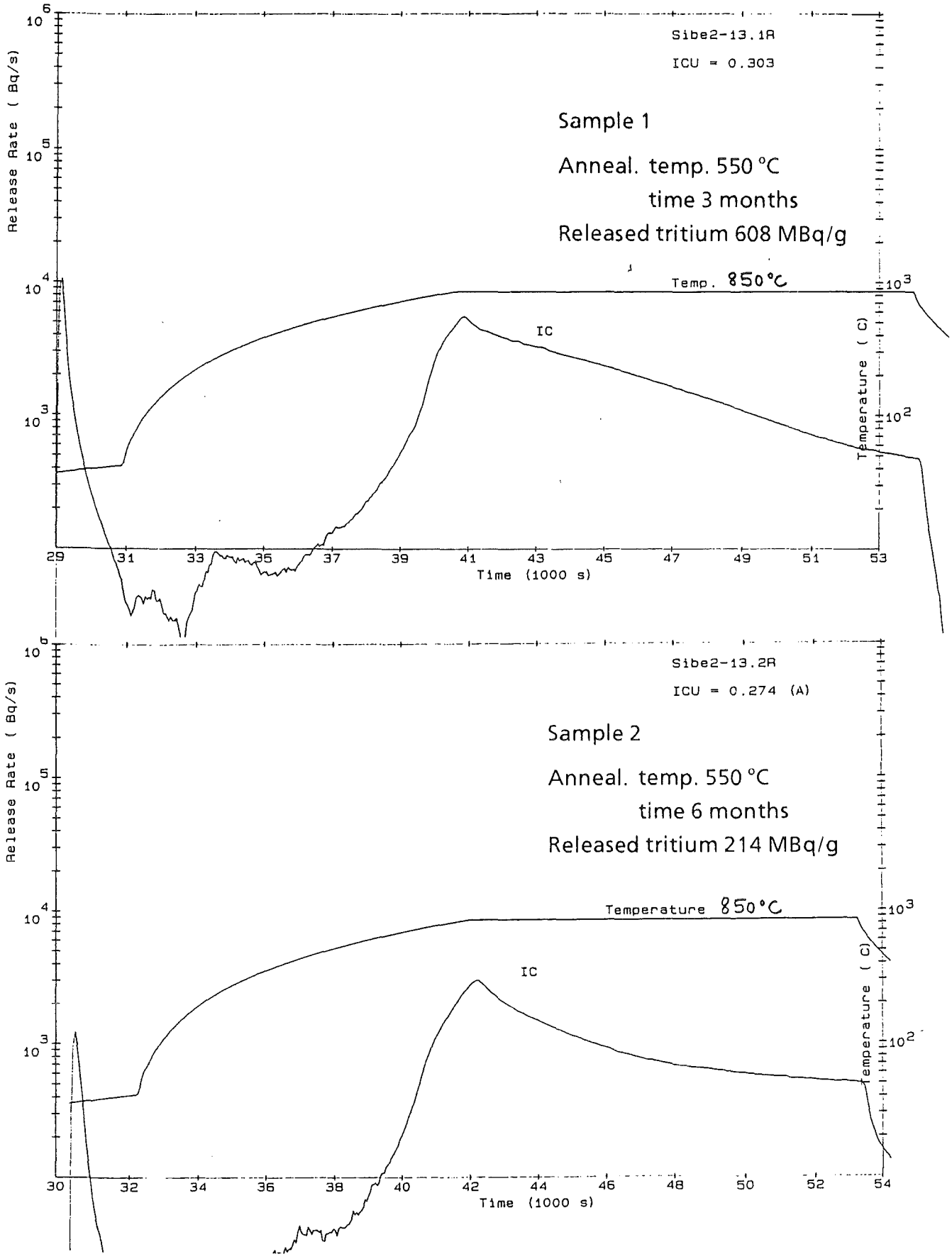

Fig. 3 Tritium release of annealed samples (capsule 2, pellet 13), ramp, 5 °C/min, purge gas He + 0.1 % H_2

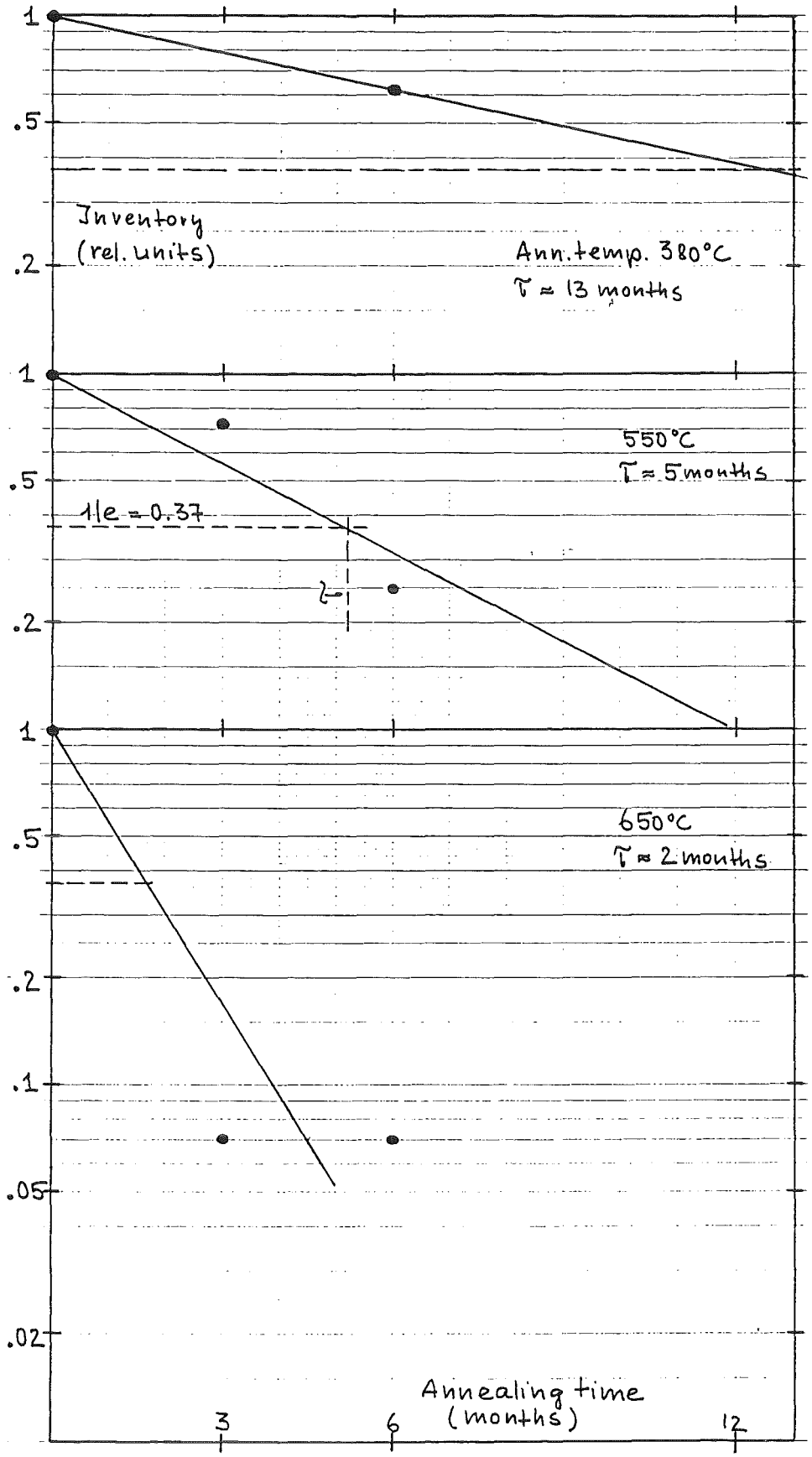

Fig. 4 Neutron-generated tritium inventory of high-density beryllium as a function of annealing time for different annealing temperatures

COMPUTER SIMULATION OF TRITIUM RETENTION AND RELEASE IN IRRADIATED BERYLLIUM

M. DALLE DONNE, F. SCAFFIDI-ARGENTINA

Kernforschungszentrum Karlsruhe, Institut für Neutronenphysik und Reaktortechnik
P.O. Box 3640, D-76021 Karlsruhe, Federal Republic of Germany

C. FERRERO

European Synchrotron Radiation Facility
B.P. 220, F-38043 Grenoble Cedex, France

C. RONCHI

Commission of the European Communities, Joint Research Centre, Karlsruhe Establishment,
European Institute for Transuranium Elements
P.O. Box 2340, D-76125 Karlsruhe, Federal Republic of Germany

ABSTRACT

The helium produced by the $^{9}Be(n,2n)2\,^{4}He$ and the oxygen impurities present in the material appear to be the main cause of tritium retention in irradiated beryllium. Because of the strong relation between the helium bubbles distribution and tritium release, it was decided to extend the code ANFIBE (ANalysis of Fusion Irradiated BEryllium), initially used to describe the helium induced swelling in beryllium, by including a new model describing the trapping effects on tritium due to chemical reactions with beryllium oxyde and capture in helium bubbles. The resulting modified code allows the calculation of tritium distribution and release from beryllium. Good agreement between calculated and experimental data was found.

1. INTRODUCTION

Since beryllium is considered as the best neutron multiplier candidate in the blanket of the DEMO Fusion Reactor [1], several studies have been required to evaluate the material behaviour under typical operating and accidental conditions. Due to transmutation reactions in beryllium, tritium is produced and released during the reactor lifetime, constituting a strong safety hazard. It is, therefore,

necessary to evaluate tritium transport behaviour and predict its release rate from irradiated beryllium. Unlike lithium-base ceramic breeder materials for which comprehensive models exist which describe the tritium transport in their interior [2], no computer codes, to our knowledge, are as yet available to account for the possible diffusion trapping processes occurring during beryllium irradiation. Based on the mathematical formulation used in the code ANFIBE [3] to describe the helium short and long-range transport, an additional tritium reaction-rate equation has been formulated to take into account the chemical trapping of this gas due to oxygen impurities.

The performance of the new version of ANFIBE was assessed by comparison with the available tritium release experiments. Additionally, analyses for a proposed EC Water Cooled Ceramic Blanket for ITER [4] and for the European BOT Solid Breeder Blanket [1] have been performed. The aim of this study is to describe the analytical approach used in the new code and to discuss the obtained results.

2. COMPUTER CODE MODEL

The model used to describe the behaviour of tritium is similar to that used to feature the helium kinetics and dynamics in beryllium [3]. The only important difference consists in an additional rate-equation accounting for the chemical trapping of tritium by oxygen impurities. Furthermore, in the case of tritium, no distinction was made between bubbles on grain-faces and bubbles on grain-edges which, for calculation purposes, were considered as a single population. Due to its relatively high solubility in beryllium, and to its much lower creation rate, it has been assumed that tritium can only be captured by helium-filled intragranular bubbles. This means that, in the modelling of tritium trapping only the simultaneously formed helium bubbles population is effective.
Schematically, the tritium behaviour is described as follows. Once it has been generated from the chain of reactions:

$$\begin{aligned} {}^{9}Be + n &\rightarrow {}^{6}He + \alpha \\ {}^{6}He &\rightarrow {}^{6}Li + \beta^{-} \\ {}^{6}Li + n &\rightarrow {}^{3}H + \alpha \end{aligned} \qquad (1)$$

it can diffuse in the lattice, or be captured by structural traps (such as intragranular helium bubbles, closed porosity, grain boundaries, etc. as in the case of helium), or it may react with beryllium oxide to form beryllium hydroxide according to the chemical reaction[1]:

$$2BeO(cr,\beta) + 2H(g) \rightarrow Be(OH)_2\,(cr,\beta) + Be(cr) \qquad (2)$$

---

1 Tritium is considered here as a gas because of its relatively small size in the Be-lattice. This hypothesis is justified within a first approximation.

the STP formation enthalpy of which is $\simeq -0.7eV$. The equilibrium concentration of soluted tritium (chemical activity) may be calculated from an Arrhenius-type relation (van't Hoff's equation) where the pre-exponential is given by the Law of Mass Action and the exponential argument is represented by the free energy of formation, namely:

$$[H] = \frac{[Be(OH)_2]^{\frac{1}{2}}[Be]^{\frac{1}{2}}}{[BeO]} e^{-\frac{\Delta G}{2RT}} \tag{3}$$

The underlying mathematical model is expressed by the following reaction-rate differential equations which describe tritium concentrations in dynamical solution, in intragranular bubbles, at the grain boundaries and in chemical traps.

Concentration of tritium in dynamical solution:

$$\frac{\partial c}{\partial t} = \beta - \chi k_i^2 D(c - \xi) - k_g^2 Dc + \eta b - \psi c - 4\pi R_t N_t D(c - \xi) \tag{4}$$

Concentration of tritium in intragranular bubbles:

$$\frac{\partial b}{\partial t} = \chi k_i^2 D(c - \xi) - \eta b - \psi b \tag{5}$$

Concentration of tritium at the grain boundaries:

$$\frac{\partial g}{\partial t} = k_g^2 Dc + \psi(c + b) \tag{6}$$

Concentration of tritium in chemical traps:

$$\frac{\partial m}{\partial t} = 4\pi R_t N_t D(c - \xi) \tag{7}$$

For the definition of the symbols used in these equations the reader is referred to the nomenclature at the end of this paper. Equations 4 to 7 are integrated by using the He-related quantities (i.e. bubble radius, bubble distribution, etc.), calculated in the remaining equations of the total governing system of coupled equations [3]. The integration of the whole system is carried out by using additional bubble expansion equations resulting from the interplay of all forces (i.e. gas pressure, capillarity stresses, internal stresses, etc.) acting on the intragranular and grain-face bubbles. The most important material properties used in the code are listed in Tab. 1.

3. RESULTS

Data on tritium release are available from the post-irradiation annealing experiments of Baldwin (for both moderately irradiated 99%-dense and highly irradiated 100%-dense beryllium) [6] [7], and from the SIBELIUS experiment for a low-irradiated 98%-dense beryllium [8]. These experiments cover a wide range of temperatures and oxygen impurity concentrations. Experimental results for in-situ tritium release are not yet available. In Baldwin's experiments [6] [7] the beryllium samples contained a relatively high quantity of oxygen (0.9-1.7 wt% BeO), and the initial irradiation at low temperature (75 °C) was followed by out-of-pile annealings at temperatures from 300 to 900 °C. As it can be seen from Fig. 1, for temperatures up to 700 °C tritium release is mainly governed by a single-energy thermally activated process (demonstrated by the linear trend of the fractional release shown in the Arrhenius plot) controlled by the chemical trapping described by equation (2). A comparison of ANFIBE predictions with Baldwin's experimental data for the 99%-dense beryllium [6], under five successive temperature annealing steps up to 700 °C, is shown in Fig. 2.

In the SIBELIUS specimens, due to the very low oxygen content (BeO < 300 ppm) and low irradiation fluence (6.0 10^{20} n/cm^2), tritium release is predominantly due to atomic diffusion through the lattice, with both chemical and He-bubble trapping playing a minor role.

As it can be seen from Fig. 3, the agreement between calculated and experimental out-of-pile annealing data at the end of each annealing step is good (mean error 4.7%, standard deviation 21.5%), whereby the discrepancies are probably due to the uncertainty in the experimental conditions (i.e. fast flux, tritium generation rate, etc.) and in knowledge of the relevant beryllium properties (i.e. tritium diffusion coefficient, etc.) which may be affected by the manufacturing processes and by the amount of impurities.

In order to evaluate tritium release during normal reactor operating conditions, calculations for beryllium pebbles containing 0.3 wt% BeO, under a variety of irradiation temperatures appropriate to the European BOT DEMO blanket have been carried out.

As shown in Fig. 4, the approximately linear dependence of the logarithm of release on 1/T up to about 450 °C (temperature at which an upswing in helium release is observed), shows that a single-energy thermally activated process, namely chemical trapping, is predominant up to this temperature. Above 450 °C there is a strong effect in release by tritium trapped in helium bubbles, as indicated by the departure from linearity of the fractional-release curve in the Arrhenius plot.

Referring to a EC Ceramic Blanket proposed for ITER [4], a transient analysis to predict the likely effects of an accidental temperature excursion was also performed. A neutron fluence corresponding to 1 MWy/m^2, a beryllium oxygen content of 2 wt% BeO, and a working temperature of 350 °C have been considered. Fig. 5 shows the time dependence of the release during the normal operating conditions of the EC ITER reactor. It can be noted that, due to the low beryllium temperature, at the end of the irradiation under normal reactor operating conditions only 1% of tritium is expected to be released. In order to investigate the tritium release danger during an accidental temperature increase of the beryllium, a temperature ramp up to 700 °C within 30 s was applied at the end of the blanket life. If the transient peak temperature of 700 °C is kept constant for 6 hours (a situation which seems, however, rather unlikely to occur) the resulting tritium release would be less than 5%

of the total inventory, as shown in Fig. 6 and Fig. 7. The end-of-life tritium inventory in beryllium being about 780 g [4], several hours at this temperature would thus be required in order to obtain an integral release of more than 40 g tritium.

4. CONCLUSIONS AND FUTURE WORK

The modified ANFIBE code describes satisfactorily tritium retention and release in beryllium although, at this stage, not all the mechanisms governing the release of tritium might have been considered. Comparison of the code predictions with experiments indicates that, for the cases considered [6] [7] [8] so far, the most important phenomena are accounted for in the model. However, to improve the reliability of the code predictions, further in-pile experiments at high temperatures and neutron fluences are clearly required. Additional code development is also needed in order to describe both the behaviour of beryllium at temperatures higher than 700 °C (as some of the correlations used in the code are valid only up to this temperature) and the behaviour of beryllium with fabricated open porosity.

NOMENCLATURE

b	gas atoms in bubbles per unit volume of beryllium (moles/cm^3).
c	intragranular gas atoms in dynamical solution per unit volume of beryllium (moles/cm^3).
D	atomic diffusion coefficient of the gas (cm^2/s).
g	index to define grain boundary.
g	gas atoms in the face bubbles per unit volume of beryllium (moles/cm^3).
i	index to define intragranular variables.
k_g^2	sink strength of the grain boundary (1/cm^2).
k_i^2	sink strength of the intragranular bubbles (1/cm^2).
m	gas atoms in the chemical traps per unit volume of beryllium (moles/cm^3).
N_t	concentration of the chemical traps (1/cm^3).
R_t	mean trap radius (cm).
t	irradiation time (s).
t	index to define trap variables.

Greek letters

β gas production rate (moles/cm^{3}s).

η atomic resolution rate (atoms/s).

ξ chemical tritium activity (moles/cm^3)

χ precipitation delaying factor due to bubble overpressure.

ψ grain-boundary sweeping rate due to the grain growth under irradiation. (1/s).

ACKNOWLEDGEMENTS

This work was performed in the framework of the KfK Nuclear Fusion Project and is supported by the European Communities within the European Fusion Technology Program.

REFERENCES

[1] M. Dalle Donne et al., in: Proc. of the 17th Symposium on Fusion Technology (Rome, 1992) p. 1236.

[2] G. Federici et al., J. Nucl. Mater. 187 (1992) 31.

[3] M. Dalle Donne et al., "Modelling of Swelling and Tritium Release in Irradiated Beryllium", Presented at the ICFRM-6 (Stresa, 1993).

[4] M. Dalle Donne et al., "EC Water Cooled Ceramic Blanket for ITER with Li_4SiO_4 Pebbles", KfK Internal Report, Kernforschungszentrum Karlsruhe (1993).

[5] G.R. Longhurst, "Tritium Behaviour in ITER Beryllium", EG&G Idhao Report, EGG-FSP-9304 (1990).

[6] D.L. Baldwin and M.C. Billone, "Diffusion/Desorption of Tritium from Irradiated Beryllium", Presented at the ICFRM-6 (Stresa, 1993).

[7] M.C. Billone et al., Fusion Technol. 19 (1991) 1707.

[8] W. Dienst et al., "Tritium Release of Li_4SiO_4, Li_2O and Beryllium and Chemical Compatibility of Beryllium with Li_4SiO_4, Li_2O and Steel (SIBELIUS Irradiation)", KfK Report, Kernforschungszentrum Karlsruhe, 5109 (1992).

[9] Brush Wellman Inc., Private Communication (1992).

[10] "Ullmann's Encyclopedia of Industrial Chemistry", Vol. A4, (VCH, Weinheim, 1985) p. 12

[11] L. Murr, "Interfacial Phenomena in Metals and Alloys", (Addison-Wesley Publishing Company, Reading, 1975) p. 130.

[12] J.M. Dupoy et al., Mém. Scientif. Rev. Metallurg. 63 (1966) 481.

[13] C Ronchi, J. Nucl. Mater. 84 (1979) 55.

[14] N.P. Pinto, "Beryllium Science and Technology", (Plenum Press, New York, 1979) p. 342.

Tab.1 Material properties.

Properties	Correlations used in the code		Ref.
Solid surface tension [dyn/cm]	$\gamma = 3130.24$ $\gamma = 1960 - 1.5 \times (T - 1560.16)$ $\gamma = 1960$	$T < 780\ K$ $T < 1560\ K$ $T \geq 1560\ K$	[9] [10]
Grain boundary surface energy [erg/cm^2]	$\gamma_{gb} = 1076.08$ $\gamma_{gb} = 686 - 0.5 \times (T - 1560.16)$ $\gamma_{gb} = 686$	$T < 780\ K$ $T < 1560\ K$ $T \geq 1560\ K$	[11]
Self-diffusion coeff. [cm^2/s]	$D_{v\perp} = 0.52 \times \exp(-18916.15/T)$ $D_{v\parallel} = 0.62 \times \exp(-19844.55/T)$ $D_v = 3.14 \times 10^{-6} \times \exp(-9105.03/T)$	$T \geq 838\ K$ $T \geq 838\ K$ $T < 838\ K$	[12]
Surface-diffusion coeff. [cm^2/s]	$D_{v\perp} = 0.52 \times \exp(-18916.15/T)$ $D_{v\parallel} = 0.62 \times \exp(-19844.55/T)$ $D_v = 3.14 \times 10^{-6} \times \exp(-9105.03/T)$	$T \geq 838\ K$ $T \geq 838\ K$ $T < 838\ K$	
Bubble-diffusion coeff. [cm^2/s]	$D_b = (3\lambda^3/2\pi r^3 f)D_v + (3\lambda^4/2\pi r^4)D_s$		[13]
Tritium-diffusion coeff. [cm^2/s]	$D_T = 9.18 \times 10^{-3} \times \exp(-7702.89/T)$ $D_T = 1.73 \times 10^{-5} \times \exp(-2225.16/T)$	$T \geq 873\ K$ $T < 873\ K$	[7]
Vapour pressure [atm]	$\log p = 6.186 + 1.454 \times 10^{-4} \times T - 16734/T$		[14]

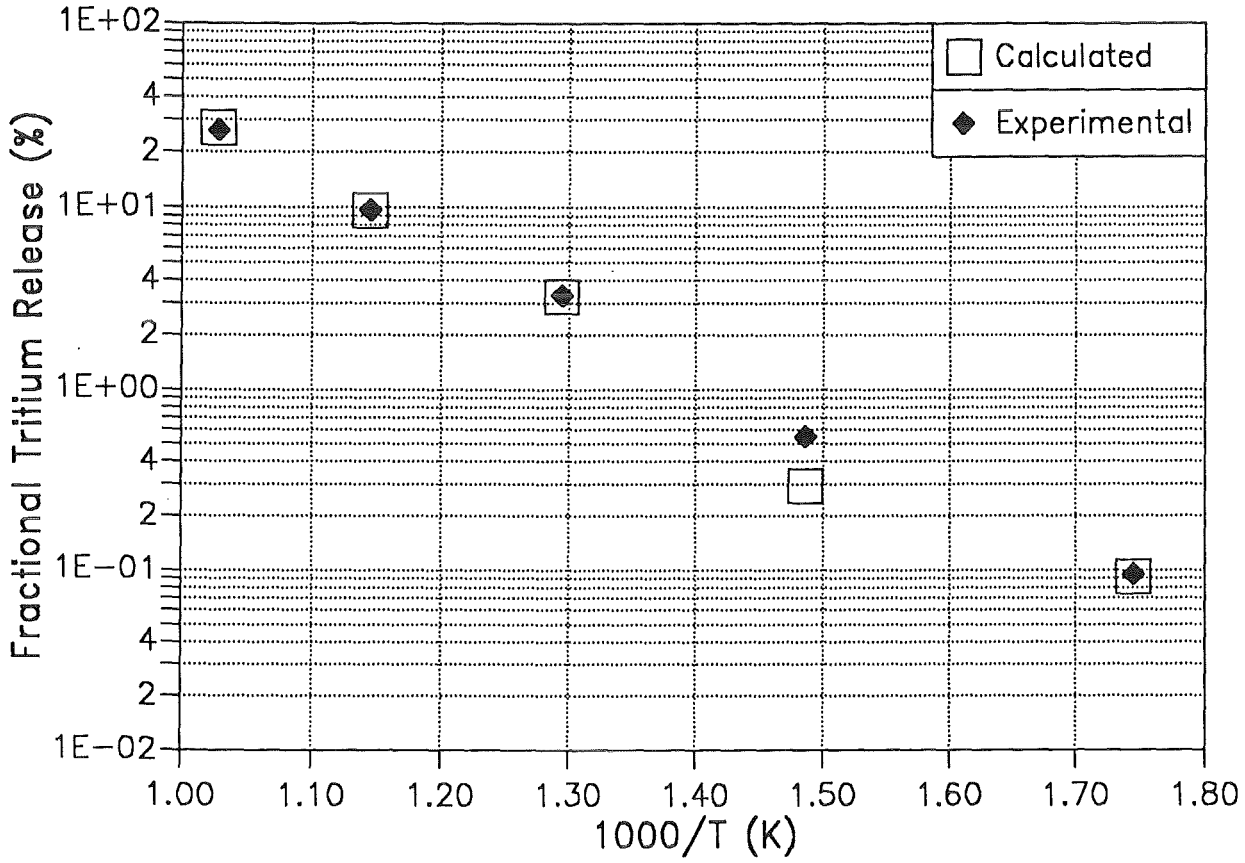

Fig.1 Arrhenius plot of the cumulative out-of-pile annealing fractional tritium release in the experiments of Baldwin [6] for 99%-dense beryllium, as compared to calculated results.

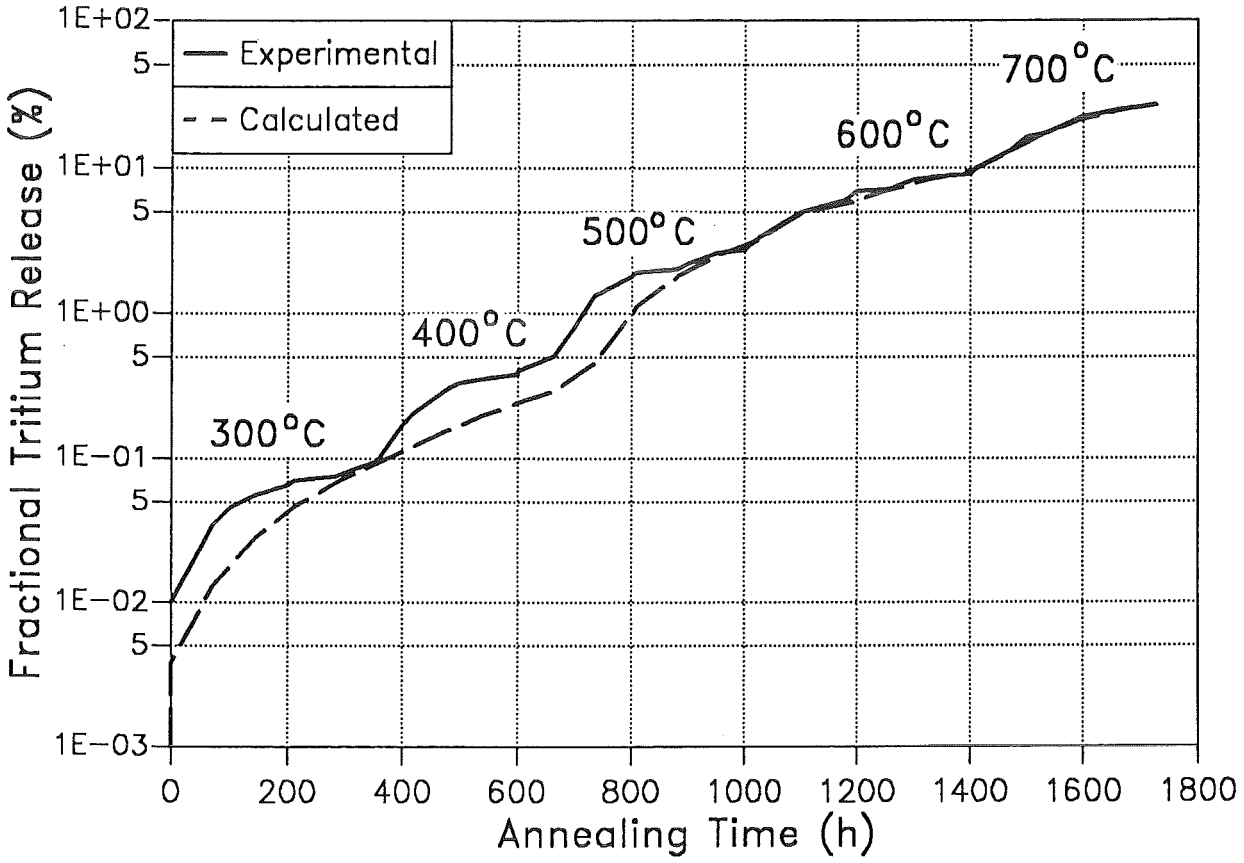

Fig.2 Time dependence of fractional tritium release from 99%-dense beryllium of the Baldwin's experiment [6], as compared to calculated results.

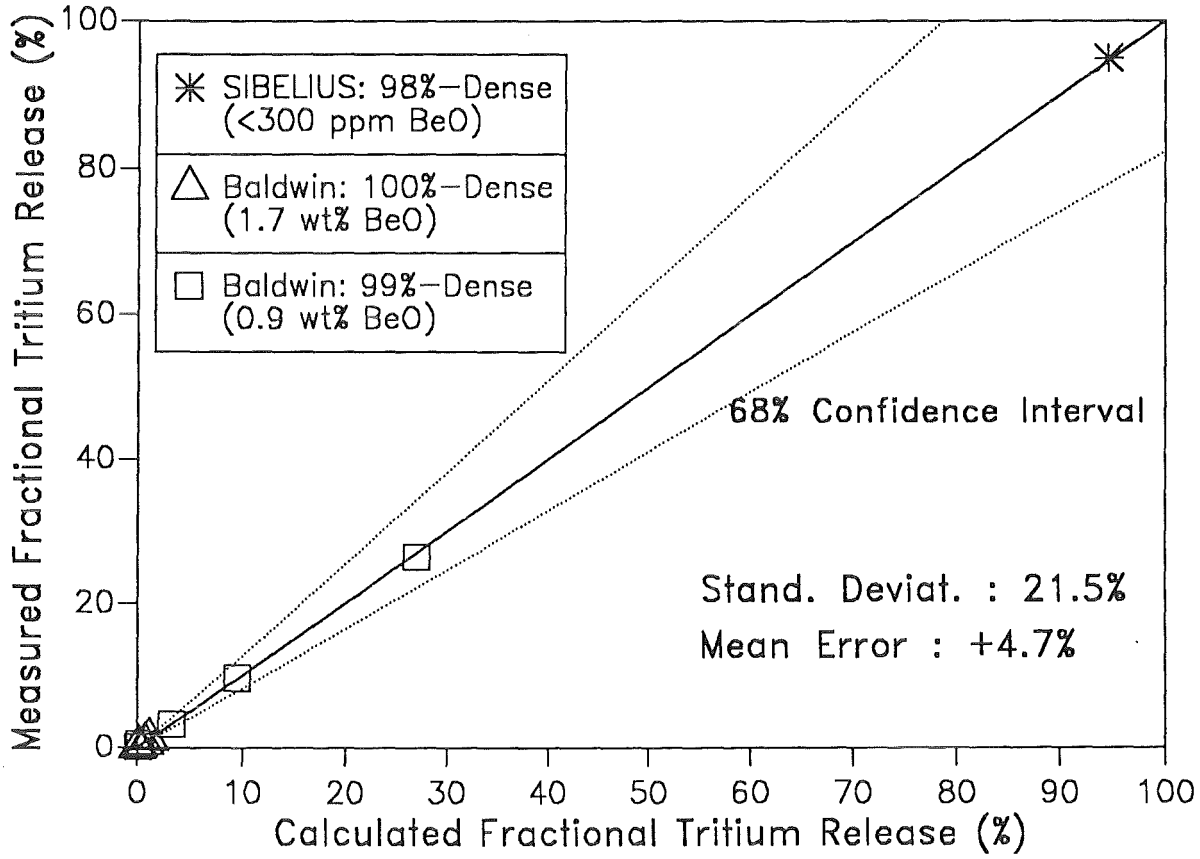

Fig.3 Comparison of cumulative fractional tritium release calculations with experimental data, for out-of-pile annealed beryllium [5] [6] [8].

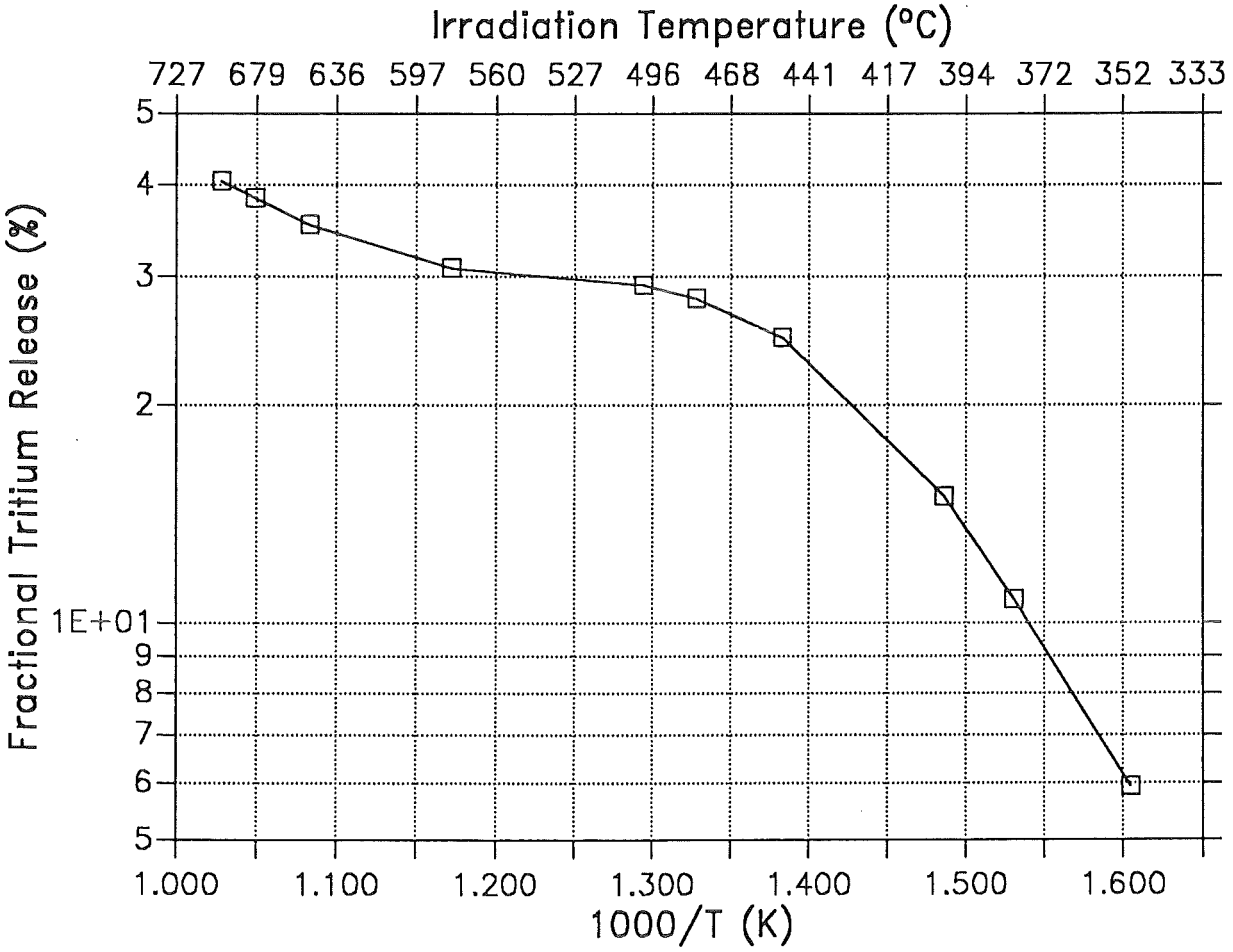

Fig.4 Arrhenius plot of the cumulative in-pile-irradiation fractional tritium release vs. irradiation temperature, for the DEMO BOT [1] beryllium, as predicted by ANFIBE.

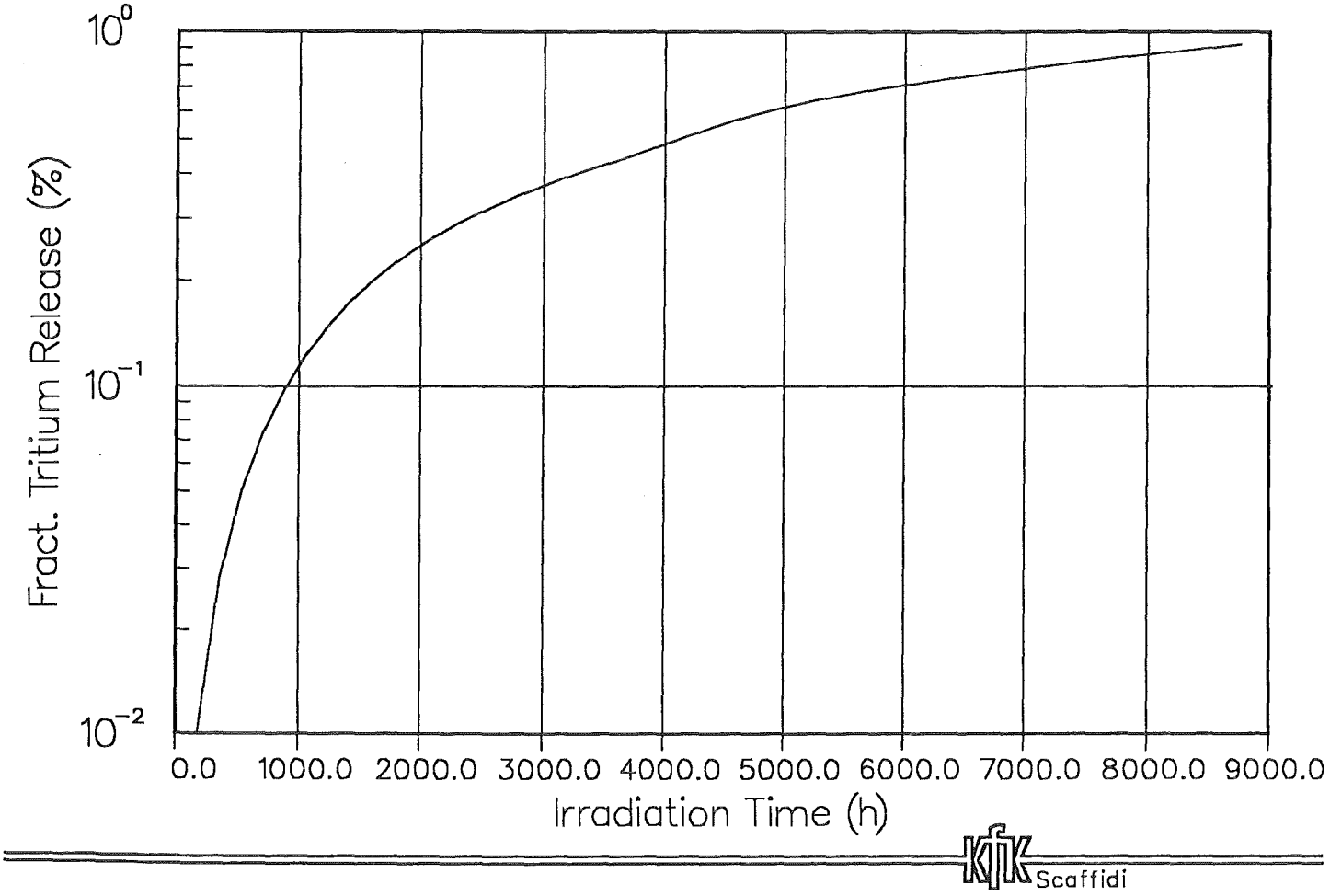

Fig.5 Time dependence of fractional tritium release from beryllium during the normal operating conditions of the EC ITER reactor [4], as predicted by ANFIBE.

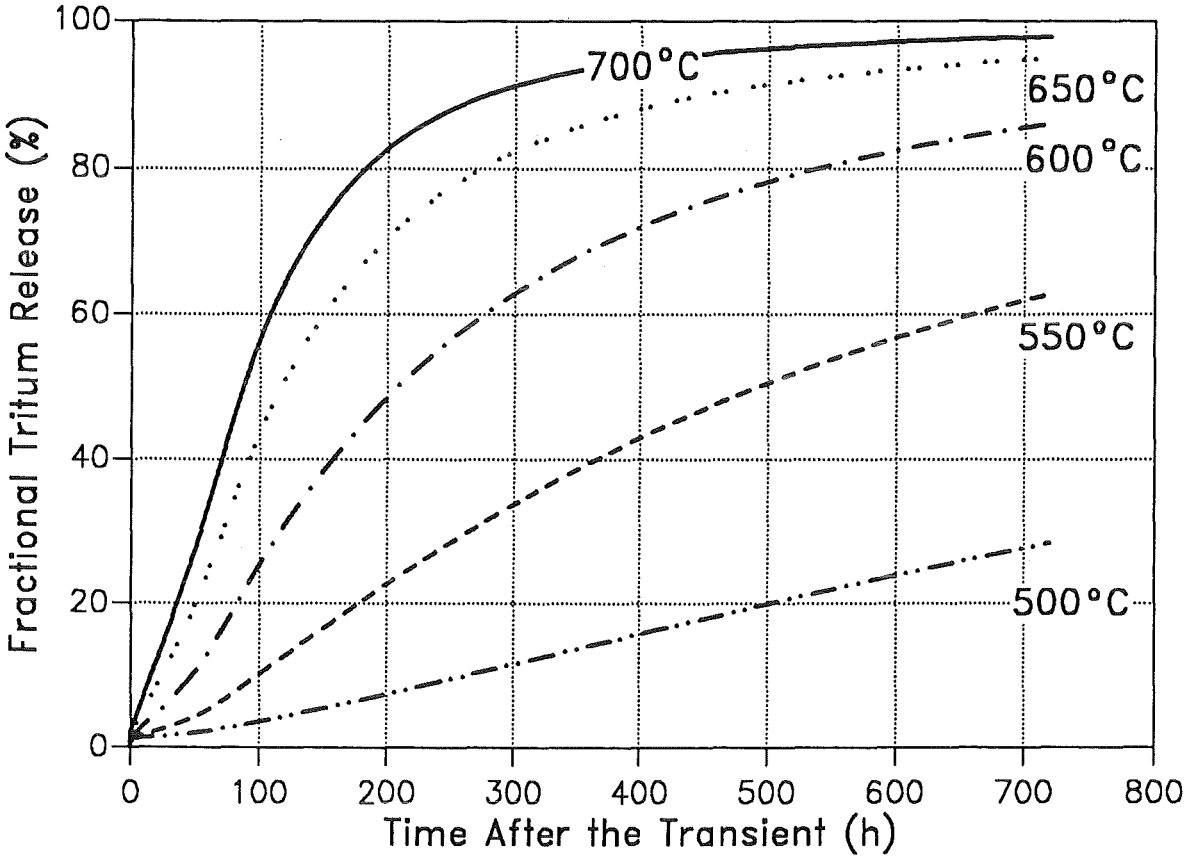

Fig.6 Fractional tritium release from beryllium during a temperature transient after $1 MWy/m^2$ operation time at 350 °C for the EC ITER reactor [4], as predicted by ANFIBE.

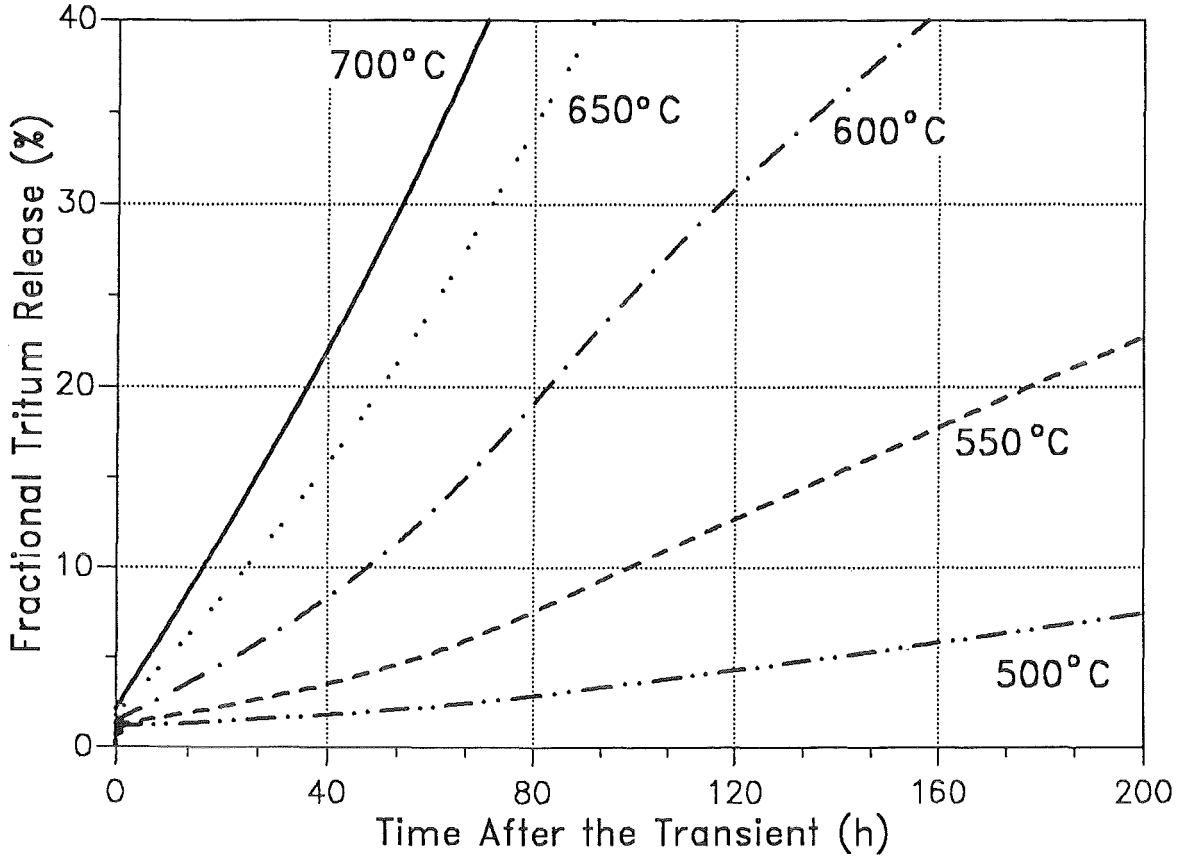

Fig.7 Fractional tritium release from beryllium during a temperature transient after $1 MWy/m^2$ operation time at 350 °C for the EC ITER reactor [4], as predicted by ANFIBE (first hours of the transient).

RESEARCH OF BERYLLIUM SAFETY ISSUES[a]

G. R. LONGHURST, R. A. ANDERL, T. J. DOLAN, M. R. HANKINS, AND R. J. PAWELKO
Idaho National Engineering Laboratory, P.O. Box 1625, Idaho Falls, Idaho 83415, USA

Beryllium has been identified as a leading contender for the plasma-facing material in ITER. Its use has some obvious advantages, but there are also a number of safety concerns associated with it. The Idaho National Engineering Laboratory (INEL) has undertaken a number of studies to help resolve some of these issues. One issue is the response of beryllium to neutron irradiation. We have tested samples irradiated in the Advanced Test Reactor (ATR) and are currently preparing to make measurements of the change in mechanical properties of beryllium samples irradiated at elevated temperatures in the Fast Flux Test Facility (FFTF) and the Experimental Breeder Reactor II (EBR-II) at the INEL. Mechanical tests will be conducted at the irradiation temperatures of 375-550°C. Other experiments address permeation and retention of implanted tritium in plasma-sprayed beryllium. In one test the porosity of the material allowed 0.12% of implanted ions and 0.17% of atoms from background gas pressure to pass through the foil with essentially no delay. For comparison, similar tests on fully dense hot-rolled, vacuum melted or sintered powder foils of high purity beryllium showed only 0.001% of implanting ions to pass through the foil, and then only after a delay of several hours. None of the molecular gas appeared to permeate these latter targets. An implication is that plasma-sprayed beryllium may substantially enhance recycling of tritium to the plasma provided it is affixed to a relatively impermeable substrate. To further evaluate safety issues associated with tritium interaction with beryllium, the Tritium Plasma Experiment (TPE) is being assembled at Los Alamos National Laboratory after its first installation at Sandia National Laboratories, Livermore. This test apparatus will enable testing under full-scale divertor conditions. The first experiments in that facility will examine tritium retention and permeation in a beryllium duplex structure. Test plans are now being formulated for a project that involves several laboratories and industrial participants.

1. Introduction

Beryllium is a strong candidate as a plasma-facing material for the International Thermonuclear Experimental Reactor (ITER) and as a neutron multiplier and energy absorber in fusion breeding blankets. It has many excellent qualities for these applications, however, because of other qualities of this material there are concerns from a safety perspective regarding its use. These concerns are shared by designers working to optimize performance of the material.

At the 1991 Beryllium Technology Workshop (Longhurst [1]) dimensional stability under neutron irradiation was singled out as requiring the most urgent attention. The next most urgent was the effect of neutron irradiation on mechanical properties, and after that was tritium interactions with beryllium. Concerning the effect of neutron irradiation on beryllium, there have been numerous studies in the neutron spectra of fission reactors of the effects of neutron irradiation on mechanical strength and swelling. Beryllium is used routinely in fission reactors, but it requires periodic replacement. Another issue related to the neutron irradiation is the buildup of tritium inventory caused by neutronic transmutations of the beryllium itself. That inventory must be considered when estimating the consequences of a loss of coolant accident (LOCA).

Experience with beryllium in neutron environments has so far been limited mostly to thermal fission reactors. Results from fast fission reactor irradiations are in process but are not yet available. Additional work is needed in the 14-MeV spectrum of a fusion neutron source.

Another issue for plasma-facing components is the permeation of tritium through to the coolant streams. The characteristics for permeation and retention of tritium impinging form the plasma have begun to be investigated, but they are strongly dependent on the fabrication history and condition of the beryllium. They also depend on the plasma particle flux density and energy in very complicated ways. Additional experiments are needed to investigate these issues.

In this paper we describe some of the work in progress at the INEL to explore the bases for concern in these areas and offer considerations for research to resolve unknowns and design features to mitigate risks.

2. Neutron Irradiation Effects

A program has been initiated to examine the effects of neutron irradiation on beryllium mechanical properties. In this section we examine the particular conditions for beryllium application and the progress of the program to gather the needed information.

[a]Work performed for the U. S. Department of Energy, Office of Energy Research under DOE Idaho Field Office Contract DE-AC07-76ID01570.

2.1 Conditions

The service temperatures of the various applications for beryllium in fusion vary substantially. Whereas in the ITER Conceptual Design Activity (CDA) the main application for beryllium was in a breeding blanket, the present Engineering Design Activity (EDA) application is as a plasma-facing material.

Applications near the plasma will experience a very "hard" neutron spectrum, one with a strong 14-MeV component and a more prevalent fast neutron spectrum compared with regions well out into the blanket or shield where comparatively more thermal neutrons would be expected.

There is a range of requirements regarding the form of the beryllium and its manufacturing/installation processes. For plasma-facing components, for instance, full density is required to get thermal conductivities high enough to prevent excessive surface temperatures. Plasma spraying is being considered for these components because of the difficult geometries and the need for remote, in-situ replacement of eroded material. In some blanket designs, on the other hand, the beryllium density needs to be substantially lower than the maximum attainable. This is specifically to reduce heat transfer, thus maintaining higher temperatures in the breeding ceramic that may lie next to the beryllium.

2.2 Irradiations

Beryllium of varying densities, prepared by compaction and hot iso-static pressing of powder, has been and is being irradiated in fission reactors. Twelve beryllium samples comprised of two densities, 80% and 100% dense, were irradiated in the Advanced Test Reactor (ATR) to a fast neutron fluence of 2.6×10^{25} n/m^2 (E > 1 MeV) at an average temperature of 75°C. Ten of these samples were subjected to mechanical testing at the INEL and compared with tests of non-irradiated samples from the same lot. Beeston et al. [2] found that the irradiation caused the specimens to swell by about 0.2% ($\Delta L/L$), to increase in strength by about four times, and to drop to about one fourth of their original ductility.

A number of additional mechanical-test samples have been or are being irradiated. Thirty six samples with densities ranging from 80.5% to 100% of theoretical density are currently in the COBRA facility at EBR-II where they are being irradiated at temperatures ranging from 425°C to 525°C. An additional 28 samples with similar densities were irradiated in the MOTA-2B experiment at temperatures from 370°C to 549°C and fluences from $1.0\text{-}5.8 \times 10^{22}$ n/cm^2 (E > 0.1 MeV). There are also another ten specimens of 86% density from MOTA-1G/2A, irradiated under approximately the same conditions.

This work was initiated under the sponsorship of the Blanket/Shield task area in the U.S. ITER program, but with the diminished emphasis on breeding blankets for ITER, funds have not yet been released to remove these specimens from their lithium/sodium laden canisters. As a consequence, we have not been able to complete the mechanical testing planned. Nevertheless, with the expectation that funds will soon become available, we are making preparations to conduct the mechanical testing at elevated temperatures.

2.3 Testing

The arrangement for doing that is illustrated in Figure 1.

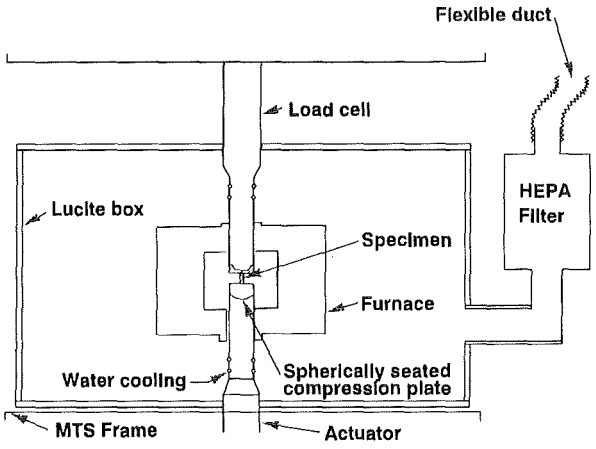

Figure 1. Schematic of apparatus for testing of irradiated beryllium specimens at elevated temperatures.

The enclosure is a Lucite chamber shown schematically in Figure 2. It contains the radioactive fragments, dust, and tritium that result when the specimens fail. The heated length is approximately 5 cm. The furnace has four quartz lamp heaters in elliptical reflectors with a rated power of 2 kW. It opens in clamshell fashion to facilitate installing the specimens. The housing is water-cooled as are the load anvils to prevent overheating of the chamber. The testing machine is conventional with load and displacement instrumentation built in.

A test consists of measuring the compliance of the load-bearing structures without the sample in place, then placing the sample between the two anvils with just enough load to get alignment and hold the sample securely. The furnace is then closed around the specimen and heated to the required temperatures. These temperatures are measured with a combination of

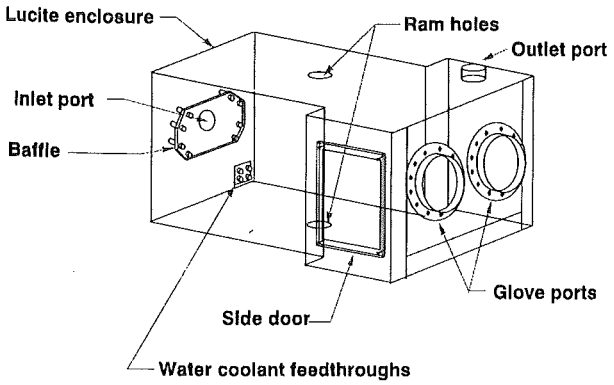

Figure 2. Configuration of the Lucite enclosure.

thermocouples and an optical pyrometer looking through a window in the furnace wall. Furnace heat is automatically controlled to provide the required sample temperature. When the sample is at the same temperature at which it was irradiated, the load is applied, and stress-strain data are gathered as the sample is loaded to failure in a period of approximately a minute.

Prior to the mechanical testing, samples are measured for swelling and density changes. During the test a tritium monitor gathers data about tritium release. This is observable, especially at the failure point. Following the testing, additional tritium content data are taken if desired on the failed specimens by thermal desorption.

The numbers of irradiated samples available is limited, but the information to be gained from these tests will significantly increase our understanding of the response of this material to neutron environments. Those data will assist in making the ITER design better.

3. Plasma-Sprayed Beryllium

Plasma-sprayed beryllium is a potentially useful material for application to plasma-facing components. As part of our work in the Fusion Safety Program to evaluate tritium retention and permeation in potential plasma-facing components for ITER, we have conducted an experiment to evaluate these characteristics in a sample of plasma-arc sprayed beryllium. This material was fabricated by Battelle Columbus Laboratory, Columbus, Ohio. In this section we describe the specimens, the tests performed, the results of those tests, and the implications of those results.

3.1 Specimens

Beryllium powder was plasma-arc sprayed onto 2.54-cm diameter copper substrates. Nominal coating thicknesses were 0.1 mm. The coating and substrate were separated for the specimens intended for free-standing sample permeation tests. These samples were fragile, and only two were delivered in this form. Only one of those was suitable for plasma-driven permeation testing.

Detailed surface analyses for the representative plasma-arc sprayed specimens were made using Scanning Electron Microscopy (SEM) and Auger Electron Spectroscopy (AES). Figure 3 shows in relatively low magnification the appearance of the surface in the region where the AES was performed. SEM analysis indicated that the surface was highly textured and pocketed. There was evidence of surface-connected porosity. Figure 4 shows at higher magnification how rough and apparently porous the surface really was.

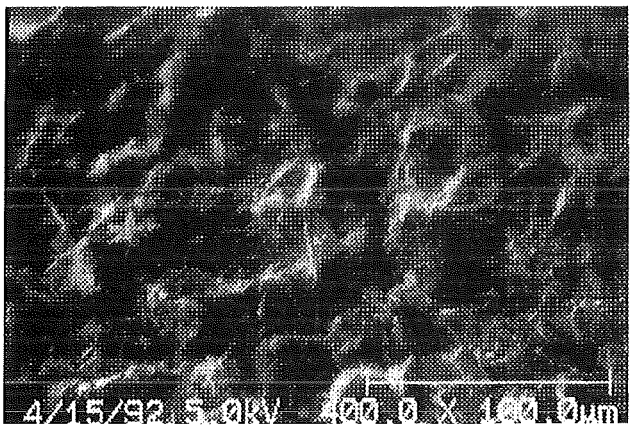

Figure 3. SEM image of plasma-arc sprayed beryllium at 400X showing general surface texture.

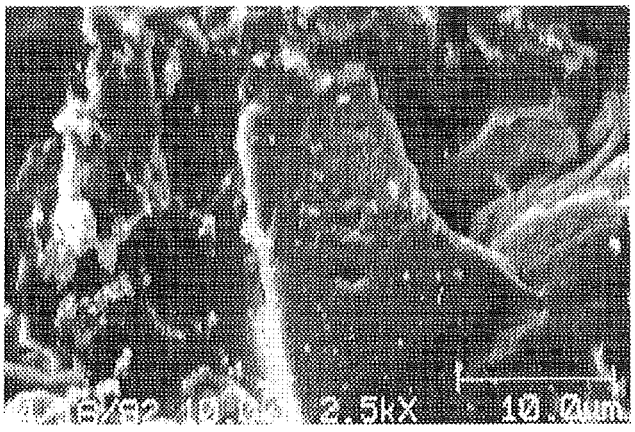

Figure 4. SEM micrographs at 2500X showing highly textured and pocketed surface.

The results of AES analysis at a point approximately in the center of Figure 4 are shown in Figure 5. Measurements were made while sputtering for 20 minutes with a 3-keV argon beam. Before sputtering, the Be signature was at an Auger electron energy of approximately 97 eV, which corresponds with the BeO form. After sputtering commenced, it shifted to the 107-eV signature of elemental Be. The fall-off with time of the oxygen signature indicates the depth of the oxide on the surface. The residual oxygen level is consistent with levels expected in the bulk of powder-metallurgy product beryllium. Although the sputter rate is not known exactly, for the conditions of this measurement the sputter rate through a Si_3N_4 standard is 10 nm/min. That suggests an oxide thickness of approximately 5 nm.

Auger analysis prior to sputtering indicated a small presence of C, Cu, and Al. That signature was not there after the sputtering was completed, suggesting it was a surface contamination. The C is probably related to CO_2 pickup from air exposure. The Cu and Al probably came from the plasma-arc system. Considering the method for making the specimen, these analyses indicate that the plasma-arc sprayed beryllium has a reasonable purity in the bulk.

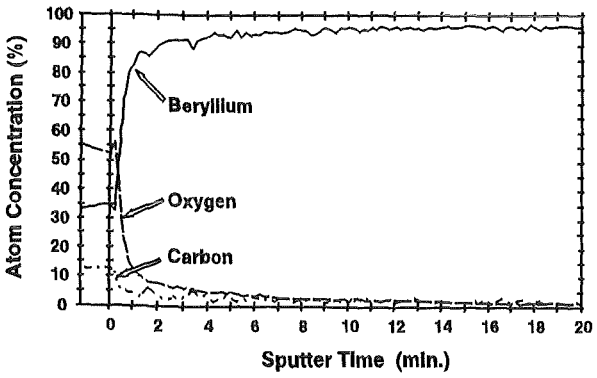

Figure 5. Depth-profile Auger analysis showing variation in species atom concentrations derived from raw Auger electron spectroscopic data.

3.2 Implantation/Permeation Experiment

The apparatus used for conducting the plasma-driven permeation experiments has been described previously by Anderl et al.[3] and by Holland and Anderl[4]. Briefly, it consists of an ion source that accelerates hydrogenic ions to 10 keV, a magnetic mass separator, deceleration stages, and a heated target assembly with a faraday cup, secondary ion mass spectrometer (SIMS), and quadrupole residual gas analyzers (RGA) to examine permeation and reemission behavior. With the use of calibrated standard leaks in the chambers upstream and downstream of the target, the RGAs function as flowmeters for re-emission and permeation of deuterium implanted into the target.

The effective sample diameter after mounting in this fixture was 1.65 cm. After the specimen was installed, the upstream and downstream chambers were each evacuated to the mid 10^{-8}-torr range. The test chambers and sample fixture assembly were subsequently heated to approximately 100°C and 200°C, respectively, and the system was vacuum baked for 64 hours. The system was heated further to a sample temperature of 360°C for two more hours. With the sample heated to 390°C at the end of that time the upstream and downstream pressures were 7.1×10^{-8} torr and 1.9×10^{-8} torr, respectively.

Table I. Implantation system parameters.

Ion beam:	D_3^+
	3 keV
	54 μA = 5.05×10^{19} D/m^2.s
Beam aperture:	2.0×10^{-5} m^2
Specimen temperature:	390°C - beam off
	397°C - beam on
Upstream gas pressure:	2.2×10^{-7} torr (beam on target)
	1.0×10^{-7} torr (beam stopped in accelerator)
Downstream gas pressure:	2.0×10^{-8} torr

Prior to the implantation/permeation measurement, the upstream and downstream quadrupole mass spectrometer RGAs were calibrated using standard deuterium leaks. The implantation/permeation experiment was conducted over a period of 292 minutes. Specific parameters for this experiment are in Table I. The most significant test results are upstream and downstream RGA signals for mass-4, which correspond to D_2 molecules either as re-emission plus background on the upstream side or as permeation on the downstream side. These data are shown in Figure 6.

In analyzing these data, we note first that a downstream mass-4 signal is observed not only for the condition of the beam striking the target specimen, but also for the cases when the beam is stopped in the Faraday cup or by the beam stop, both of which are near the upstream side of the target specimen. No background signal is observed when the beam is stopped in the accelerator, which is differentially pumped from the target chamber. This observation indicates that there is some

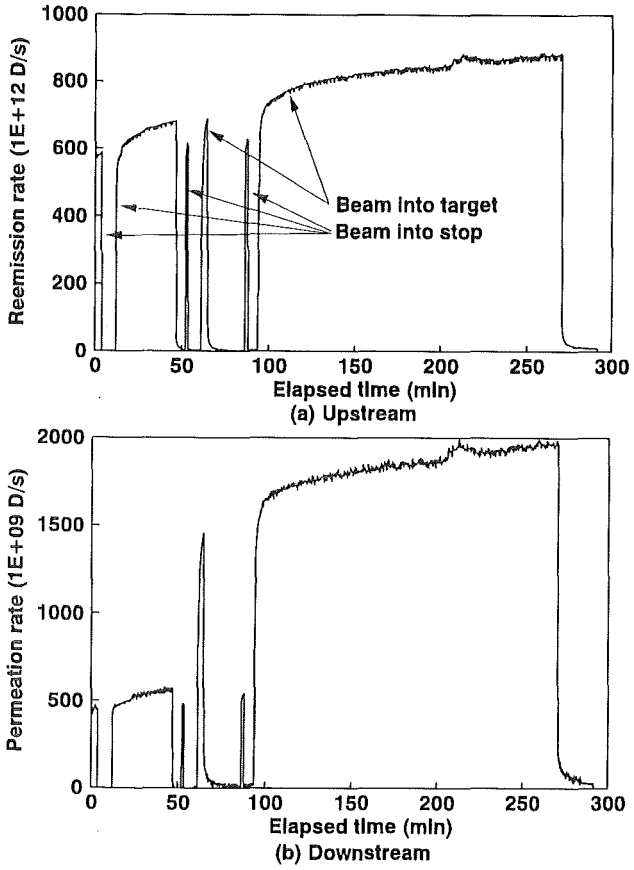

Figure 6. Re-emission (a) and permeation (b) data obtained by the RGAs on the implantation test of plasma-sprayed Be.

leakage or permeation of neutral deuterium molecules from the upstream side to the downstream side of the target specimen. Note further that the level of the downstream mass-4 signal under the Faraday-cup and beam-stop conditions is related to the deuterium partial pressure upstream, and there is effectively no time lag from the upstream change to the downstream response. When the beam strikes the target however, there is the same immediate jump seen in the other two cases, but there is an additional component with a small time lag, making the beam-on-target response much greater than the others.

We postulate that this response in the downstream mass-4 signal is due to two parts. One is the movement through the porous structure of deuterium molecules surrounding the upstream side of the target. The other is the permeation of some of the implanted deuterium ions through the sample. More than likely, this permeation is over a very short pathway, much less than the specimen thickness, to a channel where many of the molecules formed by recombination drift or migrate to the downstream side of the specimen. In similar tests on solid beryllium specimens Anderl et al. [5] showed that under approximately identical conditions, hours were required for deuterium to permeate whereas in these tests this permeation occurred very quickly (few minutes). In the solid beryllium tests, only about one atom in 10^5 was found to permeate. Here the apparent permeating fraction of implanted ions is 5×10^{-3}. The ratio of downstream deuterium molecules from the beam compared with those due to ambient upstream gas pressure, as determined from pressure measurements and gas kinetic theory, is approximately 2.1:1. Approximately 0.12% of implanted atoms and 0.17% of molecules striking the surface were estimated to permeate the specimen.

3.3 Implications

The apparent porosity of the plasma-sprayed material represented by the sample has both positive and negative ramifications. We suspect its thermal conductivity is lower than would be desired to handle heat loads in tokamak plasma-facing applications. We also suspect it will behave differently under neutron irradiation than fully dense beryllium. Swelling due to helium bubble growth may cause significant cracking or failure of the grain interfacial zones resulting in breaking away of beryllium grains. These are speculative suppositions, however.

With respect to tritium interactions, this material appears to have advantages if placed on a relatively impermeable substrate. The most notable response would be a very high recycle rate to the plasma of deuterium and tritium implanting into the surface. This is because these hydrogen isotopes would diffuse only a short distance until they find a free surface where they can recombine. Molecular drift back to the plasma would strongly dominate dissociation on the surface of the substrate, especially if the substrate were an interstitial occluder as opposed to a hydride former. That response means a substantial reduction in the amount of tritium likely to get through to the first-wall coolant stream. Again, this would only work if the plasma-sprayed beryllium were on a dense substrate.

A second apparent advantage is that with the short diffusion paths, there will probably be substantially less inventory of implanted tritium, and possibly of neutron bred tritium, in the plasma-sprayed beryllium as compared with fully dense material. This has safety advantages in the event of a loss-of-cooling event or other thermal transient. Less tritium would be available, both in the plasma-sprayed beryllium layer and in the substrate, to contribute to a possible accidental dose to the public or workers, as compared with a fully dense beryllium layer.

4. Tritium Plasma Experiment

A final activity reviewed here is our participation in the Tritium Plasma Experiment (TPE). This facility, built to resemble the PISCES facility at UCLA (Schmitz et al. [6]) was originally assembled at Sandia National Laboratories, Livermore, California (SNLL), with the notable difference that it was intended to be used with tritium as a working gas. With the closure of the Tritium Research Laboratory at Sandia, the experiment was relocated to the Tritium Systems Test Assembly (TSTA) at Los Alamos National Laboratory. The general configuration of the facility is shown in Figure 7.

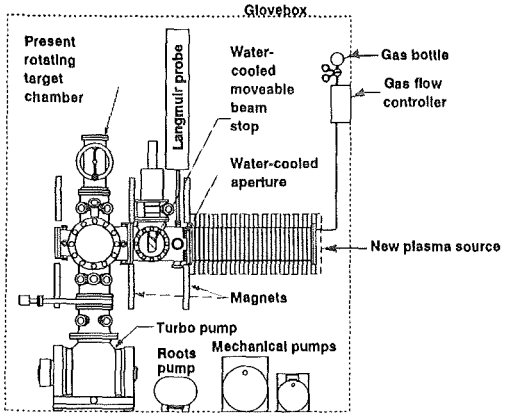

Figure 7. The Tritium Plasma Experiment will be used to examine safety issues for plasma-facing components.

Details of the program for making use of this facility have been provided elsewhere by Longhurst et al. [7], but here we note a few highlights and progress.

The experimental apparatus has a nominal particle flux of 2×10^{23} ions/m^2.s, a background gas pressure of about 13 m Pa, a plasma density of 2×10^{19} ion/m^3, an electron temperature of 15 eV, and a magnetic field intensity of 0.25 tesla. It is able to simulate to a very good approximation the loading in both heat and particle flux experienced by first walls and divertors. Tritium may be used in this system, either as a tracer or in concentrations up to 50% in mixture with deuterium.

4.1 Experiments

The first experiments are currently in the planning stages. They will evaluate permeation rates and tritium retention under nominal operating conditions. This will be done by operating the plasma column in a temporal pattern and at plasma conditions typical of those expected for the ITER divertor. The simulated ITER divertor section to be used for the experiment is currently being designed. It will feature parameters such as those listed in Table II.

Table II. Tritium Plasma Experiment parameters sought for ITER divertor simulations.

Radial beam profile uniformity	±10%
Surface heat flux maximum	3 MW/m^2
Surface temperature range	400-650°C
Peak surface ion flux density	6×10^{22} ion/m^2.s
Area exposed to plasma	30 cm^2
Coolant	H_2O or He

The materials that will makeup the plasma-facing surface remain to be fixed by the ITER design, but at present, the first choice will probably be a 2-mm thick layer of beryllium on a copper substrate. That substrate may change to vanadium.

Permeation rates will be estimated by monitoring tritium concentrations in the coolant stream at regular intervals. Calculations using the TMAP4 code (see Longhurst et al. [8], [9]) suggest that the characteristic breakthrough time for 2 mm of beryllium on a 5-mm thick copper substrate operating at a heat flux of 3 MW/m^2 with a coolant temperature of 100°C (beryllium surface temperature near 650°C) may vary from about half an hour to two months depending on the amount of trapping that is operative. Steady state permeation rate through a 5-cm diameter interaction area would be about 1.8 Ci/day if the plasma were 1% tritium.

Once the basic operating characteristics of the experiment are evaluated, experiments will be conducted to evaluate tritium retention and release processes for various accident scenarios. Loss of flow accidents (LOFA) or even loss of coolant accidents (LOCA) can be simulated and the evolution of tritium to both to the plasma side and to the coolant side can be monitored. Supplementary heating may be used to simulate gamma-decay heat from neutron activation. Consequence mitigation techniques in design and operating processes can be evaluated also.

Supporting experiments are expected at INEL and SNLL. The implantation facility at the INEL, described in Section 3 above, operates with about 0.1% of both the beam area and beam intensity. Its advantage is that the time and cost to conduct small scoping experiments are much less than would be required to conduct such experiments on the TPE. Typical scoping experiments may be to examine permeation and re-emission rates over a range of coating densities for a particular material-coating combination. If an optimum is found, that would be selected for evaluation in greater depth in TPE.

4.2 Progress

The equipment that makes up the TPE has been shipped from Livermore, California to Los Alamos, New Mexico. The room destined to receive the experiment is in the TSTA area there. It has been enlarged and refurbished to accommodate the experiment.

The experiment was housed in a high-velocity air hood when at Livermore, but in the new location it must be inside a glovebox. That glovebox is currently being designed. It will feature a removable section that will allow convenient changeout of the test hardware. It will also probably have its own intermediate cooling system for heat removal from the experiment. That system will transfer heat to water from the building potable water supply.

Also currently in the design stage are the diagnostics that will be used to make measurements on these experiments. Material characterization will include dimensional measurements, fabrication history, composition, microstructure, and information on surfaces and interfaces between strata. Instruments considered essential for that characterization include optical microscopy, scanning electron microscopy, and Auger analysis. Experiment conditions to be monitored include coolant composition, temperatures, biasing voltage from the target to the plasma, and ion flux/fluence measurements. These can be met with standard thermometry and electric meters for the most part. Accounting for secondary electron emission from the target surface poses some difficulties in accurately measuring flux, however. Standard chemical analysis tools should suffice for coolant analysis. Plasma density and temperature are determined by a fast acting Langmuir probe already part of the hardware. This must enter and leave the plasma in a very short time to prevent overheating of the probe. Neutral gas pressure and composition at the target should be measurable by capacitance manometers, ionization gages, and RGAs.

Permeation rates to the coolant side can be measured for water coolant by sampling periodically and performing scintillation counting on the samples. For helium coolant, the stream can be monitored with an ion chamber. Different requirements exist for the levels of tritium that must be used in these two cases. Re-emission rates will be difficult to measure, but it should be possible to examine them using isotopic replacement techniques. For example, the target could be preloaded with protium then tested with deuterium or a mixture of deuterium and tritium. Watching the buildup of protium in the upstream gas/plasma region would give an indication of re-emission rates. Retention and trapping characteristics will show up in permeation transient data. Post test experiments involving thermal desorption, nuclear reaction analysis, and related techniques will also be useful.

A computer-based data acquisition system will be used for recording data from differentially pumped RGAs, key TPE operating parameters, fast Langmuir probe data, system pressure and temperature data, and voltage and current information.

5. Conclusions

The use of beryllium in fusion reactors has advantages, but there are liabilities as well. Many of these liabilities are related to safety regarding the beryllium itself along with its interactions with tritium. At the INEL, we are engaged in research activities that are helping to resolve some of these issues.

The program for examining the effects of neutron irradiation on the mechanical properties of beryllium offers some very important information. Additional funding is needed to complete the disencapsulation and to perform the actual testing on the samples. We are prepared to conduct the tests soon after that happens.

The tritium interactions observed with plasma-sprayed beryllium offer some interesting opportunities for safety in design of plasma-facing structures. There is yet much to do to in developing the processes required to make this material form attractive from fabrication and thermal perspectives, but results and analyses regarding tritium interactions suggest it may have substantial advantages for low tritium permeation into the coolant streams and low tritium inventories.

The TPE along with operating fusion machines such as TFTR, JET, and DIII-D, together with the codes now becoming available for edge plasma physics modelling, offers an important test bed to evaluate design options for plasma-facing components.

References

1. G. R. Longhurst, Ed., "Beryllium Technology Workshop, Clearwater Beach, Florida, November 20, 1991," EGG-FSP-10017, December 1991, Idaho National Engineering Laboratory, Idaho Falls, ID.

2. J. M. Beeston, G. R. Longhurst, R. S. Wallace, and S. P. Abeln, "Mechanical Properties of Irradiated Beryllium," *Journal of Nuclear Materials 195* (1992) 102-108.

3. R. A. Anderl, D. F. Holland, G. R. Longhurst, and D. A. Struttman, "Permeation of Deuterium Implanted into Fusion Reactor Material," *Fusion Technology 8* (1985) 2299.

4. D. F. Holland and R. A. Anderl, "Implantation-Driven Permeation in Vanadium Alloy Fusion Reactors," *Fusion Technology 14* (1988) 707.

5. R. A. Anderl, M. R. Hankins, G. R. Longhurst, R. J. Pawelko, and R. G. Macaulay-Newcombe, "Hydrogen Transport Behavior of Beryllium," 10th International Conference on Plasma-Surface Interactions in Controlled Fusion Devices, Moneterey, California, March 30 - April 3, 1992.

6. L. Schmitz, L. Blush, G. Chevalier, R. Lehmer, Y. Hirooka, P. Chia, G. Tynan, and R. W. Conn, "Impurity transport and retention in a gas target divertor: simulation experiments in PISCES-A and modeling results," *Journal of Nuclear Materials 196-198* (1992) 841-847.

7. G. R. Longhurst, R. A. Anderl, J. R. Bartlit, R. A. Causey, and J. R. Haines, "Using the Tritium Plasma Experiment to Evaluate ITER PFC Safety," IAEA Technical Committee Meeting on Developments in Fusion Safety, June 7-11, 1993, Toronto, Canada; to be published in *Journal of Fusion Energy*.

8. G. R. Longhurst, D. F. Holland, J. L. Jones, and B. J. Merrill, "TMAP4 User's Manual," EGG-FSP-10315, June 12, 1992, Idaho National Engineering Laboratory, Idaho Falls, Idaho, USA.

9. G. R. Longhurst, S. L. Harms, E. S. Marwil, and B. G. Miller, "Verification and Validation of TMAP4," EGG-FSP-10347, July 8, 1992, Idaho National Engineering Laboratory, Idaho Falls, Idaho.

MEASUREMENTS OF THE HEAT TRANSFER PARAMETERS OF MIXED BEDS OF BERYLLIUM AND LITHIUM ORTHOSILICATE PEBBLES

M. Dalle Donne*, A. Goraieb and G. Sordon**

Kernforschungszentrum Karlsruhe

Institut für Neutronenphysik und Reaktortechnik

Postfach 36 40

D-76021 Karlsruhe

Germany

The Karlsruhe solid breeder blanket design for the DEMO is based on the use of a mixed bed of 2 mm beyllium and 0.1 - 0.2 mm Li_4SiO_4 pebbles with and without 0.08 - 0.18 mm beryllium pebbles. This arrangement allows to withstand better the neutron irradiation effects on beyllium (swelling, embrittlement). The proposed mixed beds should have high heat transfer parameters (thermal conductivity, wall heat transfer coefficient) due to the high packing factor (~ 80 %) and to the fact that the contact between the high conducting metallic pebbles is maintained. This is important, because the maximum pebble bed temperature in the blanket should be less than 700 °C. The bed heat transfer parameters have been measured in an annular test section having on the axis an electrically heated rod. Three beds have been investigated: a bed of 2 mm beryllium pebbles, a mixed bed with 2 mm beryllium pebbles and 0.1 - 0.2 mm Li_4SiO_4 pebbles and a mixed bed with 2 mm beryllium pebbles and a mixture of 50 % 0.1 - 0.2 mm Li_4SiO_4 and 50 % 0.08 - 0.18 mm beryllium pebbles. The measurements have confirmed that the heat transfer parameters of the mixed beds, especially those of the bed with the small beryllium pebbles, are considerably higher than those of the bed with the 2 mm beryllium pebbles.

* Delegated from the European Community to the Karlsruhe Nuclear Center
** Joint Research Center, Petten, Holland

1. Introdcution

The European B.O.T. (breeder out of tube) solid breeder blanket design for the DEMO is based on the use of a binary bed of 2 mm beryllium pebbles and of smaller pebbles of 0.1 - 0.2 mm Li_4SiO_4 at the back of the blanket and of a tertiary bed of 2 mm beryllium pebbles, 0.1 - 0.2 mm Li_4SiO_4 and 0.08 - 0.18 mm beryllium pebbles at the front of the blanket where the highest power densities are expected [1]. The packing factor of the 2 mm beryllium pebbles is about 60 %. The bigger pebbles form the structure of the bed. The smaller pebbles are poured in the already settled bed of bigger pebbles and occupy about 50 % of the remaining place available in the bed. The resulting packing factor is about 80 %. This kind of arrangement offers various advantages:

a) In case of large beryllium irradiation-induced volume swelling, contrary to the case with beryllium plates [2, 3], the beryllium pebbles are pressed against the cooling tube and against each other. This increases the bed thermal parameters and thus decreases the bed temperature. This, in turn, reduces the further swelling of beryllium [1].

b) The direct contact of the highly heat-conducting bigger beryllium pebbles and the high packing factor gives a pebble bed with high thermal conductivity.

c) The use of relatively small beryllium pebbles, rather than bigger beryllium plates, reduces the temperature differences in the beryllium pieces, thus decreasing the thermal stresses and the stresses caused by differential volume swelling. The danger of beryllium disintegration under irradiation is practically eliminated.

d) The volume ratio of beryllium to Li_4SiO_4 is 3.6 and 8 for the binary and the tertiary bed respectively. The mixing between beryllium and Li_4SiO_4 is very thorough and without steel in between. This arrangement is most desirable to obtain a high tritium breeding ratio.

However, the thermal conductivity of the mixed bed is lower than that of fully dense beryllium and there are beryllium and Li_4SiO_4 pebbles in contact also in the regions of maximum bed temperature (see Fig. 1). It is therefore necessary to know the heat transfer parameters of the mixed beds, namely the effective thermal conductivity and the wall interface heat transfer coefficient, with sufficient precision to guarantee that, during reactor operation, the maximum bed temperature remains below the compatibility limit between beryllium and Li_4SiO_4.

This limit si 700 °C [4]. It was therefore decided to measure the bed transfer parameters of the following pebbles beds:

1. A bed of single size beryllium pebbles of about 2 mm diameter (bed 1).
2. A binary bed with 2 mm beryllium and 0.1 - 0.2 mm Li_4SiO_4 pebbles (bed 2).
3. A tertiary bed with 2 mm beryllium, 0.1 - 0.2 mm Li_4SiO_4 and 0.08 - 0.18 mm beryllium pebbles (bed 3).

The Li_4SiO_4 pebbles have been developed in collaboration between KfK and the firm Schott-Glaswerke Mainz and the beryllium pebbles have been made by the firm Brush-Wellman.

2. Experimental Apparatus

Fig. 2 shows schematically the experimental apparatus to measure the heat transfer parameters of the bed. The pebble bed is contained between two concentric tubes. The inner tube contains an electrically heated rod. Helium can flow in the axial direction through the bed. The radial distribution of the temperature in the bed is measured either in one or in two axial positions in the central part of the test section, where the axial temperature gradients are negligible in comparison to the radial ones, by means of banks of 32 thermocouples each, placed at various radii at four different azimuthal angles. For the present experiments only one bank of 32 thermocouples placed at the middle axial position of the test section was used. Furthermore the temperatures on the inner and outer tube surface are measured by thermocouples placed into the walls. The temperature level of the bed has been varied by cooling the outer tube surface either with water coils, or by radiation and natural convection to the ambient, or by surrounding it by a thermal insulation.

The heat transfer measurements were performed with helium flowing at very low velocity so that the heat transfer parameters are not affected by the helium convection. This is also the case for the pebble bed in the blanket, where the velocity of the purge helium flow is very small (10 - 30 cm/sec).

3. Experimental Results

Preliminary tests were performed in a plexiglas annulus about 12 cm high and having the same cross section of the test section (annular cross section with R_1 = 0.8 cm and R_2 = 5.1 cm) (Fig. 3). These tests showed that, after vibration, a packing factor of 63.3 % was achieved with the 2 mm beryllium pebbles. Afterwards,

the 0.1 to 0.2 mm Li_4SiO_4 pebbles were poured into the bed. The small pebbles flowed quite well in between the bigger pebbles, filling about half of the remaining volume. The resulting filling factor of the Li_4SiO_4 pebbles was 17.5 % of the total bed volume. After filling with small pebbles the height of the pebble bed did not increase showing that the contact between the beryllium pebbles is maintained.

The actual heat transfer measurements were performed in the steel test section which was filled up to a height of 483 mm. The test section was placed vertically. A steel ring of about 300 g weight was placed on the upper surface of the bed. This was sufficient to avoid demixing of the mixed beds during the tests. The packing factors were the same as in the plexiglas annulus. In the case of the mixed bed with small beryllium pebbles (bed 3) the filling arrangement was the same: after filling the test section with the 2 mm Be pebbles the previously mixed smaller Be and Li_4SiO_4 pebbles (volume ratio 1 to 1) were poured into the bed. The packing factors were about the same as in the Be/Li_4SiO_4 mixed bed (bigger particles 63.3 %, smaller ones 17.6 %).

Fig. 4 shows a typical radial temperature distribution in the tertiary bed (bed 3) at the measurement axial position along the test section. This test was performed with the outer tube simply cooled by radiation and natural convection to the ambient. Also shown are the measured temperatures at the inner tube surface ($r = R_1$) and at the outer tube surface ($r = R_2$). With a constant radial heat flow and bed thermal conductivity the theory predicts a straight line in a semilogartihmic diagram temperature versus log r/R_2. Fig. 4 shows that the experimental points are correlated quite well by a straight line in such a diagram. This was always the case for all the tests performed during this experiment. The slope of the temperature line allows the calculation of the effective thermal conductivity of the bed. The difference between the measured temperature on the inner tube wall and the extrapolated temperature from the bed to the wall allows the calculation of the heat transfer coefficient at the wall. This temperature difference is always smaller at the outer tube surface, so that the obtained heat transfer coefficients for the outer tube scatter considerably more than those for the inner tube and were not used to the correlation.

Fig. 5 shows the radial temperature distribution for another test for bed 3, this time, however, with water cooling of the outer tube. The average bed temperature is about the same as that of Fig. 4, however the radial temperature gradient is much higher and the resulting thermal conductivity and wall heat transfer coefficient are almost two times higher than in the previous case. This phenomenon

was already observed for a pebble bed of aluminum and a mixed bed of aluminum and Li_4SiO_4 pebbles, but not in the case of a bed formed of Li_4SiO_4 pebbles only [5]. The increase in the heat transfer parameters is due essentially to the compression that the better cooled outer tube wall is exerting on the pebble bed. The differential thermal expansion between bed and bed containment walls ("interference") produces a compression on the bed which increases the contact surface area of the pebbles. This of course has a much greater effect on the heat transfer parameters of the bed in the case of the highly heat conducting metallic pebbles than in the case of ceramic pebbles which are harder and have a much lower thermal conductivity.

Table 1 shows a resumè of the heat transfer measurements for the beds 1, 2, 3. The data are correlated with equations of the type:

$$k = C_o \left(1 + C_1 \frac{\Delta l}{l}\right) \left(1 + C_2 T_m\right) \tag{1}$$

$$\alpha_1 = C_o \left(1 + C_1 \frac{\Delta l}{l}\right) \left(1 + C_2 T_{W1}\right) \tag{2}$$

where k is the bed thermal conductivity and α_1 its heat transfer coefficient to the inner wall, T_m [°C] the average temperature of the bed, T_{W1} [°C] the temperature of the inner wall and $\Delta l/l$ the "interference", i.e. the difference between the thermal expansion of the bed and that of the confinement walls. This is given by:

$$\frac{\Delta l}{l} = \alpha_{Be} \left(T_m - T_o\right) + \alpha_{St} T_o - \alpha_{St} \frac{R_2 T_{W2} - R_1 T_{W1}}{R_2 - R_1} \tag{3}$$

where $l = R_2 - R_1$ is the thickness of the bed, R_1 and R_2 the inner and the outer radius of the annular cross section of the test section, T_o the room temperature, T_m the average temperature of the bed, T_{W1} and T_{W2} the inner and the outer temperatures of the confining walls and α_{Be} and α_{St} the thermal expansion coefficients of beryllium and of the confinement walls of stainless steel respectively. The coefficients C_o, C_1, C_2 are given in Table 1 for the three beds investigated.

The thermal conductivities of the mixed beds are about 45 % and 65 % higher than that of the beryllium pebble bed for the binary and the tertiary bed respectively. This shows quite clearly the advantage of using the mixed beds here proposed: the thermal conductivities of beds with single size beryllium and Li_4SiO_4 pebbles with the same beryllium /Li_4SiO_4 volume ratio would have been about 30

% and 20 % lower of that of the beryllium pebble bed respectively [6]. As mentioned in the introduction, this large increase in thermal conductivity (a factor 2) is due to the direct contact of the highly heat-conducting bigger beryllium pebbles and to the high packing factor. As can be seen from Table 1 the coefficient C_1, increases with the volume ratio beryllium/Li_4SiO_4. This reflects the fact that the interference has a stronger effect on the thermal conductivity in the case of beryllium rather than Li_4SiO_4 pebbles.

The wall heat transfer coefficient increases by decreasing pebbles diameters due to the increase in the number of contact points to the wall per unit surface (coefficient C_o). This effect is moderate from bed 1 to bed 2 due to the relatively low thermal conductivity of the Li_4SiO_4 pebbles, but it is considerably higher for bed 3 due to the fact that 50 % of the smaller pebbles are in this case of beryllium.

4. Conclusions

The results of the heat transfer experiments have confirmed what was already found in previous experiments using aluminum pebbles [5]. Namely, that the heat transfer parameters (bed thermal conductivity and wall heat transfer coefficient) of the binary and tertiary mixed beds are considerably better than those of beds with single size beryllium or mixed beryllium and Li_4SiO_4 pebbles.

These results are very encouraging for the new design of the European B.O.T. DEMO-relevant Solid Breeder Blanket. This design is based on the use of a binary bed of 2 mm beryllium pebbles and of smaller pebbles of 0.1 - 0.2 mm Li_4SiO_4 at the back of the blanket and of a tertiary bed of 2 mm beryllium pebbles, 0.1 - 0.2 mm Li_4SiO_4 and 0.08 - 0.18 mm beryllium pebbles at the front of the blanket. Preliminary calculations for this blanket design indicate that the maximum temperature is the mixed beryllium-Li_4SiO_4 pebble beds is about 650 °C , i.e. considerably lower then the temperature limit of 700 °C.

Acknowledgements

The authors wish to thank E. Bogusch and R. Schmidt of Siemens for the help in performing the experiments.

This work was performed in the framework of the KfK Nuclear Fusion Project and is supported by the European Communities within the European Fusion Technology Program.

References

[1] M. Dalle Donne et al., Proc. 17th Symp. Fusion Technology, Rome 14. - 18. Sept. 1992, p. 1326.

[2] M. Dalle Donne et al., Fusion Technol. 14 (1988), 1357.

[3] M. Dalle Donne et al., "Demo-relevant Test Blankets for NET/ITER, BOT Helium Cooled Solid Breeder Blanket", Kernforschungszentrum Karlsruhe, Report KfK 4929 (November 1991).

[4] P. Hoffmann and W. Dienst, J. Nucl. Mater, 171 (1990) 203

[5] M. Dalle Donne, A. Goraieb, G. Sordon, J. Nucl. Mater. 191 - 194 (1992) 149.

[6] M. Dalle Donne and G. Sordon, Fusion Technol. 17 (1990) 597.

Table 1 Resumè of Heat Transfer Results

Bed effective thermal conductivity [W/mk]							
Pebble bed no.	No. of experi-ments	C_0	C_1	C_2	Standard deviation %	Temp. range (°C)	Interference range %
1	23	2.293	353	6.358×10^{-4}	10.6	30 - 590	0 - 0.24
2	21	4.721	206.4	0	14	40 - 490	0 - 0.16
3	18	5.478	320.2	0	13	30 - 520	0 - 0.16
Wall heat transfer coefficient [W/cm^2 °C]							
1	23	0.06438	287.6	3.379×10^{-3}	18.8	90 - 690	0 - 0.24
2	21	0.0932	196.8	1.654×10^{-3}	8.8	60 - 550	0 - 0.16
3	18	0.2120	383.1	9.239×10^{-4}	13	50 - 580	0 - 0.16

1: 2 mm Be pebbles; packing factor 63.3 %

2: 2 mm Be + (0.1 - 0.2 mm) Li_4SiO_4; packing factors 63.3 % + 17.5 %

3: 2 mm Be + (0.1 - 0.2 mm) Li_4SiO_4 + (0.08 - 0.18 mm) Be pebbles; packing factors: 63.3 % + 8.8 % + 8.8 %

For the definition of C_0, C_1, C_2 see equation (1) and (2).

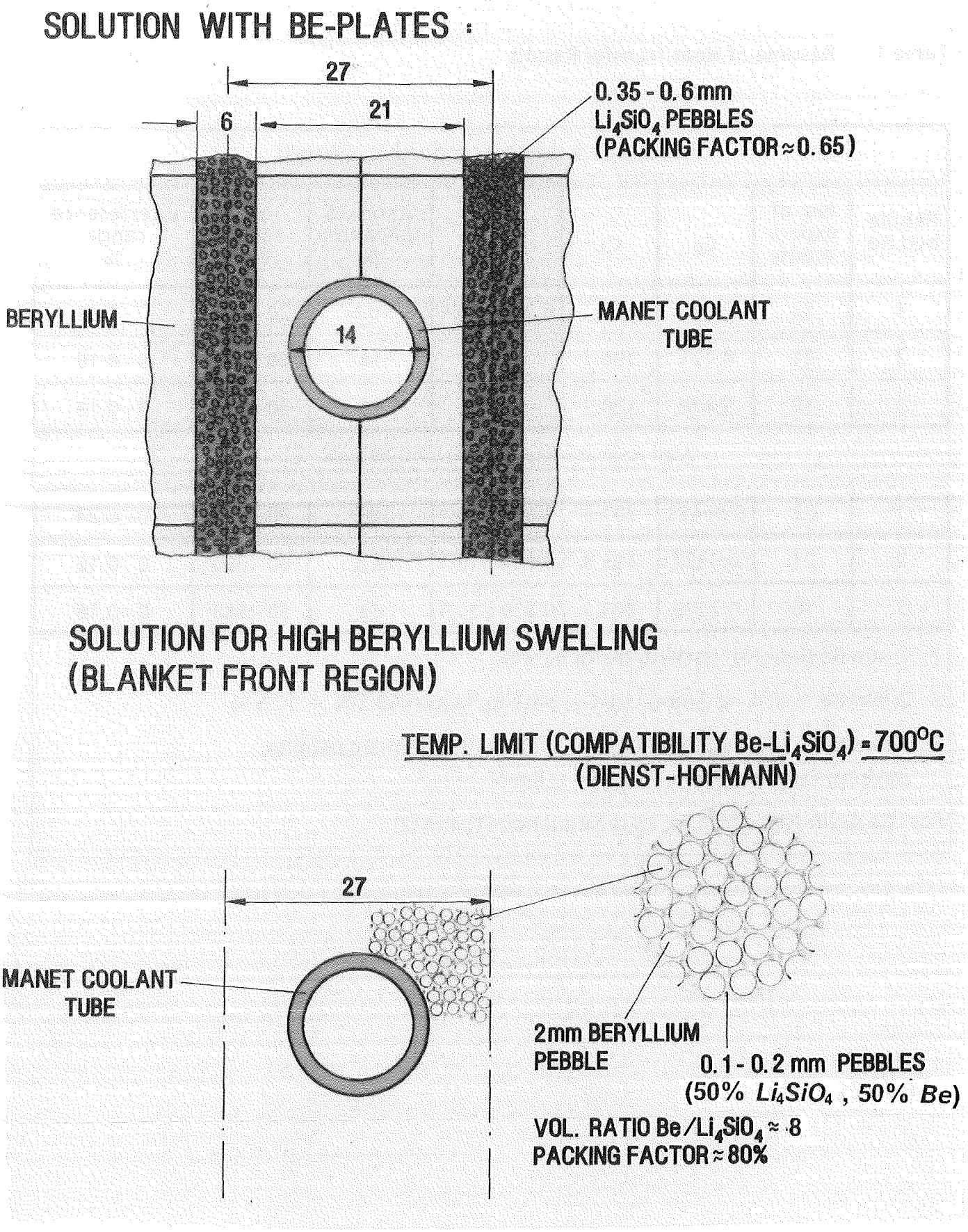

Fig. 1 Breeder-multiplier arrangement in the European B.O.T. Solid Breeder Blanket (poloidal-toroidal cross section).

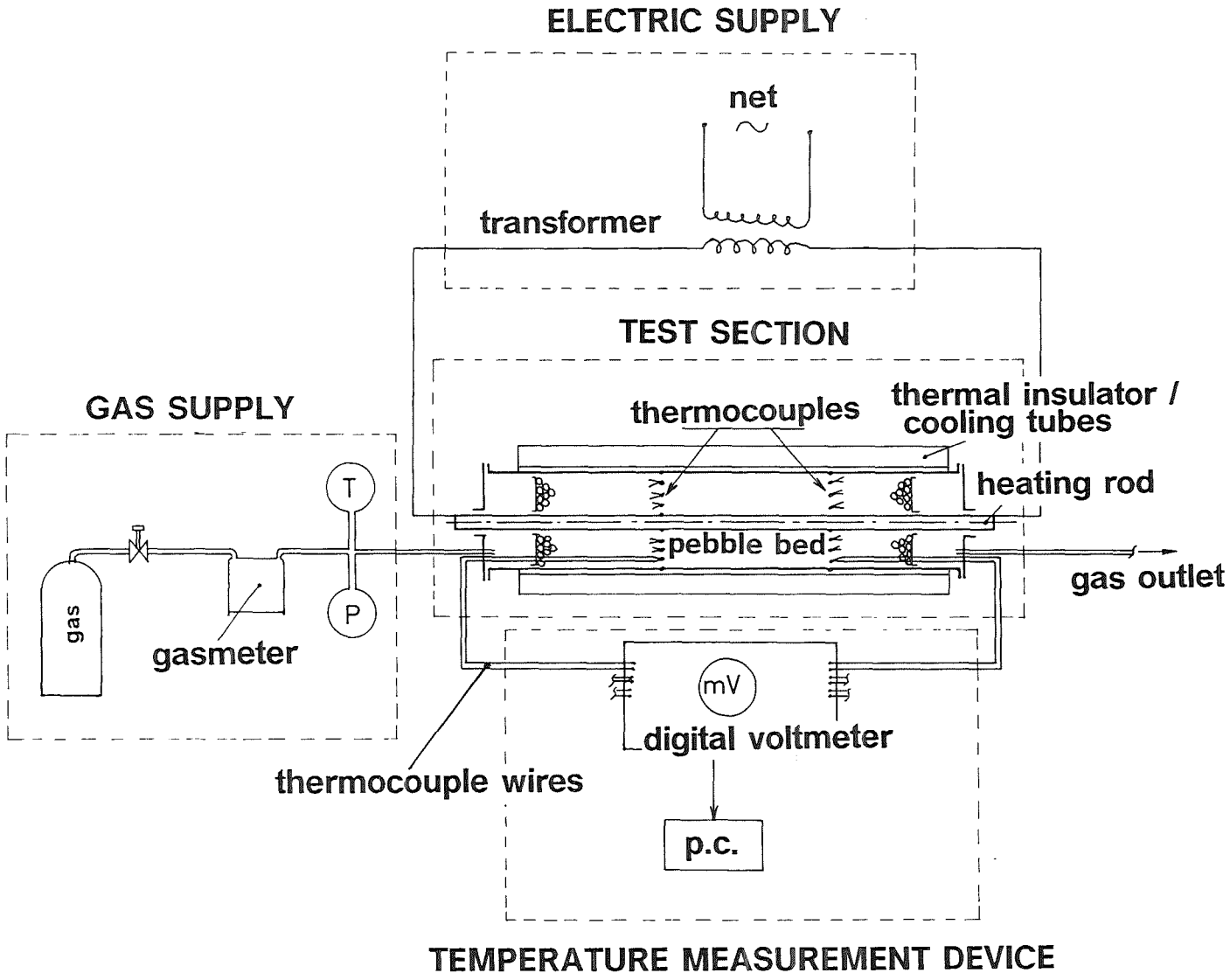

Fig. 2 Experimental apparatus to measure the heat transfer parameters of a pebble bed.

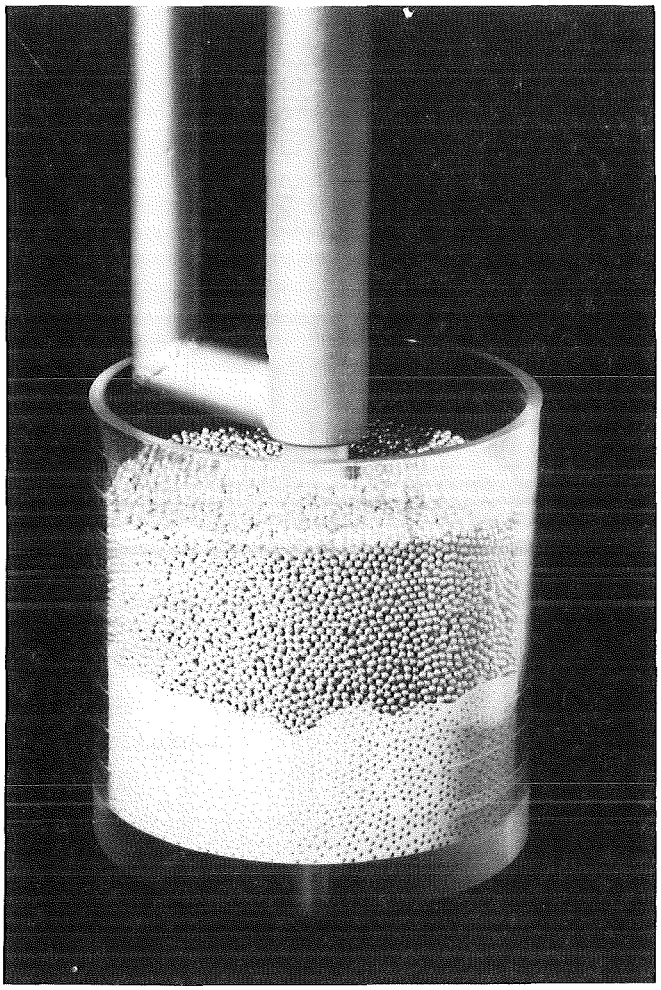

Fig. 3 Binary bed of 2 mm beryllium pebbles and 0.1 - 0.2 mm Li_4SiO_4 pebbles in the plexiglas annulus used for the preliminary tests (measurement of the packing factor).

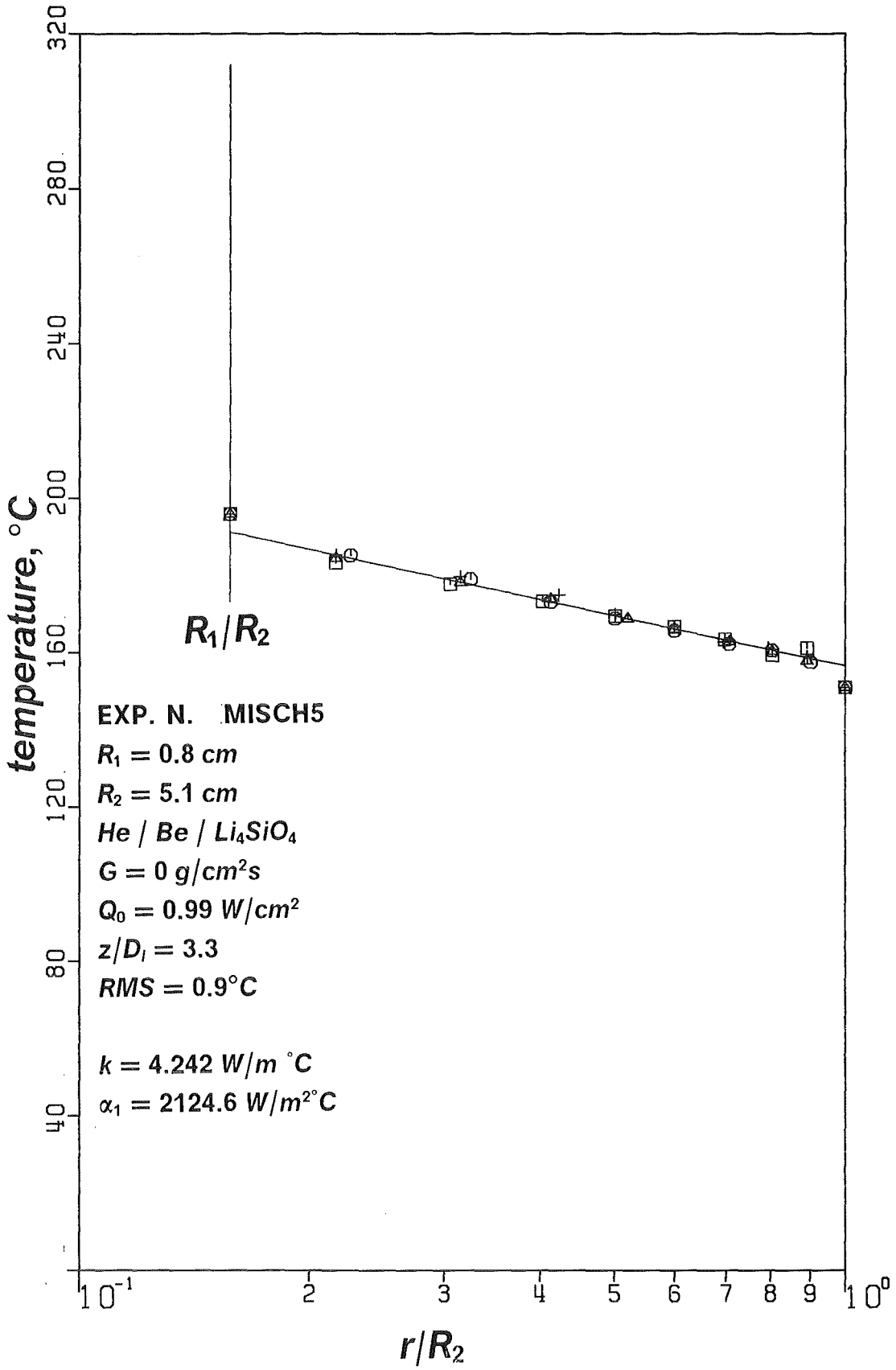

Fig. 4 Radial temperature distribution in the testing pebble bed (bed 3, air cooled outer wall).

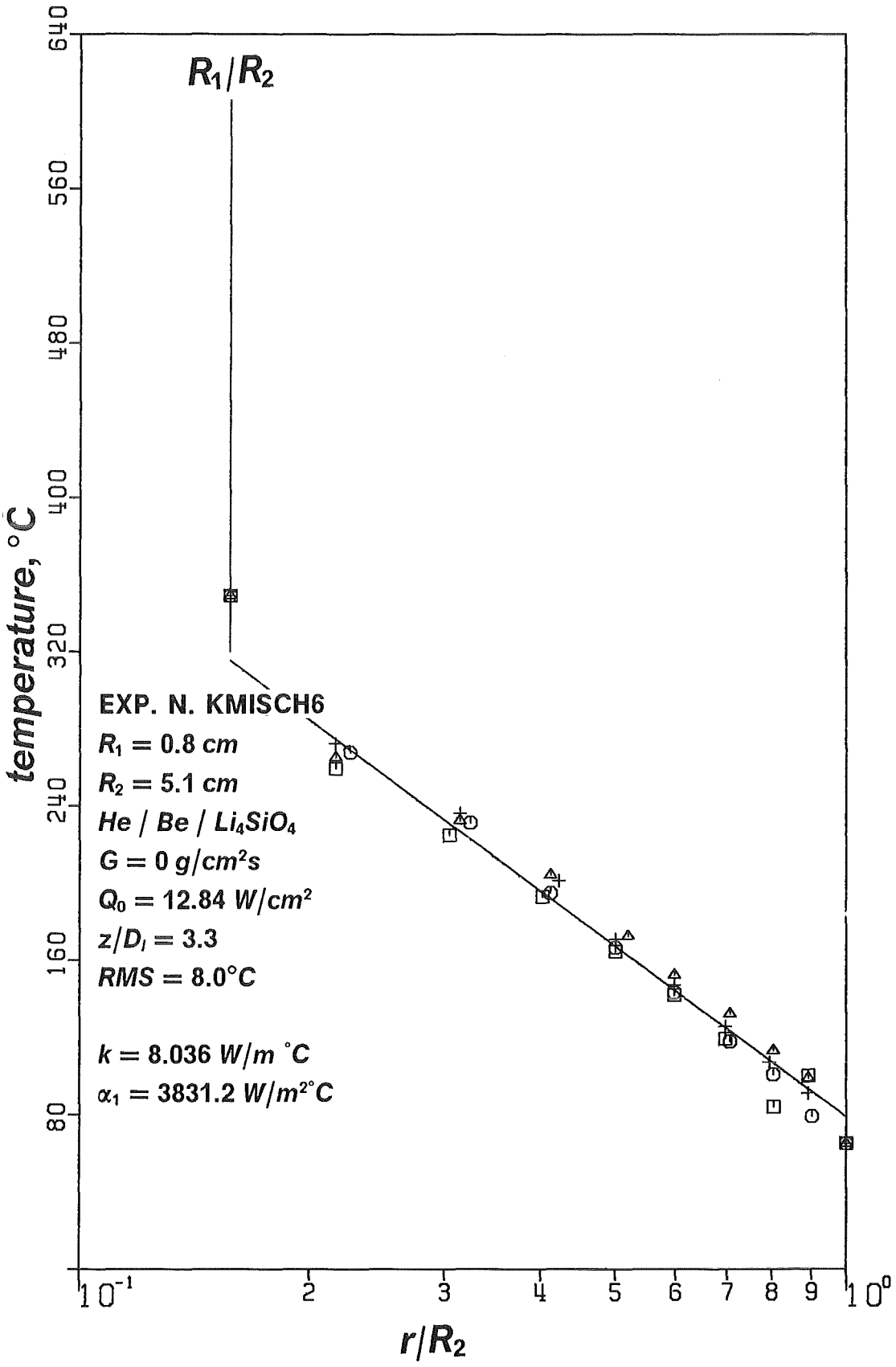

Fig. 5 Radial temperature distribution in the testing pebble bed (bed 3, water cooled outer wall).

Beryllium Workshop, Karlsruhe, KfK
October 4–5, 1993

Beryllium Research Activity in JAERI

Hiroshi Kawamura and Etsuo Ishitsuka

Japan Atomic Energy Research Institute, Oarai Research Establishment, Oarai-Machi, Higashi Ibaraki-Gun, Ibaraki-Ken 311-13 Japan.

The present status of Beryllium study in JAERI will be presented in this work. Some new programs are attempting in JAERI; compression test, vacuum heating, so on. The low impurity and low cost pebble production were developed by using improved rotating electrode method. The thermal expansion coefficient and specific heat of the unirradiated pebble samples were measured by the laser interferometer and differential scanning calorimetry (DSC), respectively. These thermal properties were almost corresponded with the balk beryllium. The compression test was conducted for the evaluation of mechanical property. The irradiated pebbles of total first neutron fluence of $1.3 \times 10^{25}(n/m^2)$ were tested at the room temperature. The embrittlement of irradiated beryllium pebbles was found from these results.

1. Introduction

The pebble-typed tritium breeder blanket have been proposed in Japan, and the in-pile mock up test is prepared in Japan Materials Testing Reactor (JMTR). The beryllium pebbles have been started to develop before three years, and basic characteristics have been investigated for the design of in-pile mock up test. In this paper, the production technology, thermal and mechanical properties of the beryllium pebbles were discussed.

2. Present status of Beryllium study in JAERI

Some beryllium study are conducting or preparing in JAERI(OHP 1, 2 and 3).

The compression test was introduced to evaluate the mechanical property of beryllium pebbles, the irradiated pebbles in JMTR were tested. The beryllium pebbles irradiated in EBR2 will be test on November.

The vacuum heating equipment of irradiated beryllium, which could be simultaneously measured with helium and tritium generated by the neutron irradiation, was almost established. This equipment will be useful to consider the tritium release from beryllium and swelling of beryllium by helium gas bubbles.

Be/BeO composite, Be/Be_2C composite and $Be_{12}Ti$ metal are planned to irradiate in JMTR on next year. These Be-content materials are interested as first wall material or neutron multiplier material of fusion blanket because these materials have high melting temperature compared with beryllium metal.

The irradiation behavior analysis code and the thermal absorption experiment were preparing in JAERI.

3. Production

The rotating electrode method(OHP 4) was most suitable production method of beryllium pebbles for the mass production and impurity control. By changing from the hot-pressed beryllium electrode to the vacuum cast beryllium electrode(OHP 5), the impurity and production cost of beryllium pebbles were improved. It was made clear that the oxide layer on pebble surface could be controlled by changing oxide concentration of vacuum chamber.

Generally, the hot-pressed beryllium were used as the popular application because beryllium metal were difficult to process (cutting or grinding etc.). In the conventional rotating electrode method, the hot-pressed beryllium was used as electrode, but content of beryllium oxide and production cost were higher. Using the vacuum cast process, the electrodes were directory produced, and production cost of pebbles were down. Further more, the impurity were decreased by the refinement effect of vacuum casting. It is clear that the impurity of pebbles were depended on chemical composition of electrode (OHP 6).

4. Thermal property

For the unirradiated pebble samples, thermal expansion coefficient and specific heat were measured to compare with normal beryllium sample. It was clear from these data that the inner pore of beryllium pebbles did not affect in the thermal expansion and specific heat.

4.1 Thermal expansion

The thermal linear expansion was measured by the laser interferometer, and the thermal expansion coefficient was calculated using thermal linear expansion data (OHP 7). The thermal expansion coefficient of pebbles were almost corresponded with normal beryllium data obtained by N.P.Pinto [1].

4.2 Specific heat

The specific heat were measured by differential scanning calorimetry (DSC) with reference sample of α -alumna (OHP 8). The specific heat of pebbles were corresponded with normal beryllium data of G.E.Darwin and J.H.Buddery [2].

5. Compression test

The compression test was conducted for the evaluation of mechanical property. The unirradiated and irradiated pebbles were tested at the room temperature. The total first neutron fluence (<1.0 MeV) of irradiated pebbles was $1.3 \times 10^{25}(n/m^2)$, temperature was about 330℃. OHP 9 shows the compression equipment for beryllium pebble. The compression speed was 0.2 mm/min. The load signal, displacement signal, acoustic emission (AE) signal and acoustic emission (AE) pulse number signal were collected by computer.

The measured data of unirradiated pebble and irradiated pebble show OHP 10 and 11, respectively. The rapid change of load signal that mean the pebble break did not observe for the half number of unirradiated test pebbles, and small changes of load signal were observed for another half test pebbles. However, the big change of load signal was observed for the all irradiated test pebbles, and the peak of AE signal was generated by cracking.

Using the loaded area "S" of pebble which assumed as pellet, measured data were compared with another data. OHP 12 shows the breaking stress. The JMTR surveillance tensile test [3] and compression test of tube [4] were showed in same figure. The breaking stress of beryllium increased at 10^{24}–10^{25} n/m^2 and decreased at over 10^{25} n/m^2. The surrounding temperature will be more important factor for breaking stress [4].

References

[1] N.P.Pinto, in *Beryllium Sience and Technology*, edited by D.R.Floyd and J.N.Lowe (Pienum, New York, 1979), Vol.2, 319–350.

[2] G.E.Darwin and J.H.Buddery, *Metallurgy of the rare metals – 7 Beryllium*, Butterworths Scientific Publications, London (1960) 170.

[3] T.Takeda, H.Amezawa and K.Tobita, JAERI–M 86–007 (1986).

[4] J.M.Beeston et al., J. Nucl. Mater. 122&123 (1984) 802–809.

OHP-1

Beryllium Resarch in JAERI

Production	pebble porous
Surface treatment	mechanical polishing electrode polishing
Irradiation behavior	swelling gas generation mechanical property thermal property analysis code
Compatibility	with breeder materials with structure materials with coating material
Hydrogen behavior	release absorption transmission, diffusion retaintion surface analysis distribution analysis
New materials	metal compound
Oxidation	oxide layer

OHP-2

Running program of 1993–1994

Compression test

Irradiated pebble in JMTR	Testing
Irradiated pebble in EBR2	Nov. 1993–

Vacuum heating

Simultaneous measurement of He and Tritium

Preparing of equipment	– Oct.1993

Irradiation of new materials

Be/BeO composite Be/Be_2C composite $Be_{12}Ti$	27 Jan. 1994–

Irradiation behavior analysis code

Diffusion model	+ Oxidization model	– Mar.1994
Swelling and surface effects		1994–

Thermal absorption

Preparing sample : Single crystal	1993–

OHP-3

Beryllium Study for In-pile Test

Pebble Production

- Mg reduction method
- Rotating electrode method

Pebble Evaluation

- Compatibility
- Mechanical property
- Thermal property

Evaluation of Pebble Bed

- Packing property
- Sweep gas property
- Thermal property

(Effective thermal conductivity)

Irradiation Test

- Tritium release
- Swelling property
- Mechanical property

Capsule for In-pile Mock-up Test

OHP-4

Rotating Electrode Method

Improved points

- *Beryllium electrode*

  Hot-press → Vacuum cast

  ↓

  High purity and cost down

- *Reduction of residual gas*

  Metal gloss was appeared on surface

  ↓

  Surface oxide layer control

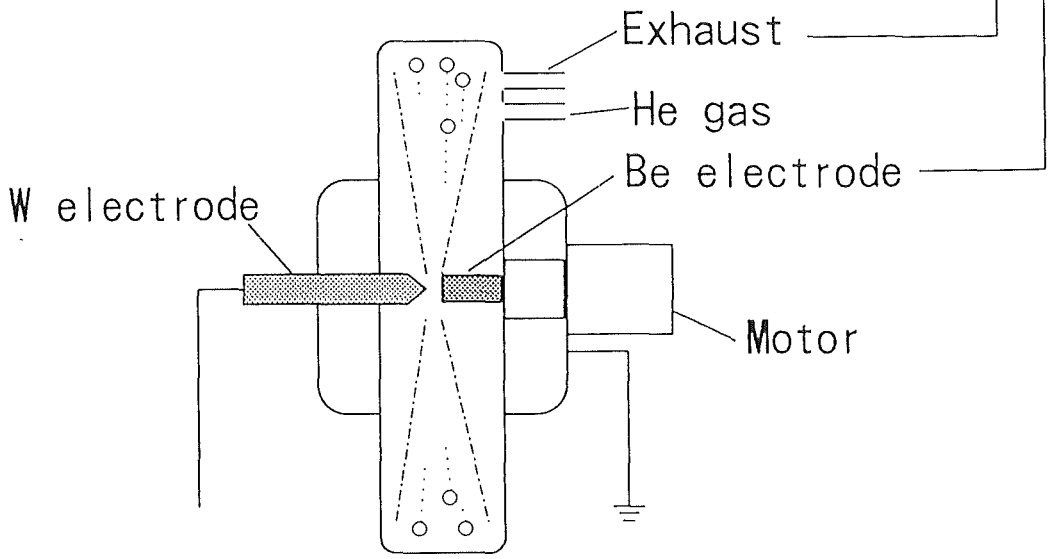

OHP-5

Production Process of Be Electrode

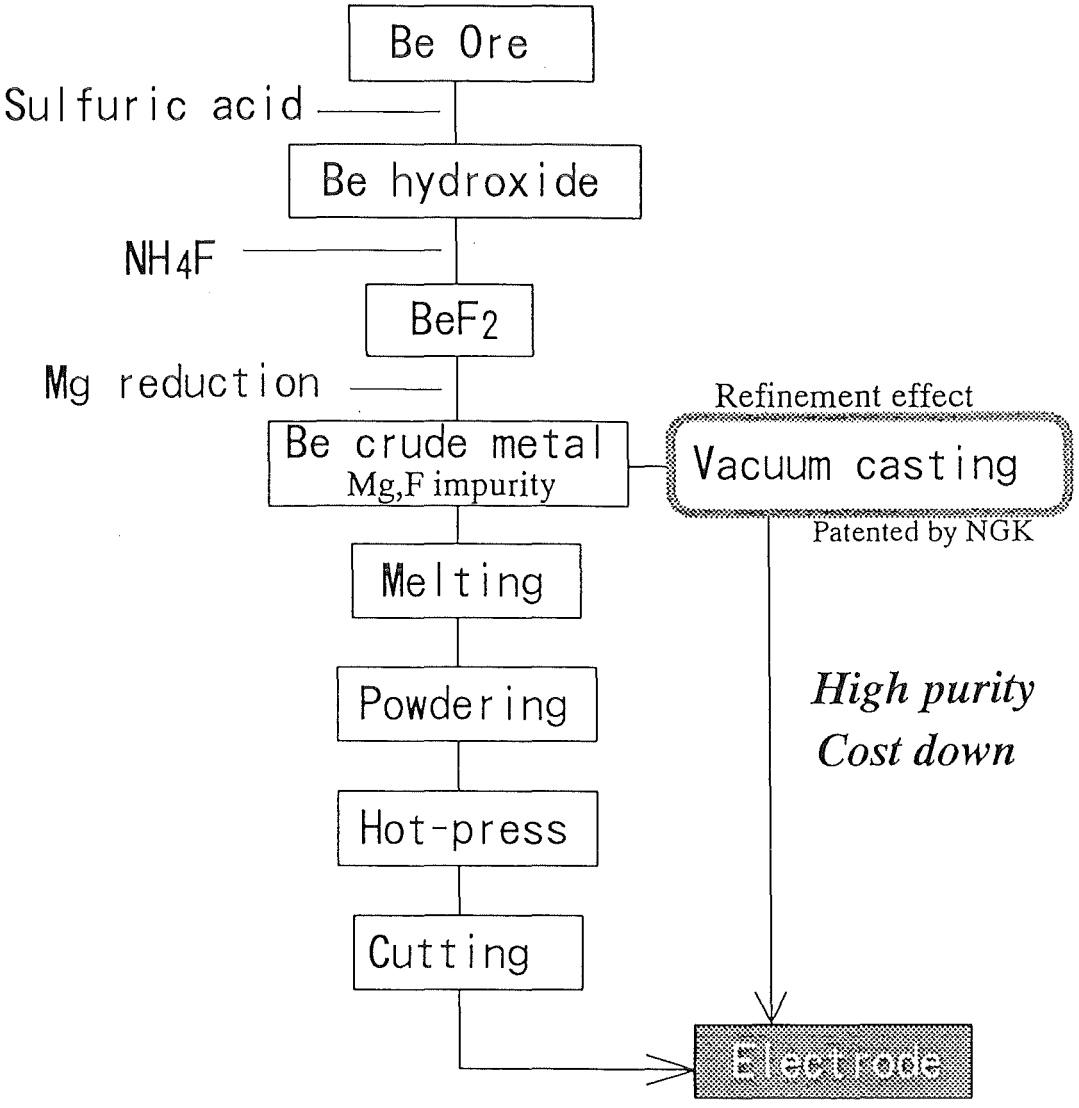

Chemical Composition of Pebble

		Chemical Composition (wt.%)								
		BeO	Al	Fe	Mg	Si	Mn	Cr	F	Co
Hot-pressed	Electrode	1.25	0.047	0.085	0.037	0.029	0.007	0.009	0.07	<0.001
	Pebble	1.36	0.048	0.084	0.031	0.022	0.002	0.003	0.05	<0.001
Vacuum cast	Electrode	0.53	0.047	0.028	0.005	0.092	0.008	0.008	0.04	<0.001
	Pebble	0.57	0.044	0.033	0.004	0.088	0.010	0.005	0.03	<0.001

OHP-6

OHP-7

Thermal Expansion Coefficient

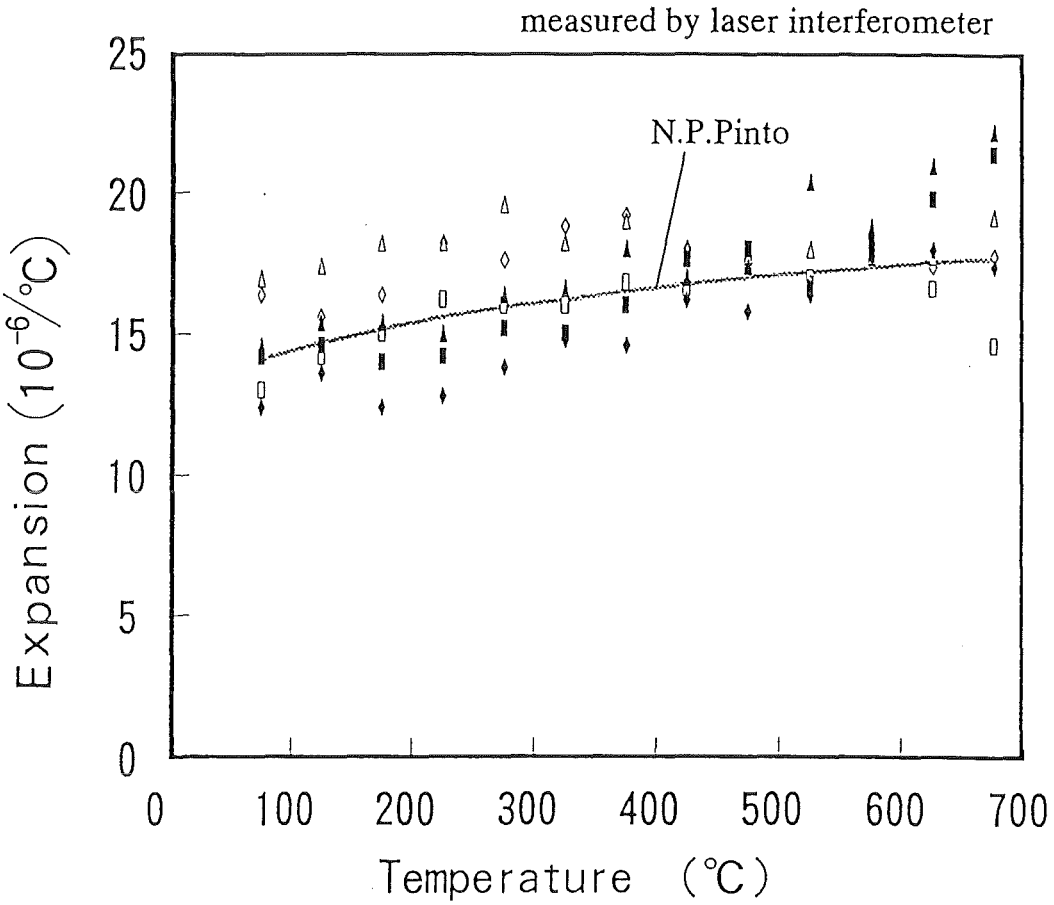

OHP-8

Specific Heat

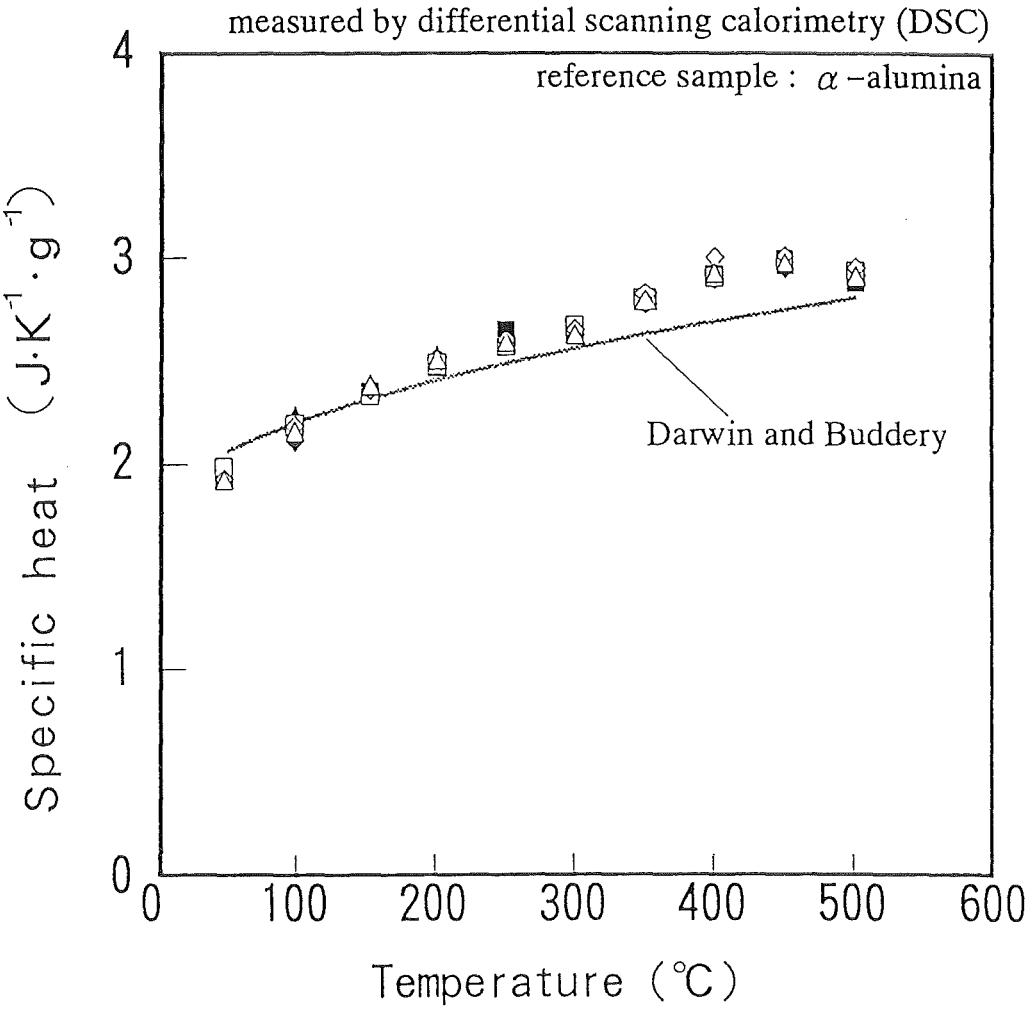

OHP-9

Pebble compression equipument

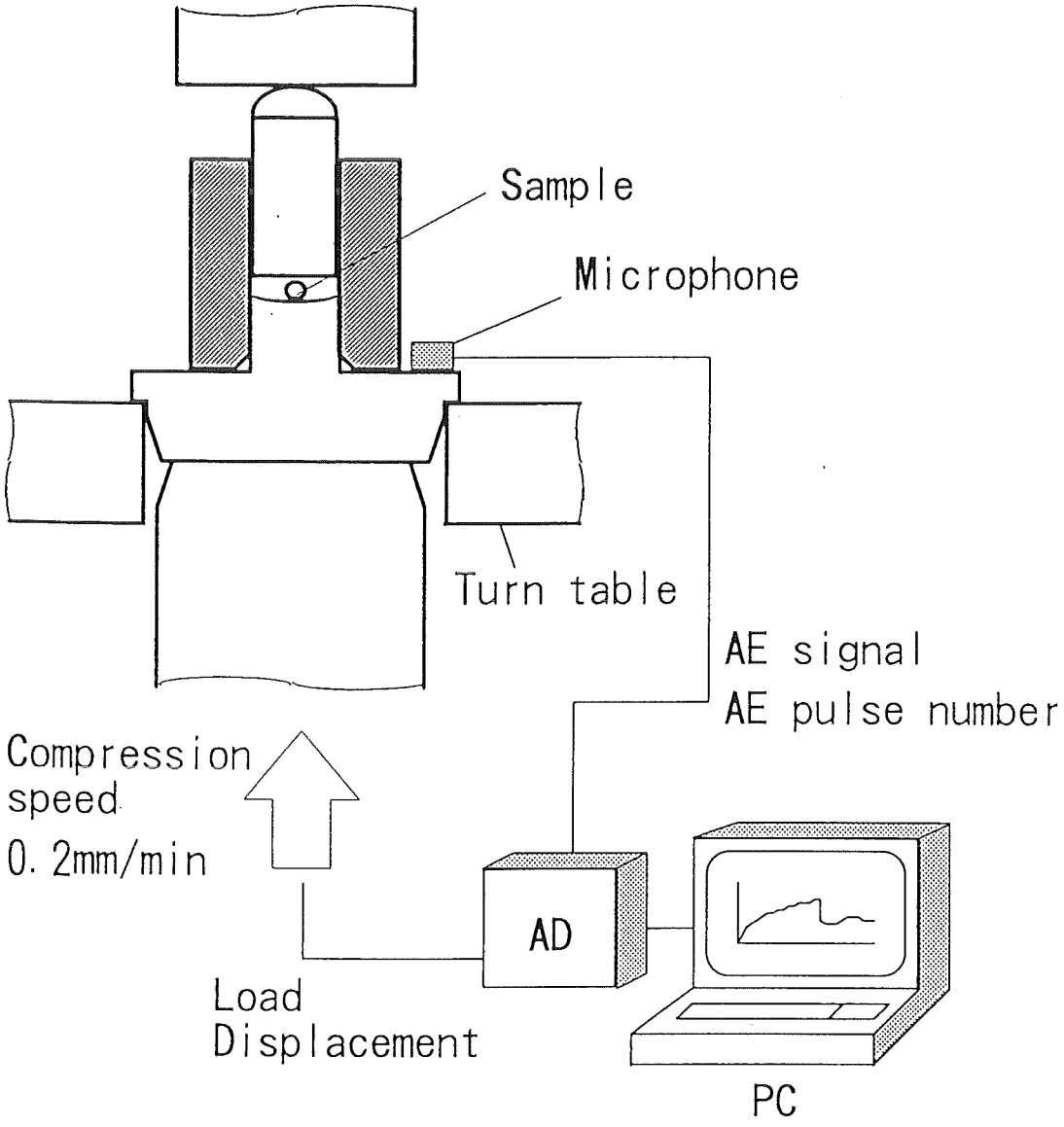

OHP-10

Unirradiated pebble
(Rotating electrode method)

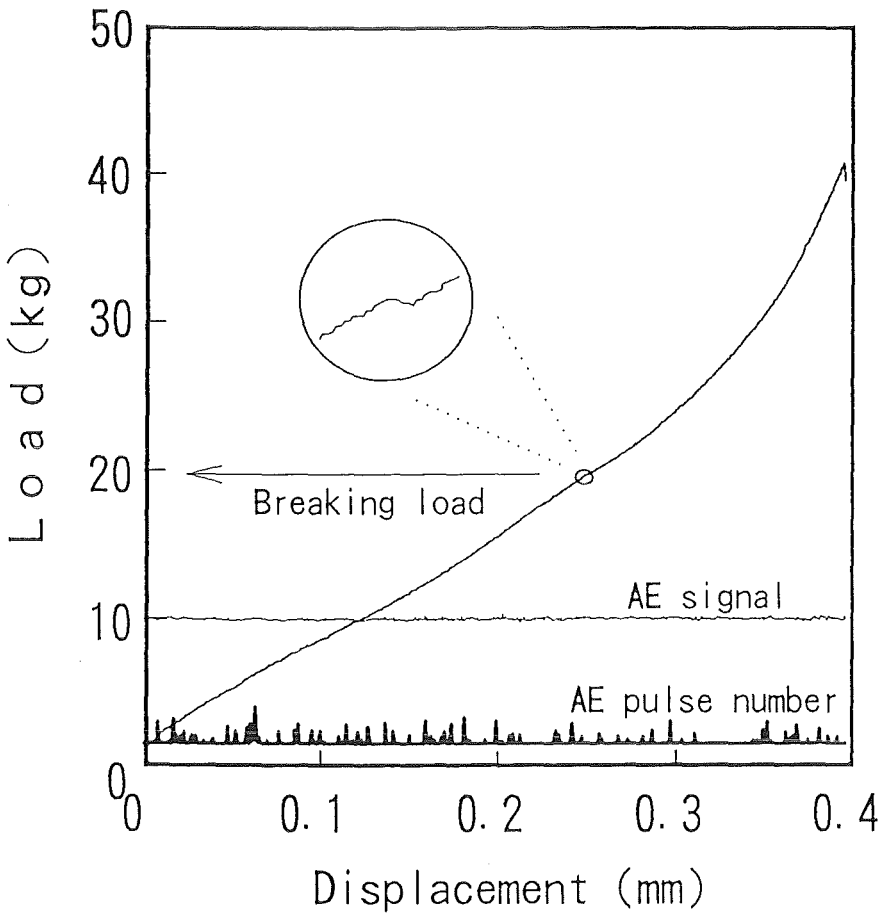

OHP-11

Neutron irradiated pebble
(Rotating electrode method)

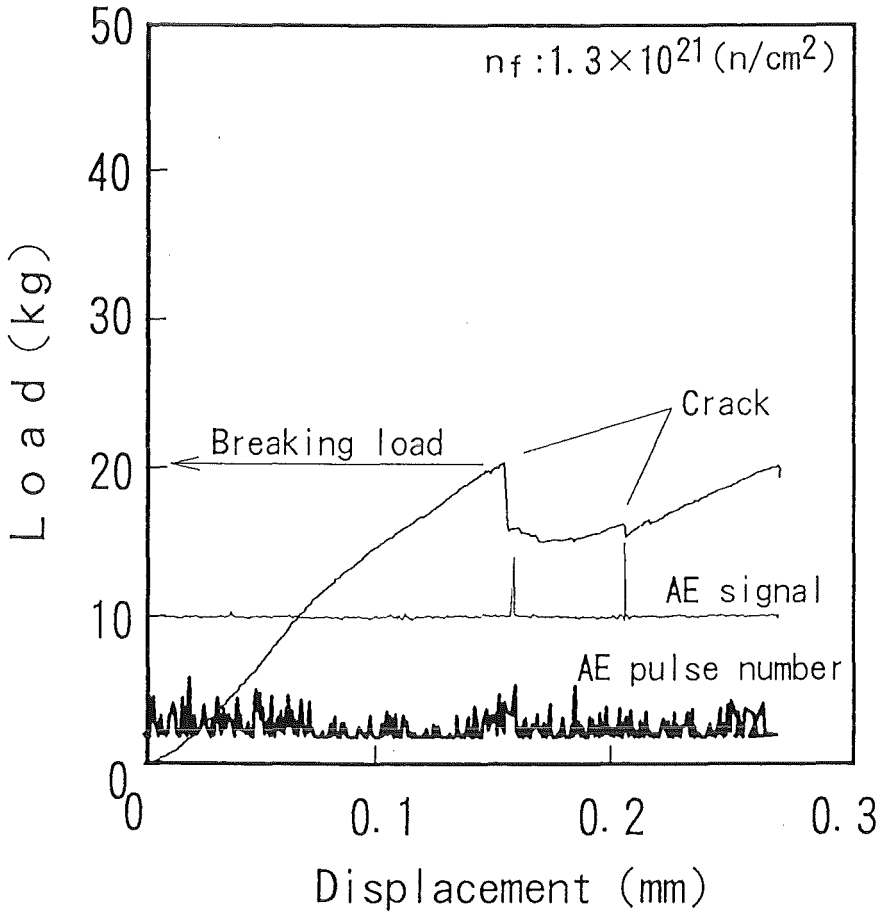

OHP-12

Irradiation effect of compression

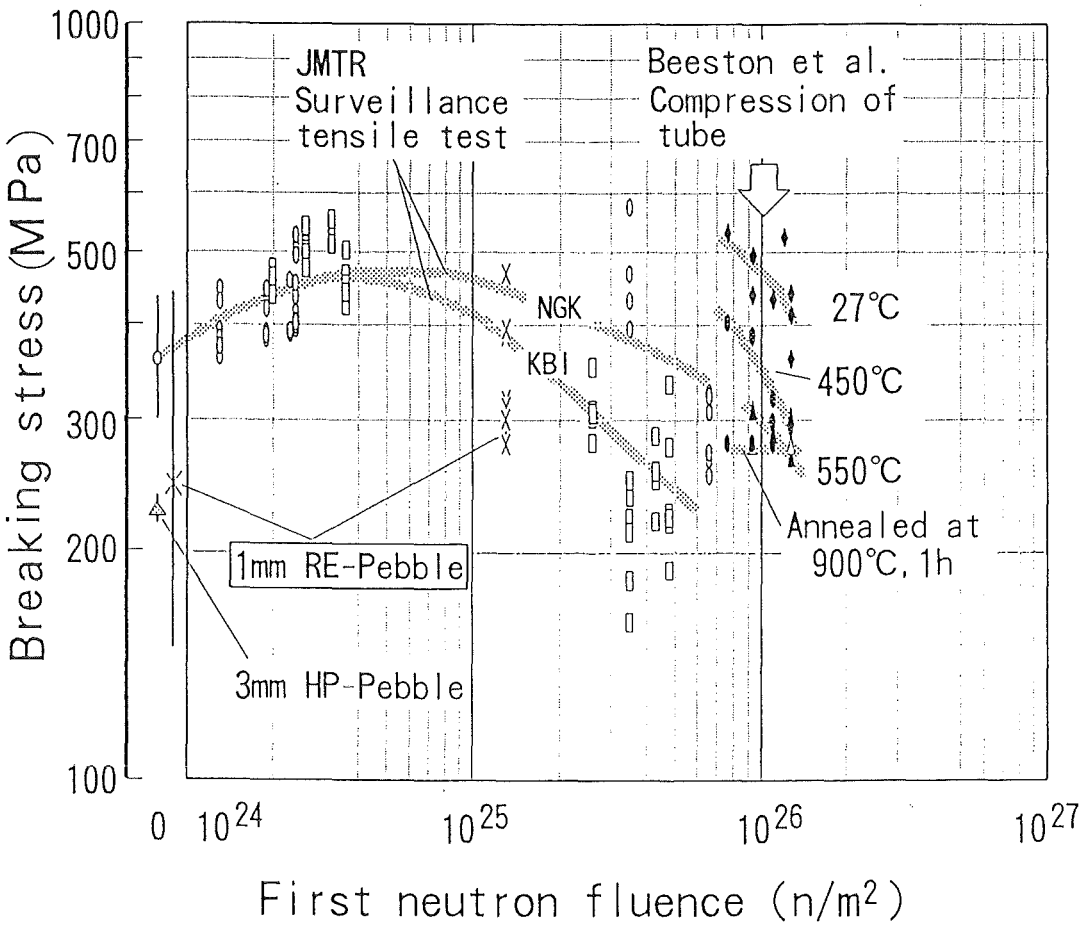

COMPATIBILITY BETWEEN BERYLLIUM AND STAINLESS STEEL

M.Kato*[1] and H.Kawamura*[2]

*[1] NGK Insulator Co., Ltd., Maegata-Cho 1, Handa-Shi, Aichi-Ken, 475 Japan.
*[2] Japan Atomic Energy Research Institute, Oarai Research Establishment,
Oarai-Machi, Higashi Ibaraki-Gun, Ibaraki-Ken, 311-13 Japan.

Beryllium has been used for the neutron multiplier in fusion blanket, and inserted into the structural material. And, 316 Stainless Steel has been proposed as the structural material. However, the elementary process of reaction between beryllium and 316SS did not clear in detail. Therefore, we conducted the diffusion couple test in order to make clear the elementary process of reaction between beryllium and 316SS. The combinations of the diffusion couple were three kinds, i.e., Be/316SS, Be/Fe・Cr alloy and Be/Ni. Each diffusion couples was sealed in capsule with high purity Helium(6N) by TIG welding, and was annealed for 100, 300 and 1000h per at each temperature, i.e. 400, 600 and 800 ℃.

1. Introduction

Beryllium is necessary for fusion blanket as the neutron multiplier. When Beryllium is inserted in the structural material, compatibility between beryllium and structural material become important. Therefore, the study for the compatibility have been conducted([1] ~ [4])(OHP 1). However, the compatibility between beryllium and structural material, austenitic or ferritic stainless steel are bad at high temperature(above 600℃) and elementary process of reaction was not obvious(OHP 2 and OHP 3). Therefore, the diffusion couple tests for making clear the reaction process were conducted.

2. Experimental method

Capsule which was used for diffusion couple test was sealed with high purity Helium(6N) by TIG welding(OHP 4). Diffusion couples are Be/316SS, Be/Fe・Cr alloy and Be/Ni and the compositions of 316SS and Fe・Cr alloy were shown in OHP 5. And, the capsules were annealed for 100, 300 and 1000h per at each temperature, i.e. 400, 600 and 800℃. The annealing test at 700℃ was conducted as the additional condition(OHP 6). As an analysis after annealing, X-ray diffraction, observation of cross section by optical microscope and EPMA analysis were conducted(OHP 7).

3. Results and discussion

3.1 The formation of reaction products

From the result of X-ray diffraction, BeNi and $Be_{21}Ni_5$ were identified as the reaction products

which were containing nickel, Be_2Fe and $Be_{11}Fe$ were identified as the reaction products which were containing iron(OHP 8). BeNi in 316SS and $Be_{21}Ni_5$ in Fe•Cr alloy were formed at 600℃. And the Be_2Fe and $Be_{11}Fe$ were formed at 800℃. From the results, it was considered that the Ni-containing compounds were more easy to form than Fe-containing compounds, because forming activation energy of the former was lower than that of the latter.

Change of X-ray peak intensity with annealing time at 800℃ was shown in OHP 9. The intensity of BeNi and $Be_{21}Ni_5$ were almost constant. On the other hand, the intensity of Be_2Fe was increased at 100h annealing, and decreased at 1000h annealing. Additionally, the intensity of Be 11Fe was increased remarkably over 100h annealing. Change of X-ray peak intensity of Be_2Fe and $Be_{11}Fe$ with annealing time at 800℃ was shown in OHP 10 as the comparison of 316SS and Fe•Cr alloy. The intensity of Be_2Fe in the Fe•Cr alloy is almost linear up to 1000h annealing. It was observed that the forming behavior of Be_2Fe and $Be_{11}Fe$ in 316SS were different from that in Fe•Cr alloy. Probably, it was considered that the difference of formation behavior of Be_2Fe and $Be_{11}Fe$ was the effect by the existence of nickel.

3.2 Change of reaction layer thickness

The change of the thickness of reaction layer with annealing time at 800℃ was shown in OHP 11. The difference of reaction was remarkable among Be/Ni, Be/316SS and Be/Fe •Cr alloy.

The change of the thickness of total reaction layer at 1000h annealing test with the increase of annealing temperature was shown in OHP 12. The reaction between beryllium and 316SS occurred above 600℃ as same as that between beryllium and nickel. And the reaction between beryllium and Fe•Cr alloy occurred first in 316SS, Ni, and Fe •Cr alloy at 800℃.

3.3 Distribution of elements on cross-section

The distribution of elements in 316SS, Ni and Fe•Cr alloy were shown in OHP 13, OHP 14 and OHP 15, respectively. From OHP 13, the reaction layer of 316SS was divided into two layers. We defined reaction layer as the outer layer at reaction interface side and the inner layer at 316SS bulk side. In inner layer, it was observed that nickel was segregated at the grain boundary. From OHP 14, existing place of beryllium and nickel in the reaction layer agreed closely. From OHP 15, the reaction layer was divided into two layers, and concentration of elements in each layer was almost constant.

4. Conclusion

The main results obtained from these test are shown as follows(OHP 16).

(1) It was observed that the reaction between beryllium and nickel occurred above 600℃, and the reaction between beryllium and iron occurred at 800 ℃.

(2) The reaction between beryllium and iron, i.e. Be_2Fe and $Be_{11}Fe$, changed with annealing time at 800℃, and the chemical reaction process changed by the existence of nickel.

(3) On 316SS, the formation of $Be_{21}Ni_5$, which is the beryllium richer compound, was inhibited by the existence of iron.

(4) Chemical reaction between beryllium and iron did not occur at 600 ℃

(5) It was easier to form $Be_{11}Fe$ which is a beryllium richer composite by existence of nickel.

References

[1]P.Hofmann and Dienst, J.Nucl.Mater., 171(1990)203-214

[2]A.Terlain, D.Herpin et.al., Fusion Technology, 1179-1183(1989)

[3]T.Flament, P.Fauvet and J.Sannier, J.Nucl.Mater., 155-157(1988)496-499

[4]T.Flament, D.Herpin et.al., J.Nucl.Mater., 191-194(1992)163-167

Study review concerning the compatibility between beryllium and structural materials

	Specimens		Atmosphere	Annealing condition		Note
	Beryllium	Structural material		Temp.(℃)	Time(h)	
Hofmann et.al.	• Be	• AISI316	Ar seal	600～900	100～1000	1990
Terlain et.al.	• Be(High Oxygen)*1 • Be-Ca Alloy (Polishing by diamond)	• 316SS • 1.4914 (mechanical polishing)	Vacuum (0.5~1.0Pa)	550～700	500～3300	1988
Flament et.al.	• Be(High Oxygen)*1 • Be-Ca Alloy (Polishing by diamond)	• 316LSS • HT9 • 1.4914 (mechanical polishing)	Vacuum (0.5~1.0Pa)	600～700	500～1500	1988
Flament et.al.	• Be(High Oxygen)*1 • Be(LowOxygen)*2 • Be-Ca Alloy (Polishing by diamond)	• 316LSS • 1.4914 (mechanical polishing)	Vacuum (0.5~1.0Pa)	550～750	500～3000	1992
Kawamura and Kato	• Be(Hot press) (Polishing by diamond)	• 316SS (Polishing by diamond)	He seal	400～800	100～1000	1992

＊1：Oxygen 0.1～0.5wt%　　＊2：Oxygen 0.005～0.01wt%

OHP 1

Review of the results of compatibility between beryllium and 316SS

Study	Reaction temperature	Analysis of reaction products	Remark
Terlain et. al.	Reaction occurred above 580℃.	Not identified	1988
Flament et. al.	Reaction occurred above 600℃.	Be-Fe-Cr chemical compound (EDS)	1988
Hofmann et. al.	Reaction occurred above 600℃.	BeNi(AES)	1990
Kawamura and Kato	Reaction occurred above 600℃.	Reaction products were different by annealing temp.. At 600℃ : BeNi At 800℃ : Be_2Fe, $Be_{11}Fe$ and $Be_{21}Ni_5$ (XD,EPMA)	1992

OHP 2

Review of the results of compatibility between Be and ferritic stainless steel

Study	Reaction temperature	Analysis of reaction products	Remark
Terlain et. al.	Reaction occurred above 650℃.	Not identified	1988
Flament et. al.	Reaction occurred above 600℃.	Be-Fe-Cr chemical compound (EDS)	1988
Kawamura and Kato	Reaction did not occur at 600℃,but at 800℃.	Be_2Fe, $Be_{11}Fe$ was identified at 800℃. (XD)	1992

OHP 3

Outline of the capsule

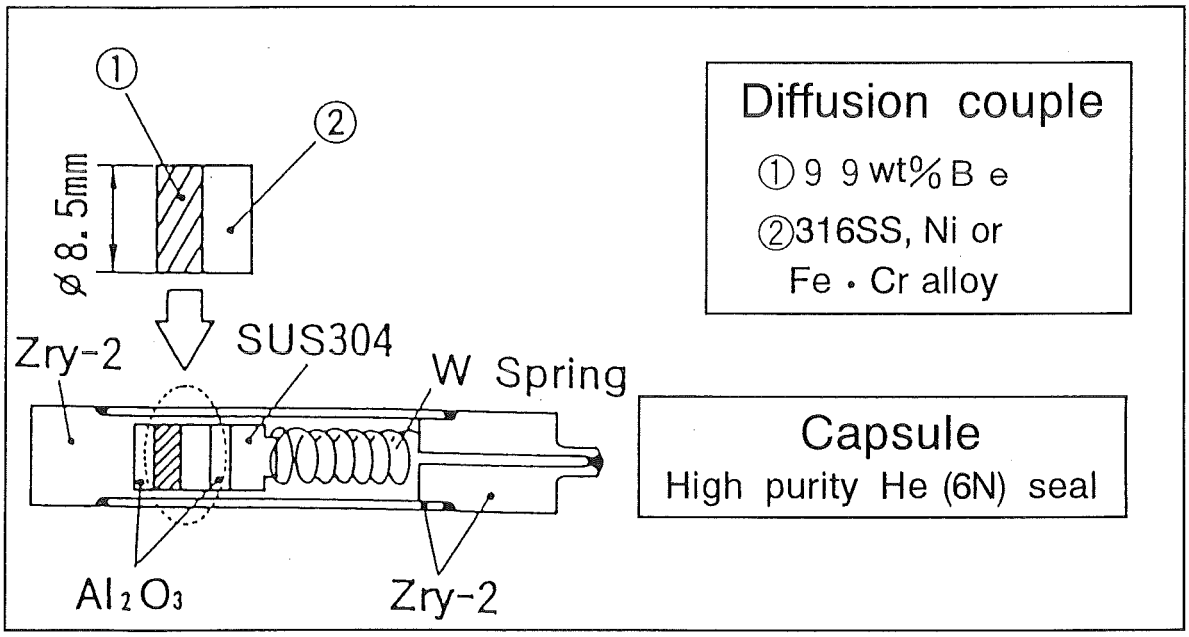

Chemical component

(wt.%)

Element / Material	Fe	Cr	Ni	Mo	Mn	Si	P	C
316SS	bal.	17	10	2	1.5	0.41	0.03	0.05
Fe·Cr alloy (410SS)	bal.	12.9	—	—	0.86	0.45	0.0015	0.0013
1.4914	bal.	11.2	0.7	0.6	0.48	0.04	—	0.2

OHP 5

Annealing condition

Temp. (°C) \ Time (h)	100	300	1000
400	○	○	○
600	○ ● ◎	○ ● ◎	○ ● ◎
700	○	○	
800	○ ● ◎	○ ● ◎	○ ● ◎

○ : Be/316SS
● : Be/Ni
◎ : Be/Fe·Cr alloy

Tests after annealing

Items	Evaluation
X-ray diffraction	Identification of reaction products
Observation of cross-section	Thickness of reaction layer
EPMA analysis	Distribution of elements in the reaction layer

Reaction products identified by X-ray diffraction

Annealing time: 1000h

Sample / Temp. (℃)	316SS	Ni	Fe·Cr alloy
400	——	——	——
600	BeNi	$Be_{21}Ni_5$	——
800	$Be_{21}Ni_5$ Be_2Fe $Be_{11}Fe$	BeNi $Be_{21}Ni_5$	Be_2Fe $Be_{11}Fe$

OHP 9

Change of X-ray peak intensity with annealing time

(316SS)

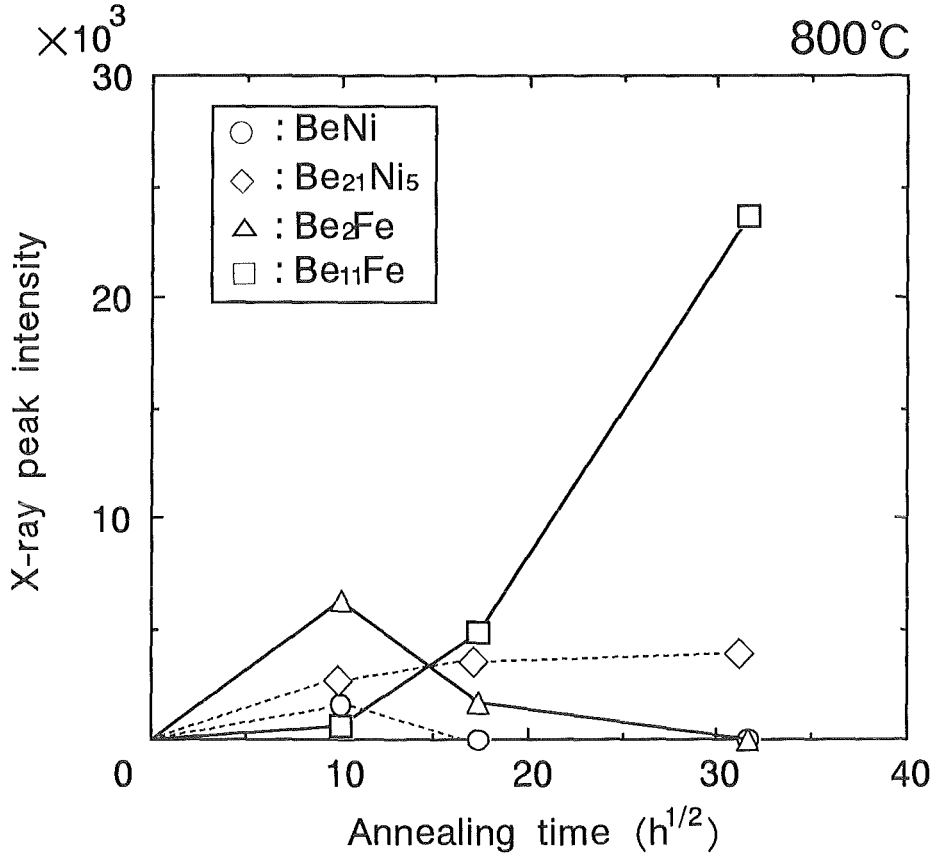

Change of X-ray peak intensity with annealing time

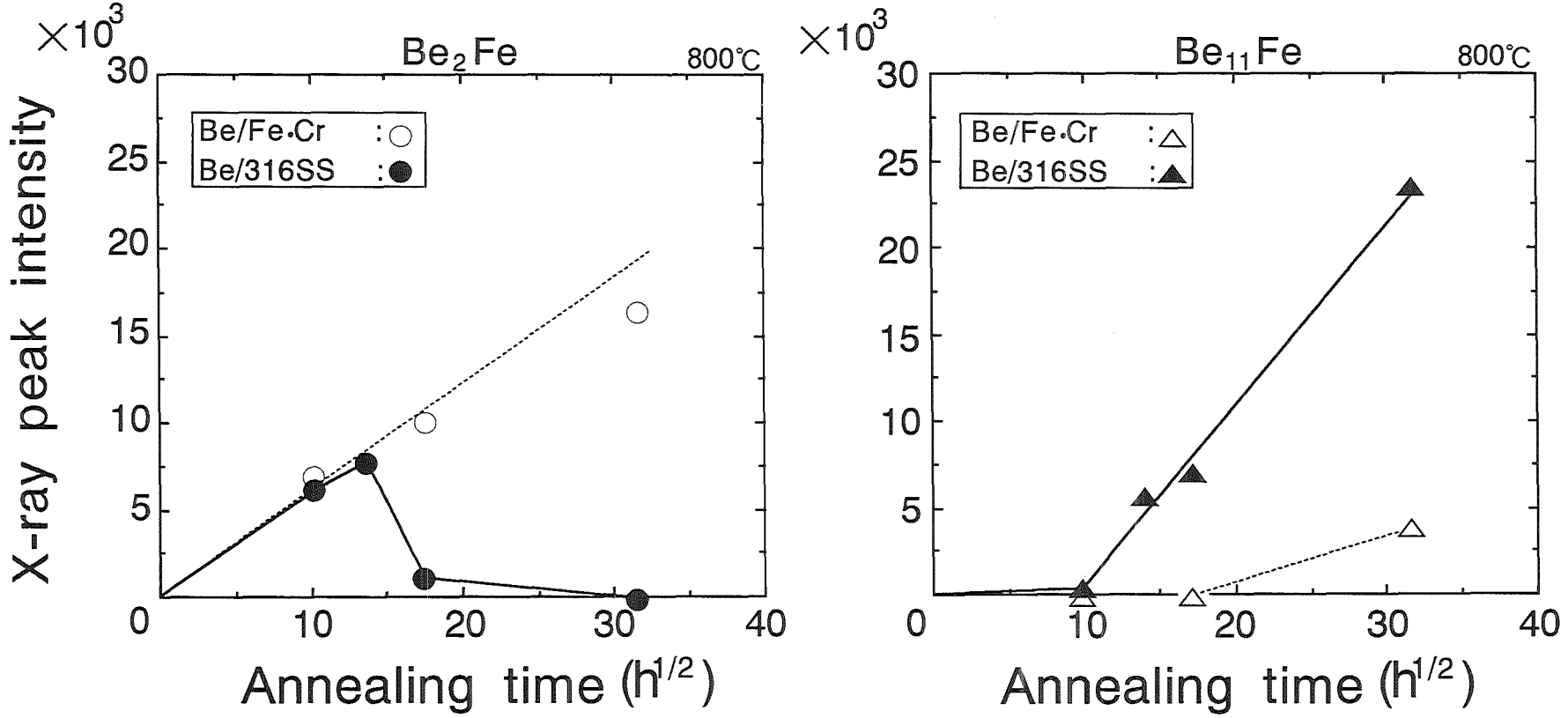

OHP 10

Changes of the thickness of total reaction layer with annealing time

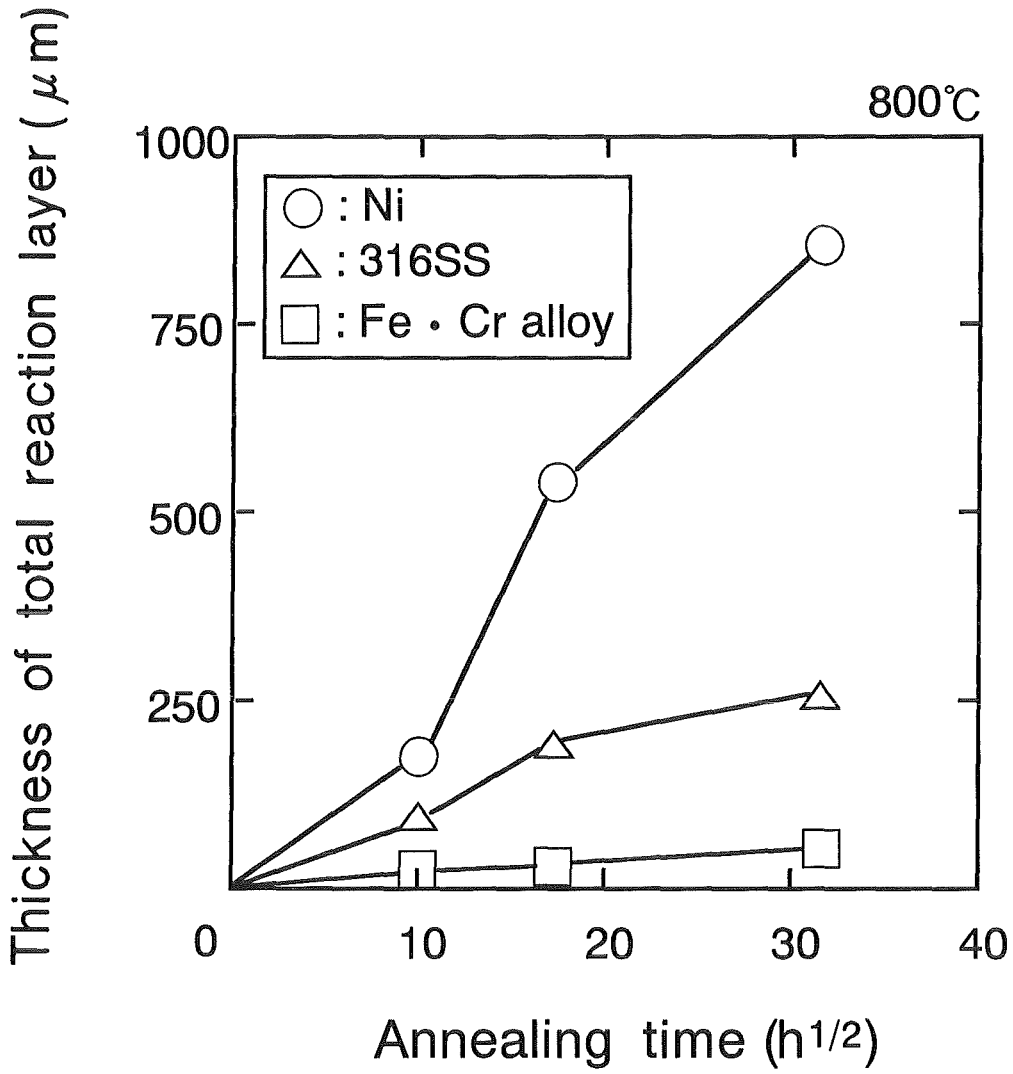

Changes of the thickness of total reaction layer with annealing temperature

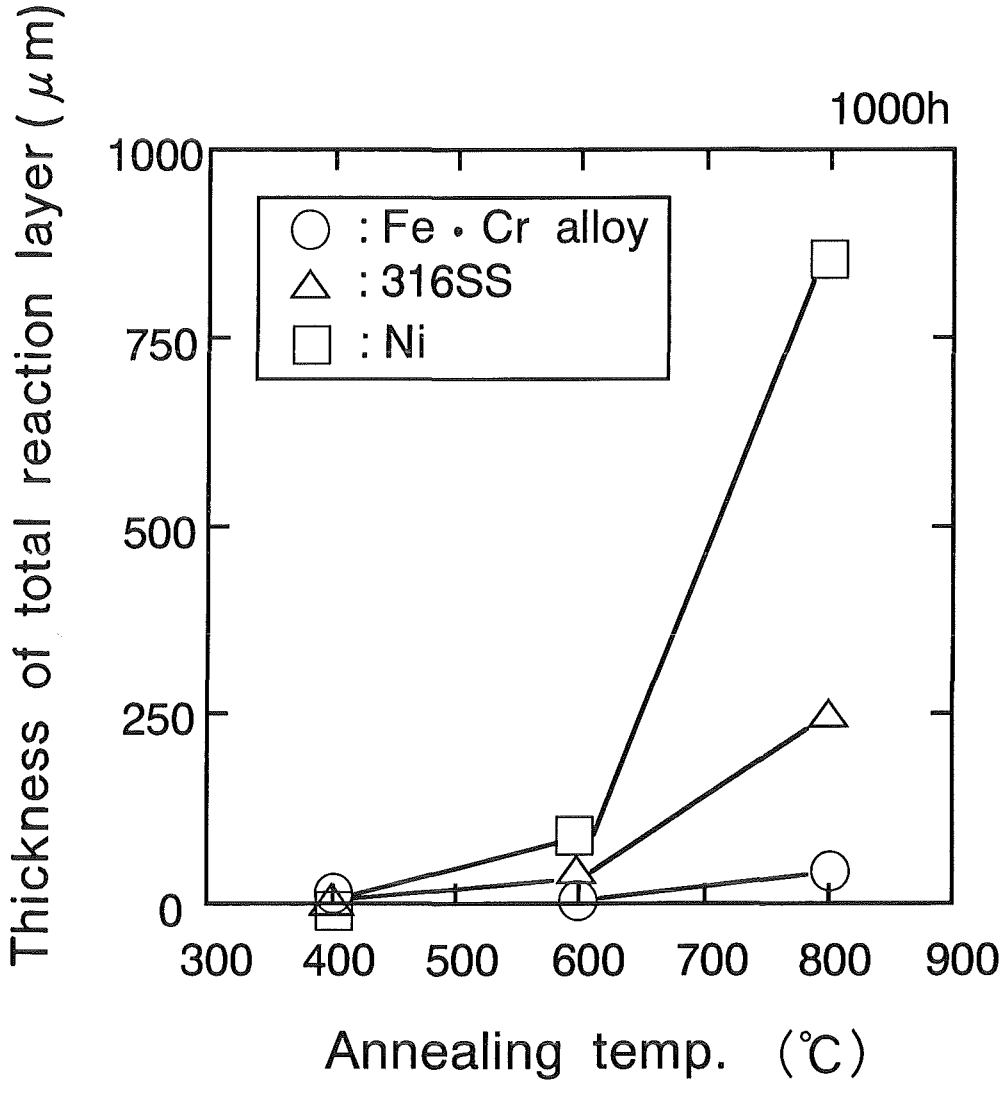

E P M A Analysis

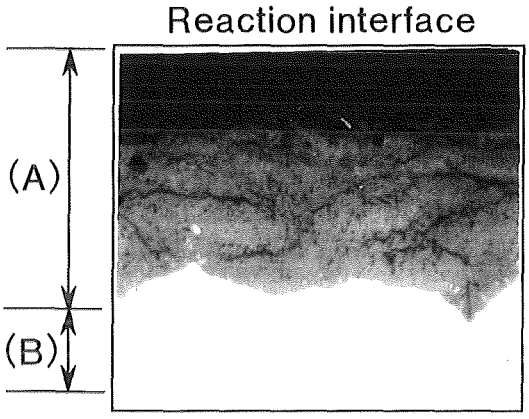

(3 1 6 SS side)

Annealing temperature : 800℃
Annealing time : 300h

(A) Outer reaction layer
(B) Inner reaction layer

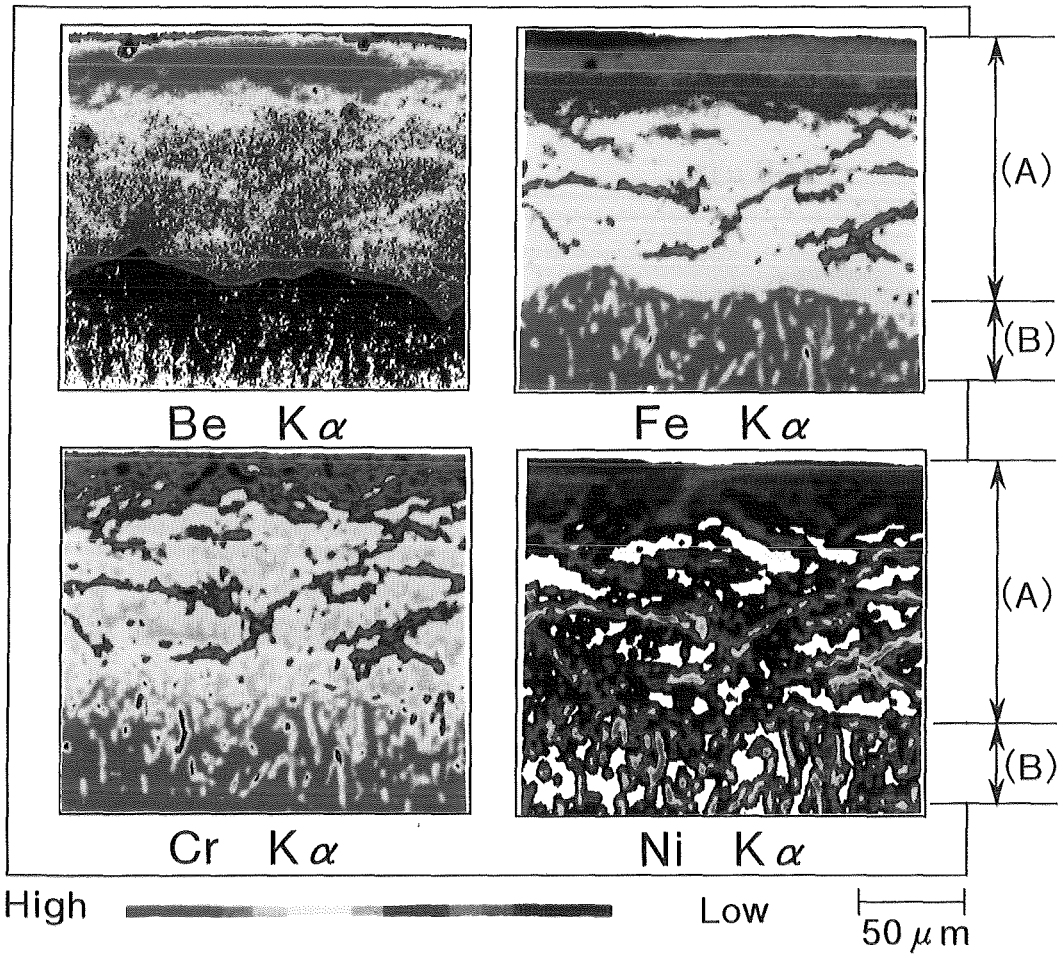

E P M A Analysis

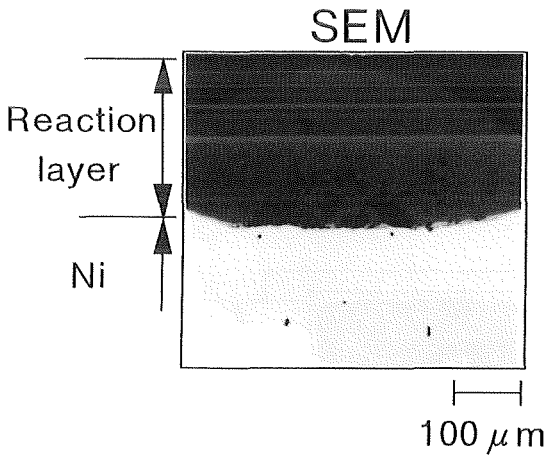

(Ni side)

Annealing Temp. 800℃

Annealing Time 1000h

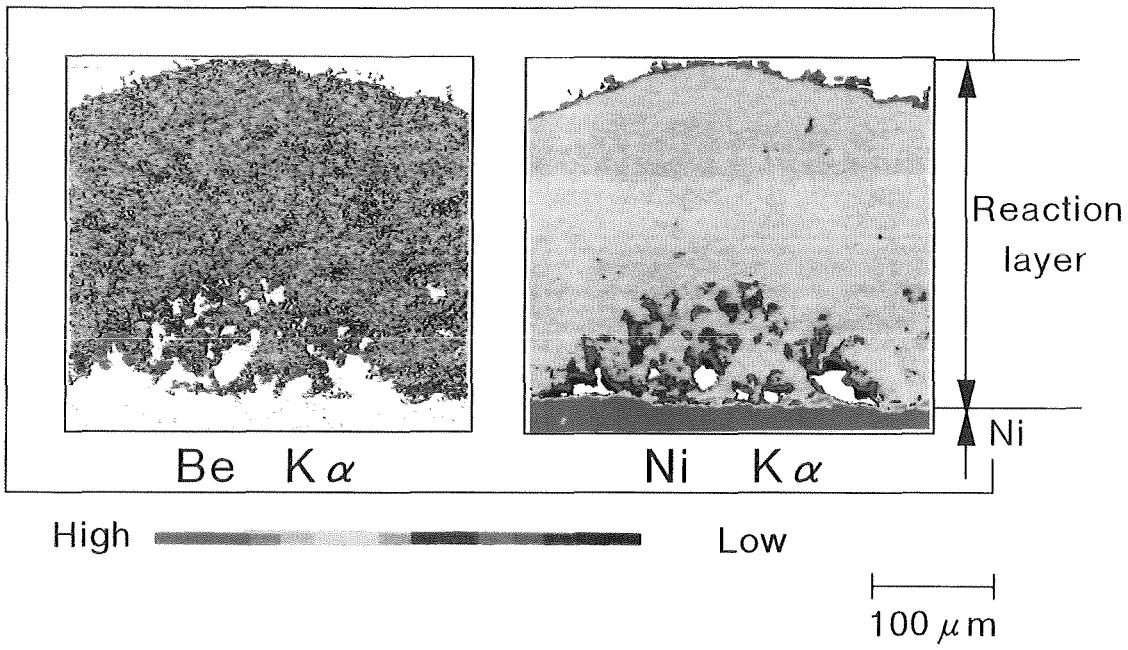

E P M A Analysis

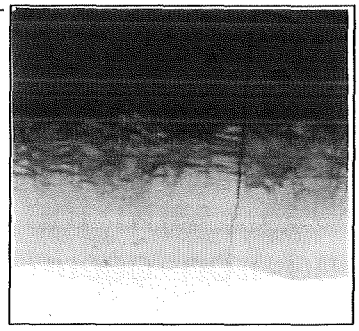

SEM

(Fe•Cr side)

Annealing Temp. 800℃

Annealing Time 1000h

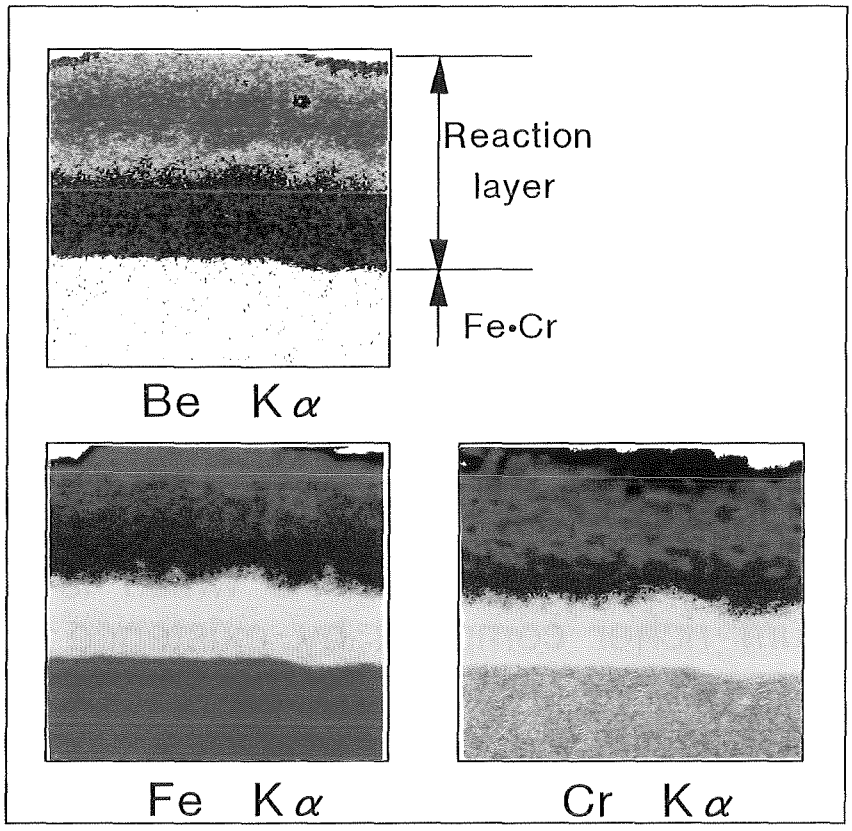

Conclusion

- It was observed that the reaction between beryllium and nickel occurred above 600℃, and the reaction between beryllium and iron occurred at 800℃.
- The reaction products between beryllium and iron, i.e. Be_2Fe $Be_{11}Fe$, changed with annealing time at 800℃, and the chemical reaction process changed by the existence of nickel.
- On 316SS, the formation of $Be_{21}Ni_5$, which is the beryllium richer compound, was inhibited by the existence of iron.
- Chemical reaction between beryllium and iron did not occur at 600℃.
- It was easier to form $Be_{11}Fe$ which is a beryllium richer composit by existence of nickel.

COMPATIBILITY BETWEEN BERYLLIUM AND CERAMIC COATING FILM

H.Kawamura[*1], M.Kato[*2] and K.Miyajima[*3]

[*1]Japan Atomic Energy Research Institute, Oarai Research Establishment,
Oarai-Machi, Higashi Ibaraki-Gun, Ibaraki-Ken, 311-13 Japan.
[*2]NGK Insulator Co., Ltd., Maegata-Cho 1, Handa-Shi, Aichi-Ken, 475 Japan.
[*3]Tocalo Co., Ltd., 4-13-4, Fukae-Kitamachi, Higashinada-ku, Kobe-shi, 658 Japan.

Beryllium is indispensable for fusion blanket as the neutron multiplier and inserted into the structural material(316SS) on Japanese blanket concept. In this case, chemical interaction between beryllium and 316SS has been observed above 600 ℃, and BeNi was formed on 316SS side at this temperature.

Therefore, we are considering a chromic oxide coating on 316SS surface as the diffusion barrier of beryllium into 316SS, because the reaction between beryllium and chromium was not observed and the component of this coating film did not contain nickel.

From the results, it made clear that ceramic coating film(50 μ m) had a function as reaction barrier completely against 316SS at 800 ℃ -300h annealing similar to 600 ℃ -1000h annealing.

1. Introduction

Beryllium is necessary for fusion blanket as the neutron multiplier. When beryllium is inserted in the structural material, compatibility between beryllium and structural material are important. However, it has been reported that beryllium react on 316SS above 600℃([1]～[4]). Therefore, for the purpose of improving compatibility between beryllium and 316SS, we considered the ceramic coating on 316SS side as reaction barrier （OHP 1）. Compatibility between beryllium and ceramic coating film(CDC film) was examined by the diffusion couple test.

2. Experimental method

Ceramic coating was conducted by Chemical Densified Coating method(CDC method)(OHP 2). This ceramic coating film has high hardness, strong adhesion and good thermal properties. This coating film contains 70% Cr_2O_3 and 30% SiO_2, and SiO_2 is dispersed in the Cr_2O_3 matrix. The diffusion couple test was conducted in order to make clear the compatibility between beryllium and CDC film (about 50 μ m) formed on 316SS. The diffusion couple was sealed in capsule filled with high purity Helium(6N) by TIG welding(OHP 3). It was annealed for 100, 300 and 1000h per at each temperature, i.e. 400, 600 and 800℃. The annealing test at 700℃ was conducted as the additional condition （OHP 3）.

As the analysis after annealing, reaction products were identified by X-ray diffraction.

Subsequently, the cross-section of CDC film on 316SS was observed in order to measure the thickness of the reaction layer by optical microscopic observation. Additionally, the cross-section was by EPMA in order to estimate the distribution of Be, Fe, et al. in 316SS with CDC film.

3. Results and discussion

3.1 The formation of reaction products

X-ray diffraction patterns of CDC film side after annealed for 1000h at temperatures of 400, 600 and 800℃ is shown in OHP 4. At the temperature lower than 600 ℃,reaction products were not identified, and only Cr_2O_3 and SiO_2 which were the component of CDC film were identified. However, Cr and BeO were identified at 800 ℃.

The change of intensity of X-ray diffraction peak in CDC film as a function of temperature is shown in OHP 5. Chromium and beryllium oxide were identified first at 800℃. It was considered that Cr_2O_3 was reduced by beryllium, then chromium and beryllium oxide were formed. The change of intensity of X-ray diffraction peak for chromium as a function of annealing time is shown in OHP 6. Intensity of chromium resulted in the straight line against a root of the annealing time. This result means that the forming rate of chromium is determined by the diffusion of beryllium in the CDC film.

3.2 Observation on cross-section

The result of optical microscopic observation of cross-section of 316SS with CDC film annealed at several temperatures is shown in OHP 7. It could not be observed that beryllium invaded into CDC film on the annealing test at temperatures lower than 600℃. However, it was observed that on annealing test at 800℃ beryllium invaded into CDC film and CDC film was cracked.

3.3 Distribution of elements on cross-section

The result of EPMA analysis of cross-section of the diffusion couple annealed at 800 ℃ for 1000h is shown in OHP 8. It shows the SEM image and distribution of elements. It was observed that beryllium invaded into 316SS through CDC film. Iron and nickel diffused into CDC film. Molybdenum concentrated at the interface between CDC film and the base metal(316SS). The distribution of beryllium matched to the distribution of nickel. Therefore, it seems that the reaction between beryllium and nickel is easier than that between beryllium and other element. From these results, thickness of reaction layer in 316SS through CDC film was about 50 μ m in the case of annealing test at 800 ℃ for 1000h.

3.4 Barrier effect by CDC film

The thickness of reaction layer in 316SS as a function of annealing temperature is shown in OHP

9. At lower temperature than 700℃, the reaction between beryllium and CDC film did not occur. The thickness of reaction layer with annealing time in case of annealing at 800℃ is shown in OHP 10. The thickness of reaction layer in 316SS with CDC film was reduced to about one fifth than that in 316SS without CDC film.

4. Conclusion

The main results obtained from these tests are shown as follows(OHP 11).

(1) Ceramic coating film(50 μ m) had a function as reaction barrier completely against 316SS at 600℃-1000h annealing.

(2) Ceramic coating film(50 μ m) had a function as reaction barrier completely against 316SS at 800℃-300h annealing similar to 600℃-1000h annealing.

(3) Ceramic coating film(50 μ m) could not have a function as reaction barrier completely against 316SS at 800℃-1000h annealing. However, the thickness of reaction layer was reduced to ~ 1/5 as a comparison of case without CDC film.

(4) Cr_2O_3 was reduced at 800℃ by beryllium, then chromium and beryllium oxide was generated. It was obvious that this behavior was controlled by the diffusion of beryllium.

References

[1]P.Hofmann and Dienst, J.Nucl.Mater., 171(1990)203-214

[2]A.Terlain, D.Herpin et.al., Fusion Technology, 1179-1183(1989)

[3]T.Flament, P.Fauvet and J.Sannier, J.Nucl.Mater., 155-157(1988)496-499

[4]T.Flament, D.Herpin et.al., J.Nucl.Mater., 191-194(1992)163-167

The background of this work

Beryllium will be used in a fusion blanket as neutron multiplier

Compatibility (Be/316SS) is bad above 600℃.

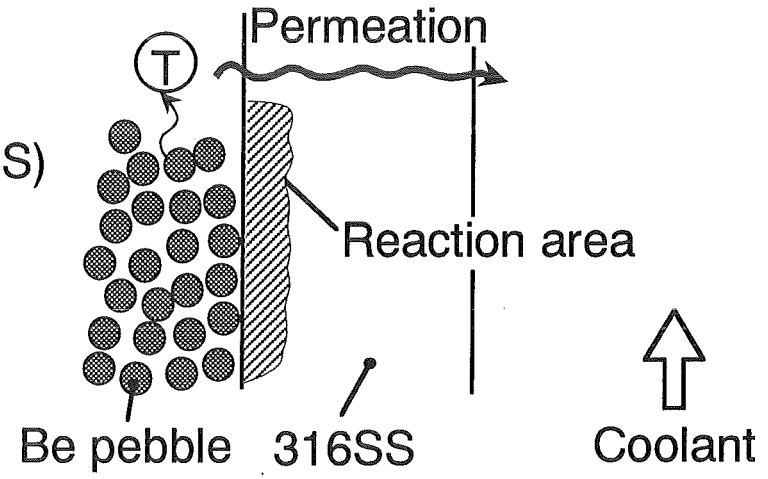

Compatibility (Be/316SS) and ^{3}H permeation are improved by the ceramic coating film.

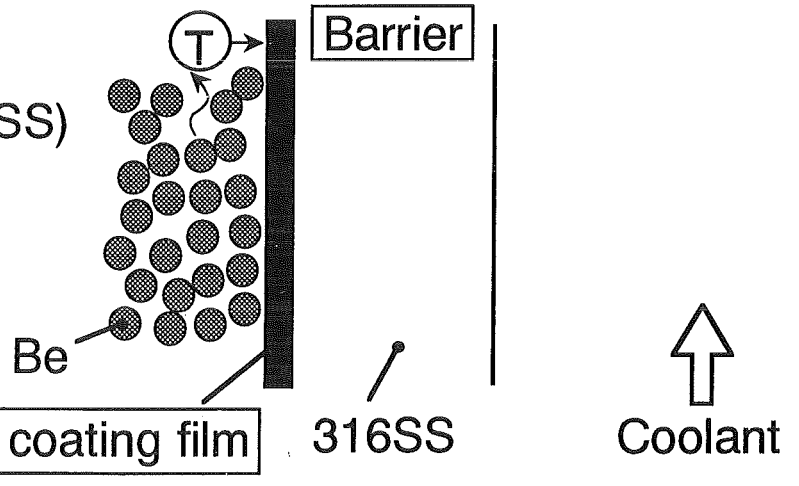

Ceramic Coating Method
(CDC : Chemical Densified Coating)

Pretreatment of Base Metal
- Degreasing
- Al_2O_3 grit Blasting

↓

Application of Ceramic Slurry
- SiO_2 Granules + CrO_3 Solution

↓

Burning

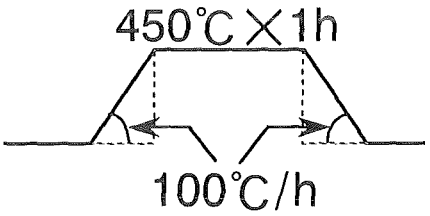

↓

Impregnating
- CrO_3 Solution

15 Times Repeat

Burning

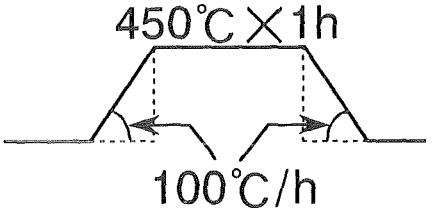

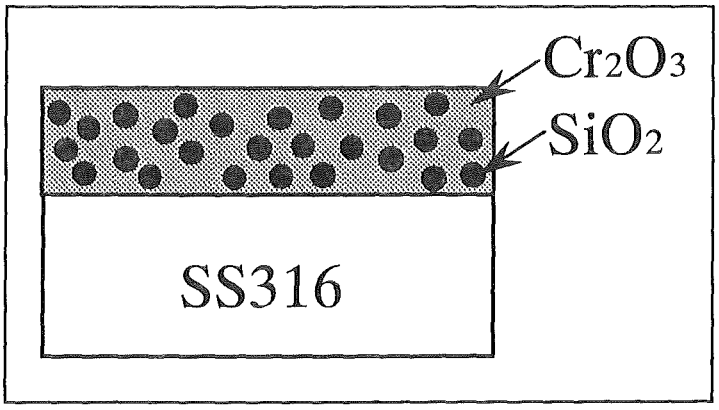

Testing method

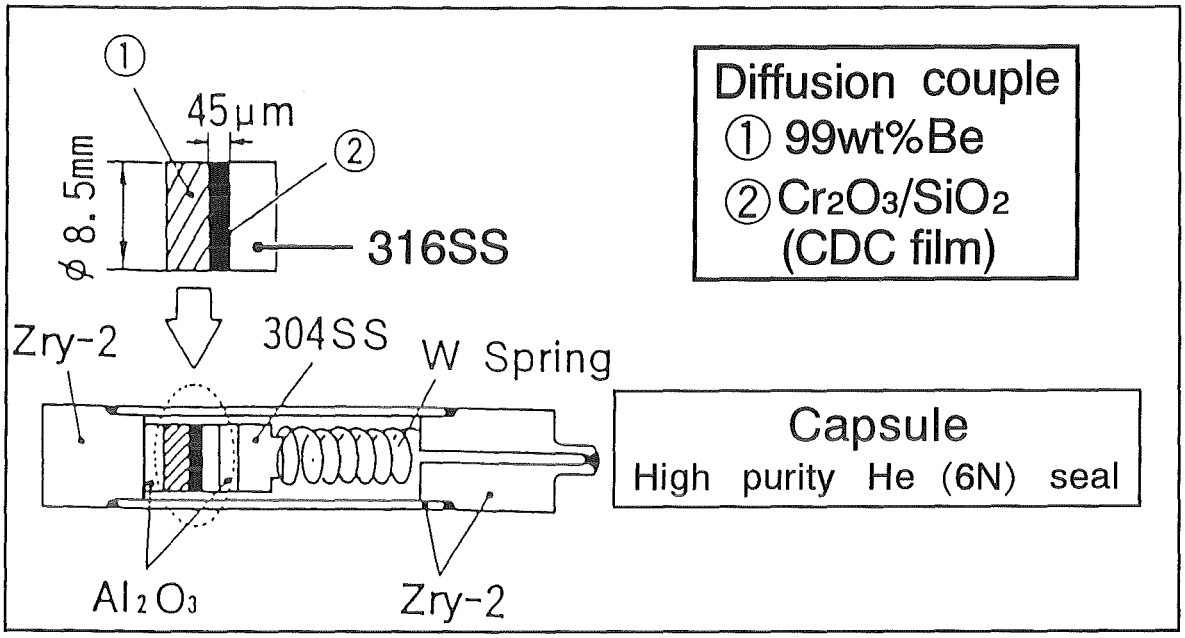

Annealing Condition

Temp. (℃) \ Time (h)	100	300	1000
400	●	●	●
600	●	●	●
700	●	●	
800	●	●	●

X-ray diffraction (CDC film)

Annealing time : 1000h

○ : Cr_2O_3, ◆ : BeO

△ : SiO_2, ■ : Cr

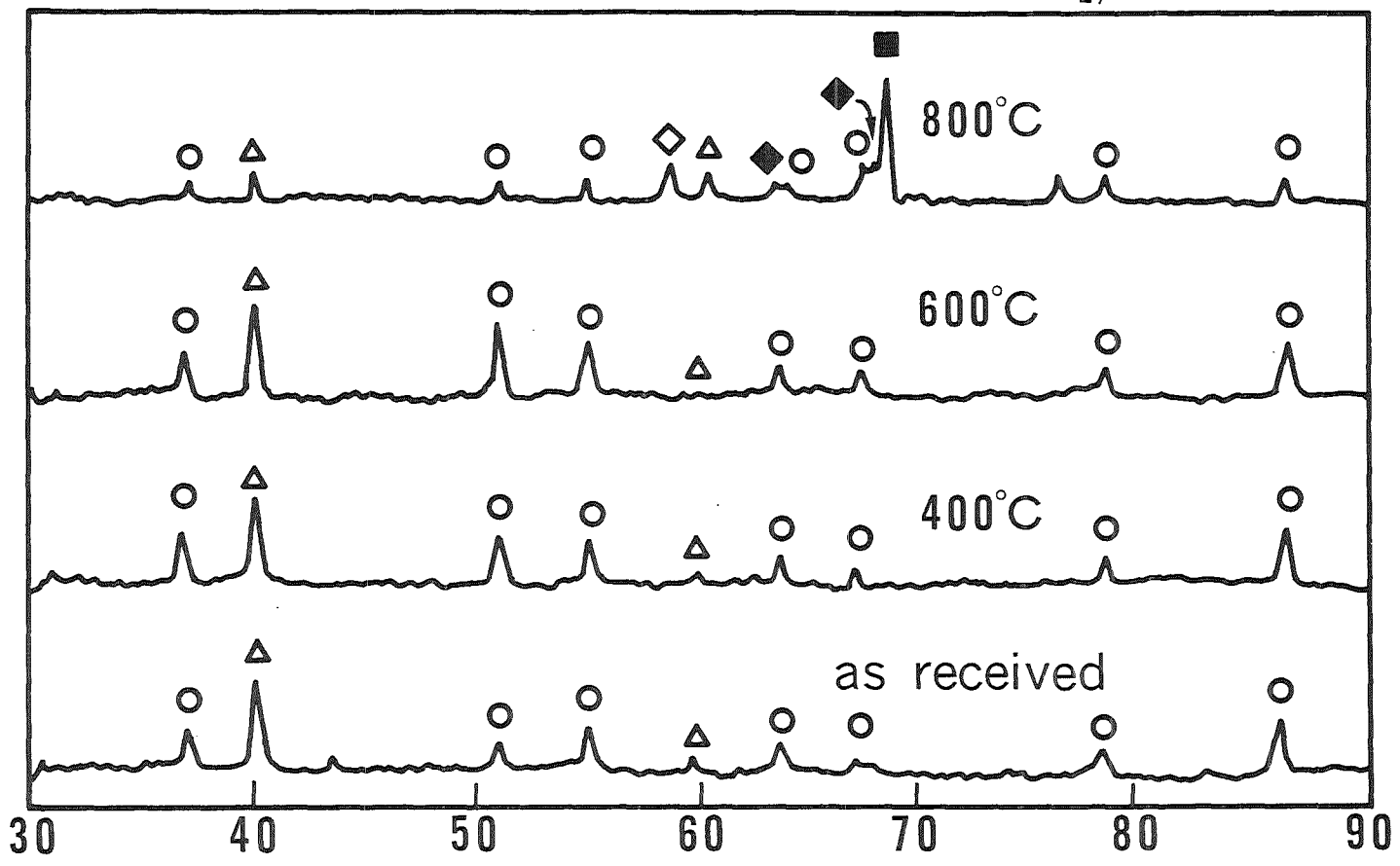

OHP 4

OHP 5

Change of intensity of X-ray diffraction peak with annealing temperature

(CDC film)

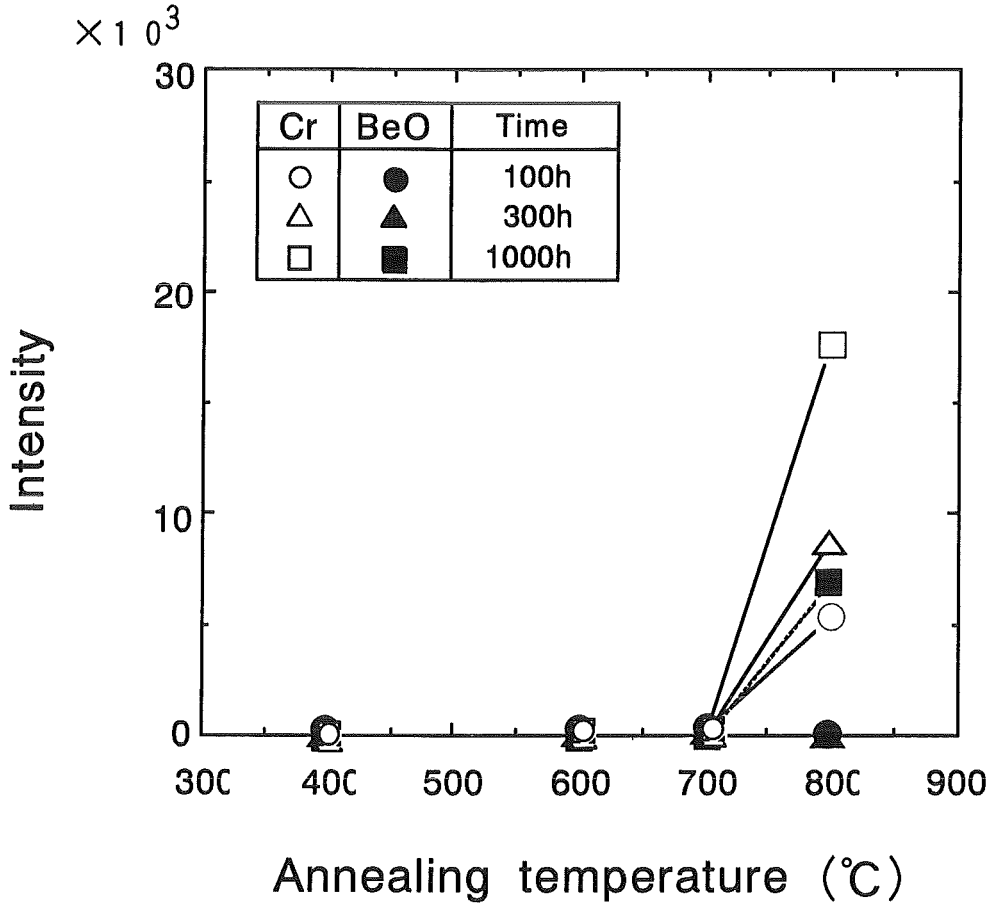

Change of intensity of X-ray diffraction peak for Cr with Annealing time

(CDC film)

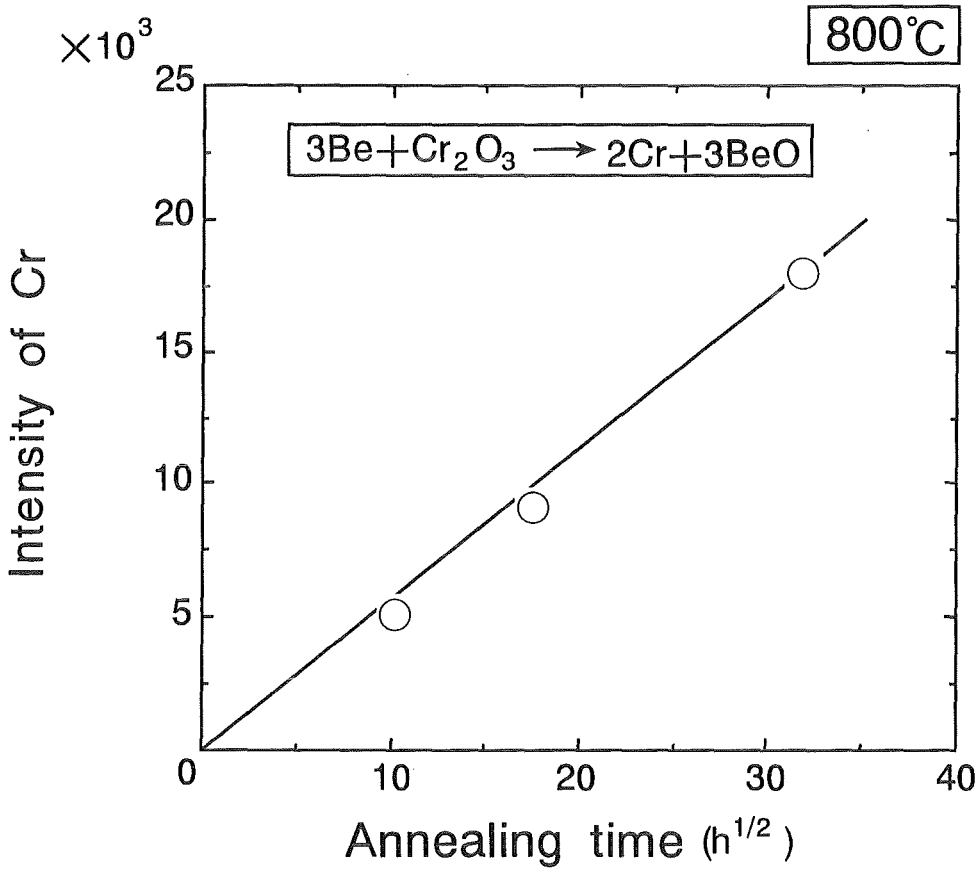

Cr_2O_3 is reduced by beryllium.

⇩

It is cleared that beryllium diffuses into ceramic coating film.

Reaction Characteristic (CDC film)

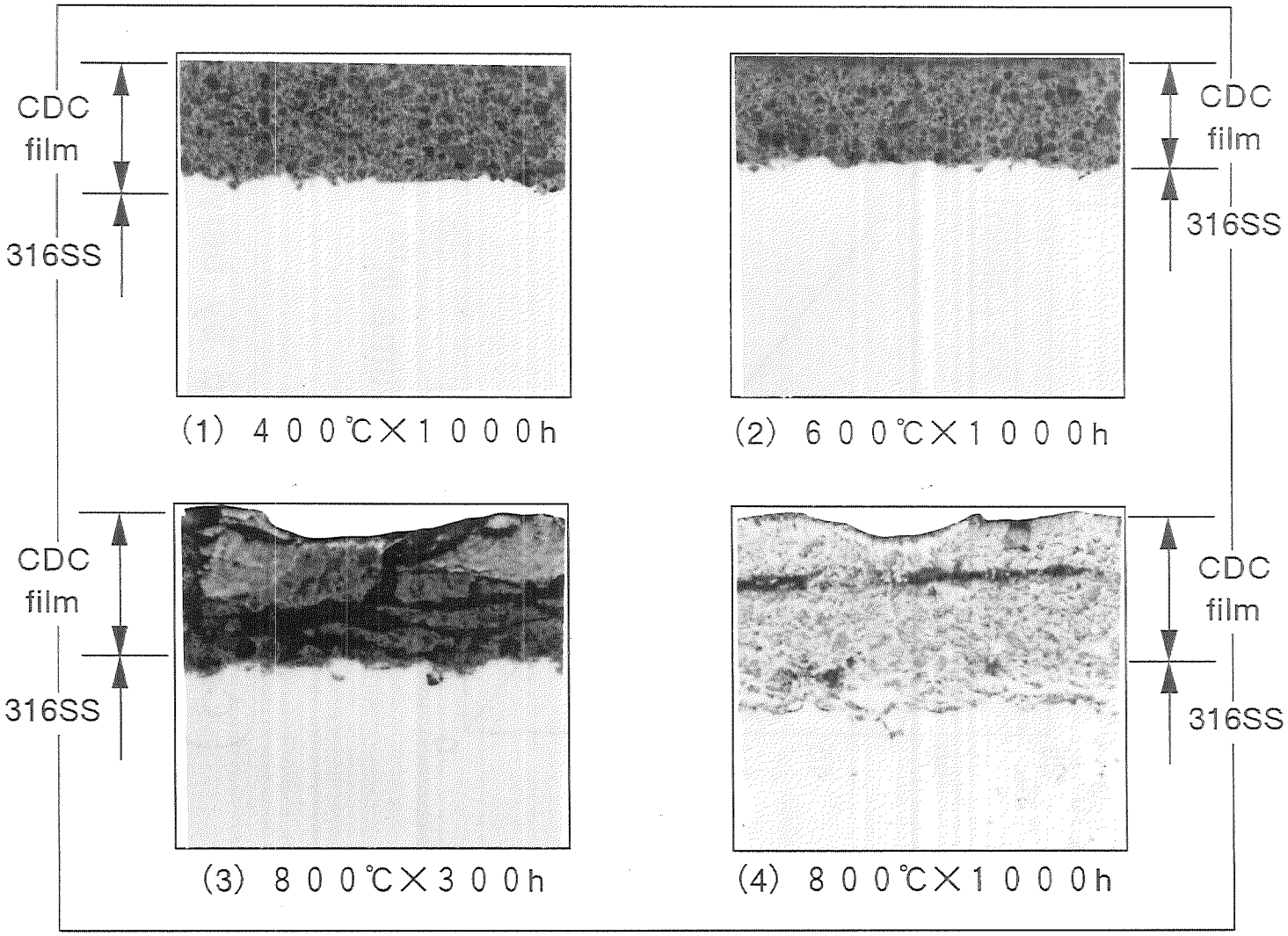

E P M A Analysis

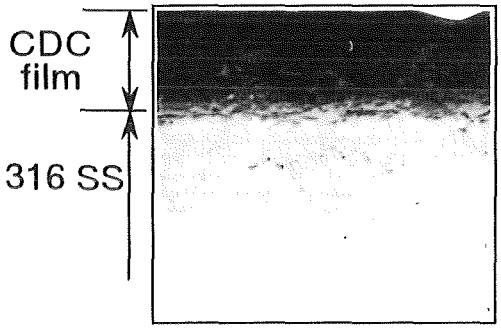

SEM

Annealing temperature : 800℃
Annealing time : 1000h

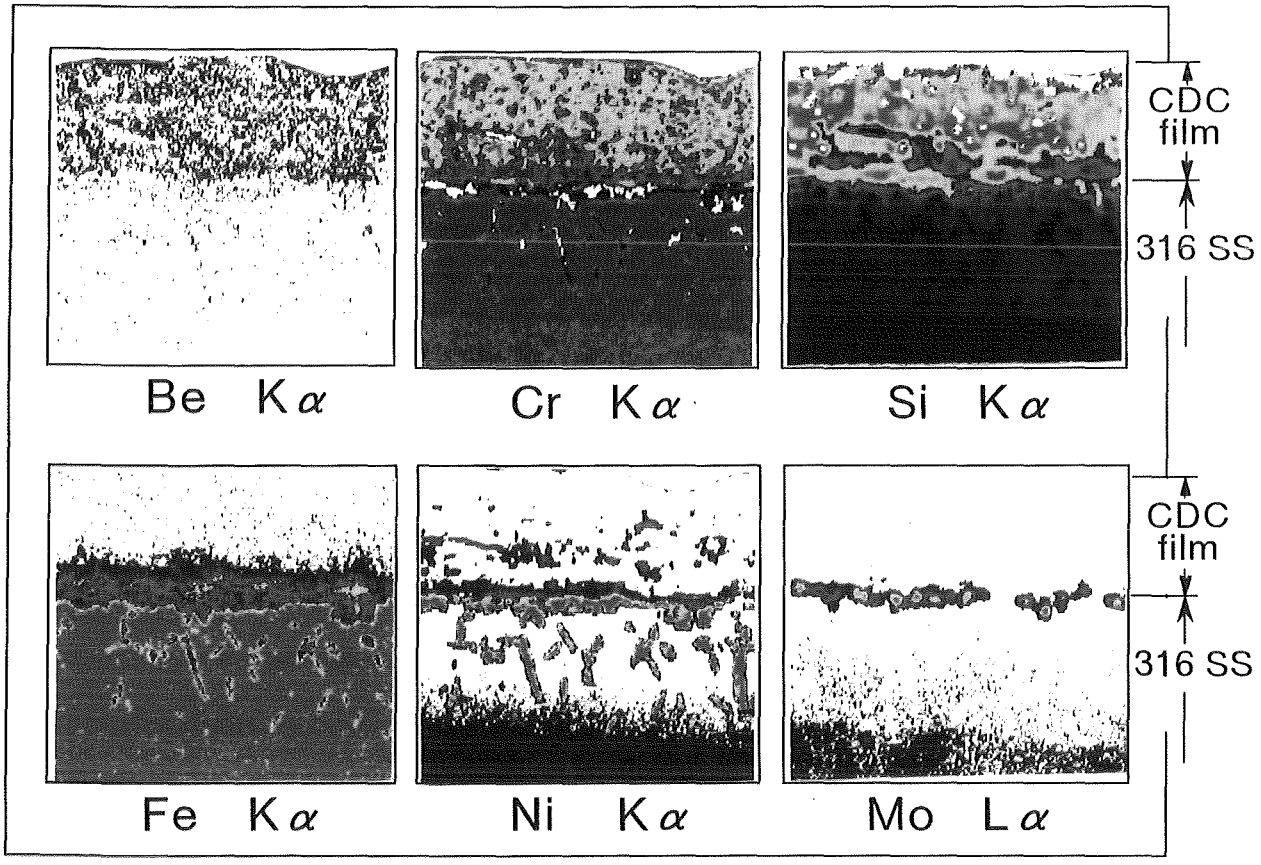

Change of thickness of reaction layer in 316SS with annealing temperature

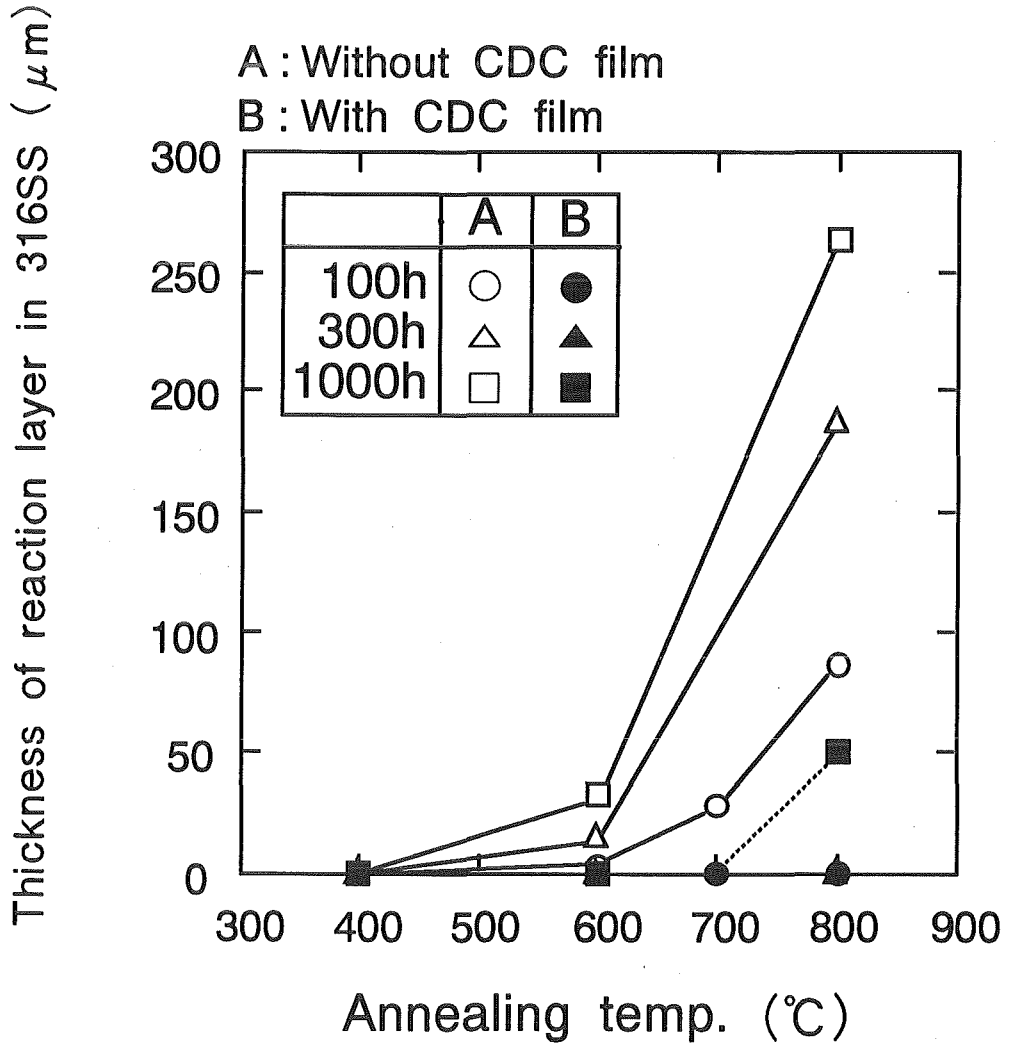

Change of thickness of reaction layer in 316SS with annealing time

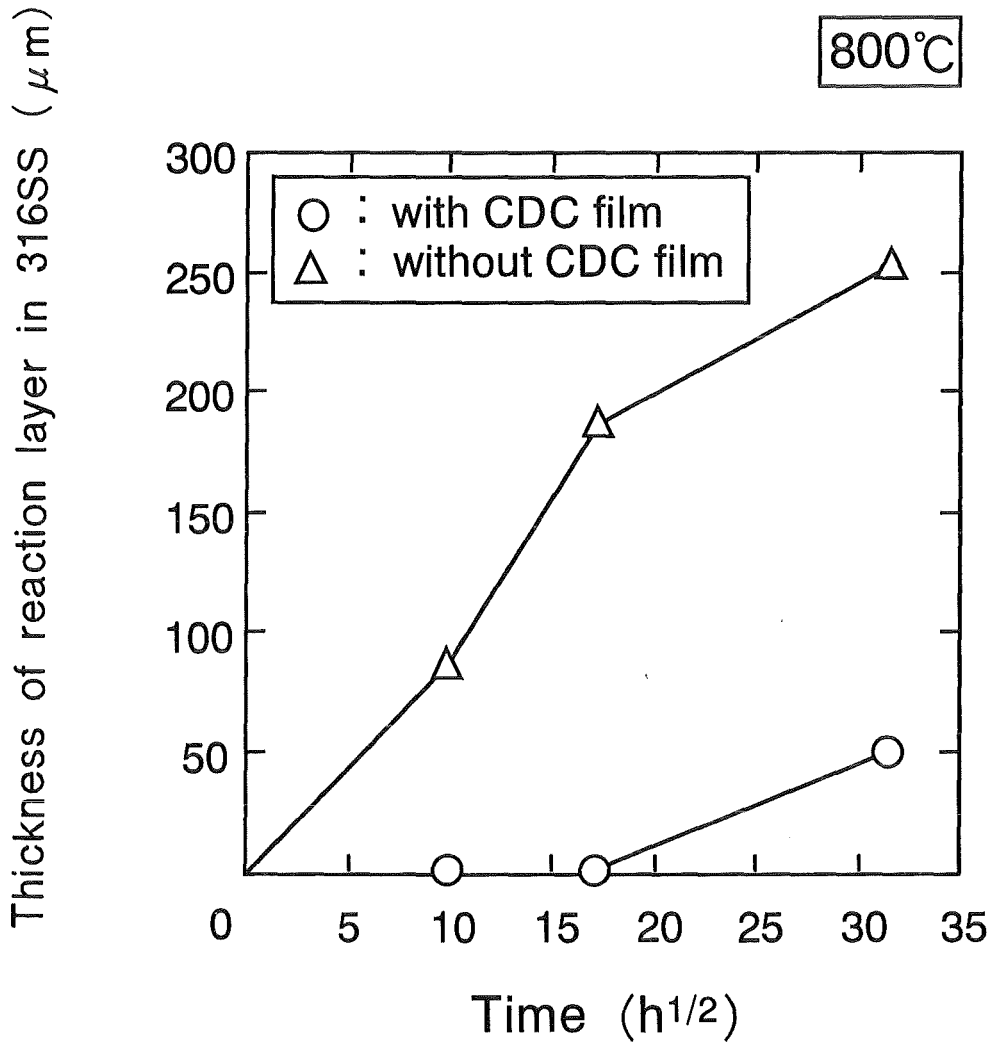

Conclusion

- Ceramic coating film(50 μm) had a function as reaction barrier completely against 316SS at 600℃-1000h annealing.

- Ceramic coating film(50 μm) had a function as reaction barrier completely against 316SS at 800℃-300h annealing similar to 600℃-1000h annealing .

  (with CDC film : reaction layer thickness 0 μm
  without CDC film : reaction layer thickness 190 μm)

- Ceramic coating film(50 μm) could not have a function as reaction barrier completely against 316SS at 800℃-1000h annealing . However, the thickness of reaction layer was reduced to ~1/5 as a comparison of case without CDC film.

  (with CDC film : reaction layer thickness 50 μm
  without CDC film : reaction layer thickness 260 μm)

- Cr_2O_3 was reducted at 800℃ by Be, then Cr and BeO was generated.
  It was obvious that this behavior was controlled by the diffusion of beryllium.

Properties of Beryllium as a Plasma facing Material

by

W.Eckstein, R.Behrisch, B.M.U.Scherzer, J.Roth

Max-Planck-Institut für Plasmaphysik, Garching, FRG

EURATOM Association

Abstract

Beryllium is investigated with respect to criteria important for plasma facing materials such as erosion, hydrogen trapping and heat removal. Beryllium tiles from JET are analyzed with SEM and the ion beam techniques of NRA, PIXE, RBS and HIERD. This paper concentrates on work performed at MPIPP.

Introduction

Beryllium as a plasma facing material has several advantages compared to carbon which is mostly used in fusion plasma machines. The advantages are the low atomic number which reduces the impact of radiation losses in the plasma, the high affinity to oxygen which keeps this impurity in the discharge at a small level, the low affinity to hydrogen with its implications on hydrogen forming compounds and tritium inventory, and its relatively good thermal properties. The biggest disadvantages of beryllium are its low melting point, high vapour pressure and its health hazard. Be as a possible plasma facing material has been discussed in [1,2].
In this contribution the investigations of ion bombardment processes and heat removal performed at IPP will be discussed.

Implantation, reflection, and erosion

The first wall of a fusion plasma machine is bombarded mainly with charge exchange neutrals, whereas limiters and divertors are hit by ions which are accelerated by a plasma sheath potential. The energy distribution of the bombarding ions can be assumed to be Maxwellian shifted due to the sheath potential by about $3qkT$, where T is the electron temperature of the edge plasma and q the charge state of the ions. These conditions determine the average penetration depth of the bombarding species in the wall material, their probability to be reflected back into the plasma, and the amount of wall material removed by sputtering. These values can be determined for a fixed energy and angle of incidence in laboratory experiments [3-7] or computer calculations [4-6,8-11] which generally good agreement with measured data [11]. For more complicated bombardment conditions like a Maxwellian energy distribution computer simulation is a better choice.

In the following some calculated results for non-monoenergetic bombardment are given. Fig.1 shows the calculated average (mean) depth of implantation versus the plasma edge temperature for a Maxwellian energy distribution including a sheath potential of $3kT$ and a uniform distribution in angle of incidence. Three plasma species are considered ; D, T, and the impurity Be. The average depth of implantation of D and T is approximately the same, whereas the average depth of Be is about a factor 3 to 4 smaller. The nearly

equal penetration depth and halfwidth of the depth distribution of D and T means that also the trapping behaviour of both species will be similar.

The backscattering or reflection of atoms from surfaces can be described by the particle reflection coefficient R_N which is the fraction of reflected to incident projectiles. Fig.2 demonstrates that for the same conditions as for fig.1 calculated R_N values are about 30% lower for T than for D. For Be R_N is at maximum only a few % , so that it can be neglected in most cases.

One important plasma impurity production process is sputtering by bombarding projectiles. Fig.3 shows calculated sputtering yields (sputtered target atoms per projectile) for the same conditions as mentioned above for figs.1 and 2. T exhibits a yield approximately 20% larger than D. Selfsputtering of Be is appreciably larger than the yield for D and T at plasma temperatures above a few eV; also the maximum yield appears at higher plasma temperatures. In fig.3 it is assumed that Be is only singly ionized; for higher charge states the yield will increase due to the sheath potential. The sheath potential accelerates ions and reduces the angle of incidence. A selfsputtering yield above unity will lead to run-away conditions for the impurity concentration of the plasma boundary.

The erosion of target material can also occur due to evaporation. This effect is especially important in the case of Be because of its high vapour pressure. The erosion rate by evaporation is determined by [12]

$$N(\mathrm{cm}^{-2}\mathrm{s}^{-1}) = 2.65 \cdot 10^{20} P(\mathrm{Pa})/(M(\text{atomic mass})T(\mathrm{K})^{1/2})$$

In fig.4 a comparison of the erosion rate due to evaporation and sputtering versus temperature is given using the vapour pressure data from [13].The sputtering yields are taken from [9]. At large ion fluxes ($10^{18}\mathrm{cm}^{-2}\mathrm{s}^{-1}$) sputtering will dominate below 1200K, whereas at low fluxes ($10^{15}\mathrm{cm}^{-2}\mathrm{s}^{-1}$, which is about a monolayer per second) evaporation dominates already above 1100K.

In contrast to graphite Be does not show a chemical erosion by forming volatile hydrides, but it has a high affinity to oxygen. While graphite forms a volatile oxide, BeO is an insulator with a high melting temperature (2260K). An oxygen free surface is only found at temperatures above 600K. Therefore, at lower temperatures, the sputtering yield of a Be wall can be an order of magnitude smaller at low projectile energies than at high temperatures due to surface oxide, see fig.5. Because of the lower atomic number and the

lower surface binding energy Be shows a larger physical sputtering yield due to hydrogen bombardment than C. Evaporated atoms have a lower mean energy (thermal energies) compared to sputtered atoms (several eV to tens of eV). Therefore, sputtered atoms have a larger penetration depth into the boundary plasma.

If more than one first wall material is used as for example Be and C in a plasma machine then an even more complicated behaviour can occur [14,15]; a C film on top of the Be may or may not form depending on the impact conditions. Surface roughness can change the physical sputtering yield quite strongly especially at oblique incidence [16]. The sputtering yields of different low Z materials are compared in [16-18].

Trapping

If hydrogen is implanted in some materials it is trapped completely at low fluences except for kinetic reflection. As an example trapping curves for D in BeO are shown in fig.6 for three implant temperatures [19]. The trapping curves show a linear increase at low fluences and reach saturation at large fluences ($> 10^{18}\mathrm{cm}^{-2}$). The ratio of trapped D atoms to BeO molecules at saturation reaches values of about 0.3 depending on the implant temperature. This value is similar to that observed for C [20]. The retained saturation amount of D in Be depends also on the energy of the bombarding D ions as shown in fig.7 for three target temperatures [21]. Postirradiation annealing leads to a decreased retained amount until at about 1000 K nearly no D can be found in Be [21], see fig.8. These results are in agreement with findings in [22]. The steep decrease at 400 K of the retention in fig.8 can be explained by the decomposition of amorphous beryllium hydride [2]. On the other hand, beryllium hydride does not form by codeposition of beryllium and hydrogen at walls or limiters. In many of these monoenergetic bombardments blistering and/or flaking can be found at high fluences [23,24].

Heat removal

The power flux densities to the walls and especially to the limiters and divertors may go up to 30 $\mathrm{MW/m^2}$ [25], mainly deposited by low energy particle bombardment. Materials with high thermal conductivity are needed to conduct heat to the coolant without surface melting and/or evaporation. The local temperature gradient which builds up at steady

state for a power density P is given by

$$dT/dx = P/k(T(x)) \quad .$$

Materials with large thermal conductivity $k(T)$ have to be used to keep the temperature gradient small. Assuming a first wall thickness L and one-dimensional thermal conduction the above equation can be integrated [26] yielding

$$P(T_1, T_2) = \frac{1}{L} \int_{T_1}^{T_2} k(T)\, dT \quad .$$

T_1 is the temperature of the cooled side and $T_2 (> T_1)$ the temperature of the plasma facing side. $P(T_1, T_2)$ gives the power flux density which can be removed through the thickness L at steady state conditions. In fig.9 the heat removal properties of Be and some other materials are compared. Be can remove similar power densities as W below 1000 K, but the maximum power density which can be removed is about a factor of four larger for W and Cu and similar for fine grain graphites such as EK98. At the same surface temperature Be is better than these graphites but worse compared to highly oriented graphites [26]. The curves are calculated for a temperature of 420 K at the cooled side of a 1 cm thick plate. In addition the vertical lines through the different curves indicate material removal by sublimation of 1 mm per day of operation. It can be seen that Be is not well suited for temperatures well above 1000 K and the removed power density is smaller than about 7 MW/m^2 (assuming the conditions mentioned above).

Be in Fusion Plasma Machines

Be has been used in three tokamaks, namely UNITOR [27], ISX-B [28] and in JET [29]. The major advantage of using Be was the reduction of impurities, especially oxygen, in the discharge [29, 30]. A thorough investigation of a Be tile of the upper belt limiter of JET (from octant 1B, position 22) was performed [29, 31]. This tile experienced about 2000 discharges. Many impurities have been found as demonstrated in the table; the numbers given in the table for the whole area of the upper belt limiter are determined from the investigation of one tile assuming azimuthal symmetry. These results show that clean Be surfaces are unlikely in a machine containing different wall materials. Several tiles show cracks, melted areas and droplets, see fig.10.

Conclusions

Computer simulation is used to obtain mean implantation depths, particle reflection coefficients for non-monoenergetic ion incidence on Be. The mean implantation depth of D and T with a Maxwellian energy distribution and isotropic incidence angular distribution are 1 nm at 10 eV to about 100 nm at 1 keV plasma boundary temperature. The corresponding ranges of Be in Be are a factor of 3 smaller. For the same conditions, the particle reflection coefficients of D and T reach values of about 30% at 2 eV whereas the Be reflection reaches a maximum of 3% at 20 eV plasma temperature. Again for the same bombardment conditions the physical sputtering yields of Be for D, T and Be are similar at low plasma temperatures; Be selfsputtering stays below 0.5 reaching a maximum at 200 eV, whereas the maximum yield for D and T is about 0.06 at 50 eV plasma temperature. Chemical sputtering due to volatile hydride and oxide formation is not observed. At temperatures above 1100 K thermal sublimation is an important erosion mechanism, the temperature where evaporation exceeds sputtering depending on the ion flux. The retained fraction of D in Be can reach 0.3 (D/Be) at room temperature and decreases to zero at 1000 K. Heat loads up to 7 MW/m^2 can be removed by thermal conduction which is more than a factor of four lower than what can be removed by highly oriented graphites or CFC's but larger than by fine grain graphites. Surface layers of Be tiles from JET are largely modified during the JET discharges. They contain large amounts of D and O as well as C, Cl, K, Ca, Ti, Cr, Fe, Ni and Zn. Molten areas, droplets and cracks can be found on these tiles.

References

1 M.F.Smith, W.Mullendore: J. Nucl. Mater. **122&123**, 855 (1984)

2 K.L.Wilson, R.A.Causey, W.L.Hsu, B.E.Mills, M.F.Smith, J.B.Whitley: J. Vac. Sci. Technol. **A8**, 1750 (1990)

3 J.Bohdansky, J.Roth: J. Nucl. Mater. **122&123**, 1417 (1984)

4 J.Roth, W.Eckstein, J.Bohdansky: J. Nucl. Mater. **165**, 199 (1989)

5 C.H.Wu, E.Hechtl, H.R.Yang, W.Eckstein: J. Nucl. Mater. **176&177**, 845 (1990)

6 W.Eckstein: In *Atomic and Plasma-Material Interaction Data for Fusion*, Suppl. to Nuclear Fusion, Vol. 1, (IAEA, Vienna 1991) 17

7 J.Bohdansky, J.Roth, W.Ottenberger: IPP-Jet-Report No. 31, Max-Planck-Institut für Plasmaphysik, Garching, FRG (1985)

8 W.Eckstein, J.Bohdansky, J.Roth: In *Atomic and Plasma-Material Interaction Data for Fusion*, Suppl. to Nuclear Fusion, Vol. 1, (IAEA, Vienna 1991) 51

9 W.Eckstein, C.García-Rosales, J.Roth, W.Ottenberger: Report IPP 9/82, Max-Planck-Institut für Plasmaphysik, Garching, FRG (1993)

10 W.Eckstein, A.Sagara, K.Kamada: J. Nucl. Mater. **150**, 266 (1987)

11 W.Eckstein: *Computer Simulation of Ion-Solid Interaction*, Springer Series in Materials Science, Vol. 10 (Springer, Berlin, Heidelberg 1991)

12 L.Holland, W.Steckelmacher, J.Yarwood: *Vacuum Manual*, (E.& F.N.Spon, London 1974)

13 R.Hultgren, J.P.Desai, D.T.Hawkins, M.Gleiser, K.K.Kelley, D.D.Wagman: *Selected Values of the Thermodynamic Properties of the Elements* (Am.Soc.Metals, Metals Park, OH 1973)

14 W.Eckstein, J.Roth, E.Gauthier, J.László : Fusion Technol. **19**, 2076 (1991)

15 W.Eckstein, J.Roth: Nucl. Instrum. Methods B **53**, 279 (1991)

16 J.Roth, W.Eckstein, E.Gauthier, J.László : J. Nucl. Mater. **179 – 181**, 34 (1991)

17 J.Roth: J. Nucl. Mater. **145 – 147**, 87 (1987)

18 E.Gauthier, W.Eckstein, J.László , J.Roth: J. Nucl. Mater. **176&177**, 438 (1989)

19 R.Behrisch, R.S.Blewer, J.Borders, R.A.Langley, J.Roth, B.M.U.Scherzer, R.Schulz: Radiat. Eff. **48**, 221 (1980)

20 K.L.Wilson, R.Bastasz, R.A.Causey, D.K.Brice, B.L.Doyle, W.R.Wampler, W.Möller, B.M.U.Scherzer, T.Tanabe: In *Atomic and Plasma-Material Interaction Data for Fusion*, Suppl. to Nuclear Fusion, Vol. 1, (IAEA, Vienna 1991) 31

21 W.Möller, B.M.U.Scherzer, J.Bohdansky: IPP-Jet-Report No. 26, Max-Planck-Institut für Plasmaphysik, Garching, FRG (1985)

22 W.R.Wampler: J. Nucl. Mater. **122&123**, 1598 (1984)

23 H.Verbeek, W.Eckstein: *Applications of Ion Beams to Metals*, ed. by S.T.Picraux, E.P.EerNisse and F.L.Vook (Plenum, New York 1974)

24 B.M.U.Scherzer, R.S.Blewer, R.Behrisch, R.Schulz, J.Roth, J.Borders, R.Langley: J. Nucl. Mater. **85&86**, 1025 (1979)

25 R.Behrisch: In *Atomic and Plasma-Material Interaction Data for Fusion*, Suppl. to Nuclear Fusion, Vol. 1, (IAEA, Vienna 1991) 7

26 R.Behrisch, G.Venus: J. Nucl. Mater. **202**, 1 (1993)

27 J.Hackmann, J.Uhlenbusch: J. Nucl. Mater. **128&129**, 418 (1984)

28 P.H.Edmonds, P.Mioduszewski, J.B.Roberto, R.D.Watson, M.F.Smith: J. Nucl. Mater. **128&129**, 422 (1984)

29 A.P.Martinelli, A.T.Peacock, R.Behrisch: J. Nucl. Mater. **196 – 198**, 729 (1992)

30 A.P.Martinelli, R.Behrisch, H.Hammer, J.Hackmann: J. Nucl. Mater. **145 – 147**, 755 (1987)

31 K.Roscher, R.Behrisch, H.Kukral: Report IPP 9/94, Max-Planck-Institut für Plasmaphysik, Garching, FRG (1993)

Table : Calculated average deposition on the upper toroidal Be belt limiter of JET assuming toroidal symmetry and a limiter area of $6.5m^2$ as deduced from the deposition on one limiter tile. A is the average deposited atom density ($\cdot 10^{17} cm^{-2}$), B is the average deposited number of atoms ($\cdot 10^{22}$). The deposited Ni/Cr/Fe corresponds to about 0.2 g.

	D	C	O	Cl	K	Ca	Ni	Cr	Fe	Ti	Zn
A	2.0	1.5	3	0.8	0.07	0.012	0.17	0.035	0.18	0.022	0.008
B	1.3	1.0	2	0.5	0.05	0.080	0.11	0.023	0.12	0.014	0.005

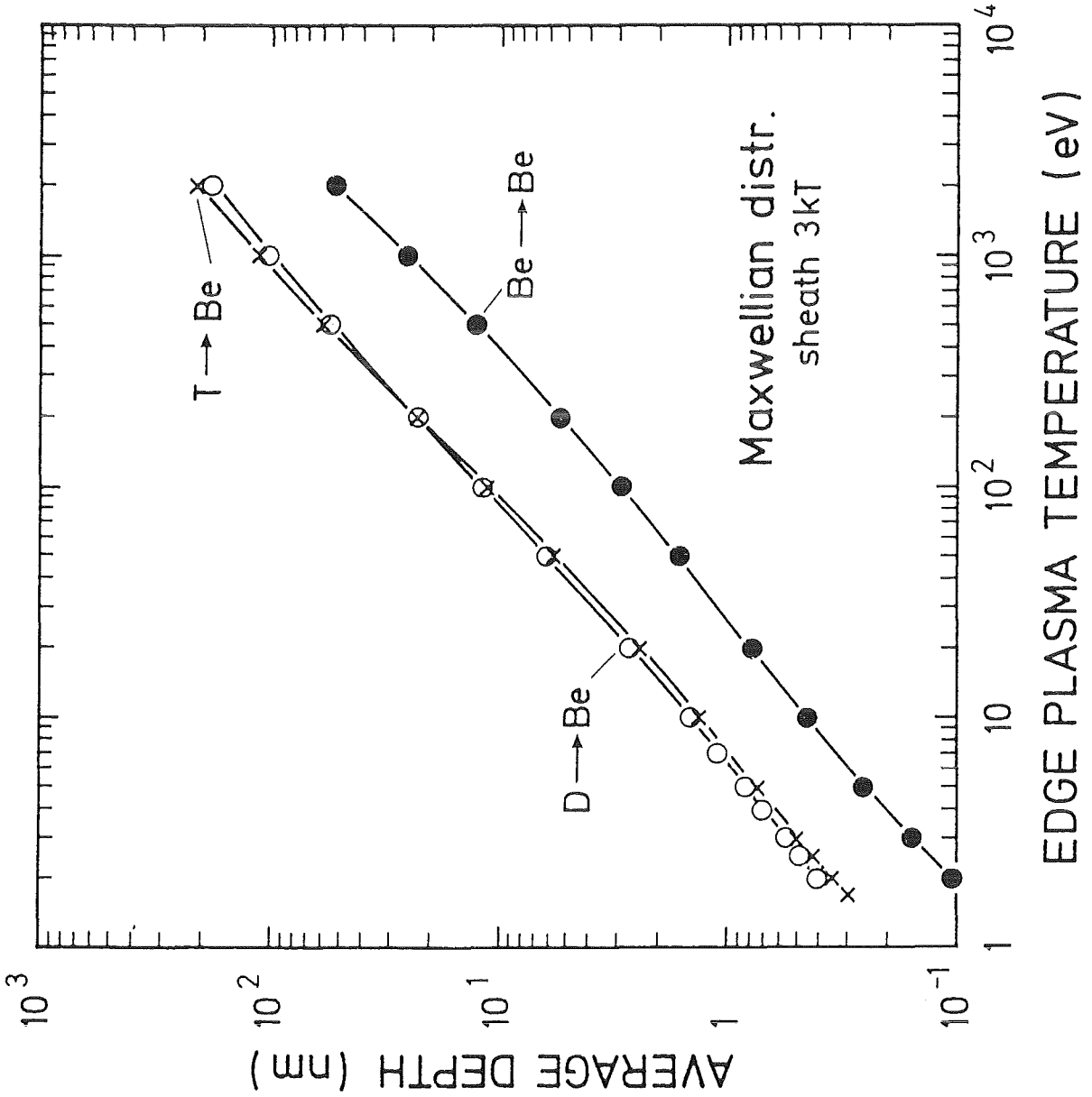

Fig. 1. The calculated mean average depth of D, T and Be in Be versus the edge plasma temperature. A Maxwellian energy distribution, an isotropic angular incidence, and a sheath potential of 3kT is assumed.

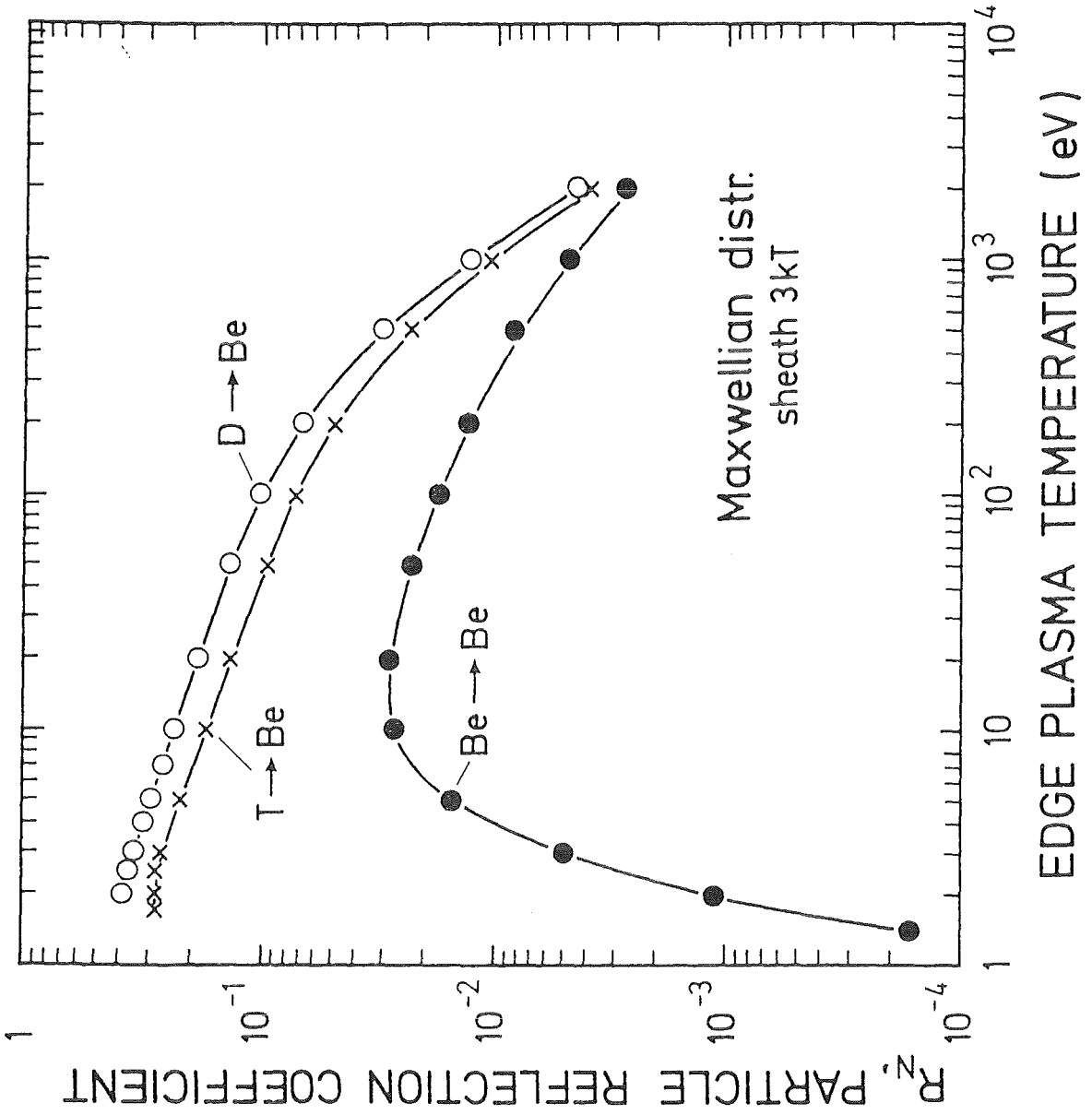

Fig. 2. The calculated particle reflection of D, T ,and Be from Be versus the edge plasma temperature. the edge plasma temperature. A Maxwellian energy distribution, an isotropic angular incidence, and a sheath potential of 3kT is assumed.

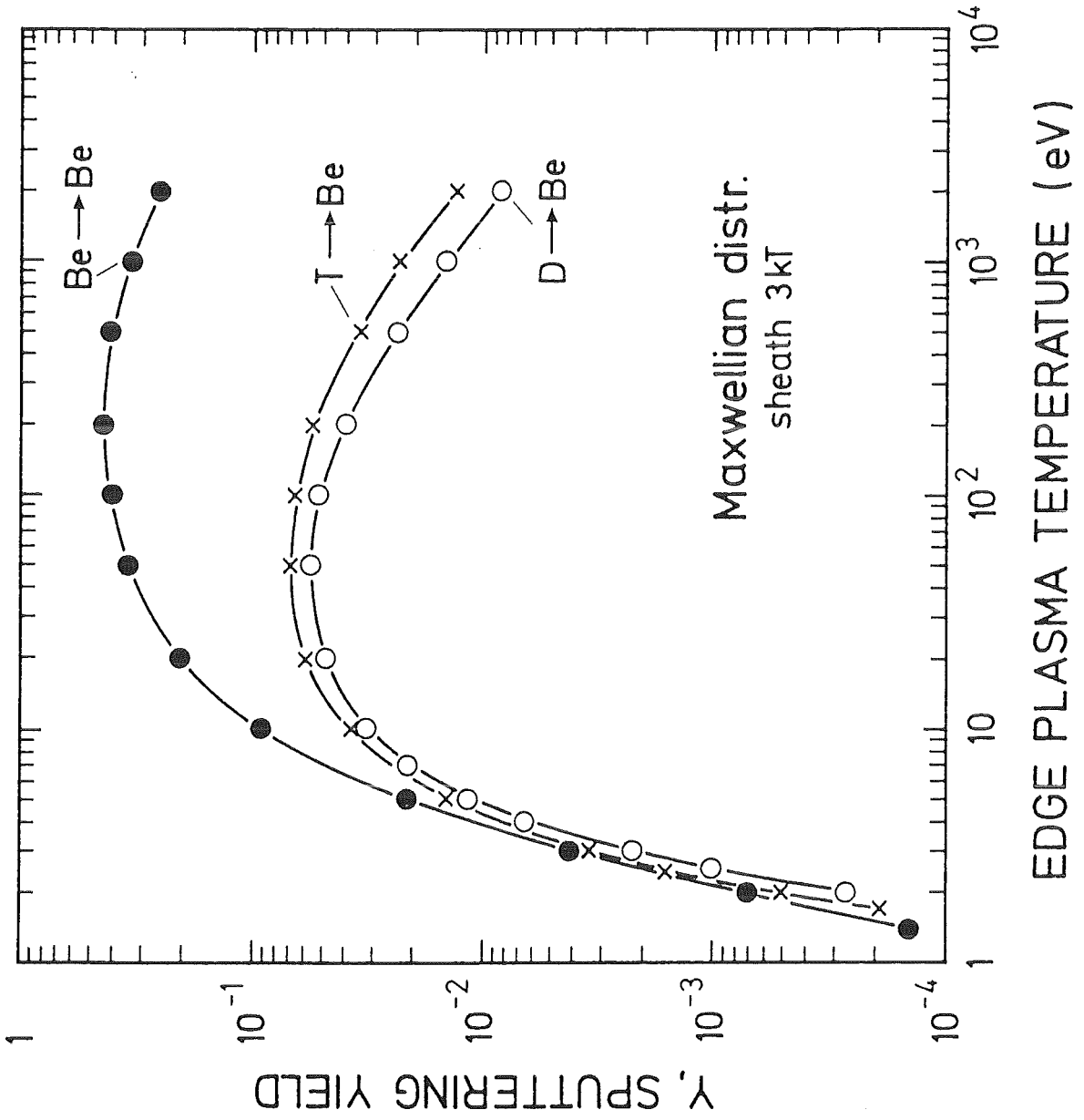

Fig. 3. The calculated sputtering yield of Be due to D, T ,and Be bombardment versus the edge plasma temperature. A Maxwellian energy distribution, an isotropic angular incidence, and a sheath potential of 3kT is assumed.

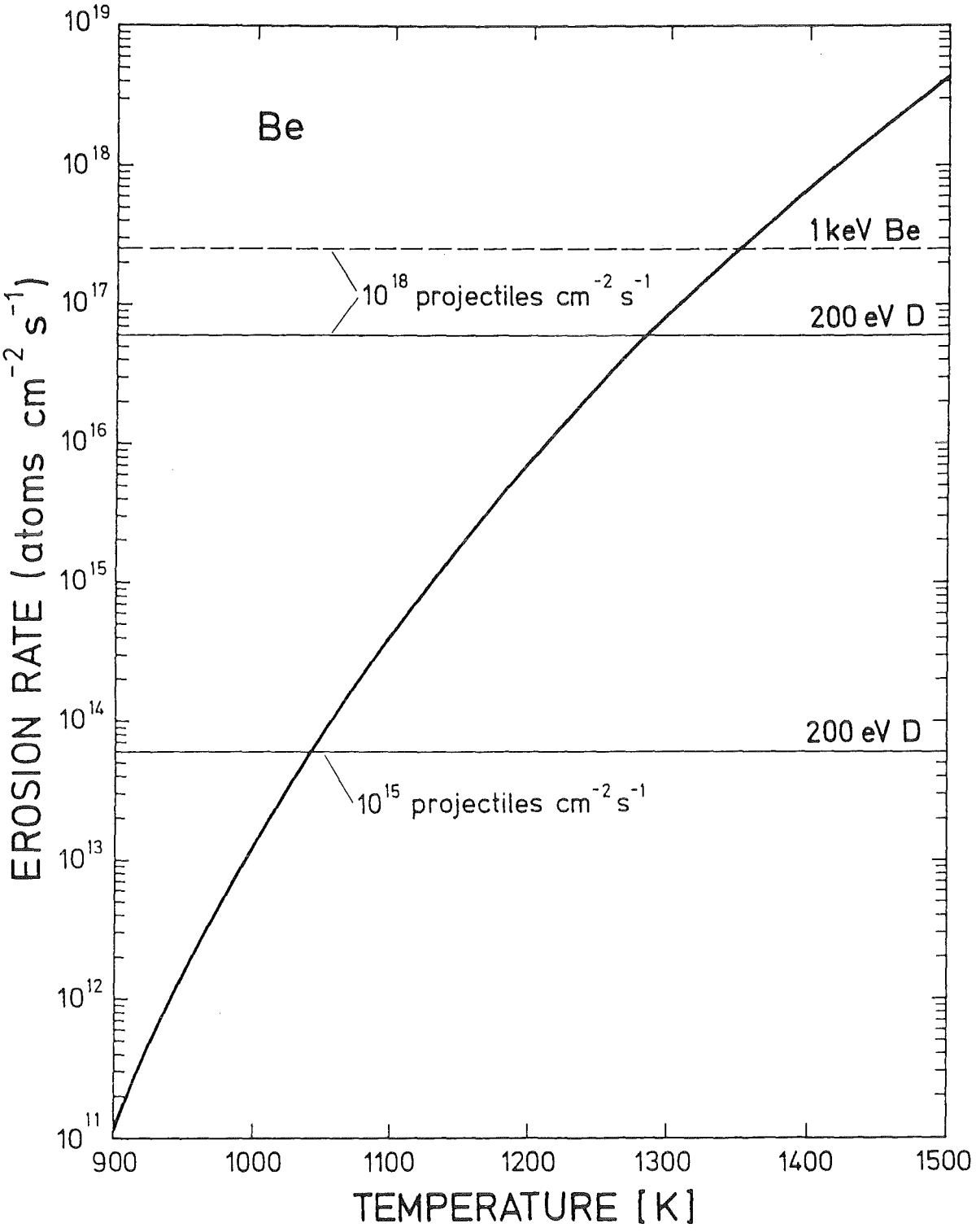

Fig. 4. The evaporation yield versus target temperature for Be. The sputtering yield of Be for different energies and normal incidence for the bombardment with D and Be is indicated by horizontal lines.

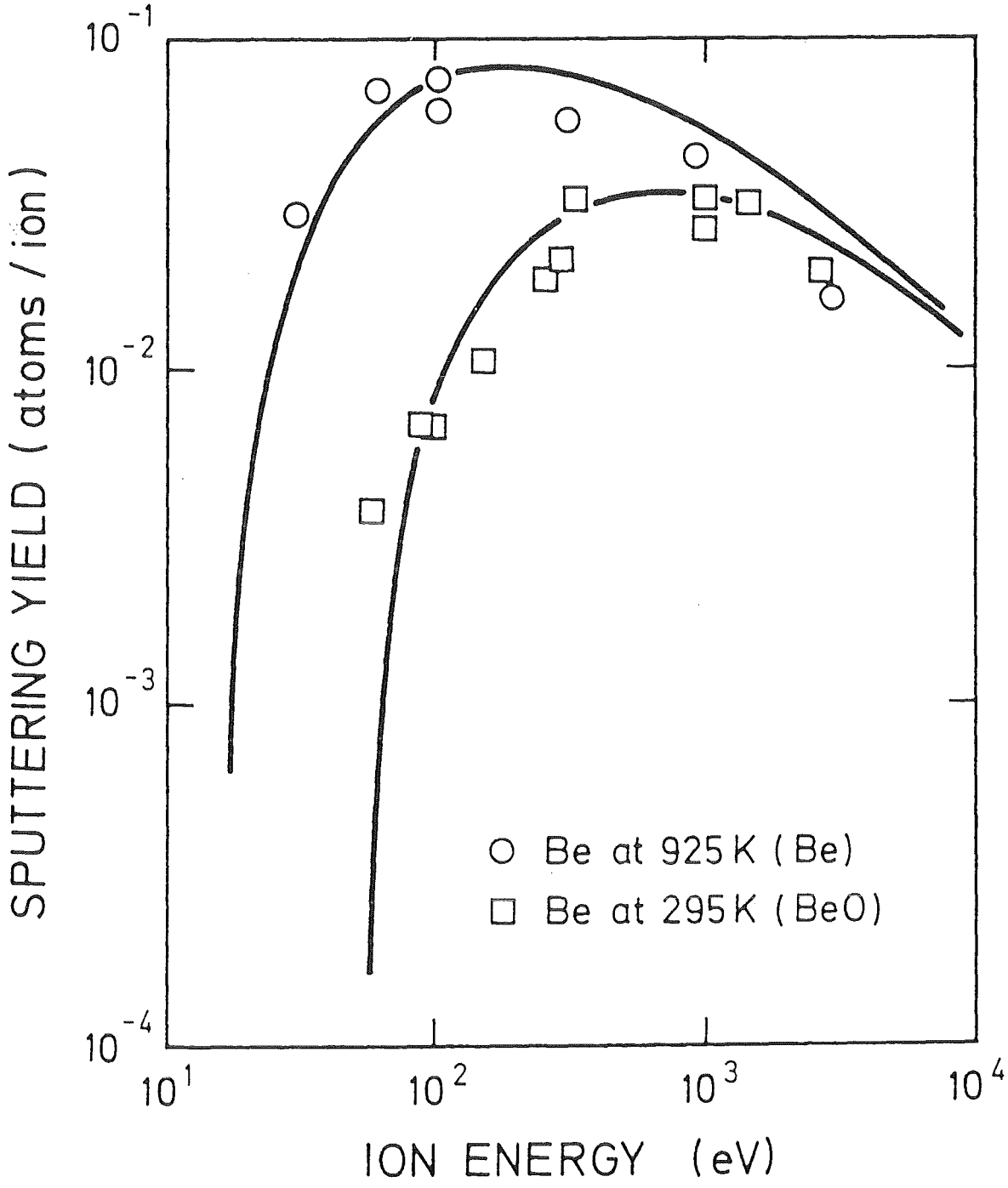

Fig. 5. The sputtering yield of Be and BeO at normal incidence versus energy of incident D at two target temperatures.

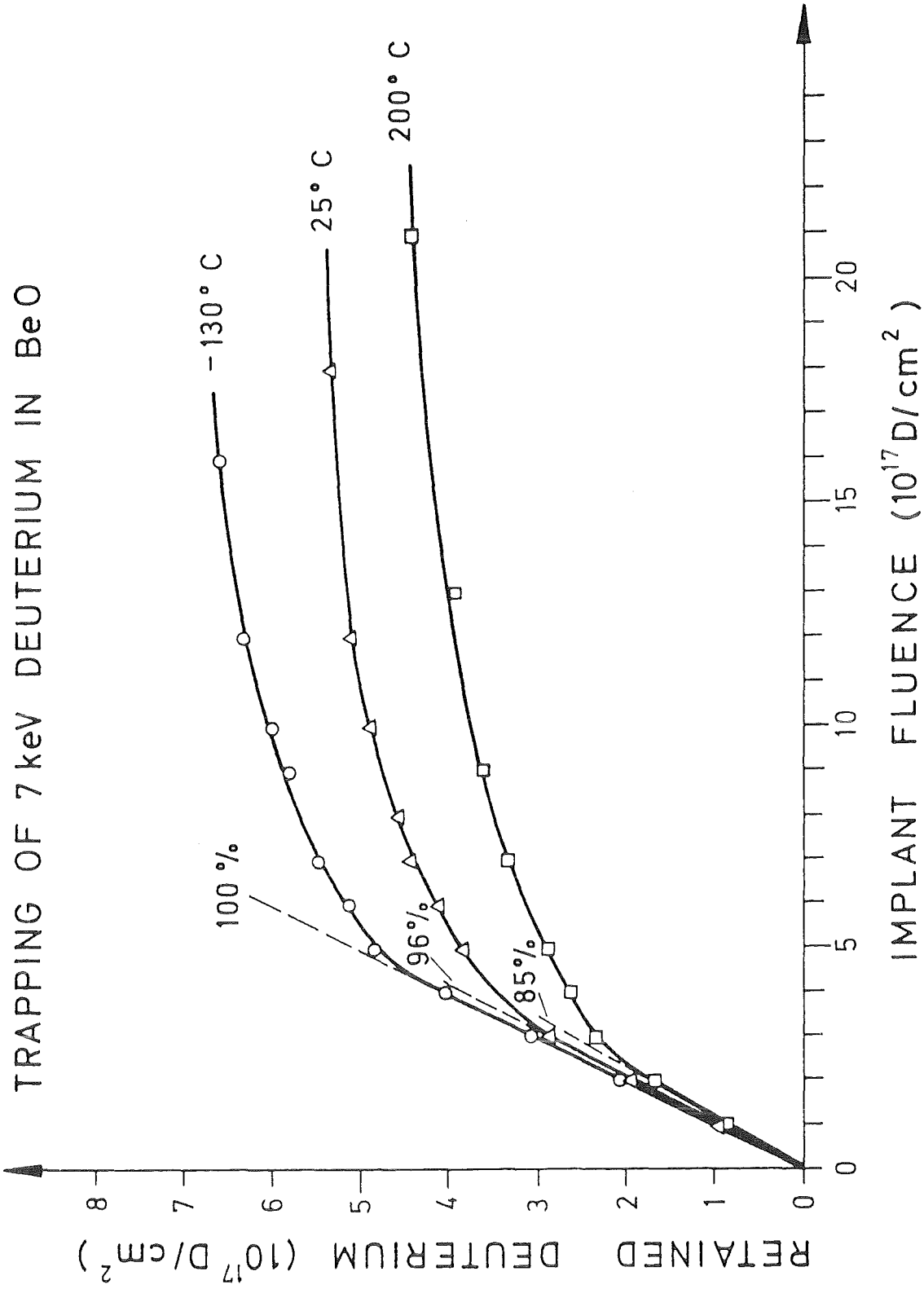

Fig. 6. Trapping curves for deuterium in a 165 nm layer of BeO versus the implant fluence at three temperatures (fig.1a of [19]).

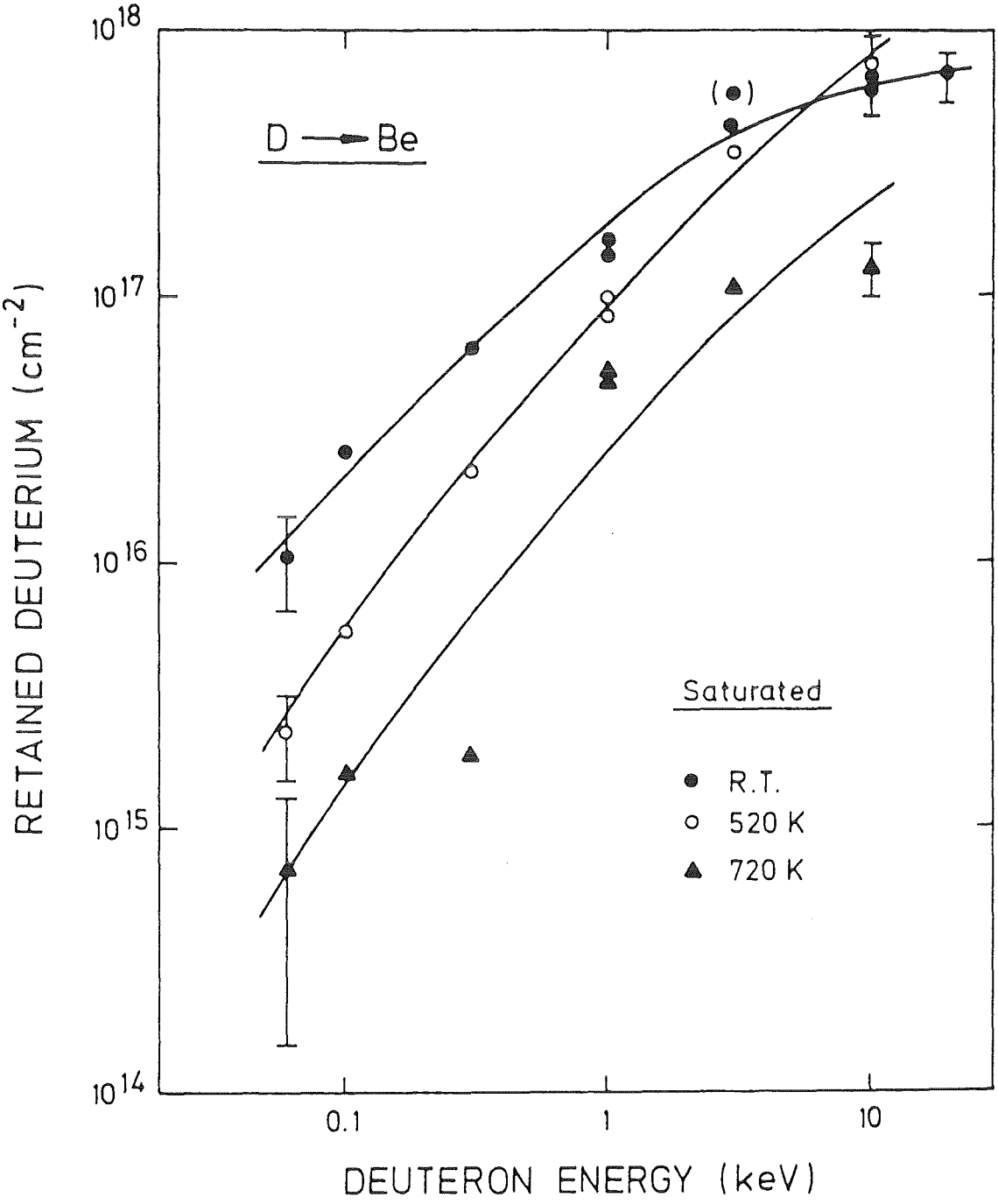

Fig. 7. Amount of deuterium retained after implantation to saturation versus the implantation energy. D is implanted at normal incidence at three temperatures. The data point in brackets may be influenced by an extraordinary thick oxide layer. The lines are drawn to guide the eye (fig.7 of [21]).

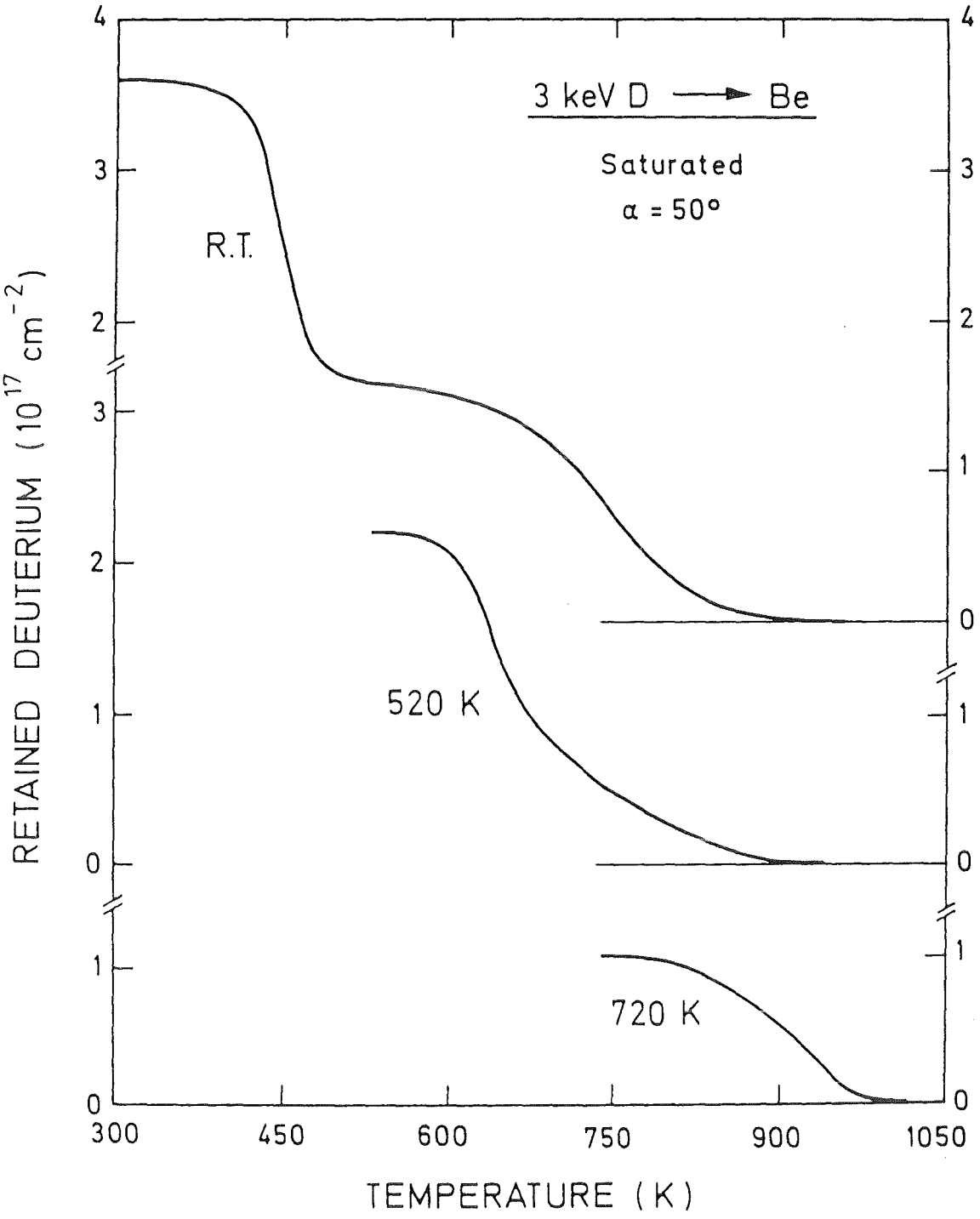

Fig. 8. Amount of deuterium retained after implantation to saturation versus the annealing temperature. 3 keV D is implanted at an oblique incidence of 50° and three target temperatures (fig.10 of [21]).

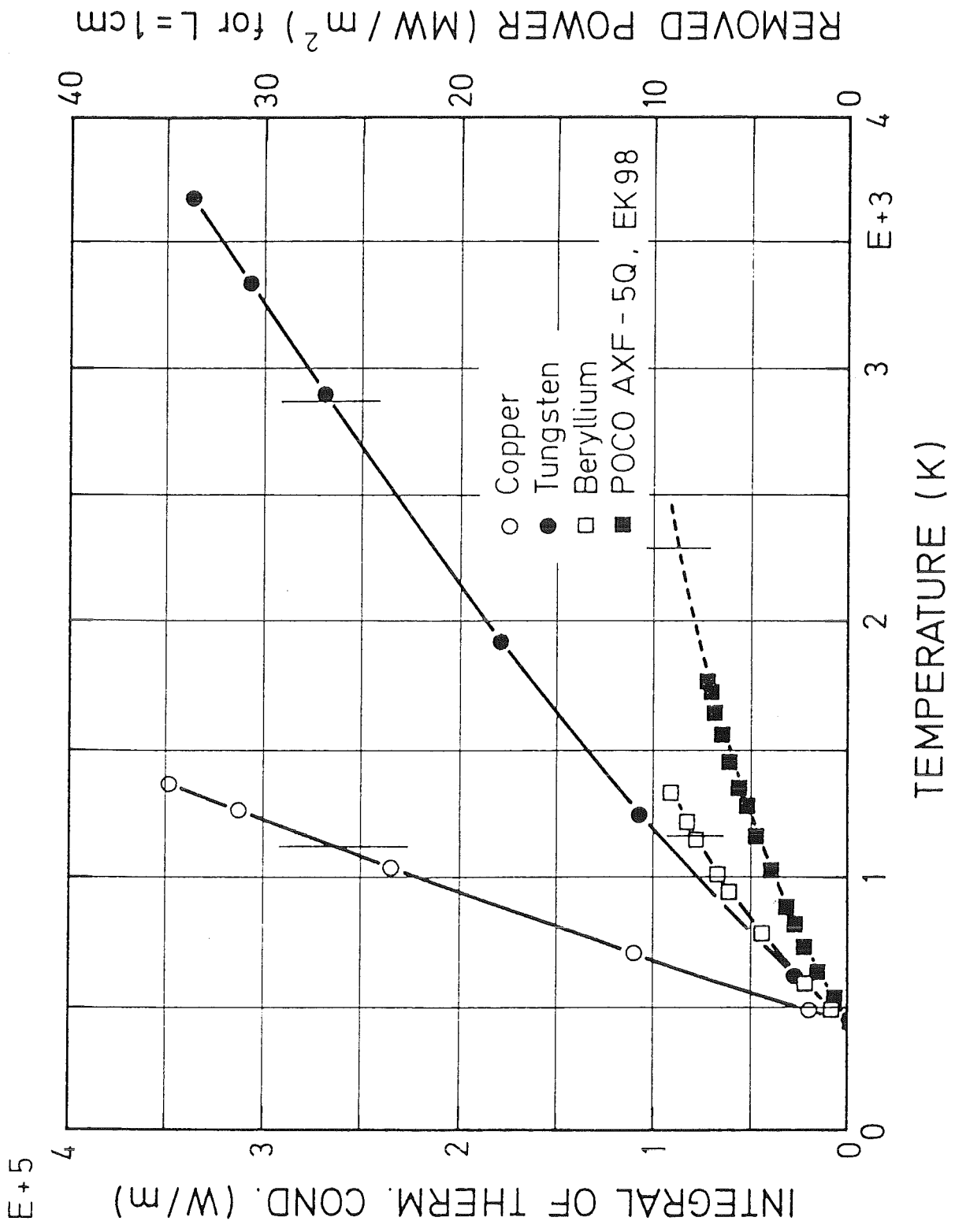

Fig. 9. The integral $\int k(T)\,dT/L$, taken between the temperature $T_1 = 423$ K on the cooled side and an upper temperature T_2, and the removed power density for $L = 1$ cm versus the plasma facing plate temperature for Cu, W, Be and graphite (EK98). Vertical lines on the curves give temperatures corresponding to sublimation of 1 mm per operating day.

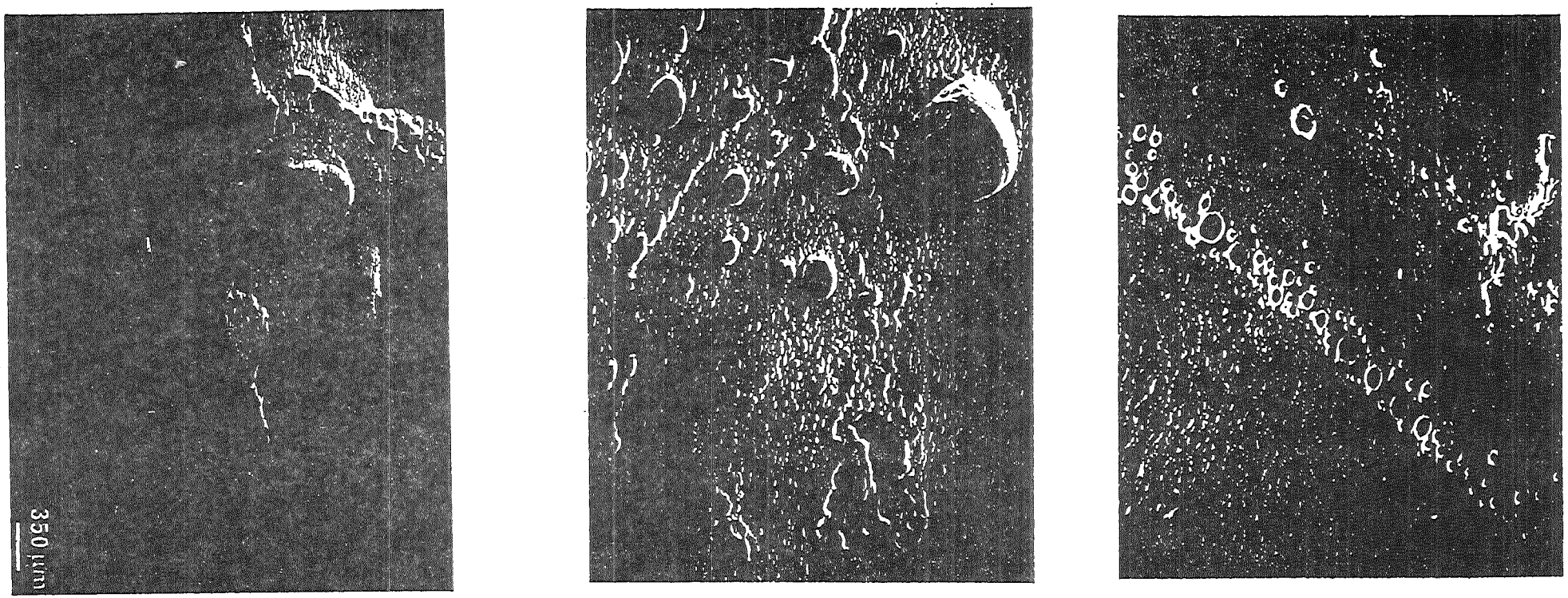

Fig. 10. SEM pictures of a Be tile of the upper limiter of JET. Cracks, droplets and melted areas can be seen.

The Effect of Processing Parameters on Plasma Sprayed Beryllium for Fusion Applications

Richard G. Castro, Paul W. Stanek and Loren W. Jacobson
Material Science and Technology Division
Los Alamos National Laboratory, Los Alamos, NM 87544 (USA)

Donald F. Cowgill
Physics of Materials Department
Sandia National Laboratory, Livermore, CA 94551 (USA)

ABSTRACT

Plasma spraying is being investigated as a potential coating technique for applying thin (0.1-5mm) layers of beryllium on plasma facing surfaces of blanket modules in ITER and also as an in-situ repair technique for repairing eroded beryllium surfaces in high heat flux divertor regions. High density spray deposits (>98% of theoretical density) of beryllium will be required in order to maximize the thermal conductivity of the beryllium coatings. A preliminary investigation was done to determine the effect of various processing parameters (particle size, particle morphology, secondary gas additions and reduced chamber pressure) on the as-deposited density of beryllium. The deposits were made using spherical beryllium feedstock powder which was produced by centrifugal atomization at Los Alamos National Laboratory (LANL). Improvements in the as-deposited densities and deposit efficiencies of the beryllium spray deposits will be discussed along with the corresponding thermal conductivity and outgassing behavior of these deposits.

1.0 Introduction

Fabrication and maintenance of surfaces that are directly exposed to the plasma in magnetic fusion energy (MFE) devices will present challenging problems in the development and design of the International Thermonuclear Experimental Reactor (ITER), the next generation magnetic fusion energy device. Plasma-spraying technology is currently being evaluated as a potential method for fabrication and maintenance of plasma facing components (PFC's) which will be subjected to severe environmental conditions as a result of either normal or off-normal operating conditions. At present, the favored armor materials for plasma-interactive surfaces are beryllium, carbon,or tungsten [1,2].

Beryllium has been selected as the prime candidate for PFC's for ITER due to some of its advantages over both carbon, and tungsten [3,4].

One advantage of beryllium over carbon is the ability to use plasma-spraying for in-situ repair of damaged components in high heat flux regions of ITER i.e., divertors. Additionally, plasma-spraying of beryllium is also being considered as a potentially large surface area deposition technique for coating first wall blanket modules made from either vanadium or stainless steel. Coating these modules with a thin (0.1-1mm) layer of beryllium will protect the underlying walls from the attack of oxygen or water and provide at the same time an acceptable plasma facing material.

Extensive investigations of plasma-spraying of beryllium were done during the late 1960's and early 1970's by Union Carbide Speedway Laboratory (UCSL) and the Atomic Weapons Research Establishment (AWRE) for a number of defense related projects. Processing conditions and the thermo-physical properties of plasma-sprayed beryllium produced during this period can be found in the book Beryllium Science and Technology, Volume 2, which was published in 1979 [5]. These investigations focused on the process optimization of beryllium plasma-spraying using state-of-the-art equipment available at that time. Deposit densities of beryllium were reported to be approximately 90% of beryllium's theoretical density (1.85 $g/cm^{3)}$ with porosity levels on the order of 10-12% in the as-sprayed condition. These levels are substantially lower than densities required for ITER (>98% dense material with 1-2% porosity). Lower porosity levels are needed in order to maximize the thermal conductivity of the spray deposits in order to transfer heat away from components in high heat flux regions of ITER.

A limited amount of research on the plasma spraying of beryllium for magnetic fusion energy devices has been reported in the recent literature [6,7]. The most recent investigations conducted by Battelle, Columbus in 1990, showed an improvement in the as-sprayed densities over results which were achieved by both AWRE and UCSL. Densities were reported to be on the order of 90 to 93% [8]. These levels were far short of early claims by Battelle of 98% dense plasma-sprayed beryllium with 95% deposit efficiency (fraction of material deposited on a surface)[6]. In all of the previous investigations, plasma spraying of beryllium was done under a controlled inert environment at atmospheric pressure.

Advances in plasma spray technology over the past decade have shown that by operating under a reduced pressure condition (<400 torr) substantial increases in the as-deposited densities can be achieved (>98%). This process technology was first introduced by Muehlberger et.al.,[9] in 1973 and has been termed LPPS^{TM} (Low Pressure Plasma Spraying). A number of factors which contribute to the increased quality of plasma sprayed deposits are:

- higher particle velocities, which result in better impacting and splatting of the liquid particles,

- transferred arc heating/cleaning of the substrate which improves deposit density and adhesion,

- broad spray patterns for coating large surface areas,

- and the ability to spray reactive materials under a protective atmosphere,

A large number of processing variables can ultimately affect the quality of the beryllium spray deposits when spraying under a reduced pressure. Operating parameters which have a direct influence on the dwell time of the injected beryllium powders will significantly affect the degree of melting of the beryllium powder feedstock. Investigations have shown that powder size, powder morphology, powder injection, particle velocity, and the heat content (enthalpy) of the plasma, can substantially change the melting behavior of the injected powders [10].

In this investigation, results will be presented on deposits of beryllium produced by low pressure plasma spraying. The effects of powder size, powder morphology and the use of helium as a secondary plasma gas on the as-deposited density will be discussed. Characterization of the beryllium spray deposits will include optical microscopy, chemical analysis, thermal conductivity and outgassing studies.

2.0 Experimental Details

2.1 Beryllium powder production

Los Alamos National Laboratory has recently been investigating the centrifugal atomization process for producing spherical beryllium and beryllium alloy powders as feedstock material for advanced consolidation processes i.e., hot isostatic pressing (HIP) and plasma spraying. The centrifugal atomization process involves vacuum induction melting of a beryllium metal charge in a MgO crucible while directing the molten beryllium metal through a ZrO_2 transfer tube onto the surface of a rapidly spinning wheel which is driven by an air turbine, Fig. 1. The liquid beryllium metal is mechanically atomized into finely divided droplets at the periphery of the spinning wheel. The droplets are solidified in flight inside the atomizing chamber by a transverse flow of helium gas that also carries the beryllium powder product into a cyclone separator. This process produces spherical beryllium powder with solidification rates on the order of 10^4-10^6

degrees C/sec. With the current equipment configuration, the beryllium powder is collected in a canister below the cyclone separator, valved off, and transferred to an inert-gas dry box for powder classification. Parameters which can influence the resulting beryllium powder size distribution are given in Table 1.

Table 1.
Parameters which can influence the size distribution of centrifugally atomized beryllium powders.

Melt temperature
Pour temperature
Superheat
Disk speed
Nozzle diameter
Atmosphere

The powders produced by the centrifugal atomization process were screened using stainless steel sieves to the following size fractions.

A. - 400 mesh (< 38 μm)
B. - 270 +400 mesh (38 μm - 53 μm)
C. - 200 +270 mesh (53 μm - 75 μm)
D. - 140 +200 mesh (75 μm - 106 μm)

Particle size fractions A,B,D, were selected for this investigation because they contained the largest fractional yields of the atomized powders and also represented a wide range of particle sizes.

2.2 Beryllium plasma-spraying

Spray deposits of beryllium were made using the low pressure plasma-spray chamber at LANL, Fig. 2. This chamber contains a commercial SG-100 Plasmadyne torch which is mounted over a translating copper-cooled substrate. Accurate control of the processing gases used in the plasma-spray process was accomplished using a multi-gas flow control system. Beryllium powder was feed into the plasma-spray torch by using a weight/loss control system which integrates a commercial powder feeder with a Toledo weight scale to measure and control the feed-rate of the beryllium powder feedstock during the spray

operation. Plasma-spraying of beryllium using this facility can be done under either a reduced pressure environment or in an argon atmosphere.

To understand the effect of processing parameters on the as-deposited densities and deposit efficiency of plasma-sprayed beryllium, parameters were changed from an initial standard operating condition which was established using commercial S-65 beryllium powder from Brush Wellman Inc., Table 2.

Table 2.
Standard Operating Condition

Spray torch	Plasmadyne SG-100
Current	700 amps
Voltage	30 volts
Primary arc gas (Ar)	30 slm
Powder carrier gas (Ar)	2.5 slm
Powder feed rate	.5 lbs/hr
Spray distance	76.2 mm
Substrate translation	39 ipm
Atmosphere	argon
Anode/Cathode	145/290

The following processing parameters were investigated:

- particle size and particle morphology
- secondary gas addition, (helium)
- chamber pressure

Spray deposits of beryllium were made on (3.175mm) thick copper substrates which were translated back-and-forth under the plasma-spray torch. A bell-shaped deposit was produced on the copper substrates after spraying for 5 minutes. Deposit thicknesses ranged from 7mm to 10mm at the thickest region of the deposit with deposit lengths on the order of 50mm. Removal of the beryllium deposits from the copper substrates for subsequent characterization was done by bending the substrate until the deposits detached. As-deposited densities of the beryllium spray deposits were measured using a water immersion technique (Archimedes principle). Measurements were made on the thickest region of the spray deposits after cutting/grinding to remove the outer fringes of the bell-shaped spray deposits.

Deposit efficiencies (the fraction of material deposited on the substrate) were determined by measuring the weight of the substrate before and after depositing beryllium. The difference in weight was compared to the total amount of beryllium powder dispensed during the plasma spray run. Since the beryllium powder feed-rate is controlled by a weight/loss system which places the powder feed hopper on a weight scale, an accurate amount of powder present in the hopper before and after the spray operation could be determined.

2.3 Deposit Characterization

2.3.1 Microstructural and Chemical Analysis

Characterization of the beryllium spray deposits in the as-deposited condition was accomplished using polarized light microscopy and chemical analysis. Spray deposits were cross-sectioned, mounted and polished for viewing in polarized light. Samples were etched with a solution containing 3%-HF, 3%-HNO_3, and 3%-H_2SO_4 for 3 to 5 seconds to determine the microstructure of the as-sprayed deposits. Chemical analysis was performed by Brush Wellman Inc., Elmore Ohio, on the centrifugal atomized beryllium powders, the beryllium plasma-spray deposits and the beryllium over-sprayed powder using a combustion analysis technique.

2.3.2 Thermal Conductivity Measurements

The room temperature thermal diffusivity was measured on free-standing beryllium samples 6mm in diameter by 5mm long. Measurements were made at Oak Ridge National Laboratory using a thermal pulse technique in which one face of the specimen was illuminated with a xenon flash lamp and the other was monitored with an IR detector. The temperature as a function of time is plotted and the thermal diffusivity is calculated from the resultant experimentally determined thermal transient. The thermal diffusivity (D) was calculated using the following expression

$$D = 1.37\frac{x^2}{\pi^2 t_{1/2}}$$

where x is the specimen thickness and $t_{1/2}$ is the time required for the back face of the specimen to reach half its maximum temperature. The thermal conductivity (κ) for the beryllium spray deposits was calculated using the following expression

$$\kappa = \rho C_p D$$

where ρ is the density and C_p is the heat capacity.

2.3.3 Vacuum Outgassing

Thermal desorption spectra were obtained on several samples of plasma-sprayed beryllium at Sandia National Laboratory, Livermore, California, to determine their vacuum outgassing characteristics. The outgassing system consisted of a turbo-pumped, ultra-high vacuum quartz tube furnace with a UTI 100^{o}C residual gas analyzer(RGA). The measurements were made on small block-shaped samples (100mg, 5x5x2 mm) by first loading them into an unheated portion of the furnace and pre-outgassing the tube to 800^{o}C to remove the contaminants resulting from air exposure. The samples were then remotely transferred into the heated zone for thermal desorption. Several samples were run at the same time to gain sufficient signal for accurate measurements. The sample temperature was ramped linearly from room temperature to 600^{o}C at 10 ^{o}C/min using a temperature programmer. For one experimental run (#2), the temperature ramp was paused at 350^{o}C for 90 minutes to examine the effect of vacuum baking at 350^{o}C. RGA signal amplitudes were converted to gas partial pressures by calibrating against carbon monoxide and hydrogen standard leaks.

3.0 Results and Discussion

3.1 Beryllium deposit densities and microstructure

The effect of processing parameters (particle size, helium gas addition and low pressure plasma spraying) on the as-deposited densities are given in Table 3.

Table 3.
The effect of processing parameters on as-deposited density

Particle size (mesh)	Standard spray condition	Secondary gas (He) addition	Reduced pressure (350 torr)	Secondary gas&reduced pressure
400 (38 μm)	88.43%	92.34	94.13%	94.89%
-270 +400 (53-38 μm)	91.8%	92.2%	91.2%	92.3%
-140 +200 (106-75 μm)	< 60.0%	<60.0%	<60.0%	<60.0%

The highest deposit densities were achieved using the beryllium atomized powders which were below 38μm. The spherical morphology of the atomized powders, Fig. 3a. allowed for better feeding of powders into the spray torch than commercially impact ground beryllium powders which are more angular and difficult to feed below 45μm Fig. 3b. Beryllium atomized powders in the size range of 53-38μm also showed relatively good deposit densities (91-92% T.D.) when spraying with the helium gas addition at a reduced pressure of 350 torr. The larger beryllium feedstock powders (106-45μm) were difficult to melt using the standard operating conditions and required an increase in the operating current from 700 amps to 800 amps in order to melt the beryllium and adhere to the copper substrates. The deposit densities (<60%) were considerably lower and did not significantly change with the introduction of the helium secondary gas and the low pressure spray environment. No further analysis was done on these spray deposits which were made from large diameter powders.

A graph of the as-deposited density, deposit efficiency and the level of porosity of plasma-sprayed -38μm beryllium powder under the various processing conditions is given in Fig. 4. The highest deposit density (94.9%) was achieved using the standard operating parameters given in, Table 2, with the addition of 15-standard liters per minute (SLM) of helium as a secondary plasma gas while operating under a reduced pressure (350 torr). This operating condition also resulted in the highest deposit efficiency (approximately 60%) with a porosity level on the order of 4 percent. These observed increases were attributed to the higher heat content (enthalpy) of the plasma jet with the addition of the helium secondary gas, and the higher particles velocities that result when spraying under a reduced pressure. Increased particle velocities improve the impacting and splatting of the melted and partially melted beryllium feedstock powders resulting in better bonding and consolidation of the deposit.

Microstructural analysis of low density beryllium plasma-sprayed deposits with density levels on the order of 90%, show a large population of unmelted beryllium particles with corresponding porosity adjacent to these unmelts, Fig. 5a. In the case of the higher density beryllium deposits, the presence of unmelted beryllium particles decreased with a corresponding decrease in porosity level, Fig. 5b. Unmelted beryllium particles were still present in the deposits although a greater degree of consolidation of the unmelts seemed to occur during low pressure plasma-spraying.

3.2 Chemical Analysis

Analysis of the -400 mesh (38μm) beryllium atomized powders, beryllium spray deposits and the over-sprayed beryllium powder (which was collected on the bottom of the spray chamber) was performed to determine the oxygen level and other impurity elements. The oxygen levels of these samples were compared to commercial SP-65 beryllium powder produced by Brush Wellman, Inc., and beryllium plasma-sprayed deposits produced by Battelle, Columbus, Fig. 6.

The oxygen level of the plasma sprayed beryllium deposits (.35%) was approximately half that of the starting atomized beryllium powder (.65%) and much lower then the over-sprayed beryllium powder (1.15%). In addition, the oxygen content of the spray deposits was lower that what was previously reported in earlier investigations done by the UCSL and AWRE [11]. Oxygen levels in the beryllium spray deposits in these investigations were reported to have increased from approximately 20 to 140 percent over the starting beryllium feedstock powder.

Metallic powders which were deposited using low pressure plasma spraying have shown oxygen levels in the spray deposits at least as high as the levels present in the starting feedstock powders. When plasma-spraying copper using hydrogen as a secondary plasma gas, oxygen levels in the spray deposits were shown to have decreased below the starting powders [7]. In this investigation, helium was used as the secondary plasma gas and should not have affected the oxygen level in the spray deposits.

The lower oxygen level in the beryllium spray deposits is not well understood but may be attributed to the plasma/particle interactions that occur when spraying beryllium powders which contain a surface layer of BeO. During melting, the powders may tend to segregate into beryllium and beryllium oxide particles due to their differences in melting points and densities (BeO-3.03 g/cm^3, M.P.-2823K and Be-1.85 g/cm^3, M.P.-1560K). This segregation may cause different particle trajectories of the Be and BeO particles as they exit the plasma torch. The BeO particles may solidify in flight before impacting the substrate and subsequently deflect off the substrate. Additionally, the BeO particles may be significantly smaller then the Be particles and become entrained in the processing gases which are deflected around the substrate. These two possibilities may account for the higher oxygen levels present in the over-sprayed powders. Further investigations are being done to understand these results.

Elevated levels of Fe, Ni, Cr were also detected in the atomized beryllium powders, and the subsequent sprayed deposits when compared to commercial impact ground SP-65 beryllium powder manufactured by

Brush Wellman, Inc. These elevated levels are a result of the erosion that occurs in the inner walls of the stainless steel cyclone separator during the beryllium powder production. Efforts are underway to coat the inside surfaces of the cyclone separator with plasma sprayed beryllium in order to minimize the contamination of the beryllium powders through impact with the stainless steel walls.

3.3 Vacuum outgassing of plasma-sprayed beryllium

The observed quantities of outgassed species per gram of sample material are given in Fig. 7. The major gas species are water vapor (18 amu) and hydrogen (2 amu). Measurable quantities of methane (16 amu), carbon monoxide or nitrogen (28 amu), and ammonia (17 amu) are also observed. Here, the NH_3 and CH_4 values are the residual amplitudes for 17 and 16 amu obtained after subtracting off the fragmentation contributions from H_2O and NH_3, respectively. Neither the interruption of the temperature ramp performed in experiment (#2) nor the size difference of the two sample sets affected the total quantities released per gram. The hydrogen released is roughly the same for the two experimental runs; however, more was released in the forms of NH_3 and CH_4 in run #1. Typical quantities outgassed from 85% and 95% dense, S-65 beryllium samples from Brush Wellman, Inc., are also given for comparison.

Much of the outgassing behavior of the plasma-sprayed samples is dominated by the presence of the large H_2O signal. It is not known whether this signal is typical of plasma sprayed material (resulting from post-processing exposure to air) or is an artifact of the specific sample pretreatment. Prior to outgassing, porosity and density measurements were done on these samples by immersing each in water. The H_2O probably resides in the oxide present on the surface of the spray deposits. BeO is know to be very hygroscopic and accommodates several waters of hydration, forming $BeO \cdot xH_2O$.

The thermal desorption spectra for the plasma-sprayed (PS) material is shown in Fig. 8. The water is weakly bound and can be desorbed at low temperatures. Hydrogen production at higher temperatures probably results from the reaction of residual H_2O with beryllium at these temperatures. Desorption spectra for the other species are compared with S-65 spectra in Fig. 9. The PS material exhibits a low temperature N_2/CO peak (28 amu) not found, or weakly present, in S-65. Most of the NH_3 detected for the PS material occurs at this lower temperature. The CH_4 increase for the lower porosity materials also occurs at a lower temperature.

Pre-baking the PS material at 350 ^{o}C for 90 minutes removes the water peak, but has little effect on the high temperature hydrogen peak. It also removes the low temperature N_2/CO peak without affecting the high temperature N_2/CO peak, as shown in Fig. 10. From careful analysis of companion mass peaks, particularly 12, 14, and 16 amu, it can be

concluded that this low temperature peak is N_2, whereas the high temperature 28 amu peak is CO. Apparently, it is the presence of weakly bound N_2 which gives rise to the formation of NH_3. This nitrogen may result from post-process absoption from air or may be due to nitrogen present in the initial powder feedstock. It also may be present in the processing gases as was described in reference [11]. If present in the powder, nitrogen may be removed by outgassing the beryllium powder feedstock prior to spraying. Other weakly-bound contaminants, including water, should also be removable by a pre-outgassing step. As mentioned above, removing the water may also reduce much of the detected hydrogen. However, experiments investigating air exposure of outgassed S-65 have shown both N_2 and H_2 rapidly return to near their pre-outgassed levels. Thus air exposure must be prevented following such a pre-outgassng.

Water outgassing from the PS material continued throughout each experiment, but varied somewhat with sample temperature, T. Even after baking at 600 ^{o}C for 90 minutes, substantial H_20 outgassing remained. Figure 11, gives the H_2O outgassing as a function of time for the PS and 85% dense S-65 materials. Each data set can be fit with an $\exp(-t^{1/2})$ function indicating diffusion-controlled release. Thus, although the water is weakly bound, probably in the oxide on the surface of each deposit, it appears to follow a very tortuous path to release. Outgassing from the PS material is substantially slower and will require a much longer pumpdown time.

3.4 Thermal Conductivity

Results of the room temperature thermal conductivity measurements are given in Table 4.

Table 4.
Room temperature thermal conductivity of plasma-sprayed beryllium

Sample	Mean Thermal Diffusivity (cm^2/s)	Specific Heat ($J/kg \cdot K$)	Density (g/cm^3)	Thermal Conductivity ($W/m \cdot K$)
A	0.2269	1750	1.7500	69.49
B	0.2145	1750	1.7141	64.34
C	0.1586	1750	1.6702	46.36
D	0.1442	1750	1.6653	42.02
E	0.1567	1750	1.6668	45.71
F	0.1246	1750	1.6997	37.06

The thermal conductivity of the beryllium spray deposits were significantly lower than that of pure beryllium which has a thermal conductivity of 218 W/m·K [12]. These results were in general agreement with previous thermal conductivity data taken for plasma sprayed beryllium produce by inert gas plasma-spraying at Battelle, Columbus [8]. An increase in the thermal conductivity also corresponded to an increase in the deposit density, except for sample F. The low thermal conductivity values in all cases can be attributed to the porosity and layered microstructure throughout the bulk of the deposit, Fig.5. The presence of interfaces created by impacting beryllium liquid particles will be a controlling factor in maximizing the thermal conductivity of the spray deposits. Improvements in the thermal conductivity of plasma sprayed beryllium can result by minimizing the splat interfaces through better melting and deposition, and also through post heat-treatments. Spray deposits of beryllium which were produced by Battelle, Columbus were heat-treated at 900°C for 1 hour to promote diffusion bonding across splat interfaces. An increase in the thermal conductivity from 25-200% over the as-sprayed beryllium resulted [8]. Since heat-treatments or consolidation by hot isostatic pressing will not be applicable for ITER, post-deposition surface conditioning techniques such as laser surface treatments should be investigated.

4.0 Conclusions

- The spherical nature of the beryllium centrifugal atomized powders, in comparison to the angular impact ground powders, allowed for better feeding of powders below 38μm into the plasma-spray torch.

- 38μm spherical beryllium powder, made by centrifugal atomization, produced the highest deposit densities under the investigated conditions.

- Increases in the deposit density and deposit efficiency of plasma-sprayed beryllium resulted when spraying under a low pressure condition (350 torr) with helium as a secondary plasma gas.

- Oxygen levels in the beryllium spray deposits produced by low pressure plasma-spraying were lower (by a factor of two) than the starting atomized beryllium powders.

- Outgassing of plasma sprayed beryllium was dominated by the presence of H_2O and H_2.

- The thermal conductivity of plasma-sprayed beryllium was significantly lower then pure beryllium. Microstructural features such as splat interfaces may be a controlling factor.

Acknowledgments

This investigation was funded through Sandia National Laboratory, Fusion Technology Department under the guidance of Dr. Robert D. Watson. The authors would like to acknowledge Oak Ridge National Laboratory for the thermal conductivity measurements, K. Elliott for the beryllium plasma-spraying and J. Montoya for sample preparation and metallography.

References

1. J.B. Whitley, K.L. Wilson and D.A. Buchenauer, *J. of Nuc. Mat.*, 155-157 (1988) 82.

2. R.F. Mattas, D.L. Smith, C.H. Wu, T. Kuroda and G. Shatalov, *J. of Nuc. Mat.*, 191-194 (1992) 139.

3. K.L. Wilson, R.A. Causey, W.L. Hsu, B.E. Mills, M.F. Smith and J.B. Whitley, *J. of Vac-Sci Techn A* 8(3) (1990) 1750.

4. K.J. Diets and the Jet Team, *Fusion Technology*, 19 (1991) 2031.

5. D. Webster and G.J. London., Ed. **"Beryllium Science and Technology"**, Vol 1., D.R. Floyd and J.N. Lowe, Ed. Vol 2., (Plenum Press, New York, 1979)

6. M.F. Smith, R.D. Watson, R.T. McGrath, C.D. Croessman and J.B. Whitley, *J. of Nuc. Mat.*, 171(1990) 158.

7. M.F. Smith, C.D. Croessman, F.M. Hosking, R.D. Watson and J.A. Koski, *2nd Plasma-Technik Symposium*, Lucerne, Switzerland,Vol 3. (1991) 43.

8. Private communication with Dr. R.D. Watson of Sandia National Laboratory, Fusion Technology Division, Albuquerque,N.M. USA.

9. E. Muehlberger, Proc. 7th Int. *Thermal Spray Conf. Proc.* London, (1973), 245.

10. D. Apelian, R.W. Smith, M. Paliwal, and W.R. Schilling, *International Metals Review*, 28(5),(1983) 271.

11. R.G. Castro, L.A. Jacobson and P.W. Stanek, *"Beryllium Processing Technology Review for Applications in Plasma-Facing Components"*, Los Alamos National Laboratory Report, LA-12545-MS, (1993).

12. Y.S. Touloukian, R.W. Powel, C.Y. Ho and P.G. Klemens, *Thermophysical Properties of Matter, Vol.1, Thermal Conductivity of Metallic Elements and Alloys*, IFI/Plenum, New York, NY (1970).

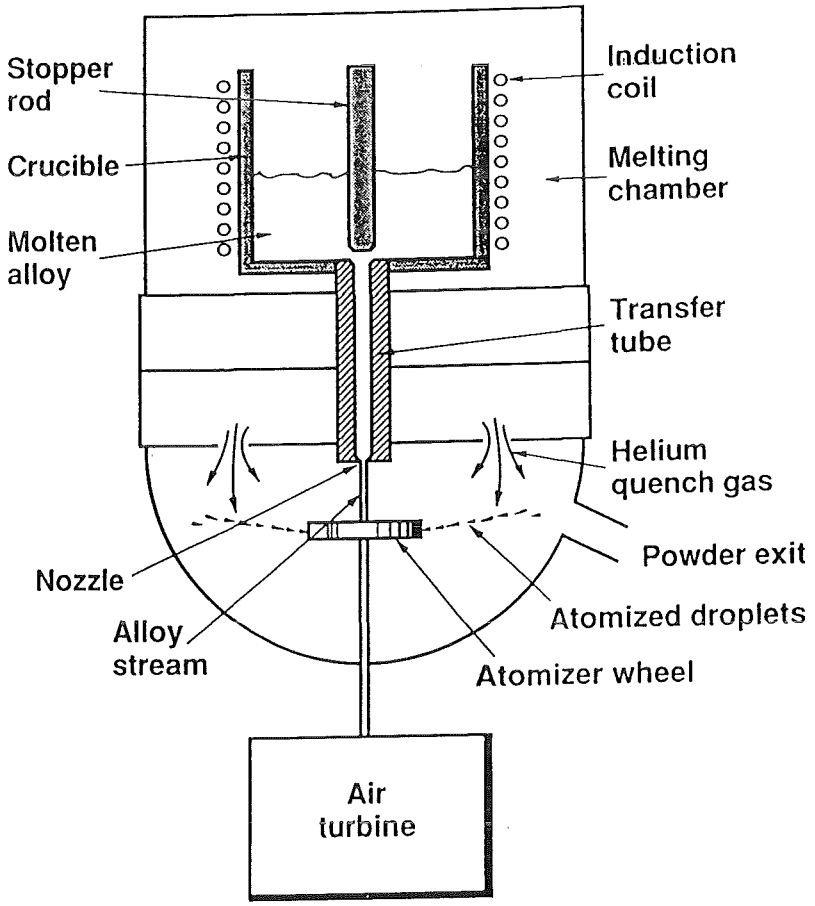

Fig. 1. Schematic of centrifugal atomization process

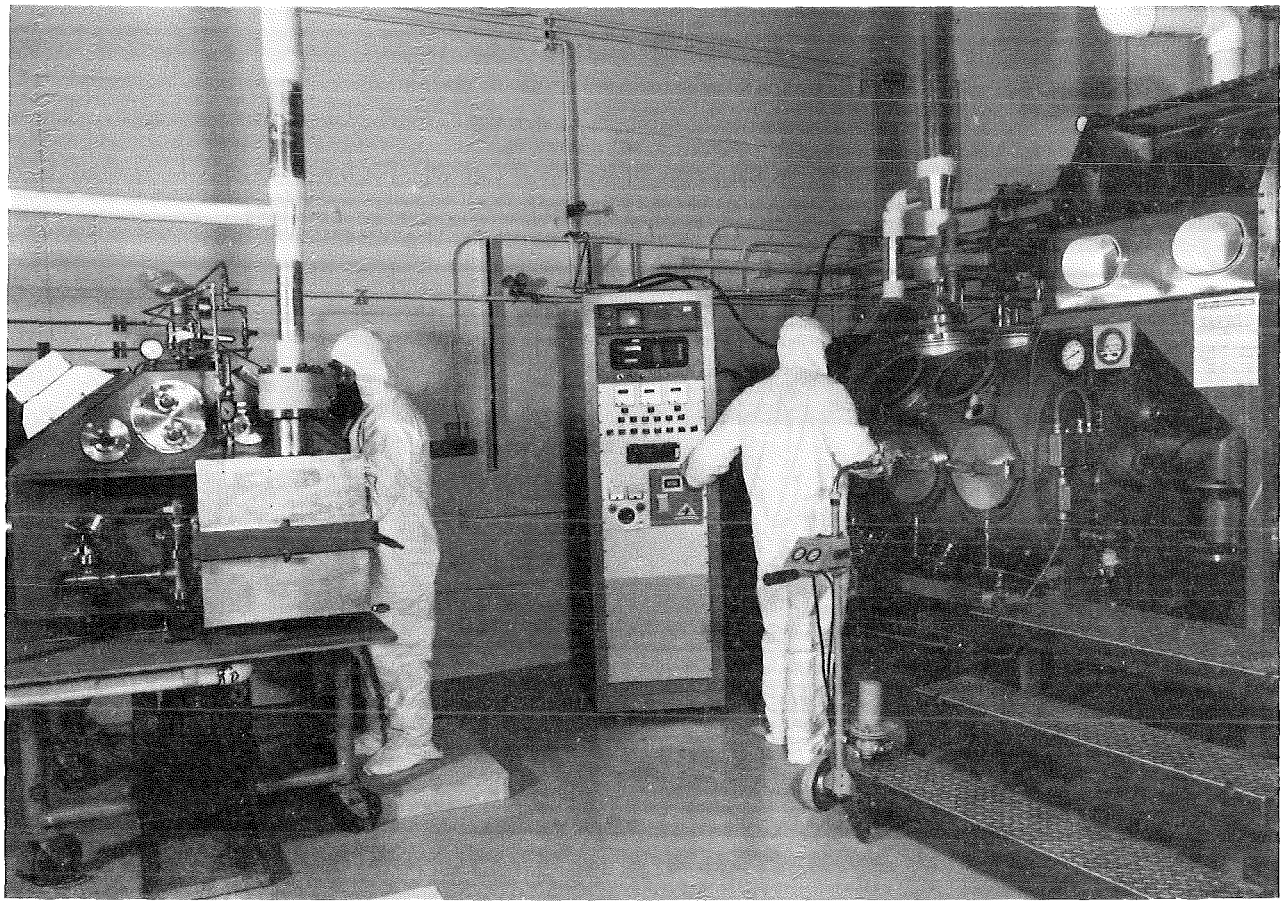

Fig. 2. Beryllium low pressure plasma spray facility at LANL.

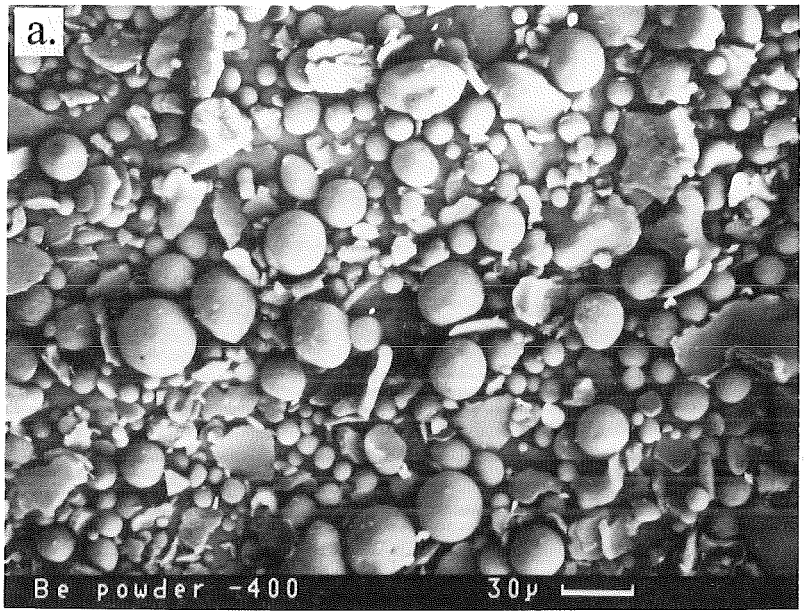

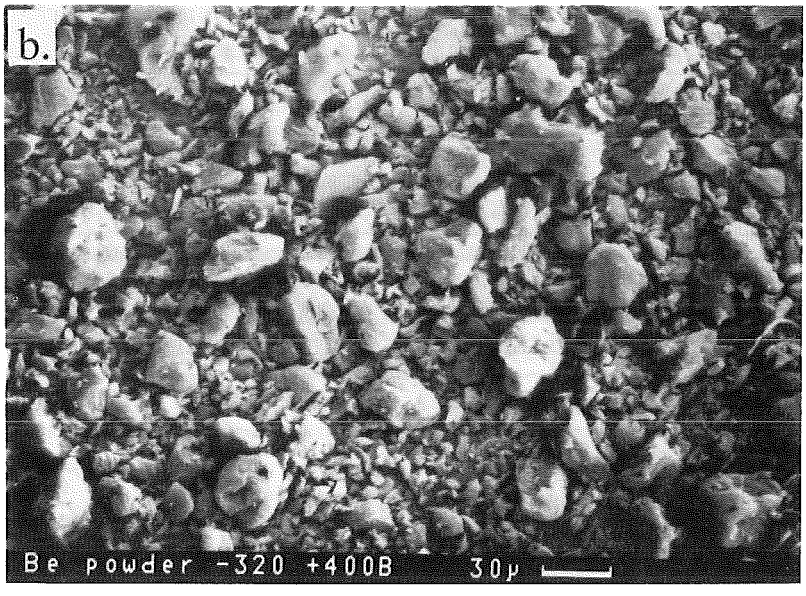

Fig. 3. a)morphology of centrifugal atomized beryllium powders, b) morphology of impact ground S-65 beryllium powders.

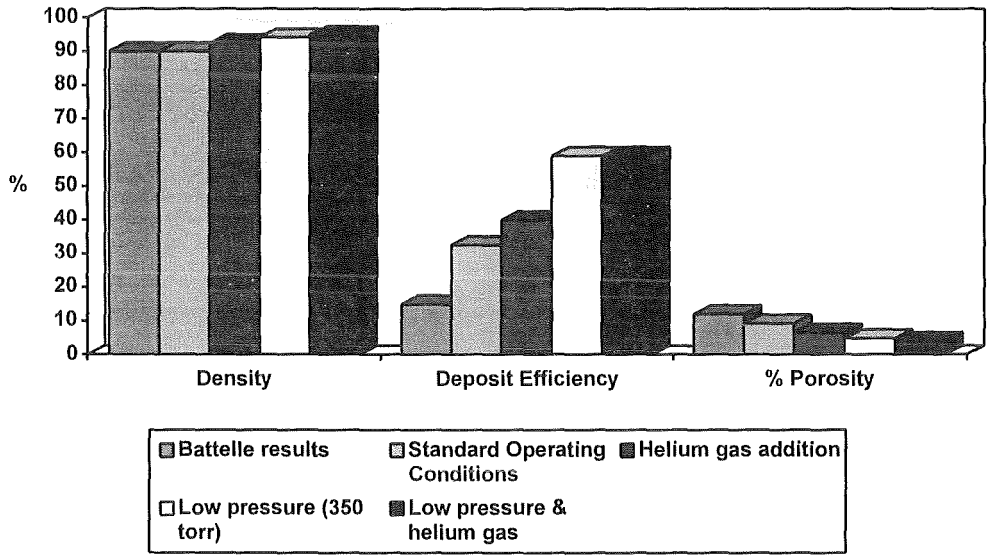

Fig. 4. As-deposited density, deposit efficiency and porosity level of plasma sprayed (-38μm) beryllium powder sprayed under the various operating conditions and compared to results previous reported by Battelle, Columbus [8].

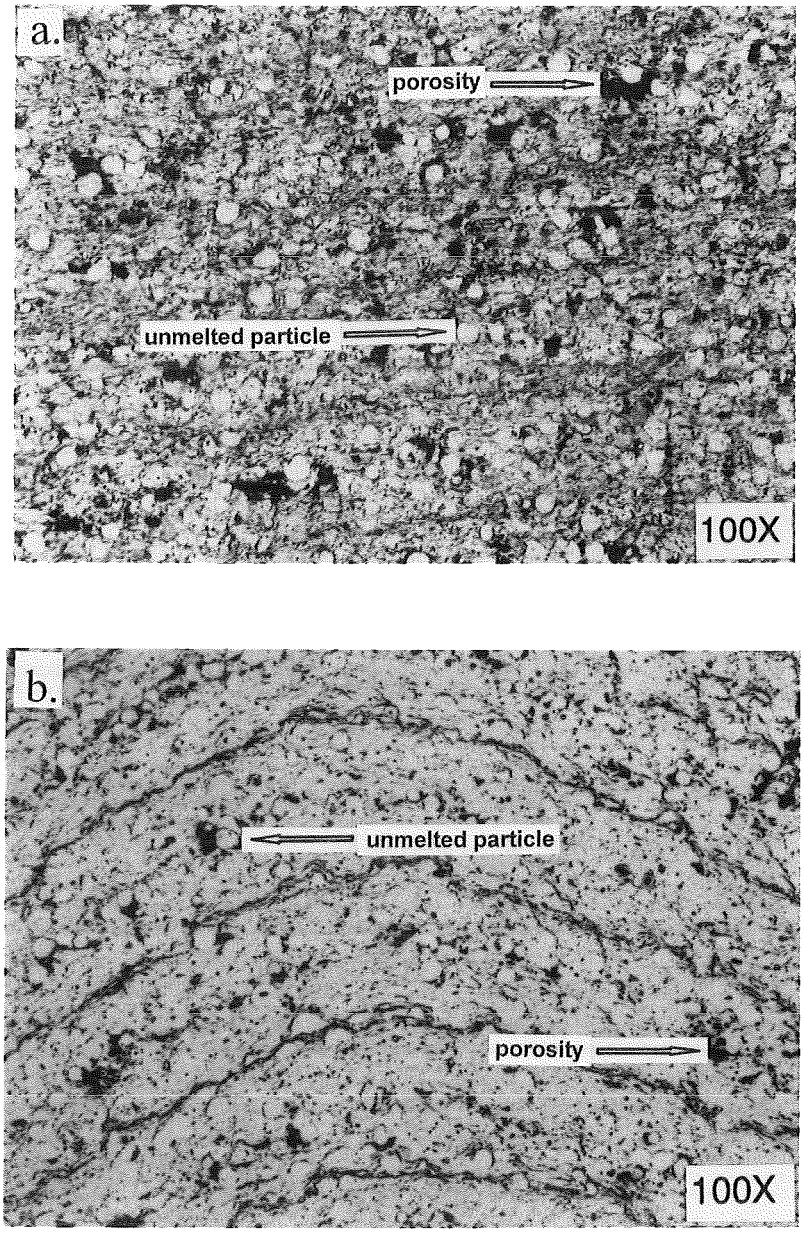

Fig. 5. a) 90% dense plasma sprayed beryllium showing presence of unmelted particles with corresponding porosity, b) 94% dense plasma sprayed beryllium showing lower porosity levels and better consolidation of unmelted particles.

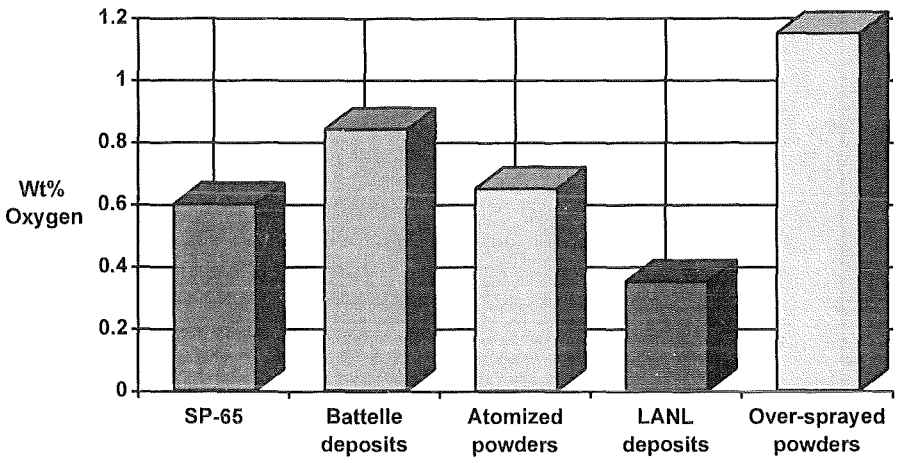

Fig. 6. Comparison of oxygen levels of commercial SP-65 beryllium powder from Brush Wellman Inc., plasma sprayed beryllium deposits produced at Battelle, Columbus, centrifugal atomized beryllium powders produced at LANL, beryllium spray deposits produced at LANL and the over-sprayed powders.

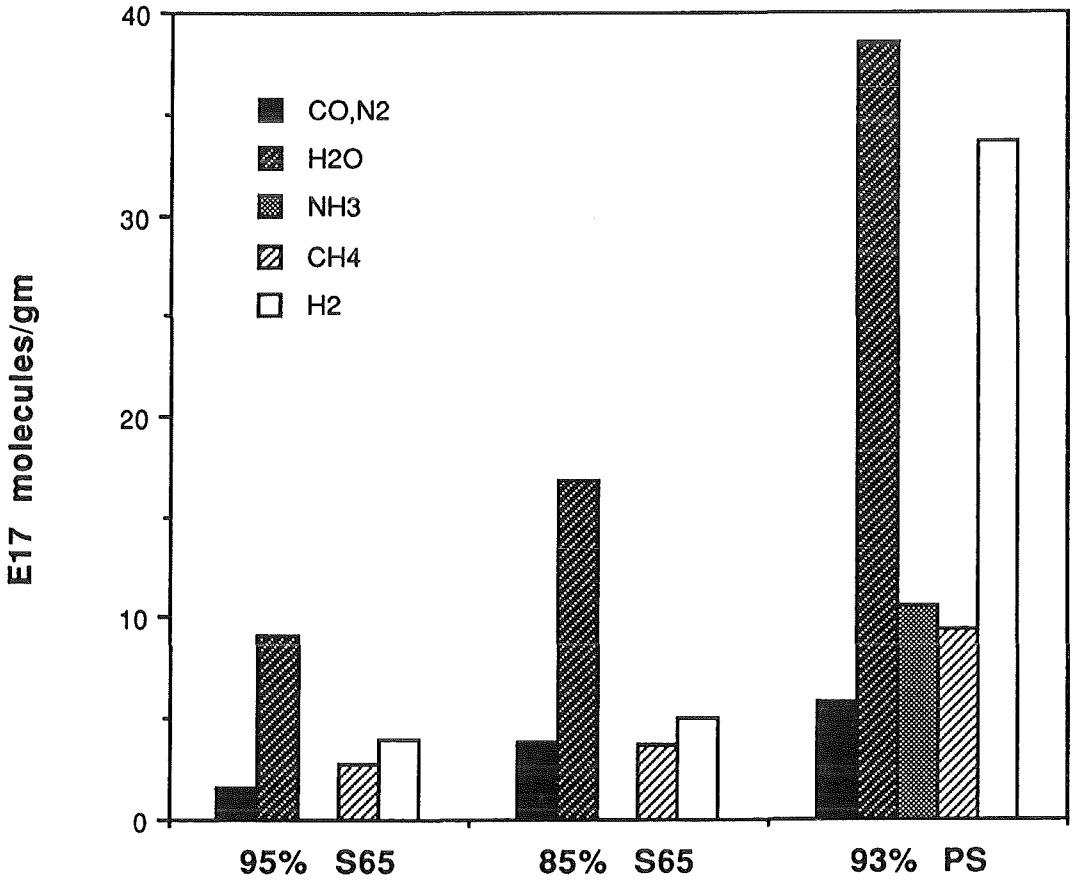

. 7. Quantities of gases produced by heating as-received plasma-ayed (PS) and S-65 materials of the indicated densities.

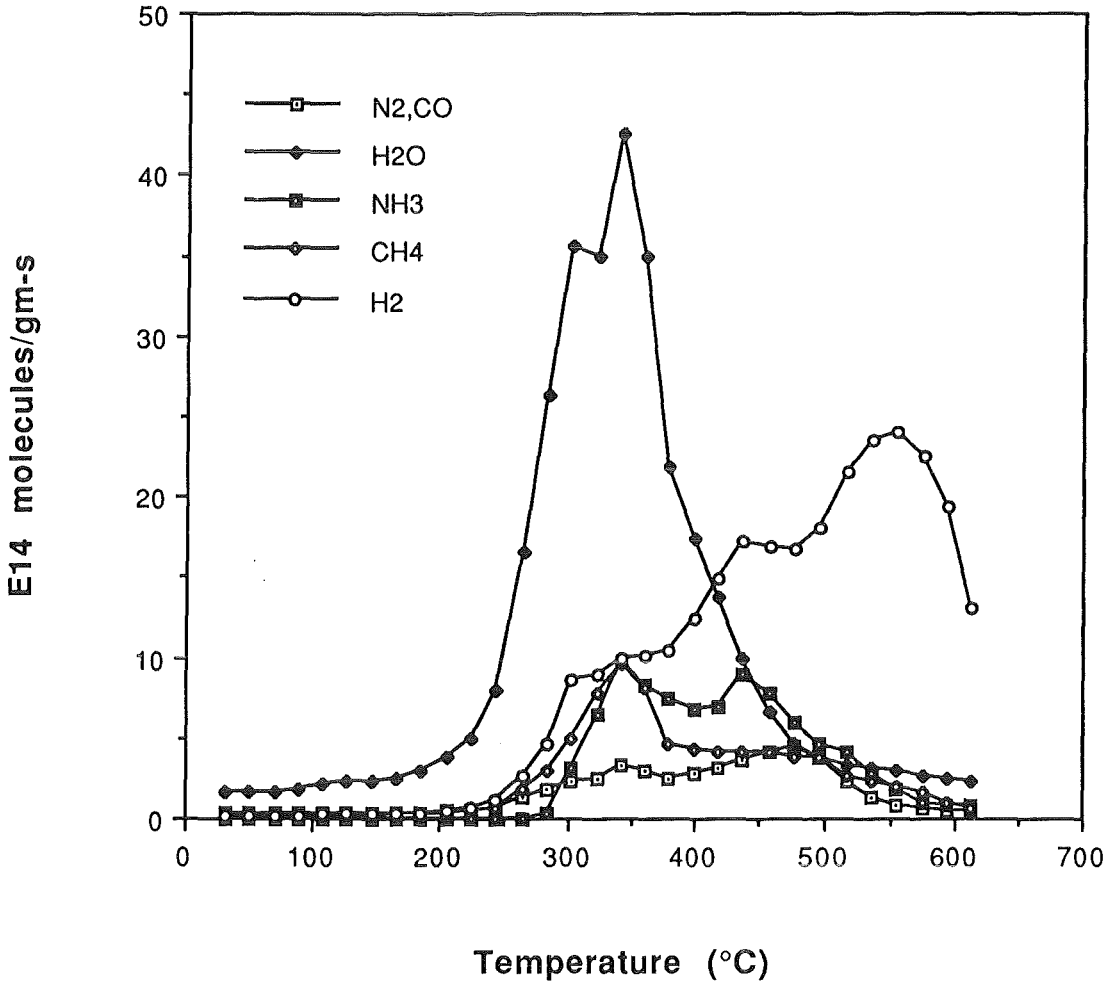

Fig. 8. Gas desorption spectra from 93% dense plasma sprayed beryllium samples.

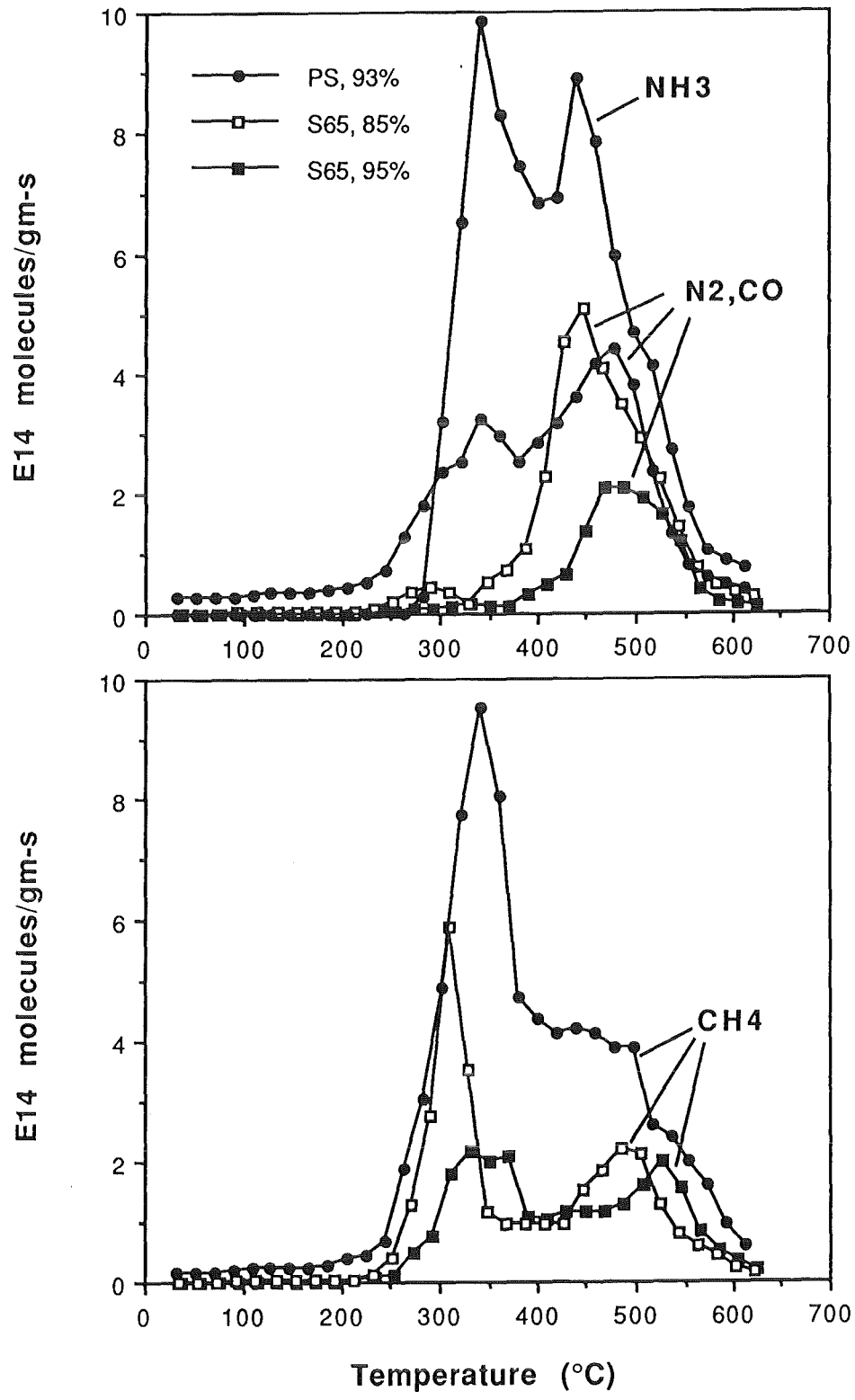

Fig. 9. Comparison of the N_2/CO, NH_3, and CH_4 desorption spectra for plasma sprayed (PS) and S-65 materials of the indicated densities.

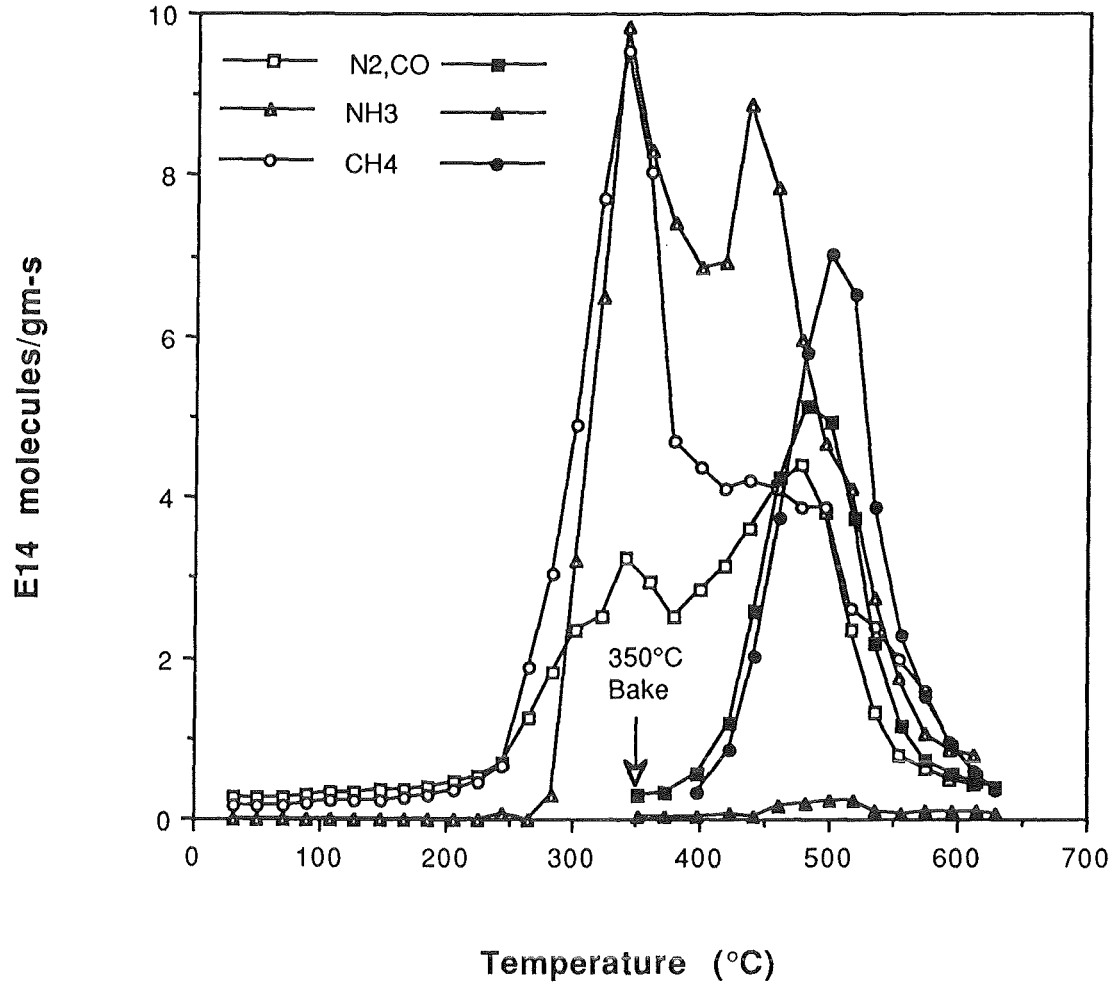

Fig. 10. Comparison of desorption spectra for (PS) material pre-baked at 350°C for 90 minutes with unbaked material. Pre-baking removed the water peak but not the water outgassing.

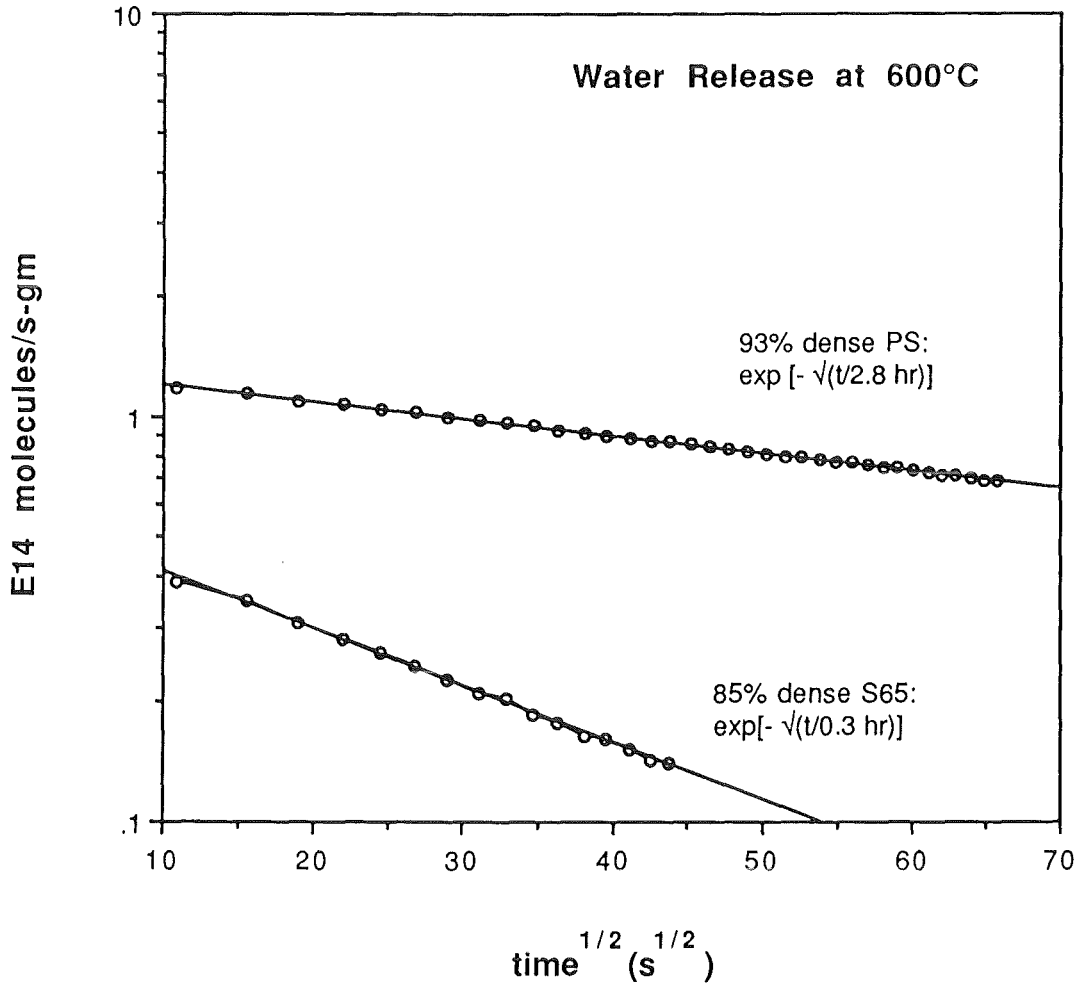

Fig. 11. Water release rate at 600°C.

BERYLLIUM HIGH HEAT-FLUX TESTS AT JET

E.B. Deksnis, H. Altmann, H. Falter, C. Ibbott, M. Pick, R. Viola

JET Joint Undertaking, Abingdon, Oxon, U.K. OX14 3EA

ABSTRACT

JET has operated with large areas of beryllium exposed to plasma in both the limiter and divertor configuration. Tests of beryllium tiles proposed for the inertial Pumped Divertor of JET suggest that castellations of 6 x 6 mm are required to sustain heat fluxes of up to 15 MW/m^2 for 5 x 10^3 pulses and no appreciable fatigue failure of the irradiated surface. However, at 27 MW/m^2 fatigue cracks appeared lateral to the irradiated surface and these cracks cause the surface to melt without fatigue failure of the hot areas. There may be a strong dependence of fatigue life of beryllium on the initial temperature of the component.

The adherence of thin layers of beryllium clad onto copper heat sinks, i.e. onto CuCrZr hypervapotrons. Brazed components have survived over 10^3 cycles at 12MW/m^2 with an ultimate power loading capability up to a minimum of 17 MW/m^2. These results have been interpreted with respect to both localised stresses and thermal fatigue at the interface.

INTRODUCTION

The Joint European Torus (JET) is the central experiment and largest project of the controlled thermonuclear fusion programme of the European Community (1). It is sited at Culham UK and the JET programme is coordinated by Euratom. JET has recently completed a highly successful period of experimental activities whereby a D-T mixture was studied for the first time in a tokamak discharge (2).

The best plasma performance for JET discharges to date have largely occurred for a divertor-like magnetic configuration. These configurations are characterised by a null in both the toroidal and poloidal fields. The target plates for such experiments have been made of solid beryllium. These have sustained up to 20 MW/m^2 for pulses of up to 1 second (3). Local melting of the beryllium is observed without loss of mechanical integrity, see figure 1.

In order to improve further the fusion parameters achievable with JET a pumped divertor configuration has been designed and is at present being installed in JET (since March 1992 with completion expected by the end of 1993) (4).

The thermal response both of inertially cooled beryllium target plates and water-cooled components have been investigated i.e. (5, 6). This paper reports recent work on beryllium clad copper heat sinks and basic studies of the fatigue of S65B beryllium. It must be noted that first operation of the new phase of JET will rely upon an inertially cooled CFC target plates (7). A full set of inertially cooled beryllium blocks has been procured and these are planned to be exchanged with the CFC material during the forthcoming experimental campaign.

ACTIVELY COOLED SANDWICH COMPONENTS

JET has relied extensively upon hypervapotrons as heat sinks with a proven capability of heat-removal at fluxes up to 15 MW/m^2 at low pressure (0.6 MPa) and at low flow speed.

Test sections prototypical of a water-cooled divertor target plate consist of castellated Beryllium tiles brazed to an actively cooled CuCrZr base with an induction brazing process using InCuSil ABA braze (27.5% Cu, 13% In and 1.25% Ti). The brazing temperature is 730°C for 1 minute. The time constant for temperature rise and cool down is 6°C/s. Test sections have a surface of 500 x 27 mm^2. The design is shown in figure 2 . The tile thickness was between 1.5 and 3 mm.

All tests reported here have been performed upon the Be clad vapotrons in the JET Neutral Beam Test Bed; a 10 MW, 160 kV ion beamline system originally used to commission the JET neutral beam injectors. The main parameters of the Test Bed are shown in Table 1.

The Beryllium test rig is a small beam line with a volume of approximately 1 m^3 that is physically separated from the main tank see figure 3. The tank is operated at the pressure required in the plasma source to produce an arc. This reduces considerably the requirement for vacuum pumping speed to less than 1000l/s. A standard JET beam source with a reduced extraction area is used. The test rig is physically separated from the main test volume.

The surface temperature of a component under test is measured with an AGA IR camera. If the design of the test sections allows sufficiently high temperatures, the IR system is calibrated during the radiative cooldown. Emissivity and transmission are then set to match the surface temperature with that measured with a thermocouple inserted into the component. Grounded hot junction CrAl thermocouples are percussion welded into 1.7 mm holes for metal substrates.

The power density is measured by water calorimetry and with inertial copper calorimeters. Water flow is measured using Taylor turbine flowmeters installed in the return line of each water channel. The water exit temperature is measured with sheathed C_rAl thermocouples sampled at a rate of 6 Hz.

The peak power density is calculated from the absorbed total energy. Power falling onto water supply and return pipes in undersized test components is taken into account by the application of a correction factor.

The tests consisted of an initial screening test for three different tile thickness followed by an endurance test of two additional test-sections.

Table 1: Parameters of the JET test facilities

	main test bed	Be test rig
heat source	ion beam	
pulse duration	20s	
max. power	2 x 4 MW	2 MW
max. power density	100 MW/m^2 per beam	> 50 MW/m^2
duty cycle	1:30	
volume	90m^3	1 m^3
access ports	up to 1500 mm i.d.	400 mm i.d.
vacuum pumping speed	10^{6}l/s	200 - 1000l/s
Cooling loop capacity available for tests:		
water flow rate and pressure head	20l/s (8 bar) & 100l/s (4.5bar)	IR. thermal imaging and high resolution CCD cameras
return water pressure	2 bar	
Diagnostics		
thermal diagnostics	>200 thermocouple channels (40 Hz)	
visual diagnostics	IR. thermal imaging and high resolution CCD cameras	
gas	residual gas analyser and spectrometer	
Shielding	Fully shielded for operation with deuterium beams.	

Screening tests produce failure and thus define performance limits. This was done for 1.5, 2 and 3 mm thick Beryllium tiles all brazed with the same process and castellated in the same way. A typical test sequence starts with 5 s long pulses to set up the beam parameters followed by modulated pulses with on/off cycles of 1 s each. After some hundred cycles at constant settings the power density is increased. The tile surface is monitored with a CCD camera and with an IR thermal imaging system. The test is terminated when several hot spots start to develop together or within a few pulses of one another.

Results of these screening tests are given in Table 2. Overheating of one or several squares is defined as a fault. A fault starts at that edge of the test section, where the power density is highest. For 1.5 and 2 mm thick Be tiles slots stopped the spreading of the melted zone and damage was confined to the area between neighbouring slots. In the case of the 3 mm thick tiles the initial damage was spread over 4 squares and within the next 30 cycles another adjacent square melted.

The first fault on the 2 mm thick tile was observed after only 44 cycles and was confined to one or two squares. The next damage occurred 400 cycles later at a higher power density. We can therefore assume that this first fault revealed a weak area not discovered by ultrasonic testing.

Two new test sections were exposed to an endurance test of more than 1000 cycles with an average power density of 12.5 MW/m^2, see Table 3. One 6 x 6 mm^2 area well outside the beam centre on the right test section became hot from the start of the test. Otherwise no deterioration of tile performance was observed and the surface temperature distribution was uniform. As shown in Table 3, more than 50% of the cycles were done with 1 second on time and 1 s off time, 90% of the equilibrium surface temperature was achieved within 1 s of beam on and the tile cooled down to less than 100°C within 1 s of power being switched off.

It is clear that any large scale delamination of the sandwich structure will lead to melting of the Beryllium tile in whole or in part c.f. figure 3. It is a basic result of the behaviour of bimetallic strips that a stress singularly always exists at the free edge of a sandwich element. The high heat flux loading tests measure, therefore, the extent of residual cracks present in any brazed component. In fact as seen in figure 4 there is a third inter-metallic layer between the two massive parts. This layer is very brittle, hardness 400-700 Vickers.

MATERIAL STUDIES

A plasma-facing component made out of beryllium that is directly cooled by water or by any other coolant is likely to suffer thermal fatigue of a different kind.

Recent studies show that inertial blocks castellated on a grid pattern of 10 x 10 mm can survive cyclic loads of up to 15 MW/m^2 (3 x 10^3) without visible cracking providing the initial tile temperature exceeds 200°C. In an earlier test (9) castellated tiles started from 70°C showed cracking as seen in figure 5 within 10^3 cycles and grew without bound (test stopped after 2.4 x 10^3 cycles). Detailed micrographs showed lateral cracks to have developed near the interface between the recrystallized columnar beryllium layer and the untouched substrate figure 6. This observation could support the hypothesis that the lateral cracks are due to the anisotropic thermal expansion of resolidified material.

Further testing was carried out for 6 x 6 mm castellations. The test sequence were adjusted such that, provided that there are no lateral cracks in the beryllium teeth, the maximum surface temperature in a pulsed mode should not exceed

Table 2: Screening test on Be tiles with 1.5, 2 and 3 mm tiles						
fault	cycles to fault	cycles <10 MW/m^2	cycles 10-12 MW/m^2	cycles 12-14 MW/m^2	cycles 14-16 MW/m^2	cycles 16-18 MW/m^2
1.5 mm thick tiles						
1	416	19.3%	37.1%	42.9%	0.7%	0
2	554	26 %	36.3 %	35.5%	1.7%	0.4%
2 mm thick tiles						
1	44	79.2%		12.5%	8.3%	0
2	436	17.3%		65.5%	9.9%	7.4%
3	451	16.8%		65.8%	9.9%	7.5%
3 mm thick tiles						
1	424	37%	9.2%	50.5%	3.3%	0

Table 3: Endurance test on 2 mm thick Be tiles.			
modulation	power density in MW/m^2		number of on cycles
	average	peak	
set-up pulses			32
6s on time	12.2	15.1	73
2s on 1s off	12.5	13.8	307
1s on 1s off	12.8	14.8	552
2.5s on 1s off	12.5	13.8	40
pulses total			1004

1000°C. These tiles were irradiated first for 3 x 10^3 stress reversals at 15 MW/m^2 and then for 500 cycles at 27 MW/m^2. Lateral cracks develop and lead to the formation of re-solidified beryllium on the surface of the tiles. The micrograph in figure 6 shows clearly that the crack develops in and propagates into virgin beryllium material. This failure was found on several teeth well outside the highest heat flux area.

The thermomechanical response of a sandwich structure comprises two distinct phases: (1) thermal shock and (2) differential thermal expansion between the two materials. Thermal shock produces no plastic deformation in a 1.5-3 mm layer of beryllium for heat fluxes 5-15 MW/m^2. Mismatch of thermal expansion produces plastic strain in beryllium for 5 MW/m^2 (3 mm layer) ~10 MW/m^2 (1.5 mm layer). At 15 MW/m^2 an uncastellated beryllium tile, i.e. essentially any tile >15 mm wide will have a predicted plastic strain of 0.25% at a surface that reaches 800°C. Castellation of thin layers of beryllium cladding have been shown experimentally to eliminate elasticity in the beryllium life for 6 x 6 mm tiles. There are additional stress problems associated with small castellated tiles, in particular the singular phases at the root of each through cut of the tiles. The range of singularities is very short, ~10^{-6} mm for Be-Cu experiments (9).

One effect of castellation is to transfer the regions of high plastic deformation to the root of castellations, see figure 7. Tests on 6x6 mm castellations 8mm deep and 12mm deep have shown that after the extended range of flux densities quoted previously a crack developed at the root of a 8 mm deep castellation. Figure 8 shows one typical crack. Examination of the roots of castellations 10-14 mm deep failed to show evidence for cracking. Clearly the depth at which the root of a castellation produces failure (stress concentration factors of ~6 can be computed for the geometry shown in figure 8) is related to the duty cycle as well as to the flux density incident on a massive tile.

CONCLUSION

This paper has presented the development of brazed beryllium-copper structures that can withstand heat fluxes of up to 12 MW/m^2 for 10^3 cycles without degradation and which have a typical failure threshold by delamination of $\geq$ 17 MW/m^2. Clearly such a component is likely to survive a much larger number of cycles for flux densities i.e. of the order of 5 MW/m^2. Finite-element modelling of the brazed sandwich structures has to date reproduced only qualitatively the behaviour observed in the test-bed. This is in part due to the extremely localised range of the stress singularity i.e. 10^{-6}mm for the beryllium - copper case and also due to difficulties in modelling the inter-metallic interlayer that is left between the copper and beryllium parts after brazing.

The vapotron principle can be adapted to a circular geometry as well as to a rectangular one. Studies on a related geometry (10) have shown that for modest heat-fluxes and for moderate flow speed in the gap between the wall of a vapotron and the line of fins extended surface heat-transfer for copper material of ~15 MW/m^2 can be safely sustained without burnout. A round vapotron with the vapotron structure cut into the exterior (flux-facing) wall has been designed. One prototype shown in figure 9 is available for testing. Preliminary heat-transfer analysis predict the onset of plastic strain at the roof of castellations for fluxes of 5-7 MW/m^2.

Basic studies of the behaviour of S65B beryllium indicate that a plasma-facing component made out of massive beryllium that is directly cooled could readily sustain up to 5 MW/m^2 steady state and possibly up to 10 MW/m^2. This is to be understood in the context of the JET experience: in the absence of radiation damage, for a small number of cycles and

in the absence of creep and embrittlement. In view of the interest in using massive beryllium components for ITER (11) further testing of such components is underway at JET.

BIBLIOGRAPHY

[1] P-H. Rebut and JET Team, Magnetic confinement fusion; recent results at JET and plans for the future, JET report JET-P(92)21.

[2] The JET Team, fusion energy production from a D-T plasma in the JET tokamak, JET report JET-P(91)66.

[3] G. Saibene et al., Power handling capability of C and Be X-point target plates in JET, paper presented at 14th PSI conference, Monterey, USA, April 1992.

[4] M. Huguet, Design of the JET pumped divertor, JET report JET-P(91)51, paper presented at 14th Symp. on Fusion Eng., San Diego USA, October 1991.

[5] E. Deksnis et al., Design of high heat-flux components for the JET pumped divertor, Proceedings 16th SOFT, Vol 1 pg 478, North Holland Press 1991.

[6] H. Falter et al., Testing of plasma facing materials for divertors in JET, paper 1997-16 presented at SPIE International Symposium on Optics, Imaging and Instrumentation, July 1993, San Diego, USA.

[7] M. Pick et al., The new first wall configuration for JET, to be presented at 15th SOFE, October 1993, Hyannisport USA.

[8] E. Deksnis et al., Fatigue of Inertial Beryllium elements for JET, Proceedings 17th SOFT, Vol I pg242, 1993.

[9] R. Viola, Stress Singularities of Sandwich Divertor Targets, JET report to be published.

[10] A. Achilli et al, Subcooled flow boiling and CHF in finned tubes, Proc. ANS Winter Meeting, San Francisco, Nov. 1991.

[11] The ITER Project, Preliminary Design Outline, March 1993.

Figure 1 Local melting of beryllium tiles.

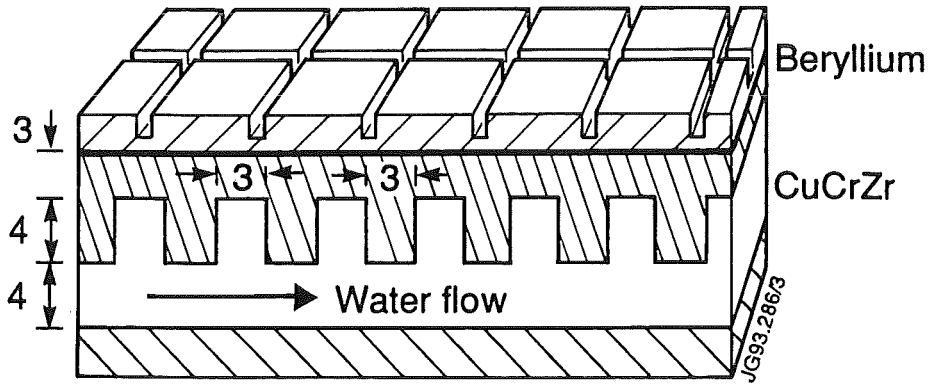

Figure 2 Castellated beryllium layer clad to copper heat sink.

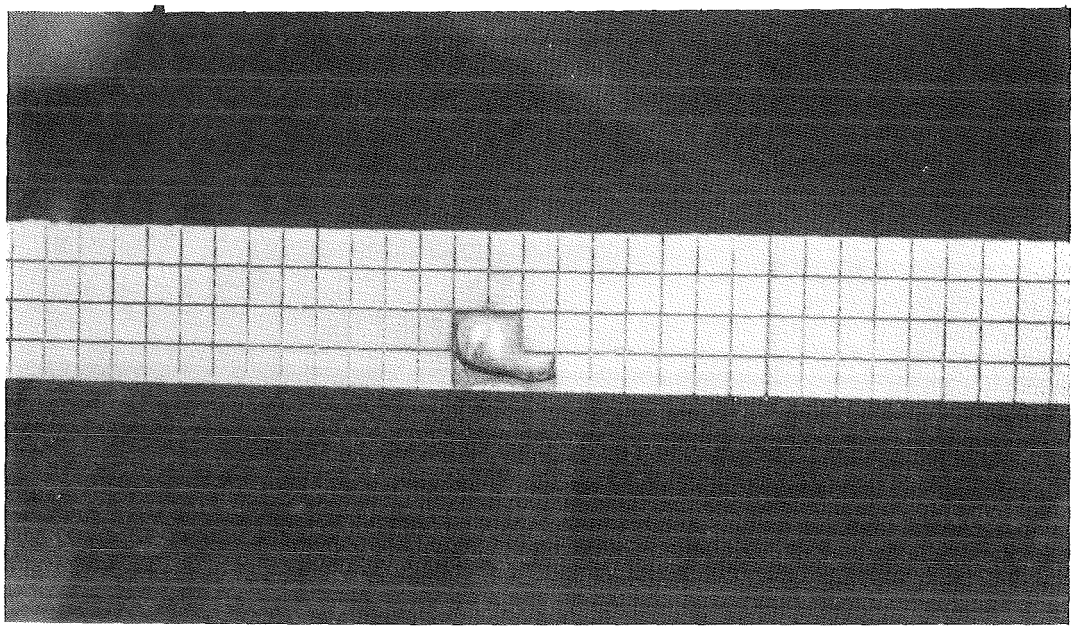

Figure 3 Melting of 3 mm beryllium cladding during screening test.

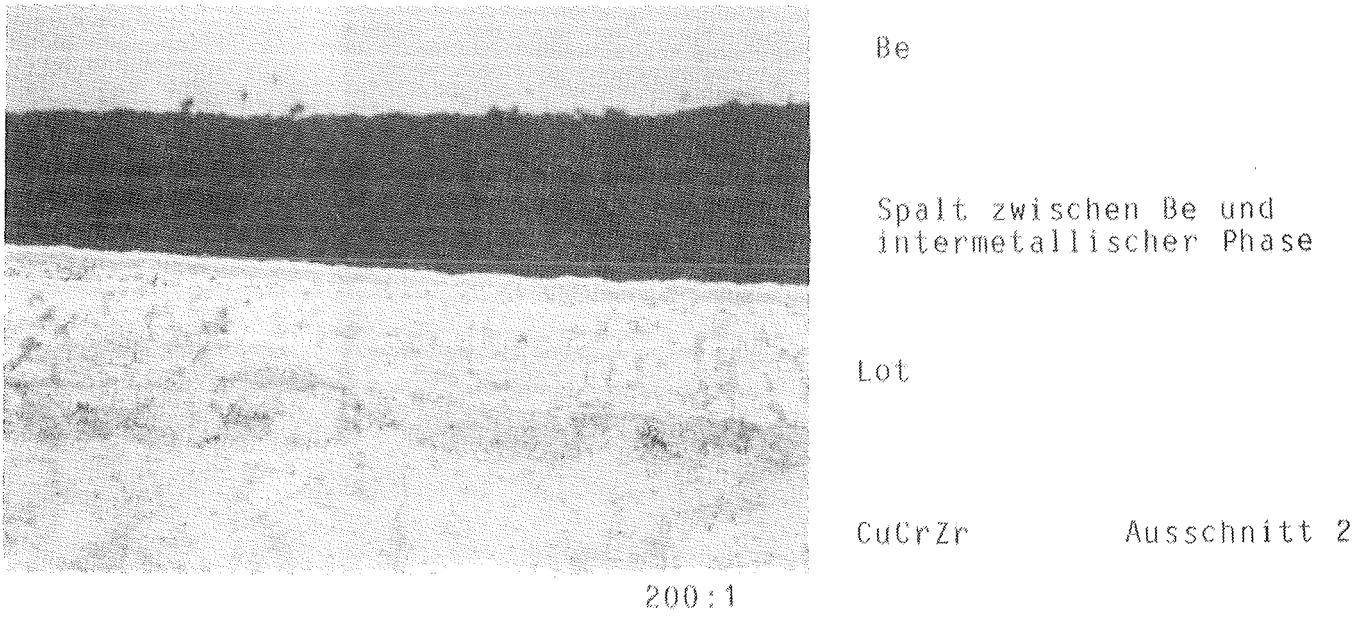

Figure 4 Micrograph of partially delaminated beryllium layer.

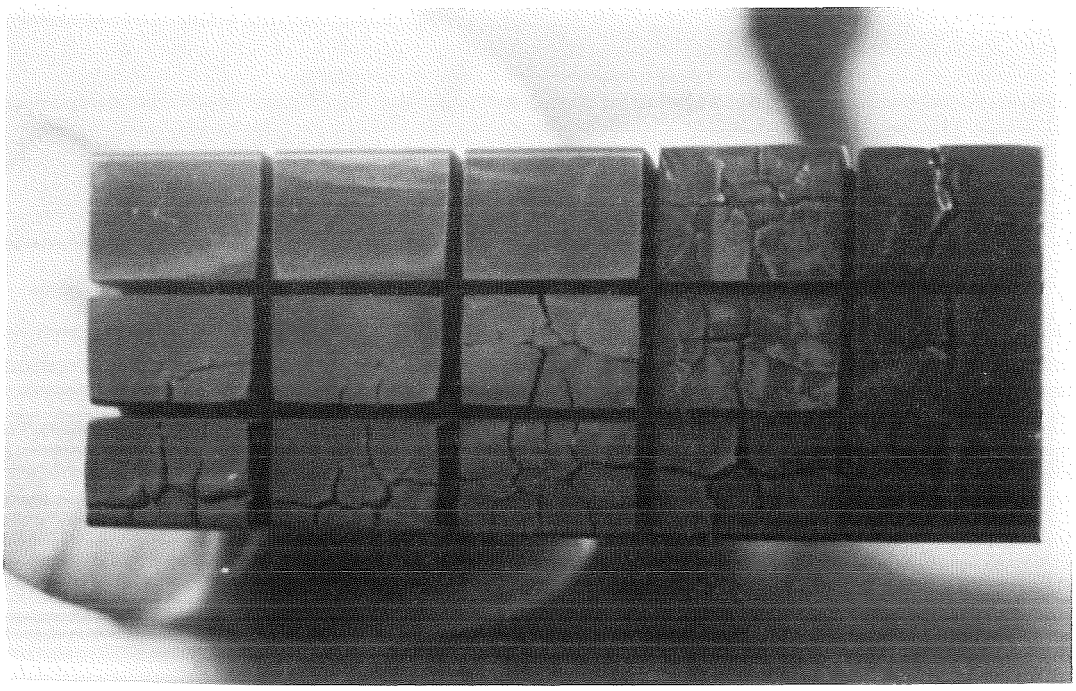

Figure 5 10 x 15 mm castellated beryllium block after 10^3 cycles 15 MW/m^2

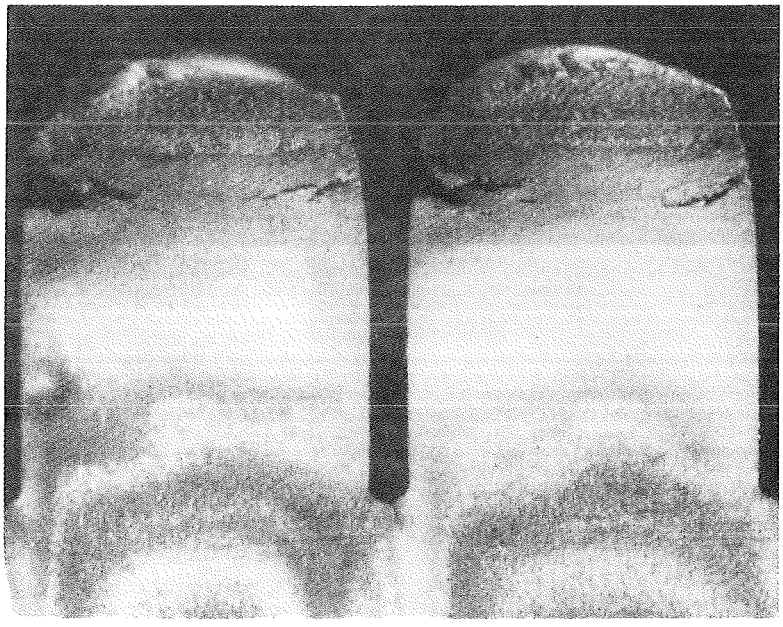

Figure 6 Side view of 6 x 6 mm castellated tooth after 3 x 10^3 cycles at 12.5 MW/m^2 and 500 cycles at 27 MW/m^2.

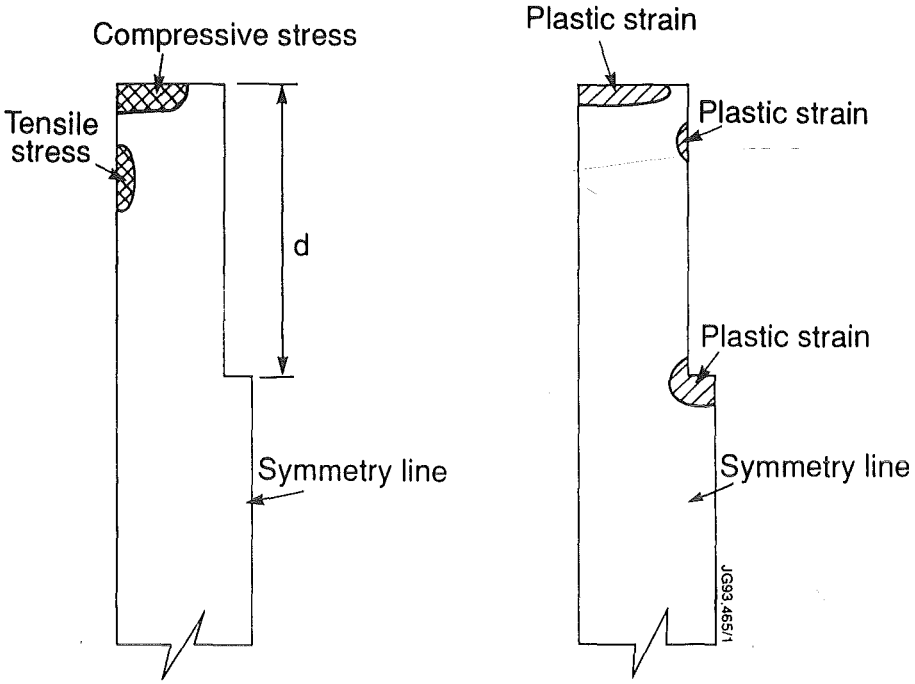

Figure 7 Castellated tile schematic.

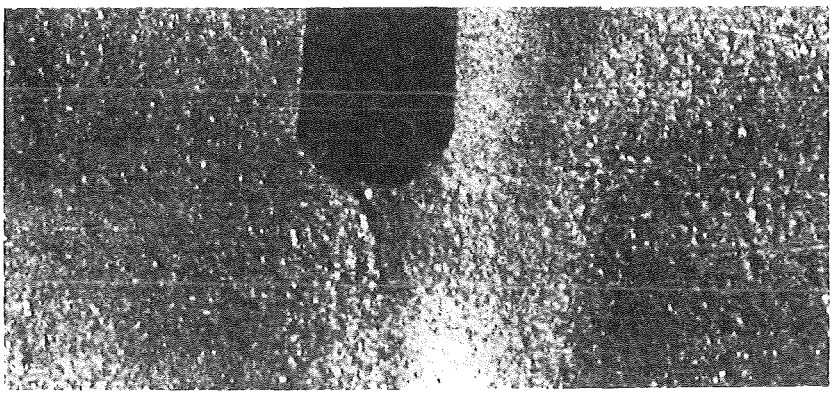

Figure 8 Micrograph of failure at root of castellations.

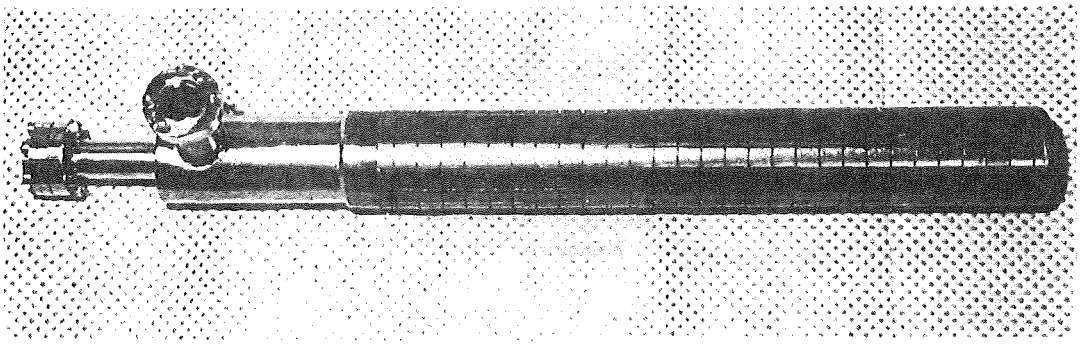

Figure 9 Thick-walled massive beryllium hypervapotron.

SOLID STATE BONDING OF BERYLLIUM TO COPPER AND VANADIUM

A Paper for the

BERYLLIUM WORKSHOP

at

Karlsruhe, Germany

October 4-5, 1993

by

Dennis R Floyd and Alan L Liby,

Manufacturing Sciences Corporation,
Oak Ridge, Tennessee, USA

and

Walter Weaver,

British Nuclear Fuels plc,
Company Research Laboratory,
Springfields Works
Preston, UK

ACKNOWLEDGEMENTS

This work was sponsored privately through the R&D budgets of Manufacturing Sciences Corporation (MSC), and British Nuclear Fuels plc. (BNFL).

Important contributions to this project were made by the following Manufacturing Sciences Corporation personnel -

Howard Hendershott	Don Davis
Mel Lundberg	Greg Landrum
Tom Muth	Norman Hood
Dave Cartwright	

Metallography and electron microscopy work was carried out respectively by Ms Sue Tanner and Mr Mike Turek of AEA Materials Characterisation Services, Risley, UK. We would like to thank Dr Dave Goddard of British Nuclear Fuels plc for expert advice on Atomic Force Microscopy.

The silver coating work was ably conducted by Dr Brian Murray, Light Metal Technologies Inc, Arlington MA.

The hot isostatic pressure bonding was done by IMT Corporation, Andover MA, where Ms Jane Lagoy was especially helpful in determining the proper outgassing conditions.

Shear testing was performed by Materials Testing and Evaluation Co, Oak Ridge, TN.

OBJECTIVE

The intent of this effort was to demonstrate that ingot metallurgy (IM) beryllium (Be) can be bonded to dissimilar metals such as copper (Cu) or vanadium (V) at low temperatures by using silver (Ag) as a bonding aid. It is hoped that success at the coupon stage will stimulate more extensive studies of the mechanical and thermal integrity of such joints, leading ultimately to use of this technology to fabricate first wall structures for ITER.

BACKGROUND

Work at the Joint European Torus (JET) in Culham, England, showed that the use of beryllium as the inner liner directly facing the high temperature plasma in which fusion occurs, caused a significant performance improvement (1). As a result, beryllium is now a strong candidate to become the first wall plasma-facing metal for ITER (2). However, since beryllium has a relatively low melting point, and because the plasma will cause high heat loading, active-cooling may be required in the first wall of ITER. Initial attempts at JET to evaluate a water-cooled first wall design involved brazing Be sheet to a Cu alloy heat exchanger. These attempts were largely unsuccessful, due to failures ascribed to intermetallic compound formation at the braze joint (3). Recently Brush Wellman Inc (BWI) has bonded their powder metallurgy (PM) Be to "Glidcop", a Cu-chromium-zirconium alloy, using the Hot Isostatic Pressing (HIP) technique (4). IM Be offers an advantage to ITER over PM Be because beryllium oxide, which is present in PM Be at a level >10,000 ppm, will contaminate the plasma during operation. The beryllium oxide content of IM Be is <100 ppm. MSC therefore felt it important to demonstrate that IM Be can also be HIP-bonded to Cu.

IM Be has other potential advantages over PM Be for ITER. It is potentially less costly because it can be made by recycling rather than using virgin metal. The manufacturing process is inherently less costly because it involves fewer steps. The elevated temperature ductility and fatigue behaviour are superior, both factors that should favourably influence thermal fatigue behaviour. Its thermophysical properties are excellent (5). The use of rolling to produce IM Be suggests roll bonding of Be to Cu or V could lead to low cost fabrication for the large quantity of plasma facing components that ITER may someday require.

In more recent preliminary design work, the ITER team is reportedly considering the use of vanadium as the primary structural material for the first wall, replacing ferritic stainless steel because of improved activation characteristics (6). Therefore, MSC included evaluation of a Be-V bond in this study.

For the present work, MSC has chosen to use silver as an intermediate layer to effect solid state bonding (SSB) between beryllium and dissimilar metals. Silver has been shown to promote high strength (~700 MPa) bonds, even when using low bonding temperatures (~200°C), and doing the bonding in an air atmosphere (7). This bond strength is much higher than that of silver and the reason such high strengths can be developed is the high state of triaxial stress that develops in the joint, due to the very thin layer of silver. This SSB approach offers great flexibility in that the silver can be coated onto nearly any metal substrate and subsequently bonded to beryllium. Also, the use of HIP to effect bonding offers joint design flexibility. For example, large plate-type samples or tube-within-tube geometries can be bonded equally well by this method.

EXPERIMENTAL

Sample Preparation

A total of 17 bond samples were prepared as follows :

- eight IM beryllium, 25mm diameter by 3mm thick,
- five OFHC copper, 25mm diameter by 9mm thick, and
- four vanadium, 25mm diameter by 9mm thick.

The beryllium was MSC-100 grade prepared by vacuum induction melting, hot rolling from 100mm to 6mm, warm rolling to 3 mm and annealing. A specification sheet for MSC-100 is provided as Figure 1.

The vanadium was supplied by Teledyne Wah Chang of Albany, Oregon, as 40mm diameter rod. The metal is typically triple-melted by the electron beam method to reduce the aluminium content. The major impurities in the heat used for this study were : Si, 390; Mo, 330; Al, 300; O, 230; and Fe, 180, all in parts per million (ppm) by weight. It was supplied in the as-worked condition to retain optimum machinability. It is normally annealed in the range 870°C to 1000°C. Although no mechanical test data was supplied with this heat, typical tensile properties in the worked condition are 350 megapascals (MPa) ultimate, 310 MPa yield and 5% elongation (8).

The oxygen-free high conductivity (OFHC) copper was purchased from a local metal supplier and its process history is unknown.

One surface of each sample was machined and lapped flat to within 5 microns to assure good contact during bonding. One sample of each metal was provided to BNFL for evaluation of the as-lapped surface and the remaining fourteen samples were sent to Light Metal Technologies to be silver-coated.

Coating

The samples were first thoroughly cleaned by chemical means. This consists of a 9-stage operation using various solvents and rinses to progressively remove contaminants and retain a clean surface immediately prior to coating. Next the samples were placed in a coating fixture within a very dry vacuum chamber, previously baked to remove all traces of water. After the chamber was evacuated, the surfaces to be coated were cleaned by ion bombardment to create a fresh, clean surface, and immediately coated with a 12 micron layer of silver by sputter deposition from a 99.99% pure silver target. Although the present samples are quite small, this chamber is sufficiently large to coat samples within an area 500mm by 200mm.

After coating, two samples, one beryllium and one copper, were sent to BNFL for characterisation of the as-coated surfaces, and the remaining 12 samples were sent to IMT for bonding.

Bonding

The samples were bonded about two weeks after the surfaces were coated with silver. Six individual steel HIP cans, three containing Be-Cu, and three containing Be-V bond couples, were used. Each was separately evacuated through a tube while being heated to 250°C to drive off gaseous contaminants within the cans. This vacuum outgassing step also served to remove the silver oxide film that forms on silver in an air atmosphere, but that decomposes in vacuum at 225°C. The evacuation tubes leading into the HIP cans were crimp-sealed while the tubes were still being pumped, and the cans were held at 250°C. The cans were then cooled to ambient and the HIP cycle was carried out more than a day after the tubes were sealed. The HIP cycle involved heating the cans to 400°C and holding in a pressure of 69 MPa for 1 hour. All six couples were bonded in the same run. Subsequently, the samples were sent to MSC for removal from the HIP cans.

Sample Evaluation

All six bonded samples were removed from the HIP cans by band sawing. An intact can and one from which a bond couple has been removed are shown in Figure 2. One of each type was saved for future evaluation, and the other two were sectioned for metallographic evaluation and shear testing, as depicted in Figure 3. Single-shear testing, as shown in Figure 4, was conducted on each shear test specimen, two tests from each material combination. Loading was done on a standard tensile test machine.

The samples sent to BNFL were examined as follows :

> Coupon surfaces were examined by low voltage electron microscopy, and by atomic force microscopy before and after silver coating, to establish their morphology and structure. HIPed samples were mounted in resin, cross-sectioned, then examined optically. After shear testing, one sample of each type was examined by low voltage electron microscope to establish the path and nature of the fracture.

RESULTS

Shear Testing

The shear test data are presented in Table 1.

Microstructural Evaluation

The results of the microstructural examination are shown in Figures 5-13 and summarised in Table 2. The main points to note are :

a) The as-lapped surfaces (Fig. 5) were relatively coarse with some loose particles, particularly on the beryllium.

b) Silver sputter coating reduced the surface roughness of the beryllium, but not the copper - the silver layer having a pronounced crystal structure of its own (see Figs. 6-8).

c) Cross-sectioning of the HIP bonded samples (Fig. 9) showed an intact silver layer in each case, with no diffusion zones or intermetallic compound formation evident at x500.

d) Examination of the shear tested samples showed :

i) Be/Ag/V

Fracture principally along the central Ag/Ag bond line, but a small proportion at the Ag/Be and Ag/V interfaces (see Figs. 10&11). The fracture surfaces showed low ductility, with some evidence of oxidation at the Ag/Ag joint.

ii) Be/AG/Cu

Mainly brittle fracture at the Be/Ag interface, but a small region which failed in a ductile manner in the Ag interlayer (see Figs. 12 & 13).

DISCUSSION

This is obviously a very preliminary study. It was designed to demonstrate that IM beryllium can be successfully bonded to metals of interest to ITER for first wall construction and to permit active-cooling.

The results indicate only partial success. The silver interlayer was effective in preventing the formation of intermetallic compounds between the beryllium and the copper or vanadium. The shear test results, however, gave joint efficiencies of at best 23% for the Be/Cu and 4% for the Be/V, clearly leaving considerable room for improvement.

Microstructural examination revealed two particular factors which contributed to these low bond strengths :

a) Excessive fragmentation of the Be surface prior to bonding.

b) Incomplete deoxidation of the silver surfaces prior to bonding.

Niether of these should prove difficult to correct in any subsequent trials.

FUTURE WORK

MSC and BNFL do not plan further work on this project without stimulus from the ITER community. If the interest for additional work does exist within ITER there are many obvious possibilities. These include :

1. Optimisation of bonding parameters,
2. Evaluation of larger samples,
3. Bonding of other geometries such as coaxial tubes,
4. Fabrication of integrally-cooled test hardware,
5. Simulation testing of plasma conditions,
6. Evaluation of alternate substrate materials,
7. Evaluation of alternate bonding methods such as roll-bonding, press-bonding, fixture-bonding, explosive cladding, etc.

We are perfectly willing to discuss how we might proceed to conduct such investigations with interested parties. The points of contact are :

Dr Alan L Liby
Manufacturing Sciences Corporation
3265 Fenton Street
Denver
CO 80212

Tel. 303-237-8576
Fax 303-233-2993

Dr Dennis R Floyd
Manufacturing Sciences Corporation
804 Kerr Hollow Road
Oak Ridge
TN 37831

Tel. 615-481-0455
Fax 615-481-3142

Mr Walter Weaver
Company Research Laboratory
British Nuclear Fuels plc
Springfields Works
Salwick
PRESTON PR4 0XJ

Tel. 0772 763928
Fax 0772 760283

REFERENCES

(1) Thomas, P R - "Results of JET Operation with Beryllium", Journal of Nuclear Materials 176 & 177 (1990) p 3-13.

(2) Rebut, Paul H - Keynote address to US National ITER Meeting, San Diego, Ca, US ITER News, Vol. 3, No. 1, January 1993.

(3) Altmann, Henk - "A Study of Beryllium Bonding on Copper Alloy". Paper presented at Beryllium Technology Workshop, Clearwater Beach Fl, 20 November 1991, EGG-FSP-10017, December 1991.

(4) Watson, Robert, Sandia National Lab, Albuquerque, Private.

(5) Floyd, Dennis R - "Thermophysical Properties of a New Ingot Metallurgy Beryllium Product Line".
Paper presented at Beryllium Technology Workshop, Clearwater Beach Fl, 20 November 1993, EGG-FSP-10017, December 1993
Communication, 3 March 1993.

(6) Harries, Don - Private Communication reporting on ITER Preliminary Design Meeting held in Garching, Germany in March 1993, 18 May 1993.

(7) Olson, D L and Liby, A L - "Diffusion Bonding", Chapter 14 in Beryllium Science and Technology, Volume 2, Plenum Press, New York, 1978. p 275-295.

(8) Edstrom, C E, CME Metallurgical Consultants, Unpublished Data, 8 September 1993.

Table 1

Results of Shear Testing Solid State Bonded Samples

SAMPLE	SHEAR STRESS (MPa)
Be-Cu #1	32.5
Be-Cu #2	15.7
Be-V #1	8.7
Be-V #2	5.7

Table 2

SUMMARY OF MICROSTRUCTURAL EXAMINATION

	Beryllium	Vanadium	Copper
as-lapped surface appearance	coarse, fragmented	flat, fissured	flat, fissured
as-lapped surface roughness (Ra)	0.23 microns	0.18 microns	0.27 microns
silver coated surface appearance	granular		orange peel
" " roughness (Ra)	0.12 microns		0.26 microns
silver coating thickness	12 microns		16 microns

SAMPLE	COMMENTS
AS-BONDED COUPONS	
Be / V	23 micron thick Ag layer Ag/V boundary distinct but detail not resolvable at x 500 Ag/Be boundary distinct, some voids/fissures no diffusion zones or intermetallics evident
Be / Cu	27 micron thick silver layer (cf 28 microns prior to bonding) Ag/Cu boundary void free, some angular particles Ag/Be boundary voids and debris present no diffusion zones or intermetallics evident
AS SHEARED COUPONS	
Be / V	Fracture at the Ag/Ag bond line, oxide present
Be / Cu	Fracture at the Be/Ag interface, Be surface appears contaminated

Figure 1

MATERIAL SPECIFICATION

MATERIAL

MSC-100 Ingot Metallurgy Beryllium Sheet & Foil

SCOPE

Ingot metallurgy beryllium produced by vacuum induction casting and hot-rolling to thicknesses less than .220". Sheet and foil thicknesses less than .035" may be warm bare rolled.

Maximum sizes normally available are 24" wide and lengths up to 84". Final surfaces may be as-rolled, ground or etched.

Foil is available to thicknesses down to .001". Vacuum tightness, when required, is measured by helium mass spectrometer leak detector, with sensitivity of 2 X 10E-08 atm cc/sec.

TENSILE PROPERTIES

	Fully-Annealed		Stress-Relieved	
	Minimum	Typical	Minimum	Typical
Ultimate, psi	40,000	45,000	50,000	55,000
Yield (0.2%), psi	20,000	25,000	35,000	40,000
Elongation, %	3	4	2	3

CHEMISTRY

Element	Amount (by weight)
Be	99.5% minimum
BeO	<100 ppm
Fe	<1500 ppm
Al, Si, C	<1000 ppm each
Cr, Mo, Ni, U	<250 ppm each
All Other	<100 ppm each

CERTIFICATION

Certification of compliance with this specification shall be furnished upon request.

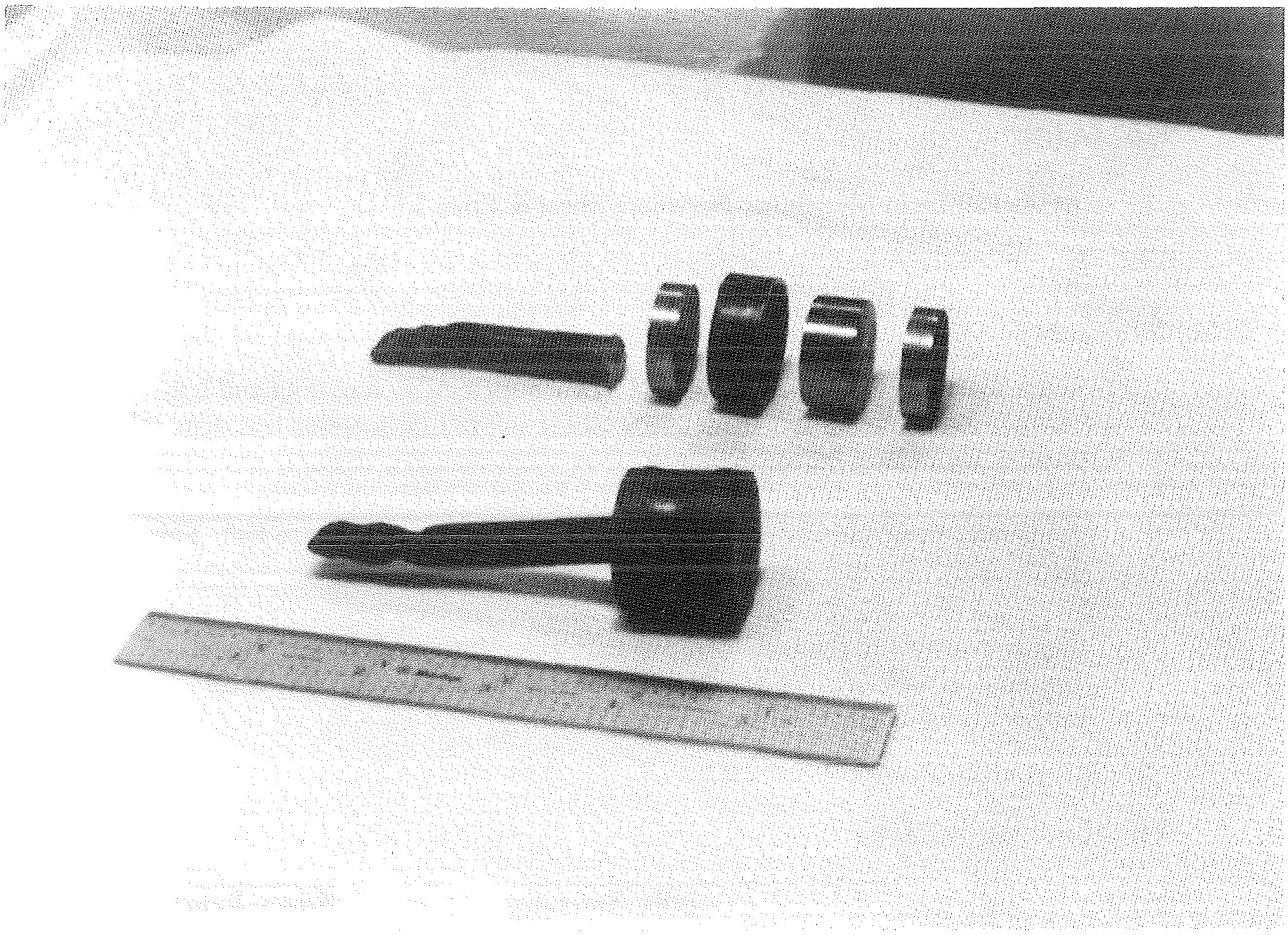

Figure 2

Photograph of a HIP can (foreground) and a disassembled HIP can. The copper-beryllium coupon is second from the right. The tubular body of the can is on its left. The remaining two items are end caps that are welded to the can body. The evacuation tube is on the far left. The ruler is 12 inches (30mm) long.

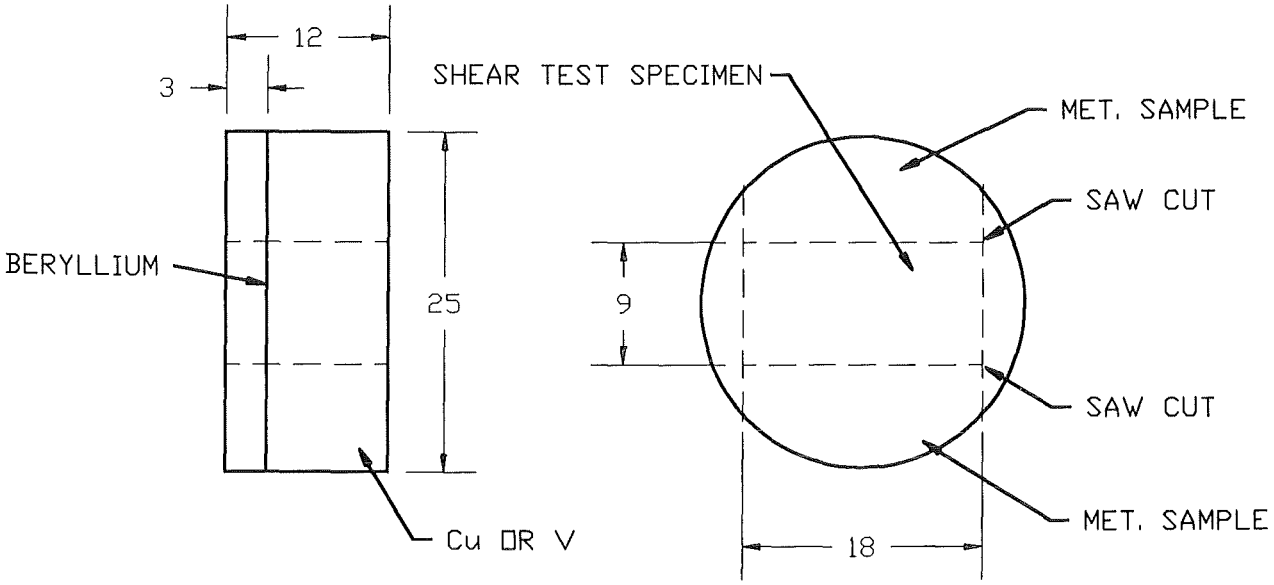

Dimensions in mm

Figure 3

View of coupons used to bond ingot metallurgy beryllium to copper or vanadium by the silver interlayer solid state process. Locations of shear test and metallographic (MET.) samples are also shown.

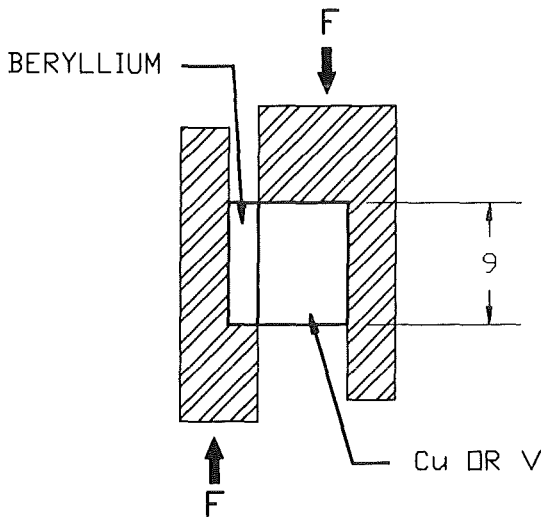

Figure 4

Sketch of set-up used for single-shear testing of solid state bonded beryllium and copper or vanadium specimens. The force (F) is applied hydraulically. The sample are 18mm deep, so the shear area is 162 sq. mm.

FIG 5 : SURFACES PRIOR TO SILVER COATING

LOW VOLTAGE SCANNING ELECTRON MICROGRAPHS

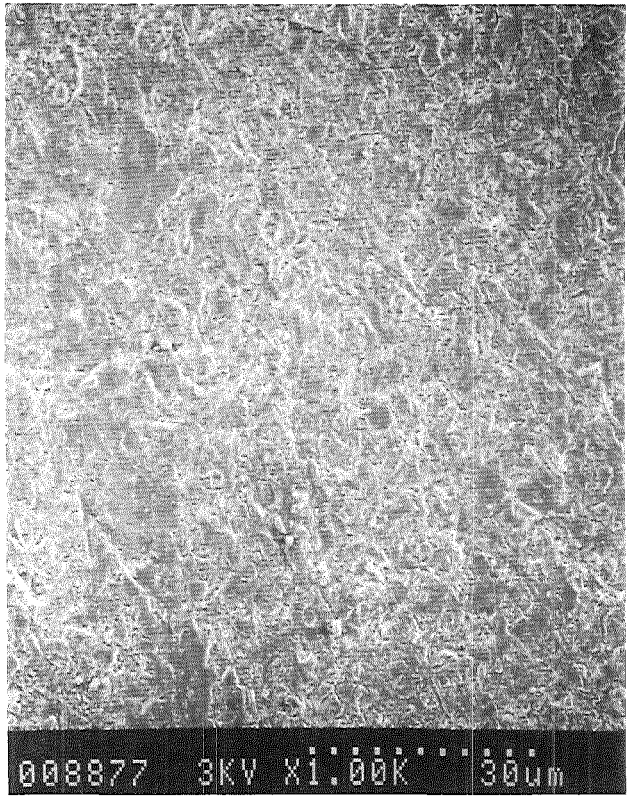

BERYLLIUM

VANADIUM

COPPER

FIG 6 : SILVER COATED SURFACES

LOW VOLTAGE SCANNING ELECTRON MICROGRAPHS

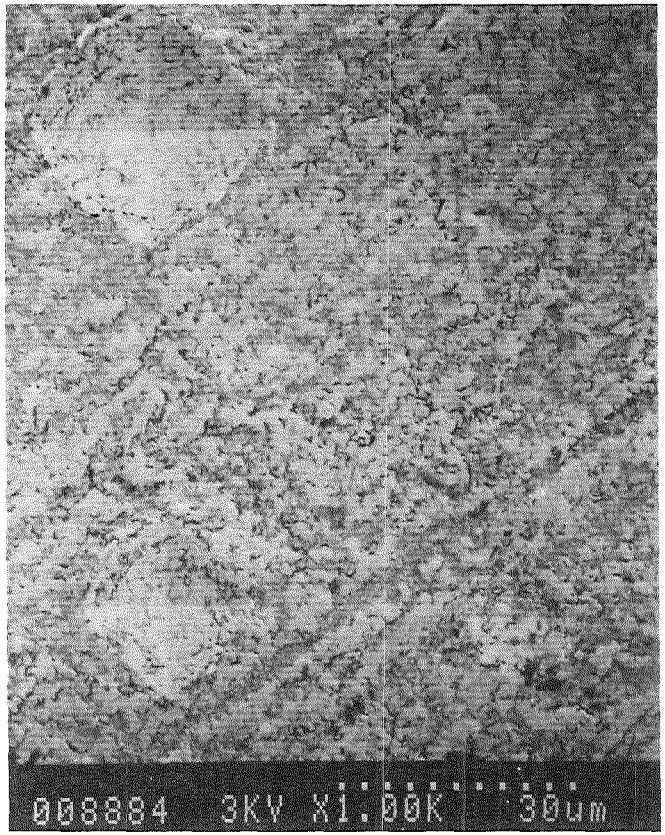

BERYLLIUM / SILVER

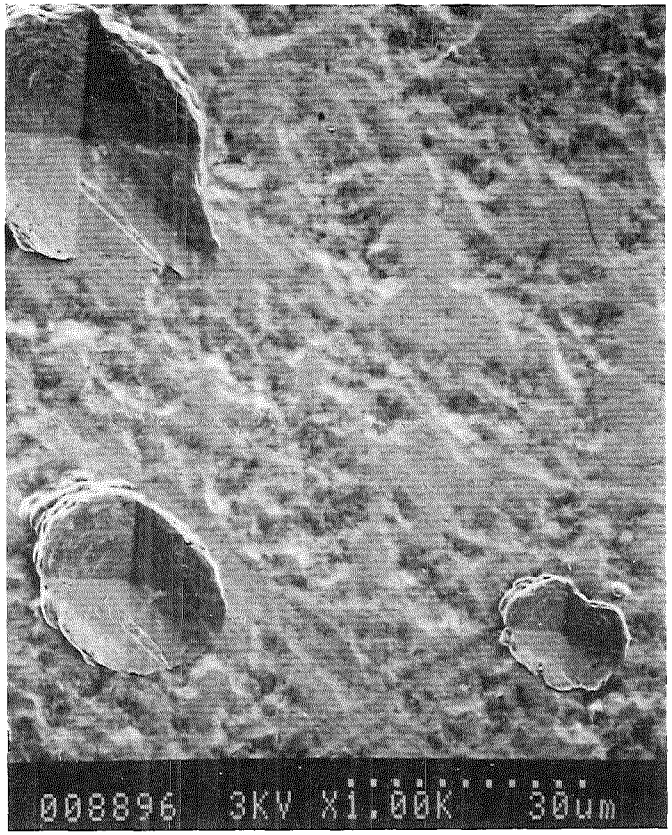

COPPER / SILVER

FIG 7 : ATOMIC FORCE MICROSCOPE SCAN OF SILVER COAT ON COPPER

PERSPECTIVE VIEW

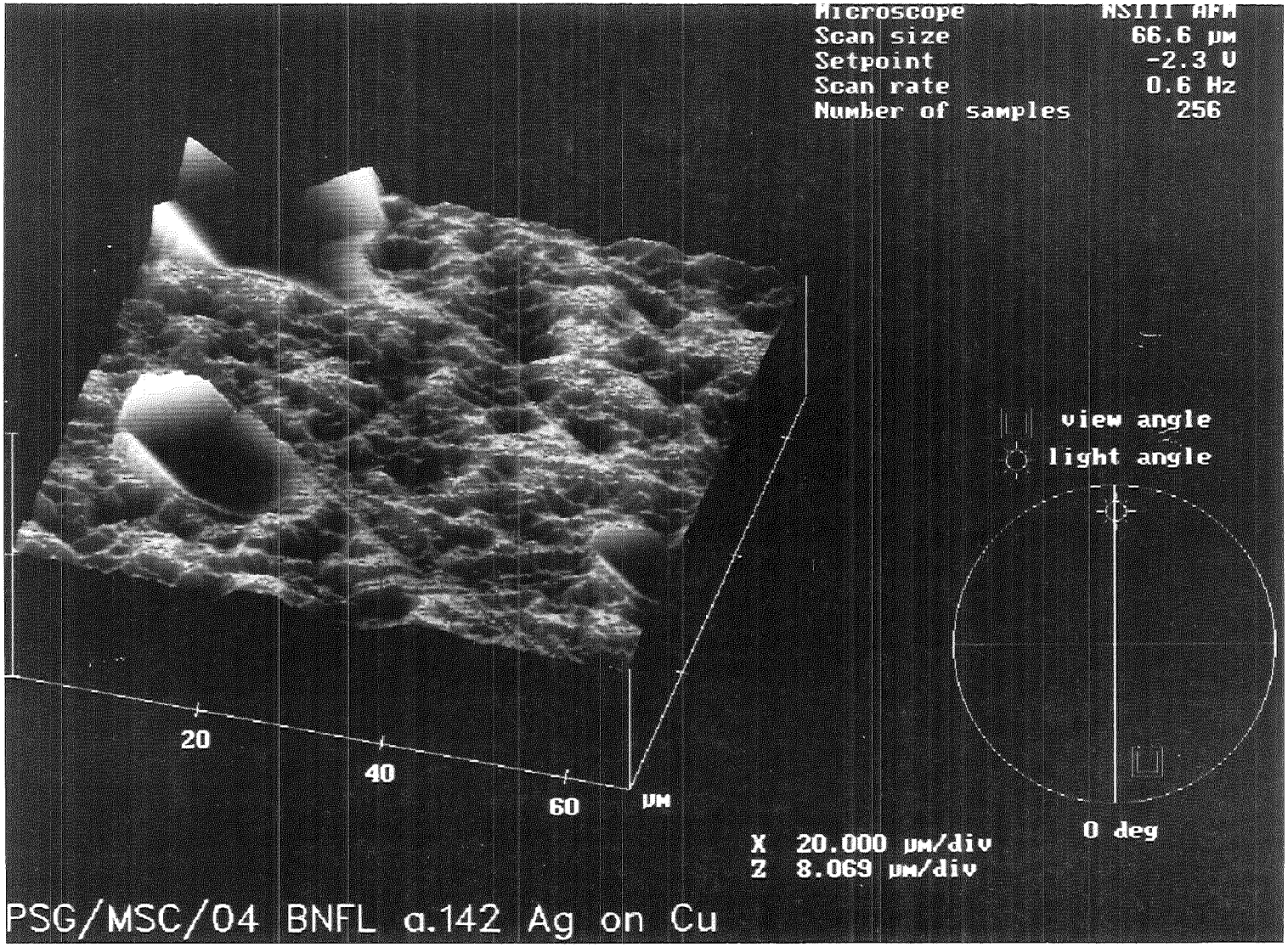

FIG 8 : ATOMIC FORCE MICROSCOPE SCAN OF SILVER COAT ON COPPER

ROUGHNESS MEASUREMENT

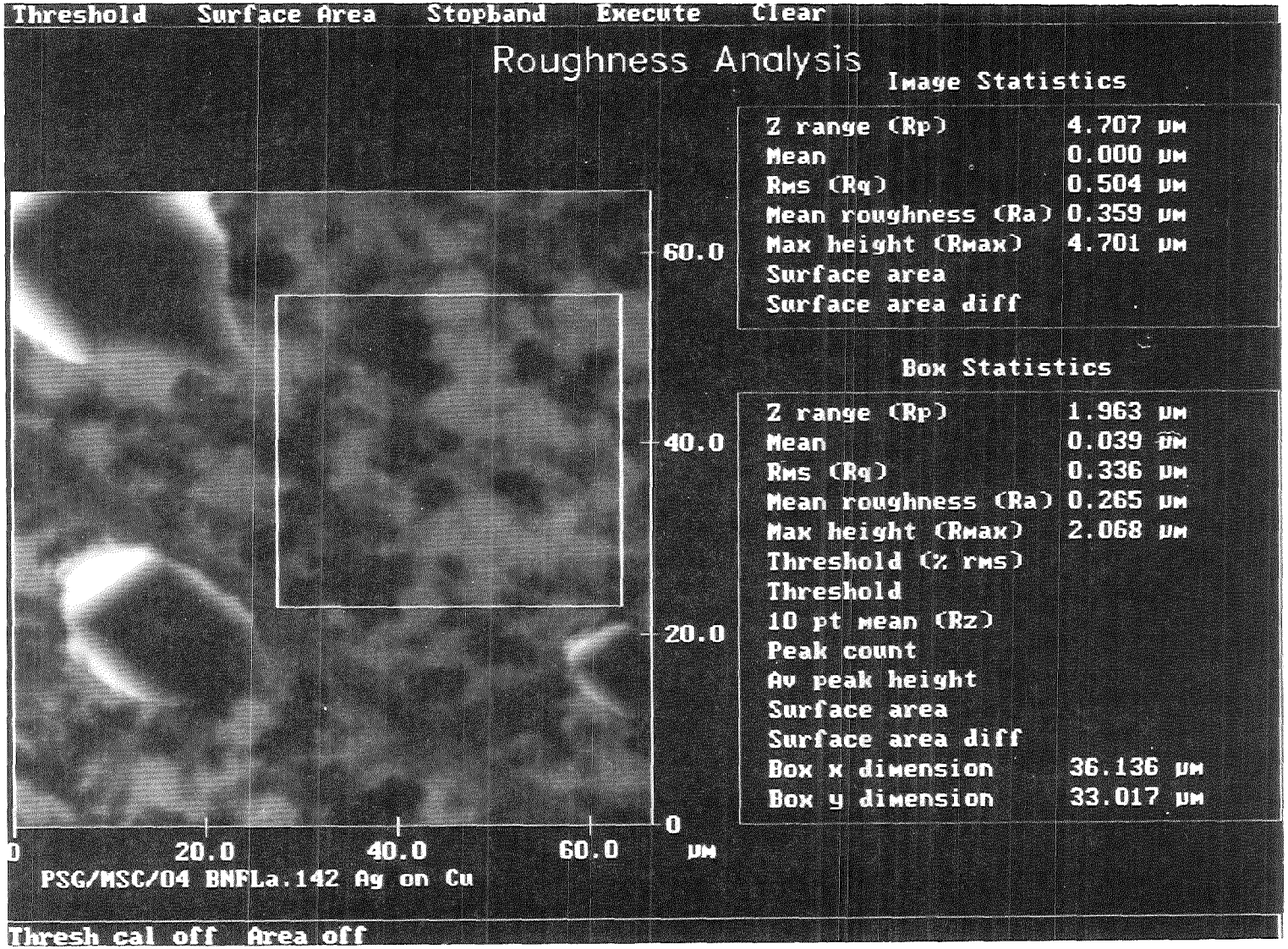

FIG 9 : COUPONS AFTER HIPPING

METALLOGRAPHIC CROSS SECTIONS VIEWED OPTICALLY AT X500

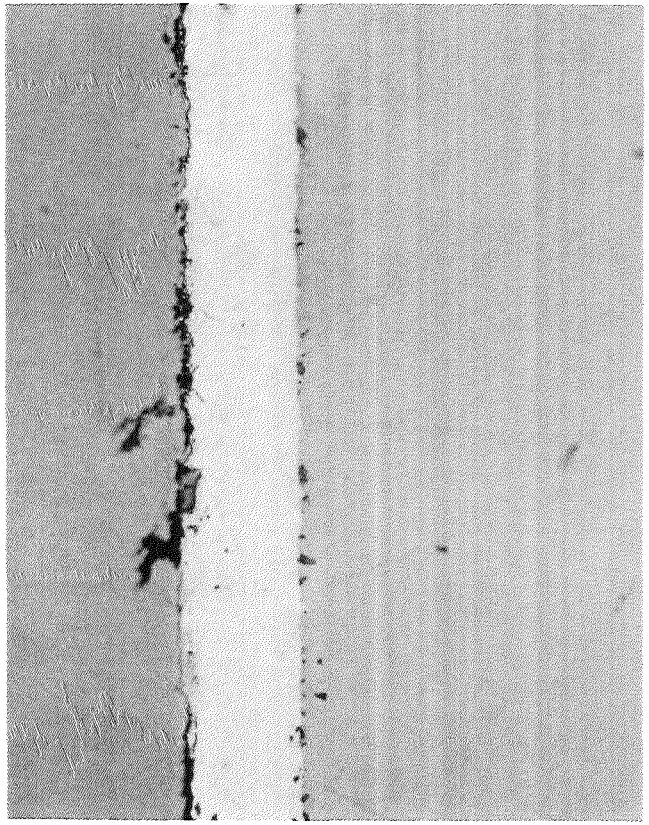

BERYLLIUM / SILVER / COPPER

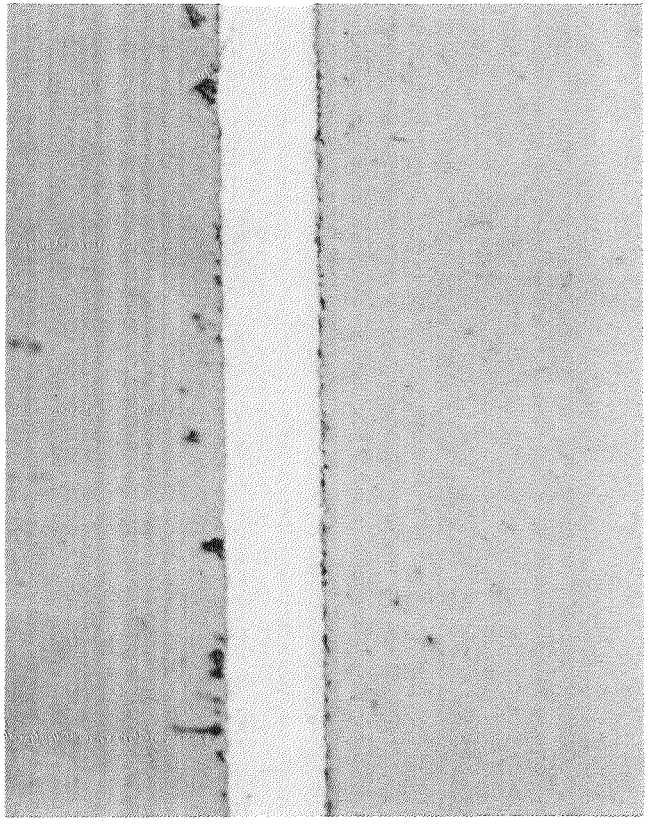

BERYLLIUM / SILVER / VANADIUM

FIG 10 : Be / V AFTER SHEAR TEST

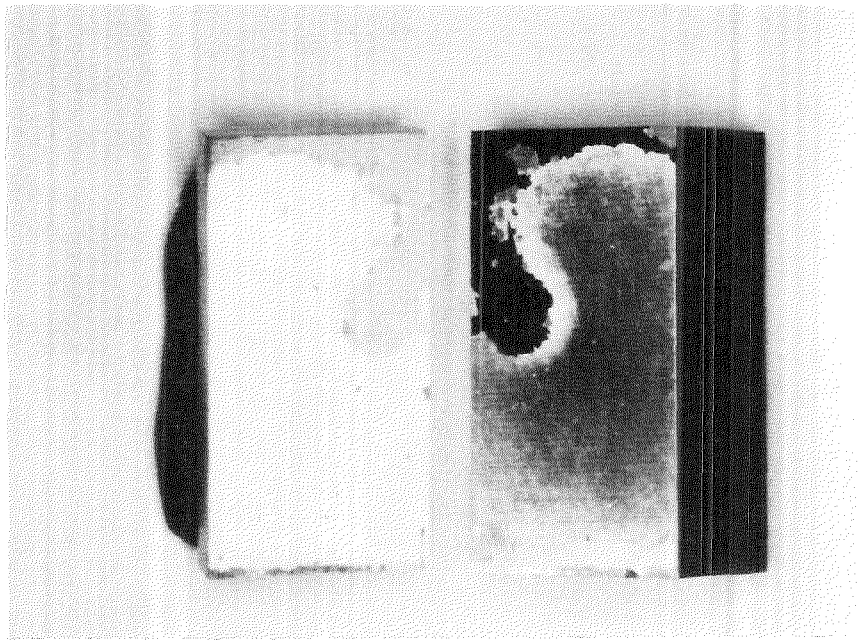

Be-V #1

FIG 11 : L V SEM MICROGRAPHS OF FRACTURE SURFACES

Be / V SAMPLE

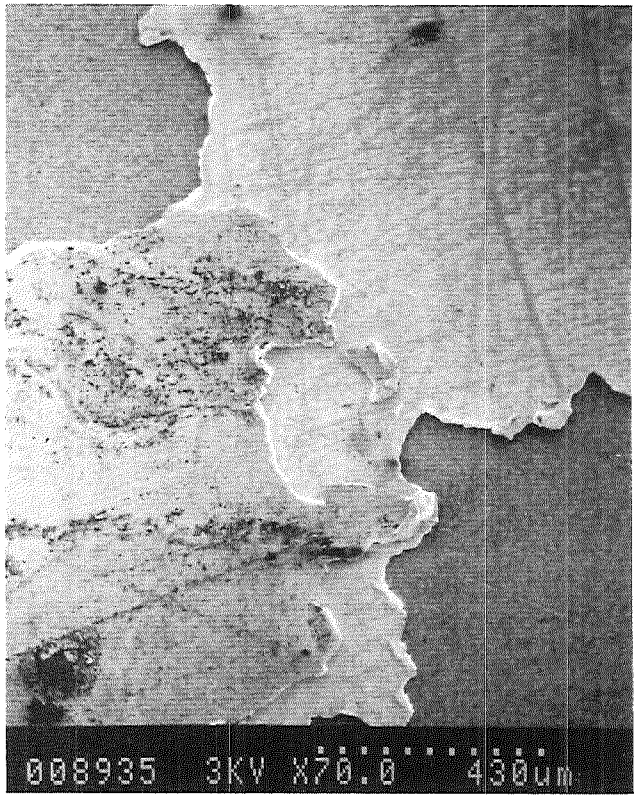

FRACTURE AT ALL THREE INTERFACES

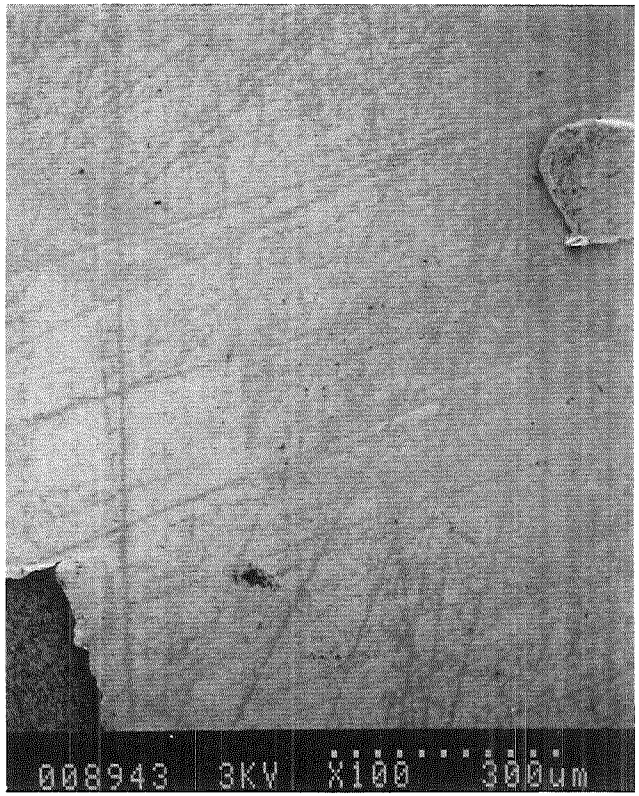

Ag / Ag INTERFACE

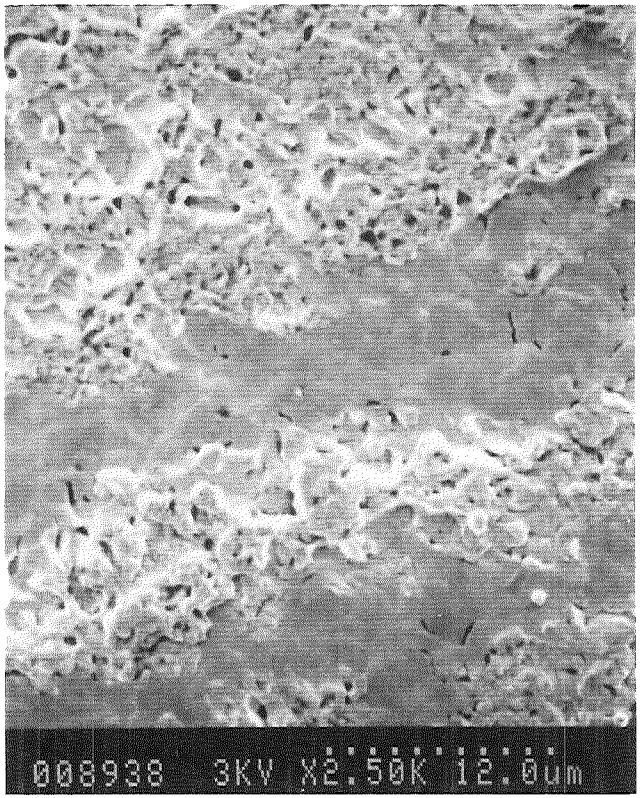

Ag INTERFACE SHOWING SIGNS OF OXIDATION

FIG 12 : Be / Cu AFTER SHEAR TEST

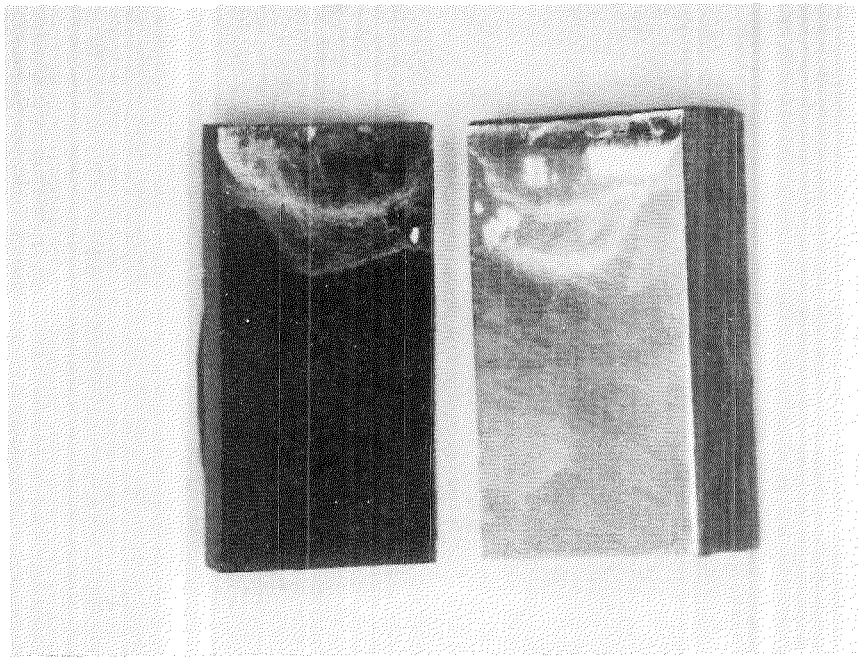

Be-Cu # 1

FIG 13 : L V SEM MICROGRAPHS OF FRACTURE SURFACES

Be / Cu SAMPLE

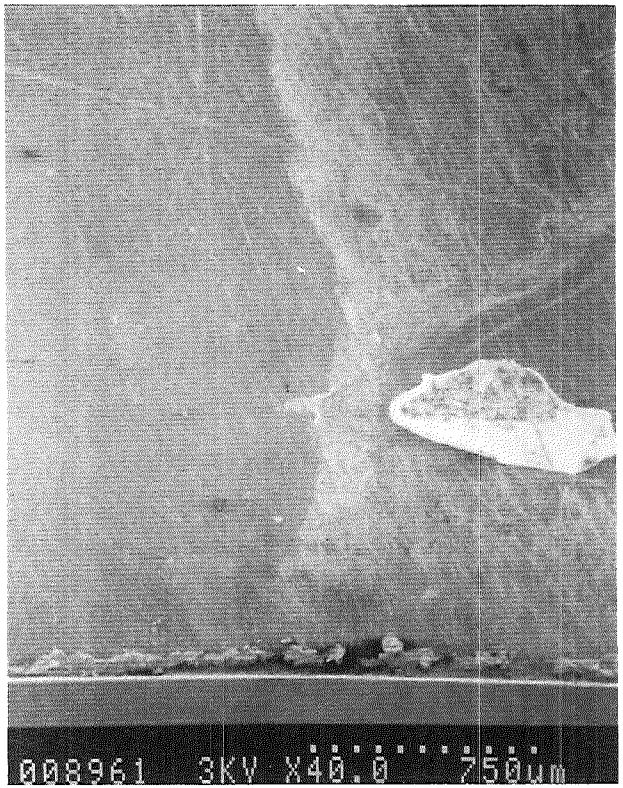

Be SURFACE SHOWING THREE REGIONS

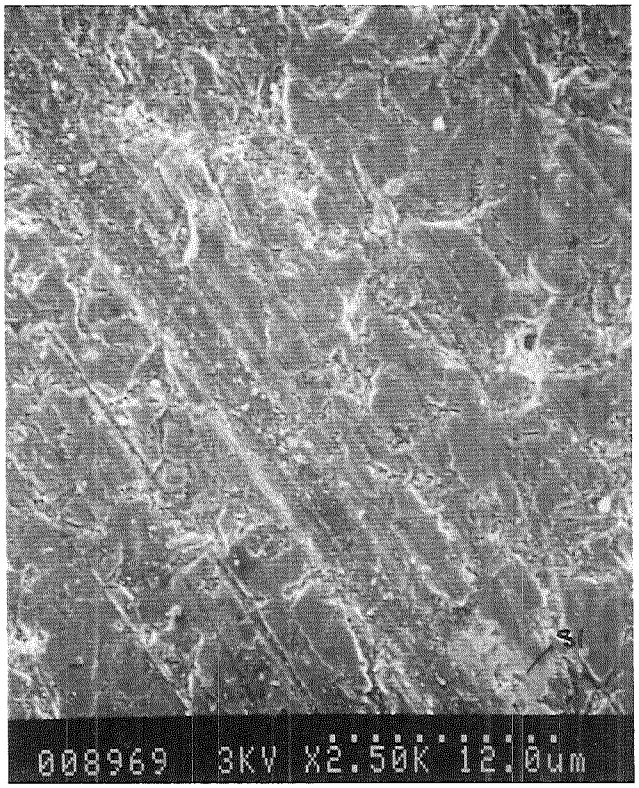

Be SURFACE

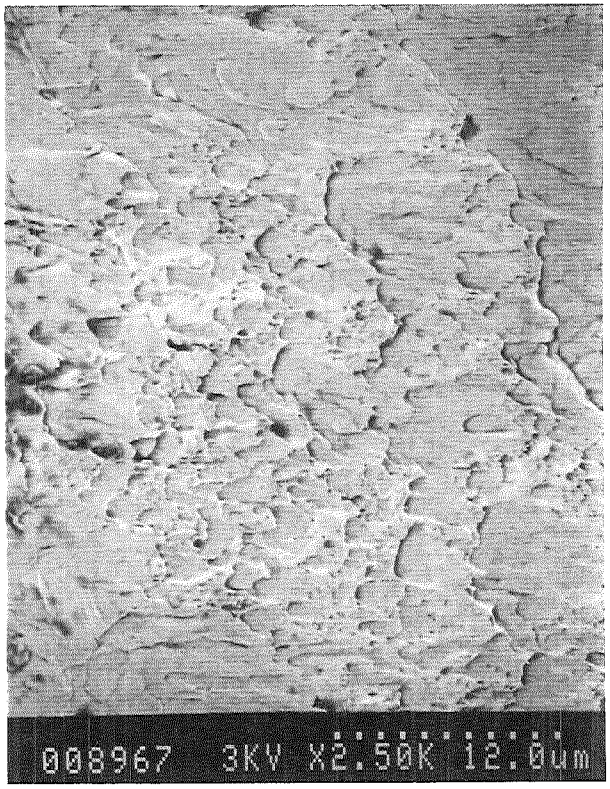

DUCTILE FAILURE IN SILVER INTERLAYER

The NET Team

N/R/3300/8/A
2nd October 1993

The Feasibility of Beryllium as Structural Material for the ITER Plasma-Facing Components (PFC)

G. Vieider, A. Cardella, H. Gorenflo

IEA Workshop on Beryllium for Fusion Applications
Karlsruhe, 4th - 5th October 1993

Abstract

Be as plasma-facing armour has attractive features including excellent plasma compatibility, no T-retention via co-deposition and the potential for in-situ repair via plasma spraying. In order to avoid the bonding of the Be-armour to a heatsink structure in e.g., Cu-alloys, the ITER Joint Central Team (JCT) proposed for the divertor tubular elements with monolithic Be, both as plasma-facing and structural material. The analysis of these Be-tubes with 5 mm wall thickness at a heat load of 5 MW/m^2 showed that even for the most favourable assumptions thermal stresses exceed by far the allowed values according to design codes. Damage by neutrons and disruptions would worsen further the case for Be as monolithic plasma-facing and structural material. For PFC at heat flux significantly above 1 MW/m^2 it appears evident that Be should be used merely as armour bonded to a suitable structural material as heatsink.

1. Background

Be as plasma facing armour has attractive features compared to C based on JET experience [1]:

- improved plasma performance
  - no density limit disruptions
  - less violent disruptions
  - strong oxygen getter
- no T-retention due to co-deposition
- the potential for in-situ repair via plasma spraying

Bonding of Be-armour onto heat sink structures (e.g. Cu-alloys) is a critical issue - in particular concerning reliability. Hence, for maximum simplicity and reliability, the ITER Joint Central Team (JCT) proposed for the divertor:

- about 2 m long tubular elements acc. Fig. 1 with 5 mm thick, monolithic Be both as plasma-facing and structural material [1]

- major R&D tasks on the development of
  - ductile Be [2]
  - manufacture of Be-divertor elements [3]

In view of the importance of this monolithic Be divertor design for the R & D program, an assessment of the basic feasibility of this component was performed.

2. Analysis of the JCT Tubular Be Divertor Design

2.1 Thermo-mechanical analysis at 5 MW/m^2, 5 mm thick Be

Source	Coolant	Peak Be Temp. °C	Peak Be, von Mises - Therm. Stress, MPa
NET Fig. 2 - 6 acc. to [4] A. Cardella H. Gorenflo	He 300 °C, 20 MPa 100 m/s	865	920 (free, 30 cm bending) 2200 (no bending)
	H_2O 250°C, 5 MPa 8 m/s	~560	~1240 (no bending)
JAERI acc. to [5] M. Akiba	He 300°C	840	~1300
McDonnell Douglas acc. to [6] F. Williams	He 150°C 20 MPa ~150 m/s	650	524 (3D-free, 30 cm bending) 1960 (3D-no end bending)

The table summarizes the main results by several ITER home teams:

- for linear elastic analysis at 5 MW/m^2 steady-state one-sided heat flux

- bending restriction by supports is required for the 2 m long tube to avoid large deformations and large electro-magnetic stresses

- He-cooling with realistic assumptions requires ~100 MW pumping power and results in unacceptable peak temperatures and peak stresses.

- water cooling due to better heat transfer would lead to significantly lower temperatures and stresses.

It should be noted that similar results were obtained by the JCT in a parallel study [7].

2.2 Allowed Thermal Stresses and Heat Fluxes

The allowed thermal stresses σ_T are limited according to design codes such as ASME or RCC-MR assuming a ductile material:

- By $\sigma_T + \sigma_P \leq 3$ Sm to avoid progressive deformation, where σ_P is the primary stress and 3 Sm (for Be) is the ultimate tensile strength depending on product quality and temperature, typically [8, 9]:

200°C	300 - 500 MPa
400°C	200 - 350 MPa
600°C	100 - 200 MPa
800°C	30 - 60 MPa

- By the allowed fatigue stress range, which should have a margin against failure of at least a factor 2 on stresses and a factor 20 on number of cycles. This allowed fatigue stress is estimated for a target life of 10^4 cycles to 100 - 220 MPa at room temperature depending on product quality and notch effects on the basis of scarce data - see Fig. 7 [9, 10]. At higher temperatures the fatigue strength should be reduced proportional to tensile strength, i.e. by about 50 % at 500°C.

Consequently, for a maximum allowed thermal stress of ~150 MPa the allowed heat flux on the Be-divertor tubes should be:

~0.8 MW/m^2	with water cooling
~0.4 MW/m^2	with He cooling

3. Discussion and Conclusions

- Be as ~5 mm thick monolithic structural material in tubular PFCs is shown to be feasible only at heat fluxes < 1 MW/m^2 based on thermal stress considerations and the usual design code rules, which include safety margins against failures. Cooling with He would only permit about half of the heat flux allowed for water despite extreme pressure and pumping power required for He.

- These results for ITER differ from basic studies at JET which "indicate that a plasma-facing component made of massive Be could readily sustain up to 5 MW/m^2 and possibly up to 10 MW/m^2 for a small number of cycles and in the absence of creep and embrittlement" [11]. This difference is explained by:
  - the safety margins according to design codes assumed for ITER in view of requirements for licensing and reliability.
  - the need to restrict bending via supports for the long ITER divertor tube, which results in 2 - 4 times higher stresses than for a short, free bending component.
  - the short pulses (mainly 1 -2 sec.) and the low number of cycles (~10^3) in JET Be-testing.

- The case for Be as PFC-structure material for ITER is further worsened considering damage from:
  - neutrons: rapid loss of ductility at < 1 dpa
  - disruptions: melting (~0.1 mm/event) followed by cracking and electromagnetic loads.

- For high-heat flux PFCs at significantly higher heat loads than 1 MW/m^2 Be can only be used as small armour tiles bonded to a heat sink structure, e.g. in Cu-alloys. Hence, the ITER R & D plans should be adjusted by giving:
  - more emphasis on bonding of Be to substrates,
  - less emphasis on development of "ductile Be".

4. References

[1] ITER Director: *ITER Divertor Design Developments*, 3rd ITER TAC Meeting, Naka, 9th - 11th Sept. 1993

[2] ITER JCT: *Beryllium Development and Study of Manufacturing Techniques*, Draft Request DPI-1, Garching, 28th June 1993

[3] ITER JCT: *Development, Manufacture and Test of High-Heat Flux Elements*, Draft Request DPI-2, Garching 28th June 1993

[4] A. Cardella, H. Gorenflo, G. Vieider: *Thermo-mechanical Analysis of a Be Tubular Divertor Module*, NET Note N/I/3330/14/A, 12th July 1993

[5] M. Akiba: *Simple Calculation Results on JCT Divertor Element Design*, JAERI, Naka, July 1993

[6] F. R. Williams, C. C. Brimer: *Thermal and Structural Analysis of Be-Divertor Tube*, McDonnell Douglas Datafax, 21st July 1993

[7] S. Chiocchio, B. Esser: *Evaluation of the Thermal Stresses in the Divertor Armour Pipe*, ITER-JCT Garching, 9th July 1993

[8] H. Kamura et al: *Beryllium Database for In-pile Mock-up Tests*, JEARI-M 92-190, Naka, Nov. 1992

[9] D. R. Floyd, J. N. Lowe et al: *Beryllium Science and Technology*, Vol. 2, Plenum Press, New York, 1979

[10] D. V. Miley: *Bending Fatigue of Ingot Source Beryllium*, Rocky Flat Project - 1534, Oct. 1970

[11] E. B. Deknis et al: *Beryllium High-Heat Flux Tests at JET*, Be-Workshop at KfK, Oct. 1993

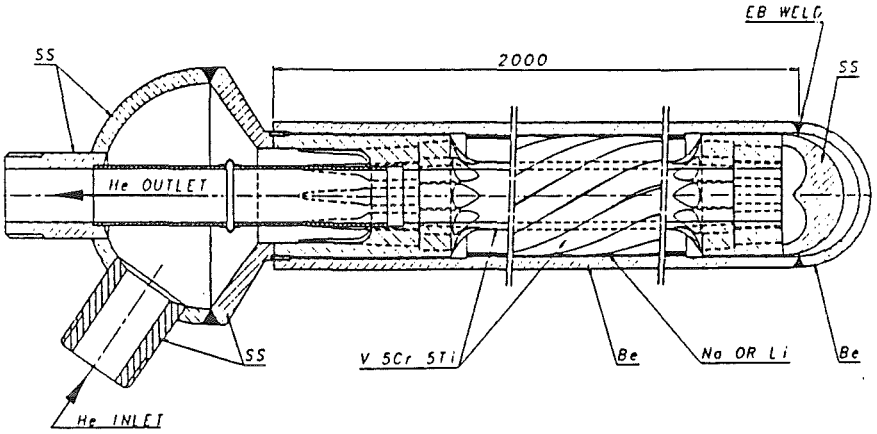

PROTOTYPE COOLING ELEMENT

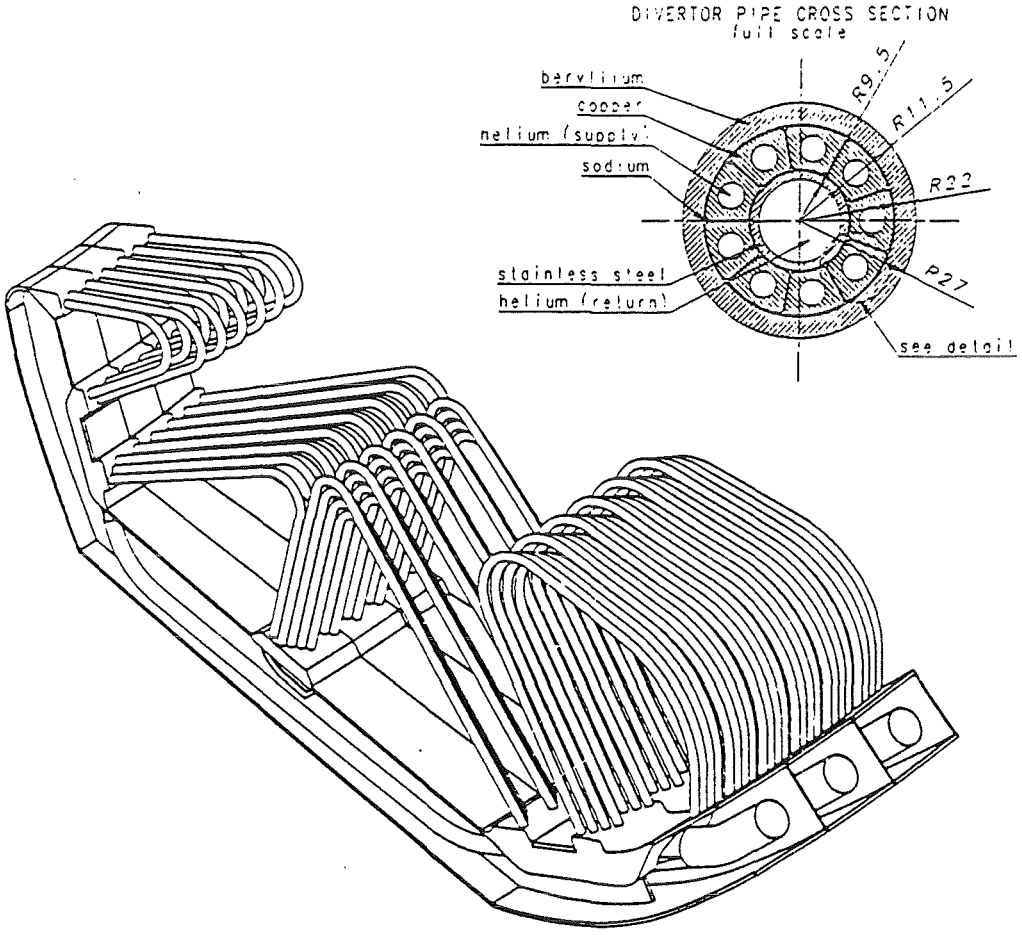

Fig. 1 Divertor Design Proposed by ITER-JCT

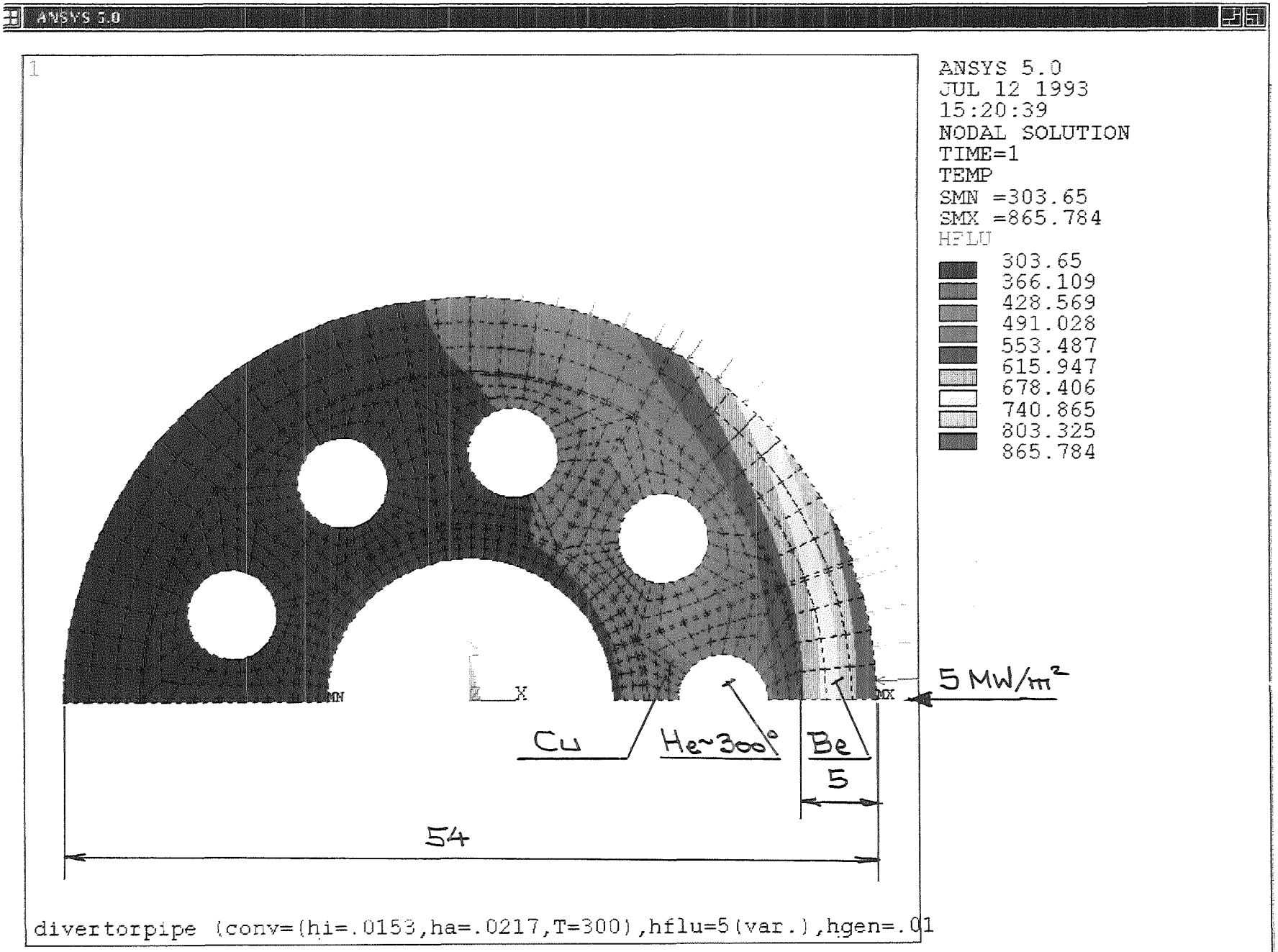

Fig. 2 Temperatures in Be-divertor pipe at 5 MW/m^2 cooled by 300°C He

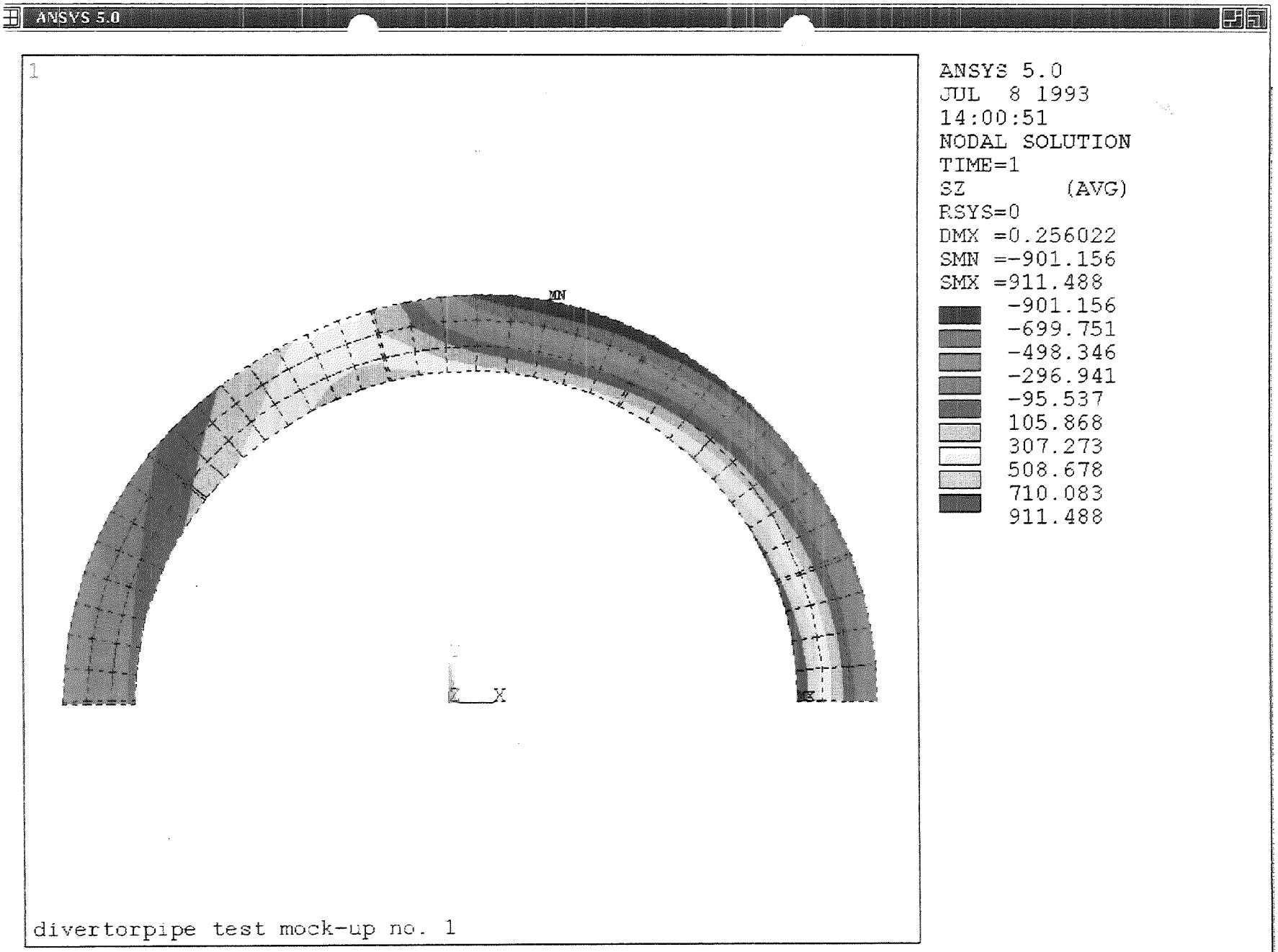

Fig. 3 Axial thermal stresses in He-cooled Be-divertor pipe at 5 MW/m^2 with free bending (~30 cm)

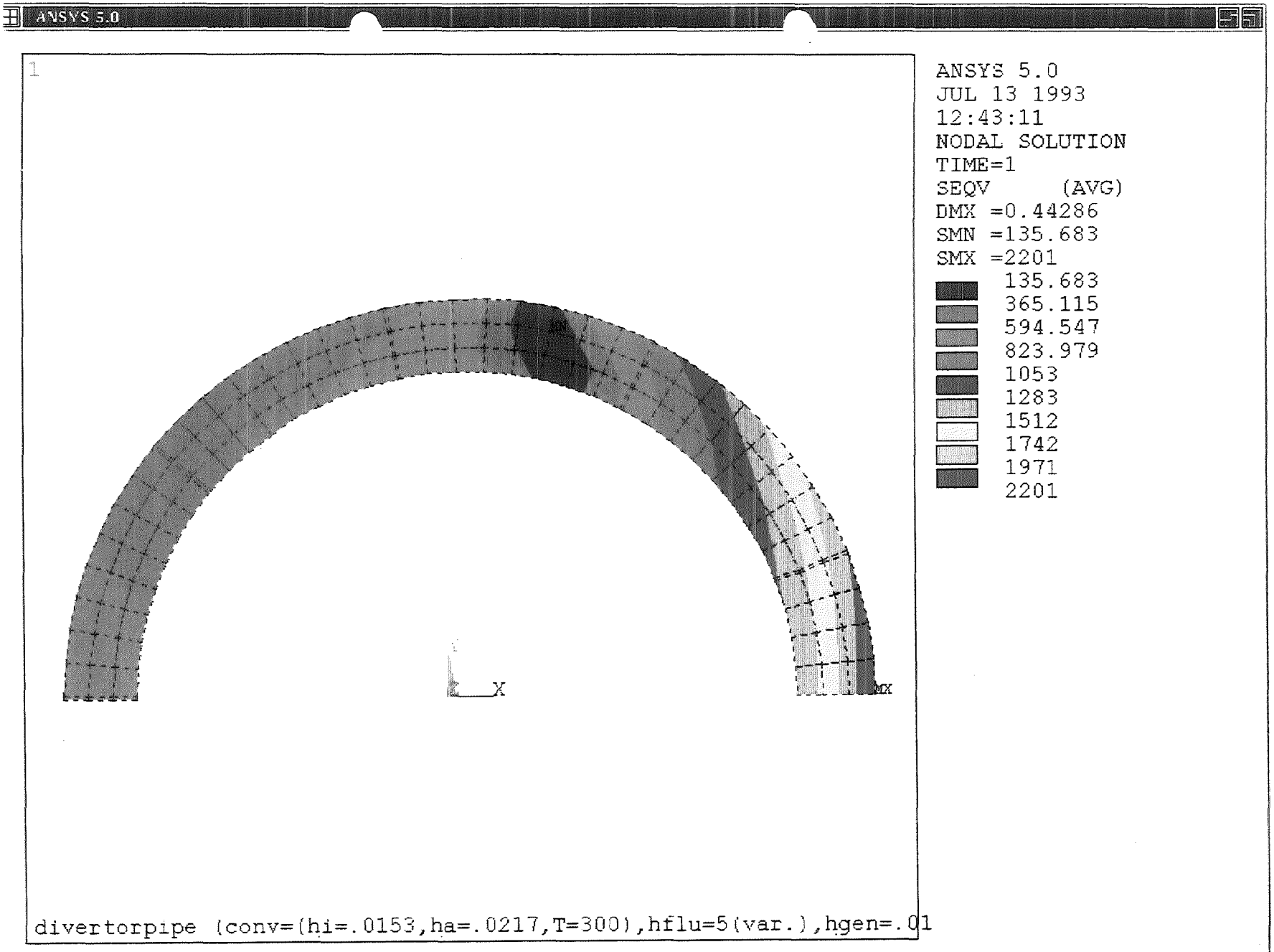

Fig. 4 Von Mises thermal stresses in He-cooled Be-divertor pipe at 5 MW/m^2 with restrained bending

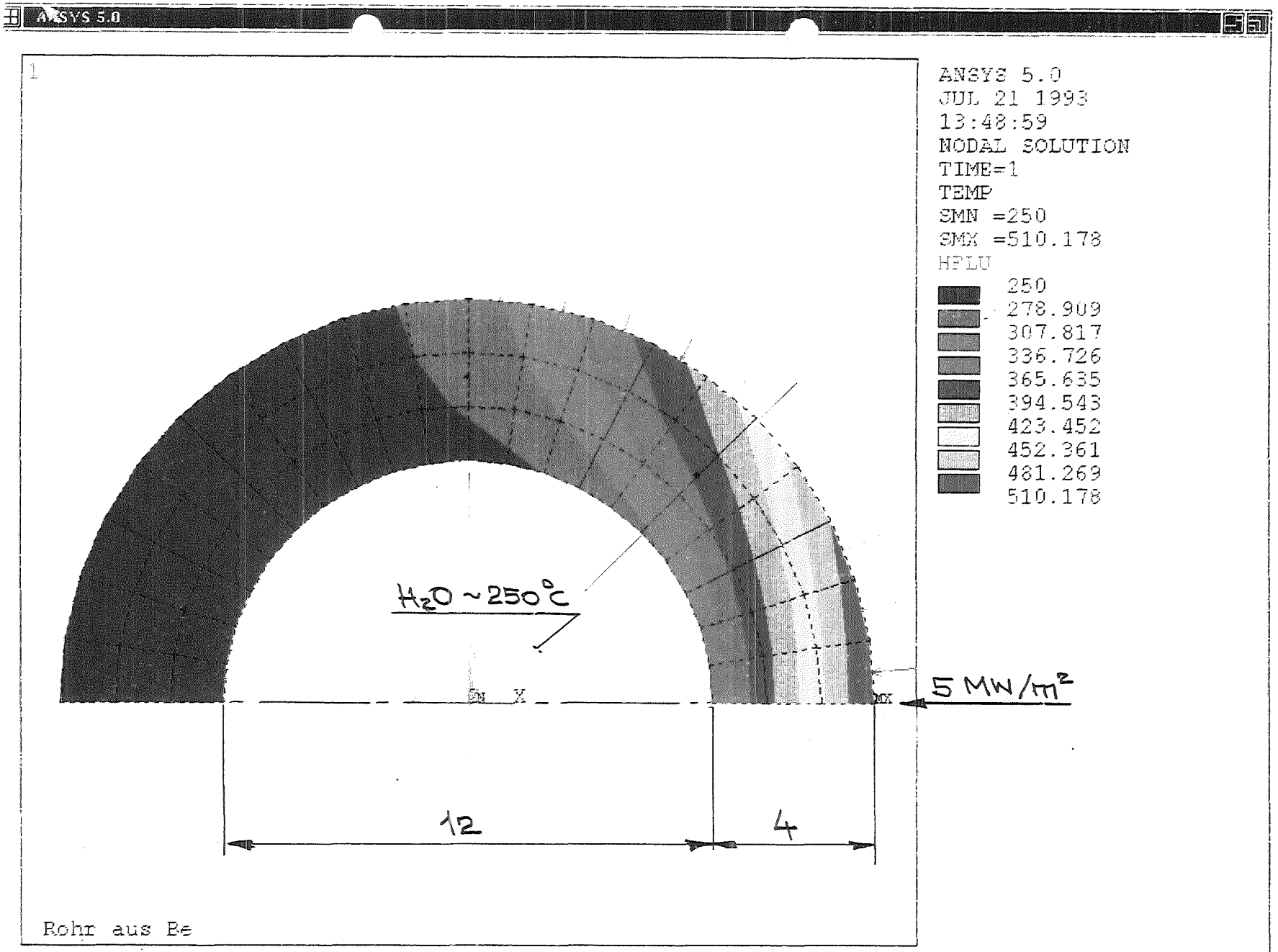

Fig. 5 Temperatures in Be-divertor pipe at 5 MW/m^2 cooled by 250°C water

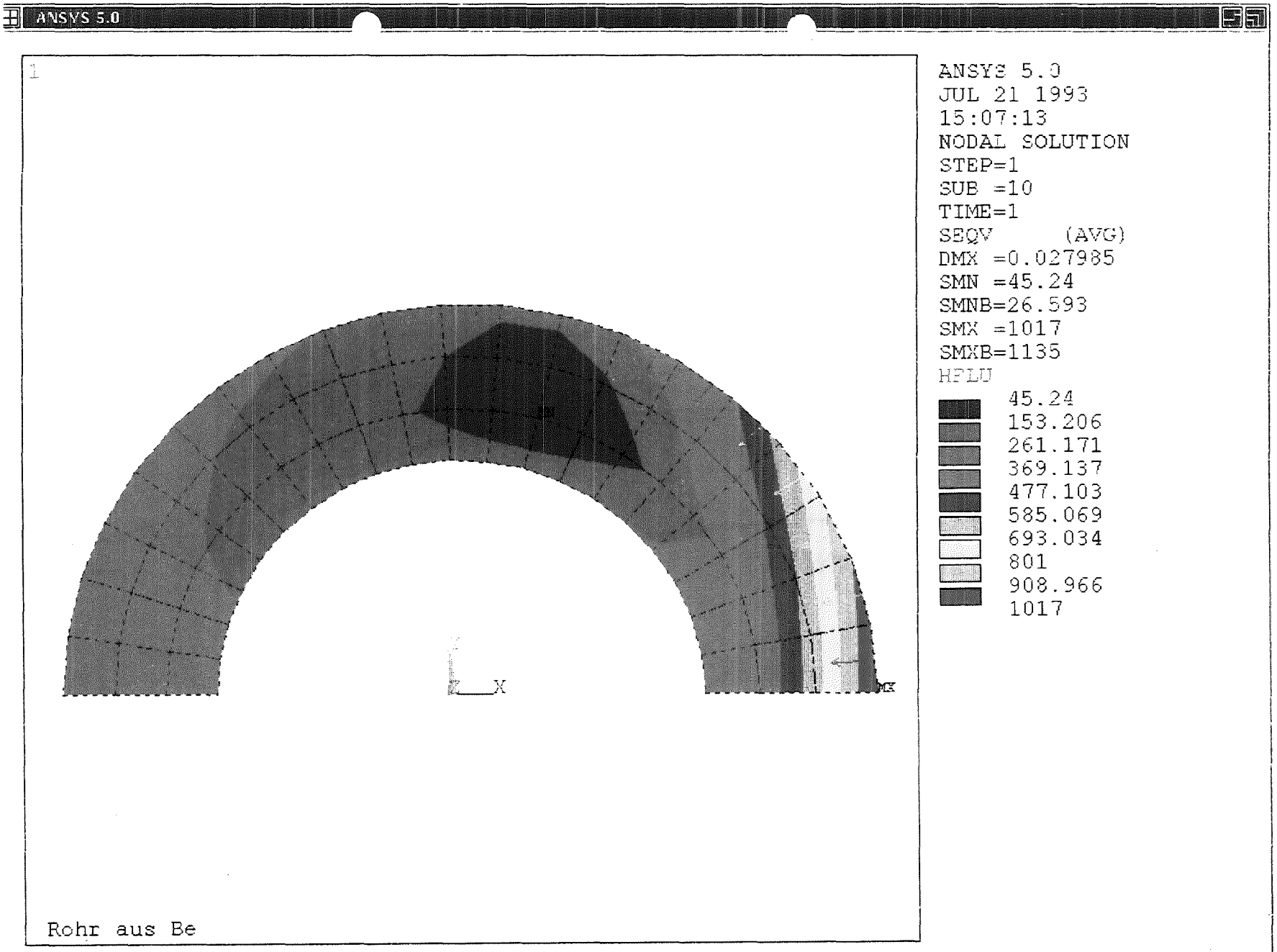

Fig. 6 Von Mises thermal stresses in water-cooled Be-divertor pipe at 5 MW/m^2 with restrained bending

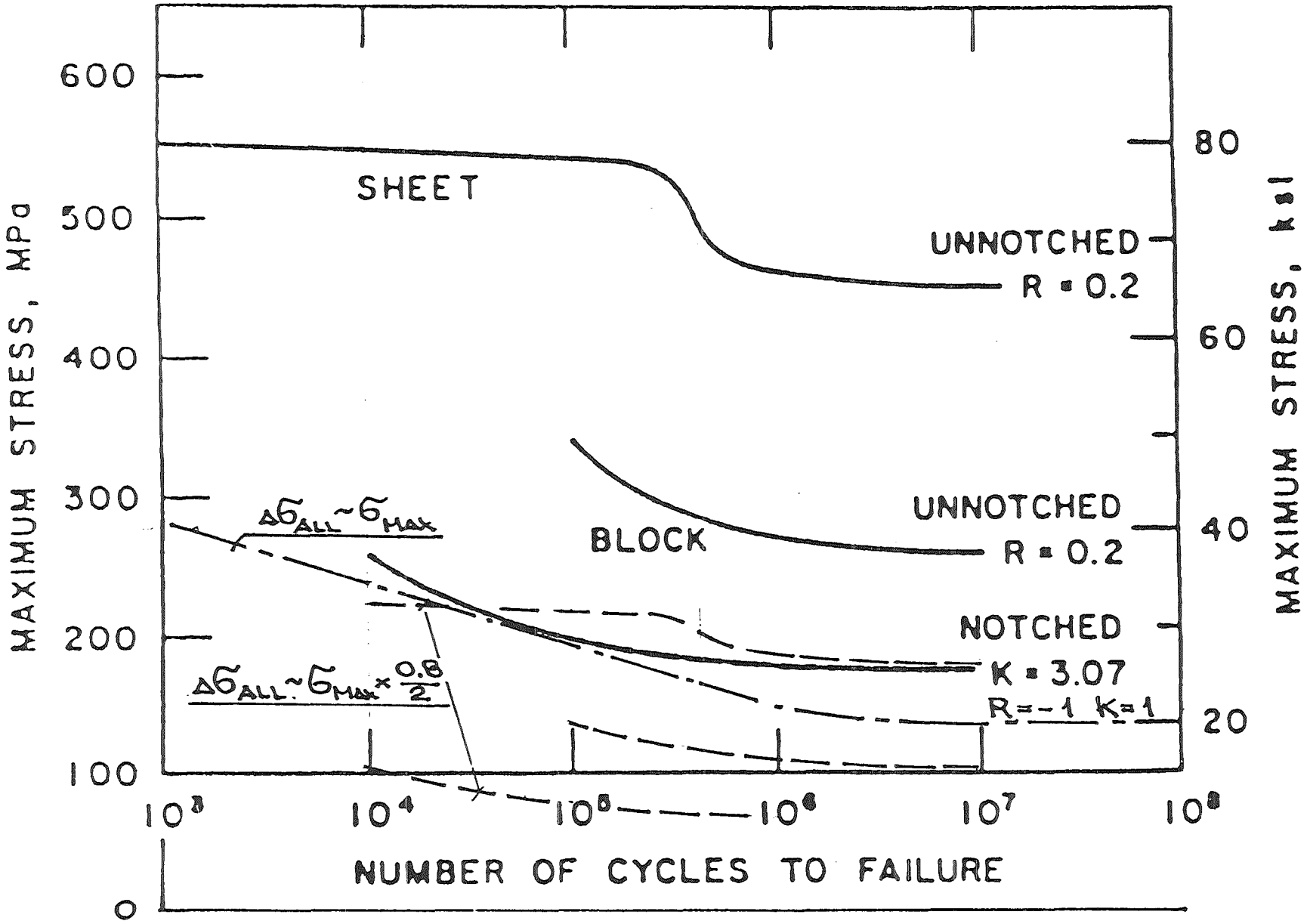

FIG 7

Fatigue curves for normal-purity beryllium block and sheet at room temperature. R is the ratio of minimum stress to maximum stress, and K is the stress concentration factor [9,10].

Laser desorption and depth profiling study of hydrogen and deuterium implanted in beryllium

D. Kéroack, F. Schiettekatte, B. Terreault and G.G. Ross
INRS-Énergie et matériaux, Université du Québec,
C.P. 1020, Varennes, Québec, Canada J3X 1S2

Pulsed laser desorption was used to investigate the reemission of deuterium implanted in beryllium. The amount of H_2 or D_2 molecules released and the evolution of the H and D depth profiles as a function of the laser energy density was measured on samples with different implantation energies and doses. Numerical modelling of our results indicates that detrapping and diffusion are the limiting processes. At low fluence the data are best fitted with second order detrapping with a trap energy of 1.7 ± 0.1 eV and the effective diffusion coefficient is described by the equation $D = (8 \pm 1) \times 10^{-4} \exp(-0.32 \pm .02 \text{ eV/kT}) \text{ cm}^2/\text{s}$. At high fluence the detrapping energy is ≤1 eV/molecule and extremely rapid migration has to be considered. The transition between these two regimes corresponds approximatively to the fluence for which blistering becomes detectable.

Introduction

The behaviour of hydrogen isotopes in beryllium, a prime candidate as plasma facing material in fusion reactors, is of growing interest. The utilisation of Be in the JET tokamak demonstrated good wall pumping properties [1-3]. The knowledge of the diffusion coefficient, D, the recombination coefficient, K, and the detrapping energy, E_B, the main parameters governing recycling properties of a material, is of crucial importance. The reported values for diffusivity vary widely [4-7]. The influence of beryllium oxide on the sample surface is critical [4,5] and careful analysis is mandatory. The experiments of Abramov *et al.* [4] on deuterium permeation through beryllium provide a diffusion coefficient of $6.7 \times 10^{-5} \exp(-0.29/\text{kT}) \text{ cm}^2/\text{s}$ for high purity beryllium, in a temperature range limited to 620 K to 775 K. Comparison with data gathered at room temperature or at high temperature like that of a tokamak limiter working temperature is not straightforward. In thermal desorption, Wampler [7] found two release stages, one around 675 K and a second one around 400 K in samples with D/Be concentrations from 0.05-0.1 up to saturation (D/Be ≈ 0.3), corresponding to trap energies of 1.8 eV and 1.0 eV respectively. Causey *et al.* [8,9] found a good agreement between their results on tritium retention and the DIFFUSE model using the activation energies of Wampler and the diffusivity of Jones [6].

In recent years, laser flash desorption has been applied [10] to near-surface implanted ions, providing some important advantages (negligible desorption from sample bulk and none from sample holder, desorption time negligible compared to pumping or wall degassing time). But the most important features come from the short heating time (e.g. 10 ns) followed by the rapid quench (≤100 ns) [11]. Consequently, the thermodynamic properties can be investigated in different conditions than in slow annealing, favoring the kinetics of the process against the energetics (which dominate under equilibrium conditions). A quantitative kinetic simulation of the desorption process [11] can be used to deduce its fundamental parameters. The simulations showed that depth profiling of partially desorbed samples provides essential information. For instance, in this way, limitation by diffusion would be directly manifested by profile broadening,

and not only inferred from a mathematical fit. Similarly, a surface barrier would give rise to a flat and very wide profile, and retrapping by defects to a shift of the peak of the profile.

We investigated hydrogen and deuterium desorption from beryllium and studied the profile modification after pulsed-laser desorption at medium to high fluences using a laser desorption technique developed in our laboratoty [12].

Experiment

Samples of 99.4 % pure beryllium (Brush-Wellmann specification PF-60) have been polished by means of a SiO_2 suspension with a finish of 0.04 μm. Rutherford backscattering analysis showed the presence of $\approx 1 \times 10^{16}$ O atoms/cm^2 at the surface (equivalent BeO thickness = 1.4 nm). After ultrasonic cleaning in CCl_4, acetone and methanol, the samples were introduced into the implantation chamber where the base pressure was 5×10^{-8} Torr. They were implanted at room temperature with hydrogen or deuterium ions at energies varying from 0.5 keV to 5.0 keV per atom and at mean concentration ranging form 2 % up to 20 %. From the nuclear profiling analysis [13], the mean implant depth is known and ranges from 19 nm at 0.5 keV to approximately 100 nm at 5.0 keV.

The samples were transferred in air from the implantation chamber to the desorption chamber whose base pressure is $\leq 10^{-6}$ Pa. The laser desorption technique has been described in detail earlier [12]. By removing neutral density filters, the samples were submitted to a series of increasing energy laser shots from a Q-switched ruby laser (694 nm and 25 ns FWHM light pulses) up to 3 J/cm^2 on a average 2.5 mm^2 surface. Most of the laser shots were directed to different locations on the substrate, but for some experiments, successive shots of increasing energy were accumulated on the same spot (hereafter named "ramp"). The energy uniformity of the laser beam is better than 2 % through careful design of the optics. The incident energy as well as the specularly reflected energy are monitored for each shot with good precision (±5 %). The reflectivity is found to be constant at 44 % for samples implanted at concentrations below 15 % H (or D)/Be, close to the reported nominal value for beryllium at the ruby laser wavelength, ranging form 44 % to 54 % depending on surface preparation [14]. Since our setup is not optimized for reflectivity measurements the agreement is satisfactory and the stability of the reflectance during the experiment demonstrated that no extensive blistering occurred during the desorption. For the samples with D/Be concentrations above 15 %, the reflectivity is low (~35 %) but increases up to a value near 46 % when the laser energy reaches 1.2 /cm^2, at which point the surface is believed to have melted (see below). Small blisters (~1 μm) can be seen by optical microscopy on the surface of samples with D/Be mean concentrations higher than 15 %. Those surfaces, as we saw, have a lower reflectivity due to blisters enhancing the diffuse reflection of light.

Depth profiling was performed on irradiated and non-irradiated zones by means of the ERD **ExB** technique [15]. The 350 keV probing beam was ^{4}He for H profiling and ^{3}He for D profiling. Since the ion beam can also induce desorption, the fluence was limited to $\approx 2.5 \times 10^{15}$ He/cm^2. The profiles were corrected for the depth varying resolution by means of a deconvolution procedure which uses constrained B-spline and delta-function [16].

Results and discussion

The advantage of the laser desorption technique over classic thermal ramp desorption is the possibility of exploring short time-scale non-equilibrium situations, e.g. high hydrogen concentrations at high temperature. The evolution of the implanted species in the material is computed as a function of time and space and is compared to the experimental data. The computations carried out with the finite difference code DTRLAS [11] require the optical and thermal properties of the material, which were found in the literature. At each time step Δt and for each layer of thickness Δx, the temperature is evaluated and the deuterium evolution is calculated assuming that the diffusion coefficient can be modeled by:

$$D = D_o \exp(-E_D / kT) , \quad (1)$$

and detrapping of order n by the equation:

$$\partial C_T / \partial t = -\nu V^{n-1} C_T^n \quad (2)$$

where ν is the attempt frequency given by

$$\nu = \nu_o \exp(-E_B / kT) , \quad (3)$$

where V is a reaction volume, E_B the trap activation energy and C_T the trapped concentration. The maximum temperature attained in the first layer increases linearly with the laser energy in the case of Be and this value is reported on the graphs below as the top horizontal axis. The predicted energy at which the top layer of the sample starts melting is around 1.2 J/cm^2. At this energy, only the first layer (Δx = 10 nm) actually melts and it remains in the liquid phase for less than 20 ns. SEM analysis on a deliberately scratched sample confirms this prediction: the marks disappear for an energy density between 1.1 and 1.3 J/cm^2. Since the thermal properties of liquid beryllium and the dynamics of the liquid-solid interface are not fully included in the code, only the low energy part of the desorption data are used for diffusion and detrapping parameter fits, but calculations are performed over the whole energy ramp.

Figure 1 shows the integrated deuterium desorbed per unit area as a function of laser energy density (ramp) on five samples implanted with deuterium at 1.5 keV and at nominal concentrations of 2 % to 14 %. The computer calculations using the first degree detrapping model (dashed lines) and the second order detrapping model (solid lines) are also shown. One can see that the desorption threshold appears at a lower energy density when the nominal concentration is higher. In order to reproduce this energy shift with the first order model, the detrapping frequency or the diffusivity has to be progressively increased when the D/Be concentration increases. In the second order model only slight adjustments are needed. This is easily explained since in the second order model the detrapping frequency increases as the square of the local concentration of the implanted species (equation (2)), which leads to an apparent energy shift.

Typical parameters for the first order detrapping model are for the diffusion coefficient: D = (5±2) x10^{-4} exp(-0.32±0.02 eV/kT) cm^2/s and for the detrapping frequency ν_o= (1.0±0.5) x10^{13} s^{-1} and E_B= 1.7±0.2 eV/molecule. For the second order detrapping we found D= (8±1) x10^{-4} exp(-0.32±0.02 eV/kT) cm^2/s and for the detrapping frequency $\nu_o V$ = (1.5±0.5) x10^{-9} cm^{3}s^{-1} with E_B= 1.7±0.1 eV/molecule. The large error bars for the detrapping and the diffusion coefficients of the first order model reflect the fact that we have either to increase the detrapping energy or to decrease the diffusion coefficient when the mean deuterium concentration increases in order to reproduce the desorption data with this model.

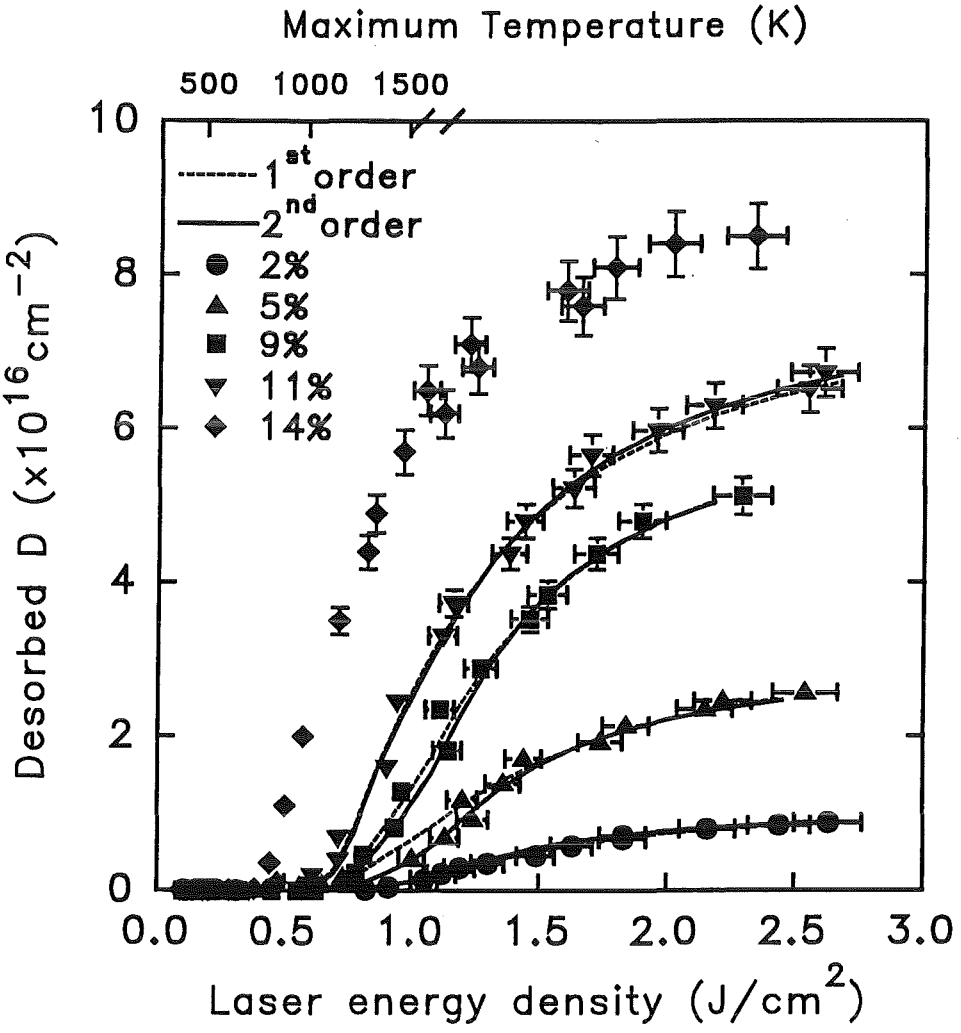

Fig. 1 Cumulative desorption as a function of laser energy for deuterium implanted at 1.5 keV. The curves represent numerical calculations (see text).

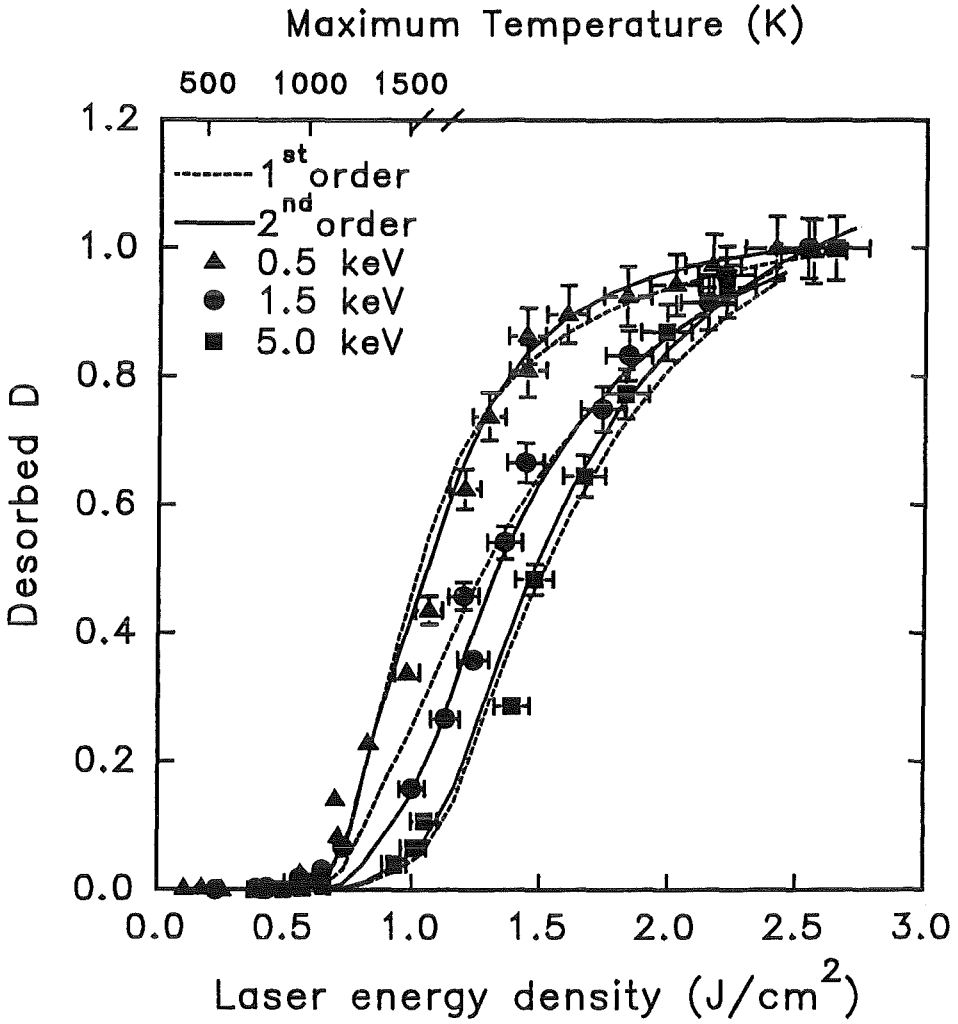

Fig. 2 Cumulative desorption as a function of laser energy for 3 samples implanted at 0.5 keV (triangles), 1.5 keV (circles) and 5.0 keV (squares) and at nominal D/Be concentration of 5 %. The curves represent numerical calculations (see text).

Our preexponential factor for diffusion is at least one order of magnitude higher than Abramov's [4] and many orders of magnitude higher than Wampler's [7]. As pointed out by Macauley-Newcombe *et al.* [5], the apparent diffusion coefficient they found was largely influenced by the BeO layer thickness on the surfaces of the samples. They have concluded that their low diffusion coefficients, similar to the values measured by Wampler, are more appropriate to the diffusion of deuterium in beryllium oxide than in beryllium.

Figure 2 shows the cumulative desorption for three samples implanted at 0.5 keV (circles), 1.5 keV (triangles) and 5.0 keV (squares) and at D/Be nominal concentrations of 5 %, normalised to the total desorption signal for each set of data. Here again, the data are best reproduced by a second order detrapping model with the same diffusion and detrapping parameters used in the preceding simulations, adjusting the initial deuterium profiles with the proper implantation mean range and variance for each ion energy. One can see that the energy threshold for deuterium desorption shifts to higher energy density when the implanted ion energy is greater. This phenomenon reflects the fact that diffusion, as well as detrapping, is a limiting process for deuterium reemission. The deuterium implanted at higher energy has to diffuse from deeper inside the sample and consequently in a diffusion limited process the laser energy required to initiate desorption has to be higher.

The saturation concentration, measured by the ERD **ExB** method, is reached for a fluence of 0.4×10^{17} at/cm^2 for both H and D implanted with an energy near 1 keV into Be. The samples implanted with fluences beyond this limit contained less H or D than just saturated samples, which suggests gas release from blister exfoliation in oversaturated samples. When D is implanted at high fluence, mean concentration $\geq$ 14 %, the desorption process begins well below the previous threshold (see figure 1) and data cannot be reproduced by computation with the above mentionned parameters. It can be reproduced however by two different models. One is a detrapping-limited model in which two traps of 1.0 and 0.8 eV (maybe actually a distribution of traps) are initially populated and the detrapped molecules instantaneously migrate to the surface and desorb (suggestive of a short-cut to the surface). The second is a diffusion-limited model with a low activation energy (0.18 eV). In this last case, simulations show that the diffusion process would transport a large part of the D atoms deeper into the bulk and so, the mean depth of the profile would be strongly shifted. Figure 3 shows the measured and the simulated D depth profiles corresponding to this experiment. It is clear that the experimental depth profiles are much better reproduced by the two-trap desorption model than by the diffusion-limited model.

Figure 4 shows results of the profile evolution following laser desorption of H implanted to different fluences into Be. In Fig. 4(a), the H was implanted with a fluence of 0.42×10^{17} H/cm^2 at 1.5 keV. A single laser shot with an energy of 1.7 J/cm^2 was used. The evolution of the measured H profile is reproducible when the same parameters as for D at low fluence are used. In Figs. 4(b) and 4(c), H was implanted with an energy of 1.5 keV and a fluence of 1.5×10^{17} H/cm^2, and with an energy of 0.7 keV and a fluence of 0.9×10^{17} H/cm^2, respectively. One single laser shot of 0.5 J/cm^2 and an energy ramp to 0.9 J/cm^2 (0.8 J/cm^2 for Fig. 4(c)) were used. Both profile evolutions were reproduced by means of two traps with energies of 0.9 and 0.6 eV/molecule. As it was observed for D behaviour in Be, the gas desorption curves can be reproduced by a detrapping-limited model with an instantaneous migration to the surface, or with a diffusion-limited model that is weakly activated (0.1 eV). Mean depths and variances of the measured depth profiles as well as those obtained from the simulated profiles according to the diffusion-limited and the detrapping-limited models are compared in table 1. It is clear that the detrapping-limited model is the most appropriate.

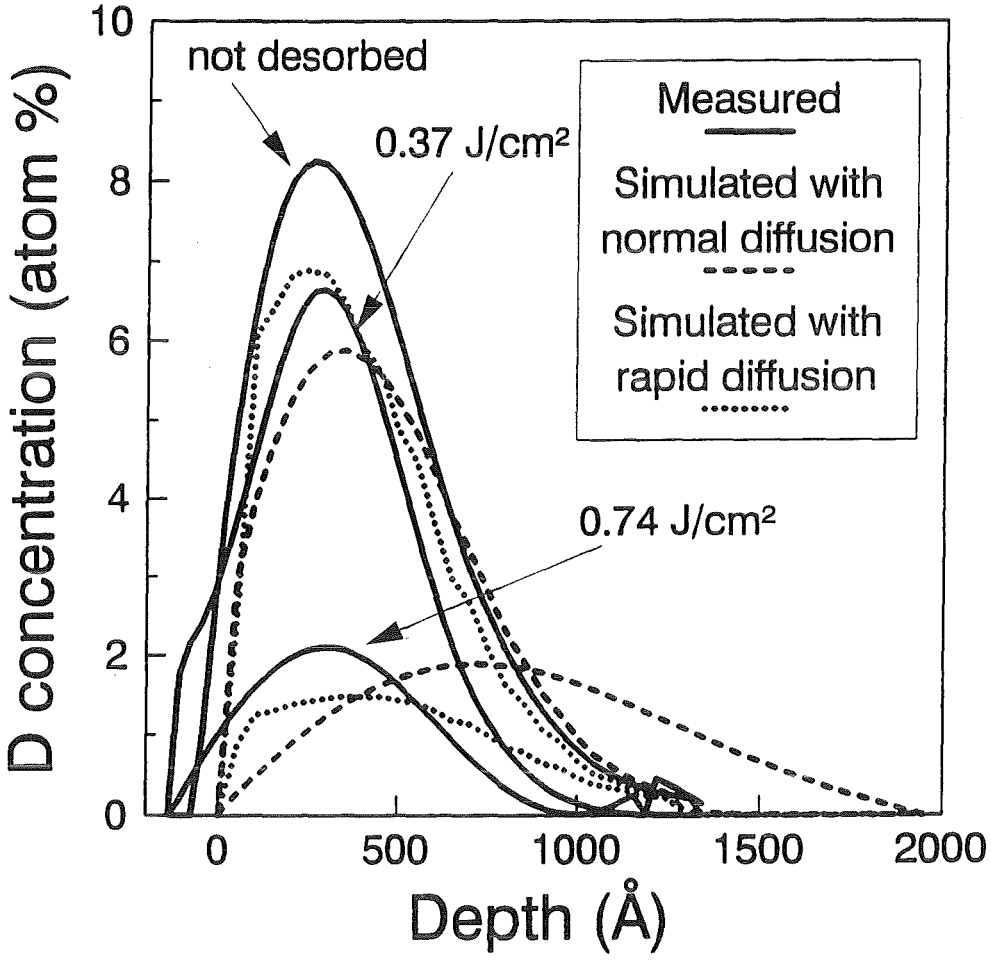

Fig. 3 Depth profile evolution after laser energy shot of 0.37 J/cm^2 and energy ramp to 0.74 J/cm^2: experimental (———), and simulated with diffusion-limited (-----) and detrapping-limited (·····) processes. The Be sample was implanted at 1 keV with 1.1x10^{17} D/cm^2.

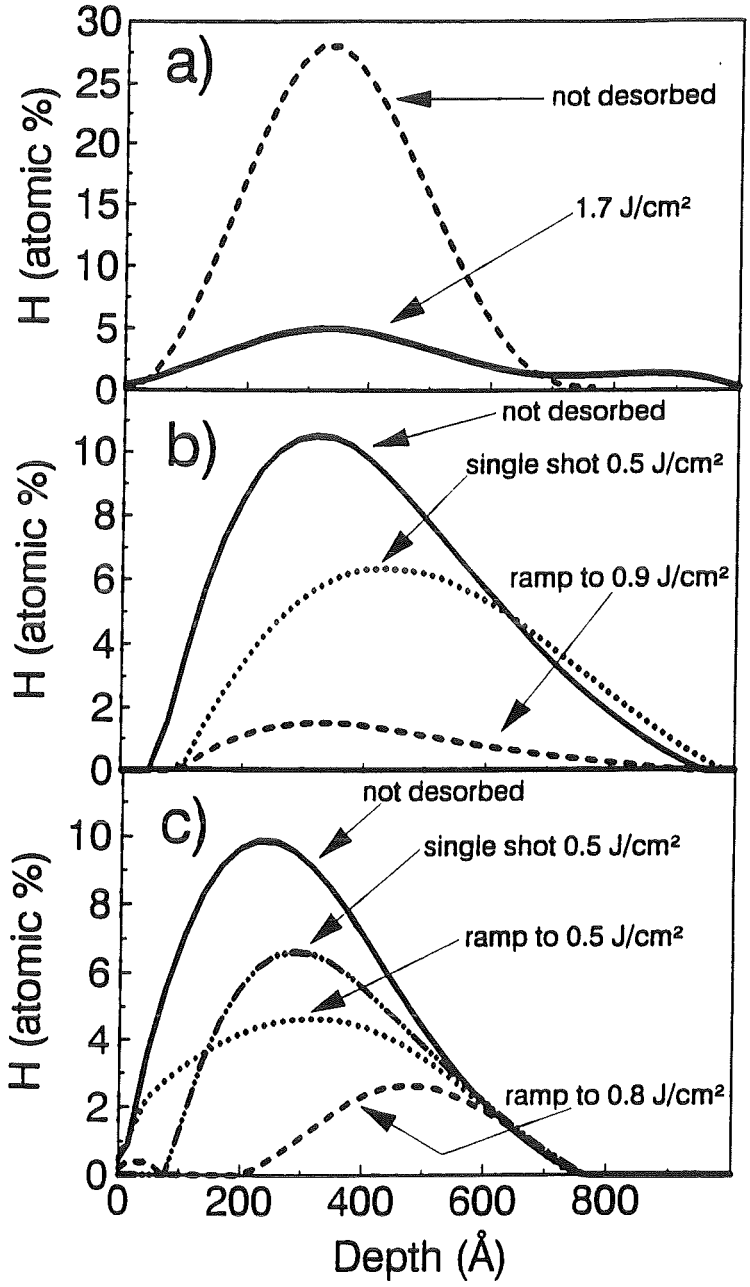

Fig. 4 Depth profiles of H implanted in Be at an energy of 1.5 keV: (a) 4.2×10^{16} H/cm^2 and desorbed with a single laser shot of 1.7 J/cm^2, (b) 1.5×10^{17} H/cm^2 and desorbed with a single laser shot of 0.5 J/cm^2 and by a energy ramp to 0.9 J/cm^2; (c) 0.9×10^{17} H/cm^2 (energy of 0.7 keV) and desorbed with a single laser shot of 0.5 J/cm^2 and by energy ramps to 0.5 J/cm^2 and to 0.8 J/cm^2.

Laser energy	Mean depth (Å)			Variance (Å)		
	Measured	Detrapping	Diffusion	Measured	Detrapping	Diffusion
Fig. 5b 0.5 J/cm^2 shot	505	424	678	216	244	478
Fig. 5b 0.9 J/cm^2 ramp	526	562	996	280	280	443
Fig. 5c 0.5 J/cm^2 shot	378	345	632	171	192	363
Fig. 5c 0.5 J/cm^2 ramp	349	350	840	189	195	431
Fig. 5c 0.8 J/cm^2 ramp	445	435	994	190	232	443

Table 1: Mean depths and variances for the profiles in Fig. 4 (b and c): measured values calculated from the experimental profiles; "detrapping" and "diffusion" values obtained from the profiles simulated with detrapping-limited and diffusion-limited models respectively.

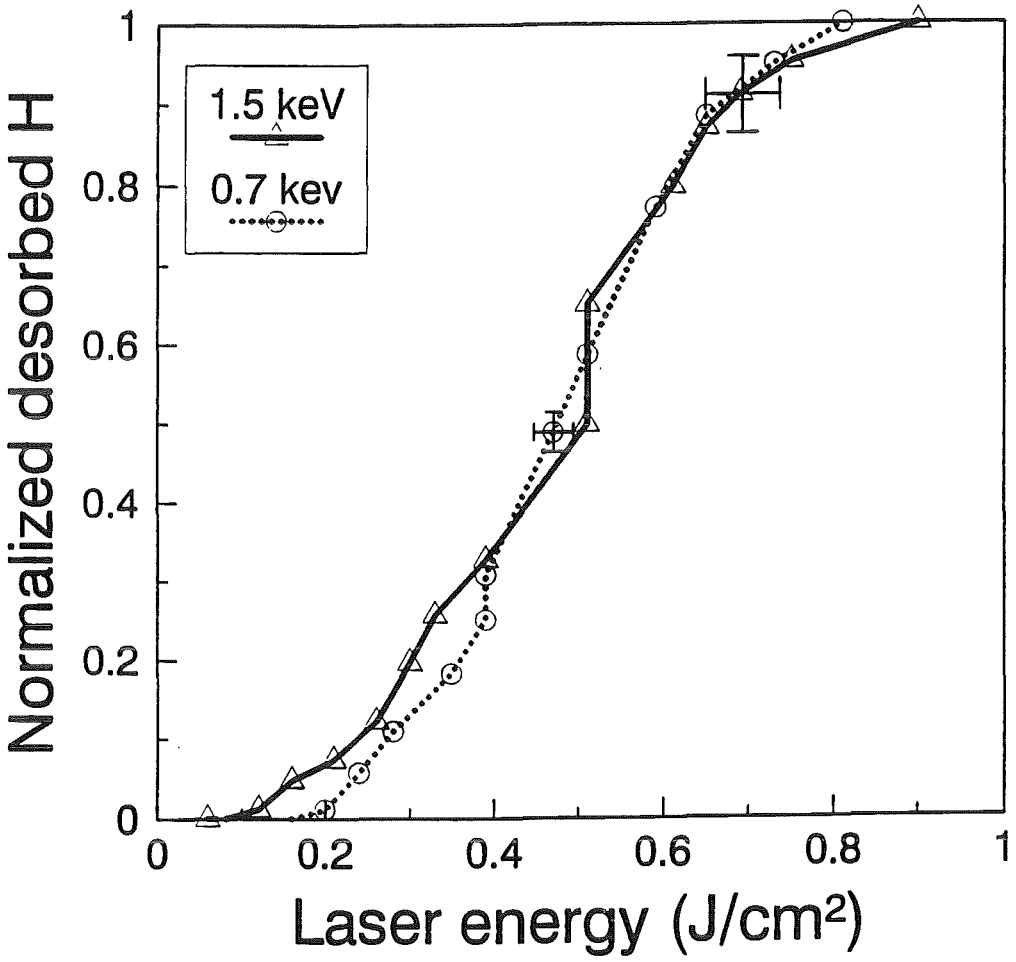

Fig. 5 Normalized hydrogen release after laser desorption from a Be sample implanted with two different energies of 0.7 keV (○) and 1.5 keV(△).

This last fact is confirmed by Fig. 5 which shows the normalised gas desorption curves corresponding to the profiles in Fig. 4 (b and c). Although the two implantations were done at two different energies (1.5 and 0.7 keV, mean ranges of 38 nm and 21 nm) the desorption curves coincide, which means that the desorption is not diffusion-limited.

The detrapping energy found for H or D implanted at low fluence (1.7 eV) is consistent with that of Wampler's [7] strong trap (1.8 eV), while the activation energies found at high fluence (0.6 to 1.0 eV) are fairly close to that of his weak trap (1.0 eV). According to Wampler the strong trap was filled first (up to a D/Be atom ratio of 5-10%), followed by filling of the weak trap until its saturation. However, none of our data can be similarly described by two well separated stages. Rather, it appears that when the strong trap becomes oversaturated (for D/Be $\geq$ 14%), a transition takes place which leaves all the H or D more loosely bound. It remains to be seen if this difference is connected with the rapid heating and quench produced by the laser. Ongoing microscopy work is aimed at studying this question [17]. The two different types of detrapping occur at fluence values comparable to, but somewhat less than, those for which blistering starts to be clearly observed. Then the desorption process which was diffusion-limited becomes independent of the diffusion. In addition, the laser desorption of such samples reveal dislocation lines ending on grain boundaries [17]. These lines could facilitate the H and D migration from the bulk of the material to the grain boundaries and then to the surface. More work, especially microscopy, are needed to characterize the desorption mechanism in the high fluence domain.

Conclusion

Beryllium samples were implanted with keV deuterium atoms and then desorbed by a Q-switched ruby laser. The H or D depth profiles were measured at various stages of the process. The computations indicated that the surface temperature reached the melting point at a laser energy density around 1.2 J/cm^2. At low fluence the desorption results can be explained by second order detrapping from a single trap at 1.7 eV/molecule. The diffusion coefficient was found to be higher under the present conditions than the reported values and appears to be with detrapping a limiting process for deuterium migration in beryllium.

On the other hand, for high fluences, where blistering and cracking appear, the trapping energies are shifted from 1.7 eV to below 1 eV/molecule. Moreover, a comparison between measured and simulated H or D depth profiles before and after the laser desorption shows that the process becomes independent of the diffusion (direct migration to the surface) and is limited by detrapping only. This observation is confirmed by the behaviour of the desorption yield versus laser energy which is the same for two different energies of implantation.

Acknowlegments

The authors are thankful to D. Thériault for the implantation work and to J. Pelletier for the excellent operation of the accelerator. We are also most grateful to P. Zheng for useful discussions. This work is supported by the National Science and Engineering Research Council.

References

[1] P.R. Thomas and the JET team, J. Nucl. Mater. 176 & 177 (1990) 3.
[2] K J. Dietz and the JET team, Fusion Technol. 19 (1991) 2031.

[3] R.E. Nygren and M.F. Smith, Fusion Technol. 19 (1991) 2092.
[4] E. Abramov, M.P. Riehm and D.A. Thomson, J. Nucl. Mater. 175 (1990) 90.
[5] R.G. Macauley-Newcombe, D.A. Thompson and W.W. Smeltzer, Fusion Eng. Des. 18 (1991) 419.
[6] P.M.S. Jones and R. Gibson, J. Nucl. Mater. 21 (167) 353.
[7] W.R. Wampler, J. Nucl. Mater. 122 & 123 (1984) 1598.
[8] R.A. Causey, W.L. Hsu, B.E. Mills, J. Ehrenberg and V. Phillips, J. Nucl. Mater. 176 & 177 (1990) 654.
[9] W.L. Hsu, R.A. Causey, B.E. Mills, J. Ehrenberg and V. Phillips, J. Nucl. Mater. 176 & 177 (1990) 218.
[10] G.G. Ross, B. Terreault, C. Boucher, R. Boivin, J. Vac. Sci. Technol. A 4 (1986) 1243.
[11] B. Terreault, J. Appl. Phys. 62 (1987) 152.
[12] R. Boivin, G.G. Ross and B. Terreault, J. Appl. Phys. 73 (1993) 1936.
[13] L. Leblanc and G.G Ross, Nucl. Instrum. and Meth. B (in press).
[14] E.T. Arakawa, T.A. Callcott and Yun-Ching Chang, Handbook of optical constants of solids II (Academic Press, San Diego, 1991) p. 421.
[15] G.G. Ross, B. Terreault, G. Gobeil, G. Abel, C. Boucher and G. Veilleux, J. Nucl. Mater. 128&129 (1984) 730; G.G.Ross and L.L. Leblanc, Nucl. Inst. and Meth. B26(1992) 484.
[16] F. Schiettekatte, R. Marchand and G.G. Ross, "Deconvolution of noisy data with strong discontinuity and uncertainty evaluation" submitted to Nucl. Instr. and Meth.
[17] P. Zheng, private communication; K. Touhouche, to be presented at the Materials Research Society Symposium (Boston, Nov. 1993).

THERMAL DESORPTION OF IMPLANTED HELIUM FROM BERYLLIUM

Y.M. Zakaria, R.G. Macaulay-Newcombe and D.A. Thompson

Department of Engineering Physics, McMaster University,
Hamilton, Ontario, L8S 4L7, Canada

ABSTRACT

Hot isostatic pressed foils of 99.5 wt.% beryllium have been implanted at room temperature with 30 keV helium to fluences ranging from 10^{20} to 10^{21} He^+/m^2. Linear ramp thermal desorption measurements up to 1073 K ($\approx 0.7\ T_m$) were performed to study the mechanisms by which the helium is trapped. Some of the samples have been deliberately corroded to investigate the effect of the surface contamination on the helium release.

As the implantation fluence is increased the number of trapping sites increases and the threshold temperature for the helium release falls from 955 K at 10^{20} He^+/m^2 to 650 K at 10^{21} He^+/m^2. Assuming that the desorption is not diffusion limited, the helium desorption peak temperatures are correlated to entrapment at vacancy type defects.

The effective activation energies of thermal desorption for the peaks are calculated from the observed peak temperatures. All samples show a principal detrapping energy of 2.95 ± 0.25 eV that is ascribed to a helium-vacancy dissociation mechanism. At higher implantation fluences, where higher vacancy concentrations are generated, a lower release energy of 2.3 ± 0.1 eV was also observed which may be related to larger helium-vacancy clusters. The total amount of desorbed helium lies below 65% of the implantation fluence after desorption up to 1073 K. This suggests the presence of deeper trapping sites. Some samples show a progressive change in the desorption spectra as the samples age. This may indicate the movement of helium between neighbouring trapping sites at room temperature.

Samples with a thick oxide surface layer show an additional

broad high temperature (> 950 K) desorption peak. This implies that the corroded surface contains additional trapping sites which delay the release of the helium detrapped from the bulk.

1. Introduction

Beryllium is a prime candidate as a plasma facing material and breeder blanket neutron multiplier in fusion reactors. In addition to its low atomic number and excellent thermal conductivity, beryllium is a good oxygen getter and has a low tritium affinity. These properties have contributed to the performance improvement achieved in recent JET tokamak experiments [1]. In the breeder blanket, beryllium has the greatest potential as a neutron multiplier due to its low (n,2n) threshold and also because it is a low activation material.

The thermal, mechanical and tritium trapping performance of beryllium will be strongly affected by the presence of helium. Helium is introduced to the wall components of the fusion reactor either directly by implantation of α-particles from the plasma or indirectly by nuclear transmutation reactions. Such processes are usually associated with the production of Frenkel defects. As a result of the low solubility of helium in metals [2] and its tendency to reside substitutionally in the host lattice [3], it can be strongly trapped at vacancy-type defects.

There have been a few experimental studies on helium effects in beryllium covering mainly two major areas of interest:
(a) helium-induced swelling in neutron-irradiated beryllium [4-7] and (b) blister formation of beryllium surfaces due to high-fluence helium implantation [8-10]. Macaulay-Newcombe et al. [11] reported initial helium thermal desorption data from beryllium. Most recently, Jung [12] presented the first experimental results on the diffusion and retention of implanted helium in beryllium foils.

In this paper, trapping of 30 keV helium in hot isostatic pressed (HIP) beryllium is investigated for room-temperature implantations with fluences ranging from 10^{20} to 10^{21} He^+/m^2. In addition, the effect of having a contaminated beryllium surface on the helium release is reported. An interesting phenomenon has been

observed that suggests the possibility of the rearrangement of the trapped helium atoms among neighbouring trapping sites at room temperature.

2. Experiment

The samples used in the present study are 0.5 mm thick foils of PF-60 high purity beryllium from Electrofusion Corporation. This material is 99.5 wt.% pure Be with about 0.45 wt.% O and 0.05 wt.% Fe as the major impurities. The foils were roughly polished and ultrasonically cleaned before shipment. Prior to the helium implantation all samples were mechanically polished to a near-mirror finish and the polishing particles cleaned off by ultrasonic cleaning in acetone.

Some of the samples were annealed at 1023 K for 1 hour in a vacuum of 10^{-6} Pa to increase the thickness of the surface oxide layer. Rutherford Backscattering (RBS) was used to analyze the surface contaminants. The results indicate a BeO thickness of 3.3 nm on the unannealed samples and a nonuniform layer of beryllium "oxycarbide", with average thickness of 27.8 nm, on the deliberately corroded surfaces.

Ion implantation was carried out at room temperature with a 30 keV He^+ ion beam normal to the sample surface. To minimize beam heating effects, the sample holder was water-cooled during the implantations. The total irradiation fluences ranged from 10^{20} to 10^{21} ion/m^2. For each set of samples, the He^+-beam current at the target was maintained at a constant level. The implantation flux varied between 4-10 mA/m^2 from run to run. The projected range in beryllium for 30 keV He^+ ions (R_p) and the range straggling (ΔR_p) were obtained using TRIM-91 [13] and found to be 241 and 33 nm, respectively.

Details of the thermal desorption system were given in a previous publication [14]. Samples were heated at a constant rate up to 1073 K. Two rates, 3 and 5 K/min, were used to display the dependence of the thermal desorption on the heating rate. A cryogenic pump in the form of a liquid nitrogen trap was used to keep the background pressure well below 10^{-6} Pa during the

desorption period. The release rate of helium atoms was monitored with a quadrupole mass spectrometer that was calibrated with a fixed deuterium leak. In order to investigate the mobility of the implanted helium atoms, some samples were allowed to age at room temperature for periods up to 37 days before being thermally desorbed.

3. Results and Discussion

3.1. Desorption as a function of fluence

The thermal desorption spectra of samples ramped at 5 K/min are shown in fig. 1. All measurements were stopped at 1073 K ($\approx 0.7\ T_m$) to minimize the sublimation of the beryllium samples. From fig. 1 it can be seen that: (a) the shape of the thermal release curves and the number of desorption peaks display a clear dependence on the implantation fluence. Up to a fluence of 5×10^{20} He^+/m^2, only one peak was observed (peak A). The amount of helium release associated with this peak increased with increasing fluence. However, a significant drop in the population of peak A was detected at the highest fluence (10^{21} He^+/m^2). This may be an indication that the concentration of the trapping site A has reached saturation. The variation of the population of peak A with the implantation fluence is depicted in fig. 2.
(b) The threshold temperature for the helium release falls notably as the fluence increases. At the lowest fluence (10^{20} He^+/m^2), no helium desorption was detected below 955 K with our apparatus, which has a detection limit of 10^8 atom/s. At an implantation fluence of 10^{21} He^+/m^2, the helium release starts more than 300 K sooner, at 650 K.

3.2. Effect of the heating rate on desorption

The nature of the desorption peaks was further examined by varying the heating rate between 3 and 5 K/min. The peak temperatures for both peaks show the normal drop when the samples were heated at a slower rate. In a number of cases, lowering the ramping rate makes it possible to detect finer structure in the peaks. Fig. 3 shows that what appears to be one desorption peak at 5 K/min can be resolved into two overlapping peaks by lowering the

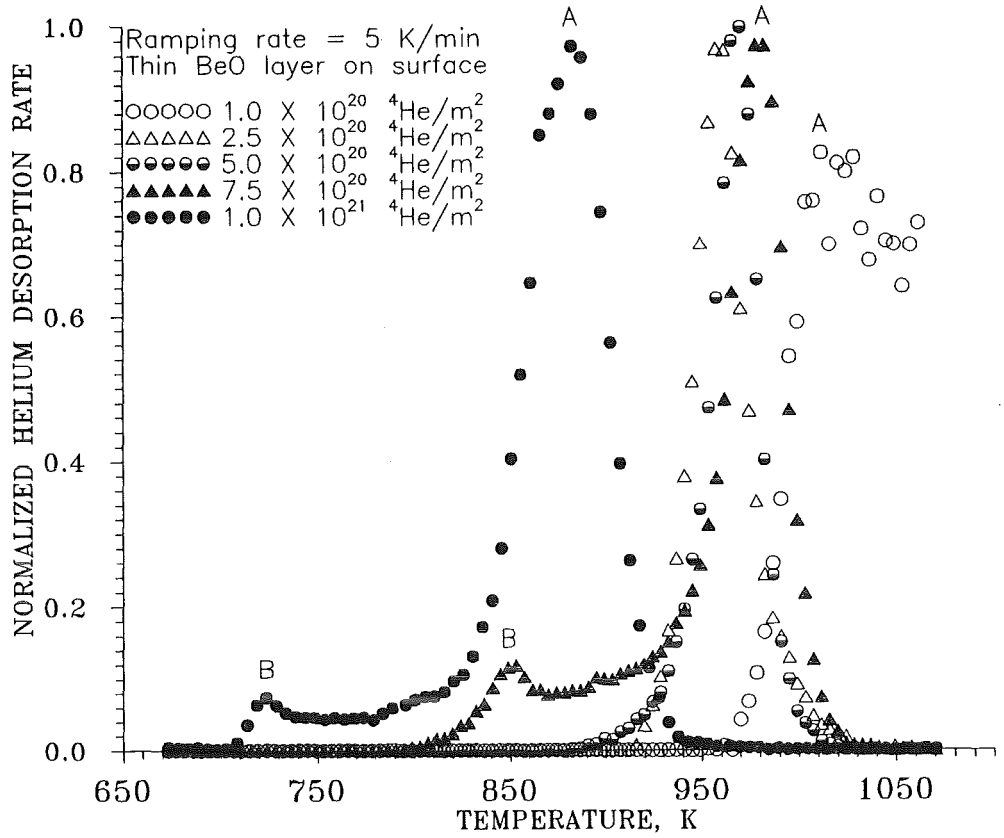

Fig. 1. Normalized thermal desorption spectra of He implanted into Be to various fluences.

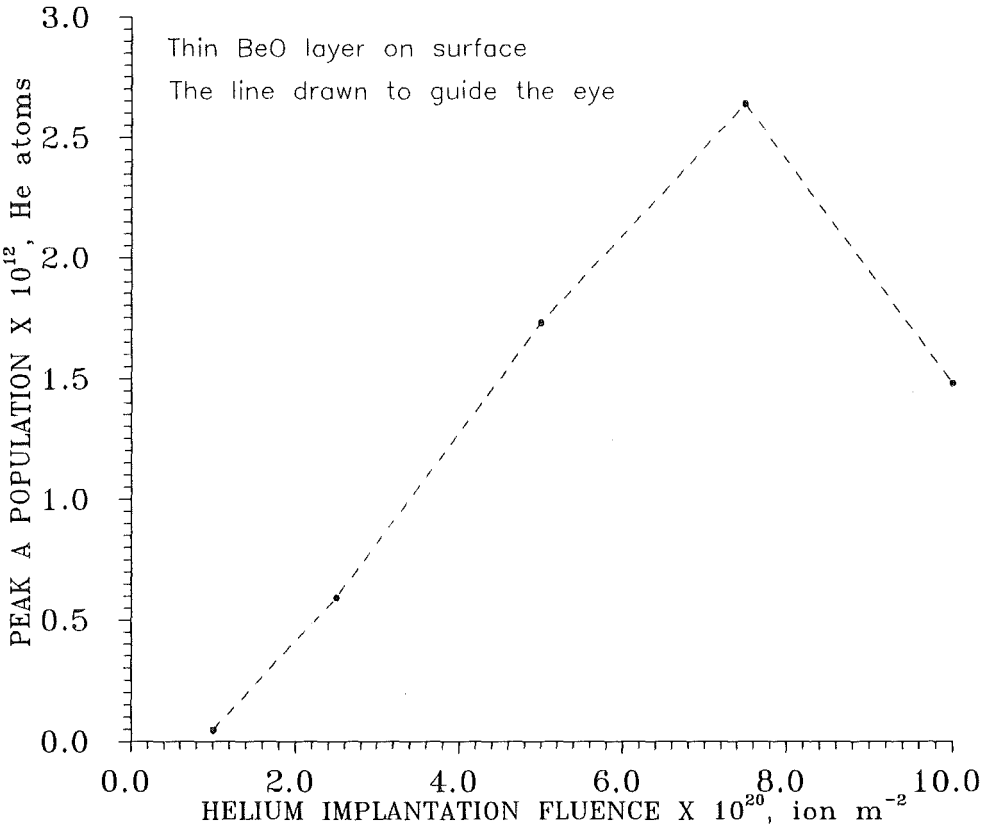

Fig. 2. The population of peak A as a function of the implantation fluence.

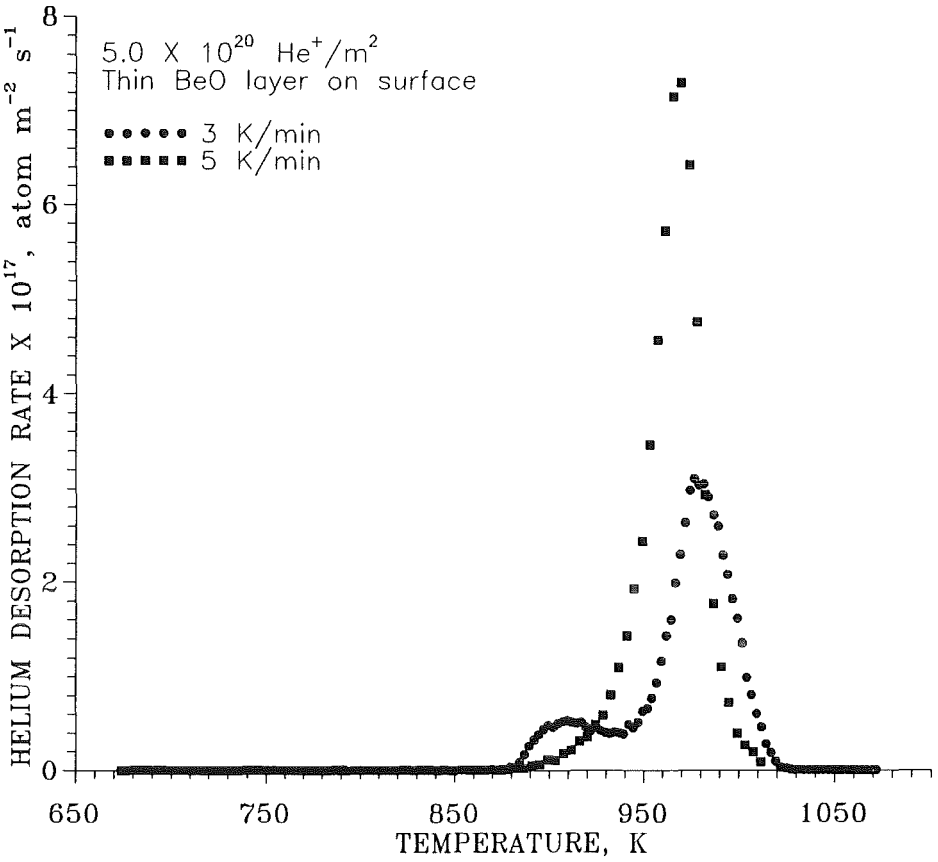

Fig. 3. Thermal desorption of implanted He from Be at different ramping rates.

heating rate, where the amount of released helium is 58% of the implanted fluence (5×10^{20} He^+/m^2) in both cases. A similar response was also found at 2.5×10^{20} He^+/m^2.

3.3. Analysis of the desorption peaks

The desorption spectra were analyzed using two basic assumptions: (a) that the helium release is not limited by diffusion in the beryllium bulk and (b) that the thermal release process is a one-step, first-order reaction. The first assumption was discussed briefly in the most recent study of helium diffusion in beryllium [12]. Jung reported an effective diffusion coefficient at low temperatures that would result in a diffusion length of more than ≈ 800 nm over 1800 s at 800 K. This is more than three times the projected range for the implantation. The second assumption is justified by the fact that helium will be only

released in its atomic form. Based on this, the observed peaks were ascribed to trapping sites in which radiation-produced vacancies are the primary centres.

Since the desorption measurements were carried out at constant ramping rates, the detrapping activation energy is given by [15],

$$2 \ln T_P - \ln \beta = E / kT_P + \ln (E / k\nu)$$

where T_P is the desorption peak temperature in K, β the ramping rate in K/sec, E the desorption activation energy, k Boltzmann's constant and ν the desorption frequency factor (assumed as 10^{13} s^{-1}).

Application of this analysis to desorption peak A results in an activation energy of 2.95 ± 0.25 eV. This is much higher than the reported values of 1.71 and 1.63 eV for beryllium self-diffusion [16]. Previous modelling of helium interatomic potentials in metals [17] and experimental observations [18,19] indicates that such high energy is usually associated with substitutional detrapping of the helium atoms; i.e. trapping at mono-vacancies. As for peak B, its detection after the apparent saturation of peak A implies that it is related to a higher order helium-vacancy cluster with an activation energy of 2.3 ± 0.1 eV.

3.4. Effect of sample aging on desorption

Once the fine structure of the desorption peaks was observed at the lower ramping rate, trials were made to reproduce the results. A set of six samples was implanted to a fluence of 5 × 10^{20} He^+/m^2. Two of the samples were desorbed with a heating rate of 5 K/min, one at 3 days and one at 16 days after the implantation. They produced almost identical spectra with one desorption peak clearly observed around 970 K. The other four were desorbed at the lower rate (3 K/min) at 4, 18, 25 and 37 days after the implantation, respectively. Fig. 4 shows three of the four desorption spectra; the 25-day sample has been omitted for clarity.

The results show a gradual movement of the trapped helium atoms from the higher energy trap to a lower one. These results were reproduced at a fluence of 2.5 × 10^{20} He^+/m^2 with the same

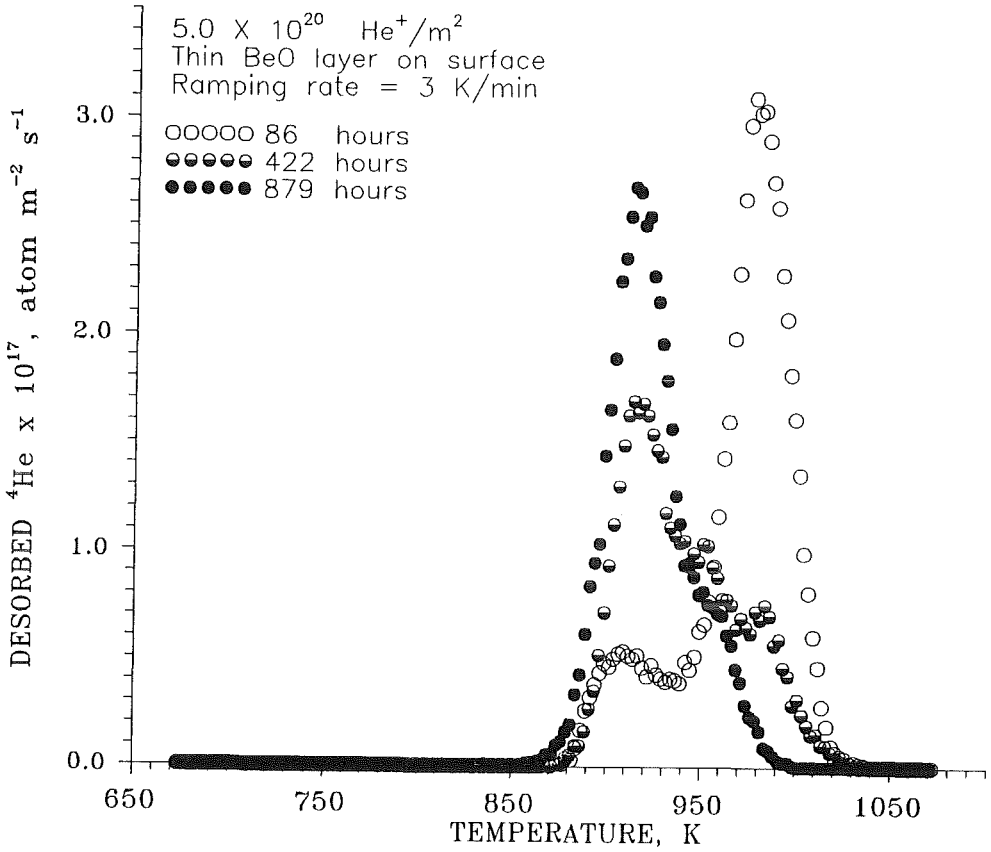

Fig. 4. Thermal desorption spectra of He implanted into Be after aging to various periods.

ramping rate. The progressive change with time and the fact that these variations cannot be detected at 5 K/min are two strong indications that either the helium atoms moved between two or more adjacent kinds of trapping sites; or the nature of the trap changed at room temperature.

3.5. Effect of surface corrosion on desorption

Figure 5 shows thermal desorption data for beryllium samples with deliberately corroded surfaces compared to the spectrum of a sample with a "clean" surface. The corroded samples show an additional broad high temperature (> 950 K) desorption peak. The fact that the other two peaks were as sharply reproduced as the uncorroded sample should disqualify the possibility that the corroded surface is acting as a diffusion barrier for the released helium. The high temperature peak is therefore attributed to

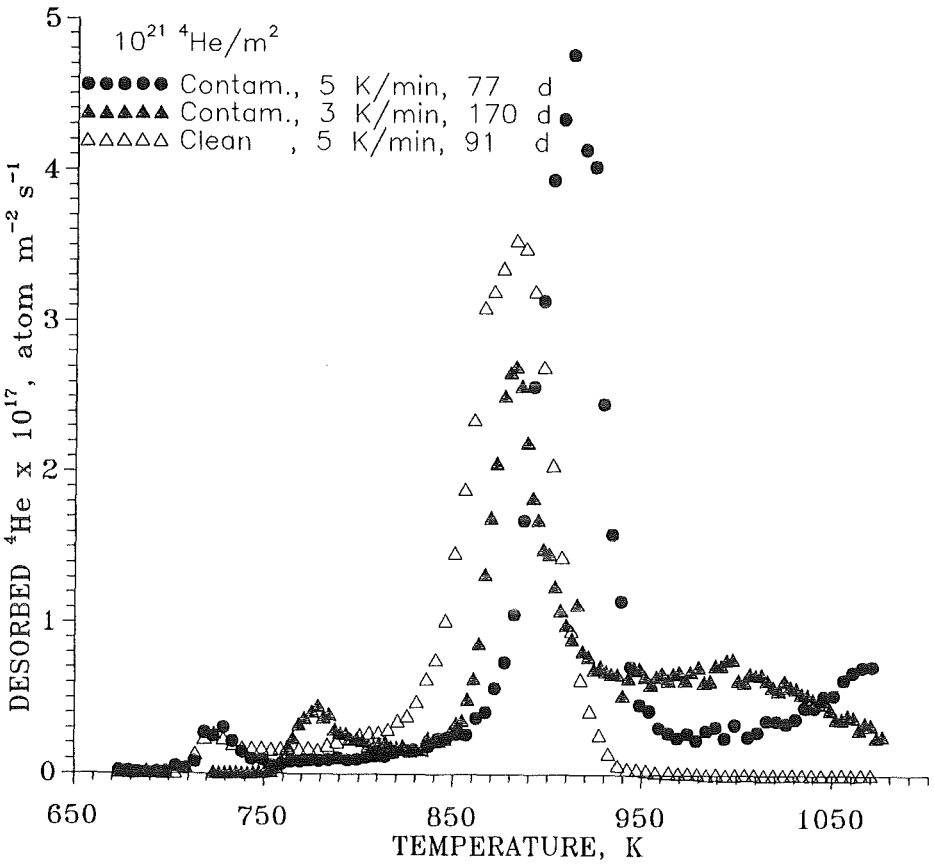

Fig. 5. Effect of surface contamination on the implanted He release from Be.

additional sites trapping the helium atoms after they were originally detrapped from the beryllium.

Finally, a common observation for all of the beryllium spectra in this experiment is that the absolute amount of desorbed helium is a strong function of both the number of available trapping sites and the implantation fluence. The average fraction of retained helium decreased from 77% for an implantation fluence of 10^{20} He^+/m^2 to 46% at a fluence of 5×10^{20} He^+/m^2. However, at the highest fluence of 10^{21} He^+/m^2, where the probability of the helium trapping to larger clusters increased, the fraction of retained helium increased again to 70% of the implantation fluence. Figure 6 gives the variation of the fraction of desorbed helium with the implantation fluence.

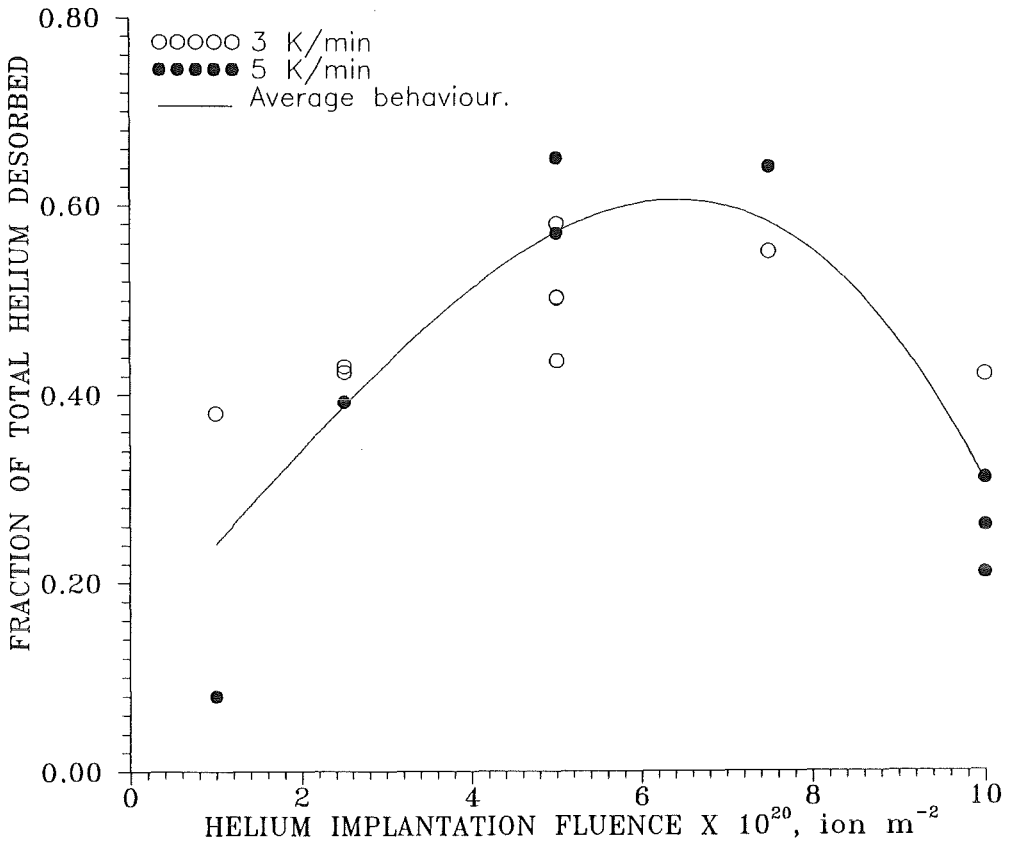

Fig. 6. Variation of the fraction of desorbed helium with the implantation fluence.

4. Conclusions

The above results and discussion lead to the following conclusions:

(a) Thermal desorption of implanted helium from beryllium has a strong dependence on the implantation fluence since it determines both the concentration of helium atoms in the material bulk and the amount of radiation damage that can serve as trapping sites.

(b) Trapped helium atoms may be locally mobile at room temperature; i.e. either movement has been detected between neighbouring trapping sites, or else the nature of the traps changed.

(c) Surface contaminants on the beryllium surface are likely to increase the amount of helium retained at lower temperatures.

(d) A high fraction of the implanted helium appears to reside at

deep traps with a possible release only near the melting point.

Acknowledgments

We gratefully acknowledge the efforts of D. Stevanovic and B. McClelland in carrying out the helium implantations. This work is supported by the Natural Sciences and Engineering Research Council of Canada and by the Canadian Fusion Fuels Technology Project.

References

[1] P.R. Thomas and the JET Team, J. Nucl. Mater. **176&177** (1990) 3.
[2] H.J. von den Driesch and P. Jung, High Temp. High Pressures **12** (1980) 635.
[3] M.I. Baskes and C.F. Melius, Phys. Rev. **B20** (1979) 3197.
[4] C.E. Ells and E.C.W. Perryman, J. Nucl. Mater. **1** (1959) 73.
[5] J.M. Beeston, L.G. Miller, E.L. Wood, Jr. and R.W. Moir, J. Nucl. Mater. **122&123** (1984) 802.
[6] W.G. Wolfer and T.J. McCarville, Fusion Tech. **8** (1985) 1157.
[7] M.C. Billone, C.C. Lin and D.L. Baldwin, "Tritium and Helium Behavior in Irradiated Beryllium," Proc. of the 9th Topical Meeting on the Technology of Fusion Energy, Oak Ridge, Illinois, Oct. 7-11, 1990.
[8] R.A. Langley, J. Nucl. Mater. **85&86** (1979) 1123.
[9] G. Ross and B. Terreault, J. Nucl. Mater. **89** (1980) 383.
[10] B. Terreault, J. Nucl. Mater. **93&94** (1980) 707.
[11] R.G. Macaulay-Newcombe, D.A. Thompson and W.W. Smeltzer, Fusion Engineering and Design **18** (1991) 419.
[12] P. Jung, J. Nucl. Mater. **202** (1993) 210.
[13] J.F. Ziegler, J.P. Biersack and U. Littmark, **The Stopping Range Of Ions In Solids** (Pergamon, New York, 1985).
[14] S.-Q. Shi, E. Abramov, D.A. Thompson and W.W. Smeltzer, J. Nucl. Mater. **182** (1991) 128.
[15] P.A. Redhead, Vacuum **12** (1962) 203.
[16] J.-M. Dupouy, J. Mathie and Y. Adda, Mem. Sci. Rev. Met. **63** (1966) 481.
[17] W.D. Wilson and R.A. Johnson, in: **Interatomic Potentials and Simulation of Lattice Defects**, P.C. Gehlen, J.R. Beeler, Jr. and R.I. Jaffee, eds. (Plenum Press, New York, 1972) 375.
[18] E.V. Kornelsen, Radiat. Eff. **13** (1972) 227.
[19] M.B. Lewis, J. Nucl. Mater. **149** (1987) 143.

List of Participants

D. Baldwin (BPNL, U.S.A.)

B. Bielak (CE, France)

M. Billone (ANL, U.S.A.)

R.G. Castro (LANL, U.S.A.)

R.A. Causey (SNLL, U.S.A.)

S. Chiocchio (ITER, Germany)

M. Dalle Donne (KfK, Germany)

F. Dammel (KfK, Germany)

E.B. Deksnis (ITER, U.K.)

W. Dienst (KfK, Germany)

L. Dörr (KfK, Germany)

D.E. Dombrowski (BW, U.S.A.)

W. Eckstein (MPIP,Germany)

G. Federici (ITER, Germany)

C. Ferrero (TU, Germany)

A. Fiege (KfK, Germany)

U. Fischer (KfK, Germany)

D.R. Floyd (MSC, U.S.A.)

A. Goraieb (KfK, Germany)

R. Gambie (BW, U.K.)

D.S. Gelles (BPNL, U.S.A.)

M.L. Grossbeck (ORNL, U.S.A.)

D.R. Harries (Oxford, U.K.)

D. Hermanuz (KfK, Germany)

M. Kato (NGK, Japan)

H. Kawamura (JAERI, Japan)

D. Kéroack (INRS, Canada)

K. Kleefeldt (KfK, Germany)

G.R. Longhurst (INEL, U.S.A.)

P. Lorenzetto (NET, Germany)

D. Lupton (Heraeus, Germany)

R. Macaulay-Newcombe (McMaster Univ., Canada)

R. Matera (ITER, Geramny)

K. Miyajima (Tocalco, Japan)

F. Moons (SCK-CEN, Belgium)

F. Mücklich (MPIM, Germany)

C. Nardi (ENEA, Italy)

A. Rahn (KfK-Mol, Belgium)

M. Rödig (KFA, Germany)

C. Ronchi (TU, Germany)

M. Rubel (R.I.T., Sweden)

L. Sannen (SCK-CEN, Belgium)

F. Scaffidi-Argentina (KfK, Germany)

S. Tanaka (ITER, Germany)

H.T. Tsige-Tamirat (KfK, Germany)

G. Vieider (NET, Germany)

E. Vietzke (KFA, Germany)

W. Weaver (BNF, U.K.)

A. Weisenburger (KfK, Germany)

H. Werle (KfK, Germany)

C.H. Wu (NET, Germany)

Y. Yao (NPIC, China)